

Generation and propagation of acoustic emissions in buried steel infrastructure for monitoring soil-structure interactions

By

Helen Heather-Smith

A Doctoral Thesis

Submitted in partial fulfilment of the requirements

For the award of

Doctor of Philosophy of Loughborough University

February 2020

Abstract

Soil-structure systems (e.g. pipelines, pile foundations, retaining structures) deteriorate with time and experience relative deformations between the soil and structural elements. Whether a result of age, working conditions, or environmental conditions, deformations have the potential to cause catastrophic social, economic, and environmental issues, including limit state failure (fatigue, serviceability, ultimate). The UK spends £100s of millions a year spent on infrastructural maintenance; the early detection of deterioration processes could reduce this spend by an order of magnitude.

Techniques to monitor ground instability and deterioration are consequently increasing in use, with most conventional approaches providing localised information on deformation at discrete time intervals. Nascent technologies (e.g. ShapeAccelArray, fibre optics) are however beginning to provide continuous measurements, allowing for near real-time observations to be made, although none are without either technical limitation or prohibitive cost.

A novel monitoring system is proposed, whereby pre-existing and newly built steel infrastructure (e.g. utility pipes, pile foundations) are employed as waveguides to measure soil-steel interaction-generated AE using piezoelectric sensors. With this, a two-stage quantitative framework for understanding soil-steel interaction-generated AE and its propagation through steel structures is also developed where (stage 1) informs the creation of an adaptable sensor network for a variety of infrastructure systems, and stage (2) informs interpretations of the collected AE data to allow for decision makers to take appropriate action. Timely actions made possible by such a framework is of great significance to practitioners, having the potential to reduce the direct and indirect impacts of deterioration and deformation, whether long- and short-term.

Stage 1 used an extensive programme of computational models, alongside small- and large-scale physical models, to enable attenuation coefficients to be quantified for a range of soil types. It was shown that both the structure and bounding materials, i.e. the burial system, significantly influenced propagation and attenuation through steel structures. In free-systems, though, the frequency-thickness product was more influential; propagation distances of 100s of metres are obtained at products <0.5 MHz-mm but reduce to 10s of metres by 1 MHz-mm. Guidelines for three generic systems, free bound, soil bound, and soil bound with an internal water environment, were developed.

Stage 2 used a programme of large direct-shear box tests to allow for relationships between AE and normal effective stress, mobilised shearing resistance, and shearing velocity to be quantified. This enabled for quantitative interpretations of soil-steel interaction behaviours to be made using various AE parameters. Both the magnitude of values, and the rates of change of the parameters, could be used in the interpretation of behaviours. Shearing and stress conditions of sand could also be determined, increasing proportionally with AE activity, whilst the point at which full shear strength mobilisation occurs was also identifiable.

Key words: Acoustic Emissions (AE), Buried infrastructure, Deformation, Geotechnical Engineering, Monitoring, Soil-structure interaction.

Acknowledgements

Firstly, I would like to express my gratitude to the Engineering and Physical Sciences Research Council (EPSRC) and Loughborough University for providing the funding and resources necessary to carry out this research. None of this would have however been possible without the many people who have contributed to this work.

Most importantly, I would like to acknowledgement the help provided by my supervisors, Dr Alister Smith, Prof. Neil Dixon, and Dr James Flint. It is whole-heartedly appreciated that your great advice for this study has proven monumental towards its success. Alongside your technical guidance, your ongoing support with the organisation of the research and encouragement to gain both internal and external experiences, developing my academic skills, were truly appreciated. The interest you took in the work pushed me to expand my thinking, making me more accomplished.

Furthermore, I would also like to say thanks to Lewis Darwin, Neil Parkes and Jim Muddimer for the assistance provided during laboratory work. The experimental work performed would not have been possible without your help in terms of technical support, but also moral support when things did not go well.

Additionally, I would like to thank Michael Lowe for the ongoing email advice provided with respect to computational modelling with Disperse. Your assistance in the use of the program was invaluable.

Finally, thanks should also be given to my internal assessor, Giorgio Barone, who helped guide this work, allowing to continue, as well as all my friends and family who have believed in me, proofread text, judged graphics, and provided ongoing encouragement throughout all the ups and downs. Thank you.

List of publications and conference articles

Smith A, Heather-Smith H, Dixon N, Flint JA and Pennie D (2020) Acoustic emission generated by granular soil-steel structure interaction. *Géotechnique Letters*, 10 (2), 1-9.

Smith A, Biller T, Heather-Smith H, Dixon N and Flint JA (2019) Acoustic emission monitoring in geotechnical element tests. 17th European Conference on Soil Mechanics and Geotechnical Engineering, Reykjavik Iceland, 1-6 September 2019

Heather-Smith H, Smith A, Dixon N and Flint JA (2018) Monitoring buried infrastructure deformation using acoustic emission. 9th European Workshop on Structural Health Monitoring, Manchester UK, 10-13 July 2018

Contents

Thesis Access Conditions and Deposit Agreement.....	i
Abstract	iii
Acknowledgements	iv
List of publications and conference articles.....	v
List of figures	x
List of tables.....	xxiii
List of equations.....	xxvi
Chapter 1: Introduction	1
1.0 Introduction	2
1.1 Research justification.....	2
1.2 Research aim and objectives.....	4
1.3 Contributions to knowledge.....	4
1.4 Thesis structure.....	6
1.5 Chapter summary.....	7
Chapter 2: Literature review	9
2.0 Literature review.....	10
2.1 Background: Deteriorating soil-structure systems	10
2.1.1 The effects of deterioration	11
2.2 Monitoring soil-structure systems	13
2.2.1 Acoustic emission monitoring.....	16
2.3 Waves: AE generation in soil-structure systems	21
2.3.1 The influence of soil properties.....	21
2.3.2 AE generating mechanisms	25
2.3.3 Characterising AE	31
2.4 Waves: AE propagation and attenuation in soil-structure systems.....	37
2.4.1 Wave forms.....	37
2.4.2 Waves in plates and shell structures	39
2.4.3 Attenuation	42
2.4.4 Using steel infrastructure as waveguides	48
2.5 Modelling methods	59
2.5.1 Physical modelling of AE propagation	60
2.5.2 Physical modelling of soil-structure interaction	61
2.5.3 Computational modelling of AE propagation	64
2.6 Summary	68
2.6.1 Gaps in knowledge	69

Chapter 3: Methodology.....	70
3.0 Methodology.....	71
3.1 AE data acquisition equipment	71
3.2 Small-scale laboratory tests	75
3.2.1 Input signals	79
3.2.2 Sensor-structure contacts	80
3.2.3 Sensor bias	81
3.2.4 Propagation distance	82
3.2.5 Pipe geometry and couplings	82
3.3 Water flow tests.....	85
3.4 Characterising soils	86
3.5 Shear box tests.....	88
3.5.1 Setting up a test	90
3.5.2 Running a test	93
3.6 Large-scale laboratory tests	95
3.7 Computational modelling with Disperse	101
3.8 Chapter summary.....	109
3.8.1 Small-scale laboratory tests	110
3.8.2 Water flow tests.....	111
3.8.3 Shear box tests.....	112
3.8.4 Large-scale laboratory tests	113
3.8.5 Computational modelling.....	116
Chapter 4: Results: Propagation and attenuation.....	119
4.0 Results: Propagation and attenuation.....	120
4.1 Computer modelling with Disperse.....	120
4.1.1 Validating the modelling approach	120
4.1.2 Investigating wall thickness.....	135
4.1.3 Investigating shell radius.....	136
4.1.4 Investigating external environments.....	137
4.1.3.1 Soils	138
4.1.3.2 Other materials	142
4.1.5 Investigating internal environments	145
4.1.6 Case studies	150
4.1.6.1 Buried utility pipes	150
4.1.6.2 Pile foundations: Cylinder and H style.....	153
4.1.6.3 Pile foundations: Off-shore monopiles.....	156

4.2	Small-scale laboratory experiments	158
4.2.1	Investigating pipe radius using propagation distances	159
4.2.2	Investigating screw jointed pipes	161
4.3	Large-scale laboratory experiments	164
4.3.1	Propagation within a free bound pipe	164
4.3.2	Propagation in a buried pipe system	169
4.4	Chapter summary	171
Chapter 5: Results: Characterising AE signals		173
5.0	Results: Characterising AE signals	174
5.1	Soil-steel interaction generated AE: Shear box testing	174
5.1.1	Compression	174
5.1.2	Shearing	182
5.1.3	Influence of plate roughness	197
5.2	Soil-steel interaction generated AE: Laboratory experiments	199
5.3	AE equipment	202
5.3.1	Signal input sources	202
5.3.2	Sensor-structure coupling	204
5.3.3	Sensor bias	205
5.4	Extraneous AE: Water flow	208
5.5	Chapter summary	212
Chapter 6: Discussion: The development of a framework		214
6.0	Discussion: The development of a framework	215
6.1	Stage 1: Employing steel infrastructure as waveguides	215
6.1.1	Step 1: Hardware	217
6.1.2	Step 2: Software	218
6.1.3	Step 3: Deployment	219
6.1.4	Stage 1: Summary	222
6.2	Stage 2: Interpreting AE behaviours in buried infrastructure systems	225
6.2.1	Step 1: Collection and processing	225
6.2.2	Step 2: Analysis	227
6.2.3	Step 3: Actions and outcomes	234
6.3	Chapter summary	236
Chapter 7: Conclusions, limitations, and future work		239
7.0	Conclusions, limitations, and future work	240
7.1	Conclusions	240
7.1.1	Objective 1	240

7.1.2	Objective 2	241
7.1.3	Objective 3	242
7.1.4	Objective 4	243
7.1.5	Objective 5	243
7.2	Recommendations for future work	244
References		246
Appendices		263
AP1.0	Landslides	263
AP2.0	Windowing	265
AP3.0	Large-scale testing: Repeatability tests	267
AP4.0	Piezoelectric transducers	273
AP5.0	Technology Readiness Levels (TRLs)	275
Glossary		276
GL1.0	General terminology	276
GL2.0	Wave terminology	279
GL2.1	Wave parameters and properties	279
GL2.2	Wave types	280
GL2.3	Wave attenuation	281
GL3.0	Material instability terminology	282
GL3.1	Landslide movement classifications	282
GL3.2	Soil mechanisms and interactions	283
GL4.0	Signal processing terminology	284
GL4.1	Processing and characterisation methods	284
GL4.2	WFT window classifications	286
GL5.0	AE measurement systems	286

List of figures

Figure 1.1 The distribution and number of reported fatalities for landslides globally between 2007 and 2017 (From Kostis, 2018).	2
Figure 1.2 The continuous AE monitoring concept applied to a buried pipe undergoing deformation and consequent damage during a land slump.	3
Figure 1.3 The understanding required to develop a framework for understanding soil-steel generated acoustic emissions in buried steel structure systems.	8
Figure 2.1 The potential effects of utility pipe deformation and damage.	12
Figure 2.2 Example forms of damage to a pipe.	13
Figure 2.3 Cracking caused by the differential settlement of a building. Adapted from Geotech (n.d).	13
Figure 2.4 A basic single-channel AE monitoring system for recording AE counts and count rates. From Koerner et al. (1981).	17
Figure 2.5 Components of a modern-day ‘active waveguide’ system for passively monitoring AE. From Dixon et al. (2003).	17
Figure 2.6 Measured cumulative acoustic emission counts with percentage failure stress for four tested soils. From Koerner et al. (1981).	18
Figure 2.7 The measured relationship between RDC rates (per minute) on a log scale and time for four shearing velocities representing standard qualitative categorisations. From Dixon and Spriggs (2007).	19
Figure 2.8 The four stages of slope failure as depicted by Lorouiel (2001). From Smith and Dixon (2015).	20
Figure 2.9 The measured relationships between velocity (mm/h) and AE rates (RDC/h) with time. Adapted from Smith and Dixon (2015).	20
Figure 2.10 Measured AE rate (per hour) as a function of velocity (mm/hour) for 21 large-scale tests. From Smith and Dixon (2015).	20
Figure 2.11 Measured AE rate (per minute) with increasing shear strain for three triaxial tests (cell pressure of 300 kPa) at axial displacement rates of 1, 3 and 6 mm/hr. From Smith and Dixon (2019).	21
Figure 2.12 Measured (a) stress verses AE behaviour of a sand, silt and clay tested under identical conditions, adapted from Koerner et al. (1981), along with measured (b) AE rates (RDC/min) and (c) volumetric strain (%) with shear strain (%) for drained triaxial shearing tests performed on LBS 1.0-2.0 at effective confining pressures of 100, 200 and 300 kPa and axial displacement rates of 1 mm/hr, from Smith and Dixon (2019).	23

Figure 2.13 (a) The differing measured frequency spectra of sand, silt and clay soils under identical test conditions and nearing failure and (b) the effects of different soils on the evolving amplitude of generated AE. From Koerner et al. (1981).	24
Figure 2.14 The proposed source mechanisms for AE generation in geological materials. Showing: (1) liquid bridge rupture, (2) crack development, (3) release of force chains, (4) grain friction, (5) grain cementation fracture, and (6) rupture of soil fibres (Michlmayr, 2013).	26
Figure 2.15 Diagrams showing some of the different grain-grain interactions potentially producing AE events. (a) Inter-molecular force rupture. (b) Capillary bridge breakage. (c) Sliding friction. 28	
Figure 2.16 Measured relationships between displacement (mm), rainfall (mm) and cumulative RDCs as a function of time at cluster 3 at the Hollin hill landslide field laboratory. From ^a Smith et al. (2014).	34
Figure 2.17 Deviator stress (kPa) (a), volumetric strain (%) (b) (dilation shown as positive), AE rate (RDC/min) (c), and <i>b-value</i> (d) measurements versus shear strain (%) from a drained triaxial shearing test performed on LBS 0.25-3.35 at an effective confining pressure of 300 kPa and axial displacement rates of 1, 3 and 6 mm/hr (Test 15). Adapted from Smith and Dixon (2019).	35
Figure 2.18 ‘Example use of AE for interpreting pre- and post-peak shear strength mobilisation and accelerating deformation behaviour. The example is based on measurements from LBS 1.0-2.0 at an effective confining pressure of 300 kPa’. From Smith and Dixon (2019).	36
Figure 2.19 Levels of mechanical wave classification for standard wave types.	39
Figure 2.20 The three forms of plate (Lamb) wave: asymmetric (A), symmetric horizontal (S_H), symmetric (S).	40
Figure 2.21 A hodogram showing surface wave particle motions as a function of distance from a source and depth for Rayleigh waves (solid red), Stoneley waves (dotted black), and Scholte waves (dashed blue). From Hernández-García et al. (2014).	42
Figure 2.22 Measured ‘attenuation curves for different external (air and wet sand) and internal environments (air and water)’. From Shehadeh et al. (2008).	47
Figure 2.23 ‘Attenuation measurements as a function of frequency in the dry sand case for three different over burden pressures, 1 bar (black), 0.5 bar (light grey) and no applied pressure (dark grey), for (a) T(0,1) mode and (b) L(0,2) mode. Diamonds and triangles correspond to 16.5 kHz central frequency and squares and circles to 23.5 kHz central frequency.’ From Leinov et al. (2015).	48
Figure 2.24 Measured ‘attenuation response of different soil types contrasted to rock/coal and iron/steel’. From Koerner et al. (1981).	49

Figure 2.25 Simplified typical cross-sectional geometries for infrastructure with the potential to be employed as AE waveguides.	50
Figure 2.26 The typical geometry and environment of a railway track (top left), cross-sectional geometry (top right) and, rail jointing methods (bottom).	51
Figure 2.27 A butt-welded pipe with welded seam.	53
Figure 2.28 Different types of wind turbine foundation (Adapted from Bhattacharya, 2014).	57
Figure 2.29 (a) A schematic diagram of an example ring shear set up and photographs of the (b) lower and (c) upper interface for a soil (sand 7/14) sample during experimentation. Adapted from Ho et al. (2011).	62
Figure 2.30 A schematic diagram, of an example direct shear experiment and photographs of (b) smooth and (c) rusted steel plate surfaces used as interfacing boundaries. Adapted from Han et al. (2018).	62
Figure 3.1 The general experimental process.	71
Figure 3.2 (a) Components of a magnetic holder for (19 OD x 22.4 H mm) piezoelectric transducers (b) coupled using a pea sized amount of silicone gel between the ceramic and structure.	72
Figure 3.3 AE acquisition equipment set up for small-scale and shear box laboratory testing.	73
Figure 3.4 Photograph of the AE data acquisition equipment in an example laboratory experiment.	73
Figure 3.5 Set up of the AE acquisition equipment for large-scale laboratory testing.	74
Figure 3.6 Example AE waveforms with superimposed threshold. (Figure 4 from Smith and Dixon, 2019, ‘Example waveforms recorded using the AE measurement system showing the 0.01 V threshold level: (a) background environmental and electronic noise, and (b) during soil deformation’). From Smith and Dixon (2019).	74
Figure 3.7 A diagram of the controlled pipe set up with which, unless otherwise stated, all controlled pipe experiments were performed. Labels describe individual components.	76
Figure 3.8 Example photograph of a controlled pipe set up for a 48 mm diameter pipe in which two dampening sponges were required. Labels describe individual components.	77
Figure 3.9 A Dirac delta function in the time and frequency domains.	77
Figure 3.10 Measured peak amplitudes with distance for numerous individual pencil lead break tests.	78
Figure 3.11 The tested input signals: pencil lead breaks (left) and dropping a guided ball bearing (right).	79
Figure 3.12 The locations of input source tests (numbered blue arrows) with respect to a sensor (red square) on a steel pipe.	80

Figure 3.13 Photographs for some of the sensor-structure contact methods tested: attachment with sticky tape (method 2), the use of an excessive amount of silicone gel (method 6), the use of a ‘normal’ amount of silicone gel (method 5), and the use of no silicone gel couplant (method 4) (left to right).....	81
Figure 3.14 The location of the varied sensor-structure contact tests (numbered blue arrow) with respect to a sensor (red square) on a steel pipe.	81
Figure 3.15 The locations of the sensor bias tests (numbered blue arrows) with respect to a sensor (red square) on a steel pipe.	82
Figure 3.16 The location of propagation distances tests (numbered blue arrows) with respect to a sensor (red square) on a steel pipe.	82
Figure 3.17 The locations of pipe radii propagation tests (numbered blue arrows) with respect to a sensor (red square) on a steel pipe.	83
Figure 3.18 Photograph of the screw threaded pipe joint, connecting two 48 mm diameter and 3 mm wall thickness pipes, with superimposed labels.....	84
Figure 3.19 The varying locations of screw joint propagation tests (numbered blue arrows) with respect to a sensor (red square) on a steel pipe of insignificant length (dashed lines). Relative positionings drawn to scale.....	84
Figure 3.20 A photograph of the overall equipment set up of the flow rates study.	85
Figure 3.21 Photographs of specific equipment set ups used in the water flow rate tests: (a) the pipe system, (b) attachment of the sensor within a magnetic holder, and (c) the bucket for measuring water flow.	86
Figure 3.22 Example high resolution grain outlines for LBS with superimposed circles used as part of an algorithm to calculate sphericity and roundness.	87
Figure 3.23 Over-end turning process during a bell jar test to characterise soil density.	88
Figure 3.24 Side and cross-sectional views of the shear box testing set up.....	90
Figure 3.25 A photograph of the bolted steel plate with rubber dampening material.	90
Figure 3.26 Step by step diagrams of how the steel plate interface was set up for shear box testing.	91
Figure 3.27 (a) Locations and orientations, with respect to the AE sensor, of the roughness measurements taken with the (b) portable roughness device before each shear box test. Sixteen orientation combinations resulted.	91
Figure 3.28 Filling the top box of the shear box with soil.	92
Figure 3.29 Photographs showing: (a) positioning of the nylon block, (b) positioning of the loading ram, and (c) the addition of LDVT to measure surface movements.....	92

Figure 3.30 The sensor placement for shear box testing, where the sensor is represented by a blue rectangle. (left) plan view. (right) side view.	93
Figure 3.31 The limited travel distance as a result of piezoelectric transducer placement during shear box tests shown (a) near the beginning and (b) at the end of a test.....	94
Figure 3.32 Large-scale experiment set up.	96
Figure 3.33 Photographs of the large-scale experiment (a) before filling (photograph taken at the source input end) and (b) after filling (photograph taken from the sensor end).	97
Figure 3.34 (a) The screw joint connecting the large-scale test pipe and (b) connection of the piezoelectric transducer to the large-scale test pipe using silicone grease couplant and a magnetic holder.	97
Figure 3.35 Creation of a dampening lip at the entry and exit holes of the large-scale testing box. ...	98
Figure 3.36 (a) Performing pencil lead break tests (b) to a standard.....	98
Figure 3.37 A photograph of the tamping rod used for densification and a diagram showing the systematic densification process.	99
Figure 3.38 Photographs of the systematic densification process during set-up of large-scale tests.	99
Figure 3.39 Weight towers constructed on a block and used to apply a normal stress and force soil-steel interactions in large-scale laboratory experimentation.	100
Figure 3.40 The six partial waves propagating within a material layer where S waves refer to shear waves in both horizontal (H) and vertical (V) planes, and L waves refer to longitudinal waves.	102
Figure 3.41 The splitting of a physical modelling problem (e.g. an air-filled buried steel pipe: air-steel-sand) into material layers which when assembled describe wave behaviours for the whole system in the form of a matrix of $6(n-1)$ equations.	102
Figure 3.42 Example global matrix for (a) solid, (b) liquid and (c) vacuum half-spaces where each layer is formed from six partial equations (three for the bounding layers). Copied from Pavlakovic et al. (1997).	104
Figure 3.43 The dialogue box(s) for defining a model geometry in Disperse where (a) defines the system type, (b) adds or deletes material layers and allows for new materials to be defined, (c) is the overall dialogue box, (d) allows for the thickness of layers to be defined – including the unit, (e) defines the system environment as either free, vacuum, or embedded, and (f) allows for pre-defined materials layers to be selected.	104
Figure 3.44 Example plate and cylinder model systems.	105
Figure 3.45 Defining a standard soil for computer modelling.....	106
Figure 3.46 A user’s control over the automatic tracing parameters within Disperse.....	108

Figure 4.1 Modelled frequency-attenuation dispersion curves compared against measured attenuation values for the L(0,2) wave mode. From Leinov et al., 2015.	121
Figure 4.2 Modelled (••), calculated (-) and measured (●) attenuation as a function of frequency for the flexural wave mode in a 19 mm diameter steel rod immersed in water. From Aristegui et al., 2001.	121
Figure 4.3 Modelled (- -) and measured (-) attenuation results normalised against frequency for an 8.1 mm bar embedded in grout. From Pavlakovic et al. 2001.	121
Figure 4.4 (a) Published and (b) recreated Disperse results for a 16 mm steel plate in an air environment plotted as group velocity against frequency thickness. From Maji et al. (1997)..	122
Figure 4.5 (a) Published and (b) recreated Disperse results for a 10 inch bore (254 mm), 16 mm wall thickness cast iron pipe. From Long et al. (2003).	123
Figure 4.6 (a) Published and (b) recreated Disperse results for phase velocity as a function of frequency-thickness for a steel plate embedded in grout. From Pavlakovic et al. (2001).	123
Figure 4.7 Annotated amplitude-time results for measured pencil lead break tests conducted by Shehadeh et al. (2008) at 0 and 5 m propagation (left and right respectively) for four pipe environments: air-steel-air, water-steel-air, air-steel-sand, and water-steel-sand (top to bottom respectively). Adapted from Shehadeh et al. (2008).	126
Figure 4.8 Annotated frequency spectra for measured pencil lead break tests conducted by Shehadeh et al. (2008) at 0 and 5 m propagation (left and right respectively) for four pipe environments: air-steel-air, water-steel-air, air-steel-sand, and water-steel-sand (top to bottom respectively). Adapted from Shehadeh et al. (2008).	127
Figure 4.9 Attenuation models created in Disperse for the four experimental pipe environments: (a) air-steel-air, (b) water-steel-air, (c) air-steel-sand, and (d) water-steel-sand.	128
Figure 4.10 Measured signal strength with propagation distance for three different pipe systems: air-pipe-gravel, air-pipe-clay, and air-pipe-air. From Smith et al., 2017.	129
Figure 4.11 Disperse models for a 3 mm wall thickness, 22 mm radius pipe in a free-steel-free environment (left) and an example free-steel-soil environment (right).	129
Figure 4.12 Results of air-pipe-air laboratory experiments for (a) a 48 mm diameter 2.6 m long pipe, (b) a 20 mm diameter 4.85 m long pipe, and (c) different sensors.	131
Figure 4.13 Disperse models showing (a) attenuation-thickness with frequency-thickness for an air-steel-air plate model and (b) the corresponding signal strengths with propagation at 0.5 and 0.8 MHz-mm frequency-thicknesses.	132
Figure 4.14 Average signal strength (%) with propagation distance (m) for measured large-scale free bound (i.e. air) and LBS buried steel pipe systems.	133

Figure 4.15 Signal strength (%) with propagation distance (m) for a free-steel-LBS plate system modelled in Disperse.	133
Figure 4.16 Modelled Disperse results of symmetric (S) and asymmetric (A) wave modes for: (a) attenuation as a function of thickness for thicknesses between 1 and 25 mm, (b) attenuation as a function of thickness collated from local maximum and minima, and (c) the relationship between attenuation and frequency as thickness products for the fundamental symmetric and asymmetric wave modes.	135
Figure 4.17 Disperse models showing the effect of shell radius on attenuation of symmetric (S) and asymmetric (A) wave modes as (a) a function of frequency-thickness for numerous shell radii (mm) and (b) a function of shell radius at a frequency-thickness of 1.5 MHz-mm.	137
Figure 4.18 Disperse models showing the influence of a soil's density (0.5 to 10 kg/m ³) on symmetric (S) and asymmetric (A) wave attenuation within plates (PL) and shell structures (Sh).	139
Figure 4.19 Disperse models showing the influence of a soil's Poisson's ratio (0.1 to 0.45) on symmetric (S) and asymmetric (A) wave attenuation within plates (PL) and shell structures (Sh).	140
Figure 4.20 Disperse models showing the influence of a soil's Young's modulus (0.02 to 1 MPa) on symmetric (S) and asymmetric (A) wave attenuation within plates (PL) and shell structures (Sh).	140
Figure 4.21 Calculated coefficient relationships describing attenuation-thickness as a function of (a) density and frequency-thickness and (b) Young's modulus and frequency-thickness.	141
Figure 4.22 Disperse models showing the effects of external materials (E) on symmetric (S) and asymmetric (A) wave attenuation in tri-layer plate (PL) systems.	143
Figure 4.23 Ratio relationships for parametric properties of different external materials.	145
Figure 4.24 Disperse modelling results for attenuation-thickness as a function of frequency-thickness with internal liquid environments and a soil external environment.	146
Figure 4.25 Disperse modelling results for attenuation-thickness as a function of frequency-thickness with internal liquid environments and a free external environment.	146
Figure 4.26 The generalised Disperse models for internal liquids of similar densities (gases, water, and oils/alcohol) with an external soil environment.	147
Figure 4.27 Disperse modelling results for attenuation-thickness as a function of frequency-thickness with internal polymeric materials and an external soil environment.	149
Figure 4.28 Disperse modelling results for attenuation-thickness as a function of frequency-thickness with internal solid materials and an external soil environment.	150
Figure 4.29 The four pipe model systems investigated (Cases 1 to 4).	150

Figure 4.30 Variations in typical soil properties for London Clay and Leighton Buzzard Sand as a function of depth.	151
Figure 4.31 Disperse modelling results for the buried utility pipe case studies.....	152
Figure 4.32 The eight pile model systems investigated (Cases 5 to 12).	153
Figure 4.33 Results showing calculated signal strengths with depth for the two pile models investigated: cylindrical with a 10 mm wall thickness (top), and H-piles with 10 mm and 30 mm web thicknesses respectively (middle and bottom).	155
Figure 4.34 The monopile system model investigated (Case 13).	156
Figure 4.35 Environmental results for the offshore monopile model as dB measurements within each metre's depth.	158
Figure 4.36 Environmental results for the offshore monopile model.....	158
Figure 4.37 The measured effect of shell radius on wave propagation at various distances for steel pipes of different radii.	159
Figure 4.38 (a) The measured relative signal strengths (% initial) and (b) how this changes over 0.25 m intervals with propagation through 20 mm and 48 mm diameter steel pipes in air.	160
Figure 4.39 The sensor-joint set ups for investigating (a) signal transmission through a screw joint and (b) signal reflection at a screw joint.	161
Figure 4.40 The measured effect of a screw joint on wave transmission for different propagation distances.	162
Figure 4.41 The measured effect of a screw joint on wave reflection for different propagation distances.	163
Figure 4.42 Averaged measured frequency spectra for the propagation of (a) a 0.5 mm pencil lead break signal and (b) a 0.9 mm pencil lead break signal through a 9 m, jointed steel pipe forming a free-steel-free system.	165
Figure 4.43 Example measured signal amplitudes with propagation along a 9 m, 42.4 mm OD diameter, 3.2 mm wall thickness steel pipe in a free-steel-free environment. Signals were measured at (a and c) 0.05, (b and d) 5.5, and (e and f) 6.5 metres and input using a Bic 0.9 mm pencil lead and standard 0.5 mm pencil lead.....	166
Figure 4.44 Average measured wave velocities (m/s) for propagation in an air-steel-air or air-steel-LBS pipe system before and after transmission through a screw joint.	167
Figure 4.45 Average measured peak amplitudes (V) for propagation in air-steel-air and air-steel-LBS pipe systems before and after transmission through a screw joint.	168
Figure 4.46 Signal strength with propagation distance in a modelled air-steel-air (free bound) system at frequency-thicknesses between 0.3 and 1 MHz-mm.....	168

Figure 4.47 Averaged measured frequency spectra for the propagation of (a) a 0.5 mm pencil lead break signal and (b) a 0.9 mm pencil lead break signal through a 9 m, jointed steel pipe forming a free-steel-LBS (buried) system.	170
Figure 5.1 Normal stress with time for (a) stepped rate LBS tests, (b) stepped rate PG tests, (c) constant rate LBS tests and (d) constant rate PG tests for their duration.....	179
Figure 5.2 Cumulative RDCs with time for (a) stepped rate LBS tests, (b) stepped rate PG tests, (c) constant rate LBS tests and (d) constant rate PG tests during compression only.	180
Figure 5.3 RDC rate/minute with time for (a) stepped rate LBS tests, (b) stepped rate PG tests, (c) constant rate LBS tests and (d) constant rate PG tests during compression only.....	180
Figure 5.4 Vertical displacement with time for (a) stepped rate LBS tests, (b) stepped rate PG tests, (c) constant rate LBS tests and (d) constant rate PG tests during compression only.	180
Figure 5.5 Frequency dominance with time for (a) stepped rate LBS tests, (b) stepped rate PG tests, (c) constant rate LBS tests and (d) constant rate PG tests during compression only.	181
Figure 5.6 Amplitude with time for (a) stepped rate LBS tests, (b) stepped rate PG tests, (c) constant rate LBS tests and (d) constant rate PG tests during compression only.....	181
Figure 5.7 b-values with time for (a) stepped rate LBS tests, (b) stepped rate PG tests, (c) constant rate LBS tests and (d) constant rate PG tests during compression only.....	181
Figure 5.8 Statistical analysis on the occurrence of dominant frequencies (within 10 kHz bins) during shearing for stepped and constant rate tests with LBS (top) and PG (bottom).....	184
Figure 5.9 Number of higher (>35 kHz) AE events for every 5 mm displacement during stepped shear rate tests.....	190
Figure 5.10 RDC rate/second with shear displacement for (a) stepped rate LBS tests, (b) stepped rate PG tests, (c) constant rate LBS tests and (d) constant PG tests.....	191
Figure 5.11 Vertical displacement with shear displacement for (a) stepped rate LBS tests, (b) stepped rate PG tests, (c) constant LBS tests and (d) constant rate PG tests during shearing only.	191
Figure 5.12 Shear rate with shear displacement for (a) stepped rate LBS tests and (b) stepped rate PG tests.	191
Figure 5.13 Shear stress with shear displacement for (a) stepped and constant rate LBS tests and (b) stepped and constant rate PG tests.....	191
Figure 5.14 Dominant frequencies with shear displacement for (a) stepped rate LBS tests, (b) stepped rate PG tests, (c) constant rate LBS tests and (d) constant rate PG tests.	192
Figure 5.15 Amplitude with shear displacement for (a) stepped rate LBS tests, (b) stepped rate PG tests, (c) constant rate LBS tests and (d) constant rate PG tests.....	192

Figure 5.16 b-values with shear displacement for (a) stepped rate LBS tests, (b) stepped rate PG tests, (c) constant rate LBS tests and (d) constant rate PG tests. 192

Figure 5.17 Separated and averaged RDC rates/minute with normal stress for (a) stepped rate LBS tests, (b) stepped rate PG tests and (c) constant rate LBS tests and PG tests (at target normal stress)..... 193

Figure 5.18 Cluster behaviours for dominant frequencies with normal stress for (a) stepped rate LBS tests, (b) stepped rate PG tests, (c) constant rate LBS tests and (d) constant rate PG tests during compression (before target normal stress) and shearing (at normal stress). 193

Figure 5.19 Cluster behaviours for b-values with normal stress for (a) stepped LBS tests, (b) stepped PG tests, (c) constant LBS tests and (d) constant PG tests during compression (before target normal stress) and shearing (at normal stress). 193

Figure 5.20 Cluster behaviours for RDC rate/minute with vertical displacement for (a) stepped rate LBS tests, (b) stepped rate PG tests, (c) constant rate LBS tests and (d) constant rate PG tests. 194

Figure 5.21 Cluster behaviours for dominant frequencies with vertical displacement for (a) stepped rate LBS tests, (b) stepped rate PG tests, (c) constant rate LBS tests and (d) constant rate PG tests. 194

Figure 5.22 Cluster behaviours for b-values with vertical displacement for (a) stepped rate LBS tests, (b) stepped rate PG tests, (c) constant rate LBS tests and (d) constant rate PG tests. 194

Figure 5.23 Cluster behaviours for RDC rate/minute with shear stress for (a) stepped rate LBS and PG before and (b) stepped rate LBS and PG tests after mobilisation, and (c) constant rate LBS tests and PG tests before and (d) constant rate LBS tests and PG tests after mobilisation. 195

Figure 5.24 Cluster behaviours for dominant frequencies with shear stress for (a) stepped rate LBS and PG and (b) stepped rate LBS and PG tests, and (c) constant rate LBS tests and PG tests and (d) constant rate LBS tests and PG tests. 195

Figure 5.25 Cluster behaviours for b-values with shear stress for (a) stepped rate LBS and PG and (b) stepped rate LBS and PG tests, and (c) constant rate LBS tests and PG tests and (d) constant rate LBS tests and PG tests. 195

Figure 5.26 Cluster behaviours for RDC rate/minute with shearing rate for (a) a variety of LBS tests and (b) a variety of PG tests after mobilisation, and (c) constant rate LBS tests and PG tests during shearing. 196

Figure 5.27 Cluster behaviours for dominant frequencies with shearing rate for (a) stepped rate LBS and PG and (b) stepped rate LBS and PG tests, and (c) constant rate LBS tests and PG tests and (d) constant rate LBS tests and PG tests during shearing. 196

Figure 5.28 Cluster behaviours for b-values with shearing rate for (a) stepped rate LBS and PG and (b) stepped rate LBS and PG tests, and (c) constant rate LBS tests and PG tests and (d) constant rate LBS tests and PG tests during shearing.	196
Figure 5.29 Plate roughness measurements taken before the programme of shear tests commenced as a (a) a distribution plot of defect depths, (b) profile of depth along a cross-section against the grain of the plate, and (c) a 3D model of the profile.	197
Figure 5.30 Plate roughness measurements with respect to position, orientation and time during shear box experiments. Superimposed arrows depict the general trend of each dataset.	198
Figure 5.31 Signal amplitude (Volts) with relative time (seconds) during the addition of 100 lbs of weights to the top of a free-steel-soil pipe system.	199
Figure 5.32 Frequency spectra measured during the addition of 100 lbs of weights to the top of a free-steel-soil pipe system.	200
Figure 5.33 Signal amplitude (Volts) measured with relative time (seconds) during the addition, removal and re-addition of weights to the top of a free-steel-soil pipe system in 20 Lb increments.	201
Figure 5.34 Raw waveforms for the measured amplitudes (Volts) of a pencil lead break test (left) and a dropped ball bearing test (right) after 4 m propagation in a steel pipe.	202
Figure 5.35 Calculated frequency spectra for a pencil lead break test (left) and a dropped ball bearing test (right) after 4 m propagation in a steel pipe.	203
Figure 5.36 (a) Measured and (b) averaged voltages of pencil lead break signals with different sensor-structure couplings.	204
Figure 5.37 Average measured signal amplitudes with propagations distance for four different piezoelectric transducers.	206
Figure 5.38 Average measured frequency spectra for four piezoelectric transducers: (a) R.45, (b) R3, (c) R15, and (d) R80.	207
Figure 5.39 Raw waveforms (amplitude (v) verse time (seconds)) for water flow tests: (a) 7 (variable flow rate), (b) 17 (0.07 m/s), (c) 26 (0.24 m/s), and (d) 19 (0.56 m/s).	211
Figure 5.40 Average measured AE signal amplitude with water flow rate where the blue dots represent data point, the black dashed line is a third order polynomial best fit, and the red dashed lines represent typical boundaries defining the flow regime.	211
Figure 5.41 Whole test frequency spectra for water flow tests: (a) 7 (variable flow rate), (b) 17 (0.07 m/s), (c) 26 (0.24 m/s), and (d) 19 (0.56 m/s).	212
Figure 6.1 The factors influencing wave propagation and attenuation within an example pipe burial system where the pipe is considered a waveguide.	216

Figure 6.2 The three steps to developing a physical sensor network (stage 1), choosing appropriate hardware, choosing appropriate software, and deploying the physical network, for the collection, analysis and interpretation of AE data (stage 2). 217

Figure 6.3 The proposed hardware required for employing steel infrastructure as waveguides in the field. 218

Figure 6.4 The cyclical nature of questions to consider when setting data capture (i.e. sampling) rates. 219

Figure 6.4 Suggested and realistic source-sensor spacings as a result of omni-directional AE sources in the field. 220

Figure 6.5 Signal strength with propagation for five burial systems and the consequent suggested sensor spacings for an air-steel-air system at different frequency-thickness products. 223

Figure 6.6 Signal strength with propagation and consequent suggested sensor spacings for (a) water filled burial systems in air and LBS and (b) air filled burial systems in LBS and clay for frequency-thickness products of 0.5 and 0.8 MHz-mm. 224

Figure 6.7 The three steps for interpreting AE behaviours in buried infrastructure systems (stage 2), collecting and processing AE data via a physical sensor network (stage 1), analysing the collected data, and using the analysis to interpret the conditions of the buried infrastructure system and provide relating actions and outcomes. 225

Figure 6.8 Scalar frameworks for determining the state of an LBS type soil-steel system using parameter-time linear gradients over 5- and 10-minute periods. The parameters include RDC rates (per minute), amplitude (dBV) and b-values. The suggested soil states have been colour coded to represent the risk posed by a system where green indicates least risk and red indicated most risk. 230

Figure 6.9 Frameworks for determining the likely normal stress and shear state of an LBS-steel system using observed parametric ranges of frequencies (kHz) and b-values for the conditions tested. 231

Figure 6.10 Shear rates (mm/minute) as a function of RDC rate (per minute) for three normal stresses, 75, 150, and 225 kPa. The points represent a mixture of constant and stepped rate shear tests. 231

Figure 6.11 Shear rate (mm/minute) as a function of measured amplitude (dBv) at different normal stresses where red points were recorded under 75 kPa, green points under 150 kPa and blue points under 225 kPa. The points represent a mixture of constant and stepped rate shear tests. 232

Figure 6.12 (a) RDC rate, (b) amplitude, and (c) b-value data with time for an LBS sample test under 150 kPa and sheared at 1 mm/minute over 40 mm. The data is plotted in 5 minute time intervals, as denoted by changing colours, for which linear gradients have been superimposed. The grey rectangle represents the period during which the sample was being compressed, as labelled, whilst the black dashed arrow indicates the point at which mobilisation of the shear plane occurred.	234
Figure 6.13 The summarised development of a two-stage framework for understanding soil-steel generated AE in buried steel structures, split into six steps.....	237
Figure 6.14 A two-stage framework for deployment of a sensor network and subsequent interpretation and understanding of soil-steel generated AE in buried steel structures.	238
Figure AP2.1 Exemplar frequency spectra calculated in DIAdem from collected waveform data using three windows: rectangular (red), Hanning (green), and Cauchy (blue).	265
Figure AP2.2 An example of the difference between a rectangular and Hanning window for FFT calculations.	265
Figure AP2.3 An example of the difference between a rectangular and Cauchy window for FFT calculations.	266
Figure AP3.1 Raw waveforms for empty (free-steel-free) large-scale laboratory tests investigating propagation and using a Bic 0.9 mm pencil.	269
Figure AP3.2 Raw waveforms for empty (free-steel-free) large-scale laboratory tests investigating propagation and using a standard 0.5 mm pencil.	270
Figure AP3.3 Raw waveforms for empty (free-steel-free) large-scale laboratory tests investigating sensor placement and using a Bic 0.9 mm pencil.....	271
Figure AP3.4 Raw waveforms for empty (free-steel-free) large-scale laboratory tests investigating sensor placement and using a standard 0.5 mm pencil.	272
Figure AP4.1 The measured sensitivities of the (a) R.45, (c) R15, and (d) R80 sensors used during laboratory experiments and the (b) suggested sensitivity of the R3 sensor.	274
Figure AP5.1 Technology Readiness Levels (TRLs) as described by NASA, 2017.	275

List of tables

Table 2.1 The advantages and disadvantages of different techniques and instruments for monitoring buried infrastructure systems.	14
Table 2.2 The influence on behaviour of soil properties for multiple soil types (Smith, 2015).	25
Table 2.3 Proposed AE generating mechanisms within soils, and standard terminologies for each, from combined literature.	26
Table 2.4 Comparing distinguishable stages of compression-based destabilisation for: granular media, rock and, singular particles; and their observed AE characteristics, proposed by different authors.	31
Table 2.5 AE sources and their measured characteristic frequencies for both granular and non-granular media. Taken from a range of authors as stated.	32
Table 2.6 A summary of mechanical wave types and waveforms.	38
Table 2.7 Wave attenuation mechanisms and processes.	43
Table 2.8 A summary table comparing the typical: materials, geometries and, environments, for different forms of infrastructure with the potential to be employed as AE waveguides.	49
Table 2.9 Pipe connection methods (Adapted from FT pipelines).	54
Table 2.10 A summary of monopile geometries and environments.	59
Table 2.11 Comparing the main features of three computer modelling programs (Abaqus, ComSol Multiphysics and Disperse) with reference to modelling wave propagation and attenuation through soil-structure systems.	68
Table 3.1 Programme summary for small-scale laboratory tests.	75
Table 3.2 Summarised specifications for four piezoelectric transducer, R.45 α , R3 α , R15 α and R80 α , from National Instruments alpha series.	81
Table 3.3 Screw joint tests sensor and signal input positionings with respect to one another for each test.	84
Table 3.4 Programme summary for water flow tests.	85
Table 3.5 Test programme for soil characterisation.	87
Table 3.6 Programme summary for shear box testing.	89
Table 3.7 Details of the stepped rate shear box test.	94
Table 3.8 A summarised programme of the large-scale laboratory tests.	95
Table 3.9 Test procedures and timing for weighted large-scale laboratory experiments.	100
Table 3.10 Summarised programme of computational models.	103
Table 3.11 Materials properties used for computer modelling.	107
Table 3.12 The properties of soils used for computer modelling.	107

Table 3.13 Full programme of conducted small-scale laboratory tests.	110
Table 3.14 Full programme of conducted water flow tests.	111
Table 3.15 Full programme of conducted shear box tests.....	112
Table 3.16 Full programme of conducted large-scale laboratory tests.....	114
Table 3.17 Full programme of conducted computer models.....	116
Table 4.1 Summary of points of interest from the results of Shehadeh et al.'s (2008) pipe experiments.	124
Table 4.2 Material properties defining Shehadeh et al. (2008) model recreations in Disperse.	125
Table 4.3 Summary of Disperse attenuation results as attenuation rates and percentage signal strengths (after 5 m propagation) for the A and S wave modes in varying environments and at different frequencies.	125
Table 4.4 Calculated attenuation rates for different pipe systems.....	129
Table 4.5 Model parameters used to describe different soil environments and their corresponding attenuation rates for the S0 mode at select frequencies.....	130
Table 4.6 A summary of experimental study results for different air-pipe-air experiments.....	131
Table 4.7 Attenuation rates with select frequencies in an air-steel-air plate model.	132
Table 4.8 The percentage error between relationships for the c and d coefficients and the scale factors for relationships for the m and n coefficients.	142
Table 4.9 Comparing parametric properties of different materials as ratios.....	145
Table 4.10 Typical parametric value ranges for describing London Clay and Leighton Buzzard Sand to a depth of 40 m.....	151
Table 4.11 Specific plate geometries for the pile foundation models (Cases 5 to 12).	153
Table 4.12 The measured average, calculated strength and change in strength of signals propagating through air-steel-air pipe systems of different diameters.	160
Table 5.1 Initial densities and related density data for shear box tests using LBS and PG materials.	176
Table 5.2 Goodness of fit as R^2 values for second order polynomials superimposed onto the amplitude data.....	184
Table 5.3 A comparison of the signal characteristics for a pencil lead break and a dropped ball bearing.....	203
Table 5.4 Specifications summary for alpha series piezoelectric transducers (MISTRAS).....	206
Table 5.5 The spectral features for different transducers at different propagation distances.	208
Table 5.6 A comparison of frequency, flow speed, and sensor information for published works on fluid flow in pipes.....	210

Table 6.1 Comparing the framework interpretations for various parameters at different time intervals with known processes.	233
Table 6.2 Suggested actions as a result of interpretations using qualitative AE levels. From Koerner et al. (1981).....	235
Table AP1.1 A modern adaptation of Varnes (1978) landslide classification system containing 32 sub-categories for six movement types. From Hungr et al. (2014).	263
Table AP1.2 The mechanical properties of different soils in the field (From Hungr et al., 2014).	264
Table AP1.3 Landslide velocity scale (From Cruden and Varnes, 1996).....	264
Table AP3.1 Amplitude, attenuation, and wave velocity results for empty (free-steel-free) large-scale laboratory tests investigating propagation and using a Bic 0.9 mm pencil.	267
Table AP3.2 Amplitude, attenuation, and wave velocity results for empty (free-steel-free) large-scale laboratory tests investigating propagation and using a standard 0.5 mm pencil.....	267
Table AP3.3 Amplitude, attenuation, and wave velocity results for empty (free-steel-free) large-scale laboratory tests investigating sensor placement and using a Bic 0.9 mm pencil.	268
Table AP3.4 Amplitude, attenuation, and wave velocity results for empty (free-steel-free) large-scale laboratory tests investigating sensor placement and using a standard 0.5 mm pencil.....	268
Table AP4.1 A comparison of the main features of four piezoelectric transducers (R.45, R3 α , R15 α , and R80 α) by Physical Acoustics.	273
Table GL1.0 A glossary of general terminology.	276
Table GL2.2 A glossary of wave types.	280
Table GL2.3 A glossary of wave attenuation terms.	281
Table GL3.1 A Glossary of landslide movement classifications.....	282
GL3.2 A glossary of soil mechanisms and interactions.....	283
Table GL4.1 A glossary of signal processing and characterisation methods.	284
Table GL4.2 A glossary of WFT window classifications.	286
Table GL5.0 A glossary of AE measurement systems.....	286

List of equations

Equation 2.1	$F = \frac{4}{3}R^{\frac{1}{2}}\frac{E}{1-v}\delta^{\frac{3}{2}}$	28
Equation 2.2	$\frac{\delta^2 y(x,t)}{\delta x^2} = \frac{1}{v^2} \frac{\delta^2 y(x,t)}{\delta t^2}$	39
Equation 2.3	$E(x) = E_0 e^{-kx}$	44
Equation 2.4	$E(x) = E_1(x) + E_2(x)$	44
Equation 2.5	$E(x) = [mn]^{ax} E_{0,1} e^{-k_1 x} + E_{0,2} e^{-k_2 x}$	44
Equation 2.6	$A \propto e^{-aR} = e^{-\pi f Q^{-1} \frac{R}{v}}$	45
Equation 2.7	$Q_{ij} = S_i(f) I_j(f) R_j(f) B_{ij}(f)$	45
Equation 2.8	$Q_{ij} = \frac{\Omega_0 f_c^Y}{f_c^Y + f^Y} \exp[-\pi f(t_{ij}^* + t_{station})] = \frac{\Omega_0 f_c^Y}{f_c^Y + f^Y} \exp[-\pi f \kappa]$	45
Equation 3.1	$Fl = \frac{Vol_{water}}{\pi t R^2}$	86
Equation 3.2	$\Phi = A_{(L)} e^{i(k \cdot x - \omega t)} = A_{(L)} e^{i(k_1 x_1 + k_2 x_2 + k_2 x_3 - \omega t)}$	101
Equation 3.3	$\psi = A_{(S)} e^{i(k \cdot x - \omega t)} = A_{(S)} e^{i(k_1 x_1 + k_2 x_2 + k_2 x_3 - \omega t)}$	101
Equation 4.1	<i>attenuation = m/thickness</i>	135
Equation 4.2	<i>frequency (kHz) × thickness (mm) = attenuation – thickness (kHz – mm)</i>	136
Equation 4.3	$50 \text{ kHz} \times 10 \text{ mm} = 500 \text{ kHz} - \text{mm} = 0.5 \text{ MHz} - \text{mm}$	136
Equation 4.4	$Att - Thickness = m\rho^c$	139
Equation 4.5	$Att - Thickness = nE^d$	139
Equation 6.1	$k = 20 \log \frac{Voltage_{in}}{Voltage_{out}}$	221
Equation 6.2	$Voltage_{out} = \frac{Voltage_{in}}{\frac{k}{10^{\frac{20}{k}}}}$	221

Chapter 1: Introduction

1.0 Introduction

1.1 Research justification

The land on which we stand is a dynamic entity, restructuring and sometimes failing dependent on the conditions imposed upon it. This can affect not only the structural integrity of the land, but also the infrastructure built in and/or on it.

Above the surface, case studies such as Aberfan in Wales, Mam Tor in Derbyshire, and Holbeck Hall in Scarborough, give examples of problems that can arise as a result of landslides in the UK with high and long-term physical, social and environmental costs. Worldwide however, landslides are also known to regularly displace, and even kill, thousands of people every year. The Global Landslide Catalogue (Kostis, 2018) for example, states that there were 10,804 reported rainfall induced landslides between 2007 and 2017 (Figure 1.1), of which 2435 caused fatalities.

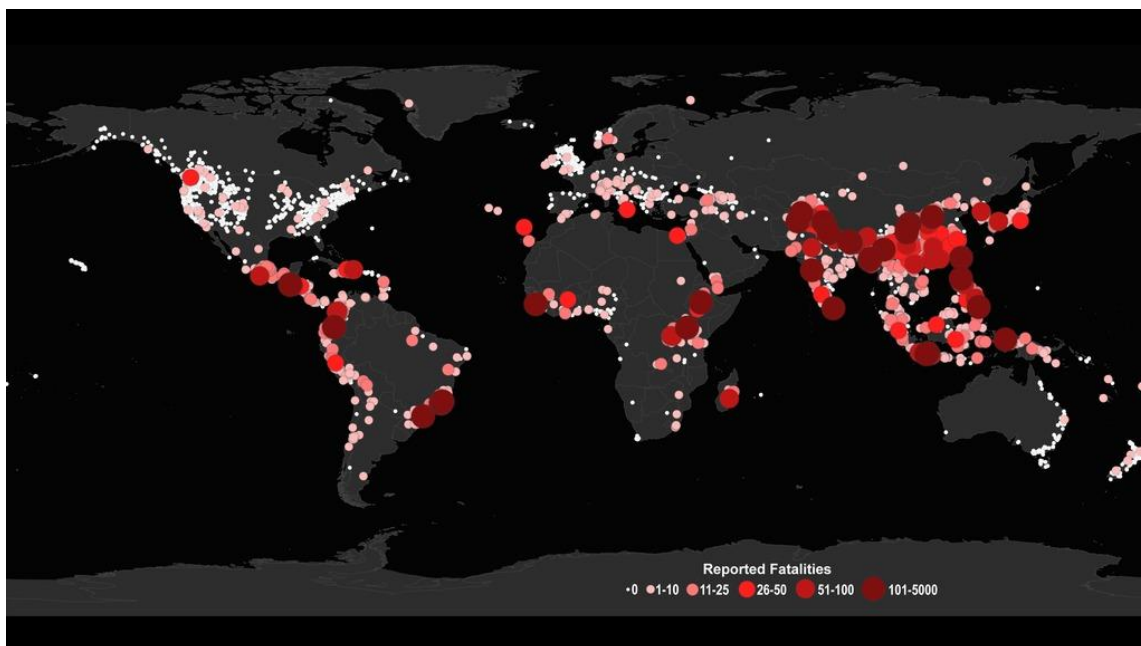


Figure 1.1 The distribution and number of reported fatalities for landslides globally between 2007 and 2017 (From Kostis, 2018).

Below the surface however, although harder to see, landslide and instability related problems are just as devastating. Buried infrastructure is a crucial component of modern-day society, transporting utilities (e.g. water, oil, and gas), ensuring environments are safe (e.g. rock bolts and retaining walls), and forming the foundations of structures (e.g. pile foundations and offshore monopile foundations). In the UK, for example, there are around 343,865 km of water pipeline, however 3183 million litres of water leaks from these every day (DiscoverWater, 2018). Furthermore, Dijkstra and Dixon (2010) suggest that approximately 7% of our main transport network is in potentially unstable areas.

Instability related problems, whether resulting from deterioration with age, working conditions or environmental conditions, have the potential to cause major social, economic and environmental issues above, as well as below, the surface. A need to further understand, monitor and where appropriate remediate materials and structures, is therefore becoming increasingly important.

Significant research effort has focused on the development of infrastructural and environmental monitoring systems using equipment and techniques such as geophysical instruments (Wilkinson et al., 2016), extensometers (e.g. Hu et al., 2015, Afandi et al., 2018), fibre-optic strain sensing (Pelecanos et al., 2017), photogrammetry (Pannese et al., 2019), acoustic emission (AE) monitoring (e.g. Koerner et al., 1980, Smith, 2015) and non-destructive testing (NDT) (e.g. Beard and Lowe, 2003, Shehadeh et al., 2019). Instruments and techniques to monitor geotechnical assets therefore exist, although none are without technical limitation. Furthermore, conventional approaches typically provide localised information on deformations/ground water at discrete time intervals.

Nascent technologies are however beginning to provide continuous measurements whereby the condition of an asset throughout its life-cycle can be communicated in near real-time. Such technologies include ShapeAccelArray and fibre optics systems, as well as geophysical methods. But, to retrofit hundreds of thousands of kilometres of assets with such systems would be prohibitively intrusive and expensive.

Smith (2015) consequently developed a relatively inexpensive and continuous AE monitoring system with which it was shown that rates of ground movement, and changes in rate, could be differentiated to a greater precision than an order of magnitude. The system detects AE using piezoelectric transducers attached to steel waveguides. The research contained in this thesis therefore proposes to exploit and extend the approach developed by Smith (2015), making use of buried monitoring networks in the form of existing and/or newly built buried steel structures such as utility pipes and pile foundations. The advantage of this proposed approach is that sensors could be retrofitted to existing, ageing infrastructure assets at discrete locations, for example at regular spacings, to provide high spatial and temporal resolution information for use in early warning of adverse deformation behaviour, which will enable targeted and timely interventions by asset owners and operators. Figure 1.2 illustrates the AE monitoring concept applied to buried structures.

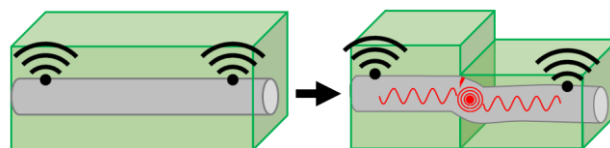


Figure 1.2 The continuous AE monitoring concept applied to a buried pipe undergoing deformation and consequent damage during a land slump.

1.2 Research aim and objectives

The overall aim of the research reported was to develop a framework for understanding soil-steel interaction-generated acoustic emissions and their propagation in buried steel structures. To achieve this, the following five key objectives were formulated:

- OB1 To review knowledge of soil and AE behaviours, as well as the current monitoring systems for soil environments.
- OB2 To identify and characterise AE sources and behaviours in soil-steel systems.
- OB3 To investigate the propagation of AE through buried steel structures.
- OB4 To develop a framework to inform the deployment of an AE sensor network.
- OB5 To develop a framework to inform the interpretation of detected AE.

1.3 Contributions to knowledge

This study has investigated the use of pre-existing and newly built steel infrastructure as passive waveguides to soil-steel interaction-generated AE and the information that can be gained from such systems. From the research, extensions to existing knowledge as well as new and original knowledge within the field of study have been contributed. Such contributions include:

- Relationships have been quantified between soil-steel interaction-generated AE and imposed mechanical conditions and behaviours (e.g. stresses, shearing velocity) (OB2). These have been obtained from an extensive programme of laboratory tests and computational models for which the results are shown in Chapter 5: Results: Characterising AE signals. Key findings are summarised below:
 - The stress conditions imposed on a soil-steel system significantly influence the generated AE during both compression and shearing; AE activity increases proportionally with normal stress.
 - Shearing rate and shearing regime similarly affected the acoustic behaviours. For the range of shear rates investigated (0.002 to 2 mm/minute, equivalent to slow to moderately-rapid soil movements) AE generation as a results of soil-steel interactions could be empirically related to the shearing rate by second order relationships. In addition, the measured AE was related to the mobilised shear stress whereby the transition between mobilising and fully-mobilising shear stress was identifiable from the AE data. All AE parameters investigated (e.g. RDCs, amplitude and b-values),

except dominant frequency, were found to be related to shearing rate and mobilised shear stress.

- An understanding of signal propagation within typical buried steel structure systems (OB3) was obtained from an extensive programme of computational modelling. Moreover, the computational method was validated using a series of small and large-scale laboratory tests and published literature. The results of this work are presented in Chapter 4: Results: Propagation and attenuation.
 - For shell type structures such as pipes and cylindrical piles, radius has a negligible effect on the propagation and attenuation of fundamental wave modes whilst the effects of wall thickness can be accounted for using frequency-thickness and attenuation-thickness products. Pipe structures may therefore be accurately modelled using plates.
 - Attenuation (dB/m) is heavily influenced by the internal and external burial materials of a system with example pipe and monopile models demonstrating that:
 - 0.01% of an AE signal's initial signal is still measurable after >20 m propagation through a cylindrical pile.
 - For H-piles, this decreases to around 10 m for the same wall/web thickness, although increases for greater wall/web thicknesses.
 - Propagation within an off-shore monopile is dependent on the origin of the signal; for adequate signal strengths to be measured it is expected that the sensor would need to be under the water line.
 - The value of attenuation-thickness (dB-mm/m) can be mathematically related to the material properties of density (kg/m^3) and Young's modulus (E) (kPa) using exponential relationships of different coefficients.
 - A mixture of small- and large-scale, primary and secondary experimental data, including both computational and physical tests, showed that Disperse provides accurate wave velocity and attenuation models for a variety of wave modes in a variety of burial systems.
- Synthesis of the results produced by computational models, shear box testing, and small- and large-scale experiments enabled a framework to be developed informing the creation of sensor networks and that was adaptable to varying forms of buried infrastructure within different environments (OB4). The framework formed stage one of an overall two stage framework, developed in Chapter 6, for understanding soil-steel AE generation in buried infrastructure.

- This framework contained three steps: (1) choosing appropriate hardware to form a desired network, (2) choosing appropriate software to control the network and collected desired data with relevant temporal resolution, and (3) deploying the sensors at appropriate spacings to form a network at a relevant spatial resolution.
- Spacings are dependent on the signal frequency (kHz) of interest and structural thickness (mm) (i.e. wall thickness), especially in air-steel-air systems, and heavily influenced by any internal and/or external system materials.
- A framework to inform the interpretation of collected AE (OB5) was created using the results from a programme of large direct-shear testing. The development of the AE framework is shown in Chapter 6 and formed stage two of an overall two stage framework for understanding soil-steel AE generation in buried infrastructure.
 - This framework also contained three steps: (1) the collection and processing of relevant AE data, (2) analysis and interpretation of this data, and (3) choosing appropriate actions as an outcome of the interpretations.
 - Both absolute values and rates of change of AE parameters can be used to interpret soil-structure interaction behaviours. Using a combination of both the absolute values and temporal gradients for different parameters (i.e. RDCs, amplitude, b-value, etc.) improves the level of interpretation, though an uncertainty is still present due to the range of factors that can influence AE generation.

1.4 Thesis structure

The thesis has been split into multiple chapters introducing, presenting the results of, and concluding the numerous studies conducted as part of the overall investigation. Additionally, summaries collating the information presented within each chapter have been provided at the end of individual chapters. The basic structure is shown in Figure 1.3 which illustrates the entire research project pictorially.

Chapter One is an introduction to the research. It provides a justification for completion of the work, states the research aim and objectives and summarises the structure and content of the thesis.

Chapter Two provides a literature review of current knowledge regarding: soil and AE behaviours relating to instability and infrastructure; instability and damage monitoring systems; AE generation and characterisation; wave propagation and attenuation, including within typical infrastructure environments; and modelling and analytical methods for wave propagation (OB1).

Chapter Three describes and justifies the methodologies and approaches adopted in the data collection and analysis stages of the research.

Chapter Four shows the results of investigative work regarding wave propagation and attenuation (OB3). This includes computational modelling, and small- and large-scale laboratory experimentation.

Chapter Five shows the results of studies concerning the characterisation of AE (OB2) including shear box testing, large-scale laboratory experimentation, and water flow testing.

Chapter Six presents a discussion of the findings of the research, synthesis of the results, and development of an overall framework for understanding soil-steel generated AE that propagates in buried steel structures. This culminates in the development of a two-part framework to inform the deployment of an AE sensor network (OB4) and interpret the AE measurements (OB5).

Chapter Seven provides the conclusions drawn from individual and combined studies, as well as the final framework, within the whole investigation. Limitations of the work and recommendations for further research are also given.

1.5 Chapter summary

An overview of the work within this thesis has been provided including a background to the problem, the consequent aim and objectives of the work and a summary on the content of each of the chapters. Additionally, original contributions to knowledge as a result of the research were detailed.

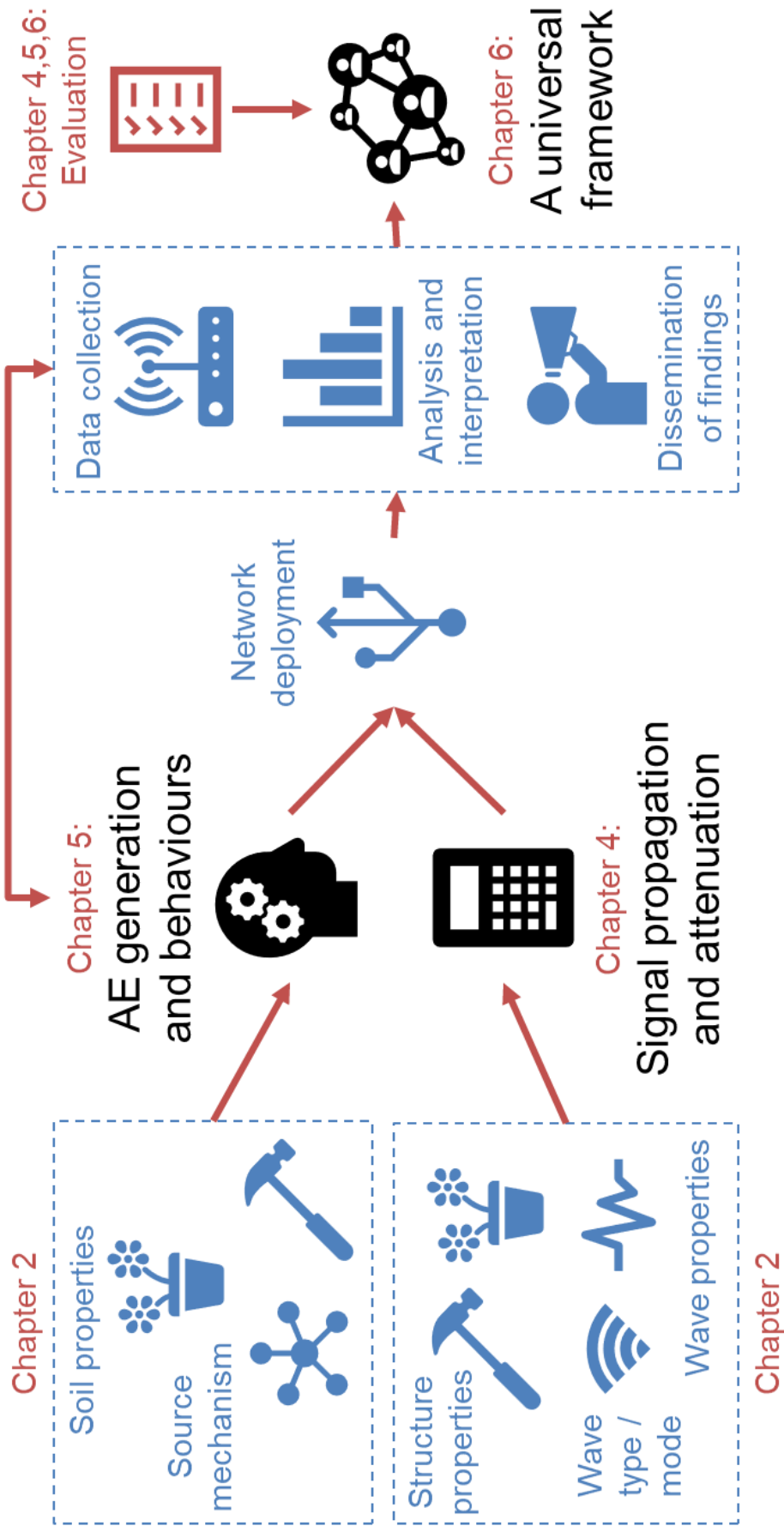


Figure 1.3 The understanding required to develop a framework for understanding soil-steel generated acoustic emissions in buried steel structure systems.

Chapter 2: Literature review

2.0 Literature review

2.1 Background: Deteriorating soil-structure systems

The deterioration and consequent instability of soils, buried structures, and composite soil-structure systems can be influenced by numerous natural and anthropogenic factors. Identifying and studying these factors not only aids in our understanding of the causes behind the deterioration but can also help in the mitigation of associated processes like structural damage and deformation by detecting them in their early stages.

It is known that deterioration within soils can occur as a result of both internal and external changes. These may be natural, such as weathering, or anthropogenic, such as loading. Consequently, there can be multiple deterioration mechanisms and forces involved in deformation.

Terzaghi (1950) summarises this concept with two statements in reference to landslides:

1. External causes result in an increase in shearing stress. These shearing stresses increase along the surface of failure until the time of failure.
2. Internal causes result in a decrease in the shearing resistance of the material.

Brunsdon and Prior (1984) then further this concept by broadly categorising some of the internal and external processes into nine categories:

External processes:

1. Geometrical changes (undercutting, erosion stream incision, artificial excavation leading to changes in slope height, length or steepness)
2. Unloading (erosion, incision, artificial excavation)
3. Loading (addition of material, increase in height, etc.) including undrained loading
4. Shocks and vibrations (artificial, earthquakes, etc.)
 - Associated processes: (a) Liquefaction
 - (b) Remoulding
 - (c) Fluidisation
 - (d) Air lubrication
 - (e) Cohesionless grain flow
5. Drawdown (lowering of water in lake or reservoir)
6. Changes in water regime (rainfall, increase in weight, pore pressure)

Internal processes:

1. Progressive failure (following lateral expansion or fissuring or erosion)
2. Weathering (freeze-thaw, desiccation, reduction of cohesion, removal of cement)
3. Seepage erosion (solution, piping, etc.)

If landslides intersect buried structures (Section AP1.0), soil-structure interactions can cause relative deformations between the soil and structural elements. Relative deformation as a result of soil-structure interactions though, may also be caused by other processes including:

- Differential settlements in soil supporting infrastructure;
- The in-service loading of pile foundations;
- Operating temperature fluctuations causing cyclic axial displacement within pipelines;
- Cyclic axial and lateral loading of offshore monopiles (i.e. resulting from wind and wave action);
- Upheaval buckling of deep-sea pipelines; and
- Lateral earth pressures acting on retaining structures.

The effects of such deformation should not be underestimated. To fully understand the effects however, an understanding of the mechanisms behind such processes and the measurable outcomes of these mechanisms should first be gained.

2.1.1 The effects of deterioration

With buried and surface infrastructure often essential to modern day society, relative soil-structure deformations can be very costly both economically and environmentally. Buried pipes, for example, carry substances including oils, gases and water; The UK Petroleum Industry Association (UKPIA) (2019) states that the 'UK is criss-crossed by a vast network of pipelines' which 'transport over 30 million tonnes of fuels each year', 'equivalent to about one million road tanker journeys'. Similarly, the CLH Pipeline System (CLH-PS) (n.d.) (formally the Government Pipeline and Storage System, GPSS) have pipelines covering 2000 km, transporting over 1 million cubic metres and providing 50% of the UK's aviation needs, whilst DiscoverWater (2018) suggest that there are 343,865 km of water pipeline servicing the country.

DiscoverWater (2018) also state that 3183 million litres of water is leaked from the UK pipe system every day as a result of deteriorated and damaged pipes. Thames Water (2019) suggest that they are investing £1 billion a year into the continual upgrade of water pipes, sewers and facilities in order to improve their networks and reduce leaks. Damages, deterioration, and eventual failure (i.e. serviceability and ultimate limit state) of buried infrastructure can consequently cause a large financial burden, as well as significant environmental damage.

Stein (2004) suggest that there are three overall causes of such infrastructural deterioration:

- When there is a non-adherence to standards and regulations;
- Damages caused during installation (whether in transport, storage, laying, bedding, backfilling, compacting, etc.); and
- The general effects of wear/fatigue with time while in service.

The non-adherence to standards and regulations during the installation of buried structures and the general wear of structures with time can directly influence the deterioration and stability of the burial environment (i.e. soil) as well as the buried structure. Damages caused during installation, however, may not be directly attributed to a degrading environment but can influence its degradation. The health of a buried structure and its burial environment are thus interlinked.

Figure 2.1 for example shows an unstable soil slope and the effect it could have on a utility pipe intersecting it. In Figure 2.1, a slope can be seen to fail where slumped material loads and deforms an intersecting pipe. This can lead to larger problems such as tensile and buckling failures which can cause water or gas leaks, further destabilising the slope and potentially requiring the complete shut-down of a local utility network. If left without intervention, damage can cause a spiral of decline.

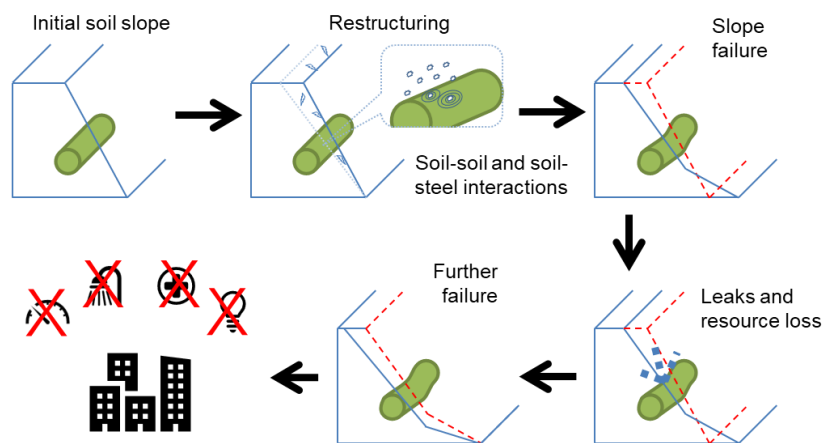


Figure 2.1 The potential effects of utility pipe deformation and damage.

Furthermore, from this example it may also be deduced that the severity and type of damage is an important consideration which may change over time. Additionally, structural materials (e.g. structural reinforcements) and external environments (i.e. their presence and condition) can influence the damage effect (Stein, 2004).

The shape, depth, width, and location of damages should be considered; Damages can range from a slight deformation or corrosion and cutting, to notches, holes, cracks and crack growth as shown in

Figure 2.2. Cracks and crack growth are of particular importance as these can result from tensile stresses during pipe bending, for example, or the differential settlement of a building (Figure 2.3).

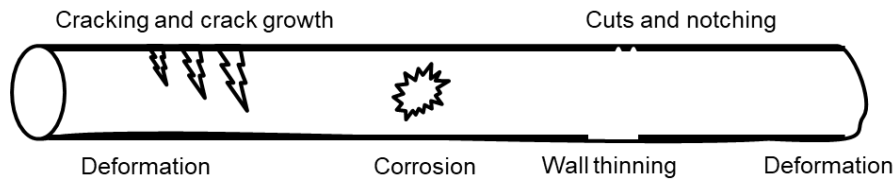


Figure 2.2 Example forms of damage to a pipe.



Figure 2.3 Cracking caused by the differential settlement of a building. Adapted from Geotech (n.d).

Focusing on cracking, Stein (2004) therefore suggests four criteria for monitoring damage severity and the evolution of damage through time:

- Alterations with time: It can be seen from alterations whether the crack has come to rest, is still propagating, or is accelerating.
- Depth: Is the crack only superficial, or does it extend throughout the entire component?
- Course: The course of the crack provides information on the direction of the force acting on it.
- Mutual displacement of the crack edges: This provides information on the direction of the force acting on it as well as the danger of failure.

2.2 Monitoring soil-structure systems

Stability monitoring can provide the information necessary to adequately remediate or eradicate stability related problems faced by current and to-be-built structures and systems through both knowledge and design (Uhlemann et al., 2016). Additionally, monitoring the performance of material infrastructure can provide an understanding on the condition of buried assets and allow for improvements to their system designs to be implemented.

There are numerous methods for monitoring the condition and behaviour of buried infrastructure. These include measuring surface and sub-surface deformation, monitoring temporal and spatial changes in wave propagation, and measuring changes in the water table and internal material stresses. Both Uhlemann et al. (2016) and Smith (2015), however, suggest that no singular method can be employed to fully understand failure and movement mechanisms and instead, various combinations should be used.

A summary of some of the monitoring methods currently in use is given by Smith (2015). The methods are categorised by monitoring area with advantages and disadvantages of relating factors such as the accuracy and resolution of specific instrumentation presented. Uhlemann et al. (2016) similarly detail the use of a suite of different monitoring instruments specifically installed at the Hollin Hill landslide field laboratory. The instruments measure both surface and sub-surface deformations, as well as changes in the ground water. Furthermore, other publications investigate and compare the use of these and other monitoring methods including, but not limited to, non-destructive testing (NDT) (Ghandourah, 2015), AE (Mair et al., 2007, Korkolis and Niemeijer, 2017, Smith and Dixon, 2019), and electrical resistivity (Wilkinson et al., 2016, and Boyle et al., 2017).

Table 2.1 focuses and extends the general summary provided by Smith (2015) to concentrate on the instrumentation and techniques most useful to monitoring deformation and/or damages within soil-structure systems. Additionally, example publications in which further investigations, comparisons or information on the instrumentation and techniques are given.

Table 2.1 The advantages and disadvantages of different techniques and instruments for monitoring buried infrastructure systems.

Techniques and Instruments	Monitoring focus	Advantages and Disadvantages
Non-destructive testing (NDT) (general ultrasonics)	Structural health monitoring	<ul style="list-style-type: none"> ✓ Completely non-invasive technique ✓ High spatial resolution possible with adequate instrumentation ✓ High temporal resolution possible ✓ High sensitivity to small defects ✗ High sensitivity to noise ✗ Access to infrastructure required ✗ Large amount of pre- and post-processing required and therefore relatively high computational effort • Beard et al. (2003), Hesse and Cawley (2006), Shehadeh et al. (2019)
Acoustic emissions (general)	Ground condition and structural health monitoring	<ul style="list-style-type: none"> ✓ The monitoring of vast areas with a high spatial resolution possible ✓ The monitoring of vast areas with a high temporal resolution possible ✓ High sensitivity allowing for quantitative relationships between mechanical behaviours

Techniques and Instruments	Monitoring focus	Advantages and Disadvantages
Acoustic emissions: Slope ALARMS	Ground condition monitoring	<p>and AE generation to be determined and consequently more accurate condition interpretation (i.e. detailed analysis)</p> <ul style="list-style-type: none"> ✗ Local calibration of systems can be required due to material dependence ✗ Large amounts of processing power often required (for detailed analysis) either pre- or post-. ✗ Access to an area required for system installation • Mair et al. (2007), Smith and Dixon (2014), ^aSmith et al. (2014), Korkolis and Niemeijer (2017), Smith and Dixon (2019) ✓ High temporal resolution possible with adequate instrumentation therefore allowing for early warning of slope instability ✓ Comparatively lower cost to other slope monitoring instrumentation ✗ Relatively low spatial resolution in terms of area coverage but can be high for a specific locality. ✗ Local calibration of the system can be required ✗ Access to an area required for system installation • Dixon et al. (2015), ^bSmith et al. (2014), Smith (2015)
Remote sensing (general) (e.g. LIDAR and InSAR)	Ground condition monitoring	<ul style="list-style-type: none"> ✓ Completely non-invasive technique ✓ The monitoring of vast areas with a medium spatial resolution possible ✓ Remote areas can be monitored easily ✓ Relatively high precision (mm to m scales, dependent) ✗ Low temporal resolution dependent on satellite trajectories, picture quality and processing time ✗ Relatively expensive equipment costs ✗ Affected by ground cover (i.e. vegetation)
Electrical resistivity (general)	Ground condition and structural health monitoring	<ul style="list-style-type: none"> ✓ High temporal resolution possible ✓ High spatial resolution possible with adequate instrumentation ✓ Condition dependent – therefore providing additional ground condition information ✗ Low sensitivity with non-unique solutions ✗ Dependable accuracy with the movement of instrumentation • Wilkinson et al. (2016), Boyle et al. (2017)
Strain gauges	Structural health monitoring	<ul style="list-style-type: none"> ✓ High temporal resolution possible ✓ High spatial resolution possible with adequate instrumentation (but low for an individual gauge) ✓ High sensitivity to small changes ✗ High susceptibility to noise

Techniques and Instruments	Monitoring focus	Advantages and Disadvantages
Fibre optics	Ground condition monitoring	<ul style="list-style-type: none"> ✗ Can have a high susceptibility to noisy influences ✗ Access to a structure required • Zand, 2018 ✓ The monitoring of vast areas with a high spatial resolution possible ✓ The monitoring of vast areas with a high temporal resolution possible ✓ Fibre optic cables are relatively cheap compared to other system components. ✓ High sensitivity to small changes in conditions ✗ Calibration with local changes in temperature necessary to accuracy ✗ Large amounts of processing power and expensive machinery (signal analyser) needed ✗ Access to areas required for system installation. • Michlmayr et al. (2017)
Ground Penetrating Radar (GPR)	Ground condition and structural health monitoring	<ul style="list-style-type: none"> ✓ Completely non-invasive technique ✓ Good spatial resolution possible within the study area (spatial resolution can also be changed with different antenna at the data collection stage) ✓ Cheap after initial equipment and software outlays ✗ Generally low temporal resolution ✗ Land access required to conduct surveys. ✗ Large amounts of post-processing and analysis usually required for interpretation ✗ Affected by ground conditions, especially water • Zhang et al. (2014), De Pue et al. (2015)

2.2.1 Acoustic emission monitoring

The first published work regarding AE monitoring in soils was conducted by Beard (1961 and 1962) with the purpose of monitoring slope stabilities (Koerner et al., 1981). Since then, AE monitoring has been investigated by many authors including Cadman and Goodman (1967), Rouse et al. (1991), Holford and Pullin (2007), and ^aSmith et al. (2014) with the methods employed evolving over time.

Koerner et al. (1981) suggest a basic and passive AE monitoring system set up as shown in Figure 2.4. Modern day systems have changed little with Dixon et al. (2003), for example, proposing an 'active waveguide' system (Figure 2.5) (slope ALARM field system) comprising of a waveguide, sensor, and amplification and conversion instrumentation. The design and set up of individual monitoring system components, however, has been refined over time. Dixon et al. (2003) imply that the guide material, geometry (i.e. wall thickness and diameter), connection methods (between guide lengths), and backfill

material will all influence wave propagation and attenuation, and hence measured AE. Furthermore, the sampling frequencies, resonant frequency of sensors, and effects of any filters applied during amplification and/or processing will influence later interpretation.

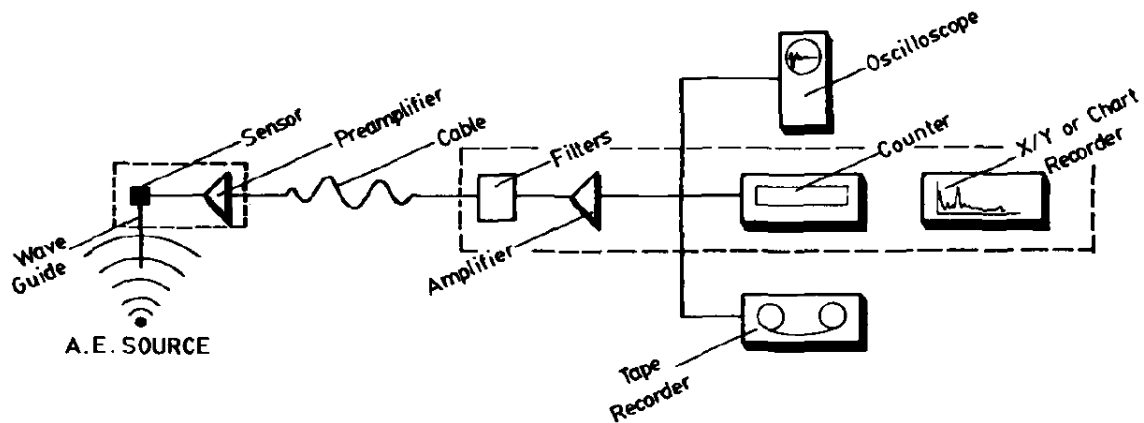


Figure 2.4 A basic single-channel AE monitoring system for recording AE counts and count rates. From Koerner et al. (1981).

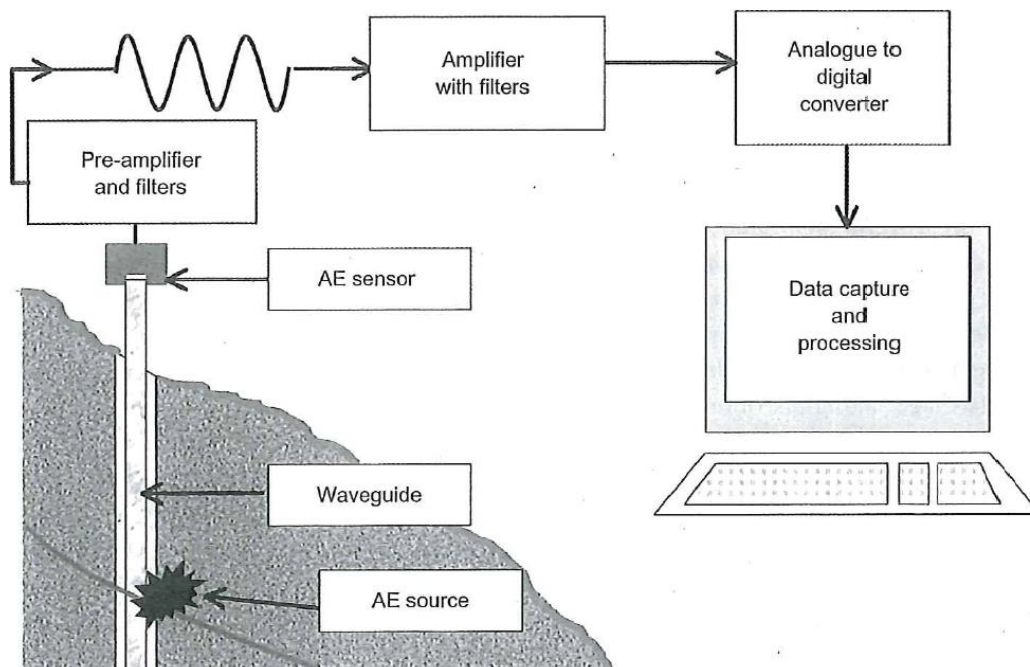


Figure 2.5 Components of a modern-day 'active waveguide' system for passively monitoring AE. From Dixon et al. (2003).

It is not just the monitoring system that is important though, the way in which the AE are recorded (i.e. full waveforms, RDCs, frequency contents) and interpreted (i.e. absolute and/or quantitative values, changes in behavioural trends) also make a difference.

Koerner et al. (1981), for example, observe a measurable difference in the frequency content and RDC rate, with respect to failure (Figure 2.6), of different soils. They therefore suggest a qualitative guide to understanding AE measurements where:

- ‘Soil masses that do not generate AE are probably not deforming and are therefore stable. Such structures are in a state of equilibrium and need not be inspected for a considerable time or until a new loading condition is imposed.’
- ‘Soil masses that generate moderate levels of AE are deforming slightly and are to be considered marginally stable. Continued monitoring is required until such time that the emissions cease or increase to the following condition.’
- ‘Soil masses that generate high levels of AE are deforming substantially and are to be considered unstable. Immediate remedial measures are required that, in the case of earth dams, could be the reduction of reservoir levels or the addition of downstream berms until equilibrium is re-established. It is important to note that if AE monitoring is continued during the time in which these remedial measures are applied, the technique can now function as a measure of construction effectiveness, giving an instant assessment of the remedial measures as they are in progress.’
- ‘Soil masses that generate very high levels of AE are undergoing large deformations and can be considered to be in a failure state. Emergency precautions to assure safety of nearby residents and their personal property should be immediately initiated.’

In this qualitative guide for AE interpretation, behavioural changes are of importance with the general trend of the data indicative of the soil behaviour. The quantitative interpretation of AE measurement would however be dependent on the soil type and conditions (Koerner et al., 1981). This has since been investigated by numerous authors including Dixon and Spriggs (2007), Dixon et al. (2015) and Smith and Dixon (2015).

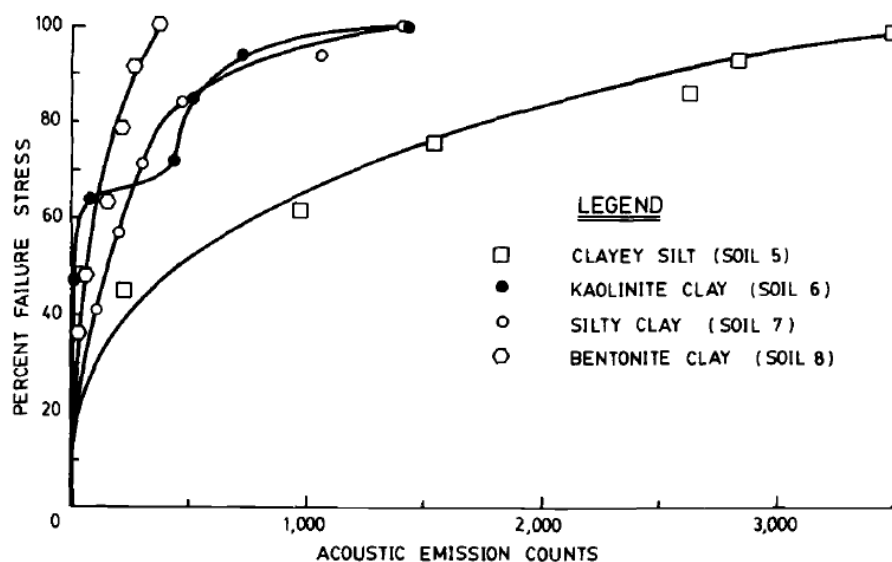


Figure 2.6 Measured cumulative acoustic emission counts with percentage failure stress for four tested soils. From Koerner et al. (1981).

Dixon and Spriggs (2007) for example, quantified slope movements as a function of AE generation rate. They found that rates could be differentiated by an order of magnitude consistent to standard landslide classifications (Appendix 1.0). This is illustrated in Figure 2.7 where RDCs as a result of interactions between a river gravel and steel waveguide are plotted.

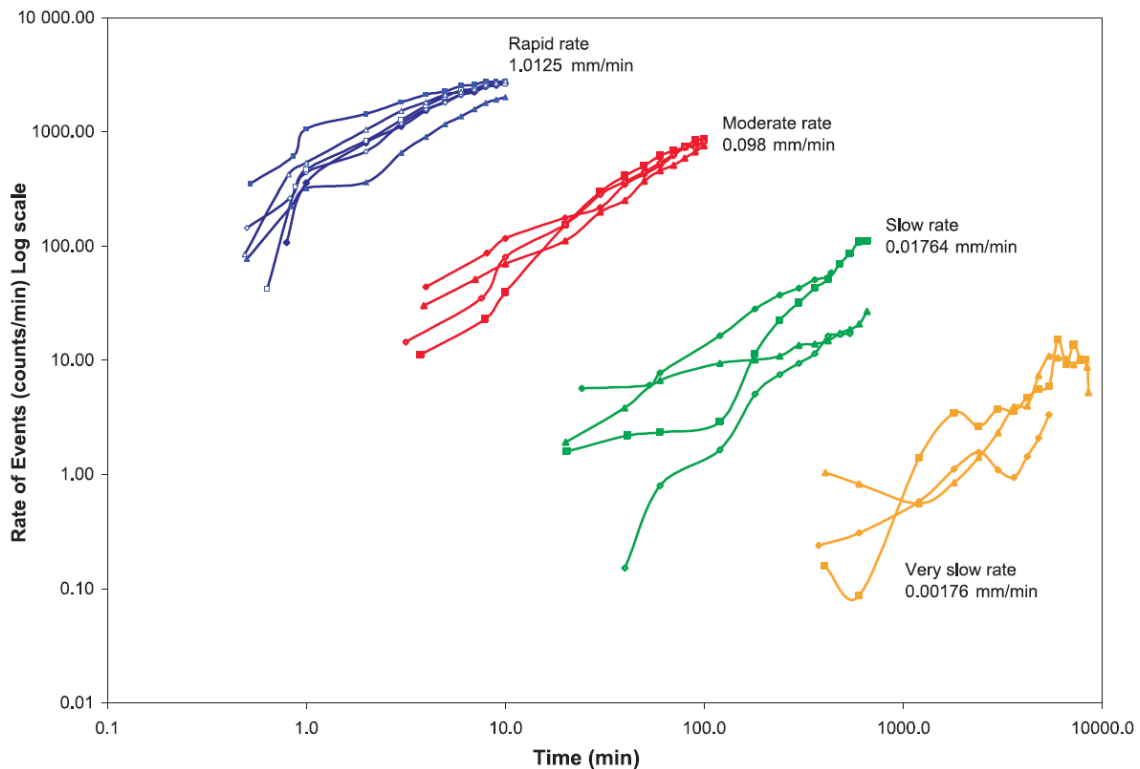


Figure 2.7 The measured relationship between RDC rates (per minute) on a log scale and time for four shearing velocities representing standard qualitative categorisations. From Dixon and Spriggs (2007).

In addition, using Lerouiel's (2001) definition for the four stages of slope failure (Figure 2.8), Smith and Dixon (2015) observed that the 'relationship for both first-time failures and reactivations are expected to increase exponentially with time until a peak velocity is reached, and then subsequently decay exponentially until movement ceases and equilibrium is regained'. This is reflected in AE measurements with Figure 2.9 showing the similar relationships between RDC rate and the velocity of movement with time. From this, Smith and Dixon (2015) were then able to relate AE rates with velocity for the tested soil. Exemplar relationships between AE rates and movement rates are shown in Figure 2.10, which is from 21 shearing tests performed on active waveguides installed inside pseudo-boreholes (Smith and Dixon, 2015) and Figure 2.11, which shows AE rate measurements versus shear strain from three triaxial tests performed on dense sands at the same confining stress level but different axial displacement rates (Smith and Dixon, 2019).

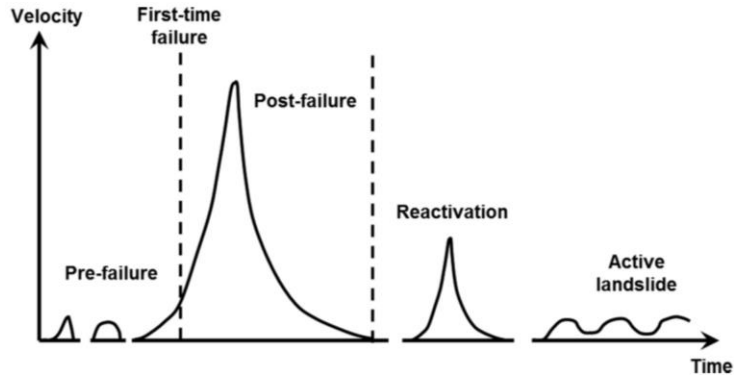


Figure 2.8 The four stages of slope failure as depicted by Lorouiel (2001). From Smith and Dixon (2015).

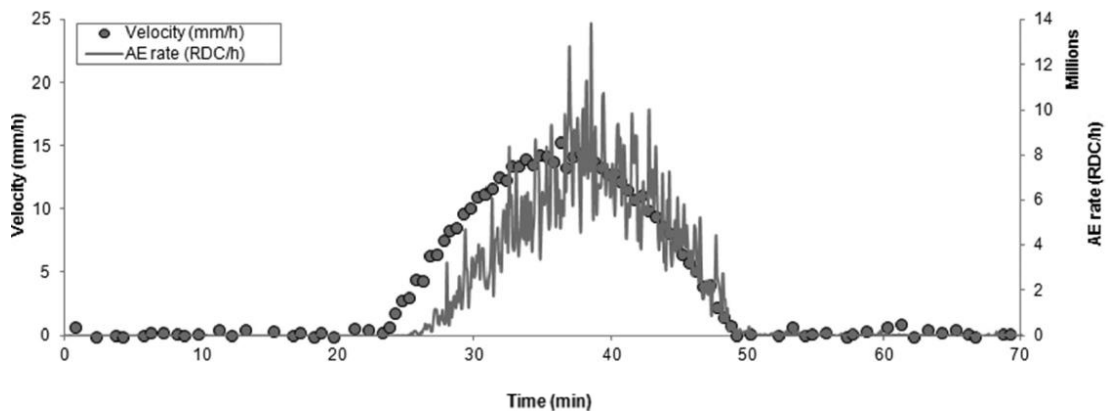


Figure 2.9 The measured relationships between velocity (mm/h) and AE rates (RDC/h) with time. Adapted from Smith and Dixon (2015).

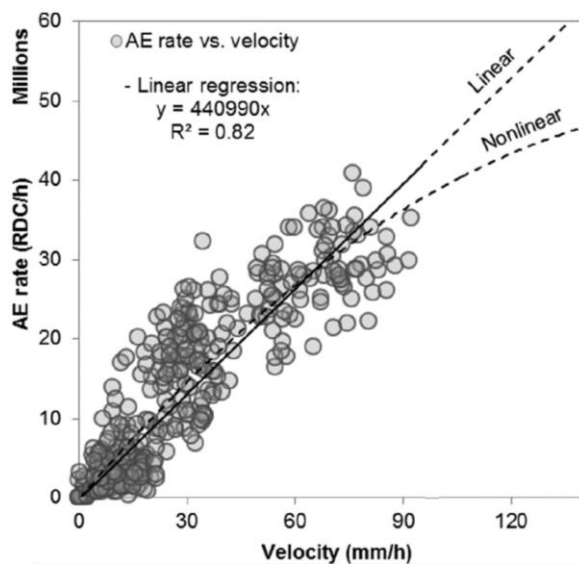


Figure 2.10 Measured AE rate (per hour) as a function of velocity (mm/hour) for 21 large-scale tests. From Smith and Dixon (2015).

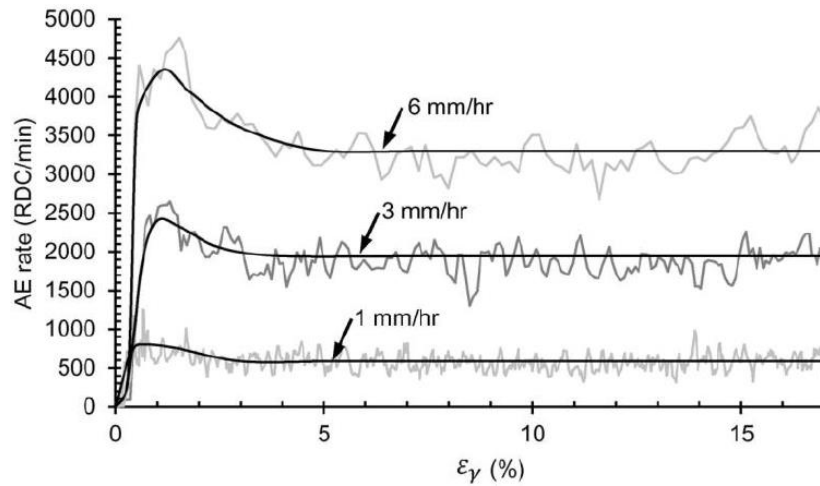


Figure 2.11 Measured AE rate (per minute) with increasing shear strain for three triaxial tests (cell pressure of 300 kPa) at axial displacement rates of 1, 3 and 6 mm/hr. From Smith and Dixon (2019).

2.3 Waves: AE generation in soil-structure systems

AE may be defined as ‘the class of phenomena whereby transient elastic waves are generated by the rapid release of energy by a localized source or sources within a material, or the transient elastic wave(s) so generated’, (ASTM E1316-20, 2000). In buried structure systems, AE is primarily caused by mechanical interactions, or frictional processes, between soil particles with other soil particles (soil-soil), and soil particles with buried steel structures (soil-steel). Other non-frictional processes such as rearrangement and damages, however, can also generate AE.

Jiang et al. (2017) state that AE generating processes are often a result of ‘fluctuations of internal forces’ which release stored elastic energy, the events from which then manifest as high frequency (kHz to MHz) elastic waves, i.e. AE. The processes and interactions, or AE generating mechanisms, are known to occur at a range of scales from grain-grain through to grain assemblages in soil bodies, whilst multiple micro-scale interactions can lead to macro-scale failures (^aMichlmayr et al. 2012, ^bMichlmayr et al. 2012, Naderi-Boldaji et al., 2017).

2.3.1 The influence of soil properties

Steel structures can be buried and embedded in an array of different materials. Rock bolts for example can be driven directly into rock but may also be embedded using epoxy resins (Design Manual for Road and Bridges, 1999). Similarly, utility pipes can be buried directly into the in-situ soil but may also be embedded using a sandy backfill material. The properties of the sandy backfill material, however, can vary significantly from one site to another; particle size and grading, as well as compaction method, can significantly impact the fabric. Moreover, a material’s fabric and stress state can evolve with time due to variations in pore water pressures and external loading.

The properties of a soil govern its acoustic behaviour. Mao and Towhata (2015) for example suggest that a medium's behaviour is dependent on the constituent particle properties such as mineralogy and shape configuration, whilst Smith (2015) states that soil behaviour is also dependent on the overall properties of particle assemblages (i.e. fabric structure, stress history, grading). Furthermore, Noda and Hyodo (2013) and Yamada and Oshima (2016) suggest that the fines content, grain size, and plasticity of a material affect soil behaviours. It may therefore be inferred that acoustic behaviour and AE generation are a result of both the constituent particles (e.g. angularity) and overall soil body properties (e.g. stress history or water content).

AE behaviour within different soils has been studied by a variety of authors including Koerner et al (1981, ^a1984 and, ^b1984), Oelze et al. (2002), Mao et al. (2015), Smith (2015), Yamada and Oshima (2016), and Smith and Dixon (2019). Koerner et al. (^a1984 and ^b1984), for example, found that the stress history of a material is of importance to AE behaviours and were able to determine, within around 10% accuracy, the pre-consolidation behaviours of a soil based on AE. Relatedly, both Mao et al. (2015) and Smith and Dixon (2019) showed that the relative density of soil affects its AE generation (Figure 2.12), whilst Koerner et al. (1981) and Yamada and Oshima (2016) suggest that the grading of a soil, and importantly grain shapes, affect the emissivity (Figure 2.12), amplitude and frequency of emissions (Figure 2.13) which can evolve differently during the failure of a material.

Using this information, Smith (2015) summarises a selection of material characteristics that influence AE behaviour including both particle-scale, and macro-scale (i.e. assemblages of particles) properties (Table 2.2). These factors are not limited to soils though, with the properties also applicable to alternative burial materials such as epoxy, concrete, and rock.

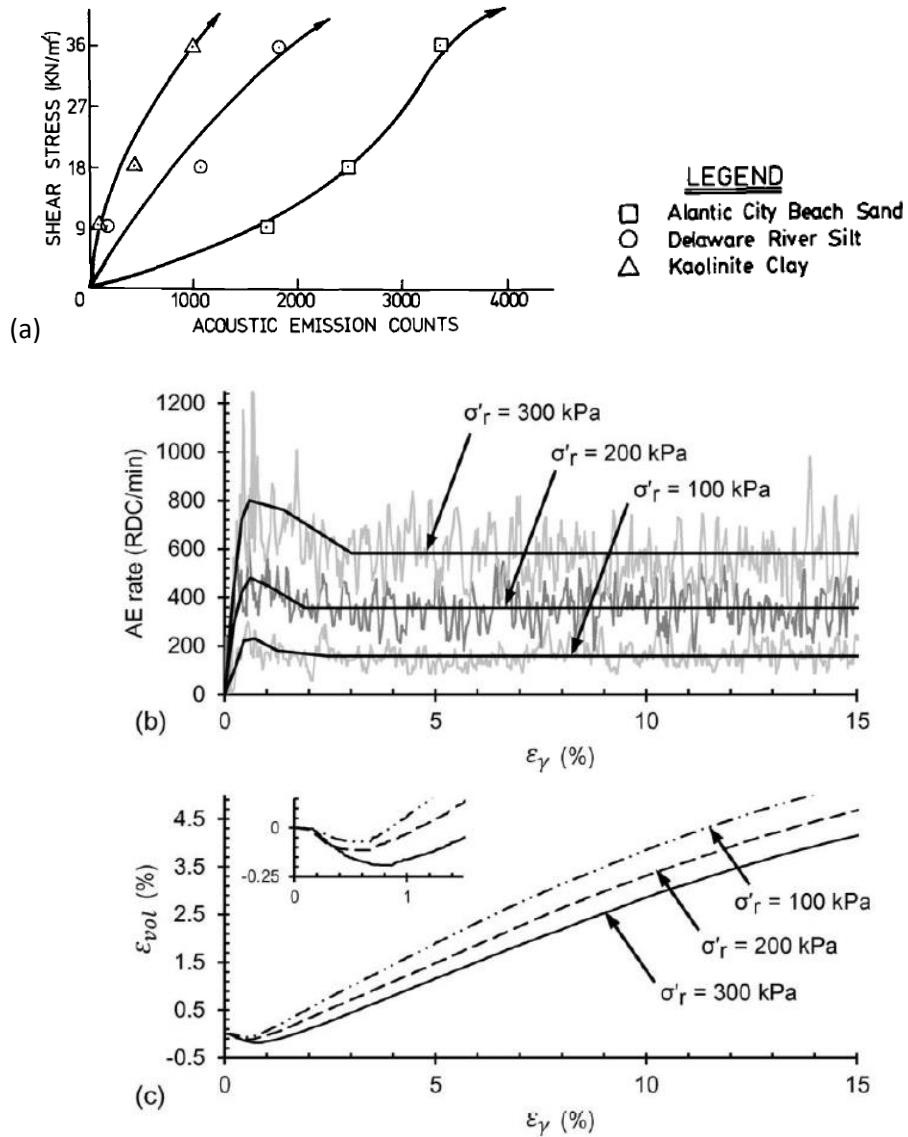


Figure 2.12 Measured (a) stress versus AE behaviour of a sand, silt and clay tested under identical conditions, adapted from Koerner et al. (1981), along with measured (b) AE rates (RDC/min) and (c) volumetric strain (%) with shear strain (%) for drained triaxial shearing tests performed on LBS 1.0-2.0 at effective confining pressures of 100, 200 and 300 kPa and axial displacement rates of 1 mm/hr, from Smith and Dixon (2019).

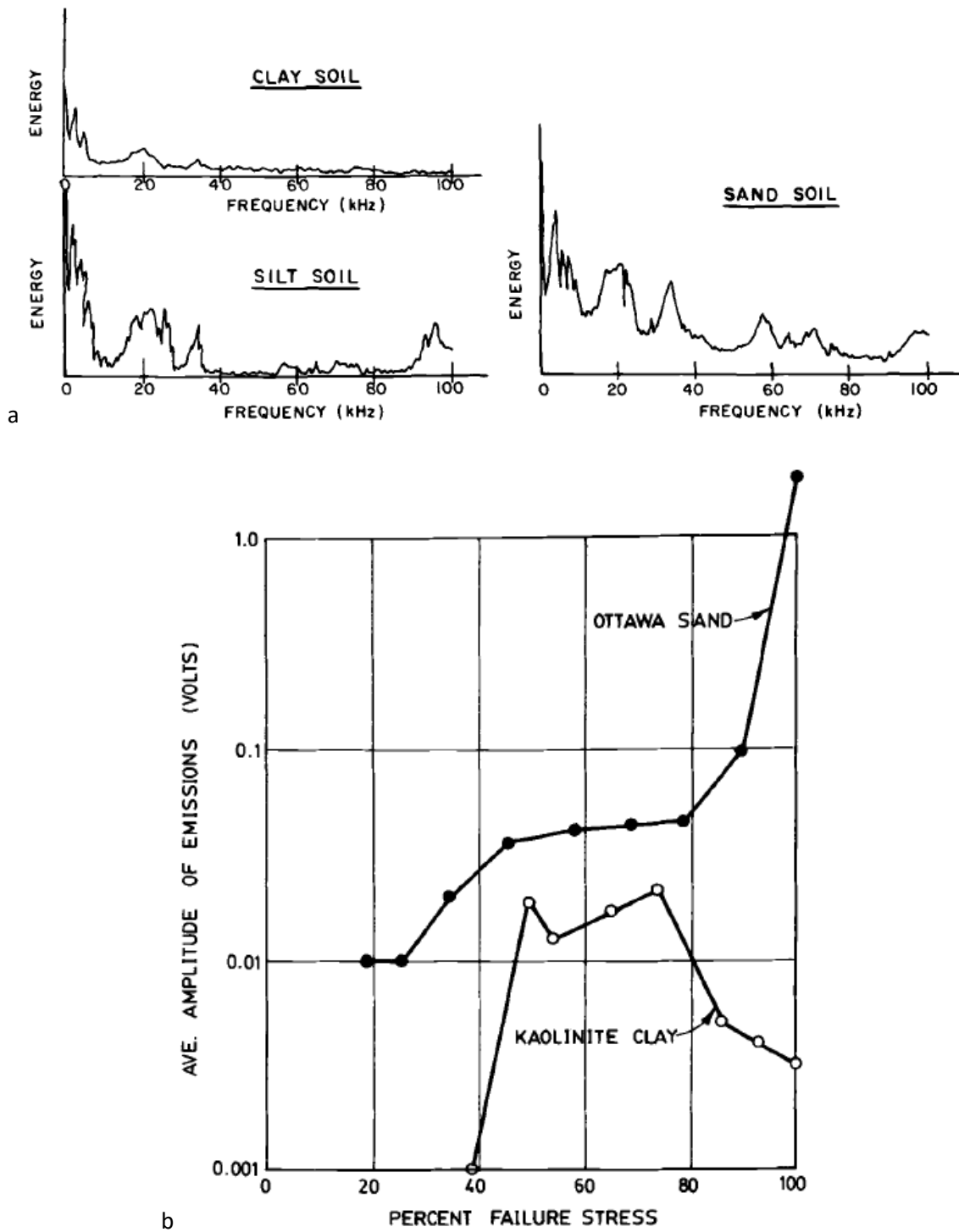


Figure 2.13 (a) The differing measured frequency spectra of sand, silt and clay soils under identical test conditions and nearing failure and (b) the effects of different soils on the evolving amplitude of generated AE. From Koerner et al. (1981).

Table 2.2 The influence on behaviour of soil properties for multiple soil types (Smith, 2015).

	Property	Influence on behaviour
Granular soil	Coefficient of uniformity	Soils with more uniform grading and larger values of coefficient of uniformity produce greater AE. This is because a greater surface area is achieved over which frictional interactions can occur.
	Particle shape	Angular particles generate greater magnitude AE than rounded particles.
Fine-grained soil	Particle size	Soils with larger particles generate AE with greater magnitude than those with smaller particles; however, smaller particles give rise to a greater number of AE events (due to a greater number of particle-particle interactions per unit volume).
	Plasticity index	The higher the plasticity index the lower the AE response of the soil. This is partly due to the higher clay content (i.e. greater proportion of 'quiet' soil grains) found in high plasticity soils. The influence of clay mineralogy is yet to be investigated.
General factors	Water content	The higher the water content, and thus lower the inter-particle contact stresses, the lower the AE response.
	Soil structure	The majority of research has been conducted on remoulded samples and therefore the AE response of samples containing discontinuities (e.g. fissures) has not yet been investigated. It is anticipated that the soil structure will have a significant influence on the AE generated, and therefore understanding the influence of soil structure will be important when interpretation of AE from undisturbed soil is required.
	Stress history	Due to the Kaiser effect*, soils have been shown to exhibit greatly increased AE activity when stress levels exceed the pre-stress/preconsolidation pressure (e.g. Koerner et al. ^a 1984 and Koerner et al. ^b 1984).

*The Kaiser effect is an absence of AE at loads not exceeding the previous maximum load level (e.g. is a clear phenomenon when materials experience repetitive loading)

2.3.2 AE generating mechanisms

Although interest is with soil-steel interactions, rather than soil-soil, it is important to understand the generation mechanisms and consequent signals arising from soil-soil interactions. Within soils, Smith (2015) suggests the two dominant mechanisms behind AE generation are particle-particle interactions and particle contact network rearrangements, whilst other non-dominant mechanisms include the breakage of adhesive bonds, degradation of particle asperities and capillary bridge ruptures. Similarly, Michlmayr (2013) found that there are six major source mechanisms for soil generated AE: liquid bridge rupture, crack development, release of force chains, grain friction, grain cementation fracture and the rupture of soil fibres; these are depicted in Figure 2.14.

Work conducted by Rumpf (1962) on granular bonding also discusses what may be approximated as five bonding mechanisms between soil particles: capillary bridges, inter-molecular forces, electrostatic

forces, solid bridges and closed bonds. Given both Smith (2015) and Michlmayr (2013) suggest the breaking of several of these bonds to produce AE, it may be assumed that the breakage of any of these bonds are AE generating.

Combining these three works, eight AE generating mechanisms can therefore be concluded as a result of soil-soil interactions, although bond breakages are only relevant to bonded soils. Table 2.3 compares and synthesises these, also providing a standard terminology describing each which will be used hereafter.

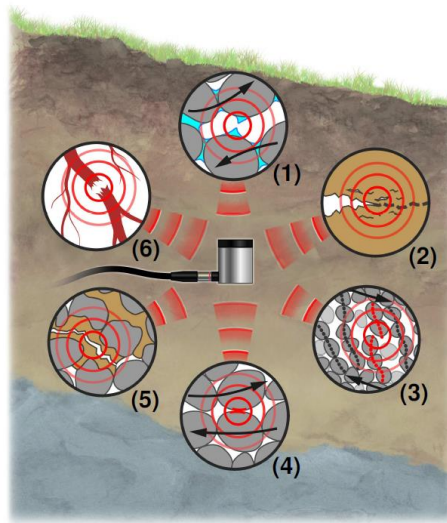


Figure 2.14 The proposed source mechanisms for AE generation in geological materials. Showing: (1) liquid bridge rupture, (2) crack development, (3) release of force chains, (4) grain friction, (5) grain cementation fracture, and (6) rupture of soil fibres (Michlmayr, 2013).

Table 2.3 Proposed AE generating mechanisms within soils, and standard terminologies for each, from combined literature.

AE generating mechanisms	Smith (2015)	Michlmayr (2013)	Rumpf (1962)
Capillary bridge breakage	Capillary bridge rupture	Liquid bridge rupture	Capillary bridge breakage
Adhesive bond breakage	Adhesive bond breakage	Grain cementation fracture	Solid bridges
Grain friction	Particle-particle interactions	Grain friction	Closed bonds
Force chain rupture	Force chain rupture	Release of force chains	-
Soil (e.g. root) fibre rupture	-	Rupture of soil fibres	-
Crack development (within a soil mass)	-	Crack development	-
Inter-molecular force severing	-	-	Inter-molecular force severing
	-	-	Electrostatic force severing
Asperity breakdown	Degradation of particle asperities	-	-
Soil-structure interactions (all interaction types)	-	-	-

Of the eight mechanisms suggested, the severing of inter-molecular forces should intuitively produce the smallest AE in terms of energy content. Inter-molecular forces (Figure 2.15) are very weak atomic attractions between individual particles that provide true cohesion within a soil (Rumpf, 1962). Attraction is caused by either electrostatic or Van de Waals forces. Rumpf (1962) estimated theoretical values of Van der Waals forces to be in the order of 1×10^{-20} kg/cm², whilst electrostatic forces are around 1×10^{-5} kg/cm². These are very weak and, although their influence on grain behaviour is of importance, it is reasonable to assume that inter-molecular force breakage has a negligible effect on measurable AE production.

Capillary bridges (Figure 2.15) on the other hand, are liquid bridges connecting two or more grains in partially saturated soils as a result of meniscus forces providing apparent cohesion. The bridges create capillary forces between grains, which Scholtès et al. (2009) found to be distributed homogeneously throughout a medium. This finding agrees with the work of Rumpf (1962) on free-bridges but not viscous binders. It can therefore be inferred that the force distribution is dependent on the involved liquid type and content which then affects the distribution of generated AE.

Similarly, adhesive bonds connect two or more grains with a solid material bridge; they may also be referred to as solid bridges for which Rumpf (1962) suggests the existence of five formation processes:

- Sintering (where heat and pressure causing solidification without melting)
- Chemical reactions
- The melting of extremities and the outer surface of particles (this can create molten bridges which then solidify to create connections)
- Inorganic bonding agents (these can create liquid bridges which then solidify to form solid connections)
- Mineral crystallisation (dissolved materials can crystallise and create solid bonds between particles, such as with mineral veins within rocks)

Mishra and Thornton (2001) argue that capillary bridges are stronger than adhesive bonds, lasting longer and generating higher energy AE. Wang and Santamarina (2007) however suggest that capillary bridge breakages provide a very low energy loss. Regardless, the breakage of both types of bonds occurs when an imposed strain exceeds their elastic thresholds (Wang and Santamarina, 2007); Mishra and Thornton (2001) suggest that this produces measurable AE outputs.

Overcoming the elastic threshold by an imposed strain is also the time definition for frictional forces gaining dominance between two resistive objects (e.g. granular particles, or particle at a steel surface). In terms of friction generated AE, there are two types: rolling and sliding, although for AE

measurements Lord and Koerner (1974) suggest that sliding friction is more important. A frictional force may be defined as a resistive force between two surfaces moving across one another. For sliding friction, this is a transverse movement, whilst for rolling it essentially a torque opposing the relative rotation between two contacting spheres (Zhou et al., 1999).

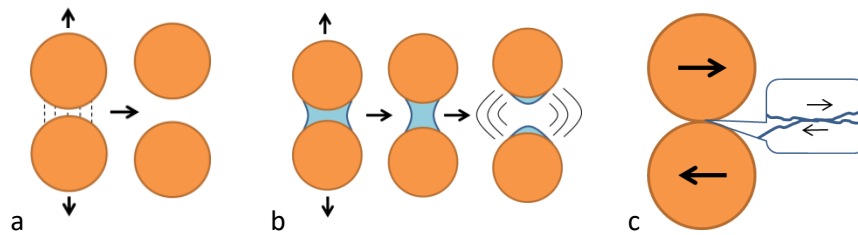


Figure 2.15 Diagrams showing some of the different grain-grain interactions potentially producing AE events. (a) Intermolecular force rupture. (b) Capillary bridge breakage. (c) Sliding friction.

As suggested, frictional forces become relevant when an imposed strain exceeds the elastic threshold (i.e. resistive forces). The magnitude of friction is dependent on the grain contact, something McLaskey and Glaser (2011) describe as an ‘ensemble of μm -scale contacts’ collectively forming a contact area. This contact area may then be expressed using the non-linear Hertzian contact law (Equation 2.1) assuming frictionless, and therefore apparent, contact:

$$F = \frac{4}{3} R^{\frac{1}{2}} \frac{E}{1-\nu} \delta^{\frac{3}{2}} \quad [2.1]$$

where: F is the force (N), R the effective particle radius ($1/R_1 + 1/R_2$ where R_1 and R_2 are the radii of the contacting spheres) (m), E Young’s modulus (GPa), ν Poisson’s coefficient, and δ the change in deformation.

The Hertzian contact law has numerous implications for the understanding of acoustic wave behaviours (^bMichlmayr et al., 2012), including propagation (Liu and Nagel., 1992, Coste and Gilles, 1999). Logically, higher Hertzian contact (i.e. higher particle contact areas over which frictional forces may exist) will result in higher AE generation. Its validity has however been challenged by both Chai et al. (2014), Coste and Gilles (1999) who were only able to confirm the law to hold at high frequencies. This is of little consequence to buried structure systems though as the AE is known to be higher frequency (>10 kHz) (Michlmayr et al., 2013, Smith and Dixon, 2019).

Hertzian contact between grains is also important to the stick-slip behaviours (i.e. rearrangement) observed within granular materials. Slip behaviour results from slipping contacts, slips occurring when the inter-particle Coulomb friction is overcome, and the boundary can therefore move freely. Stick behaviour on the other hand, describes sticking contacts which are below their Coulomb friction or

interlocking (i.e. there are other non-frictional forces and moment resistance provided by surrounding particles).

Grain contacts are constantly changing between slipping and sticking dependent on both the forces being exerted on them and the fabric of the material. Furthermore, the number of contacts can also change. For example, dense and interlocked granular materials may experience dilation during shearing, reducing the number of grain contacts and forming shear zones in which strain is concentrated. Loose materials on the other hand, experience contraction and create more contacts. Nevertheless, as a material approaches failure there is a clear increase in micro-slip events and the number of slipping contacts (Ferdowsi et al., 2013, Johnson et al., 2013, Korkolis and Niemeijer, 2017) with McLaskey and Glaser (2011) relating AE formed from a multitude of discrete slip events usually lasting 1 μ s. It may therefore be inferred that slipping contacts result in frequent but small energy events.

Welker and McNamara (2011) however suggest that the exact number of sticking or slipping contacts is not of importance, instead the spatial and temporal patterns of contact numbers govern stability. At a small-scale, this observation relates to coordination numbers which depict the number of contacts per particle and therefore relate to density. Coordination numbers are consequently important to dilation and contraction behaviours with shearing, as previously implied.

As an influence to AE, McLaskey and Glaser (2011) found that the spatial density of surface contacts affects the production of emissions, whilst both Korkolis and Niemeijer (2017) and Welker and McNamara (2011) observed that there was a presence of highly concentrated AE groups, potentially indicating local variations, within their experiments. Additionally, Majmudar and Behringer (2005) and Staron et al. (2006) identified anisotropy in the development of force chains and grain contact behaviours during arising instability. Staron et al. (2006) suggest that friction may therefore be expressed as multiple localised coefficients of friction within the fabric of a material.

Both Korkolis and Niemeijer (2017) and Zigone et al. (2011) also found that inhomogeneous spatial evolution of grain contacts is non-random. Both Majmudar and Behringer (2005) and Staron et al. (2006) agreed, observing that contact orientations follow the principal stress direction (Staron et al., 2006), and clusters of critical contacts (at the boundary of stick-slip behaviour) grow as a result of local perturbations propagating through neighbouring contacts. These behaviours occur at both small and large scales with clusters originating in areas of locally low friction. It can therefore be concluded that friction plays an important role in the development and rupture of force chains.

Force chains occur as highly stressed contacts align to the direction of the principal stresses and form pillars of strongly loaded grains. The pillars then affect stress transmission and distribution within a medium (Michlmayr, 2013). This implies that force chains predominantly occur in materials undergoing shear. Majmudar and Behringer (2005) however state that force chains can be correlated over shorter ranges, regardless of direction, and in systems undergoing isotropic stress too. The rupture of force chains produces relatively infrequent but significant AE events in sheared systems, and infrequent but weak events in systems undergoing isotropic stress. In either system however, force chain ruptures represent considerable granular restructuring of a permanent nature (Korkolis and Niemeijer, 2017).

The final AE mechanism identified within Table 2.3 is asperity breakdown and grain crushing. Grain crushing and asperity breakdowns are the development and propagation of micro-fractures within a singular grain and the subsequent fragmentation of grains and their asperities. Understandably, poorly rounded and angular grains with low particle density and strength are more susceptible.

Experiments conducted by Korkolis and Niemeijer (2017) found that there was no 'significant particle size reduction' of the material used (soda-lime glass beads) under 2 MPa, however under 5 MPa around 47% of the material, by weight, maintained its original size with significant particle size reduction therefore occurring. This suggests that grain crushing and asperity breakdown only occur in late stage and significant deformation. Given these observations, the mechanism is likely one of the last to occur before the ultimate failure of a body. Other studies such as by Mao and Towhata (2015) used singular grains under significant loading to further study and understand the processes. From these it may be concluded that asperity breakdowns and fragmentation cause relatively strong AE events, compared with other grain scale interactions, that are high frequency (>100 kHz). They may also be considered to occur in the plastic deformation stage along with crack development.

Various studies suggest that there is a sequential structure to the occurrence of the different AE mechanisms discussed during material deformation. Under soil loading for example, Zhang et al. (1990) found that there are two stages of AE production: a creep stage (compaction creep), and a crushing stage, which are separated by AE activity. Mao and Towhata (2015) however considered there to be three stages: a grain densification stage, an elastic deformation stage, and a plastic deformation stage; although these are for the loading of a singular grain rather than soil body. Similarly, for the destabilisation of rock bodies, Montoto et al. (1984) concluded that there were three stages of AE: inner modifications, elastic redistribution, and plastic deformation. This three-stage concept is also adopted by He et al. (2010) to explain observed AE behaviours. Table 2.4 provides a comparison of all three sequences.

Table 2.4 Comparing distinguishable stages of compression-based destabilisation for: granular media, rock and, singular particles; and their observed AE characteristics, proposed by different authors.

Author	Suggested stages of destabilisation	Observed AE characteristics	Suggested (and implied) AE mechanisms involved
Zhang et al. (1990) (soil body) (increasing pressure)	1. Creep	Minority < 10 kHz	Friction
	2. Crushing	Majority	Asperity breakdown and fragmentation
Mao and Towhata (2015) (singular grain)	1. Grain densification	High rate Low amplitude Low frequency (52 kHz)	Granular restructuring Friction Inner crack readjustment
	2. Elastic redistribution	Inactive rate	-
	3. Plastic deformation	Substantial rate High amplitude High frequency (210 kHz)	Crack growth and propagation Asperity breakdown and fragmentation
Montoto et al. (1984) and He et al. (2010) (rock)	1. Inner modifications (balancing period)	High rate Low amplitude High frequency (170-190 kHz)	Crack closures in rock Friction
	2. Elastic redistribution	Weak rate	-
	3. Plastic deformation	High rate High amplitude Low frequency (60-100 kHz)	Growth and coalescence of cracks Asperity breakdown and fragmentation

A definitive comparability between the sequences can be identified, despite being proposed for different media and on different scales. Of the three authors compared, two conclude there to be three distinguishable stages of AE behaviour during destabilisation: material restructuring, plastic deformation, and plastic/brittle deformation. The observed behavioural characteristics within each stage are however contradictory leading to a secondary observation: the significance of different AE generating mechanisms may vary dependent on the material. For example, although it is agreed by all three authors that the first stage of AE (material restructuring) involves frictional mechanisms, Mao and Towhata (2015) characterised the AE as relatively low frequency (<52 kHz). Montoto et al. (1984) however suggest characteristic frequencies of 170-190 kHz, which are much higher.

2.3.3 Characterising AE

To determine the stability state of a material, an ability to distinguish between AE mechanisms, AE based stability stages, and/or related behaviours is required via signal characterisation. Signal characterisation can be done using numerous signal properties including frequency, amplitude and wave energy, ring down counts (RDC), wave shape(s) clustering, and directionality. Additionally, further properties such as b-values may be calculated from collected data.

Frequency characterisation is popular within literature (e.g Table 2.4) with other characterising properties, such as amplitude, often becoming distorted during propagation and therefore unreliable. Dixon et al. (2003) and ^bMichlmayr et al. (2012), for example, suggest that AE signals can be highly attenuative dependent on the material in which they are propagating, as well as subject to contamination from other sources. Table 2.5 provides a summary of some of the measured characteristic frequencies for various AE mechanisms. These have been compiled from multiple authors using a range of experimental and analytical processes and include both granular and non-granular sources.

The table shows that recorded frequencies for different AE mechanisms can range in value and suggests that they may be distinguishable using the property. Singular AE generating mechanisms (i.e. grain friction), however, have also been observed to generate a variety of frequencies suggesting the frequencies generated may be dependent on numerous factors, not just the generation mechanism. Additionally, factors such as instrumental bias (i.e. the resonant frequencies of sensors) should, for example, be considered whilst pre- and post-data processing methods may also affect results.

Table 2.5 AE sources and their measured characteristic frequencies for both granular and non-granular media. Taken from a range of authors as stated.

Source mechanism	Proposed characteristic frequency (kHz)	Reference(s)
Adhesive bond breakage	100	Read et al. (1995)
Asperity breakdown (and crushing)	210	Mao and Towhata (2015)
	137	Mao et al. (2016)
Capillary bridge breakage	-	-
Grain friction (rolling and sliding) (slip and grain collision)	10-20	Cody et al. (1996)
	20-80	Jiang et al. (2007)
	<10 (grain-steel)	Gardel et al. (2009)
	40-60 (salt)	Zigone et al. (2011)
	30-80	Michlmayr et al. (2013)
	40	Johnson et al. (2013)
	52	Mao and Towhata (2015)
	90-100 (glass)	Doanh et al. (2017)
	4-40	Mao et al. (2016)
Fluid flow (in pipes)	50-150	Fang et al. (2013)
Pressurised fluid leakage (from pipes)	0-400 (dominant at 150 and 300)	Mostafapour and Davoudi (2013)
Fluid seepage	0.8-10	Hung et al. (2009)
	0.8-10	
Force chain rupture (and particle network rearrangements)	<20	Michlmayr et al. (2013)
Matrix microcracking (crack initiation)	0-50 (plastics)	Gutkin et al. (2011)
	>300	Aggelis et al. (2011)
Matrix cracking (crack propagation)	100-600	Read et al. (1995)
	50-150 (plastics)	Gutkin et al. (2011)
	120-150	Aggelis et al. (2011)

Despite these uncertainties, the general characterisation of frictional mechanisms is still possible. Using frequency characterisation, Michlmayr et al. (2013) found that high frequency AE events (30 to 80 kHz) were continuously generated throughout their experiment whilst low frequency AE events (<20 kHz) were episodic and correlated to stress jumps within the material. They therefore concluded that higher frequency AE events were a result of small-scale grain-grain interactions, and lower frequency AE events related to larger structural scale interactions.

Similarly, Mao et al. (2016) reported comparable findings using amplitude characterisation where significantly more low amplitude AE events than high amplitude AE events were measured during pile penetration tests. Using these findings, it may therefore be concluded that low amplitude, grain scale events contain relatively high frequencies and occur frequently whilst larger structural interactions produce lower frequency, less frequent, and higher amplitude events.

Extending these observations, Mao et al. (2016) and Mao and Towhata (2015) also found the dominant frequency created by two particles sliding against one another (i.e. sliding friction) is centred around 52 kHz whilst the presence of higher frequencies is practically negligible. Relatedly, Zigone et al. (2011) found that low amplitude, frictional and tremor like signals contain frequencies between 40 and 60 kHz. Interestingly though, Zigone et al. (2011) suggest that the tremor like signals occurred systematically before slip events with Michlmayr et al. (2017) similarly observing a significant acceleration in the rate of AE activity preceding failures. AE rates (i.e. RDCs) may therefore be used as a signal characterisation tool.

This concept was investigated by Smith and Dixon (2019) who found that AE activity is proportional to imposed stress levels, strain rates, fabric coordination numbers and work done by boundary stresses. Changes in these factors can result from environmental changes such those discussed in Section 2.1. Figure 2.16 for example shows the relationship between rainfall, displacement and cumulative RDCs with time. These AE measurements were obtained from an active waveguide installed through a reactivated landslide in North Yorkshire, UK. The periods of rainfall caused periodic elevation in pore-water pressures, which caused the slope to move. The measured shear surface displacement and AE activity show comparable behaviour.

Moreover, Smith and Dixon (2019) show that b-values (calculated from full waveform amplitude data) can be used to illustrate similar relationships (Figure 2.17). When a waveform is dominated by low-amplitude events, such as with tremor like signals, the b-values are high. When the proportion of higher amplitude events then increases, indicating increasing energy release, the values then decreases (Smith and Dixon, 2019). This is not surprising as Lockner (1993) suggests that 'a close analogy exists between the AE activity during failure of soil and other geologic materials and the

natural seismic activity within the Earth's crust'. Additionally, Smith and Dixon (2019) developed an interpretation framework demonstrating how AE measurements could be used to identify the transition from contractive to dilative behaviour, the mobilisation of peak shear strength, and quantify accelerating deformation behaviour that typically accompanies shear zone development in dense soil bodies (Figure 2.18).

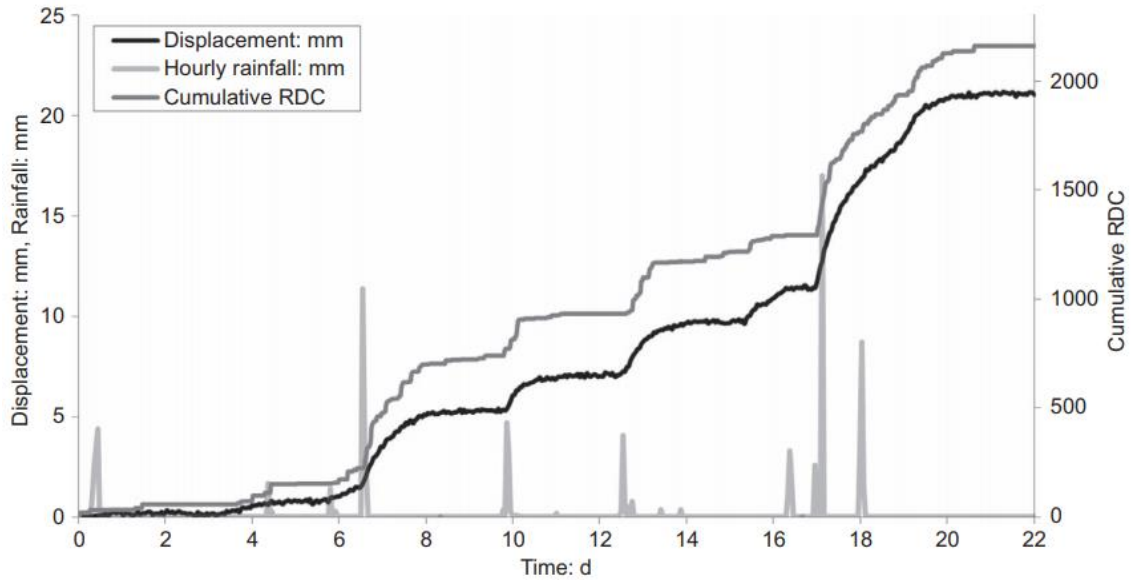


Figure 2.16 Measured relationships between displacement (mm), rainfall (mm) and cumulative RDCs as a function of time at cluster 3 at the Hollin hill landslide field laboratory. From ^aSmith et al. (2014).

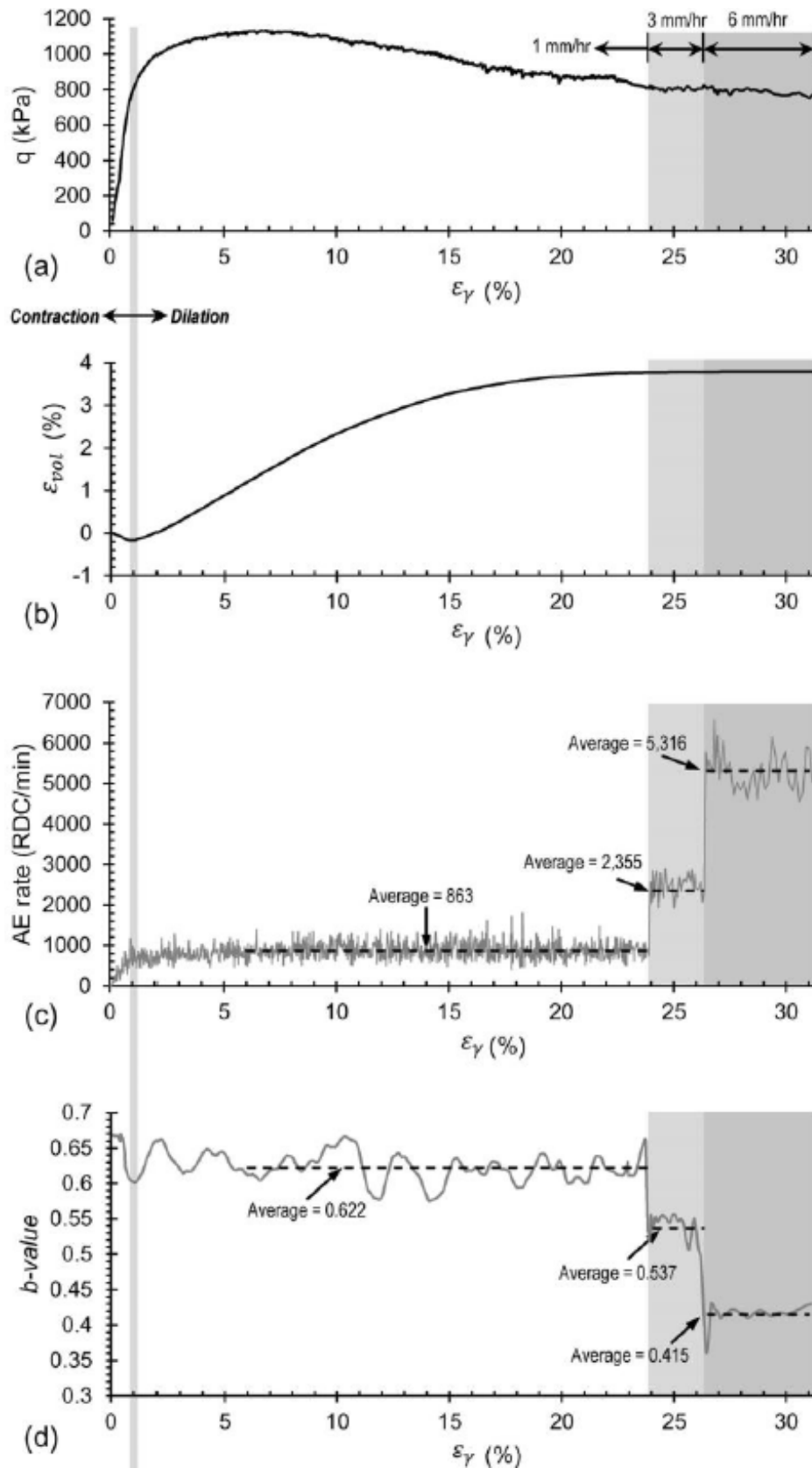


Figure 2.17 Deviator stress (kPa) (a), volumetric strain (%) (b) (dilation shown as positive), AE rate (RDC/min) (c), and b -value (d) measurements versus shear strain (%) from a drained triaxial shearing test performed on LBS 0.25-3.35 at an effective confining pressure of 300 kPa and axial displacement rates of 1, 3 and 6 mm/hr (Test 15). Adapted from Smith and Dixon (2019).

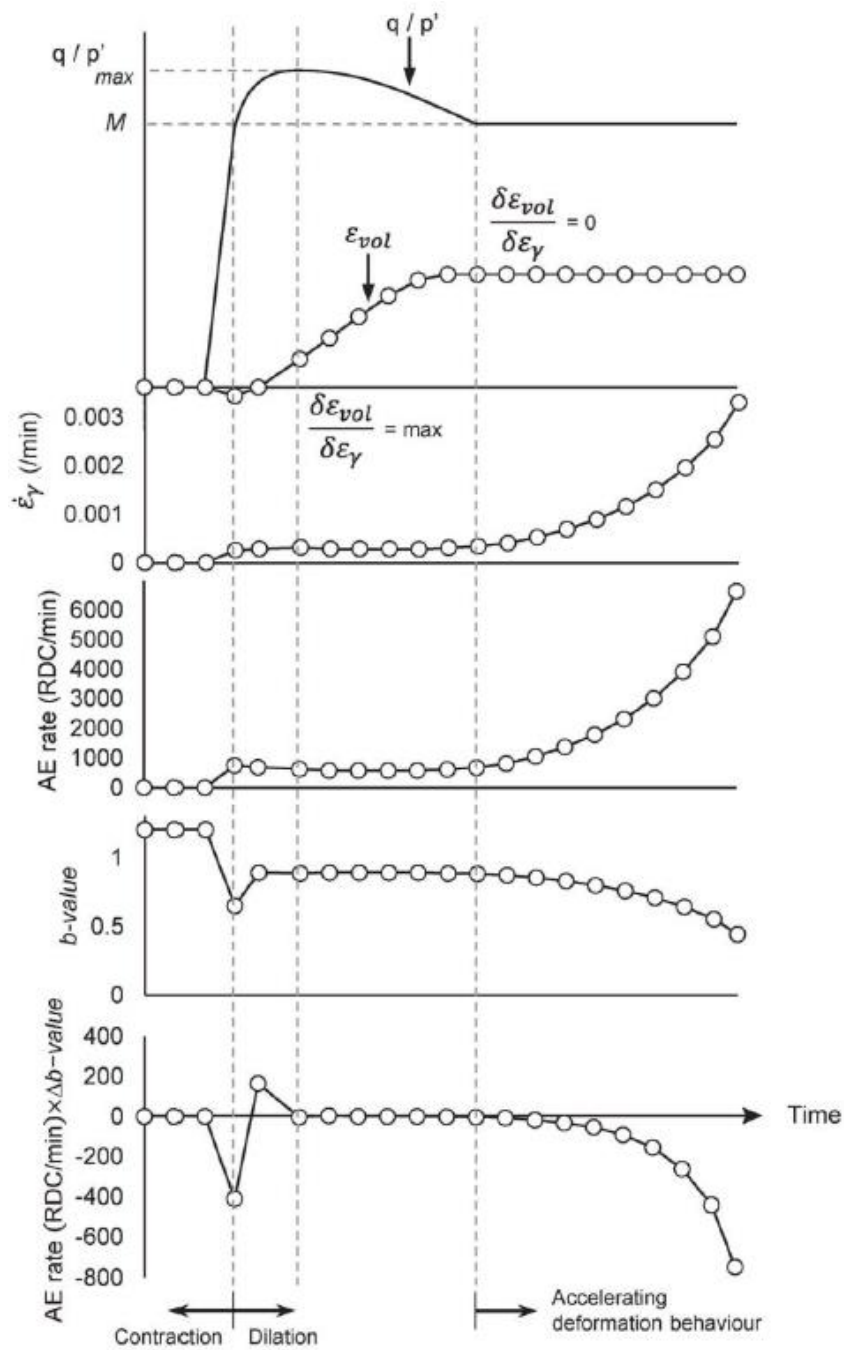


Figure 2.18 'Example use of AE for interpreting pre- and post-peak shear strength mobilisation and accelerating deformation behaviour. The example is based on measurements from LBS 1.0-2.0 at an effective confining pressure of 300 kPa'. From Smith and Dixon (2019).

2.4 Waves: AE propagation and attenuation in soil-structure systems

AE propagates as waves. The ^aOxford dictionary defines a wave, with respect to physics, as ‘a periodic disturbance of the particles of a substance which may be propagated without net movement of the particles, such as in the passage of undulating motion, heat or sound’. The term ‘wave’ is however broad and may be broken down into multiple categories and sub-categories classifying the different wave forms, types and behaviours found in nature. This is necessary in order to further understand the propagation and attenuation behaviours of the waves resulting from generated AE.

2.4.1 Wave forms

Three major types of wave exist: matter, electromagnetic and mechanical. Matter waves are only found in singular electrons or particles, whilst electromagnetic waves are disturbances within electric and magnetic fields and may travel through a vacuum. Mechanical waves however, for which AE may be classified, are particle displacement patterns requiring a medium in which to propagate.

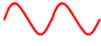
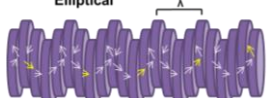


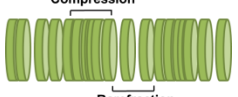

AE propagation therefore occurs as energy is transferred between particles within a medium. The mechanical waves can propagate in three ways: transient, harmonic and standing. Transient waves refer to single signal pulses propagating through a material, also known as travelling waves. Transient waves should not be confused with harmonic waves, which are steady state rather than pulsed. This is also opposed to standing waves which do not travel and are instead fixed between nodal points. AE may generally be assumed as transient in form.

Alongside the different forms of propagation, mechanical waves may additionally be distinguished dependent on where they propagate within a material, their particle motions, and in some cases the material in which they will propagate.

In terms of locational propagation, there are three types of wave: bulk, or body waves; surface waves; and plate waves. Body waves, such as the primary and secondary waves often referred to in seismology, travel through a whole material. Surface waves, however, only travel on or along the surface of a material. Similarly, plate waves travel through materials which are only a few wavelengths thick.

Given the range of waves that exist, Table 2.6 describes and defines some of these in more detail whilst Figure 2.19 provides an overview of how the different levels of mechanical wave classification relate to one another.

Table 2.6 A summary of mechanical wave types and waveforms.

Abb.	Term	Definition
-	Bulk (body) wave 	Bulk, or body, waves travel through the bulk of a material and therefore within a material’s body rather than at or on its surface. Bulk waves can be shear or longitudinal. They do not occur in plates (the definition of a plate being relative to the wavelength).
-	Elliptical wave 	Elliptical waves have a rotational particle motion with respect to axes perpendicular to the direction of propagation. They are consequently a cross between longitudinal and flexural waves.
-	Flexural (shear) wave 	Sometimes known as secondary or shear waves, flexural waves have particle motions which are left and right (or up and down) with respect to the propagation direction. Shear waves can only travel through solids or materials that have a high enough shear strength.
S, S _H or, A	Lamb wave 	Lamb waves are also known as plate waves and propagate in whole layers up to a few wavelengths thickness. This is opposed to surface waves which only propagate within the first few wavelengths thickness of a larger body. Lamb waves may also sometimes be referred to as normal modes for which there are three forms: S, S _H , and A. S waves have symmetric, and A waves are have asymmetric movements.
-	Longitudinal (compressional) wave 	Sometimes known as primary or compressional waves, longitudinal waves have particle motions going forwards and backwards with respect to the propagation direction. Respectively, these movements create compressions (dense areas of particles) and rarefactions (less dense areas of particles) during propagation.
-	Love wave	Love waves are asymmetric surface waves that propagate with particle motions perpendicular to the direction of travel but aligned to the surface.
-	Plate wave	See Lamb wave.
-	Rayleigh wave	Rayleigh waves are surface waves that propagate at solid-free boundaries. They have an elliptical, retrograde particle motion.
-	Scholte wave	Scholte waves are surface waves that can form at the boundary of solid-liquid half-spaces. They have elliptical, retrograde particle motions.
-	Stoneley wave	Stoneley waves are surface waves that can form at the boundary of solid-solid half-spaces. They have clockwise, elliptical particle motions.
-	Surface wave 	Surface waves form in materials greater than a few wavelengths thick. They are displacements that decay exponentially with distance from a surface (Achenbach, 1973) and will therefore only ever appear to propagate within a few wavelengths of a surface or boundary. There are three types of surface wave: Rayleigh, Scholte, and Stoneley, their formation dependent on the boundary at which they form.
-	Torsional wave 	Torsional waves are body waves that propagate with particle motions rotating back and forth around an axis in the direction of propagation. They effectively produce a twisting motion where, in cross-section, a particle will first rotate clockwise and then anti-clockwise.

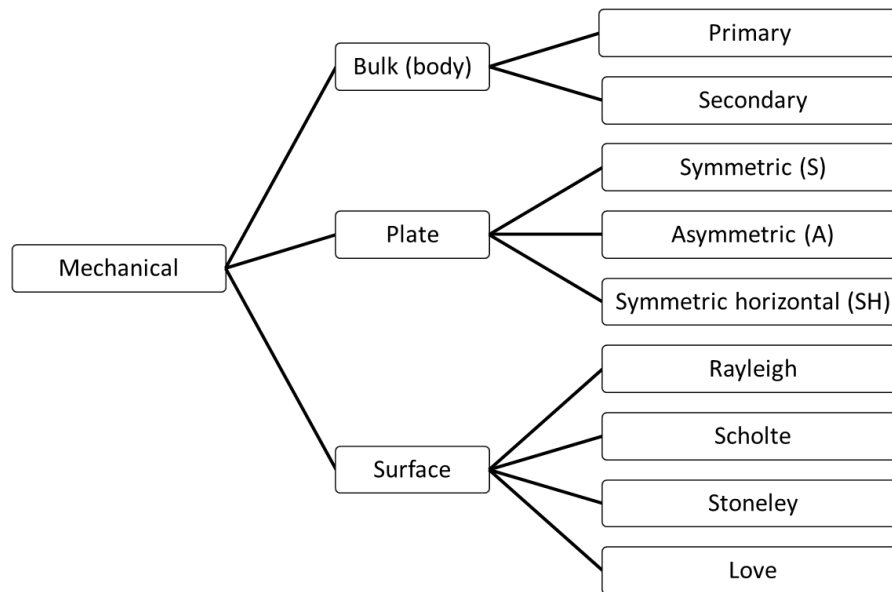


Figure 2.19 Levels of mechanical wave classification for standard wave types.

Despite the different ways in which waves may be categorised, all may be expressed mathematically using variants of Equation 2.2, known as the one-dimensional wave equation.

$$\frac{\delta^2 y(x,t)}{\delta x^2} = \frac{1}{v^2} \frac{\delta^2 y(x,t)}{\delta t^2} \quad [2.2]$$

where x and y represent Cartesian coordinates, v is velocity (m/s) and t is time (seconds).

Variations of the wave equation include the addition of functions such as Bessel functions, or models such as the Euler-Bernoulli model. Adding variations to the equation allows for slightly varying solutions to be reached and reflect different real-world conditions, such as with different burial environments. Pavlakovic et al. (2001) however suggest that the solutions to both real and complex Bessel functions have only recently become achievable due to increased computing powers, whilst it is known the Euler-Bernoulli model becomes unstable at high frequencies and may only be used for near-field propagation. The choice of equation modification is therefore important.

2.4.2 Waves in plates and shell structures

Waves within plates and shell structures have been studied extensively within literature. Authors such as Poncelet and Deschamps (1997), Maze et al. (2001) and Baik et al. (2010), for example, investigated wave behaviours theoretically, whilst authors like Aristegui et al. (2001), Long et al. (2003), Greve et al. (2005), and Shehadeh et al. (2005, 2008, 2019) observed behaviours using a combination of computational modelling, laboratory, and field observations. Additionally, waves within infrastructure such as pipes and piles, modelled as shell structures, have been studied similarly by authors such as Dixon et al. (2003), Leinov et al. (2015), and Ni et al. (2017) (Sections 2.4.2.1, 2.4.2.2, 2.4.2.3).

Aristegui et al. (2001) for example, investigated propagation and attenuation within a copper pipe both computationally using Disperse, a numerical simulation program discussed in Section 3.7, and experimentally using scaled laboratory experiments. Good agreement was found between the two methods. Aristegui et al. (2001) also suggest that wave propagation within air filled pipes can be approximated well using vacuum-filled experiments and models. Consequently, it can be inferred that wave behaviours can be accurately studied using a variety of investigative methods.

From studies such as those above, it is generally agreed that two types of wave will propagate within plates and shell structures, plate waves and surface waves, the type determined by both structural and environmental factors. Propagation can be complex with the measured waves formed from numerous source signals and multiple wave modes (where wave modes are variations of a wave form, their complexity defined with subscripts, e.g. A_1 and A_2 with A_2 being more complex). Additionally, in large structures and as a result of the varying sources from which waves may be generated, waves will travel as different modes with different characteristic frequencies and wave velocities (Shehadeh et al., 2006) which may also convert to different modes at interfacing boundaries (Pollock, 1986). Long et al. (2003) for example, suggest that dependent on the system only the fundamental $L(0,1)$ mode will propagate at lower frequencies whilst the higher order $L(0,2)$ mode does not occur until a cut-off frequency in a modelled free bound iron pipe. Similarly, Shehadah et al. (2008, 2019) experimentally showed that two waves of different velocities will propagate within a steel pipe and the attenuation of one will always be greater than the other regardless of environmental conditions. Wave modes are therefore an important consideration when studying wave behaviours; signals may be formed from multiple wave types and modes which can affect their analysis and interpretation.

With respect to plate waves, which are also known as Lamb waves after the work done by Horace Lamb in 1917 (Su et al., 2006), three forms can be identified. These are symmetric (S), asymmetric (A), and symmetric horizontal (S_H). These forms are a superposition of longitudinal and shear modes (Su et al., 2006) but remain distinguishable by the plane in which they propagate (Figure 2.20), although all travel at a normal to the direction of propagation.

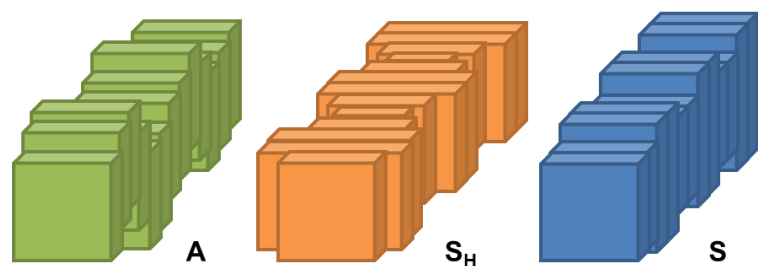


Figure 2.20 The three forms of plate (Lamb) wave: asymmetric (A), symmetric horizontal (S_H), symmetric (S).

Both the form and mode of a Lamb wave will influence its behaviour. Greve et al. (2005) state that higher modes do not exist below certain frequencies. The A1 mode for example, cuts off below frequency-thicknesses of 1.69 MHz-mm whilst the S1 mode cuts off below 2.94 MHz-mm. At the frequency-thicknesses of interest to this research, where frequency-thickness is the product of frequency (10 to 100 kHz as in Section 2.3.3) and plate/wall thickness, it may therefore be concluded that only the fundamental Lamb waves should propagate.

Additionally, Greve et al. (2005) also suggest that at frequency-thicknesses of 0.5 to 0.6 MHz-mm, the fundamental S0 mode is largely non-dispersive (i.e. the constituent frequencies travel with the same phase speed) whilst the A0 mode is contrastingly highly dispersive. Ghandourah (2015) further observed that for the same frequency, an A mode has a shorter wavelength than an S mode. This is important for monitoring as an A mode will consequently be more sensitive to defects. For condition monitoring, this is a desirable trait however limits the propagation distances over which the mode could be monitored due to distortion and attenuation effects. As a compromise, the S mode is therefore better for monitoring structures over distance due to its smaller sensitivity and minimal dispersion.

With respect to surface waves three main forms exist, Rayleigh, Stoneley, and Scholte, although as implied, the classification of Love waves is arguable with the USGS suggesting that Love waves may be classified as surface waves whilst NDT resources suggests that they are plate waves. Furthermore, Su et al. (2006) state that Love waves may also be referred to as S_H plate waves in some classification schemes.

Focusing on Rayleigh, Stoneley, and Scholte waves though, each propagate with elliptical particle motions and are distinguishable by the environment in which they propagate. Rayleigh waves, for example, are normally defined as surface waves that propagate along solid-free boundaries. Stoneley waves on the other hand propagate along solid-solid boundaries, whilst Scholte waves propagate along solid-liquid boundaries. There is however controversy surrounding these definitions.

Zhu et al. (2004), for example, proposed and investigated the existence of leaky Rayleigh waves at solid-fluid interfaces. They concluded that although Rayleigh waves will dominate at solid-air interfaces and Scholte waves will dominate at solid-liquid interfaces, both waves may still be present. However, they also note that the Rayleigh waves at solid-liquid boundaries are indistinguishable from the other waves suggesting this could arguably be used to deny their existence.

Contrastingly, other studies clearly support the proposed definitions with an example being Hernández-García et al. (2014) who developed a hodogram (a graph of particle paths) as shown in

Figure 2.21. Figure 2.21 shows a hodogram for the particle motions as a function of distance from source and depth for different surface waves detected in changing environmental half-spaces. Distinct particle path behaviours may be seen, indicating the presence of differently behaving waves. Hernández-García et al. (2014) therefore concluded that both Rayleigh and Scholte waves propagate with retrograde and elliptical particle motions, whereas Stoneley waves exhibit a clockwise and elliptical particle motion.

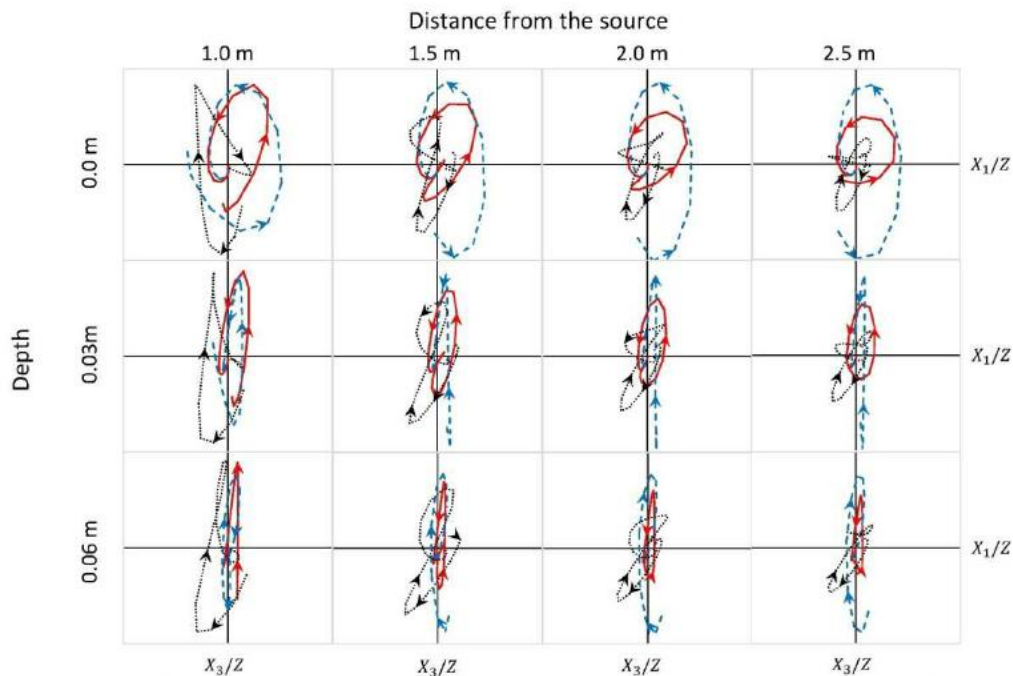


Figure 2.21 A hodogram showing surface wave particle motions as a function of distance from a source and depth for Rayleigh waves (solid red), Stoneley waves (dotted black), and Scholte waves (dashed blue). From Hernández-García et al. (2014).

Figure 2.21 also shows that the decay of Scholte waves with depth is less than that of Rayleigh and Stoneley waves, a further defining feature of the different wave types. Zhu et al. (2004) imply that this may be a result of most Scholte wave energy being carried in the coupled fluid, rather than solid, whilst the increased acoustic impedance of a fluid could also create stronger Scholte waves. The Scholte waves could therefore penetrate deeper into a solid half-space, which could account for the reduced energy losses seen by Hernández-García et al. (2014).

2.4.3 Attenuation

Attenuation may be defined as a loss of energy per wave cycle and occurs naturally as a wave propagates. It is usually assumed to refer to a decrease in wave amplitude but can also present as a decrease of parameters including amplitude, energy, intensity magnitude, and signal duration. Additionally, attenuation can affect frequency, in the form of frequency shifts; wave modes, in the

form of conversions; and the significance (i.e. dominance) of different frequencies and modes. Li et al. (2017) investigated the attenuation behaviours of five wave properties for steel strands embedded within concrete and concluded that each property responded differently. Given the different responses, it can therefore be inferred that attenuation affects different parameters to different extents. This may be a result of different attenuation mechanisms.

2.4.3.1 Attenuation mechanisms

Attenuation may generally be attributed to one or more of four processes, also known as attenuation mechanisms. These are: absorption, scattering, geometric spreading, and coupling (energy leakage). Shehadeh et al. (2008) demonstrate that coupling and absorption are most important. The mechanisms are dependent on either a material's properties, and therefore intrinsic, or on the environment and geometry of a material, and therefore extrinsic. For example, geometric spreading only occurs in materials of two or more dimensions and will vary dependent on the number of dimensions; in 2D geometries, for example, waves spread radially, whereas in 3D geometries waves spread spherically. Table 2.7 therefore defines and describes these attenuation mechanisms and related terms.

Table 2.7 Wave attenuation mechanisms and processes.


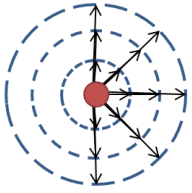
Abb.	Term	Definition
-	Absorption 	Absorption is a process of energy transformation where one energy form changes into another. In the case of propagating waves, this is usually from kinetic (vibrational) energy to heat energy. The amount of kinetic energy therefore reduces, presenting as a reduction in amplitude. The energy of the wave field, however, remains constant; the energy is still there but in a different form.
-	Coupling	Coupling occurs between adjacent bodies or layers of media. It is the effective sharing of energy between two or more adjacent bodies. Coupling therefore often presents as two or more separate waves across a boundary.
-	Extrinsic attenuation	The term extrinsic refers to an external influence. Extrinsic attenuation is therefore attenuation as a result of external influences such as the surrounding medium.
-	Geometric spreading 	Geometric spreading can occur in objects with two or more dimensions; it is not applicable to one dimensional propagation. It may be described as the spreading out of a wave's energy homogeneously around the edges, or across the surface, or a circle or sphere. As a circle or sphere grows, the energy packages remain the same in number but become less densely positioned around the edge or surface. Thus, it appears that in any one direction the energy is reducing with distance, although remains the same over the whole. It should also be noted that plates, although 2D, are treated as a one-dimensional entity; the effects of geometric spreading are negligible.

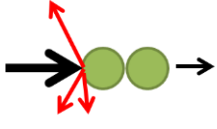
Abb.	Term	Definition
-	Intrinsic attenuation	The term intrinsic may be defined as natural to or belonging to. Intrinsic attenuation therefore refers to attenuation as a result of the material properties of the body in which a wave is propagating.
-	Scattering 	Scattering (sometimes referred to causatively, e.g. grain boundary scattering) occurs when energy is reflected and propagated in different directions to that of the main propagation. The overall energy in the wave field is maintained, however the energy in the direction of propagation is reduced. Energy is not lost or transformed during this process, only re-directed.

Table 2.7 shows that attenuation can present itself in different forms and with different significance for different wave parameters and properties. Normally however, it is measured as a relative decrease in the amplitude.

2.4.3.2 Quantifying attenuation

Shehadeh et al. (2008) suggest that attenuation may be quantified using the absorption equation for energy (Equations 2.3, 2.4, and 2.5).

$$E(x) = E_0 e^{-kx} \quad [2.3]$$

$$E(x) = E_1(x) + E_2(x) \quad [2.4]$$

$$E(x) = [mn]^{ax} E_{0,1} e^{-k_1 x} + E_{0,2} e^{-k_2 x} \quad [2.5]$$

where $E(x)$ is the energy in Joules as a function of distance in metres, E_0 is the initial source energy in Joules, k is the attenuation factor and, x is the distance travelled in metres. The parameters: k_2 , m , and n are dependent upon the impedance matching between a steel pipe and the external (k_2 and m) and internal (n) environments.

Of these equations, Equation 2.3 represents the general absorption equation, whilst Equation 2.4 splits Equation 2.3 into two components to represent the presence of two wave fronts. Equation 2.5 then extends this concept, expanding Equation 2.4 to account for changes in the contributing factors (E_0 , k and x) for both the shear and longitudinal wave fronts.

Equation 2.5 therefore represents the inferred dispersion of the shear and longitudinal wave modes as a function of distance. Shehadeh et al. (2008) however suggest that this does not occur distinctly until propagation distances > 5 m, the same boundary at which Cawley et al. (2003) suggests intermediate distance waves commence.

To successfully use Shehadeh et al.'s (2008) quantification equations, knowledge of the signal energy at both the source (or specified origin) and the point of measurement is required. Measurement, or calculation, of these values is however complex and often inaccurate due to being functions of

multiple factors. Consequently, quantification of attenuation using these values could have relatively low accuracy.

Lee and Waite (2007) instead proposed an alternative equation for quantifying the intrinsic attenuation within a system (Equation 2.6). Similarly to Equation 2.5, Equation 2.6 proposes a relationship between amplitude and energy. However, unlike Equation 2.5, does not account for the potential dispersion of different wave modes implying it may become inaccurate after this occurs. It should also be noted that amplitude losses as a result of coupling are independent of R (i.e. the distance between the source and receiver).

$$A \propto e^{-\alpha R} = e^{-\pi f Q^{-1} \frac{R}{V}} \quad [2.6]$$

where Q^{-1} is the intrinsic attenuation (or inverse quality factor), f is a linear frequency in Hz, R is the distance between the source and receiver in metres, and V is the acoustic velocity.

Haberland and Reitbrock (2001) provide a further method of attenuation quantification shown in Equations 2.7 and 2.8.

$$Q_{ij} = S_i(f) I_j(f) R_j(f) B_{ij}(f) \quad [2.7]$$

$$Q_{ij} = \frac{\Omega_0 f_c^\gamma}{f_c^\gamma + f^\gamma} \exp[-\pi f (t_{ij}^* + t_{\text{station}})] = \frac{\Omega_0 f_c^\gamma}{f_c^\gamma + f^\gamma} \exp[-\pi f \kappa] \quad [2.8]$$

where Q is the quality factor, or inverse attenuation; S , the source spectrum; I , the instrument response; R , local site amplification effects; B , the absorption along the ray path; Ω , the long-period plateau value; f_c , the corner frequency in Hz; γ , a high-frequency decay factor; t_{ij}^* , the whole path attenuation; and t_{station} , the local site receiver attenuation effects.

Equations 2.7 and 2.8 represent the attenuation experienced by large wavelength seismic signal travelling through the Earth as body waves, as opposed to the small wavelength Lamb waves expected to propagate within shell structures. The applications are comparable, although assuming a Brune type source, as is done for earthquakes, may not be appropriate to soil-steel generated AE. Consequently, an additional factor would potentially be required.

For earthquakes, the authors find that attenuation is a convolution of several factors which may be quantified using a quality factor (Q). This is not dissimilar to Equation 2.6 where factors including frequency, propagation distance and acoustic velocity are accounted for. Contrastingly however, the methods of quantification suggested by Shehadeh et al. (2008) and Lee and Waite (2007) calculated Q as a function of energy rather than a function of frequency as in Haberland and Reitbrock's (2001) equation.

2.4.3.3 Attenuation in context: the effects of adjacent materials

Attenuation within different buried and embedded structure systems has been studied extensively with the effects of varying internal and external media known to be heavily influential. Shehadeh et al. (2008) for example, experimentally compared the effects of soil saturation on wave propagation and attenuation within both air and water filled pipe systems over 5.5 m. They found that:

- Two wave modes propagated within the pipe, distinguishable after around 5 m propagation. These were suggested to be an extensional mode and a flexural mode for which other work (Pollock, 1996, Holford and Carter, 1999) observes that, at appreciable distances, the waves travel as a relatively low frequency and high-speed mode and a higher frequency and lower speed mode.
 - The presence of different wave modes that may travel at different wave speeds. Measured signals would therefore be a superposition of different waves.
- Each wave mode was affected differently by their surrounding environment. The presence of water, either internally or externally, however, increased the observed attenuation for both (Figure 2.22) whilst the least attenuating environment was air-steel-air.
 - This suggests that in the field saturated soils will be more attenuating.
- Given the calculated reflection coefficients, an air-steel-air environment provides a near total reflective boundary (i.e. total internal reflection) which is why attenuation in this environment is the smallest of those tested (Figure 2.22). Water environments on the other hand are less reflective (i.e. absorbing) and are therefore more attenuative.
- Coarse sands are less attenuating than fine sands under the same conditions.
 - Pipes buried with a surrounding coarse-grained annulus (i.e. sand or gravel) would potentially make for more efficient wave guides than pipes simply backfilled with the in-situ soil.
- There were 'significant differences in relative attenuation of high and low frequency components between the different environments' with environments containing water externally, appearing to favour lower frequencies.

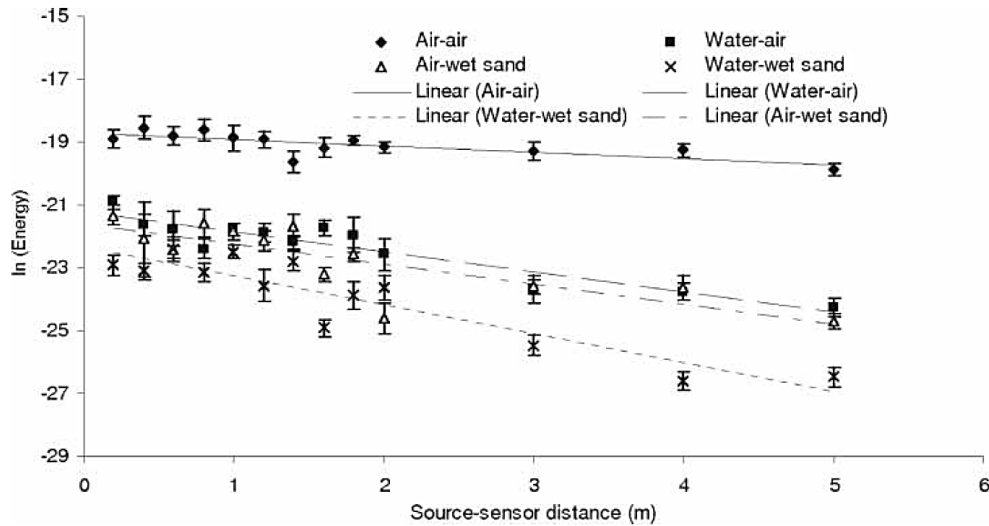


Figure 2.22 Measured 'attenuation curves for different external (air and wet sand) and internal environments (air and water)'. From Shehadeh et al. (2008).

Similarly, Leinov et al. (2015) also investigated wave propagation and attenuation for pipes buried in a variety of sands. Additionally, they compared their experimental results with those of computational models using Disperse. Leinov et al. (2015) found that:

- Attenuation ranged between 1.65 and 5.5 dB/m for the measured torsional modes and 0.98 and 3.2 dB/m for longitudinal modes. Attenuation of the torsional mode was therefore greater.
- Of the loose and compacted sand samples tested, the compacted sands were always more highly attenuating after the application of an overburden pressure. Overburden pressures, representing different burial depths, further increased the attenuation (Figure 2.23) due to modifications of the density and stress level with the observed attenuation being approximately proportional to the pressures.
 - Pipes buried at depth should therefore be more attenuating.
- The addition of water to dry sand samples increased the attenuation due to an increased density. Attenuation then further increased as the soil was consolidated and the density further increased.
 - Consequently, the effects of water to attenuation vary dependent on the initial (relative) soil conditions.
- As a result of the experimental set up, reflections from the pipe-air to pipe-sand environments could be seen.
 - This is important as it suggests that abrupt changes in the surrounding medium of a pipe would also cause acoustic reflections in the field.

- The backfilled sand was not homogeneous with what appeared to be a thin layer of higher shear velocity sand forming adjacent to the pipe. This effected the wave propagation and attenuation.

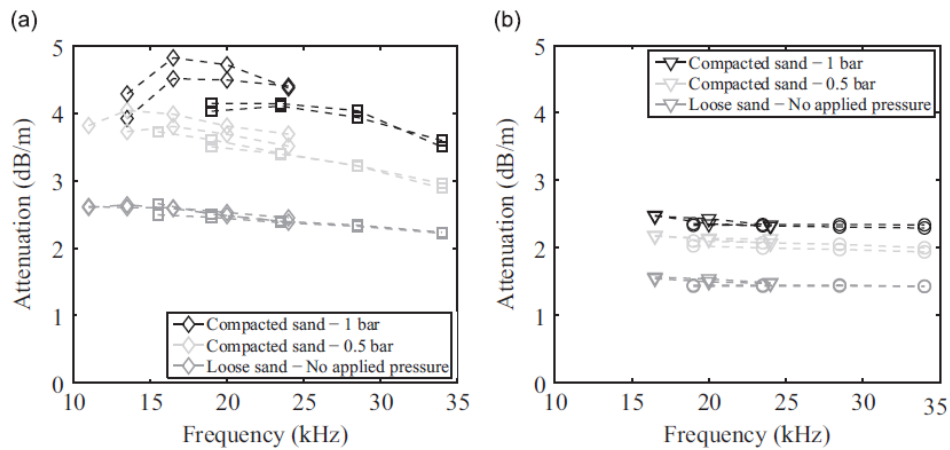


Figure 2.23 'Attenuation measurements as a function of frequency in the dry sand case for three different over burden pressures, 1 bar (black), 0.5 bar (light grey) and no applied pressure (dark grey), for (a) T(0,1) mode and (b) L(0,2) mode. Diamonds and triangles correspond to 16.5 kHz central frequency and squares and circles to 23.5 kHz central frequency.'

From Leinov et al. (2015).

2.4.4 Using steel infrastructure as waveguides

Infrastructure is defined by the ^bOxford dictionary (n.d.) as 'the basic physical and organisational structures and facilities (e.g. buildings, roads, and power supplies) needed for the operation of a society or enterprise'. Herein, the use of infrastructure however refers specifically to physical civil infrastructure assets comprising of structural elements (i.e. pipelines, pile foundations).

A selection of appropriate infrastructure has been studied in order to ascertain their suitability as waveguides. The assets for each structure were assessed using several factors either relating to their efficiency in wave propagation, for example their materials, geometry, and environment; or their practicality in location and accessibility. Regarding these assessment criteria, a focus was kept on steel-based infrastructure as they experience relatively low attenuation of AE (Figure 2.24). Table 2.8 summarises and compares the initial findings whilst Figure 2.25 shows a selection of typical cross-sectional geometries for such infrastructure.

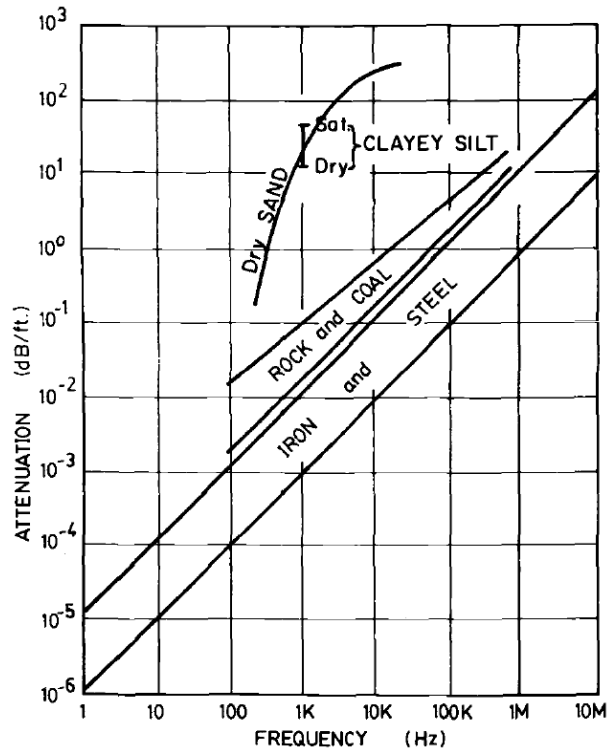
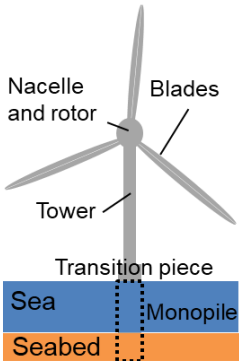
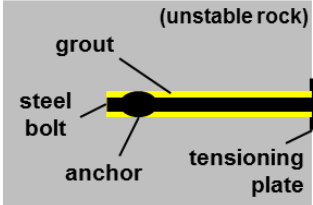
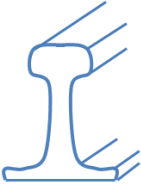


Figure 2.24 Measured ‘attenuation response of different soil types contrasted to rock/coal and iron/steel’. From Koerner et al. (1981).


Table 2.8 A summary table comparing the typical: materials, geometries and, environments, for different forms of infrastructure with the potential to be employed as AE waveguides.

	Materials	Components	Connecting methods	Typical environment
Railway tracks <u>Element / network size:</u> 0.01 to 1000s m	Steel tracks, wooden; concrete or steel sleepers	Track, joints, fastenings, sleepers	Fish plates, expansion joints, welds (flash-butt, thermit, gas pressure and enclosed arc)	
Utility pipes <u>Element / network size:</u> 0.01 to 1000s m	Steel, HDPE, iron or lead pipes; gravel, sand or host soil annulus	Pipe, joints (including branching), caps	Butt welds, socket weld joints, e joints (insulating), flanged joints, victaulic joints	
Onshore pile foundations <u>Element / network size:</u> 0.01 to 10s m	Steel, concrete, wood (or a mix)	Pile, joints, caps	Interconnecting screw joints	

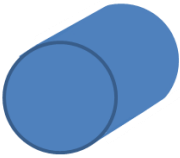
	Materials	Components	Connecting methods	Typical environment
Offshore monopiles <u>Element / network size:</u> 0.1 to 10s m	Steel with cement grout	Monopile, transition piece, tower, rotor and blades	Grouting	
Rock bolts and dowels <u>Element / network size:</u> 0.01 to 10s m	Steel or fibreglass bolts or dowels, epoxy resin or cement grout	Bolt, anchors, tensioning plate	Interconnecting screw joints	



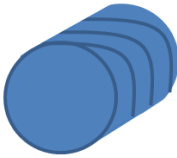
Rail track




Pipe or rock bolt or pile



Rock dowel or rock bolt or pile



Threaded rock bolt



Pile

Figure 2.25 Simplified typical cross-sectional geometries for infrastructure with the potential to be employed as AE waveguides.

Various conclusions can be drawn from both Table 2.8 and Figure 2.25:

- A common geometric shape for infrastructure is that of a hollow cylinder, also known as a shell structure. This structure for example can be used for utility pipes, foundation piles, and rock and soil bolts.
- Structures are usually formed from several parts with different types of joints, or in the case of monopiles grout, connecting them together.
- Most of the compared infrastructure can be made from steel but may also be made of other materials. Furthermore, different types of steel can be used for depending on the type and location of the structure.
- The environment in which the infrastructure may be situated is wide ranging and, although standards and recommendations generally exist, may vary dependent on local needs.

Given these conclusions, the suitability of specific structures were investigated in more detail.

2.4.4.1 Railway tracks

Railways span a large area of the country to create a transportation network. As surface structures they are easy to access, although this also makes them prone to the influence of noise. AE signals resulting from ground instability can therefore become distorted with unwanted signals such as those from trains, weather and other unpredictable interactions. The geometry of UK rail tracks is however standardised with different formats dependent on use. Theoretically, signal propagation within railway tracks is therefore predictable. A typical rail track configuration is shown in Figure 2.26.

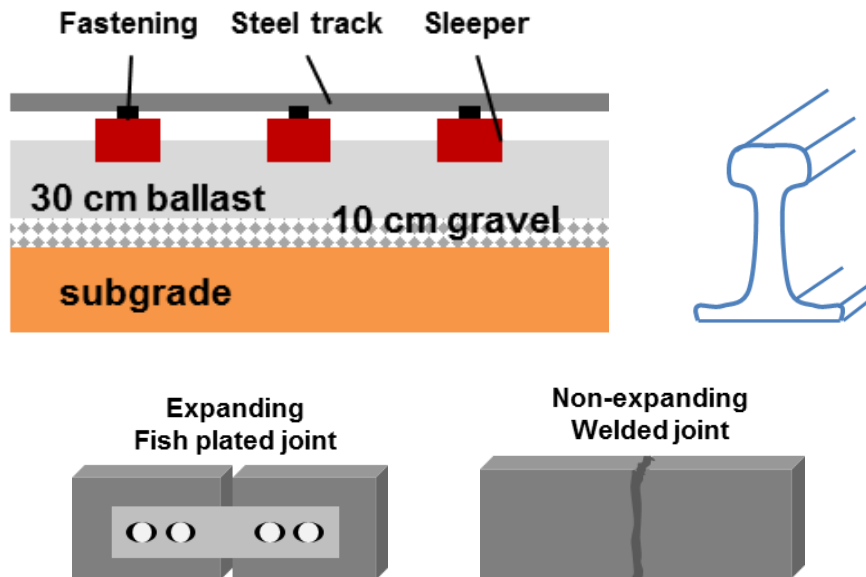


Figure 2.26 The typical geometry and environment of a railway track (top left), cross-sectional geometry (top right) and, rail jointing methods (bottom).

Studying wave propagation within railway tracks is however challenging due to the complex, multi-modal and dispersive nature of the supported waveforms (di Scalea and McNamara, 2004, and Bartoli et al., 2005). Hayashi et al. (2003) for example, suggest that there are three unnamed, dominant wave modes at the surface of a rail head with two further modes within the lateral head. Similarly, Cawley et al. (2003) found that the different measurable wave modes concentrate their energy and preferentially travel through different areas of a rail track including the head, web, and foot. The superposition of these modes and their differing characteristics can make signal analysis problematic (Wilcox et al., 2003), whilst any defects encountered during propagation will further complicate the signal through distortion and reflections. Hesse and Cawley (2006), for example, suggest that rail supported wave modes are greatly susceptible to defects and these may cause both symmetric and asymmetric modal reflections (Bartoli et al., 2005).

Contrastingly, Rose et al. (2004) found that steel railway tracks can propagate induced AE appreciable distances (> 2 km) implying that signals are easy to measure. Additionally, they also found that signal

attenuation is frequency dependent suggesting that, contrastingly to conventional thinking, higher frequencies attenuate less than lower frequencies with distance. This may be linked to the findings of Wilcox et al. (2003) who concluded that for low frequency propagation, railway tracks can be used as effective waveguides at a scale of decimetres rather than kilometres. Wilcox et al. (2003) also took account of flaws and defects in the rails when modelling propagation. As discussed, these can cause significant distortion and attenuate a propagating signal.

Specifically, Bartoli et al. (2005) concluded that railway tracks best support frequencies in the range of 10-50 kHz. Rose et al. (2004) however suggest that the relatively higher frequencies of 40-80 kHz are best supported. It should be considered though, that Rose et al.'s (2004) experiment used high powered input sources, such as trains, to induce signals within the rails. This is not representative of the small-scale soil-structure interactions of interest to this project and may therefore not be applicable.

In conclusion, railway tracks are surface structures and thus more susceptible to superimposed noise when compared to buried structures. Their complex cross-sectional geometry is shown to propagate multiple, multi-modal, and dispersive wave modes that preferentially travel through different parts of a rail's geometry making for difficult interpretation and analysis. Despite this, the suggested frequency range best supported by tracks is within that of the range in which soil-structure generated AE is known to occur (Section 2.3.3). Railway tracks are also shown to be effective waveguides at a scale of at least cm and in other cases km, with signals easily being distorted by flaws and defects within the rail. This is a useful property for asset health monitoring at a small scale, but not necessarily soil-structure monitoring over a larger scale. Arguably, this distortion is however a common problem for any steel structure containing defects.

2.4.4.2 Utility pipes

Pipes are essentially hollow tubes (shell structures) connected by varying methods to form a network. They are used to transport different substances over distances ranging from a cm to a km scale. The substances being transported vary in type and purpose and so there are consequently multiple piping networks within the UK. DiscoverWater (2018) for example suggest that there are 343,865 km of water pipes within the UK system whilst CLH Pipeline System (CLH-PS) (n.d.) (formally the Government Pipeline and Storage System, GPSS) have pipelines covering 2,000 km. Cumulatively there are therefore hundreds of thousands of km of pipelines across the country, which are vulnerable to ageing and deterioration, geohazards and ground failure processes; however, there is currently no cost-effective geotechnical technique that can be retrofitted across such a substantial infrastructure network.

The existence of regular access points to pipe networks also means that accessibility for the attachment of instrumentation is easily achievable. Furthermore, pipe cross-sectional geometries are relatively simple, for which wave propagation is well understood.

Pipes however, may be manufactured in multiple ways with the two main methods being: seamless piping, formed by the piercing of a near molten steel rod, called a billet, with a mandrel to form a hollow tube with no joints; and butt-welded piping (Figure 2.27), formed by forcing a hot steel sheet through shapers which roll it into a hollow shape. A third, less commonly used method is spiral welding where a metal sheet is twisted into a helical shape and welded at the seams (Parisher and Rhea, 2001). The way in which a pipe is manufactured is important as it can affect the propagation of AE. Welds for example can cause signal reflections and therefore a loss of energy.



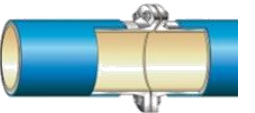

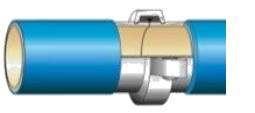


Figure 2.27 A butt-welded pipe with welded seam.

Given the range of substances transported by pipes, a range of cross-sectional dimensions (i.e. radii) are also required. Pipe dimensions are traditionally defined with three measurements: the nominal pipe size (a name, usually inaccurate), the internal diameter, and the external diameter (Parisher and Rhea, 2001), all of which are dependent on the designed purpose of a pipe and the environmental conditions to which it will be subjected. Pipes may however also be defined with just an internal diameter and wall thickness. In order to provide adequate flow rates and pressures, Thames water (2015) thus recommend varying the internal diameter of pipes for modern, plastic mains supply. The precise values are dependent on how many, and what type of, building or structure a pipe system will be servicing. At critical sites (e.g. geohazards) the pipe design, including dimensions and flexural rigidity, will however be specified to ensure that appropriate safety standards are met, and the potential of ultimate state failure is limited.

To accommodate the changes in dimensions often required within piping systems, pipes are connected to form a network. Connections can be made by multiple methods (Table 2.9) including butt welds, flange joints and socket welds, for example, all of which increase the complexity of the cross-sectional geometry.

Table 2.9 Pipe connection methods (Adapted from FT pipelines).

Term	Definition
Butt welds 	A simple weld between the edges of two pipes faced together of the same material and dimension.
E joint (insulating) 	Similar to socket welded joint but with the addition of an internal air pocket to reduce heat transfer during welding and any consequent damage to the internal pipe. Sometimes a sealing sleeve is also used.
Flanged 	Flanged joints consist of two pipes with protruding collars. These collars may be bolted together and will sometimes include an insulating ring between. There are however many forms of collar including flat, raised, ringed, tongue and groove and, male and female. Raised face collars are most common providing a positive grip whilst flat faces are usually for low pressure pipes (Parisher and Rhea, 2001). Flange joints are easy to disassemble for transportation.
Socket welds 	Similar to an E joint but without the insulation, socket joints consist of a sleeve like socket welded to one pipe and in which the other slots in to connect.
Victaulic (groove joint) 	A sleeve joint across two pipes. Two semi-circular bridges are then bolted around this to pressurise the seal.

The different methods by which pipes can be connected will therefore affect their suitability as waveguides with propagating waves potentially becoming distorted. Alleyne and Cawley (1996) suggest that unless a feature is axisymmetric, mode conversions during reflection and transmission will occur and may cause a loss in energy directionality.

Butt-welds for example, which may be assumed the main connection method despite their inherent irregularity, create reflections (Cawley et al., 2003). Field tests have however shown propagation distances of 50 m are still possible with around 5% of the input signal reflected (Alleyne and Cawley, 1996). These results imply that 95% of the original signal is still transmitted, a value also consistent with the findings of Cawley et al. (2003) who suggest that, at the frequencies being measured (i.e. kHz to MHz), material attenuation due to grain boundary scattering is very low and alumina-thermic welds (welding where the exothermic reaction uses aluminium) are readily penetrated. Similarly, Hardy (1992) also demonstrated that welds are effective transmitters, although in their work signal amplitude losses in the region of 22% are reported. Contrastingly, alternative joining methods such as

flange joints with a rubber seal have been shown to transmit very little energy and can effectively terminate a signal (Alleyne and Cawley, 1996).

It is not just the geometry of a pipe network that effects AE propagation though; the bulk pipe material, internal media, external media, and to some extent environmental factors such as temperature and pressure, are also all of importance (Shehadeh et al., 2005).

With respect to bulk material, fortunately, given the types of substances and the pressures to which these substances must sometimes be transported, there is only a small range of appropriate, non-reactive materials from which pipes may be formed. This range is further reduced when the pipe system is pressurised. In British history, pipes have therefore been made of materials such as lead, wood, and cement; modern installations are however generally made from plastics, steels, and iron.

Steel as a material has a low acoustic attenuation making it ideal for AE propagation. Less material attenuation allows for potentially longer signal propagation distances and therefore more efficient waveguides. Materials such as concrete on the other hand are highly attenuative (Li et al., 2017) and would make for a less efficient waveguide.

The attenuation within a material is, however, also influenced by bounding media through mechanisms such as coupling. Pipelines are usually buried; numerous studies on the attenuative effect of surrounding soils, i.e. the external media, have consequently been conducted over the past few decades to investigate attenuation within buried structures.

Table 2.8 suggests pipe burials are relatively standardised and repeatable showing a typical pipe environment may be considered as a pipe buried within a coarse-grained sand annulus to backfill. This backfill system is based on the recommendations of NJUG (2013) and can be found in multiple, individual utility company guidelines (Thames Water, 2017, Severn Trent Water, 2016, and Water UK, 2017).

Even with a standard, prescribed backfill, studies suggest that for pipes buried in soil, the soil properties will govern attenuation (Alleyne and Cawley, 1996, and Leinov et al., 2015). Given that soil properties are not homogeneous, attenuation is consequently variable. Alleyne and Cawley (1996) for example found that the compaction of soil against a pipe can be highly influential, suggesting that compaction is the most important governing factor. Relatedly, Leinov et al. (2015) proposed that soil stiffness has the most influence.

Combining these works, Smith et al. (2017) state that the transmission of energy between boundaries, such as a soil-structure interface, is highly dependent on the acoustic impedance at the boundary, where acoustic impedance is a function of both density and stiffness. Leinov et al. (2015) however,

found that energy leakage is controlled by the bulk velocity of the burial material relative to the phase velocity of the guided wave. They state that 'Leakage arises when the phase velocity of the guided wave is larger than the bulk velocity in the embedding material' (Leinov et al., 2015). It may therefore be inferred that attenuation within pipe-soil systems may be influenced strongly by multiple material properties.

As well as mechanical material properties, the thickness of surrounding material layers should also be considered. Extra material layers can change the way propagating waves interact within the environment, and therefore effect waveguide efficiency.

At a small scale for example, pipes may develop layers of rust or corroded materials whilst protective layers, such as paint, polyethylene or polypropylene which resist corrosion (FT pipelines), may be added before installation. Similarly, at a larger scale, it is recommended that pipes are buried within a surrounding annulus of fine sand or, when buried in buoyant ground such as a mire, weighted with a coating of cement or other suitable materials in order to maintain their positioning as well as provide reinforcement.

Studies investigating the effects of material coating have been conducted by numerous authors (Alleyne and Cawley, 1996, Shehadeh et al., 2008, Leinov et al., 2015, Tong et al., 2016, Smith et al., 2017) with Leinov et al. (2015) finding that low impedance coatings can effectively decouple them from their surrounding environments. This is beneficial to NDT, minimising the influence of an external environment and reducing wave signal leakage, however, also reduces the impact of soil-steel interactions and the consequent detection of AE. For example, Leinov et al. (2016) found that the energy loss for thin material layers (< 1 mm) has typical rates < 0.5 dB/m at 60 kHz.

Contrastingly though, coatings such as bitumen and epoxy, have been found to propagate both shear and longitudinal waves well, thus providing a good coupling potential between a pipe and coating (Alleyne and Cawley, 1996) but also energy leakage; attenuation rates of 3 to 10 dB/m observed. Consequently, Alleyne and Cawley (1996) concluded that attenuation is controlled by both the properties and the thickness of a pipe coating; the displacement of the pipe surface in all directions (radial, circumferential and axial); and the wave frequency.

In conclusion, pipes and pipe networks are highly suited to monitoring AE. Their abundance, locality, and accessibility in the UK makes them ideal candidates for monitoring and understanding AE generation as a result of relative deformations between a soil and structure, but also allows for health monitoring of the structural asset due to wave propagation within the structures being well understood and documented.

The variety of conditions in which pipes can be situated, as well as their production methods, can however somewhat complicate this understanding due to inherent irregularities. Accuracy in the interpretation of signals may therefore be lessened although information on the asset (e.g. soil conditions and pipe connections) should always be available to facilitate understanding. Additionally, behavioural trends, opposed to specific parametric quantification, can be more valuable during AE interpretation.

2.4.4.3 Pile foundations

Pile foundations are stability structures often used in the construction of civil building works both on- and off-shore. Okwori et al. (2016) state: ‘Civil infrastructures such as bridges, dams and, high-rise buildings largely depend on the use of piles for support. In addition they are used for underpinning works, for example in marine facilities as temporary platforms to facilitate construction work and especially in abnormal soil or ground conditions’. The implied large-scale use of piles means they are ideal monitoring candidates. Furthermore, pile foundations may be found in a variety of environments including offshore.

As a result of the range of locations in which piles may be found, piles may also be made from a range of materials and have a variety of geometries. These were briefly discussed in Section 2.2.4 (i.e. Figure 2.25), although further geometries such as those shown in Figure 2.28 for specific structures like wind turbines also exist.

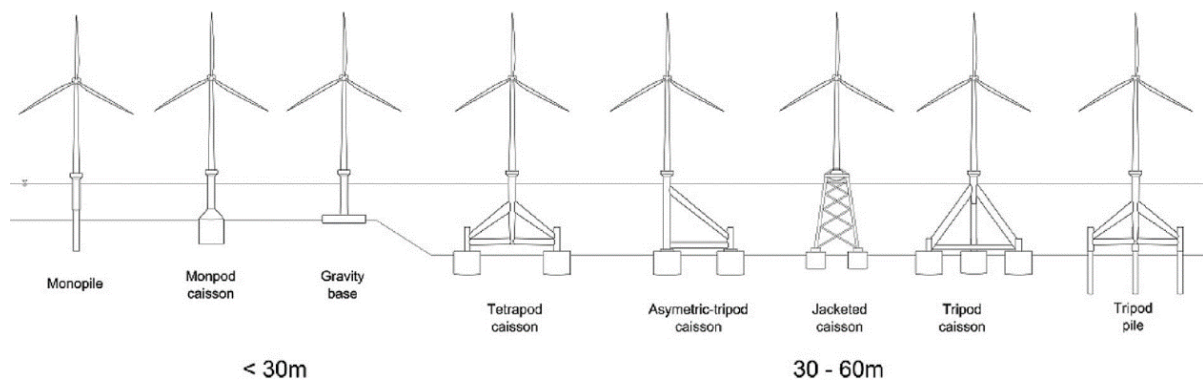


Figure 2.28 Different types of wind turbine foundation (Adapted from Bhattacharya, 2014).

Access to pile foundations, usually being a buried and often integral part of a larger structure, is not always easy. With respect to bridges for example, Lo et al. (2010) state how the task of NDT is complicated ‘because of a lack of direct access to the pile top’. Furthermore, attachments to the piles can limit the free vibration within the system therefore dampening propagating waves. Modern builds, though, are increasingly using smart infrastructure, whereby monitoring equipment is inbuilt before

and/or during installation. Lai et al. (2017) credit this, suggesting that embedded accelerometers can provide more accurate results when compared to coupled accelerometers as there is a reduction in boundary effects.

Regardless of sensor location, measuring AE propagation and attenuation through pile foundations has been investigated in many separate studies. Zheng et al. (2018), for example, present an in-depth analytical solution, in 3D, of wave propagation within a generic buried pile whilst Ni et al. (2017) tested six 6 m long piles of varying properties (hollow, buried, concrete and/or defective) in the field. Ni et al. (2017) found that defects were easily locatable using their newly developed complex continuous wave transform (CCWT) method to within 30% accuracy. Without the use of this method however, the burial environment attenuated signals to such a degree that they were not useful; Ni et al. (2017) suggest that this was also the case for work conducted by Ni et al. (2012). Consequently, it is implied that energy leakage from concrete piles within soils is significant. Beard et al. (2003) strengthen this statement by suggesting that the two dominant forms of attenuation within rods are: material damping, and energy leakage into the surrounding environment due to coupling. Attenuation is known to be dependent on material and geometry though.

Okwori et al. (2016) for example, contrastingly measured wave propagation through nine steel reinforced and solid concrete piles with known defects in laboratory conditions. They found that non-destructive sonic echo tests using the pile as a waveguide could successfully identify the extent of different types of defect damages. This implies that, as previously discussed (Section 2.4.4), steel is less attenuating.

Both studies by Okwori et al. (2016) and Ni et al. (2017) however, focused on active monitoring within concrete foundations. Piles are not just used onshore, and, as discussed, not necessarily made of concrete. Steel monopiles, for example, are often the foundation of choice for offshore wind turbines due to their simplicity, ease of installation in shallow waters (<30 m) and economic viability (Henkel et al., 2018, Bisoi and Haldar, 2014, Bhattacharya and Adhikari, 2011, 4COffshore, 2019).

Wind turbines are electric power generators in which a shaft is made to rotate by the flow of wind over a propeller. The turbines consist of multiple sections including: the foundation, a transition piece, the main tower, the nacelle and rotor, and the blades. Consequently, offshore wind turbines are situated within multiple environments including soils, seawater, and air, with numerous studies having been conducted on AE propagation within the upper (nacelle and propeller) parts of the structure/structural environments.

Early wind turbine designs consisted of monopiles with diameters around 4 m, however recent installations now typically have diameters in the region of 5-6 m and may increase to diameters around 10 m (Byrne et al., 2015). Preliminary calculations suggest that with larger diameters, the depths to which monopiles can be used may also increase with Bhattacharya (2014) suggesting depths of 45 m could be reached dependent on the ground conditions. Offshore monopiles are therefore essentially scaled up cylindrical piles.

Ground conditions are an important consideration for wind-turbine installation. Even at a local level, such as a region within a farm, individual turbines may vary structurally to suit the environmental conditions in which they are placed. Carswell et al. (2014) for example state that there is ‘a variability in soil properties from site to site (and within a site)’, whilst Henkel et al., (2018) suggest that uncertainties in soil conditions are especially pronounced when considering small strains. For the recent London Array, every turbine foundation was designed specifically to its location (London Array). Given this, Table 2.10 summarises a range of monopile geometries and environments in which wave propagation has been investigated within literature.

Table 2.10 A summary of monopile geometries and environments.

Case study	Pile diameter	Pile depth	Wall thickness	Reference
Reference model: NREL 5MW OWT	6 m	34 m clay, 20 m water	90 mm	^a Carswell et al., 2015
Reference model: NREL 5MW OWT	6 m	34 m clay, 20 m water	70 mm	Carswell et al., 2014
Reference model: NREL 5MW OWT	6 m	38.9 m	70 mm	^b Carswell et al., 2015
Reference model: NREL 5MW OWT	6 m	38.9 m	70 mm	Lesny et al., 2007
Reference model: NREL 5MW OWT	6 m	36 m undefined soil, 20 m water	60 mm	Rendon and Manuel, 2014, and Krathe and Kaynia, 2017
Barrow	4.75 m	30-40 m soil	-	C4 offshore, 2019
London Array	5.7 m	43 m soil 25 m water 21 m soil 24 m water	-	LondonArray, n.d. Iliopoulos et al., 2017
Walney extension	5.7 to 6.2 m	Up to 72.4 m 5 m water	51 to 92 mm	C4Offshore, 2019, and Menck
Amrumbank	5.2 m	19 to 24 m water	-	Menck, 2015.

2.5 Modelling methods

Modelling can be defined as either physical or computational where physical modelling employs physical components to simulate a real-world problem whilst computational modelling involves a digital simulation.

Modelling allows for a greater understanding of a variety of phenomena to be gained with the ability to control and monitor the interactions and consequences of large and small parametric changes. The data collected from modelling can then be analysed using a variety of methods, dependent on the data type.

There are numerous analytical methods, their relevance dependent on data type and application. AE data, for example, can come in a range of types from which other types may then be extracted or calculated. Such types may include signals in the form of raw waveforms (time-amplitude), RDCs (time-value), RMS (time-value), and frequency spectra. Further quantitative data such as velocities, amplitudes, energy, rise-times, durations, and statistical values such as averages may then also be calculated resulting in a large range of data types, the appropriate analysis and representation of each having the potential to be different.

2.5.1 Physical modelling of AE propagation

Physically modelling includes laboratory-scale experimentation and field-scale simulations. The design of a physical model needs to be realistic and representative in order to provide accurate results and repeatable to increase the reliability of the data. Physical models can therefore prove time consuming and expensive to conduct, dependent on the model. The value of knowledge gained from physical modelling, however, often outweighs the cost of running experiments.

Publications using physical modelling methods to investigate AE propagation in buried infrastructure systems are numerous. The methodologies adopted however vary dependent on their application and the equipment available.

In terms of signal sources, active signals (i.e. purposefully excited waves) are usually used in investigative laboratory and field studies. This is opposed to the passive AE expected with soil-steel interactions. The use of active signals in experimentation allows for controlled signals to be input. Di Scalea and McNamara (2004), Ni et al. (2008), and Lai et al. (2017) for example all used a hammer impulse to actively excite signals with Lai et al. (2017) suggesting that hammer impulse testing, or the sonic echo PIT method in particular, 'has been adopted as a standard procedure to assess the integrity of drilled shafts or cast-in-place piles by the ASTM (ASTM, 2000)'. Results obtained using this method are consequently easily comparable with others.

Both Li et al. (2018) and Li et al. (2019) on the other hand used piezoelectric transducers due to their omni-directionality and ability to excite the modes of interest to the experiment. Using dual-purpose piezoelectric transducers reduces costs and allows for precision control of the generated signals.

Precision control is however not necessarily useful for generating multi-modal, broadband frequencies as would be expected from soil-steel interactions.

Shehadeh et al. (2019) similarly use a combination of compressed air and solenoids. In previous works though, Shehadeh et al. (2005, 2008) used pencil lead breaks.

Pencil lead breaks are a widely used and long-established input source in acoustic research (Sause, 2011). They produce repeatable, short duration and broadband signals. The tests, also sometimes known as a Hsu-Nielsen source (Sause, 2011, NDT, 2007) consists of breaking a 0.5 (or 0.3) mm pencil lead of approximately 3 mm length against a surface and produces a signal resembling a natural AE source (NDT, 2007, Madarshahian et al., 2019). It has been used in numerous publications including Gorman (1991), Shehadeh et al. (2005, 2008), and Madarshahian et al. (2019).

It is not just the signal source that is of importance though, sensor placement and attachment are also key considerations (Long et al., 2003). Long et al. (2003) state that with a common sensor configuration, sensors are placed at an axis perpendicular to that of a pipe or elongate structure. As a result, the sensors are most sensitive to radial displacements.

To minimise the problems this can cause, commercial transducer rings, such as those developed by Guided Ultrasonics Ltd., were used by Leinov et al. (2015) in order to excite and measure a range of modes. Unlike other sources/receivers, such rings have the ability to excite and measure a range of controlled modes within a structure allowing for a greater understanding of propagation behaviours to be gained.

Contrastingly, although regarding the signal source rather than sensor, Aristegui et al. (2001) used a source that covered the entire end of the pipe in their experiment, rather than sitting on the side. Axial pressure was imposed on the circumference of the pipe, as well as through the wall and internal water body (Aristegui et al., 2001). This is opposed to the non-axial impulses created by pencil lead breaks on the side of a pipe. Multiple methods of signal induction and measurement can therefore be used to excite and investigate different wave modes.

Similarly to Long et al. (2003), Xie et al. (2016) suggest that a good contact between a sensor and structure is also crucial for measurement accuracy. A good contact is usually achieved by using a couplant such as silicone grease; couplants minimise the acoustic impedance between materials.

2.5.2 Physical modelling of soil-structure interaction

Interactions between an interfacing soil and steel element can be influenced by numerous parameters. These include the properties of the physical components within a soil-steel system (i.e.

the soil and steel element), and the forces influencing the relative deformation processes causing interaction (i.e. normal stress, friction, and shear stress, for example).

Ho et al. (2011) studied soil-steel interactions for two materials using ring shear experiments over 8 m shear displacements. Ring shear experiments use a hollow sample of material which is sheared in a continuous ring against an interfacing surface (Figure 2.29). Usually, the sample is saturated with water and an axial stress applied in slowly stepped increments until consolidation occurs. Observation regarding the shearing process can then be made.

This is opposed to direct shear experiments, such as those performed by Han et al. (2018), where a box sample of material is sheared linearly against an interfacing plate of material (Figure 2.30). Ring shear experiments have two main benefits over direct shear tests: (1) they are free from ends effects which can lead to stress non-uniformities, as with direct tests, and (2) they allow for unlimited shear displacement to be applied to a sample continuously; direct shear tests are limited in size.

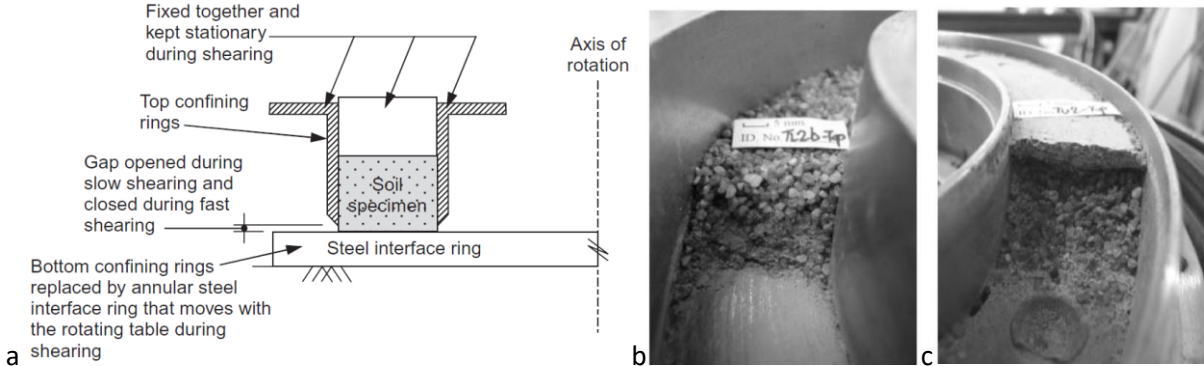


Figure 2.29 (a) A schematic diagram of an example ring shear set up and photographs of the (b) lower and (c) upper interface for a soil (sand 7/14) sample during experimentation. Adapted from Ho et al. (2011).

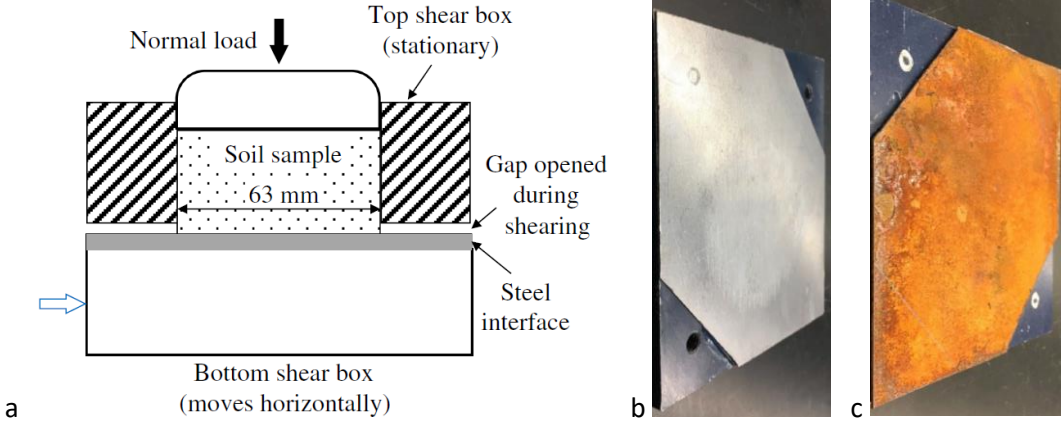


Figure 2.30 A schematic diagram, of an example direct shear experiment and photographs of (b) smooth and (c) rusted steel plate surfaces used as interfacing boundaries. Adapted from Han et al. (2018).

By focusing on the effects of different parameters to the interface friction angle (δ'), where δ' denotes the ability of a material withstand an imposed shear stress, Ho et al. (2011) come to several conclusions regarding the behaviour of δ' with respect to parameters such as displacement, normal stress and plate roughness.

With respect to displacement, the authors showed that the magnitude of shear displacement greatly affects the behaviour of δ' with three clear behavioural stages identifiable: the first few mm of travel, 10's of mm to 2 m of travel, and travel distances > 2 m. δ' is therefore strongly displacement-dependent.

Ho et al. (2011) suggest that the displacement-dependence of δ' may be a function of grain crushing and particle breakages. Grain crushing and particle breakage are more prevalent during initial shearing but become insignificant as shearing distances increase. Consequently, Ho et al. (2011) also noted that at larger shear displacements the initial grain size, as well as morphologies, had less influence on the behaviour of δ . Barmopoulos et al. (2009) observed similar behaviours, suggesting that the particle size distribution of a sample tends to stabilise after shearing displacement of around 10 m.

Relating to grain size, Han et al. (2018) observed that δ' was greater for smaller grain sizes and decreased as the grain size increased. Ho et al. (2011) similarly found that there was a weak relationship between the mean particle size (up to 5 mm) and the thickness of the shear zone at the interfacing surface. Yang et al. (2010) however, suggests that the shear zone thickness is related to the normal stress and shear displacements experienced by a sample. Moreover, Han et al. (2018) shows that plate roughness effects thickness where an increasing surface roughness increases the shear zone size.

It was however acknowledged by Ho et al. (2011) that thickness of a developed shear zone can be influenced by other factors including differences in the testing procedures (e.g. varying stress and displacement levels, and application rates).

Additionally, the position of a shear zone and the potential gravitational migration of fines created during grain crushing and breakage can affect the behaviour of δ' . This is as a result of fines accumulating within a basal shear zone. Ho et al. (2011) imply that, although this process is significant for shear distances < 2 m, the distance to which fines migrate is relatively small, despite being affected by grain size, and therefore insignificant.

In summary, several observations of importance to understanding and interpreting soil-steel generated AE may be made:

- The value of δ' effects interface behaviours and the development of shear zones, and hence a research question is: do these also effect the consequent AE generation?
- Displacement effects δ' .
 - Ho et al. (2011) show that the behaviour of δ' is dependent on the magnitude of displacement. This is likely a result of inhomogeneous changes in the grain size distribution as grain crushing and particle breakage occur. Three behaviour stages are identified: the first few mm, 10's of mm to 2 m, and > 2 m. Barmopoulos et al. (2009) however, suggest the grain size distributions stabilise after 10 m shear displacement from which a fourth stage can be inferred.
- Grain size effects δ' .
 - Up to particle diameters of around 5 mm, there may be a link between particle size and the thickness of a developed shear zone (Ho et al., 2011).
 - δ' is generally greater for smaller particle sizes and/or particles of more angular or elongated morphologies (Han et al., 2018).
- Surface roughness effects δ' .
 - Generally, δ' increases with an increasing interfacial surface roughness (i.e. the roughness of a steel element in a soil-steel system) (Han et al., 2018).

2.5.3 Computational modelling of AE propagation

Computational modelling allows for the relatively quick and cost-effective digital simulation of physical and mathematical problems. Computational modelling therefore has many advantages over traditional physical modelling, such as with laboratory and field experiments, including:

- Precision control over various and numerous parameters leading to reliable and repeatable solutions within the capabilities of the software.
- Comparably quick set-up times compared to physical models of the same problem for time and cost-effective solutions.
- Easy repeatability, even of small changes, for an increased reliability of collected data.
- Wide ranging functionalities with many pre-built software packages available for a range of modelling scenarios and often including pre- and post- data processing capabilities.

Consequently, computational modelling is becoming a popular process within both scientific and industrial communities. With advances being made in the technological industry every day, the accuracy and capabilities of available modelling software also continues to increase.

2.5.2.1 Numerical methods and modelling software

Numerical methods provide the mathematical laws from which modelling programs calculate solutions. Different modelling programs will use different numerical methods, sometimes in combination, dependent on the purpose of the modelling as each method brings its own advantages and disadvantages. Some of the most common advantages and disadvantages include differences in simulation times, instability at certain resolutions, and difference in spatial and temporal accuracies. Usually however, spatial and temporal accuracies are a trade-off with one another.

Three common numerical methods used to investigate wave behaviours have been investigated, finite difference (FD), finite element modelling (FEM), and matrix methods. Modelling software using each has also been identified below.

FD methods may be used in either the frequency or time domains. For forward modelling, FD methods are simple to apply in the time domain however become complicated in the frequency domain. Contrastingly, for inverse modelling FD methods are easy to apply in the frequency domain but complex in the time domain (Sakuma et al., 2014).

FD methods also include finite-difference time domain (FDTD) modelling. FDTD is an iterative process that calculates a solution one step into the future with each iteration step. It replaces spatial and temporal derivatives with finite approximations to form a solution with each iteration, thereby evolving in time. The method is based on Maxwell's equations, most notably Faradays and Amperes (Schneider, 2017), magnetic flux and magnetic field equations, respectively.

Although relatively simple to calculate with an ability to provide solutions to complex situations, FDTD is a computationally expensive process and can have unreliable accuracy subject to its implementation (Schneider, 2017 and Sakuma et al., 2014). Sakuma et al. (2014) state the method provides second order accuracy in time and fourth order accuracy in space. Second order accuracy, or second order behaviour, may be explained where a decrease in the input change by a factor of ten, results in a decrease in error by a factor of 100 (Schneider, 2017). The method is therefore highly sensitive often with stability problems.

FDTD as a modelling method is used by the program SimSonic. Although the program has not been considered as appropriate to the project, SimSonic is designed to model ultrasonic wave propagation through layered materials and has been used in many medical papers. Bossy et al. (2005), used the program for modelling elastic wave propagation through bones. They chose it because it could provide accurate models in both fluid and solid materials and reduce errors at boundary reflections, a common

geophysical problem (Bossy et al., 2005). Xie et al. (2016) also used FDTD modelling for ultrasonic simulation, comparing it with analytical and FEM methods.

FEM, also sometimes referred to as finite element analysis (FEA), is built upon the fundamental laws of physics expressed as discretised mathematical models. Physical laws are modelled with mathematical expressions bound by real-world conditions and therefore forming numerical models governed by physical interaction. In the case of soil-structure interactions, constitutive models, which provide the governing equations underpinning material responses, are therefore of vital importance.

FEM is advantageous as it can provide more in-depth solutions than simpler analytical methods. The complex mathematical processes behind FEM, however, make it a computer intensive process.

Examples of the use of FEM based software are widespread with many modern modelling programs using the technique due to the increased computational power of modern-day technology. The commonly used, industry standard modelling packages Abaqus and ComSol Multiphysics, for example, both use FEM. Consequently, it may be inferred that a lot of modern research and technology relies heavily on FEM.

Differently to FD and FEM, matrix methods work on the assumption that an interactive system may be considered as multiple layers. Matrix formulations can describe the propagation of elastic waves through an arbitrary number of system layers by modelling the relationships between stress and displacement. This is done by combining the dynamics of continuum and interactional conditions between interfaces (Lowe, 1995, and Rose, 2014).

The first matrix formulation to be developed was the Thomson matrix method, this was soon adapted by Haskell to improve small errors, and become the Thomson-Haskell matrix method, or transfer matrix (Lowe, 1995). The transfer matrix works by condensing a 'multi-layered system into a set of four equations relating the boundary condition at the first interface to the boundary conditions at the last'; the method therefore only describes a system using the external boundary conditions (Lowe, 1995). It is a simple technique and perfectly adequate when attenuation does not need to be considered. Given boundary conditions and material attenuation however, it becomes unstable and sensitive to changes. In particular, thick layers combined with higher frequencies produce high instability within solutions and reduce the model's reliability (Lowe, 1995, Pavlakovic, 1997, and Rose, 2014).

Various adaptations for the transfer matrix method have consequently been proposed to address these attenuation and material problems (Lowe, 1995, and Cunfu et al., 2013). Instability, although often decreased, still influences most solutions though.

In 1964, a fundamentally different matrix method, the global matrix, was then proposed by Knopoff (Lowe, 1995). The global matrix method is a single, large matrix combining multiple matrices describing the individual system layers (Lowe, 1995, and Pavlakovic et al., 2001). Each system layer is described similarly to the transfer matrix method with four governing equations satisfying the boundary conditions at each interface. As a result, there are $4(n-1)$ equations involved with n being the total number of layers (Lowe, 1995). As shown by Pavlakovic et al. (1997), the individual layers may have up to six different partial waves within them resulting in a 6-by-6 matrix for each layer. The 6-by-6 matrix is formed from each partial wave being assigned amplitude values dependent on their significance.

A major advantage of using the global matrix method is that it overcomes problems with instability at high frequency-thickness products (Lowe, 1995, Pavlakovic et al., 2001, and Pavlakovic et al, 1997), as discussed for the transfer matrix method. Furthermore, the method uses a base matrix that may be applied to many different situations such as solid or liquid propagation in vacuum with real or complex components, without the need for adaptation (Lowe, 1995, and Pavlakovic at al., 1997).

The global matrix method, however, cannot solve modes where their phase velocity is equal to one of the bulk velocities (Pavlakovic et al. 1997). Also, since the solution is calculated using all the governing equations simultaneously the method can also be very slow depending on the size of the overall matrix. Complex and/or larger systems are consequently very computationally expensive (Lowe, 1995).

Examples of the use of matrix methods include Disperse. Disperse as a piece of modelling software using FEM combined with global matrix methods (Leinov et al., 2015) to model wave propagation through plates and shells. Since its creation, the Disperse program has been shown to have successfully been used for many modelling purposes (Section 4.1.1).

Given the range of numerical methods available and the different programs which used different models, three programs, identified as being most appropriate for modelling wave propagation, were investigated further. These are Abaqus, ComSol, and Disperse. The numerical methods behind these programs are already discussed, therefore a table summarising the main features of each provides a useful comparison (Table 2.11). Additionally, notes discussing the practicalities of each program for modelling soil-structure system interactions are listed.

Table 2.11 Comparing the main features of three computer modelling programs (Abaqus, ComSol Multiphysics and Disperse) with reference to modelling wave propagation and attenuation through soil-structure systems.

	Abaqus	ComSol Multiphysics	Disperse
Cost	Free teaching version (limited usability)	Yearly subscription with additional module purchases	£3500 (lifetime license)
Numerical method	FEM	FEM	FEM and global matrix methods
Shell structures	Yes	Yes	Yes
Complex structures	Yes	Yes	No
Soil interactions	Yes	Yes	Yes
Layer interactions	Yes	Yes	Yes
Attenuation	Yes	Yes	Yes
User defined input sources	Yes	Yes	No
Additional notes	The free version is severely limited in modelling size. Requires CAD programs and/or skills to create structures for modelling with.	Requires CAD programs and/or skills to create structures for modelling with. Requires an additional purchase of several appropriate modules.	Only plate and shell structures can be modelled. Input sources cannot be modified. Single purchase with everything included. No additional skills required.

2.6 Summary

The causes and signs of deterioration within soil-structure systems, as well as the subsequent generation, propagation and attenuation (Sections 2.1, 2.3 and 2.4 respectively) of relating AE have been studied in detail using a range of literary sources. Additionally, methods for modelling AE generation and propagation both physically and computationally (Section 2.5) have been briefly investigated.

AE is shown to be a popular form of monitoring method. It is a passive method whereby signals are not purposefully induced and has evolved over the past few decades, although the required component equipment remains largely the same (Section 2.2).

Nine processes leading to the deterioration of soils and soil-structure systems, and the consequent generation of AE, have been identified (Section 2.1). These processes are a result of both natural and anthropogenic influence.

Qualitative interpretation of soil-steel generated AE is established, however quantitative interpretation of soil-steel generated AE is currently lacking. Smith and Dixon (2019) do provide some quantitative interpretation and demonstrate how AE measurements can be used to identify accelerating deformations, the change between contractive and dilative behaviours, and the

mobilisation of peak shear strength in tri-axial sand specimens, however the current application of this knowledge is limited.

2.6.1 Gaps in knowledge

The chapter has therefore enabled the identification of gaps in current knowledge. These include (1) a current lack of an adequate framework for quantifying AE attenuation within buried structure systems; and (2) a quantitative framework for interpreting AE generated by soil-structure interactions.

An understanding of AE attenuation within buried structure systems would serve as guidance in the deployment of efficient sensor networks for AE monitoring. A quantitative framework to interpret AE generated by deforming buried structure systems will enable decision makers to make targeted and timely interventions, such as to evacuate people or undertake preventative measures (e.g. remediation).

The development of an adequate framework for quantifying attenuation and interpreting AE generated within soil-structures systems will therefore be focused on throughout this thesis through: studying the effects and influences of different burial structures and environments on wave propagations and attenuation (Chapters 4 and 6); and identifying and quantifying relationships between different AE parameters (Chapters 5 and 6).

Chapter 3: Methodology

3.0 Methodology

The methodologies in this chapter detail and justify the approaches used to achieve the research aim and objectives defined in the Chapter 1. Overall, the research methodology is applied, aiming to develop a quantitative framework to interpret soil-steel interaction-generated AE and their propagation in buried infrastructure. The research is therefore also deductive, providing quantitative solutions.

Fellows and Lui (2009) describe quantitative research and solutions as allowing phenomena to be explained with the use of numerical data. By modelling a series of systems (both experimentally through laboratory testing and computationally with a Disperse study) within which variables were systematically changed, the individual influences of different variables could be isolated, understood and quantified parametrically, thereby explaining phenomena quantitatively.

Several methods of primary data collection were used (Figure 3.1). These included: physical modelling using small- and large-scale laboratory testing, including direct shear tests (OB2); and computational modelling using the commercial software package Disperse (OB3). Secondary data, in the form of published work, was then also used to compare, evaluate, and support findings in similar and different contexts.

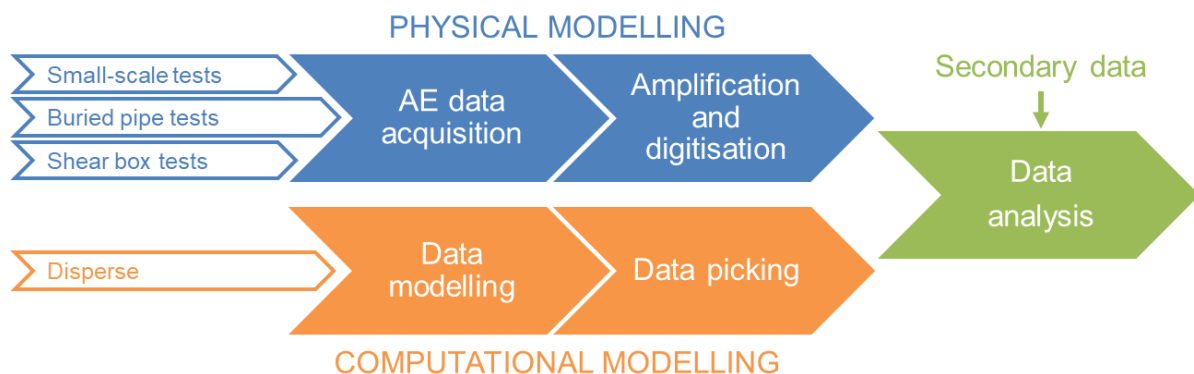


Figure 3.1 The general experimental process.

3.1 AE data acquisition equipment

It was important to maintain consistency throughout the experimental studies so the results of each could be directly compared. For the purpose of continuity all AE data was therefore collected using the same method whilst for the small-scale tests, sensor positioning was also kept the same when possible. This is with exception to the tests in which the data collection method was itself being investigated.

The AE equipment consisted of a 30 kHz resonant frequency piezoelectric transducer (MISTRAS R3 α by Physical Acoustics) which is sensitive over the range 0-100 kHz and was coupled to the structure under investigation using a purposefully designed magnetic holder and a pea sized amount of silicone gel couplant at the contact boundary (Figure 3.2).

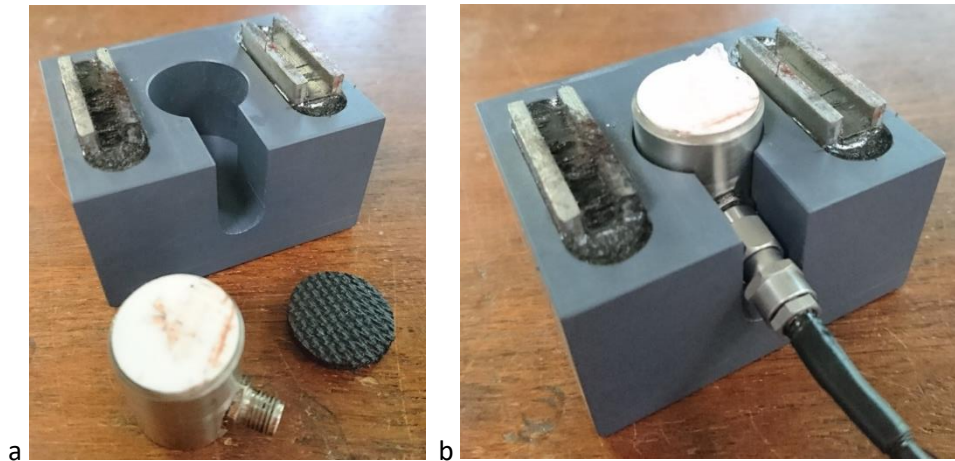


Figure 3.2 (a) Components of a magnetic holder for (19 OD x 22.4 H mm) piezoelectric transducers (b) coupled using a pea sized amount of silicone gel between the ceramic and structure.

The use of a gel couplant reduced the impedance mismatch between the materials, thus increasing the instrument sensitivity. For the small-scale and shear box tests, the transducer was then connected to a 0-1200 kHz filtered pre-amplifier, set with 20 dB gain, which lead into a secondary, 10-100 kHz main amplifier set with 3 dB gain. Although the frequency filters were inherent to the amplifiers, the amount of gain could be varied. Settings of 3 and 20 dB gain respectively, were chosen to avoid over amplification, and therefore limit the loss of data due to ‘clipping’ by the analogue to digital convertor, whilst still improving the signal to noise ratio. With the convertor having a limited voltage range, high voltage signals would be cut at the limiting value (clipping) and data would therefore be lost.

The signal was then digitised using a National Instruments analogue to digital convertor (2 MHz sampling frequency) which connected to the main amplifier. The digital signal was then directly fed into a laptop or desk computer.

For the large-scale tests however, a slightly different configuration was used as data from multiple locations was required. Three piezoelectric transducers, coupled to the structure in the same way, therefore lead into three separate and modified pre-amplifiers. The modified pre-amplifiers had inbuilt frequency filters between 10 and 50 kHz and were set with a gain of 20 dB. The modifications allowed the pre-amplifiers to be powered directly from mains power, via a moderator, rather than through a secondary main amplifier which had provided their power in other tests. This was required as the secondary amplifier only had capacity for one signal.

The pre-amplifiers were then connected directly to a PXI (PCI eXtensions for Instrumentation) DAQ (data acquisition) system, by-passing the need for a separate main amplifier and analogue to digital convertor. The PXI DAQ acted as a self-contained computer system providing the same services amplification and conversion services. A monitor was then connected to the system from which the data collection software could be run.

The entire AE acquisition equipment set up is shown in Figures 3.3 and 3.4 for the small-scale and shear box tests, whilst Figure 3.5 shows the amended set up for the large-scale laboratory tests. Both the main amplifier and analogue to digital converters required mains or alternative power as shown.

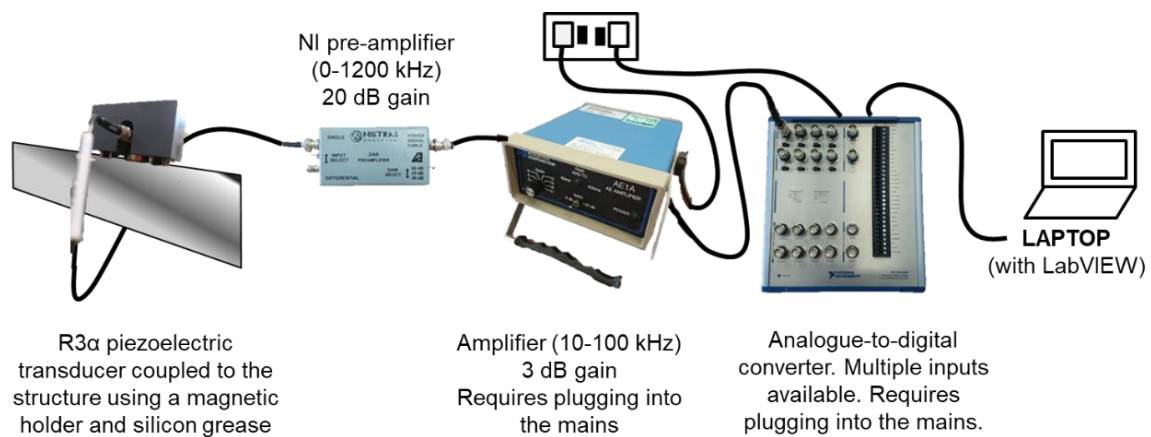


Figure 3.3 AE acquisition equipment set up for small-scale and shear box laboratory testing.

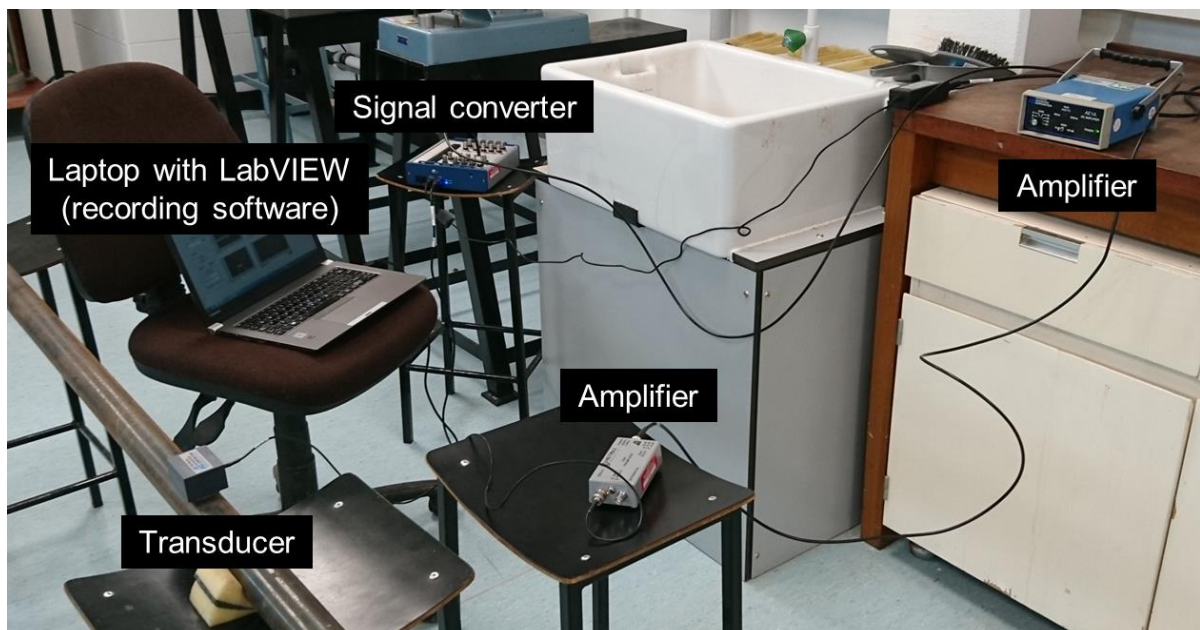


Figure 3.4 Photograph of the AE data acquisition equipment in an example laboratory experiment.

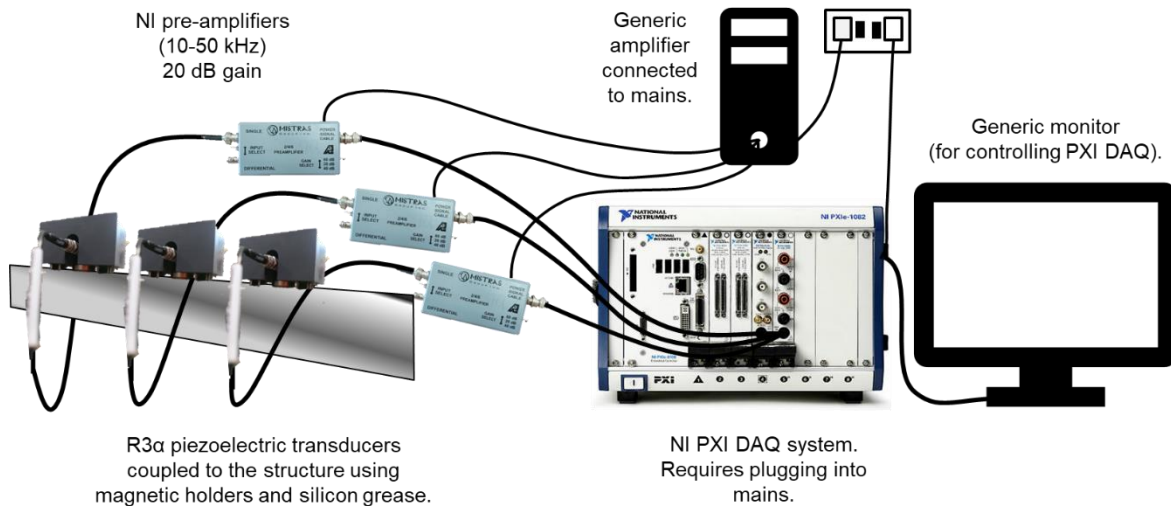


Figure 3.5 Set up of the AE acquisition equipment for large-scale laboratory testing.

The collection of AE data was orchestrated using three variations of a LabVIEW program. For the controlled pipe tests, a singular channel input was used that collected the raw waveform (voltage with time) data at a rate of one million samples per second, and cumulative ring down count (RDC) data per 10 second time interval. The RDCs were set to register whenever the voltage passed a threshold value, in this case 1 mV. A value of 0.01 V was chosen as this has been shown to sufficiently filter out background noise whilst still capturing low-level AE activity (Figure 3.6) (Smith and Dixon, 2019).

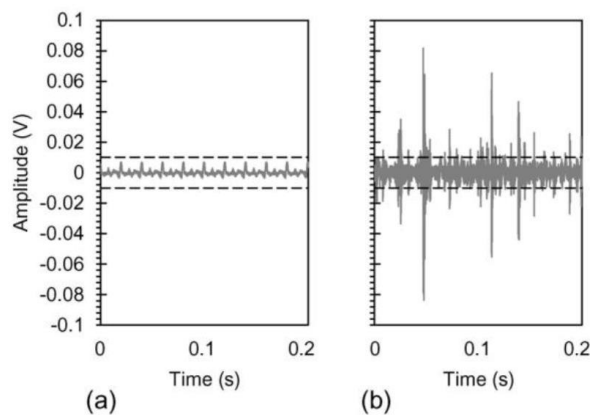


Figure 3.6 Example AE waveforms with superimposed threshold. (Figure 4 from Smith and Dixon, 2019, 'Example waveforms recorded using the AE measurement system showing the 0.01 V threshold level: (a) background environmental and electronic noise, and (b) during soil deformation'). From Smith and Dixon (2019).

For the shear box testing a more complex LabVIEW program incorporating some basic wave analysis in near real-time was applied. This version of the program allowed for the raw waveforms, cumulative RDC, and cumulative RMS data to be collected at time intervals specified by the user. In this case, unless otherwise specified, this was once per second for all the respective parameters throughout the duration of each test.

The program also allowed for a bandpass filter to be applied to recorded frequency data as well as the calculation of fast Fourier transforms (FFTs) in near real-time. Unless otherwise specified, FFTs were therefore captured every thirty seconds whilst the bandpass filter was set to allow only data between 10 and 100 kHz for the duration of each test. The FFT capture rate was chosen as a trade-off between having analysable data and sufficient temporal resolution whilst using a filter of 10 to 100 kHz removed unwanted noise thus making the system field-viable, as described by Smith (2015) and Smith and Dixon (2019). Moreover, Table 2.5 shows that most AE generated as a result of grain friction or force chain rupture, occur within this frequency range.

For the large-scale laboratory tests, a third LabVIEW program was used. This included the same variables as the second version used for capturing data during the shear box tests, but also allowed for multiple input channels to be recorded simultaneously.

Irrespective of the LabVIEW version, the AE data were recorded and written into separate files with either a .tdms extension for the waveform data, or a .lvm extension for all other data. For data with multiple channel inputs, the data for all channels was included in each file.

3.2 Small-scale laboratory tests

Multiple small-scale laboratory tests, summarised in Table 3.1, were conducted to investigate a range of factors relating to signal sources, signal measurement, signal propagation, and background noise. Specifically, the investigations studied signals from different inputs, the sensitivity of varying sensor-structure contacts, the effect of propagation distances, the effect of pipe radius, and the effect of screw joint connections to wave propagation. The effects of wall thickness were not considered and remained constant (at 3 mm) throughout experimentation.

Table 3.1 Programme summary for small-scale laboratory tests.

ID	Signal source	Pipe diameter	Couplings and joints	Sensor	Couplant amount	Attachment of sensor	
1	Input signals	Pencil lead	20 mm	None	R3α	6 mm sphere	Magnetic holder
		Ball bearing	20 mm	None	R3α	6 mm sphere	Magnetic holder
2	Pipe diameter	Pencil lead	20 mm	None	R3α	6 mm sphere	Magnetic holder
		Pencil lead	48 mm	None	R3α	6 mm sphere	Magnetic holder
3	Pipe couplings	Pencil lead	48 mm	Screw joint	R3α	6 mm sphere	Magnetic holder
4	Propagation distance	Pencil lead	20 mm	None	R3α	6 mm sphere	Magnetic holder
		Pencil lead	48 mm	None	R3α	6 mm sphere	Magnetic holder
5	Sensor-structure contact	Pencil lead	20 mm	None	R3α	None	Magnetic holder
		Pencil lead	20 mm	None	R3α	6 mm sphere	Magnetic holder
		Pencil lead	20 mm	None	R3α	10 mm sphere	Magnetic holder
		Pencil lead	20 mm	None	R3α	6 mm sphere	None
		Pencil lead	20 mm	None	R3α	6 mm sphere	Sticky tape

ID	Signal source	Pipe diameter	Couplings and joints	Sensor	Couplant amount	Attachment of sensor
6 Transducer bias	Pencil lead	20 mm	None	R3 α	6 mm sphere	Magnetic holder with cable ties
	Pencil lead	20 mm	None	R.45 α	6 mm sphere	Magnetic holder
	Pencil lead	20 mm	None	R3 α	6 mm sphere	Magnetic holder
	Pencil lead	20 mm	None	R15 α	6 mm sphere	Magnetic holder
	Pencil lead	20 mm	None	R80 α	6 mm sphere	Magnetic holder

Unless otherwise stated, Figure 3.7 shows the generic set up for a 4.85 m long, 20 mm diameter, and 3 mm wall thickness steel pipe used in each experiment. Figure 3.8 similarly shows the set up for a 48 mm diameter pipe. The pipe was balanced over four stools placed approximately equidistantly along its length and of the same height to keep the pipe horizontal. Single scourer sponges (scourer side down) were placed between the stools and the pipe to increase the acoustic impedance of the boundary and thus reduce any attenuative effects a direct contact may have induced. The pipe itself had a thin coating of red-oxide paint; representative of the protective coatings often found on buried infrastructure.

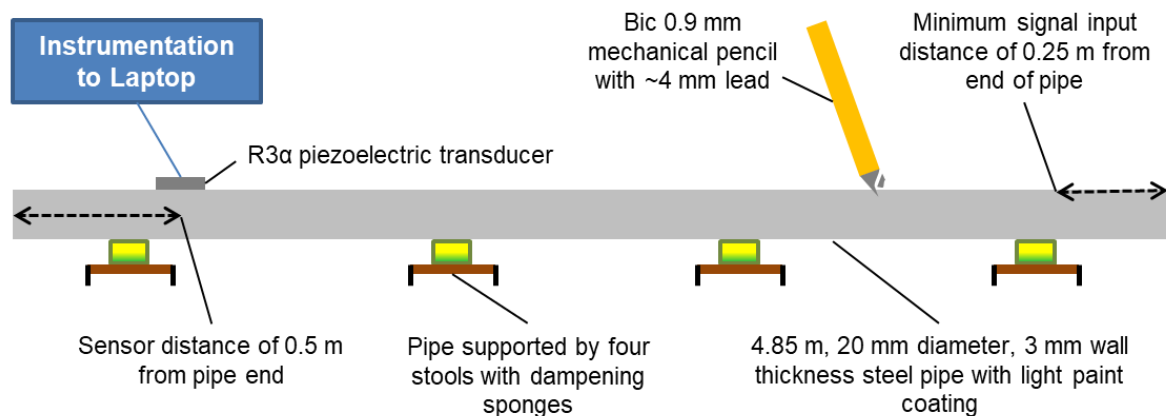


Figure 3.7 A diagram of the controlled pipe set up with which, unless otherwise stated, all controlled pipe experiments were performed. Labels describe individual components.

The piezoelectric sensor was always placed 0.5 m from the end of the pipe. This was to reduce the effect of reflections at the open end and ensure consistent conditions during experiments (i.e. defects within the pipe were always present during propagation), thus reducing errors. For the same reason, the input signals were always induced at a minimum distance of 0.25 m from the other end of the pipe.

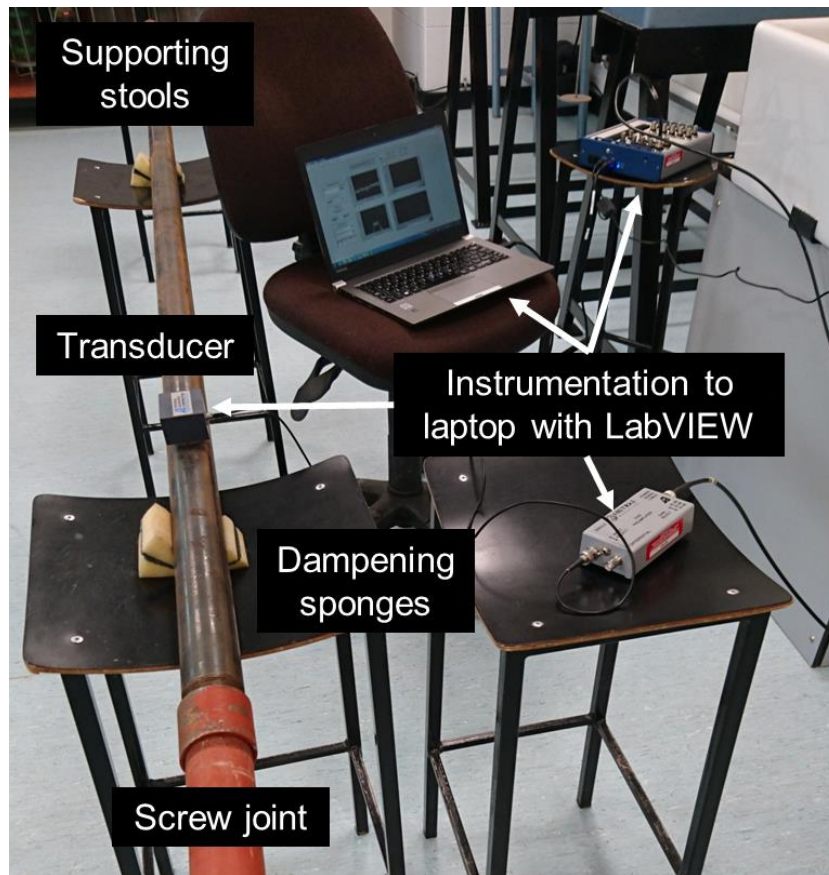


Figure 3.8 Example photograph of a controlled pipe set up for a 48 mm diameter pipe in which two dampening sponges were required. Labels describe individual components.

Figure 3.7 also shows that pencil lead breaks were used as the main input source. Pencil lead breaks have relatively broadband but short duration signals and, as a standard test method (Sause, 2011), are used in multiple published works making their results comparable. Broadband and short duration signals are good for wave analysis with the ideal signal being a Dirac delta function, a signal of infinite amplitude and infinitesimally short duration in the time domain that represents all frequencies equally in the frequency domain (e.g Figure 3.9). By representing all frequencies within experiments, a signal will always be representative of a real-world signal. Additionally, short temporal duration and transient signals allow for the determination and allocation of accurate time stamps for wave velocity and modal analysis.

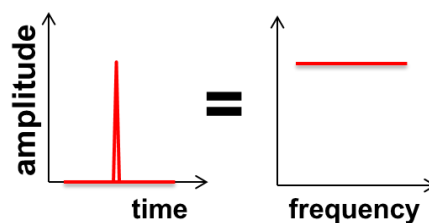


Figure 3.9 A Dirac delta function in the time and frequency domains.

At each test location (input source) at least three pencil lead break tests were conducted. Conducting three tests showed the repeatability of the method but also increased the reliability of results through averaging in later analysis. Figure 3.10, for example shows example results for pencil lead break tests, acquired from small-scale laboratory experiments, in which peak amplitudes have been plotted with distance for multiple individual tests. Good repeatability in these results may be seen with the averages being representative of the general results.

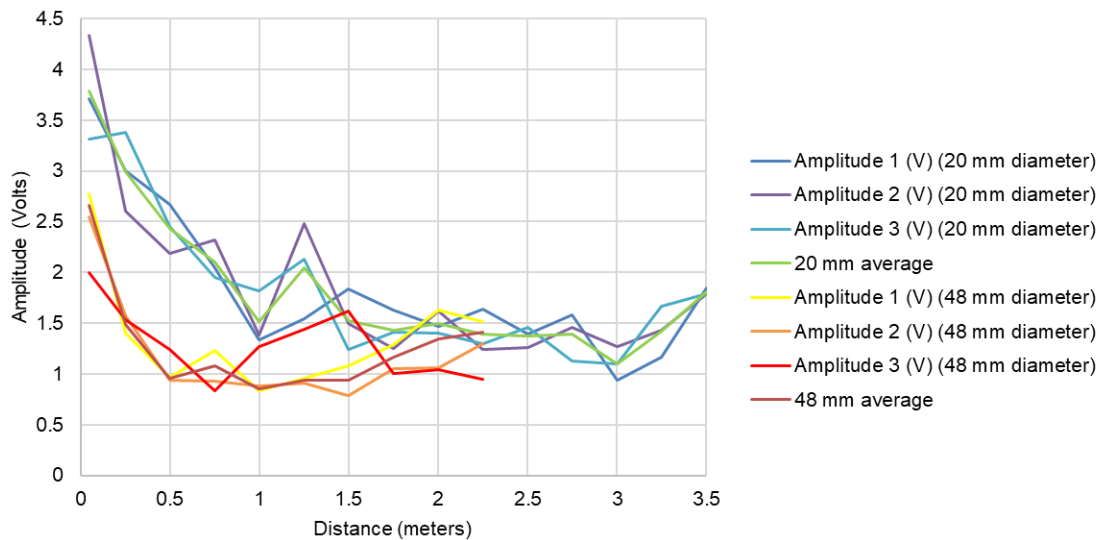


Figure 3.10 Measured peak amplitudes with distance for numerous individual pencil lead break tests.

Where possible, the same test locations were also used in order to take account of defects causing potential distortion of signals and therefore make results directly comparable. Results were recorded using the AE acquisition set up as described in Section 3.1 and the data was then analysed using a mixture of the programs DIAdem and Excel.

The computer software DIAdem is a National Instruments designed data analysis and visualisation package. It was designed in conjunction with the data acquisition system and therefore capable of analysing the .tdms data files recorded by the hardware without a need for file conversion. The program allowed for results to be viewed as either the collected raw wave forms (time-amplitude graphs) in the time domain, or calculated frequency spectra (frequency-amplitude graphs) in the frequency domain. In both cases, mathematical analysis, such as the subtraction, filtering and averaging of multiple datasets, was sometimes performed to quantitatively compare different tests.

Time-amplitude graphs could be plotted using the raw data. From these, characteristics such as the signal duration and peak amplitudes were picked (where picking in terms of seismology means to manually select and read the information for a point of interest, usually the first break of a wave).

Frequency spectra however required calculation. This was performed using an inbuilt but programable function within which calculations were performed over a rectangular window (Glossary 4.2).

Generally, the frequency spectra were calculated as an average of each whole waveform. To compare different time periods within a dataset though, multiple spectra were calculated using non-overlapping windows for a singular dataset and displayed together. Notable characteristics from analysis within DIAdem were then recorded into Excel spreadsheets for further analysis.

3.2.1 Input signals

Different input signals have different measurable characteristics whilst some sources are more repeatable than others. Several potential source signals were therefore investigated including pencil lead breaks, dropping a guided ball bearing, and electronic induction. Literature suggests that most laboratory-based propagation experiments use either pencil lead breaks or electronically induced vibrations. For practicality however, electronic inducing signals correctly for the small-scale tests would have been too time consuming. Figure 3.11 shows the two input signal tests tested: pencil lead breaks and dropping a guided ball bearing.

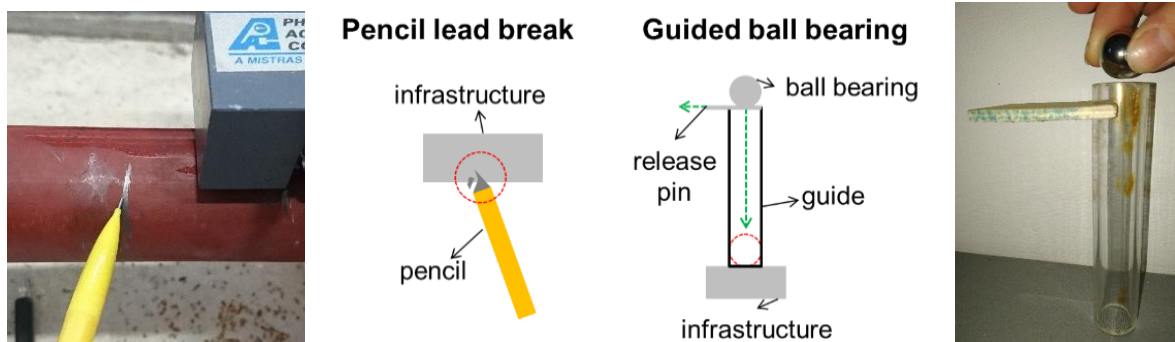


Figure 3.11 The tested input signals: pencil lead breaks (left) and dropping a guided ball bearing (right).

For the pencil lead break tests, a Bic 0.9 mm mechanical pencil with approximately 4 mm of protruding lead was used. The lead was broken by applying a quick but strong force on the lead by pressurising it against the structure. A Bic mechanical pencil was chosen due to its common availability as well as the uniformity, and therefore breaking repeatability, of the lead. Using approximately 4 mm of protruding lead allowed breaks to be easily produced using pressure, whilst still providing control. Standard tests suggest using 3 mm lead, however this was less controllable.

For the guided ball bearing drop tests, a 10 g, 14 mm diameter ball bearing was dropped into a 15 mm diameter plastic guide tube held at the structure's surface. The guide tube was held vertically to minimise any effects the guide tube may have had on the drop, whilst in direct contact with the

structure to allow for easy repeatability. The ball was dropped from a set distance of 105 mm each time using a wooden release pin fitted within the tube using a cut out notch.

Both input signal tests were conducted three times each at four different distances (centralising at 0.05, 2, 3 and 4 m) from the centre of the sensor coupling. This resulted in twelve tests for each source, as shown in Figure 3.12.

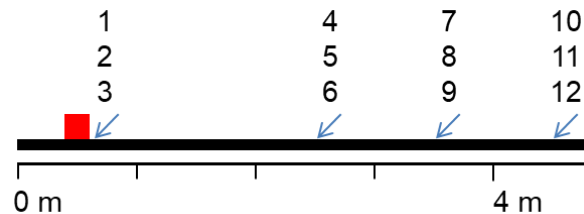


Figure 3.12 The locations of input source tests (numbered blue arrows) with respect to a sensor (red square) on a steel pipe.

3.2.2 Sensor-structure contacts

The sensor-structure contact can affect the measurement or signals. Six experiments specifically aimed at testing the effect of variations in the sensor-structure contact were conducted by focusing on two overall variables: the contact pressure, and the use of a couplant. These were performed in order to inform the deployment of a sensor-structure network and the subsequent interpretation of AE signals. The six variations included:

- (1) Light sensor pressure by balancing the sensor on the pipe.
- (2) Medium pressure by attaching the sensor with sticky tape.
- (3) Strong pressure by attaching the sensor with both a specially designed strong magnetic holder and the addition cable ties.
- (4) The use of no silicone gel and therefore no couplant.
- (5) The use of silicone gel couplant equivalent to a 6 mm diameter sphere (pea sized).
- (6) The excessive use of silicone gel couplant equivalent to a 10 mm diameter sphere.

with photographic examples shown in Figure 3.13.

Unless stated as a variable, a specially designed magnetic holder was used to attach the sensor to the pipe. Additionally, a pea sized amount of silicone gel couplant was placed between the sensor and structure in order to reduce the acoustic impedance by excluding air.

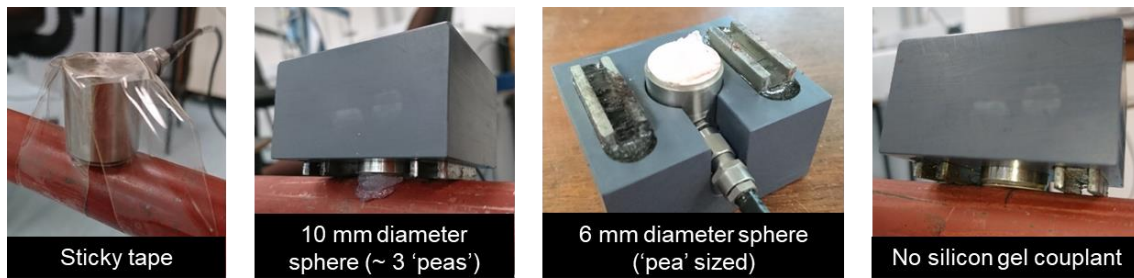


Figure 3.13 Photographs for some of the sensor-structure contact methods tested: attachment with sticky tape (method 2), the use of an excessive amount of silicone gel (method 6), the use of a 'normal' amount of silicone gel (method 5), and the use of no silicone gel couplant (method 4) (left to right).

For each variation, three pencil lead break tests were performed at 1 m from the sensor centre (Figure 3.14); overall, eighteen tests were performed.

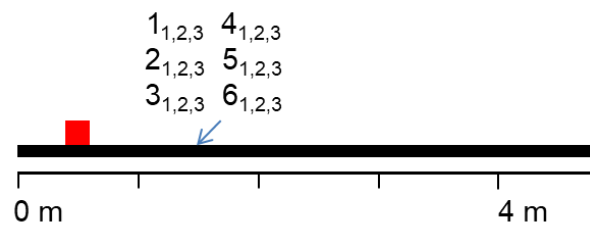


Figure 3.14 The location of the varied sensor-structure contact tests (numbered blue arrow) with respect to a sensor (red square) on a steel pipe.

3.2.3 Sensor bias

An investigation into the bias of sensors with different resonant frequencies was conducted using four piezoelectric transducers produced by Physical Acoustics: R.45 α , R3 α , R15 α and R80 α . Table 3.2 summarises the specifications of each.

Table 3.2 Summarised specifications for four piezoelectric transducer, R.45 α , R3 α , R15 α and R80 α , from National Instruments alpha series.

	R.45	R3 α	R15 α	R80 α
Size (mm)	28.6 x 40.6	19 x 22.4	19 x 22.4	19 x 21.4
Temperature range (°C)	-45 to 150	-65 to 175	-65 to 175	-65 to 175
Shock limit (g)	500	500	500	500
Resonant frequency (kHz)	20	29	150	200
Peak sensitivity (dB)	85 (m/s)	80	80	80
Weight (g)	121	41	34	32

For each sensor, three pencil lead break signals were input at four distances, 0.05, 1, 2 and 3 m, from the sensor centre. This resulted in a total of forty-eight tests, twelve for each sensor. An example set up is shown in Figure 3.15.

It should be noted that for tests involving the R.45 α transducer, the magnetic holder as described in Section 3.2.2 was not used due to the sensor's physical size. Instead, the sensor was secured using sticky tape. The results from these tests were therefore not directly comparable, however using the results from the study investigating sensor-structure coupling, the results were scalable and therefore comparable.

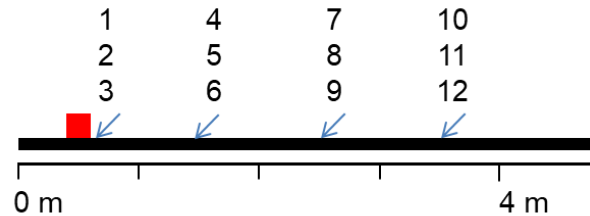


Figure 3.15 The locations of the sensor bias tests (numbered blue arrows) with respect to a sensor (red square) on a steel pipe.

3.2.4 Propagation distance

Attenuation as a result of propagation is a known phenomenon. The behaviour was investigated by measuring and comparing the results of pencil lead break tests along the length of a pipe. Signals were input at regular 0.25 m interval distances, with respect to the sensor centre, along the length of a pipe (Figure 3.16). It should be noted that a 0 m propagation distance was not possible and is instead represented a distance of 0.05 m. Overall forty-five tests were conducted, three at each position.

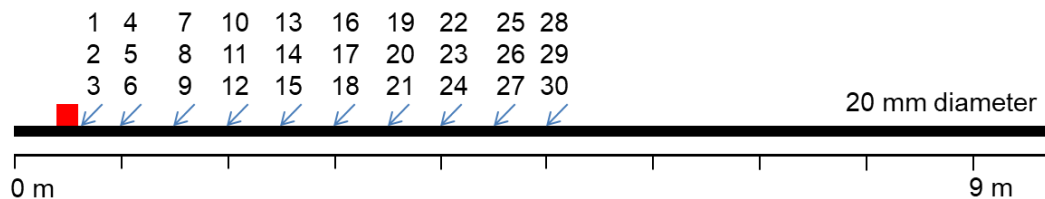


Figure 3.16 The location of propagation distances tests (numbered blue arrows) with respect to a sensor (red square) on a steel pipe.

3.2.5 Pipe geometry and couplings

Section 2.4 showed that wave behaviours are complex and can be affected by geometry. The effect of pipe geometry was investigated by looking at two major variables: the pipe radius; and connecting screw joints.

To investigate the effect of pipe radius, tests comparing the propagation of pencil lead breaks with distance for two different radii pipes were conducted. The tests used a 4.85 m long, 20 mm diameter steel pipe, as used for all previous small-scale tests, and a new 2.6 m long, 48 mm diameter steel pipe.

Both pipes had wall thicknesses of 3 mm, making them comparable, although it should be noted that, unlike the 20 mm diameter pipe, the 48 mm pipe was unpainted and slightly rusted.

Signals were input at regular 0.25 m distance intervals up to 2.25 m for each pipe (Figure 3.17). This resulted in a total of sixty tests altogether, thirty on each of the pipes and three at each test location. As with the propagation distance tests, an initial 0 m test was not possible and is instead represented by a 0.05 m test.

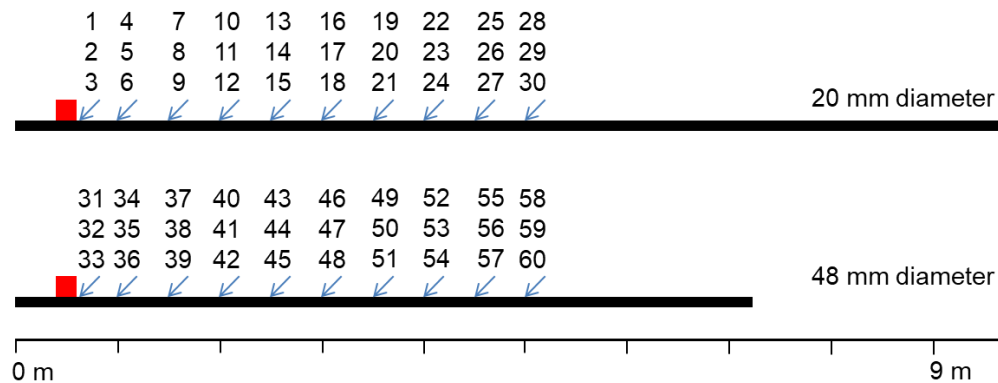


Figure 3.17 The locations of pipe radii propagation tests (numbered blue arrows) with respect to a sensor (red square) on a steel pipe.

To investigate the effect of a threaded screw joint on wave propagation, two 48 mm diameter steel pipes were connected. 48 mm diameter pipes were used as these were readily available and of the same wall thickness (3 mm).

The joint consisted of two screw threaded pipe ends connected by a threaded sleeve (Figure 3.18). It was lightly greased and tightened by hand to create a secure but relatively loose connection (mimicking a loosening joint). A similar set up to Figure 3.7 was used, however, due to the weight of the pipe, two scourer sponges were used as dampeners between the stools and pipe (Figure 3.8).

To input signals, pencil lead breaks were used at several locations and in several sensor-signal configurations around the pipe joint (Figure 3.19). Multiple configurations were used to observe the wave-joint interactions in greater depth. Overall, twenty-four experiments, including repeats, were therefore conducted with details of each given in Table 3.3. It should be noted that, as long as the pipe was of a suitable length to minimise the effect of end reflections, the total pipe length was insignificant as wave behaviours were only measured within a 0.3 m zone around the screw joint.

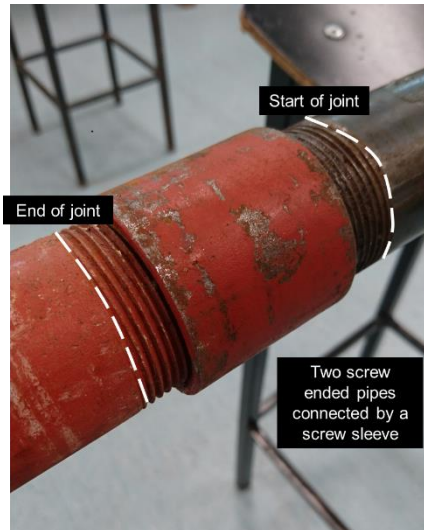


Figure 3.18 Photograph of the screw threaded pipe joint, connecting two 48 mm diameter and 3 mm wall thickness pipes, with superimposed labels.

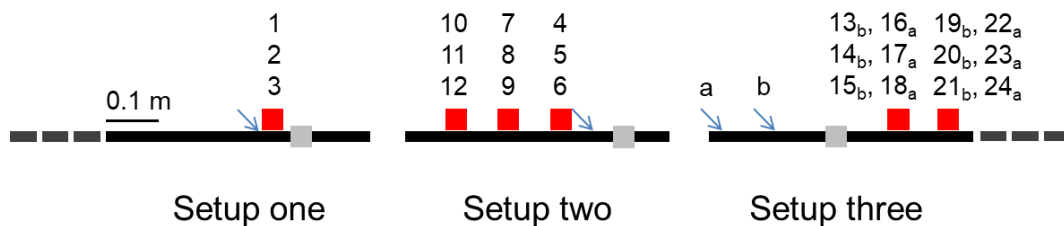


Figure 3.19 The varying locations of screw joint propagation tests (numbered blue arrows) with respect to a sensor (red square) on a steel pipe of insignificant length (dashed lines). Relative positionings drawn to scale.

Table 3.3 Screw joint tests sensor and signal input positionings with respect to one another for each test.

Test No.	Sensor positioning (centre of)	Signal input positioning
1, 2, 3	0.05 m before the start of the screw joint threading	0.05 m before the centre of the sensor (0.1 m before the joint)
4, 5, 6	0.1 m before the start of the screw joint threading	0.05 m before the start of the screw joint threading
7, 8, 9	0.2 m before the start of the screw joint threading	0.05 m before the start of the screw joint threading
10, 11, 12	0.3 m before the start of the screw joint threading	0.05 m before the start of the screw joint threading
13, 14, 15	0.1 m after the end of the screw joint threading	0.1 m before the start of the screw joint threading
16, 17, 18	0.1 m after the end of the screw joint threading	0.2 m before the start of the screw joint threading
19, 20, 21	0.2 m after the end of the screw joint threading	0.1 m before the start of the screw joint threading
22, 23, 24	0.2 m after the end of the screw joint threading	0.2 m before the start of the screw joint threading

3.3 Water flow tests

The transportation of water through pipes generates measurable AE, also known as flow noise. Flow noise was investigated using a programme of small-scale tests (Table 3.4) to study the influence of flow velocities on the measured signal. In total, thirty tests (for 8 flow regimes) measuring the AE outputs over a range of flow velocities were performed with the aim of characterising flow noise (OB3) dependent on velocity.

Table 3.4 Programme summary for water flow tests.

No.	Flow regime	Tap details	Flow rate (m/s)
1	Minimal flow	Tap turned to only just provide flow	< 0.01
2	Very small flow	Tap turned to provide a very small flow	0.01 to 0.099
3	Small flow	Approximate 1/10 turn of tap	0.1 to 0.199
4	Medium flow	Approximate 1/9 turn of tap	0.2 to 0.299
5	Medium-strong flow	Approximate 1/8 turn tap	0.3 to 0.399
6	Strong flow	Approximate 1/4 turn of tap	0.4 to 0.499
7	Very strong flow	Approximate 1/2 turn of tap	≥ 0.5
8	Varied flow	Tap position changes throughout	Varied

Figure 3.20 shows the overall set up of the study. For each test within the programme, a piezoelectric transducer was coupled to a 22 mm diameter, vertically orientated copper pipe of an unknown thickness (Figure 3.21). This pipe fed into a sink and was chosen due to its accessibility. Although the sensor was held within the magnetic holder, copper is not magnetic so the holder itself was attached using two reusable and adjustable cable ties (Figure 3.21). Reusable and adjustable cable ties were used as these could be tightened to the same amount each time thus making the results comparable.

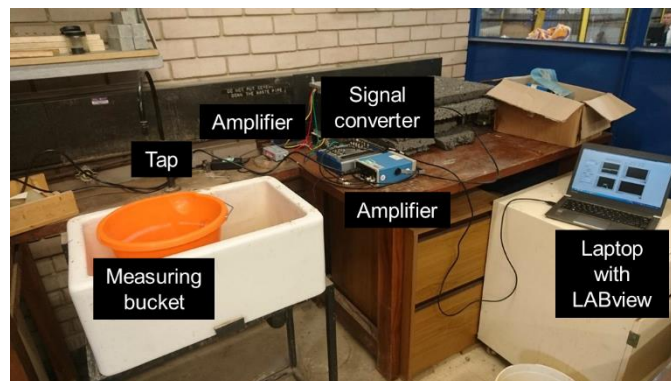


Figure 3.20 A photograph of the overall equipment set up of the flow rates study.

Flow signals were induced by opening and closing the connecting tap. The flow rate was controlled by the amount the tap was opened. Opening and closing the tap (inducing and stopping the water flow respectively) was done by turning the tap to the desired amount in one move and as quickly as possible to allow for the establishment of a steady flow. The water was collected in a measuring bucket

(Figure 3.21) over a noted time-period. It was important to collect a measured amount of water within a known time period as this allowed for the flow rate to then be calculated using the internal pipe diameter, flow time, and water volume as in Equation 3.1

$$Fl = \frac{Vol_{water}}{\pi t R^2} \quad [3.1]$$

Where Fl is the flow rate in m/s, Vol_{water} is the collected volume of water in L, t is the collection time in s, and R is the internal pipe radius in m. It should be noted however that due to the pipe thickness being unknown, the internal pipe radius was approximated using the external pipe diameter.

Contrastingly, rather than establishing a single flow rate, one test (test 7) was conducted so that the rate of flow was changed several times throughout the duration of the test. This test was performed to investigate the noise of a changing rate, achieved by opening and closing the tap to different amounts during the test.

Furthermore, unlike the other small-scale laboratory tests, the gain of the pre-amplifier was changed between 20 and 40 dB for different tests. It was noted during recording that the signals being recorded were of a very small amplitude so, for comparative purposes and later data analysis, different values of gain were tested. Details of the individual flow rate tests are summarised in Section 3.8.2.

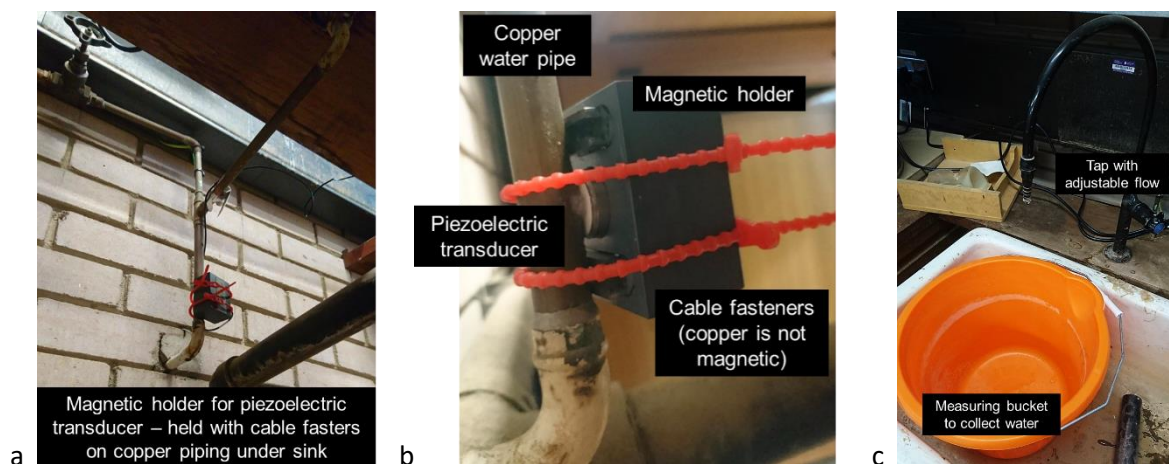


Figure 3.21 Photographs of specific equipment set ups used in the water flow rate tests: (a) the pipe system, (b) attachment of the sensor within a magnetic holder, and (c) the bucket for measuring water flow.

Like the other small-scale laboratory tests, the results of the water flow tests were processed using a combination of DIAdem and Excel.

3.4 Characterising soils

The characterisation of test soils used in experiments was important for understanding and interpreting the results of the tests. Consequently, several tests were undertaken to characterise the

different soil properties including particle size distribution, density, specific gravity, and particle morphologies (Table 3.5). Explanations for these properties are given below:

- The particle size distribution of a soil defines the relative amounts of particles present according to size.
- Packing density refers to the soil's characteristic minimum (ρ_{\max}), and maximum (ρ_{\min}) densities.
- Specific gravity is a dimensionless parameter calculated as a ratio of the substance density against a reference density. In this case the substance was a soil, and the reference density was that of water. All three parameters were obtained to standard BS1377:1990.

The processes for characterising the different properties were repeated at least once for each soil to increase the reliability of the results through later averaging. Particle size distribution, soil density, and specific gravity were all determined using standardised test as shown in Table 3.5. Particle morphologies however were determined using very high-resolution photographic outlines of individual grains. For this a test sample of ten grains was used for each soil type. High-resolution photographs were then taken (at least 200 pixels per circumscribing circle diameter according to Zheng and Hryciw, 2015), the grain outlines from which (e.g Figure 3.22) could be identified computationally and run through an algorithm developed by Zheng and Hryciw (2015) which provided values for roundness and sphericity (conforming to five common definitions) for each grain.

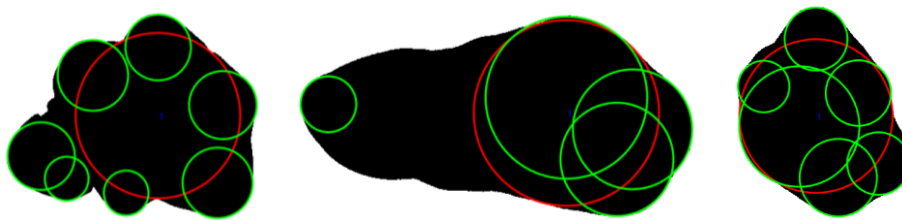


Figure 3.22 Example high resolution grain outlines for LBS with superimposed circles used as part of an algorithm to calculate sphericity and roundness.

Table 3.5 Test programme for soil characterisation.

Soil property		Methods
Particle size distribution		Gradation tests following BS1377:1990
Soil density	Characteristic minimum density Characteristic maximum density	Packing density tests using a known volume mould following BS1377:1990
Specific gravity		Bell jar test following BS1377:1990 (Figure 3.23)
Particle morphology	Roundness Sphericity	High-resolution photography and computationally assisted algorithm analysis



Figure 3.23 Over-end turning process during a bell jar test to characterise soil density.

3.5 Shear box tests

AE generation as a result of soil-steel interactions under varying conditions was studied using a Wille-Geotechnik large direct shear box. The apparatus was used to simulate an element of a buried soil-steel system (e.g. a monopile, pile foundation or utility pipe) (OB2). The shear box could perform shear tests with shearing rates between 0.00001 and 20 mm/m, thoroughly covering the range expected during soil-structure interactions, such as during landslides, and is stated as an ‘advanced and highly accurate shear box system’ with the ability to prevent tilting and wall friction during experiments (Wille-Geotechnik). This is a result of the floating top box design which allows for volumetric changes under a constant normal stress. Furthermore, technical information suggests that the equipment conforms to multiple standards including (Wille-Geotechnik):

- ASTM D-3080
- ASTM D-5607
- BS 1377-7
- CEN ISO/TS 17892-10
- JGS 0560
- JGS 0561

A programme of eighteen tests using the box was developed to study several influential factors to AE generation mechanisms and characteristics within a soil-steel system. These included:

- confining stress,
 - for which three normal stresses were applied: 75, 150 and 225 kPa. These values represent approximate burial depths of: 6, 12, and 18 m, given that bulk unit weight ($9.81 \text{ m/s}^2 \times \approx 1$) \times depth (m) = stress (kPa), and were chosen on recommendation from Alister Smith in conversation (Personal Communication). These are relatively

deep burial depths, but allow for the presence of additional stresses in the vertical plane, such as with loading, as well as variations in the burial material (e.g. compaction) and burial material properties (grain size, angularity, etc.) to be taken account of during testing.

- soil grain size,
for which two soils, LBS and PG, were used as grain size backfills typically used within industry for the burial of steel structures.
- soil packing density,
for which the soil samples were packed in relatively loose and dense states for testing.
- and shearing rate
for which set rate tests, where a constant, set shear rate was used throughout the duration of the tests; stepped rate tests, where the shear rate was increased by 0.25 mm/minute every 5 mm of travel (starting from 0.5 mm/minute); and ramped rate test, where the shear rate was increased by 0.05 mm/minute every 10 seconds (starting from 0.05 mm/minute) were used.

The listed factors were studied parametrically with details of each test summarised in Table 3.6. A detailed list of all tests is given in Section 3.8.3.

Table 3.6 Programme summary for shear box testing.

Test ID	Normal stress (kPa)	Soil	Initial density	Rate (mm/min)	Running time (hh:mm:ss)	Travel (mm)
1 LBS-75dD-1	75	LBS	Dense	1 mm/min	00:40:00	40
2 LBS-150dD-1	150	LBS	Dense	1 mm/min	00:40:00	40
3 LBS-225dD-1	225	LBS	Dense	1 mm/min	00:40:00	40
4 PG-75dD-1	75	PG	Dense	1 mm/min	00:40:00	40
5 PG-150dD-1	150	PG	Dense	1 mm/min	00:40:00	40
6 PG-225dD-1	225	PG	Dense	1 mm/min	00:40:00	40
7 PG-150dL-1	150	PG	Loose	1 mm/min	00:40:00	40
8 PG-150dD-002	150	PG	Dense	0.02 mm/min	20:50:00	25
9 PG-150dD-01	150	PG	Dense	0.1 mm/min	04:10:00	25
10 PG-150dD-stepped-1	150	PG	Dense	Stepped	07:17:30	35
11 PG-75dD-stepped-2	75	PG	Dense	Stepped	00:33:21	40
12 PG-150dD-stepped-2	150	PG	Dense	Stepped	00:33:21	40
13 PG-225dD-stepped-2	225	PG	Dense	Stepped	00:33:21	40
14 PG-150dD-ramped	150	PG	Dense	Ramped	00:20:09	25
15 LBS-150dD-stepped-1	150	LBS	Dense	Stepped	07:17:30	35
16 LBS-75dD-stepped-2	75	LBS	Dense	Stepped	00:33:21	40
17 LBS-150dD-stepped-2	150	LBS	Dense	Stepped	00:33:21	40
18 LBS-225dD-stepped-2	225	LBS	Dense	Stepped	00:33:21	40

3.5.1 Setting up a test

The main shear box consisted of a bottom box and a floating top box, over which a ram providing a defined confining stress could be placed. The boxes could be filled with different materials, whilst an interfacing material could also be put at the boundary between them.

To investigate AE generation in a free-steel-soil system, a 3 mm thick steel plate was used as an interfacing boundary. The bottom box therefore represented a free boundary, whilst the top was filled with soil (Figure 3.24). To prevent significant deformation of the interfacing steel plate however, the bottom box was not left free. Deformation would affect the propagation of signals and skew the results therefore nylon blocks were used to fill the bottom box. Plastic blocks were used due to the material's dampening effects.

After filling the bottom box, the steel plate was then placed over it. The plate was designed with holes to allow it to be bolted down. Bolting it down was important to ensure that it did not move or vibrate as a result of mechanical processes during shearing (Figure 3.25). Rubber dampening material was therefore also used underneath where the plate touched the bottom box to decrease noise and energy leakage from the box and plate respectively. Furthermore, the plate was also designed to have a large excess on one edge so that a sensor could be attached without interfering with the shearing process (Figure 3.25). Step-by-step diagrams of the overall process is shown in Figure 3.26.

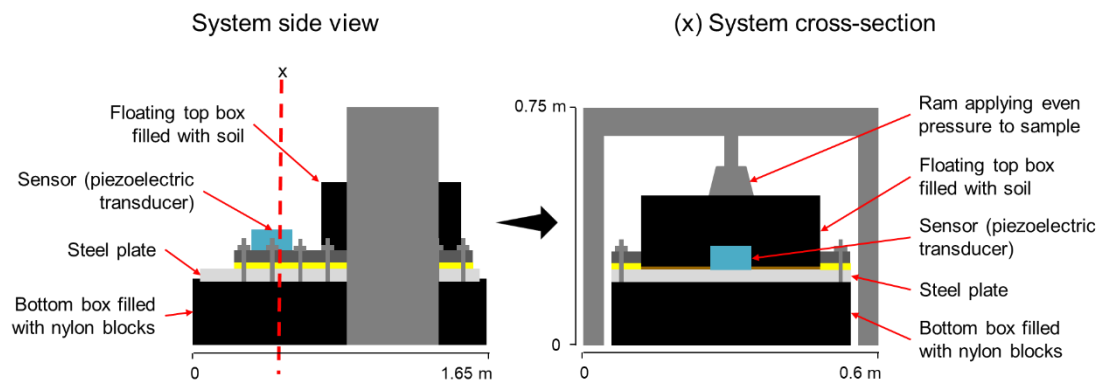


Figure 3.24 Side and cross-sectional views of the shear box testing set up.

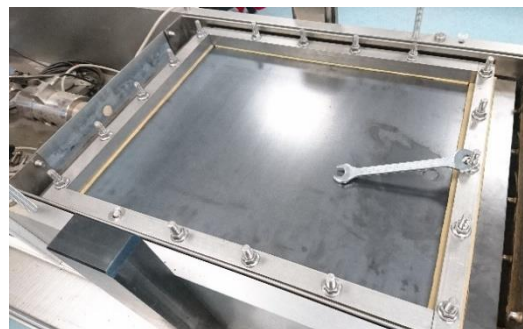


Figure 3.25 A photograph of the bolted steel plate with rubber dampening material.

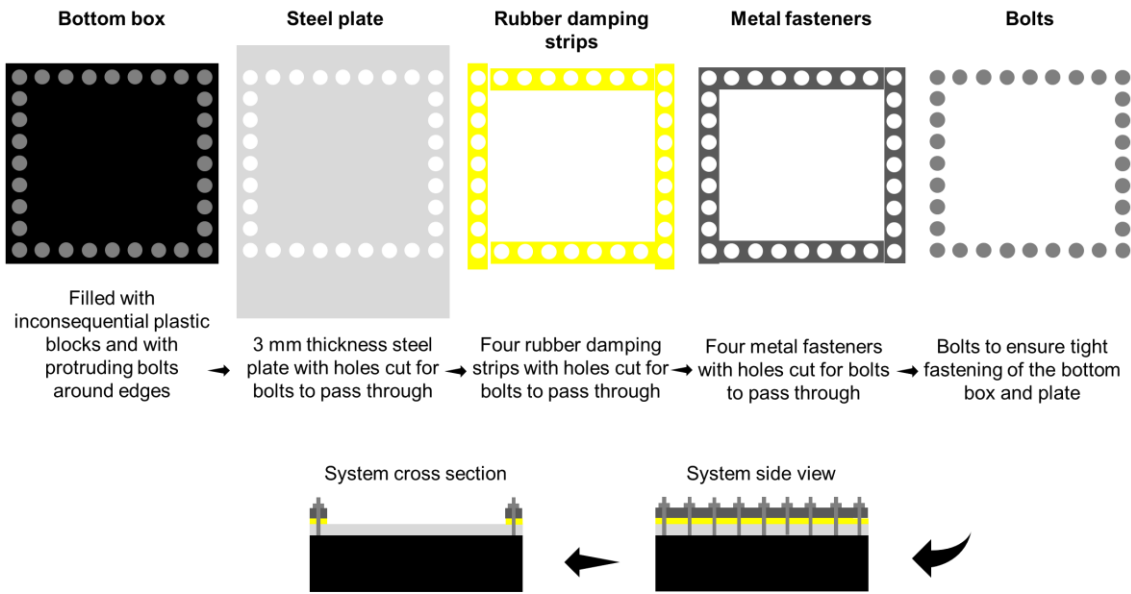


Figure 3.26 Step by step diagrams of how the steel plate interface was set up for shear box testing.

The top box could then be lifted into position over the plate. It should be noted that the top box was floating (around 0.6 mm), and therefore not in direct contact with the interfacing steel plate. The height of the gap between them was minimised, controlled using springs on which the top box sat. Leaving a gap ensured any detected AE was a result of soil-steel interactions rather than steel-steel from the box and plate.

Before filling the top box, roughness measurements of the steel plate were taken using a portable roughness device (Mitutoyo: Surf test 211). The device would drag a stylus across the plate, measuring the average amount of vertical undulation in μm . This method was chosen due to its portability and simplicity of use. The roughness measurements were taken methodically to measure approximately the same area of plate each time, making the different test results comparable. The plate was therefore split into quadrants, and four measurements at four different device orientations taken within each quadrant. This resulted in 16 roughness measurements before each shear test (Figure 3.27).

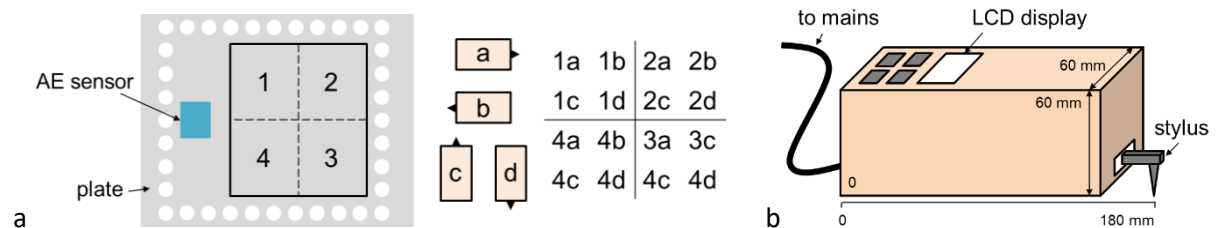


Figure 3.27 (a) Locations and orientations, with respect to the AE sensor, of the roughness measurements taken with the (b) portable roughness device before each shear box test. Sixteen orientation combinations resulted.

The top box was then filled with the test soil using a scoop (Figure 3.28). For repeatability, this was done using a controlled method. Dense soil tests therefore consisted of filling the top box to a depth of 7.5 cm using three 2.5 cm deep layers, each being compacted using a tamping rod before the next layer was added. Loose soil tests consisted of pouring the soil into the box from an approximate height of 10 cm; no compaction was performed at any point during loose filling. In both cases, the soil surface was levelled to allow for application of the loading plate (Figures 3.28 and 3.29).



Figure 3.28 Filling the top box of the shear box with soil.

After filling the top box, a 0.3 by 0.3 m nylon block was placed on top of the soil over which the loading ram was then be manually positioned (Figures 3.29a and 3.29b respectively). Using the nylon block ensured that the load was distributed equally across the surface of the soil sample whilst any mechanical noise was dampened.

To further ensure equal loading during shearing, linear variable differential transducers (LDVT) measuring the movement of the soil surface were also set up (Figure 3.29c). The LDVT measured the relative vertical position of the soil surface, feeding this information back to the machine which could then adjust its loading regime. Collecting positioning data allowed for calculations regarding volume changes (e.g. dilation and contraction) to be made.

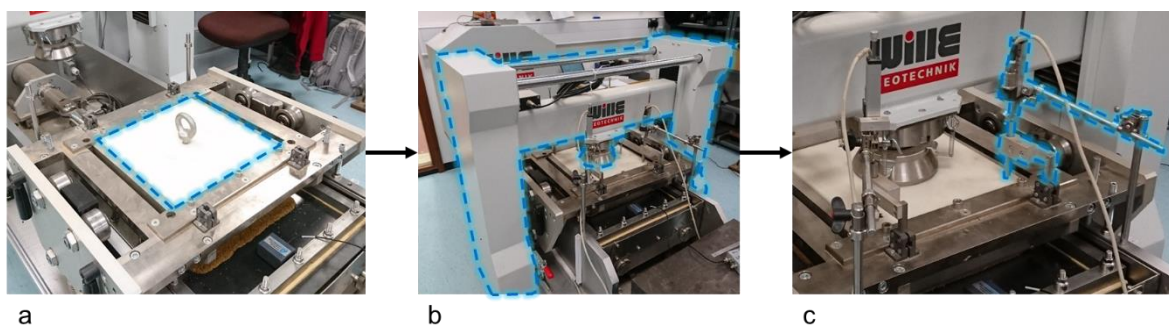


Figure 3.29 Photographs showing: (a) positioning of the nylon block, (b) positioning of the loading ram, and (c) the addition of LDVT to measure surface movements.

Once the shear box and tests specimen were configured, the AE acquisition equipment could then be attached. The piezoelectric transducer was placed centrally on the top of the pate excess and close to the edge (the holder was 1 mm from metal fasteners) to avoid interfering with shearing (Figure 3.30).

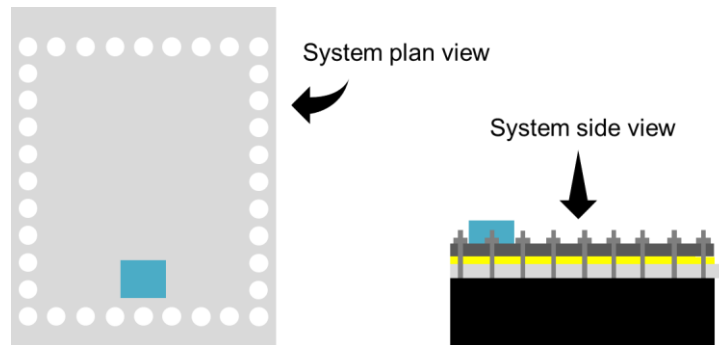


Figure 3.30 The sensor placement for shear box testing, where the sensor is represented by a blue rectangle. (left) plan view. (right) side view.

3.5.2 Running a test

The shear box was controlled computationally using the software GEOsys. GEOsys allowed for relevant parameters such as: shear rate, shear distance, and the application of a normal force to be controlled. Furthermore, it also controlled the initiation of tests and the collection of data.

To run the programme of shear tests several steps were therefore followed:

1. The creation of a logging file within GEOsys

Data collection was coordinated using a logging file. For all tests conducted, data for the parameters of time (s), shear force (kN), normal force (N), settlement (mm), and shear displacement (mm) were collected.

2. Initiation of logging

When a logging file had been created, logging could then be initiated. Initiating logging started the collection of the parameters indicated. Additionally, it allowed for further machine controls, such as shearing and the application of a normal force, to be activated.

3. Application of a normal force

A normal force could then be applied. This was done as a ramped stress (50 N/s) up to the desired value (75, 150 or 225 kPa). In the program, the stress was defined using Newtons, normal stresses of 75, 150 and 225 kPa therefore needed to be calculated as a function of the area using the equation $width \times depth \times \tau \times 1000$.

4. Shearing

When the target normal stress was reached, shearing could then begin. Shearing was conducted as a shear displacement (i.e. displacement controlled); this was usually done over 40 mm. The shearing distance was limited spatially by the presence of a transducer measuring AE (Figure 3.31), however the distance still needed to allow for peak shear stresses to be reached. A distance of 40 mm was therefore used for most tests, although varied dependent on the test type and time constraints.

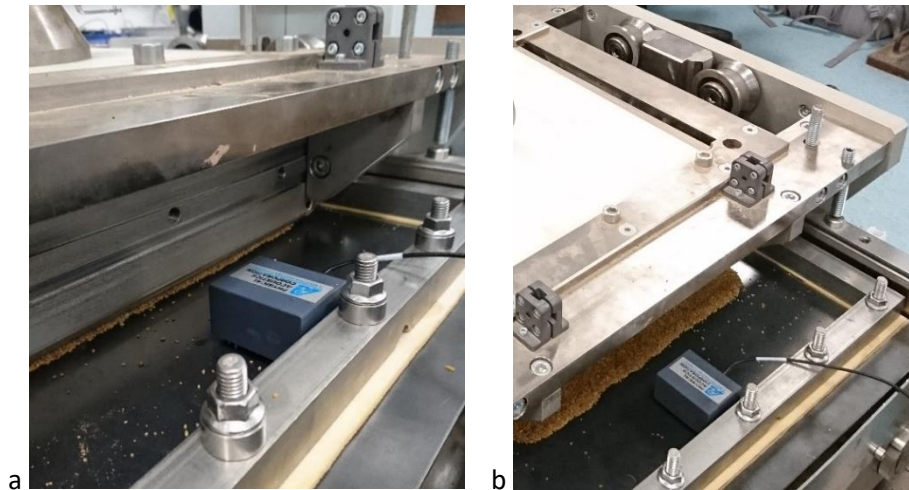


Figure 3.31 The limited travel distance as a result of piezoelectric transducer placement during shear box tests shown (a) near the beginning and (b) at the end of a test.

Most tests within the programme used a constant shearing rate. This allowed for shear rate to be removed as a variable during investigations. However, some tests used stepped (Table 3.7) or ramped shearing rates. Stepped and ramped tests were conducted to provide information on AE behaviours as a result of accelerating shearing, as well as allowing for the effects of different shear rates to be studied. Full details for each shearing test are summarised in Section 3.8.3. It should be noted that the starting time for shearing, and in the case of stepped shear tests, the changes of shear rate, were noted into an Excel spreadsheet.

Table 3.7 Details of the stepped rate shear box test.

Stepped Test: 1			Stepped Test: 2		
Shearing rate (mm/minute)	Travel (mm)	Duration (hh:mm:ss)	Shearing rate (mm/minute)	Travel (mm)	Duration (hh:mm:ss)
0.02	5	4:10:00	0.5	5	00:10:00
0.05	5	01:40:00	0.75	5	00:06:40
0.1	5	00:50:00	1	5	00:05:00
0.25	5	00:20:00	1.25	5	00:04:00
0.5	5	00:10:00	1.5	5	00:03:20
1	5	00:05:00	1.75	5	00:02:51
2	5	00:02:30	2	5	00:02:30
	Total	07:17:30		Total	00:33:21

When each test was finished, logging could be stopped via GEOsys and the collected AE and shear data saved for future analysis. The files were then converted to .txt extensions using the program GOEzip and analysis conducted using a combination of Excel and MatLab.

3.6 Large-scale laboratory tests

A programme of large-scale laboratory tests (Table 3.8) was performed to study the influence of various factors on wave propagation within a steel pipe system (OB3) as well as characterise AE generated from soil-steel interactions (OB2). These factors included: the burial system (air and soil as a burial material), system conditions (moisture and loading), and structural differences (propagation with distance and the presence of pipe couplings). The tests would also provide a means of evaluation for computational models of comparable model systems within Disperse. Consequently, the design needed to be reproducible both computationally and experimentally whilst also allowing for propagation and attenuation behaviours to be observed.

Table 3.8 A summarised programme of the large-scale laboratory tests.

Test ID	Source (pencil lead breaks at)	Sensor location (m)	Set up
Wave propagation (empty)	Bic 0.9 mm at 0.2 m	Sensor 1: 0.25 (top)	Empty
		Sensor 2: 5.7 (top)	Mechanically tightened joint at 6 m
		Sensor 3: 6.7 (top)	
Wave propagation (empty)	Bic 0.9 mm at 0.2 m	Sensor 1: 0.25 (top)	Empty, hand tightened joint at 6 m
		Sensor 2: 5.58 (top)	
		Sensor 3: 7.08 (top)	
Wave propagation (empty)	Standard 0.5 mm at 0.2 m	Sensor 1: 0.25 (top)	Empty
		Sensor 2: 5.7 (top)	Mechanically tightened joint at 6 m
		Sensor 3: 6.7 (top)	
Wave propagation (filled)	Bic 0.9 mm at 0.2 m	Sensor 1: 0.25 (top)	Filled
		Sensor 2: 5.7 (top)	Mechanically tightened joint at 6 m
		Sensor 3: 6.7 (top)	
Wave propagation (filled)	Bic 0.9 mm at 0.2 m	Sensor 1: 0.25 (top)	Filled
		Sensor 2: 5.78 (top)	Hand tightened joint at 6 m
		Sensor 3: 7.08 (top)	
Wave propagation (filled)	Standard 0.5 mm at 0.2 m	Sensor 1: 0.25 (top)	Filled
		Sensor 2: 5.7 (top)	Mechanically tightened joint at 6 m
		Sensor 3: 6.7 (top)	
Wave propagation (filled)	Standard 0.5 mm at 0.2 m	Sensor 1: 0.25 (top)	Filled
		Sensor 2: 5.78 (top)	Hand tightened at joint 6 m
		Sensor 3: 7.08 (top)	
Structural propagation (empty)	Bic 0.9 mm at 0.2 m	Sensor 1: 0.25 (top)	Empty, no joint
		Sensor 2: 5.7 (top)	
		Sensor 3: 5.7 (bottom)	
Structural propagation (empty)	Standard 0.5 mm at 0.2 m	Sensor 1: 0.25 (top)	Empty, no joint
		Sensor 2: 5.7 (top)	
		Sensor 3: 5.7 (bottom)	
Structural propagation (filled)	Bic 0.9 mm at 0.2 m	Sensor 1: 0.25 (top)	Filled, no joint
		Sensor 2: 5.7 (top)	
		Sensor 3: 5.7 (bottom)	
Structural propagation (filled)	Standard 0.5 mm at 0.2 m	Sensor 1: 0.25 (top)	Filled, no joint

Test ID	Source (pencil lead breaks at)	Sensor location (m)	Set up	
Reflections	Standard 0.5 mm at 5.45 m	Sensor 2: 5.7 (top)	Filled Mechanically tightened joint at 6 m	
		Sensor 3: 5.7 (bottom)		
	Standard 0.5 mm at 6.45 m	Sensor 1: 0.25 (top)		Filled
		Sensor 2: 5.7 (top)		Mechanically tightened joint at 6 m
Weighted	Soil-steel interactions from stress at 4.5 m / Standard 0.5 mm pencil lead breaks at 0.45 m	Sensor 3: 6.7 (top)	Filled	
		Sensor 1: 0.25 (top)	Mechanically tightened joint at 6 m	
		Sensor 2: 5.7 (top)	Weight up to 100 lbs added	
Weighted	Soil-steel interactions from stress at 3 m / Standard 0.5 mm pencil lead breaks at 0.45 m	Sensor 3: 6.7 (top)	Filled, mechanically tightened joint at 6 m	
		Sensor 1: 0.25 (top)	Weight up to 120 lbs added	
		Sensor 2: 5.7 (top)		

Figures 3.32 and 3.33 shows the laboratory set up used to perform various aspects of the experimental programme. Due to the differing focuses of each test, it should be noted that not all elements within the figures were used for every experiment.

From Figures 3.32 and 3.33, it can be seen that unlike the small-scale laboratory tests, for which a single sensor was used, the large-scale tests used three R3 α piezoelectric transducers to measure the propagating signal at different distances and positions. These were coupled to a 9 m pipe (3.2 mm wall thickness, 42.4 mm outside, and 39.2 mm inside diameter), formed from one 6 m and one 3 m section connected by a mechanically tightened screw joint (Figure 3.34a), at 0.25, 5.7 and 6.7 m unless otherwise stated. The transducers were connected using a magnetic holder and 6 mm sphere amount of silicone grease couplant (Figure 3.43b) and fed into further data acquisition equipment as detailed in Section 3.1.

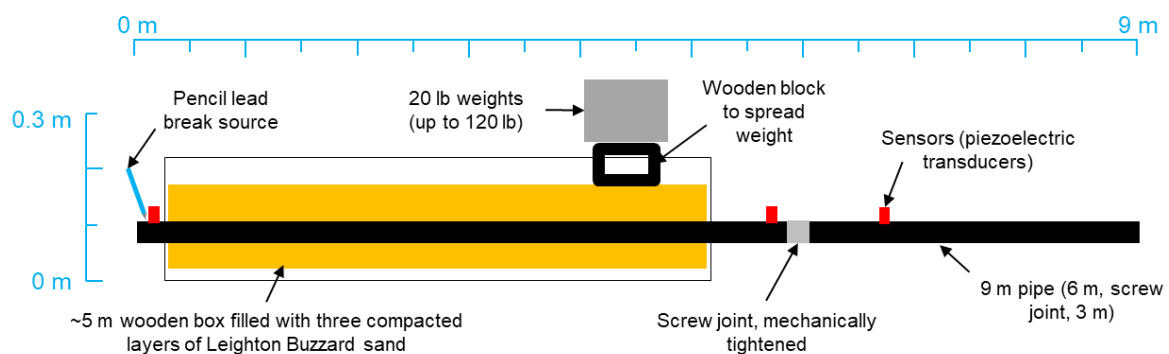


Figure 3.32 Large-scale experiment set up.

Also unlike the small-scale tests which were performed in an air environment, approximately 5 m of the large-scale test pipe was buried in an LBS annulus. This was created using a wooden test box of

external dimensions 0.22 x 4.89 x 0.22 m (wood thickness of 2 cm), in which the pipe could enter and exit through 54 mm diameter holes cut into either end (to accommodate a 42.4 mm outside diameter pipe). The diameter of the holes was made slightly larger than the diameter of the pipe in order to reduce any effects caused by contact with the box. Consequently, a lip formed from thin and flexible card was created within the holes to minimise material loss from the box (Figure 3.35). Additionally, felt was also used to dampen the pipe-box contact.



Figure 3.33 Photographs of the large-scale experiment (a) before filling (photograph taken at the source input end) and (b) after filling (photograph taken from the sensor end).

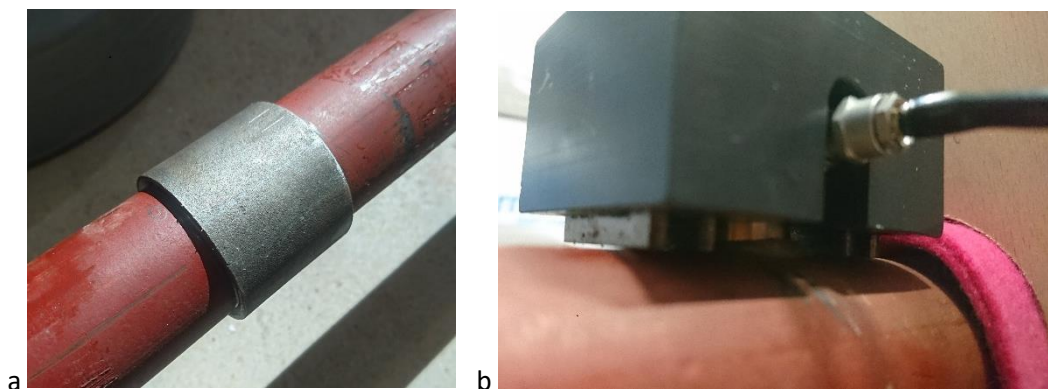


Figure 3.34 (a) The screw joint connecting the large-scale test pipe and (b) connection of the piezoelectric transducer to the large-scale test pipe using silicone grease couplant and a magnetic holder.

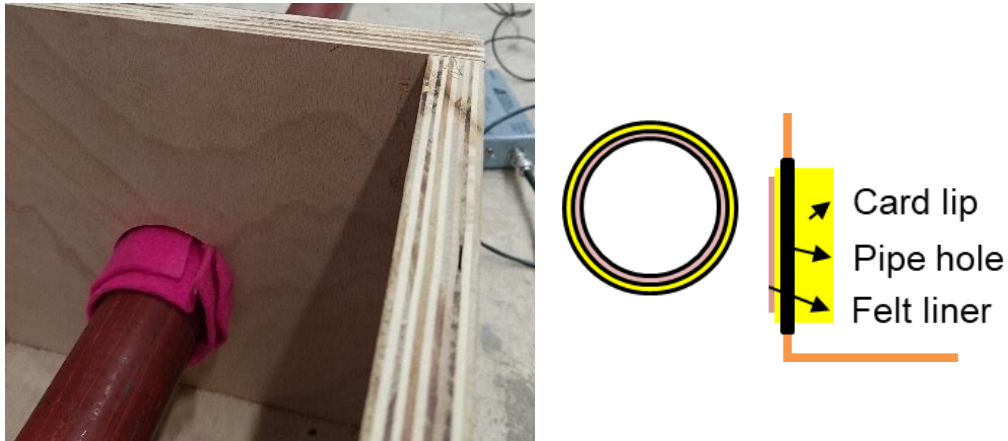


Figure 3.35 Creation of a dampening lip at the entry and exit holes of the large-scale testing box.

For the empty (i.e. air as an external environment) propagation and reflection tests, signals were input by breaking pencil leads. For these tests two types of pencil were used, a Bic 0.9 mm mechanical pencil broken at 4 mm and a 0.5 mm mechanical pencil broken at 3 mm. Additional pencil lead breaks using the 0.5 mm diameter lead pencil were performed in these tests to provide comparability with published work (Figure 3.36); 0.3 to 0.5 mm diameter lead pencil broken at 3 mm are considered a standard test (Sause, 2011).

For the filled tests, simulating a pipe burial environment, the test box was filled with LBS using a scoop as in the shear box tests (Figure 3.28). LBS was chosen to represent a typical coarse-grained material used to backfill buried pipes (, 2.2.2). The box was filled in three 5 cm layers (i.e. filled to marked lines at 5, 10, and 15 cm), each of which was compacted using a tamping rod before the next layer was added. The densification process was performed by systematically compacting the layer with a 4 cm wooden tamping rod in several lines and over two directions (Figures 3.37 and 3.38).

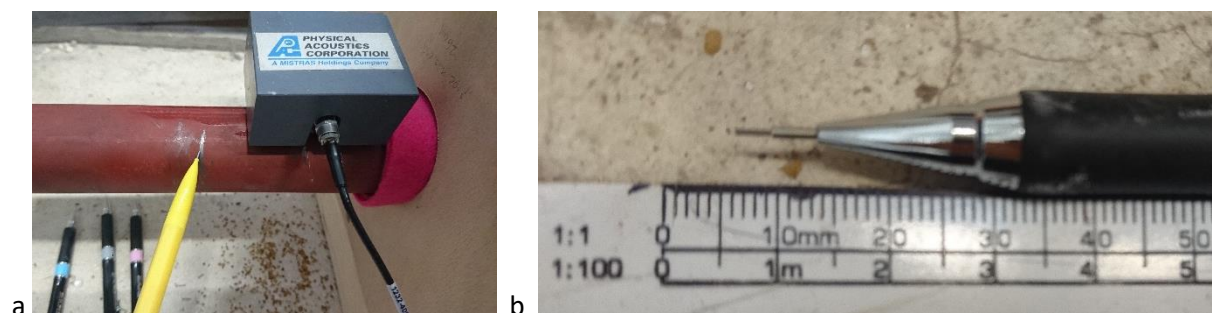


Figure 3.36 (a) Performing pencil lead break tests (b) to a standard.

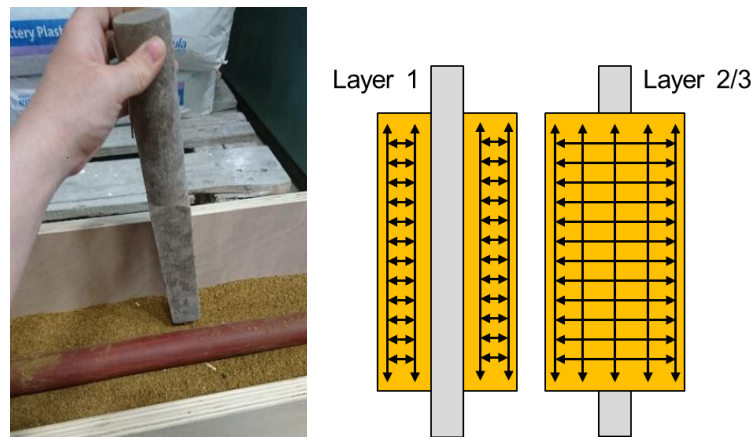


Figure 3.37 A photograph of the tamping rod used for densification and a diagram showing the systematic densification process.



Figure 3.38 Photographs of the systematic densification process during set-up of large-scale tests.

Signals from both pencil lead breaks, and soil-steel interactions could then be propagated through the pipe. Pencil lead break tests were conducted as with the empty tests whilst soil-steel interactions were generated by applying a localised normal stress to the soil using towers of 20 lb (9.07 kg) weights at various locations, simulating a compression mechanism. These were placed lightly and one by one at near-regular time intervals within the tower, the times at which they were placed, relative to each experiment start time, were noted down for later reference.

The stress provided by the weights was localised and distributed by placing them onto a wooden cube structure of a surface area 15 x 15 cm (Figure 3.39). Utilising the wooden cube structure also ensured that had material compression occurred upon application, the weights would still be acting on the LBS

rather than the burial box. Table 3.9 describes the procedures for the tests in which soil-steel AE was generated via weights. The results of the large-scale tests were then processed using a combination of the programmes DIAdem, MatLab and Excel.



Figure 3.39 Weight towers constructed on a block and used to apply a normal stress and force soil-steel interactions in large-scale laboratory experimentation.

Table 3.9 Test procedures and timing for weighted large-scale laboratory experiments.

Test ID	Time from start (minutes)	Test procedure
Weighted 1	0	Add 60 lbs at 4.5 m
	10	Pencil lead break at 0.2 m (0.5 mm)
	11	Pencil lead break at 0.2 m (0.5 mm)
	12	Pencil lead break at 0.2 m (0.5 mm)
	15	Add additional 40 lbs at 4.5 m, total 200 lbs
	18	Pencil lead break at 0.2 m (0.5 mm)
	20	Pencil lead break at 0.2 m (0.5 mm)
	21	Pencil lead break at 0.2 m (0.5 mm)
	23	Remove 100 lbs at 4.5 m
	30	Add 100 lbs at 4.5 m
Weighted 2	0	Add 100 lbs at 3 m
	5	Remove 100 lbs at 3 m
	10	Add 120 lbs at 3 m
	15	Pencil lead break at 0.2 m (0.5 mm)
	16	Pencil lead break at 0.2 m (0.5 mm)
	17	Pencil lead break at 0.2 m (0.5 mm)
	18	Pencil lead break at 0.2 m (0.5 mm)
	19	Pencil lead break at 0.2 m (0.5 mm)
	20	Remove 120 lbs at 3 m
	25	Add 120 lbs at 0.45 m
30	Remove 120 lbs at 0.45 m	
35	Add 120 lbs at 0.45 m	

3.7 Computational modelling with Disperse

The propagation and attenuation of waves through steel structures in varying environments was investigated using a series of computer models performed with the software Disperse (OB3). Disperse is a computational modelling program capable of modelling wave propagation through layered material systems. Pavlakovic et al. (1997) provide an excellent description of how the underlying numerical methods of the Disperse program work whilst Lowe (1995) further this, providing a full mathematical break down of the underlying equations. A summary of the numerical method follows.

The Disperse program uses global matrix methods to model multi-layered systems for both cartesian (plate) and cylindrical (shell structure) geometries (Pavlakovic et al., 2001). In cartesian systems, both leaky and non-leaky waves may be modelled. In cylindrical systems, which are more mathematically complex, only non-leaky waves can be modelled. This is because additional Bessel and Hankel functions are required; Gazis (1959) solutions are preferred due to their simplicity (Lowe, 1995). Additionally, for transversely isotropic systems (where the material parameters are symmetric around an axis normal to a plane of isotropy, such as with bedded rocks) solution adaptations proposed by Mirsky (1965), and Berliner and Solecki (1996) must be used.

The main advantage of using the global matrix method is that it remains stable at high frequency-thicknesses, i.e. when high frequency waves are present within layers of large thickness (Lowe, 1995, Pavlakovic et al., 2001). Leinov et al. (2015) state that the Disperse program ‘provides rigorous predictions for guided wave propagation and dispersion in pipes, allows embedding the structure in solid materials, has layering capabilities, and is applicable over a range of frequencies’. Models of numerous layers can however be computationally expensive.

Disperse works by modelling displacements and stresses using expressions provided by Hooke’s law, Euler’s equation of motion, and Navier’s displacement equation of motions, and their relationship to six partial waves (L+, L-, SV+, SV-, SH+, SH-) (Figure 3.40) within a material of a specific geometry. Two basic solutions within flat isotropic layers exist, one for longitudinal waves (L or Φ) and one for shear waves (S or Ψ) (Equations 3.2 and 3.3), which can be represented in vector form by the Helmholtz methods:

$$\Phi = A_{(L)}e^{i(k \cdot x - \omega t)} = A_{(L)}e^{i(k_1x_1 + k_2x_2 + k_3x_3 - \omega t)} \quad [3.2]$$

$$\psi = A_{(S)}e^{i(k \cdot x - \omega t)} = A_{(S)}e^{i(k_1x_1 + k_2x_2 + k_3x_3 - \omega t)} \quad [3.3]$$

Where Φ represent the longitudinal equation, Ψ represents the shear equation, k is wave number, x is displacement within an x-y coordinate system, t is time, and ω is the angular frequency. As noted above, these can be expanded and edited to include different functions relevant to different system

geometries and material properties.; the equations shown are for flat, isotropic and elastic media. Additionally, it is assumed that the guided wave field can be composed exactly by the superposition of the two longitudinal and shear solutions, i.e. without assumption or approximation, whilst the wavefront is an infinite plane which is normal to the direction of propagation and uniform (i.e. homogeneous).

The displacements and stresses are modelled using a layer matrix where each layer is studied individually by considering the amplitude of waves within adjacent layers, before then being assembled to form a single matrix describing the behaviour of the whole system (e.g. Figure 3.41). Within each layer, given boundary conditions must be satisfied.

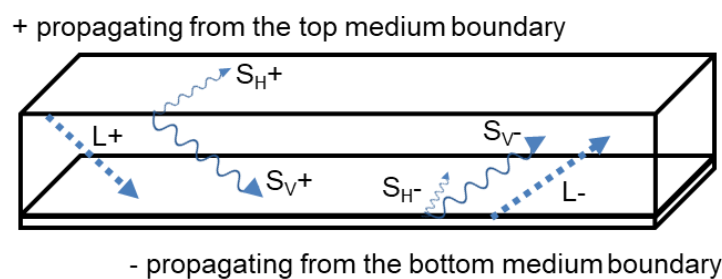


Figure 3.40 The six partial waves propagating within a material layer where S waves refer to shear waves in both horizontal (H) and vertical (V) planes, and L waves refer to longitudinal waves.

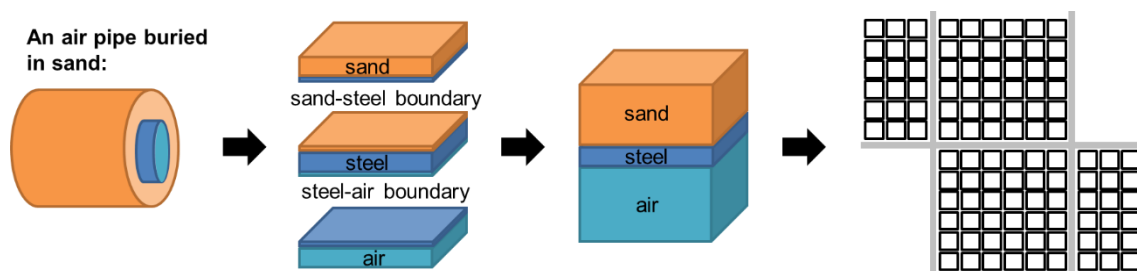


Figure 3.41 The splitting of a physical modelling problem (e.g. an air-filled buried steel pipe: air-steel-sand) into material layers which when assembled describe wave behaviours for the whole system in the form of a matrix of $6(n-1)$ equations.

It is however worth noting that the exterior bounding materials, which may be described as semi-infinite half-spaces only require relationships with three partial waves due to it being assumed that no energy may be added to the system at infinity. Consequently, global matrix systems consist of $6(n - 1)$ equations.

Dispersion curves are plotted by finding a root of the characteristic equation. This means that the absolute value of the describing matrix's determinant equals zero. The matrix if formed from the six partial waves (e.g. Figure 3.42 from Pavlakovic et al., 1997). Solutions are found by performing an iterative process over three parameter spaces, frequency, real wave number, and attenuation until convergence occurs (Leinov et al., 2015). This is initially coarse, becoming finer as a solution is neared

(i.e. minima are deduced) with the amount of convergence and tolerance of the solution an underlying assumption within the program. The next solution may then be found by taking a small step forward in parameter space, these are then connected to form a trace.

The Disperse program is commercially available software. It is consequently easy to navigate and uses a point and click user interface. The program however still provides an adequate degree of freedom allowing the user to edit and change how solutions, and the systems for which solutions, are formed.

An investigative series (Table 3.10) was designed to systematically investigate the influence of individual parameters including: plate/wall thicknesses, plate and pipe structures, pipe radius, internal materials, and external materials. Additionally, case study models for typical burial environments were also conducted.

Table 3.10 Summarised programme of computational models.

No.	Investigation	Model	Plate/wall thickness	Cylinder radius	Environment
1	Plate thickness	Plate	1, 2, 3, 5, 10, 15, 25 mm	-	Free-Steel-Free/Soil
2	Shell radius	Cylinder	5 mm	5, 10, 20, 30, 40, 50, 60, 70, 80, 90, 100, 120, 150, 200 mm	
3	Density	Plate	5 mm	-	Free-Steel-Soil
		Cylinder	5 mm	50 mm	
4	Poisson's ratio	Plate	5 mm	-	Free-Steel-Soil
		Cylinder	5 mm	50 mm	
5	Young's modulus	Plate	5 mm	-	Free-Steel-Soil
		Cylinder	5 mm	50 mm	
3	External media	Plate	5 mm	-	Free-Steel-Material
4	Internal media	Plate	5 mm	-	Material-Free-
		Plate			
5	Case study: gas pipe	Cylinder	25 mm	200 mm	Air(at 20c)-Steel-Soil
		Cylinder	25 mm	200 mm	
6	Case study: water pipe	Cylinder	25 mm	200 mm	Water-Steel-Soil
		Cylinder	25 mm	200 mm	
7	Case study: cylindrical pile	Cylinder	10 mm	50 mm	Free-Steel-Soil
8	Case study: H-pile	Plate	10 mm	-	Soil-Steel-Soil
		Plate	30 mm	-	
9	Case study: off-shore monopile	Cylinder	60 mm	6000 mm	Material-Steel-Material

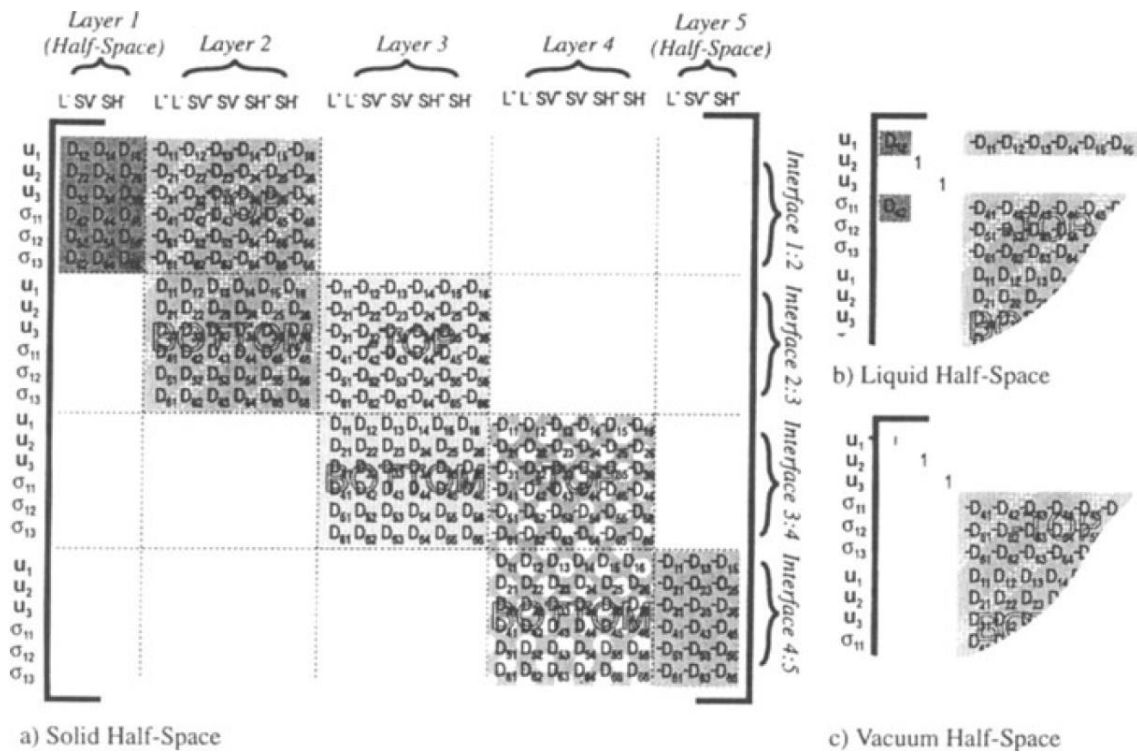


Figure 3.42 Example global matrix for (a) solid, (b) liquid and (c) vacuum half-spaces where each layer is formed from six partial equations (three for the bounding layers). Copied from Pavlakovic et al. (1997).

3.7.1 Creating a model

Modelling systems could be defined parametrically within Disperse. This allowed for a large and varied range of buried structures to be modelled. The parametric variables included: the system geometry (plate or cylinder), the system environment (free or embedded), the number of layers within the model, the layer materials, and the thickness of the layers (including geometry) (Figure 3.43).

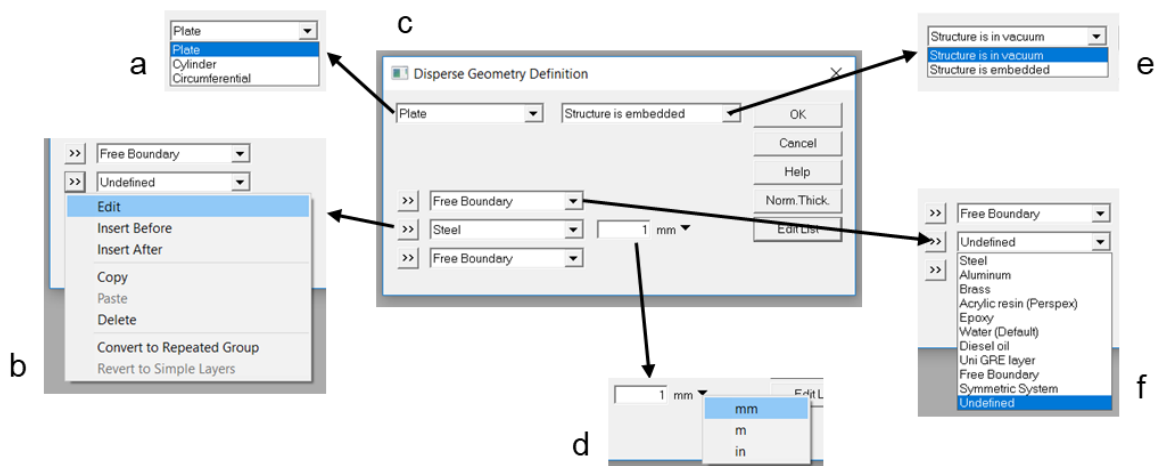


Figure 3.43 The dialogue box(s) for defining a model geometry in Disperse where (a) defines the system type, (b) adds or deletes material layers and allows for new materials to be defined, (c) is the overall dialogue box, (d) allows for the thickness of layers to be defined – including the unit, (e) defines the system environment as either free, vacuum, or embedded, and (f) allows for pre-defined materials layers to be selected.

Most models within the developed programme were produced using an embedded tri-layer plate system as this is representative of a simple buried system. To model structural influences for example, a tri-layer free-steel-free system was created (Figure 3.43b) for which the thickness of the steel layer (Figure 3.43d) was varied to represent changing plate/wall thicknesses, and the model type (Figure 3.43a) also varied to represent either plate or shell structures. Further details follow.

To investigate the effect of changing plate/wall thicknesses both plate and cylinder models (Figure 3.44) were performed allowing for differences in the system types to be identified. The cylinder models were conducted with a nominal radius of 50 mm (to remove radius as a variable). Plate/wall thicknesses of 1, 2, 3, 4, 5, 7, 10, 15 and 25 mm were tested for two environmental systems, free-steel-free and free-steel-soil. In these the properties of the steel were left as default whilst the properties of the soil were set to a standard (Table 3.10). The standard soil was considered as an isotropic material with a free boundary (Figure 3.45). Overall, thirty-six models were therefore performed.

To investigate pipe radius on the other hand, only cylindrical models were conducted with a nominal wall thickness of 5 mm (to remove the effect of thickness). Radii tested included: 5, 10, 20, 30, 40, 50, 60, 70, 80, 90, 100, 120, 150 and 200 mm. These models were conducted for a free-steel-free environment. Overall, fourteen radius models were produced.

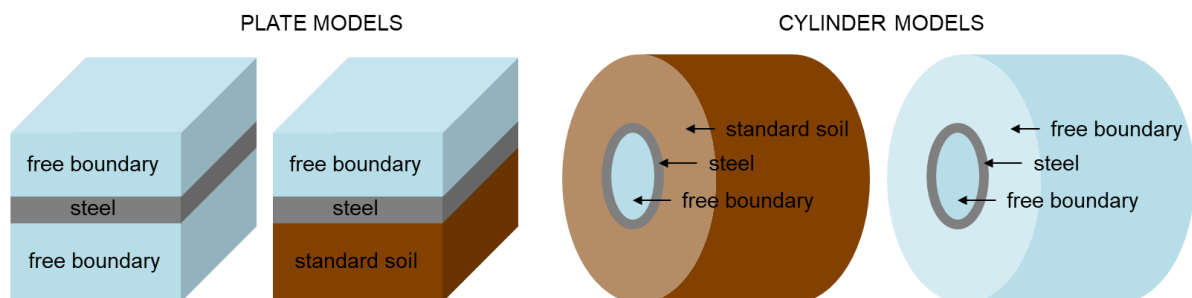


Figure 3.44 Example plate and cylinder model systems.

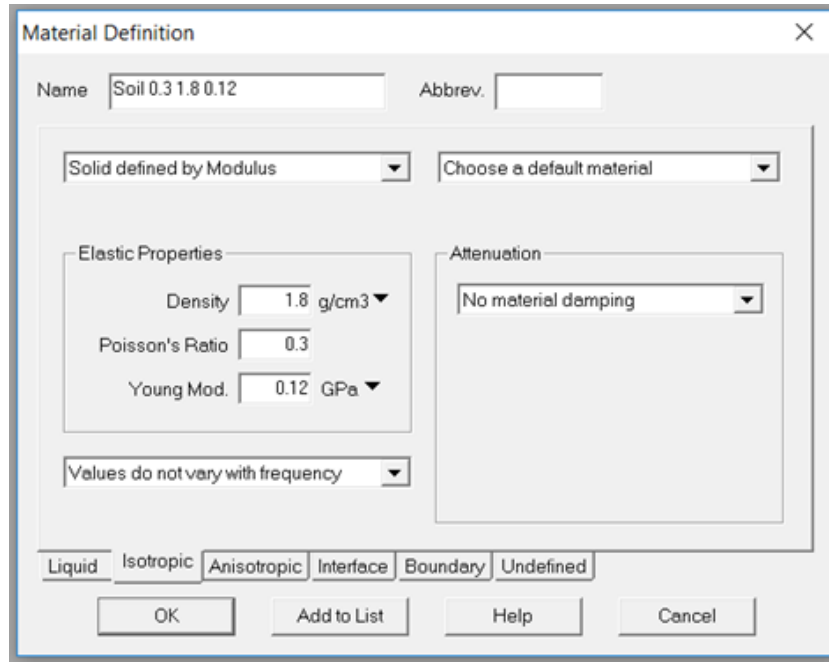


Figure 3.45 Defining a standard soil for computer modelling.

Contrastingly, to study the effect of varying environmental systems a range of both tri-layer plate and cylinder models were performed with different internal and external material layers including a baseline model of a free (air) boundary. All plate models used an arbitrary wall thickness of 5 mm (to remove the effect of thickness) whilst all cylinder models similarly used an arbitrary radius of 50 mm (to remove the effect of radius). These arbitrary measurements were kept the same as for plate/wall thickness and radius modelling to allow for results to be extrapolated from.

For investigating internal materials, only embedded tri-layer plate systems comprising of varying internal materials, steel, and an external standard soil were modelled. Internal materials were investigated categorically to compare the effects of gases, liquids, polymers and other stiff materials separately. The types and properties of the materials were pre-defined within Disperse (although editable) and can be found in Table 3.11.

Similarly, the influence of external materials was also investigated by using embedded, tri-layer plate systems comprising of a free internal boundary, steel plate, and a varying external material. In some cases, cylinder models for the same environment were also conducted to compare the effects of the different structures. The external materials modelled included all those modelled for the internal material study however was also extended to include soils of varying properties. These were density (ρ), Poisson's ratio (ν), and Young's Modulus (E) (three properties with which materials could be defined in the Disperse program and influential to fundamental wave behaviours).

The three parameters were studied systematically and parametrically over ranges found appropriate from reviewing literature (Gasparre et al., 2007, Hight et al., 2003, Nishimura et al., 2007, Cabalar et al., 2010, Kumar and Madhusudhan, 2012, Cavallaro et al., 2001). Given the parametric nature of the studies, if not the subject of investigation, the parameters were defaulted back to those of the standard soil (Table 3.11) for direct comparability. Table 3.12 therefore shows the ranges and values studied for each parameter. It should be noted that the parametric values were not equidistantly spaced within each of the tested ranges; instead they were chosen to be representative of more common soil properties. Overall, thirty-three models were performed.

Table 3.11 Materials properties used for computer modelling.

	ρ (g/cm ³)	ν	E (MPa)	Longitudinal velocity (m/ms)	Shear velocity (m/ms)
Free	-	-	-	-	-
Air (20C)	0.001	-	-	0.344	-
Water	1.000	-	-	1.500	-
Benzene	0.881	-	-	1.117	-
Castor oil	0.971	-	-	1.474	-
Diesel	0.800	-	-	1.250	-
Ethyl alcohol	0.790	-	-	1.238	-
Kerosene	0.822	-	-	1.319	-
Concrete	2.200	0.270	9.570	4.100	2.300
Epoxy	1.170	0.392	3.941	2.610	1.100
Perspex	1.180	0.311	6.327	2.730	1.430
Polystyrene	1.060	0.343	3.764	2.350	1.150
Rock	2.500	0.100	22.000	3.000	2.000
Standard	1.800	0.300	0.120	-	-
Steel	7.932	0.286	216.906	9.560	3.260

Table 3.12 The properties of soils used for computer modelling.

Parameter	Unit	Value range	Specific values tested
Density (ρ)	g/cm ³	0.5 to 10	0.5, 1, 1.5, 1.8, 2, 3, 4, 5, 8, 10
Poisson's ratio (ν)	-	0.1 to 0.45	0.1, 0.2, 0.3, 0.4, 0.45
Young's modulus (E)	GPa	0.02 to 1	0.02, 0.05, 0.08, 0.12, 0.15, 0.2, 0.3, 0.5, 0.8, 1

3.7.2 Running a model

With the geometry of a model set up, dispersion curves could then be traced. This was done by utilising the 'automatic tracing' function within Disperse.

The automatic tracing function would run a mathematical algorithm to find and mark out model solutions which would then be connected based on a best fit system. The function used an underlying global matrix system formed of multiple material layers. Within each layer partial waves were

controlled by stresses and displacements, the amplitudes of which feed into the overall global matrix to describe boundary conditions which must be satisfied (Pavlakovic et al., 1997).

Parameters regulating the modelling algorithm could be partially controlled by the user (Figure 3.46). These parameters included: the variable over which tracing would occur, the top frequency to which solutions could be found, the type of modes to be traced, the influence of attenuation to the tracing and solutions, and the convergence parameters used for iterating.

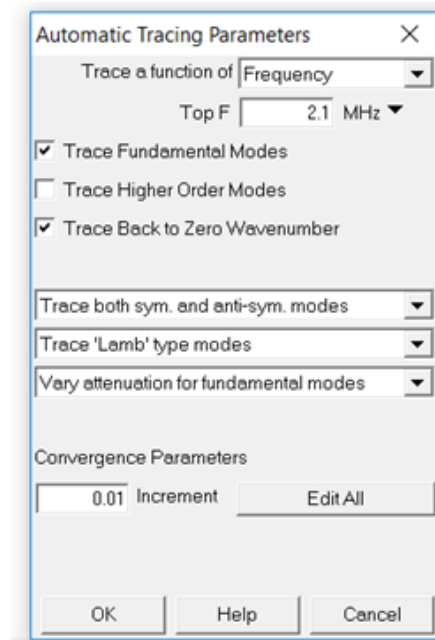


Figure 3.46 A user's control over the automatic tracing parameters within Disperse.

All models run were traced as a function of frequency for only the fundamental symmetric (S0) and asymmetric (A0) wave modes; higher modes were not of interest due to the frequencies at which they propagate. For all models, attenuation was also varied for the fundamental modes whilst the convergence parameters were kept constant. The convergence parameters were: a step type of wavenumber with an increment of 0.001; an iteration type of frequency with a search width of 0.0003 and tolerance of 5e-006 (the convergence); and a secondary iteration type of attenuation with a search width of 0.003 and tolerance of 5e-006. These values were used on the personal recommendation of Professor M. Lowe, through email (February 2018), to create an efficient model. The wave modes required sufficient resolution, in terms of solution convergence, to accurately represent their propagation whilst still being time efficient to model and within the scope of the computer power and memory.

By regulating the modelling algorithm in the same way for each model, the modelling results were comparable. The only variable that changed between models was the frequency to which solution

could be found. This value was however largely irrelevant being much higher than that of interest (i.e. several MHz opposed to kHz).

In some cases, the automatic tracing did not function appropriately. When this occurred, model solution could be manually traced for and connected using inbuilt program tools. Traces could also be split or connected manually if deemed unrealistic or needed respectively.

3.8 Chapter summary

A large variety of methods have been utilised due to the diversity of experiments performed. These included both small- and large-scale physical models, as well as computational modelling. The experiments were conducted to investigate both wave propagation and attenuation (Chapter 4), and AE generation within soil-steel systems (Chapter 5).

The Wille Large Direct-Shear Apparatus was selected because it allowed soil-steel interfaces to be subjected to compression and shearing. Moreover, the apparatus comprised a 'floating' top-box, which meant that volumetric strains (contractive and dilative behaviours) could take place under constant normal stress. The Disperse program was selected as a bespoke modelling tool for high frequency wave propagation in layered, continuous systems. Multiple published studies demonstrate the use of the software in similar applications, providing datasets for comparison with model outputs from this study.

All experiments were quantitative, parametrically quantifying the influence of different variables relevant to the overall aim of the work (Section 1.2). Categorized tables summarising all conducted experiments and method variations follow.

Additional experiments, studying alternative methodologies such as window shaped during FFTs, may also be found in the Appendix 2.0.

3.8.1 Small-scale laboratory tests

Eight small-scale laboratory tests were performed to both inform data collection (Tests 1, 5, 6) and understand wave propagation and attenuation within steel structures (Tests 2, 3, 4) (OB3). By evaluating different data collection methods, the accuracy and reliability of results collected were improved for the later development of a framework for both informing the deployment of AE sensor networks and interpreting the collected AE data (OB4, OB5).

Table 3.13 Full programme of conducted small-scale laboratory tests.

	Input signal	Pipe details	Propagation distance(s)	Sensor details	AE equipment details
1 Input signals	Ball bearing	Steel, 20 mm diameter, painted, horizontal	0.05, 2 and 3 m from centre of sensor	R3 α , pea of silicone gel, sensor attached with magnetic holder	Pre-amplifier set to 3 dB and main amplifier to 20 dB gain.
	Pencil lead	Steel, 20 mm diameter, painted, horizontal	0.05, 2 and 3 m from centre of sensor	R3 α , pea of silicone gel, sensor attached with magnetic holder	
2 Pipe radius		Steel, 48 mm diameter, slightly rusted, horizontal	Ranging between 0.05 and 3.5 m in approximate 0.25 m intervals	R3 α , pea of silicone gel, sensor attached with magnetic holder	
3 Pipe structures (joints)		Two steel, 48 mm diameter, 3 mm wall thickness pipes connected by a threaded screw joint, horizontal, one pipe slightly rusted, one pipe painted	5 and 10 cm before the start of the joint and 5 and 10 cm after the end of joint	R3 α , pea of silicone gel, sensor attached with magnetic holder	
4 Propagation distances		Steel, 20 mm diameter, painted, horizontal	Ranging between 0.05 and 3.5 m in approximate 0.25 m intervals	R3 α , pea of silicone gel, sensor attached with magnetic holder	
5 Sensor-structure coupling		Steel, 20 mm diameter, painted, horizontal	Ranging between 0.05 and 3.5 m in approximate 0.25 m intervals	No silicone gel used Pea of silicone gel Excessive silicone gel Transducer balances (resting) Transducer attached with sticky tape Transducer attached with magnetic holder and cable ties	

	Input signal	Pipe details	Propagation distance(s)	Sensor details	AE equipment details
6	Transducer biases		0.05, 1, 2 and 3 m from centre of sensor	R3 α , pea of silicone gel, sensor attached to pipe with magnetic holder	

3.8.2 Water flow tests

Water flow tests were conducted with the aim of characterising water flow noise (OB2). Characterising water flow noise allows for its influence to be removed from AE data captured in the field, improving its interpretation (OB5). Additionally, characterisation creates a reference signal where changes in flow noise as a result of deteriorating structures would be notable.

Table 3.14 Full programme of conducted water flow tests.

No.	Flow regime	Tap details	Flow details			Pipe details	Sensor details	AE equipment details
			Volume collected (L)	Time (s)	Flow rate (m/s)			
14	Minimal flow	Tap turned so only just flowing	0.5	294.0	0.005	Copper pipe, 20 mm diameter, unknown wall thickness, vertical orientation	An R3 α piezoelectric transducer with a pea sized amount of silicone gel at the sensor-structure contact. Transducer attached using the magnetic holder held in place with two adjustable cable ties due to copper being non-magnetic. This resulted in a slightly weaker attachment than other experiments.	Pre-amplifier set to 3 dB and main amplifier to 40 dB gain
18	Very small flow	Tap turned to a minimal flow	0.5	39.30	0.04			
15		\approx 1/10 turn of tap	1	47.70	0.07			
28		\approx 1/9 turn of tap	1	36.13	0.09			
30	Small flow	\approx 1/8 turn of tap	1	30.63	0.1			
17			1	28.40	0.11			
27			1	25.7	0.12			
29	Medium flow	\approx 1/7 turn of tap	1	31.23	0.2			
16			1	14.6	0.22			
26			2	26.67	0.24			
20	Medium-strong flow	\approx 1/6 turn of tap	2	17.20	0.37			
2	Strong flow	\approx 1/4 turn of tap	4	30.40	0.42			
1			4	29.10	0.44			
3			4	27.80	0.46			
5			4	27.20	0.47			

No.	Flow regime	Tap details	Flow details			Pipe details	Sensor details	AE equipment details
			Volume collected (L)	Time (s)	Flow rate (m/s)			
6	Very strong flow	≈ 1/2 turn of tap	4	25.30	0.50			
4			4	25.60	0.50			
19		≈ 3 full turns	4	22.90	0.56			
25	Very small flow	≈ 1/10 turn of tap	1	45.74	0.07			Pre-amplifier set to 3 dB and main amplifier to 20 dB gain. These settings were not appropriate to fully record the signals.
24	Small flow	≈ 1/8 turn of tap	1	25.49	0.12			
23			1	23.8	0.13			
22	Medium flow	≈ 1/7 turn of tap	2	29.92	0.21			
21			2	29.24	0.22			
7	Varying flow	Varying turns to vary flow rate	4	29.1	Average of 0.44 but varying			
13	Strong flow	≈ 1.5 turns of tap	4	27.1	0.47			
9		≈ 3/4 turn of tap	4	26.6	0.48			
10			4	26.8	0.48			
12		≈ 1.5 turns of tap	4	26.7	0.48			
8	Very strong flow	≈ 3/4 turn of tap	4	25.5	0.50			
11		≈ 1.5 turns of tap	4	24.8	0.51			

3.8.3 Shear box tests

Large-direct shear box tests were conducted to investigate AE generation and behaviours as a result of soil-steel interactions (OB1, OB2). Understanding how a soil and steel element interact, allows for the condition of buried geotechnical assets, and their burial environment, to then be passively monitored by analysing the generated AE (OB5). Fourteen tests studying interactions as a result of varying burial and deforming conditions were therefore performed.

Table 3.15 Full programme of conducted shear box tests.

No.	Test ID	Stress (kPa)	Soil	State	State	Rate (mm/min)	Running time	Travel (mm)	Sensor details
1	LBS-75dD-1	75	LBS	Dry	Dense	1 mm/min	40 m	40	An R3α piezoelectric transducer with a pea sized amount of silicone gel at the sensor-
2	LBS-150dD-1	150	LBS	Dry	Dense	1 mm/min	40 m	40	
3	LBS-225dD-1	225	LBS	Dry	Dense	1 mm/min	40 m	40	
4	PG-75dD-1	75	PG	Dry	Dense	1 mm/min	40 m	40	

No.	Test ID	Stress (kPa)	Soil	State	State	Rate (mm/min)	Running time	Travel (mm)	Sensor details
5	PG-150dD-1	150	PG	Dry	Dense	1 mm/min	40 m	40	structure contact. The sensor was attached to top of steel plate with a magnetic holder.
6	PG-225dD-1	225	PG	Dry	Dense	1 mm/min	40 m	40	
7	PG-150dL-1	150	PG	Dry	Loose	1 mm/min	40 m	40	
8	PG-150dD-002	150	PG	Dry	Dense	0.02 mm/min	20 h 50 m	25	
9	PG-150dD-01	150	PG	Dry	Dense	0.1 mm/min	4 h 10 m	25	
15	LBS-150dD-stepped-1	150	LBS	Dry	Dense	Stepped	7 h 17 m 30 s	35	
10	PG-150dD-stepped-1	150	PG	Dry	Dense	Stepped	7 h 17 m 30 s	35	
16	LBS-75dD-stepped-2	75	LBS	Dry	Dense	Stepped	33 m 21 s	40	
17	LBS-150dD-stepped-2	150	LBS	Dry	Dense	Stepped	33 m 21 s	40	
18	LBS-225dD-stepped-2	225	LBS	Dry	Dense	Stepped	33 m 21 s	40	
11	PG-75dD-stepped-2	75	PG	Dry	Dense	Stepped	33 m 21 s	40	
12	PG-150dD-stepped-2	150	PG	Dry	Dense	Stepped	33 m 21 s	40	
13	PG-225dD-stepped-2	225	PG	Dry	Dense	Stepped	33 m 21 s	40	
14	PG-150dD-ramped	150	PG	Dry	Dense	Ramped	20 m 9 s	25	

3.8.4 Large-scale laboratory tests

Large-scale laboratory tests were conducted with three purposes:

- To compare the results of identical systems physically and computationally, and therefore validate the use of Disperse as a modelling tool.
- To investigate wave propagation and attenuation behaviours within soil-structure systems (Tests 1, 2, 3, 4, 5) (OB3) with intention of informing the development of AE sensor networks within the field (OB4).
- To investigate AE generation as a result of interactions between a steel pipe and soil under loading (Tests 6, 7) (OB2) with the intention of informing the development of a framework for interpreting measured AE (OB5).

Two forms of tests were therefore performed: those using pencil lead breaks as a source signal (Tests 1, 2, 3, 4, 5) to investigate propagation and attenuation, and those investigating soil-steel interactions under loading (Tests 6, 7) and therefore investigating AE generation.

Table 3.16 Full programme of conducted large-scale laboratory tests.

No.	Test ID	Source	Input location (m)	Sensor location (m)	Screw joint	Backfill	Weights and timings
1	Wave propagation (empty)	Bic 0.9 mm	0.2	Sensor 1: 0.25 (top) Sensor 2: 5.7 (top) Sensor 3: 6.7 (top)	Mechanically tightened, 6 m	Empty	n/a
		Bic 0.9 mm	0.2	Sensor 1: 0.25 (top) Sensor 2: 5.58 (top) Sensor 3: 7.08 (top)	Hand tightened, 6 m	Empty	n/a
		Standard 0.5 mm	0.2	Sensor 1: 0.25 (top) Sensor 2: 5.7 (top) Sensor 3: 6.7 (top)	Mechanically tightened, 6 m	Empty	n/a
2	Wave propagation (filled)	Bic 0.9 mm	0.2	Sensor 1: 0.25 (top) Sensor 2: 5.7 (top) Sensor 3: 6.7 (top)	Mechanically tightened, 6 m	LBS: Three 5 cm dense layers	n/a
		Bic 0.9 mm	0.2	Sensor 1: 0.25 (top) Sensor 2: 5.78 (top) Sensor 3: 7.08 (top)	Hand tightened, 6 m	LBS: Three 5 cm dense layers	n/a
		Standard 0.5 mm	0.2	Sensor 1: 0.25 (top) Sensor 2: 5.7 (top) Sensor 3: 6.7 (top)	Mechanically tightened, 6 m	LBS: Three 5 cm dense layers	n/a
		Standard 0.5 mm	0.2	Sensor 1: 0.25 (top) Sensor 2: 5.78 (top) Sensor 3: 7.08 (top)	Hand tightened, 6 m	LBS: Three 5 cm dense layers	n/a
3	Structural propagation (empty)	Bic 0.9 mm	0.2	Sensor 1: 0.25 (top) Sensor 2: 5.7 (top) Sensor 3: 5.7 (bottom)	n/a	Empty	n/a
		Standard 0.5 mm	0.2	Sensor 1: 0.25 (top) Sensor 2: 5.7 (top) Sensor 3: 5.7 (bottom)	n/a	Empty	n/a

No.	Test ID	Source	Input location (m)	Sensor location (m)	Screw joint	Backfill	Weights and timings
4	Structural propagation (filled)	Bic 0.9 mm	0.2	Sensor 1: 0.25 (top) Sensor 2: 5.7 (top) Sensor 3: 5.7 (bottom)	n/a	LBS: Three 5 cm dense layers	n/a
		Standard 0.5 mm	0.2	Sensor 1: 0.25 (top) Sensor 2: 5.7 (top) Sensor 3: 5.7 (bottom)	n/a	LBS: Three 5 cm dense layers	n/a
5	Reflections	Standard 0.5 mm	5.45	Sensor 1: 0.25 (top) Sensor 2: 5.7 (top) Sensor 3: 6.7 (top)	Mechanically tightened, 6 m	LBS: Three 5 cm dense layers	n/a
		Standard 0.5 mm	6.45	Sensor 1: 0.25 (top) Sensor 2: 5.7 (top) Sensor 3: 6.7 (top)	Mechanically tightened, 6 m	LBS: Three 5 cm dense layers	n/a
6	Weighted	Soil-steel interactions from stress / Standard 0.5 mm pencil lead breaks	4.5	Sensor 1: 0.25 (top) Sensor 2: 5.7 (top) Sensor 3: 6.7 (top)	Mechanically tightened, 6 m	LBS: Three 5 cm dense layers	0 m: Add 60 lbs 10 m: Pencil break 11 m: Pencil break 12 m: Pencil break 15 m: Add another 40 lbs to the initial 60 lbs 18 m: Pencil break 20 m: Pencil break 21 m: Pencil break 23 m: Remove 100 lbs 30 m: Add 100 lbs
			4.5				
			4.5				
7	Weighted	Soil-steel interactions from stress / Standard 0.5 mm pencil lead breaks	3.0	Sensor 1: 0.25 (top) Sensor 2: 5.7 (top)	Mechanically tightened, 6 m	LBS: Three 5 cm dense layers	0 m: Add 100 lbs 5 m: Remove 100 lbs
			3.0	Sensor 3: 6.7 (top)			10 m: Add 120 lbs 15 m: Pencil break 16 m: Pencil break
			4.7 m				17 m: Pencil break 18 m: Pencil break
			0.45 m				19 m: Pencil break 20 m: Remove 120 lbs 25 m: Add 120 lbs

No.	Test ID	Source	Input location (m)	Sensor location (m)	Screw joint	Backfill	Weights and timings
							30 m: Remove 120 lbs 35 m: Add 120 lbs

3.8.5 Computational modelling

Numerous computational models were performed in order to study a multitude of phenomena. These included:

- Comparing and evaluating the accuracy of experimental methods in the laboratory, and vice versa (Tests 1, 6, 8).
- Studying wave propagation and attenuation within varying structural geometries, materials, and environments (Tests 1, 2, 3, 4, 5, 6, 7) (OB3).
- Modelling AE propagation and attenuation in simulated structural environments (Tests 8, 9, 10, 11, 12) (OB3) in order to inform sensor network spacings in context (OB4).

Table 3.17 Full programme of conducted computer models.

No.	Test	Model	Plate/wall thickness	Cylinder radius	Internal medium	Plate/wall	External medium
1	Plate thickness	Plate	1, 2, 3, 5, 10, 15, 25 mm	-	Free	Steel	Soil
2	Shell radius	Cylinder	5 mm	5, 10, 20, 30, 40, 50, 60, 70, 80, 90, 100, 120, 150, 200 mm	Free	Steel	Free
3	Density	Plate	5 mm	-	Free	Steel	Soil ρ: 0.5, 1, 1.5, 1.8, 2, 3, 4, 5, 8, 10 kg/m ³
		Cylinder	5 mm	50 mm	Free	Steel	Soil ρ: 0.5, 1, 1.5, 1.8, 2, 3, 4, 5, 8, 10 kg/m ³
4	Poisson's ratio	Plate	5 mm	-	Free	Steel	Soil ν: 0.1, 0.2, 0.3, 0.4, 0.45
		Cylinder	5 mm	50 mm	Free	Steel	Soil

No.	Test	Model	Plate/wall thickness	Cylinder radius	Internal medium	Plate/wall	External medium
5	Young's modulus	Plate	5 mm	-	Free	Steel	v: 0.1, 0.2, 0.3, 0.4, 0.45 Soil E: 0.02, 0.05, 0.08, 0.12, 0.15, 0.2, 0.3, 0.5, 0.8, 1 GPa
		Cylinder	5 mm	50 mm	Free	Steel	Soil E: 0.02, 0.05, 0.08, 0.12, 0.15, 0.2, 0.3, 0.5, 0.8, 1 GPa
6	External media	Plate	5 mm	-	Free	Steel	Free, Air (at 20c), Water, Epoxy, Perspex, Polystyrene, Rock, Concrete
					Water	Steel	Free, Air (at 20c), Water, Epoxy, Perspex, Polystyrene, Rock, Concrete
7	Internal media	Plate	5 mm	-	Free, Air (at 20c), Water, Castor oil, Benzene, Diesel, Kerosene, Ethyl alcohol, Epoxy, Polystyrene, MDPE, Concrete, Steel	Steel	Free
		Plate			Free, Air (at 20c), Water, Castor oil, Benzene, Diesel, Kerosene, Ethyl alcohol, Epoxy, Polystyrene		Soil
8	Case study: gas pipe	Cylinder	25 mm	200 mm	Free	Steel	Leighton Buzzard Sand ρ : 1552.5 kg/m ³ v: 0.1728 E: 0.131 GPa
		Cylinder	25 mm	200 mm	Free	Steel	Leighton Buzzard Sand ρ : 1550 kg/m ³ v: 0.1730 E: 0.13 GPa

No.	Test	Model	Plate/wall thickness	Cylinder radius	Internal medium	Plate/wall	External medium
9	Case study: water pipe	Cylinder	25 mm	200 mm	Water	Steel	Leighton Buzzard Sand ρ : 1552.5 kg/m ³ ν : 0.1728 E: 0.131 GPa
		Cylinder	25 mm	200 mm	Water	Steel	Leighton Buzzard Sand ρ : 1550 kg/m ³ ν : 0.1730 E: 0.13 GPa
10	Case study: cylindrical pile	Cylinder	10 mm	50 mm	Free	Steel	Case A, Case B, Case C, Case D
11	Case study: H-pile	Plate	10 mm	-	Case A, Case B, Case C, Case D (Figures)	Steel	Case A, Case B, Case C, Case D
		Plate	30 mm	-	Case A, Case B, Case C, Case D (Figures)		Case A, Case B, Case C, Case D
12	Case study: off-shore monopile	Cylinder	60 mm	6000 mm	Case E (Figure)	Steel	Case E

Chapter 4: Results: Propagation and attenuation

4.0 Results: Propagation and attenuation

Wave propagation and attenuation behaviours were investigated using a series of small- and large-scale laboratory experiments alongside extensive computational models. Several methods were employed in order to compare and evaluate the results. These included a variety of small-scale laboratory experiments using pencil lead break source tests (Section 4.2), large-scale laboratory testing on a buried and jointed steel pipe (Section 4.3), and numerous computational models using the program Disperse (Section 4.1).

Understanding wave propagation and attenuation (OB3), particularly within buried steel structures, was important to the development of an AE sensor network; the propagation and attenuation of AE dictates sensor spacings (OB4). Additionally, understanding wave behaviours aids in the characterisation of AE sources (OB2).

This Chapter therefore presents the results of several experiments investigating the propagation and attenuation of waves within steel structures. Furthermore, the computational modelling approach using Disperse has also been validated (Section 4.1.1).

4.1 Computer modelling with Disperse

4.1.1 Validating the modelling approach

The Disperse program was introduced in Section 3.7. It uses global matrix methods coupled with partial wave theory to calculate dispersion solutions for wave modes in both flat (plate) and cylindrical (shell structure) systems of an arbitrary number of layers (Pavlakovic et al., 2001).

4.1.1.1 Validation within published work

Disperse has been shown to accurately model wave propagation and attenuation through an array of different materials and geometries in a variety of published works. Leinov et al. (2015) for example, show how the results of their buried steel bar experiments can be reproduced within the program by modelling a small range of plausible material parameters and choosing a best fit (Figure 4.1). Similarly, Aristegui et al. (2001) show that Disperse provides a better estimate for attenuation than complex frequency solutions for a flexural mode within an immersed steel rod (Figure 4.2).

Pavlakovic et al. (2001) conducted a similar experiment in which an 8.1 mm steel bar was embedded in grout. Their results are shown in Figure 4.3 which compares the modelled and measured attenuation. The figure shows that the results are highly comparable, and it may therefore be concluded that Disperse has provided an accurate model.

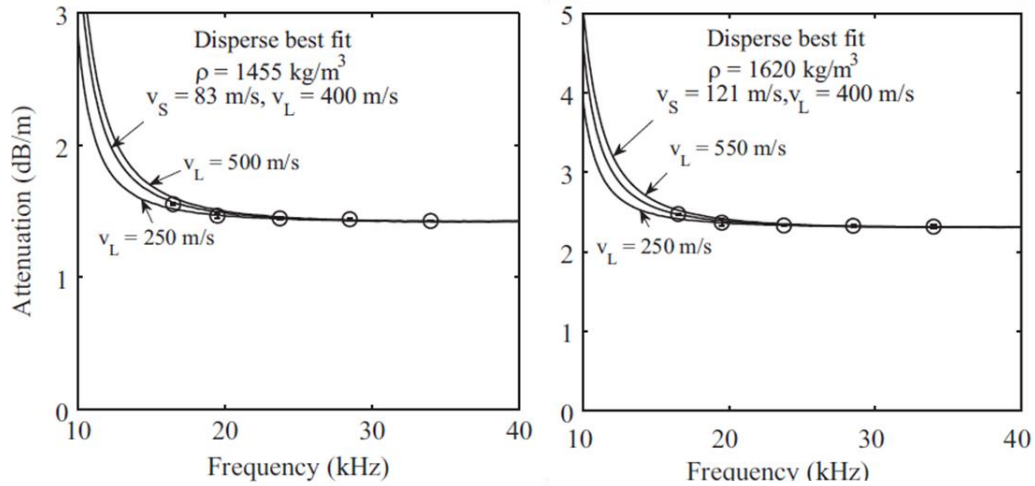


Figure 4.1 Modelled frequency-attenuation dispersion curves compared against measured attenuation values for the L(0,2) wave mode. From Leinov et al., 2015.

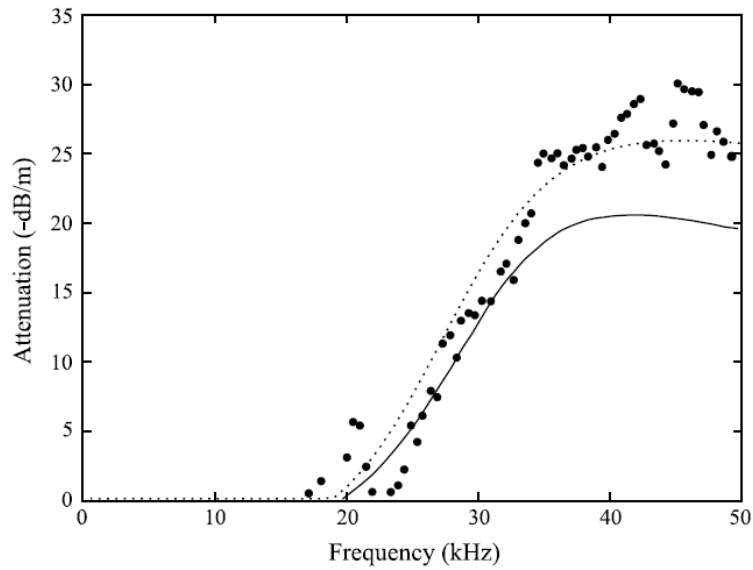


Figure 4.2 Modelled (**), calculated (-) and measured (●) attenuation as a function of frequency for the flexural wave mode in a 19 mm diameter steel rod immersed in water. From Aristegui et al., 2001.

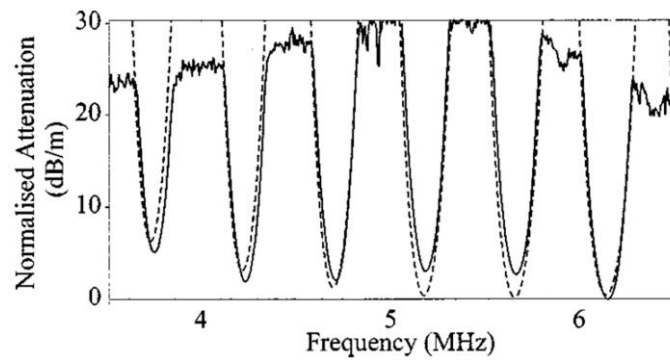


Figure 4.3 Modelled (- -) and measured (-) attenuation results normalised against frequency for an 8.1 mm bar embedded in grout. From Pavlakovic et al. 2001.

The methodology behind these validations is not however stated. Therefore, to further evaluate the use of the program in this study, a series of Disperse models aimed at reproducing published experimental work have been produced.

4.1.1.2 Recreating published work

The correct use of Disperse is important to the reliability as well as the validity of results produced. Consequently, the recreation and in some cases extension of various published works have been conducted to validate the Disperse modelling approach employed within this project.

Maji et al. (1997) show dispersion curve results by Bray and Stanley (1989) for a 16 mm steel plate in air. These are shown in Figure 4.4a. Models for the same environment have been recreated in Disperse and are shown in Figure 4.4b. It is seen that, although the wave modes are labelled differently, the results are the same. Thus, Disperse has successfully been used to recreate the published work.

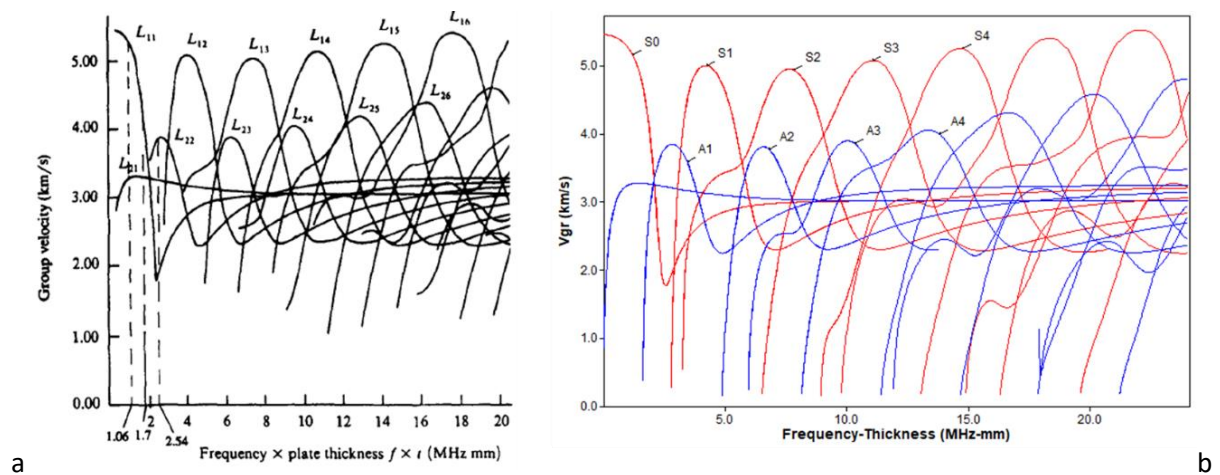


Figure 4.4 (a) Published and (b) recreated Disperse results for a 16 mm steel plate in an air environment plotted as group velocity against frequency thickness. From Maji et al. (1997).

^aLong et al. (2003) similarly model the attenuation of flexural modes in a 10 inch bore (254 mm), 16 mm wall thickness iron pipe in vacuum. Their Disperse results are shown in Figure 4.5a alongside recreated Disperse models for the same environment (Figure 4.5b).

In this case, the modelled and published results are seen to be very similar but not the same. In the published results there is a sudden drop in attenuation of the L(0,1) mode at around 4 kHz. In the modelled results this is at 2 kHz. This could however be a result of differences in the input parameters for the two modelling algorithms.

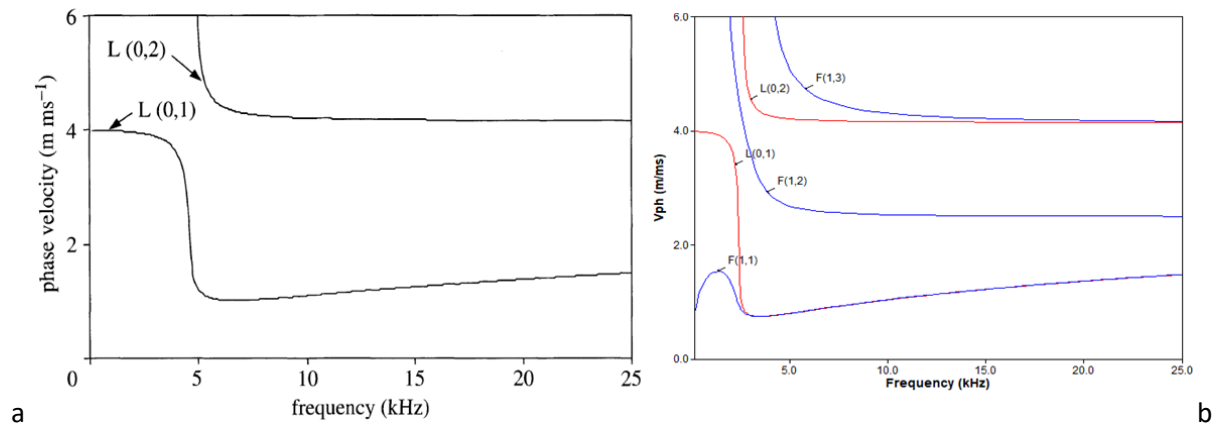


Figure 4.5 (a) Published and (b) recreated Disperse results for a 10 inch bore (254 mm), 16 mm wall thickness cast iron pipe. From Long et al. (2003).

Comparatively, Pavlakovic et al. (2001) model a more complex environment in which a steel plate of unknown thickness was embedded in grout. Their Disperse results are shown as a function of frequency-thickness (Figure 4.6a); an arbitrary value of 6 mm thickness was used to recreate these models (Figure 4.6b). The figure shows that largely the published and recreated results are the same despite the exemplar plate thickness.

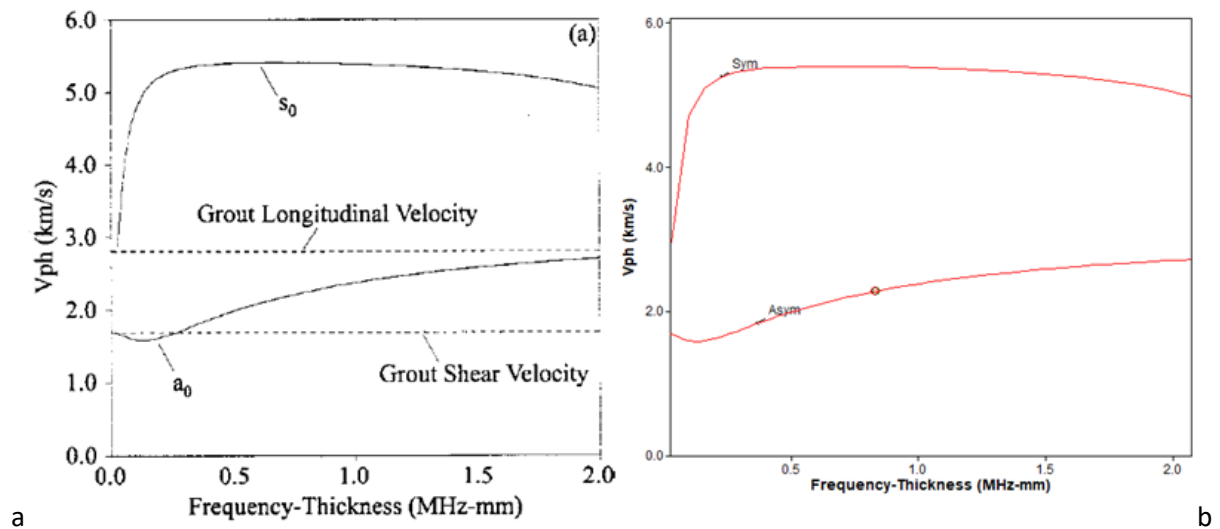


Figure 4.6 (a) Published and (b) recreated Disperse results for phase velocity as a function of frequency-thickness for a steel plate embedded in grout. From Pavlakovic et al. (2001).

Together, Figures 4.1 to 4.6 show that the Disperse program can be successfully used to recreate dispersion models for both simple and complex environments.

4.1.1.3 Validation using published work

Figures 4.7 and 4.8 show annotated pencil lead break results conducted by Shehadeh et al. (2008) for four pipe burial systems: air-steel-air, air-steel-water, air-steel-sand, and water-steel-sand. Figure 4.7

shows signal amplitudes (mV) with time, whilst Figure 4.8 shows corresponding frequency spectra (kHz).

It is clear from the figures that signal amplitudes are affected by burial materials whilst the dominance of different frequencies is also dependent on the burial system. Furthermore, the dominant frequencies change with propagation, shifting to become lower as the propagation distance increases. These observations are summarised in Table 4.1 which quantifies differences between the systems and provides calculated signal strengths for the dominant frequencies after 5 m propagation.

Table 4.1 Summary of points of interest from the results of Shehadeh et al.'s (2008) pipe experiments.

Environment	Amplitude (mV)	0.2 m propagation Dominant frequencies (kHz)	Amplitude (mV)	5 m propagation Dominant frequencies (kHz)	Strength after 5 m (%)
Air-Steel-Air	9.1	325	$4.1 + 0.5 = 4.6$	175 and 325	51
Water-Steel-Air	4.8	175 and 350	$0.4 + 0.11 = 0.51$	175 and 325	11
Air-Steel-Soil	3.8	325	$0.5 + 0.1 = 0.6$	125 and 350	16
Water-Steel-Soil	2.3	325	$0.19 + 0.04 = 0.23$	150 and 325	10

Computational models recreating the results of Shehadeh et al. (2008)'s experiments were carried out using a mixture of cylinder and plate models in Disperse. These are shown in Figure 4.9 whilst Table 4.2 details the parametric values used for modelling.

Using these models, values of attenuation for the fundamental Asymmetric (A0) and Symmetric (S0) wave modes at different frequencies were picked and recorded in Table 4.3. The picked frequencies were chosen to cover a broad spectrum whilst still being representative of the dominant frequencies identified by Shehadeh et al. (2008). Corresponding percentage signal strengths after 5 m of propagation were then calculated and may be compared to those measured by Shehadeh et al. (2008).

For the air-steel-air system, Shehadeh et al. (2008) found the dominant frequencies during propagation centred around 175 and 325 kHz. The Disperse models show that frequencies of 300 kHz will contain < 18% of their original signal strength; they are therefore unlikely to dominate the measured signal. At frequencies of 175 kHz and lower however, > 35% of the initial signal strength will be left of the A mode whilst > 56% will be left of the S mode. Given these results, and considering that the signals measured in the experiment will be a superposition of multiple frequencies and modes, it can be concluded from the Disperse models that the experimental results, for which 51% of the signal strength remained, are plausible.

For the air-steel-water system, the measured values of amplitude show that water is highly attenuating. Shehadeh et al. (2008) suggest that only 11% of the initial signal strength is measurable after 5 m propagation. The Disperse models show similar findings, with < 30% of the initial signal

strength left at frequencies > 100 kHz whilst, at 300 kHz, < 15% of the original signal strength is left. Considering the models assume perfect conditions (i.e. homogenous material properties), this value is comparable to the 11% found in experiments and therefore confirms the Disperse model to be representative.

Table 4.2 Material properties defining Shehadeh et al. (2008) model recreations in Disperse.

Material	ρ (g/cm ³)	Longitudinal velocity (m/ms)	Shear velocity (m/ms)	ν	E (GPa)
Air	-	-	-	-	-
Water	1	1.5	-	-	-
Steel	7.932	5.96	3.26	0.2865	216.9
Soil	1.2	5.2	3.9	-	-

Table 4.3 Summary of Disperse attenuation results as attenuation rates and percentage signal strengths (after 5 m propagation) for the A and S wave modes in varying environments and at different frequencies.

kHz	Air-Steel-Air				Water-Steel-Air				Air-Steel-Soil				Water-Steel-Soil			
	A		S		A		S		A		S		A		S	
	dB/m	%	dB/m	%	dB/m	%	dB/m	%	dB/m	%	dB/m	%	dB/m	%	dB/m	%
100	1.09	53.4	0.51	74.6	-	-	1.64	38.9	-	-	-	-	-	-	-	-
125	1.28	47.9	0.65	68.8	-	-	1.60	39.8	0.96	57.5	21.1	0	38.6	0	22.6	0
150	1.50	42.2	0.81	62.7	-	-	1.76	36.3	1.21	49.8	21.8	0	38.2	0	23.9	0
175	1.73	36.9	0.98	56.9	-	-	1.98	32.0	-	-	-	-	-	-	-	-
200	1.97	32.2	1.20	50.1	-	-	2.21	28.0	1.73	36.9	24.5	0	39.7	0	29.0	0
225	2.22	27.9	1.47	42.9	-	-	2.46	24.3	-	-	-	-	-	-	-	-
250	2.46	24.3	1.86	34.3	-	-	2.71	21.0	2.28	26.9	60.6	0	43.0	0	74.7	0
300	3.00	17.8	3.65	12.2	-	-	3.23	15.6	2.84	19.5	116	0	48.5	0	153	0
350	3.55	13.0	6.65	2.2	-	-	3.75	11.6	3.42	14.0	65.8	0	55.5	0	125	0

Contrastingly, for soil-structure systems, results between models and experiments start to differ. In an air-steel-soil system, experiments conducted by Shehadeh et al. (2008) show that 16% of the original signal strength should be left after propagation. Disperse models however suggest that the S mode is highly attenuative, essentially not propagating, whilst the A mode retains almost 20% of its strength at frequencies as high as 300 kHz. Consequently, the Disperse model is plausible assuming that the A mode was measured during experimentation.

In the water-steel-soil system, Disperse models show that no wave modes should be measurable after 5 m propagation. Shehadeh et al. (2008) however find that 10% of the initial signal was measurable in their experiments. This shows that the computer model is not accurate in this case, implying that are other factors affect propagation and attenuation and are not taken account of. These may include reflections and the superposition of alternative wave modes. The limitations of models are discussed in Section 4.1.1.6.

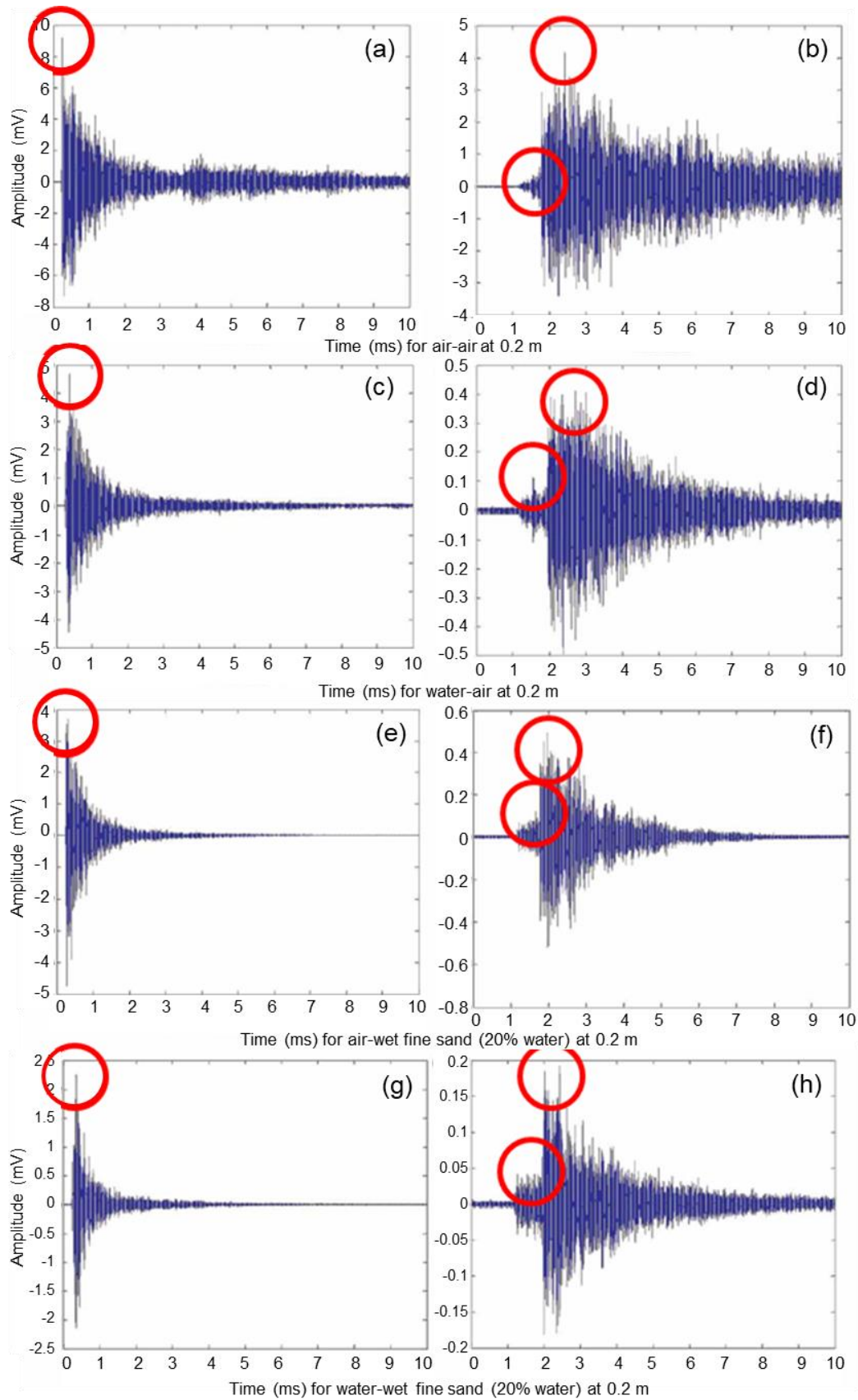


Figure 4.7 Annotated amplitude-time results for measured pencil lead break tests conducted by Shehadeh et al. (2008) at 0 and 5 m propagation (left and right respectively) for four pipe environments: air-steel-air, water-steel-air, air-steel-sand, and water-steel-sand (top to bottom respectively). Adapted from Shehadeh et al. (2008).

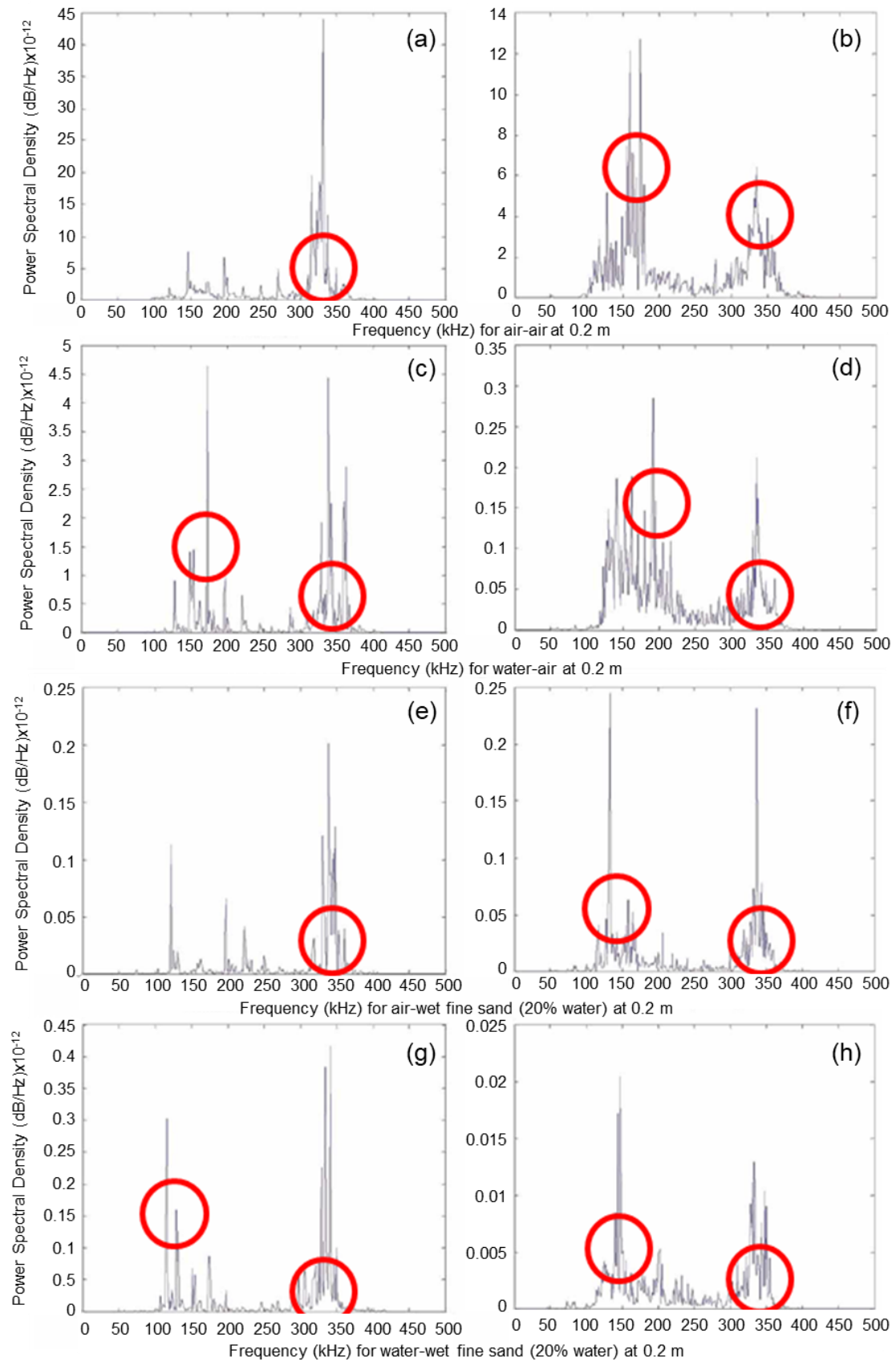


Figure 4.8 Annotated frequency spectra for measured pencil lead break tests conducted by Shehadeh et al. (2008) at 0 and 5 m propagation (left and right respectively) for four pipe environments: air-steel-air, water-steel-air, air-steel-sand, and water-steel-sand (top to bottom respectively). Adapted from Shehadeh et al. (2008).

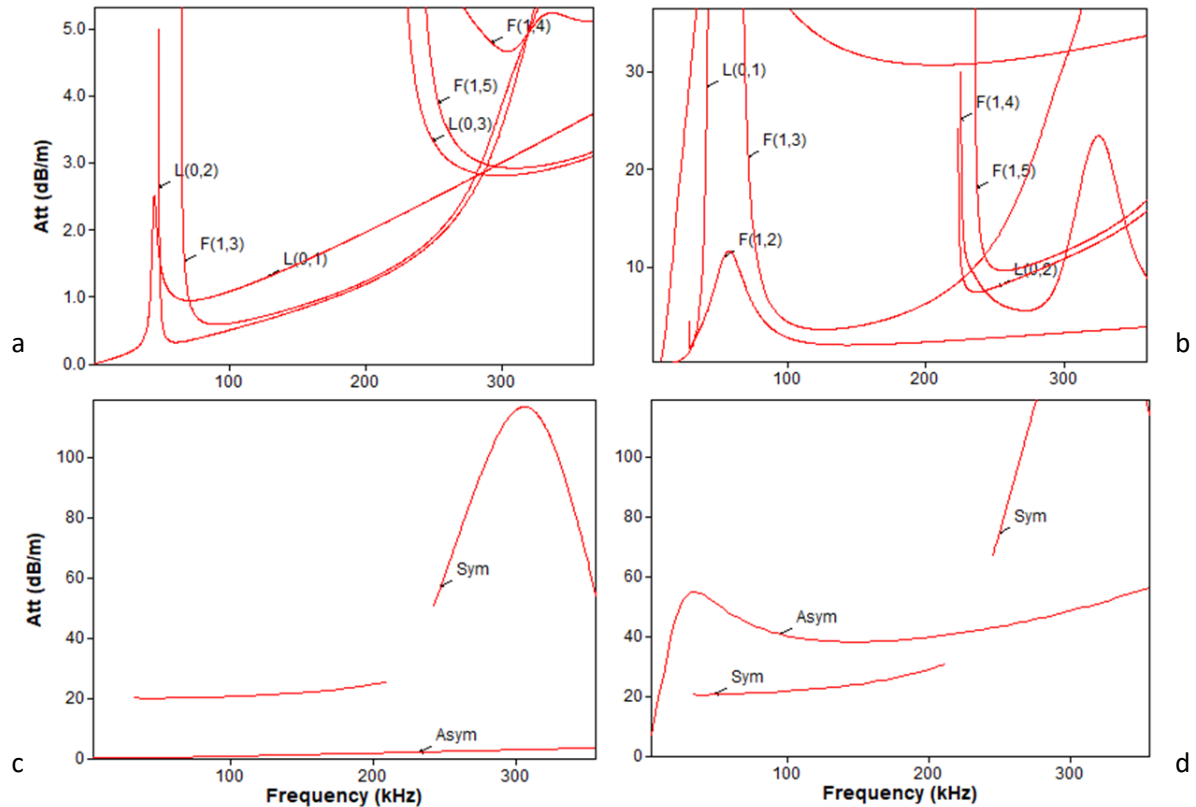


Figure 4.9 Attenuation models created in Disperse for the four experimental pipe environments: (a) air-steel-air, (b) water-steel-air, (c) air-steel-sand, and (d) water-steel-sand.

Smith et al. (2017) also investigated the effect of different burial systems on attenuation; their results are shown in Figure 4.10 as calculated signal energies (as a percentage of the original signal) with propagation distance (m). Like Shehadeh et al. (2008)'s results, it is seen that as the signal propagates it loses energy at a rate dependent on the burial system. Using Figure 4.10, Smith et al. (2017) were therefore able to calculate attenuation rates (dB/m) for each system using the conversion equation $A = A_0 e^{-kx}$, 'where A represents the magnitude of the wave at some distance, x, from the source, and A_0 represents the magnitude of the signal at the source (i.e. un-attenuated). The term e is Euler's (or Napier's) constant' (Smith et al., 2017). Their results are shown in Table 4.4 as three attenuation rates in dB/m. Burial system can be seen to effect attenuation significantly with clay having the strongest effect.

Computational models to replicate the attenuation rates were conducted in Disperse. Table 4.5 shows the parameters used to create the models alongside the corresponding attenuation rates for the S0 wave mode at three different frequencies. The results are summarised in Table 4.5.

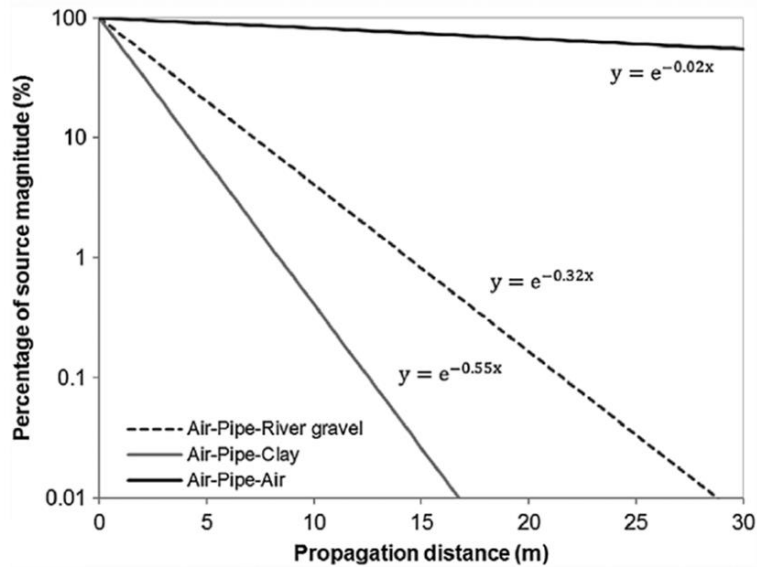


Figure 4.10 Measured signal strength with propagation distance for three different pipe systems: air-pipe-gravel, air-pipe-clay, and air-pipe-air. From Smith et al., 2017.

Table 4.4 Calculated attenuation rates for different pipe systems.

Environment	Attenuation (dB/m)
Air-Steel-Air	0.16
Air-Steel-Clay	4.75
Air-Steel-Gravel	2.78

As with the rates shown in Table 4.4, Table 4.5 shows that the external burial environments changes attenuation rates. In an air (or free) system (Figure 4.9a and 4.11a) attenuation is generally modelled at < 2 dB/m for frequencies below 200 kHz, whilst at a frequency of 30 kHz shows attenuation in the range of 0.2 dB/m. For the soil systems on the other hand (Figures 4.9c and 4.9d), attenuation is much higher with modelled rates between 3.5 and 8.2 dB/m.

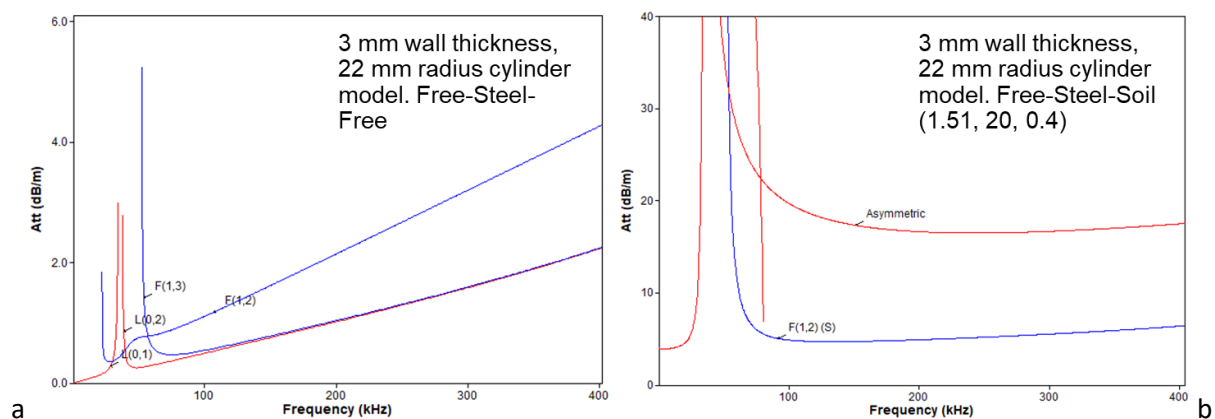


Figure 4.11 Disperse models for a 3 mm wall thickness, 22 mm radius pipe in a free-steel-free environment (left) and an example free-steel-soil environment (right).

Table 4.5 Model parameters used to describe different soil environments and their corresponding attenuation rates for the S0 mode at select frequencies.

	P (g/cm ³)	E (MPa)	ν	Attenuation (dB/m) (S0)		
				20 kHz	30 kHz	80 kHz
Clays	1.86	100	0.30	8.14	8.20	8.46
	1.86	80	0.30		7.35	
	1.86	30	0.40	4.81	4.87	5.14
	1.86	20	0.40	3.95	4.00	4.26
Sands	1.51	120	0.15		9.52	
	1.51	120	0.30		8.96	9.22
	1.51	120	0.40		8.64	
	1.51	80	0.15		7.80	
	1.51	80	0.30	7.29	7.35	7.61
	1.51	80	0.40	7.03	7.09	7.35
	1.51	60	0.40	6.11	6.16	6.42
	1.51	40	0.40	5.00	5.05	5.32
	1.51	20	0.40	3.57	3.62	3.88
	1.51	20	0.45	3.52	3.56	3.83

Considering attenuation rates of around 0.15 dB/m in an air environment were measured by Smith et al. (2017), the Disperse model can be concluded accurate for this case. For the soil environments, however, Table 4.5 suggests that to achieve the small attenuation rates calculated by Smith et al. (2017) (<5 dB/m) the soil must have a high Poisson's ratio and relatively low Young's modulus. Alternatively, the signals measured by Smith et al. (2017) could have been a superposition of wave modes and reflections and therefore accurately modellable in Disperse.

4.1.1.4 Small-scale experimental validation

Validation experiments using a small-small air-steel-air pipe system were conducted in the laboratory using two different diameter pipes and a range of propagation distances and AE sensors. By systematically varying these parameters, a robust data set could be compiled and then compared to Disperse models of equivalent burial systems. It was important to validate the Disperse models using a range of data collection methods (i.e. variations in instrumentation) as there is no one set way of collecting AE data and variations in the collection method will influence the collected AE.

Results of the study are shown in Figure 4.12. The figure shows amplitude behaviours with distance for a 48 mm diameter steel pipe, a 20 mm diameter steel pipe, and different sensor sensitivities (i.e. resonant frequencies). A source signal was induced using pencil lead break. The figure shows that generally, the measured amplitudes decrease with propagation distance. Figure 4.12c however demonstrates that this is sensor dependent.

A quantitative overview of Figure 4.12 is provided in Table 4.6 along with calculated signal strengths and corresponding attenuation rates. It should be noted that to remove the effect of end reflections,

comparisons have only been made for propagation distances between 0.5 and 2 m. Regardless, the attenuation is relatively low with rates between 0.15 and 1.40 dB/m calculated for the air-steel-air systems.

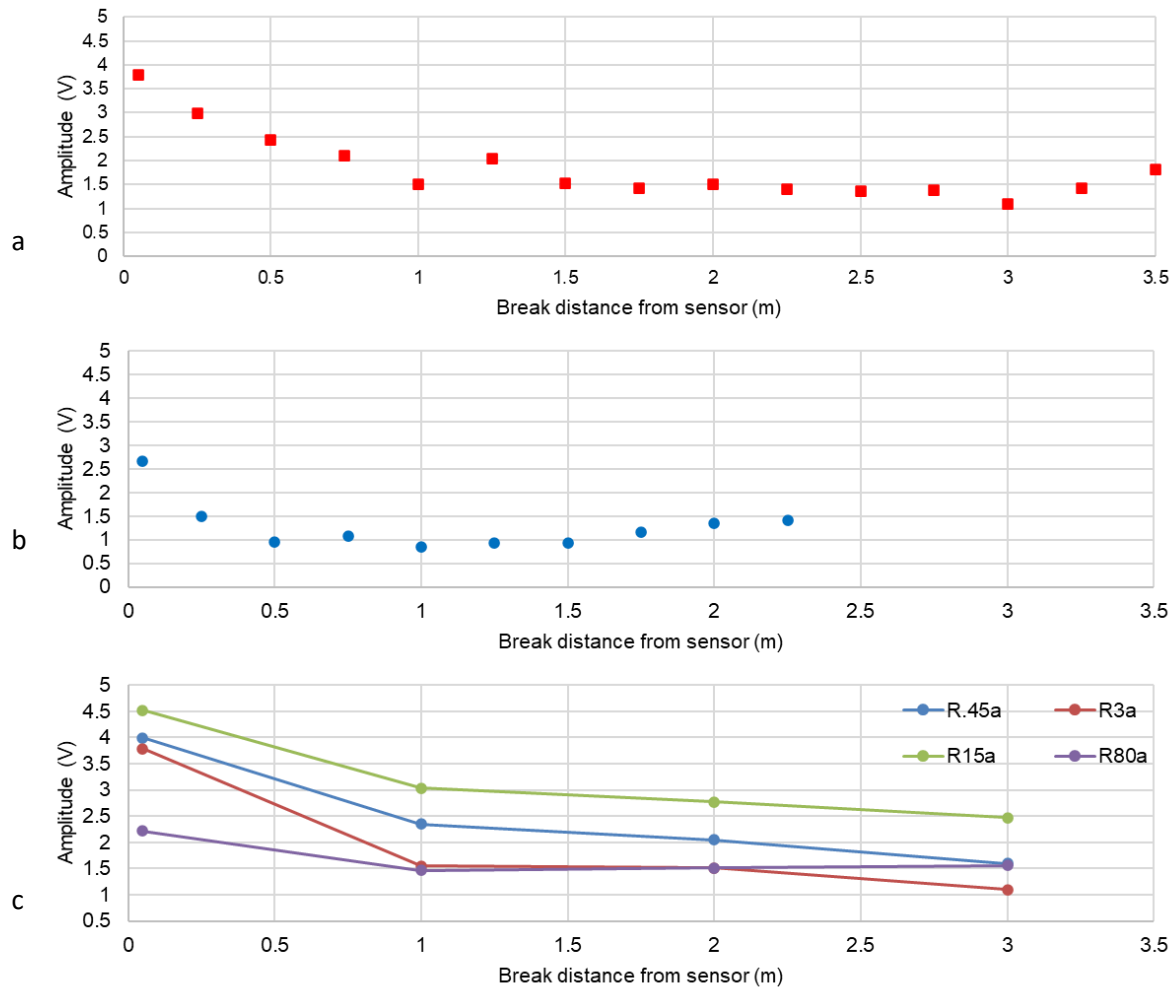


Figure 4.12 Results of air-pipe-air laboratory experiments for (a) a 48 mm diameter 2.6 m long pipe, (b) a 20 mm diameter 4.85 m long pipe, and (c) different sensors.

Table 4.6 A summary of experimental study results for different air-pipe-air experiments.

Experiment	Amplitude (V) with propagation (m)				Signal strength after propagation (%)	Corresponding attenuation (dB/m)
	0.5	1	1.5	2		
48 mm diameter	0.94	-	0.79	-	84	1.40
20 mm diameter	-	1.51	-	1.50	98	0.15
R15a sensor	-	3.04	-	2.78	92	0.70
R3a sensor	-	1.55	-	1.51	98	0.15
R45a sensor	-	2.35	-	2.05	87	1.20

Figure 4.13 comparatively shows a Disperse model for a similar air-steel-air system. Given that the effects of pipe radius are shown to have a negligible effect on attenuation (Section 4.1.3), whilst

plotting results as a function of frequency-thickness removes the effect of thickness (Section 4.1.2), the plate model used to produce the figures is representative.

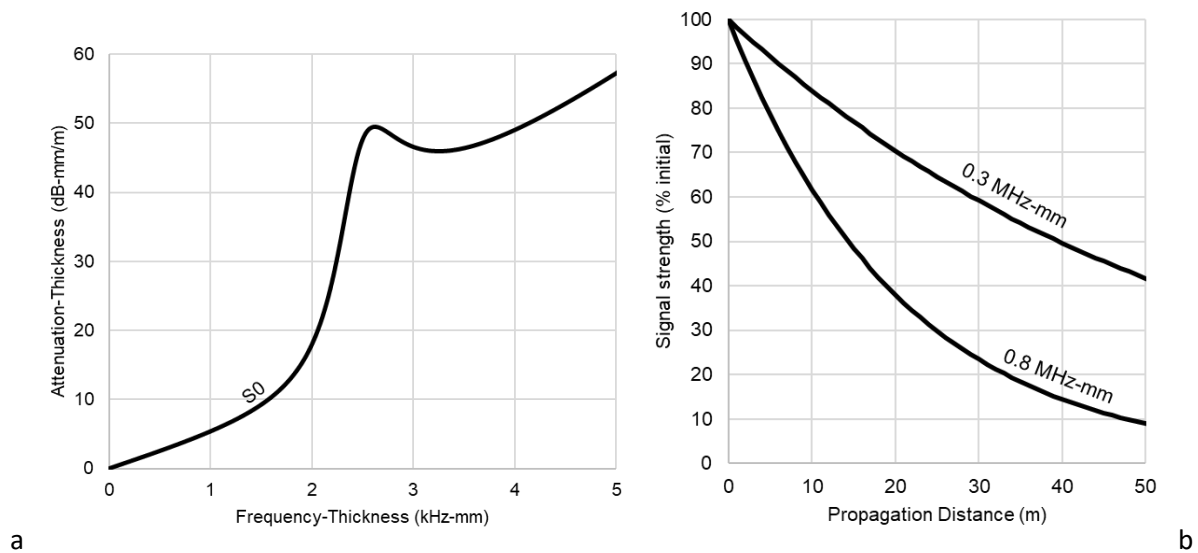


Figure 4.13 Disperse models showing (a) attenuation-thickness with frequency-thickness for an air-steel-air plate model and (b) the corresponding signal strengths with propagation at 0.5 and 0.8 MHz-mm frequency-thicknesses.

Figure 4.13a shows that attenuation of the S0 mode generally increases with an increasing frequency-thickness for an air-steel-air system. Before 1 MHz-mm, the attenuation is also relatively low at < 10 dB-mm/m. Considering that the pipes used for experimentation (Figure 4.12) had a wall thickness of 3 mm, 10 dB/mm divided by 3 mm results in maximum modelled attenuation rates of around 3.3 dB/m for frequencies below 300 kHz. Table 4.7 summarises some of the exact rates, whilst Figure 4.13b illustrates how a range of rates would affect propagation in the same system.

Table 4.7 Attenuation rates with select frequencies in an air-steel-air plate model.

Frequency (kHz)	S0		A0	
	Attenuation (dB/m)	% signal strength after 1 m	Attenuation (dB/m)	% signal strength after 1 m
20	0.16	98.2	0.16	98.2
30	0.20	97.7	0.20	97.7
50	0.23	97.4	0.66	92.7
80	0.40	95.5	0.90	90.2
150	0.76	91.6	1.5	84.1

The table shows that the Disperse model suggests attenuation rates ranging between 0.16 and 1.5 dB/m dependent on the wave mode and frequency of interest. This range is almost identical to the range measured during laboratory tests and therefore indicates that Disperse is a valid modelling tool for understanding wave attenuation in small-scale air-coupled steel structures.

4.1.1.5 Large-scale experimental validation

Large-scale experiments using both a free bound and soil (LBS) bound steel pipe system were conducted in the laboratory. From these, signal voltages and frequencies were measured for comparison with Disperse models.

Figure 4.14 summarizes the results plotting average signal strengths with propagation for a free bound (i.e. air) and a soil bound system. In both cases, the signal strength decreases with propagation although is much greater for the soil bound system. Disperse models for comparative systems are shown in Figures 4.13 and 4.15.

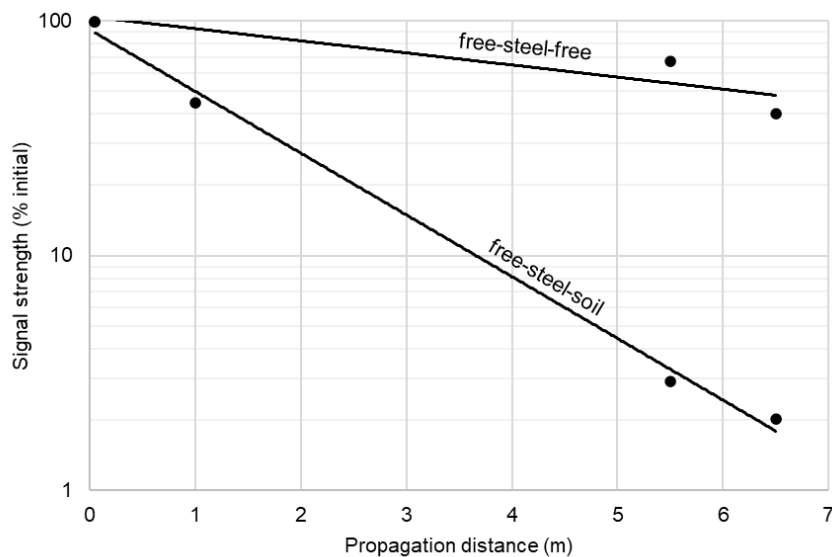


Figure 4.14 Average signal strength (%) with propagation distance (m) for measured large-scale free bound (i.e. air) and LBS buried steel pipe systems.

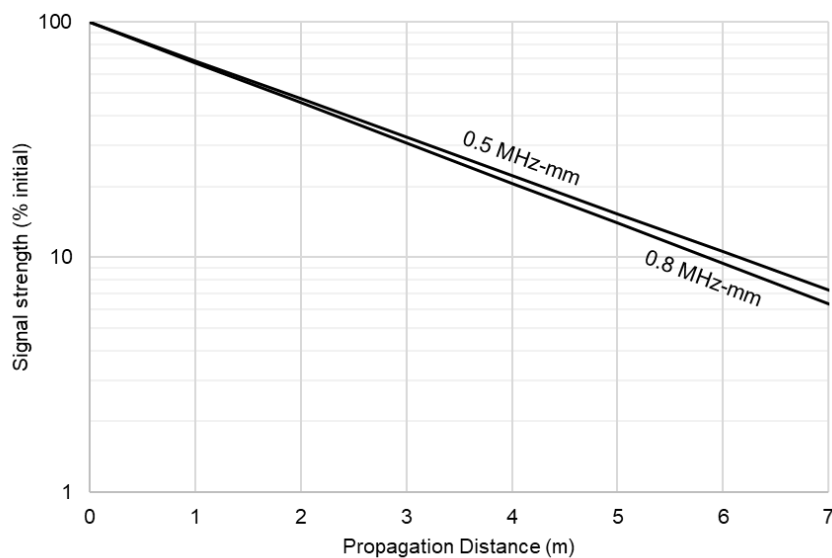


Figure 4.15 Signal strength (%) with propagation distance (m) for a free-steel-LBS plate system modelled in Disperse.

Figure 4.13 shows that after 5 m propagation between 75 and 95% of the initial signal strength should still be measurable for the S0 wave mode, dependent on frequency, in a free bound system. Figure 4.14 however shows that an average of around 60% was measurable in the large-scale experiment. Considering that the Disperse model assumes pristine conditions, the measured results are not unreasonable with defects in the pipe and the potential negative influences of sensor sensitivity, phase, noise, etc. affecting the results. Furthermore, a value of 60% has been interpolated from the regression analysis, however, at 5.5 m propagation values of 70% were measured. This suggests the accuracy of the regression line could be improved.

For a buried system however, Figure 4.15 suggests that 15% of the S0 mode should still be measurable after 5 m propagation. In the experiments, Figure 4.14 shows that < 5% of the signal was measurable after 5 m propagation. Like with the free bound system, this is a 10% difference, however as a result of the smaller strengths, is more significant.

The difference in the modelled and measured signal strength can be attributed to the effects discussed previously, whilst the accuracy of the regression analysis may again be low as a result of being formed from only three data points. Consequently, the modelled values are still plausible given the limitations of computational modelling and the results of the Disperse model are valid.

4.1.1.6 Modelling limitations and accuracy

Generally, computational models produced within Disperse can accurately recreate the results of both published and experimental works investigating propagation and attenuation within structures of varying geometries. Given the likely presence of unknown and/or un-modellable factors however, the limitations of models and their consequent accuracy should be considered.

Modelled and observed frequencies, for example, will differ as a result of processes such as aliasing and superposition, whilst in the field signals are likely to be multi-modal rather than formed from the pure fundamental wave modes. Additionally, instrumental error and signal distortion as a result of imperfect system conditions (i.e. defects causing reflections and/or inhomogeneous parametric properties) should be considered.

Despite this, it may be concluded that the underlying modelling technique of the Disperse program is scientifically valid even though an experiment may be more complex than the basic model; some factors can simply not be properly represented in models. Consequently, although the numerical methods are valid, their accuracy cannot be confirmed. Thus, a margin of error should always be acknowledged when creating and using computational models. This margin is dependent on the model and therefore not quantifiable.

4.1.2 Investigating wall thickness

Computationally, the effects of wall thickness were studied using a programme of Disperse models for which plate thickness was varied systematically between 1 and 25 mm for a tri-layer and free bound steel plate system. The results of this study are shown in Figure 4.16.

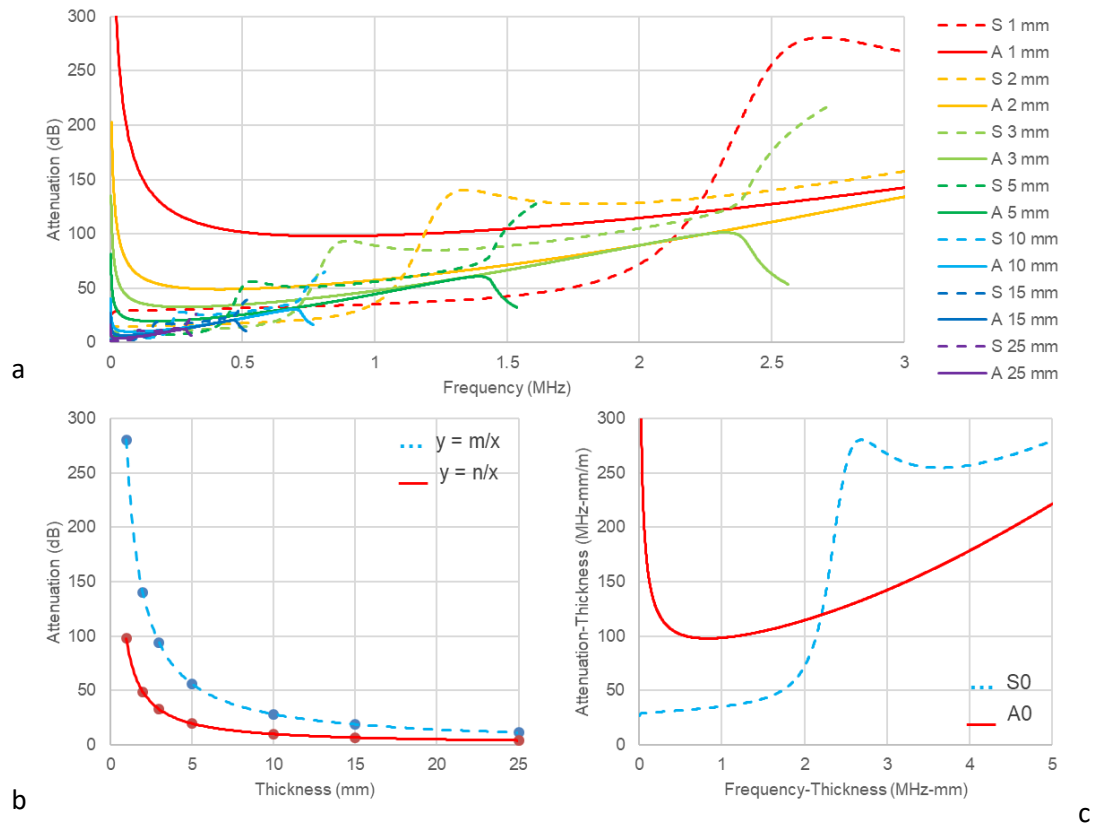


Figure 4.16 Modelled Disperse results of symmetric (S) and asymmetric (A) wave modes for: (a) attenuation as a function of thickness for thicknesses between 1 and 25 mm, (b) attenuation as a function of thickness collated from local maximum and minima, and (c) the relationship between attenuation and frequency as thickness products for the fundamental symmetric and asymmetric wave modes.

Figure 4.16a plots attenuation (dB) with frequency (MHz) for a range of all tested plated thicknesses. Figure 4.16a shows that for any specific frequency the attenuation decreases as plate thickness increases. This is also demonstrated in Figure 4.16b which shows attenuation with thickness for both the S0 and A0 wave modes at exemplar frequency thicknesses (local maxima and minima for the wave modes respectively).

Figure 4.16b shows that as plate thickness increases, attenuation decreases at a rate that may be quantified using the inverse law (Equation 4.1):

$$\text{attenuation} = m/\text{thickness} \quad [4.1]$$

Where attenuation is in dB, m (or n) are constants dependent on the wave mode and Frequency, and thickness (i.e. the thickness of the steel plate/wall) is in mm. Notably, an inverse law can be used for both the S0 and A0 wave modes by changing the constant m (or n). This is demonstrated in Figure 4.16c.

Figure 4.16c shows attenuation as a function of frequency but as thickness products, i.e. frequency-thickness (MHz-mm) against attenuation-thickness (dB-mm/m). For the S0 wave mode, attenuation increases near exponentially with an increasing frequency, peaking at around 2.3 MHz-mm, before decreasing near exponentially until around 3.5 MHz-mm and beginning to increase again. For the A0 mode, the wave behaviour is simpler and decreases rapidly to a frequency-thickness of about 0.7 MHz-mm, with respect to attenuation, before then increasing at an increasing rate over the data range shown.

By plotting the data as a thickness product, relationships at any frequency or thickness may be represented in a single plot as a result of the mathematical relationship shown in Figure 4.16b. Attenuation and/or thickness for a specific frequency or attenuation product can be obtained by multiplying/dividing either the frequency or attenuation product with/by the thickness. For example, to obtain an attenuation rate at a frequency of 50 kHz in a 10 mm thick plate, the frequency-thickness product is calculated as follows (Equations 4.2 and 4.3):

$$\text{frequency (kHz)} \times \text{thickness (mm)} = \text{attenuation} - \text{thickness (kHz} - \text{mm)} \quad [4.2]$$

$$50 \text{ kHz} \times 10 \text{ mm} = 500 \text{ kHz} - \text{mm} = 0.5 \text{ MHz} - \text{mm} \quad [4.3]$$

Given this, an attenuation-thickness value for 0.5 MHz-mm should be read from the graph in Figure c from which the value can be divided by 10 (the plate thickness) to find the attenuation in dB/m for a frequency of 50 kHz.

4.1.3 Investigating shell radius

Computationally, the influence of shell radius (i.e. pipe diameter) was investigated using a series of cylindrical Disperse models for which the shell radii were systematically varied between 5 and 200 mm. The results of the investigation are shown in Figure 4.17.

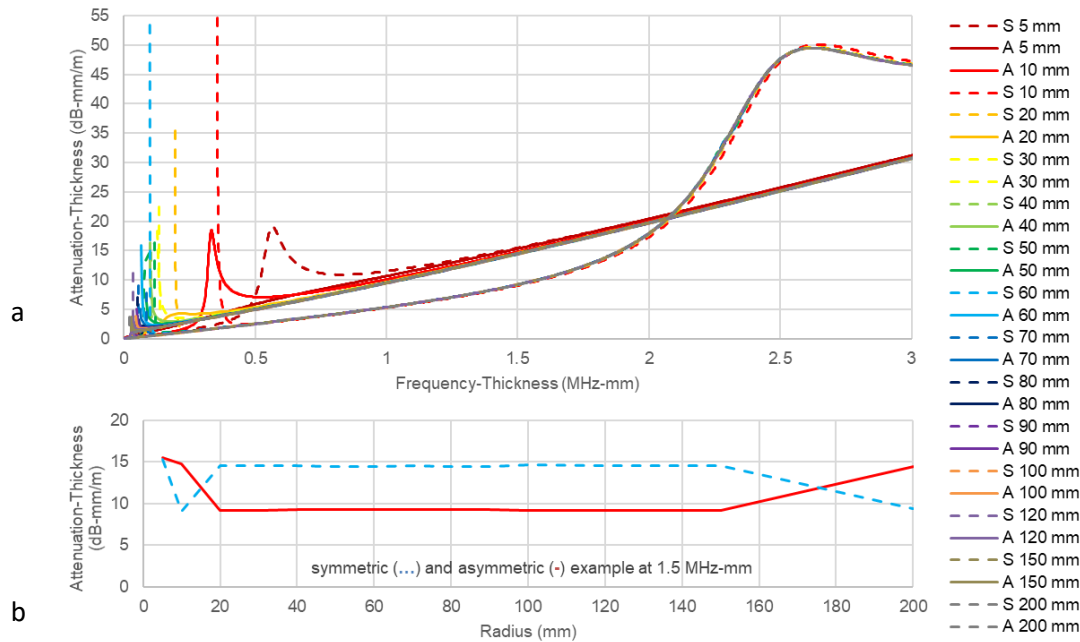


Figure 4.17 Disperse models showing the effect of shell radius on attenuation of symmetric (S) and asymmetric (A) wave modes as (a) a function of frequency-thickness for numerous shell radii (mm) and (b) a function of shell radius at a frequency-thickness of 1.5 MHz-mm.

Figure 4.17a shows attenuation-thickness as a function of frequency-thickness for numerous cylindrical models with varying radii whilst Figure 4.17b shows attenuation-thickness as a function of radius for a specific frequency-thickness of 1.5 MHz-mm. From both figures, it is shown that attenuation is relatively low before 2 MHz-mm with values < 20 dB-mm/m whilst radius appears to have a minimal effect.

Figure 4.17b shows that over the large range of radii tested (5 to 200 mm), a relatively minimal difference in attenuation can be seen despite this. Before a radius of 20 mm, the attenuation varies between around 10 and 15 dB-mm, whilst after a radius of 150 mm the attenuation again varied between the same values. Between 20 and 150 mm however, attenuation appears to remain constant at approximately 14 and 9 dB-mm/m for the S0 and A0 modes respectively. This suggests that the variation seen at the lowest and highest radii may be a result of errors during data generation and collection. Generally, however, shell radius has a negligible effect on propagation and attenuation.

4.1.4 Investigating external environments

Steel infrastructure can be buried in a range of natural as well as man-made embedding materials. Rock bolts, for example, can be driven into rock bodies but may also be drilled and embedded using epoxy. Similarly, utility pipes can be buried in their host material but may also be embedded using a sand or gravel annulus. A series of computational models investigating a variety of different burial

systems was therefore conducted to quantify the effects of different systems on wave behaviours. The series included studies on different burial systems and material types, as well as the influence of differing soil properties in soil systems. All models, unless otherwise stated, used a tri-layer plate system with a 5 mm thick steel plate and free internal boundary.

4.1.3.1 Soils

To investigate the influence of different soils, the effects of three input parameters, density (ρ), Poisson's ratio (ν), and Young's modulus (E), which describe the elastic mechanical behaviour of soils at small strains were studied. Results of the investigation are shown in Figures 4.18 to 4.20.

Figures 4.18 to 4.20 plot attenuation-thickness (MHz-mm) as a function of frequency-thickness (kHz-mm) and attenuation-thickness as a function of each parameter (accompanying numbers within each key identify the value of the parameter for which the dispersion curve was modelled). Displaying the results in this way allows for changes in the wave attenuation as well as relationships between the describing parameters to be viewed. Furthermore, the results are shown for both plate (PL) and cylinder (Sh) models in order to compare the effects of the different modelling methods whilst only the S0 and A0 (S and A) wave modes are plotted as these are the most likely to occur at the frequencies of interest.

The figures show that attenuation of the S0 mode is complex. Before 1 MHz-mm, attenuation is comparatively low (<250 dB-mm/m), before then increasing at an increasing rate to peak at approximately 2.7 MHz-mm. After peaking it then decreases to form a local minimum, around 3.7 MHz-mm, before increasing again.

Attenuation of the A0 mode, though, is relatively simple. Initially the attenuation decreases at a decreasing rate to form a minimum around 1.25 MHz-mm, after this it then increases at an increasing rate for the remainder of the parametric ranges tested. Given these behaviours, four initial observations may be made:

- There is little difference between the modelled solutions of cylindrical and plate systems within comparable systems.
- Between frequency-thicknesses of 0.5 and 2.5 MHz-mm, attenuation generally increases with an increasing frequency for both the S0 and A0 modes in all cases.
- As a function of the input parameters ρ and E , attenuation increases at a decreasing rate for both the S0 and A0 wave modes as the parameters increase.
- As a function of ν , attenuation increases as ν increases for the A0 mode but initially decreases for the S0 mode before then increasing again after 1.2 MHz-mm.

Assuming ν and E remain constant, the behaviour of the attenuation-thickness as a function of the parameter ρ can therefore be quantified using Equation 4.4:

$$Att - Thickness = m\rho^c \quad [4.4]$$

where m and c are constants dependent on the frequency of interest.

Similarly, the relationship between attenuation-thickness and E may also be quantified using the same equation but with different constants (Equation 4.5):

$$Att - Thickness = nE^d \quad [4.5]$$

where n and d are more constants dependent on the frequency of interest.

The equations show how attenuation is heavily and directly affected by changes in both ρ and E , especially at lower values of each parameter. This is important as lower parametric values are more representative of the expected soils types and conditions.

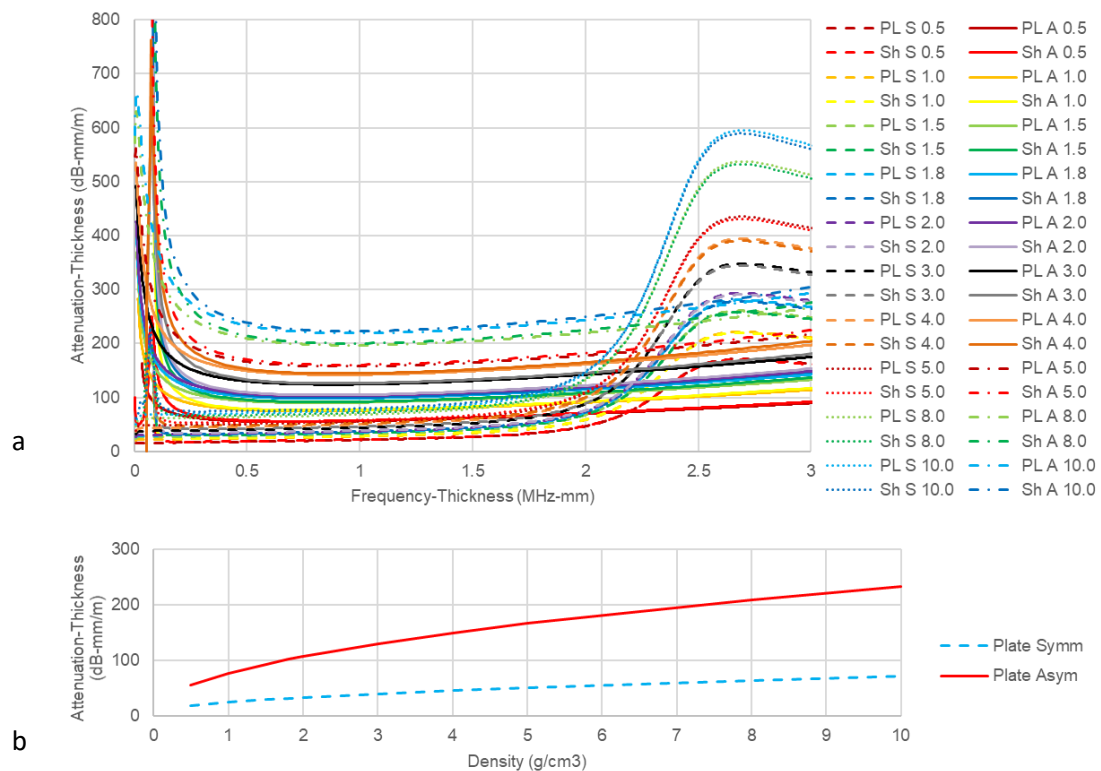


Figure 4.18 Disperse models showing the influence of a soil's density (0.5 to 10 kg/m³) on symmetric (S) and asymmetric (A) wave attenuation within plates (PL) and shell structures (Sh).

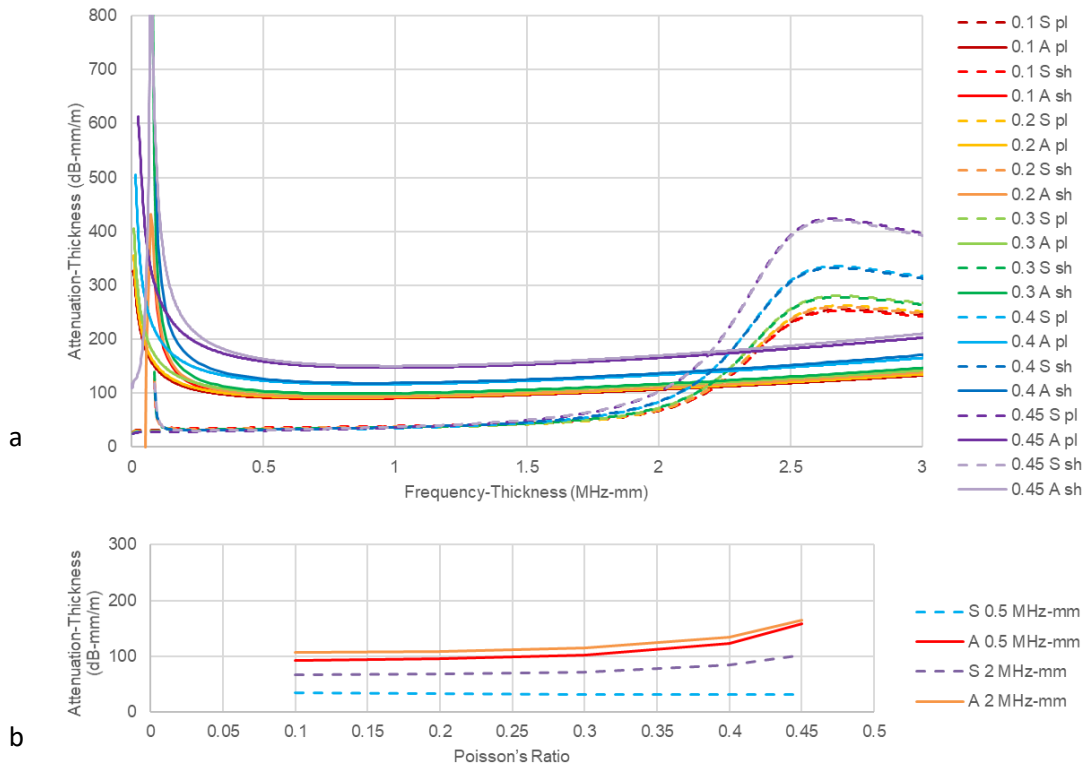


Figure 4.19 Disperse models showing the influence of a soil's Poisson's ratio (0.1 to 0.45) on symmetric (S) and asymmetric (A) wave attenuation within plates (PL) and shell structures (Sh).

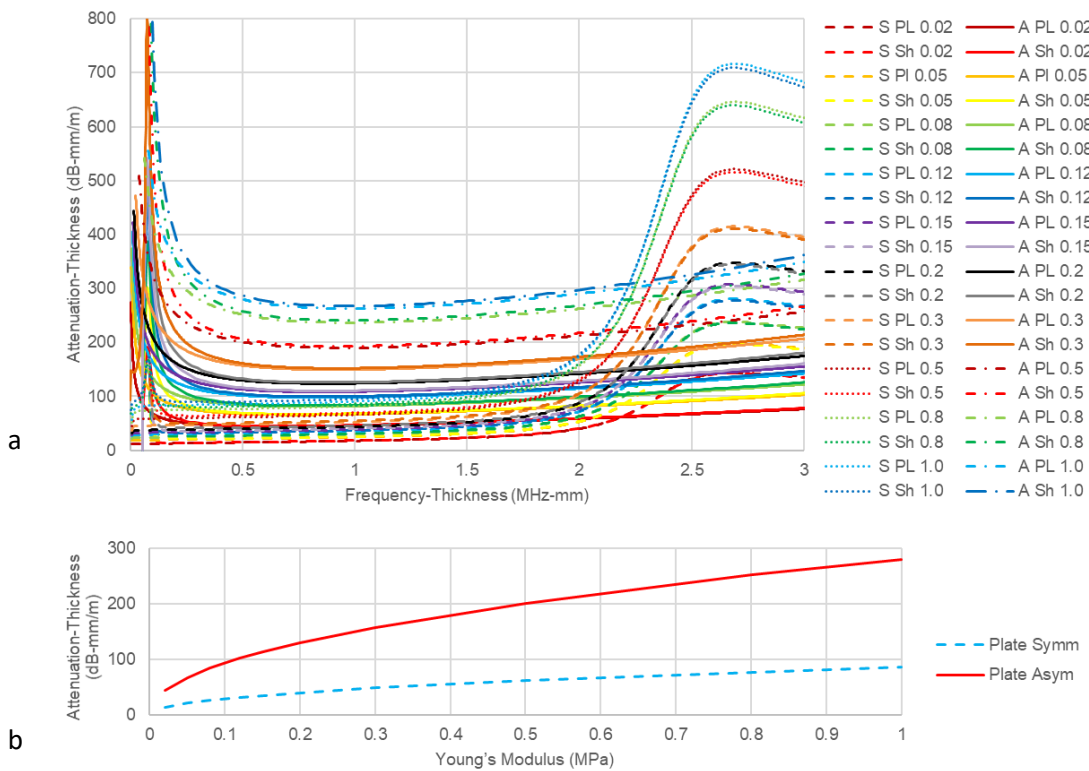


Figure 4.20 Disperse models showing the influence of a soil's Young's modulus (0.02 to 1 MPa) on symmetric (S) and asymmetric (A) wave attenuation within plates (PL) and shell structures (Sh).

As stated, attenuation with respect to ν does not show the same behaviours. Figure 4.19a shows that, at around 1.2 MHz-mm, there is a crossover point. Before this point, attenuation decreases approximately linearly but after this point it then increases at an increasing rate. These behaviours are therefore represented in Figure 4.19b as relationships for 0.5 and 2 MHz-mm (before and after the crossover).

Despite these changes in behaviour, a relationship between attenuation and ν is still not comparable to that of either ρ or E ; Figure 4.19b shows that attenuation initially decreases before then increasing at an increasing rate. For ρ and E attenuation continues to increase throughout, but at a decreasing rate. Moreover, the relationship between attenuation and ν is not quantifiable for the data shown whereas for ρ or E quantification resulted in exponential relationships defined by differing constants which changed dependent on the frequency-thickness. Relationships describing the way in which these constants changed were subsequently determined to better understand the overall behaviours. These are shown in Figure 4.21.

Figure 4.21 shows how the m , c , d , and n coefficients (for describing attenuation as a function of ρ and E) change dependent on frequency-thickness. Notably, the relationships appear very similar in their behaviour, whilst the c and d coefficients also remain close in value. The difference between the m and n coefficients, however, is much greater. Quantitative analysis comparing the coefficients has been conducted in Table 4.8.

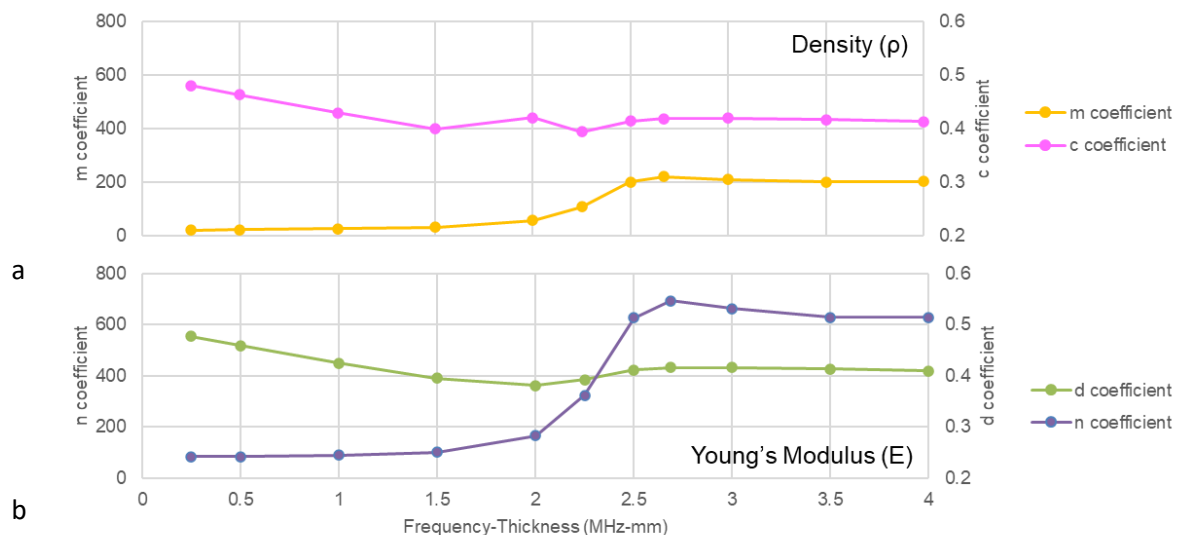


Figure 4.21 Calculated coefficient relationships describing attenuation-thickness as a function of (a) density and frequency-thickness and (b) Young's modulus and frequency-thickness.

Table 4.8 The percentage error between relationships for the c and d coefficients and the scale factors for relationships for the m and n coefficients.

MHz-mm	0.25	0.5	1	1.5	2	2.25	2.5	3	4
c	0.4816	0.4639	0.4304	0.4	0.4213	0.3946	0.4149	0.4205	0.4144
d	0.4771	0.4589	0.425	0.3952	0.3813	0.3919	0.4115	0.4163	0.4098
% error	0.9343	1.0778	1.2546	1.2	<u>9.4944</u>	0.6842	0.8194	0.9988	1.1100
m	22.801	24.186	27.625	33.938	58.292	110.17	202.76	211.63	204.46
n	83.437	84.501	88.439	100.49	166.41	322.91	626.45	662.16	629.45
scale factor	0.2732	0.2862	0.3123	0.3377	0.3502	0.3411	0.3236	0.3196	0.3248

Table 4.8 compares the c, d, m, and n coefficients. For the c and d values, a percentage difference comparing the two has been calculated. Generally, this is < 1.5% and implies that there may be a single factor controlling the behaviour. This is with exception to the values at 2 MHz-mm where the difference is inexplicably much greater (around 10%). This may however be treated as an anomaly.

The difference between the m and n coefficients is on the other hand much greater. Instead of a percentage difference, a scale factor between the two has consequently been calculated. The scale factors show that the n coefficient is always around three times greater than the m coefficient suggesting that E may have more of an influence than ρ on attenuation behaviours.

4.1.3.2 Other materials

As discussed, soils are not the only material with which steel structures may be buried or embedded. Rock bolts and utility pipes can not only be embedded in their natural environments, but also with man-made annuli. Studies concerning these alternative materials have therefore been conducted alongside the soils study, with Figure 4.22 showing the results.

Figure shows the results of Disperse models concerning alternative embedding materials to soil. The external materials have been considered infinite with the figure plotting attenuation-thickness as a function of frequency-thickness. The studies have been categorised into three groups: liquid burial systems (including air), polymeric embedding materials, and solid embedding materials. Unlike the soils study, these materials were modelled using constant parametric properties as defined by the Disperse program (Table 3.11). This was done so a focus could be kept on the effect of changing materials, rather than subtleties in the material properties. Also, given the negligible differences between plate and cylinder models, only plate models are shown.

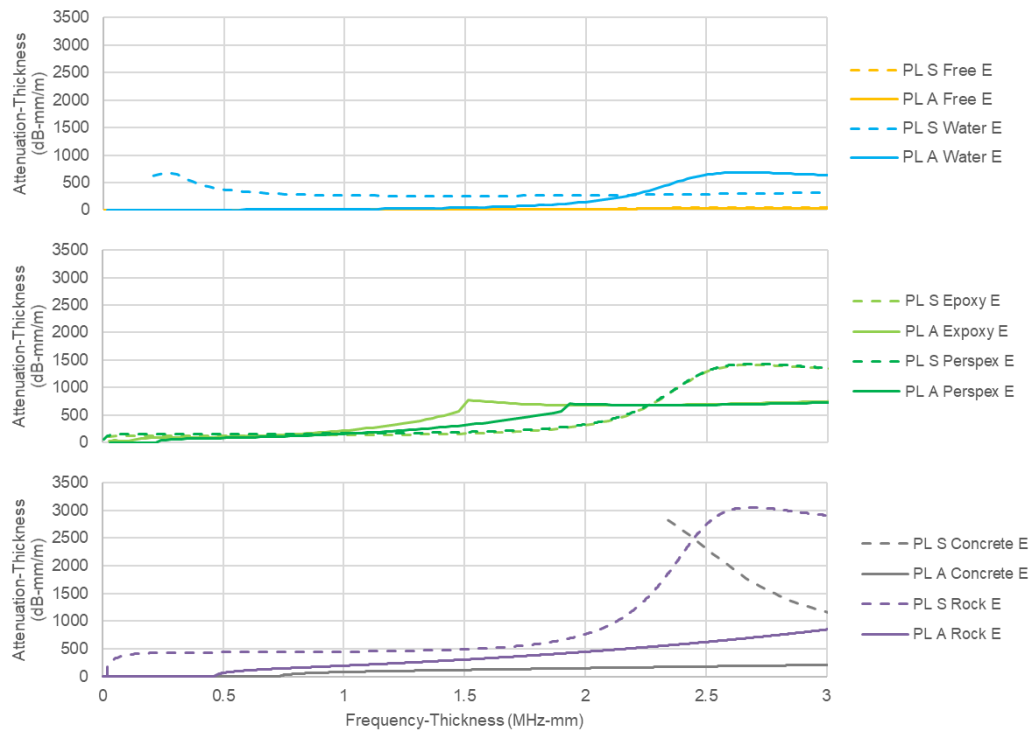


Figure 4.22 Disperse models showing the effects of external materials (E) on symmetric (S) and asymmetric (A) wave attenuation in tri-layer plate (PL) systems.

Two immediate observations made be made from Figure 4.22:

- Overall, the attenuative behaviours remain similar within different material groups; local features such as peaks and minima can be seen at constant frequency-thicknesses.
- The type of external material effects the wave attenuation to different extents.

Focusing on the overall attenuation behaviours, in the case of the S_0 mode, the wave behaviour remains similar throughout. As with previous models, attenuation remains relatively low until 1.5 MHz-mm at which point it then increases at an increasing rate to peak around 2.25 MHz-mm before then decreasing again within the range shown. This behaviour occurs for all tested materials with exception to concrete for which the program was unable to produce a complete model.

For the A_0 mode however, behaviours only remain similar within for similar materials. Within the liquid systems, the mode's behaviour follows that of previous models initially decreasing at a fast rate before then increasing slowly over the range of frequencies shown. For the polymeric systems, however, it's behaviour changes, increasing at a visibly increasing rate until 1.5 MHz-mm before then abruptly decreasing to form a local minimum at approximately 1.75 MHz-mm and then continuing to increase again. This behaviour is difficult to explain and may be a result of errors within the modelling process; it is possible multiple wave modes, rather than just the A_0 mode, have been connected.

Contrastingly, the behaviour of the A0 mode in the stiffer, solid systems is again different. Initially, attenuation is relatively low with rates <10 dB-mm/m. By 0.5 MHz-mm however the behaviours change. Within rock, for example, the attenuation increases suddenly before then continuing to increase at an increasing rate. Within concrete, it shows a similar behaviour increasingly suddenly around 0.75 MHz-mm and then increasing at an increasing rate. The different solid material systems can therefore be seen to affect wave behaviours differently.

Alongside propagation behaviours, attenuation behaviours (i.e. the magnitude and rate of attenuation) are also affected by the different material systems. For liquid systems, attenuation peaks at a maximum of around 300 dB-mm/m. For polymeric systems however, this value increases to around 800 dB-mm/m whilst for the soil systems increases to around 500 dB-mm/m. Peak attenuation occurs at around 1.5 MHz-mm. By 2.25 MHz-mm, however, the differences are even greater with attenuation rates peaking at around 700, 1400, and 3000 dB-mm/m respectively. This implies that the influence of an external material is affected by the frequency-thickness as well with higher frequency-thickness products being more sensitive.

The observed variations in attenuation are likely a result of the greatly varying material properties (Table 3.11) and consequent transmission of energy at structure-material interfaces. Energy transmission at a boundary is predominantly controlled by the differences in density of the materials present, where their relative densities then contribute to a value of acoustic impedance (Z). The characteristic acoustic impedance (Z) of water (≈ 1.5 MPa.s/m³) (where characteristic acoustic impedance is dependent on volume), for example, is more closely matched to that of steel than that of air or gas (≈ 420 Pa.s/m³) (Wolfe). Consequently, the impedance mismatch, or difference in characteristic acoustic impedances, at a steel-water interface is much smaller than that at a steel-air interface and energy transfer is higher. Given this, higher densities, such as those of polymeric and concrete materials, make the impedance mismatches of these material boundaries even smaller. Higher density materials are consequently more attenuative.

It is not just ρ that controls wave behaviours, though, with v and E also effecting attenuation as shown in Figures 4.19 and 4.20. By considering the properties of the tested materials, no clear link between v and attenuation may be determined. This suggests that v is less influential than ρ . For E however, it is clear that materials with a higher value of E are more attenuative.

The relationship between E and attenuation is shown in Figure 4.20. Previously, it was suggested that E is likely to influence the rate of attenuation more than ρ as a result of the higher coefficients seen in Figure 4.21. Table 4.9 therefore compares their influence as ratios to rock, the material which had the highest parametric values of those tested. These results are also shown in Figure 4.23.

Table 4.9 Comparing parametric properties of different materials as ratios.

Material	ρ (g/cm ³)	E (MPa)	Peak Att (dB-mm/m)	ρ ratio to rock	E ratio to rock	Att ratio to rock
Air (20C)	0.001	-	50	0.0004	-	0.016
Water	1.000	-	690	0.400	-	0.225
Epoxy	1.170	3.941	1425	0.468	0.179	0.466
Perspex	1.180	6.327	1430	0.472	0.288	0.467
Concrete	2.200	9.570	-	0.88	0.435	-
Rock	2.500	22.000	3060	1	1	1

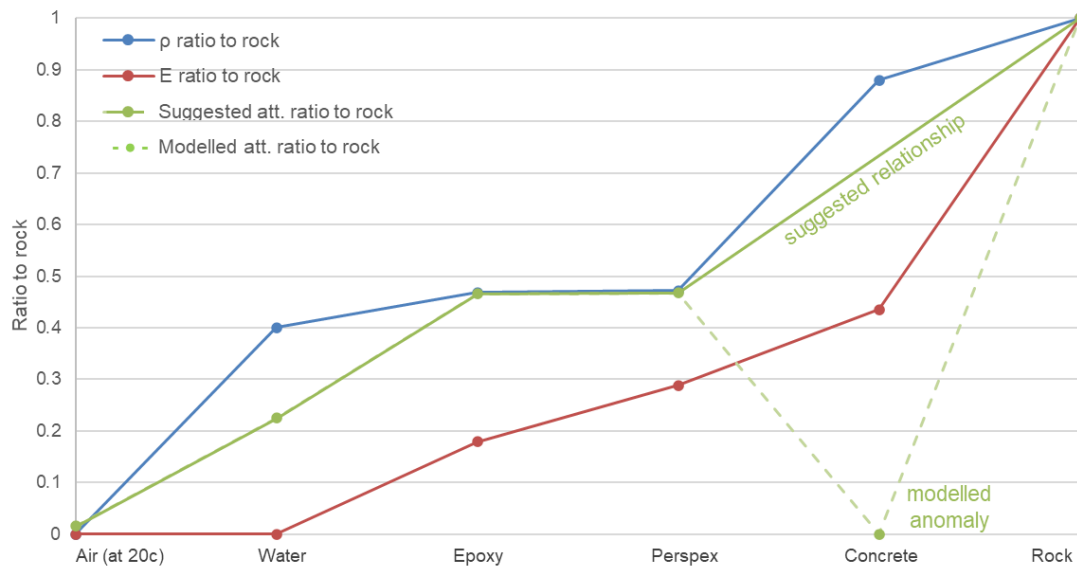


Figure 4.23 Ratio relationships for parametric properties of different external materials.

Figure 4.23 shows that although E shows a similar behavioural pattern to attenuation, the plotted ratios for ρ are even closer suggesting that ρ has the strongest influence on the observed trend. Certain parametric values have however been excluded. This makes the sample size small and consequently decreases the reliability of the result. Further factors such as material isotropy or ductility, which have not been considered, are likely influencing attenuation too.

4.1.5 Investigating internal environments

Buried pipes are used to transport varying substances whilst pile foundations, rock bolts, and other structures may be embedded using specific materials externally as well as internally. Models of these buried systems must therefore consider a wide range of potential internal environments and their influence on wave propagation and attenuation.

4.1.5.1 Fluids

Figures 4.24 and 4.25 shows the results of an investigative study looking at several common substances carried by pipes. Figure 4.25 shows attenuation-thickness as a function of frequency-

thickness for different liquid substances, including gases, within free bound systems. For comparison, these have also been modelled with an external soil (where $\rho = 1800 \text{ kg/m}^3$, $\nu = 0.3$, and $E = 120 \text{ kPa}$) (Figure 4.24). By modelling both free and soil bound systems, later extrapolation of the results for other materials can be done. Furthermore, it is shown how different internal and external material combinations may interact.

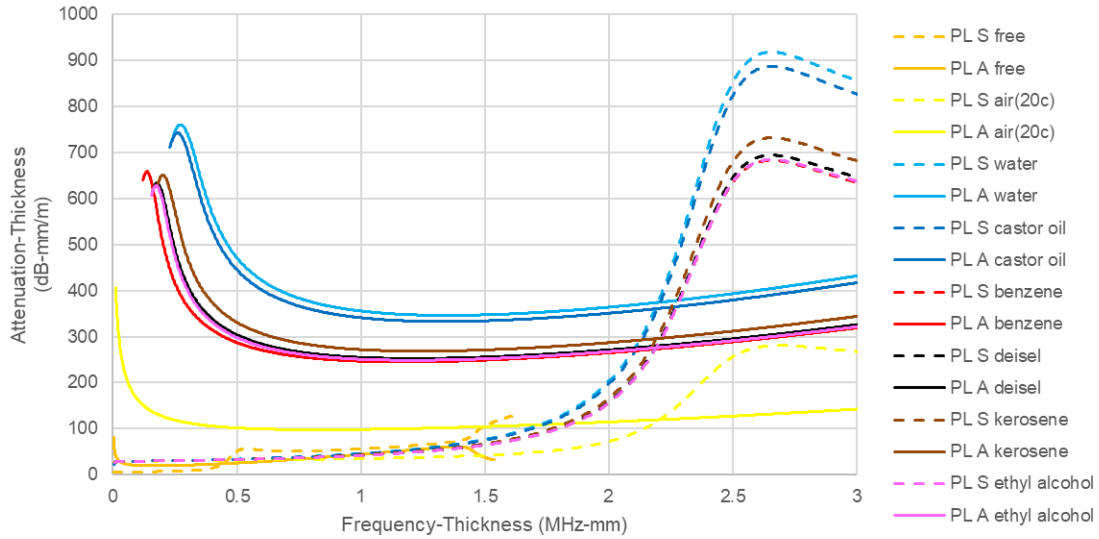


Figure 4.24 Disperse modelling results for attenuation-thickness as a function of frequency-thickness with internal liquid environments and a soil external environment.

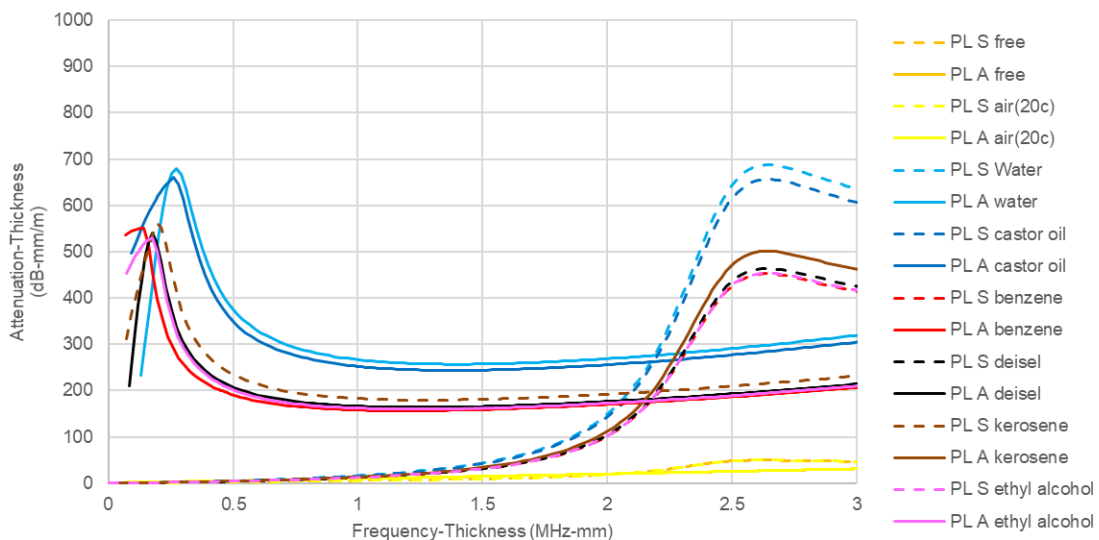


Figure 4.25 Disperse modelling results for attenuation-thickness as a function of frequency-thickness with internal liquid environments and a free external environment.

Figures 4.24 and 4.25 shows that the overall propagation behaviour remains the same as previous Disperse investigations (e.g. thickness and radius as in Section 4.1.2), implying that the internal

environment does not affect wave propagation. Also, as previously concluded, the external environment has a strong effect on attenuation with the free and soil bound models showing considerably different rates of attenuation for corresponding internal environments. Variations in internal environment however further effect the attenuation rates.

Specifically, Figure 4.25 shows that at 0.5 MHz-mm all the substances have attenuation rates between 32 and 33 dB-mm/m for the S0 mode. This is equivalent to 3.3 dB/m for a 50 kHz signal in a 10 mm thick plate. By 1 MHz-mm though, the attenuation of different substances starts to differentiate with the gases showing attenuation rates of around 35 dB-mm/m, most of the liquids around 42 dB-mm/m and the water and castor oil environments even higher at 45 dB-mm/m.

Attenuation of the A0 mode is less complex. Initially the attenuation decreases at a decreasing rate to reach a minimum at around 1 MHz-mm (e.g. 100 kHz in a 10 mm thick plate). After this point, the rate of attenuation then increases at an increasing rate for the range of frequency-thicknesses shown.

This behaviour is unexpected with lower frequencies normally being less attenuating due to fewer wave cycles. It is therefore possible that this behaviour is an artefact of the modelling algorithm but, could also show that lower frequencies are more sensitive to the burial system. Additionally, unlike with the S0 mode, Figures 4.24 and 4.25 shows that attenuation of the A0 does not differentiate with frequency for different materials. Instead, the attenuation rates stay approximately proportional to one another with different materials showing three distinctive and groupable rates based around density. Consequently, three generalised relationships may be used to describe the attenuation of the modelled internal liquid environments for both the S0 and A0 modes. These are shown in Figure 4.26.

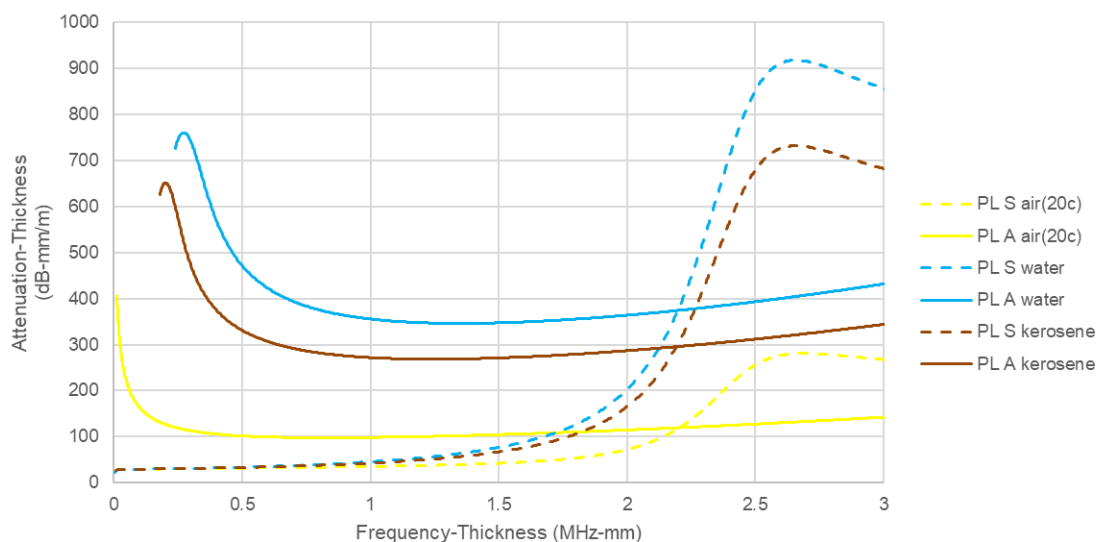


Figure 4.26 The generalised Disperse models for internal liquids of similar densities (gases, water, and oils/alcohol) with an external soil environment.

Figure 4.26 shows three generalised relationships for wave attenuation behaviour with different internal materials. The relationships shown are for air at 20°C, which can be used to represent most gases; kerosene, which can be used to represent alcohol and most oils; and water, which can be used to represent water and castor oil. These relationships have been used as worst-case scenarios, i.e. the most attenuating liquid within each sub-group, to ensure that the modelled attenuation is not underestimated for different materials. These three relationships therefore approximate attenuation within most liquid-steel-soil systems.

4.1.5.2 Solids: Polymeric materials

Steel-soil systems such as those created by rock bolts and pile foundations do not normally have internal liquids. Instead, they are often embedded with materials such as epoxy or concrete both internally and externally. Embedded structures are also not necessarily hollow, in which case the internal material is steel. To investigate such systems, further Disperse studies for polymeric and stiff solid internal materials have been performed.

Figure 4.27 shows the modelling results for a steel plate with internal polymeric materials, including epoxy. For the S0 mode the overall mode behaviours are similar to Figure 4.26, increasing at an increasing rate until around 2.27 MHz-mm. The rates of attenuation are however almost doubled. At 2 MHz-mm, for example, attenuation within an epoxy environment is modelled at 400 dB-mm/m. Comparatively, in a water environment rates of only 200 dB-mm/m were modelled.

Attenuation of the S0 mode in Figure 4.27 also differs with frequency. At 2.5 MHz-mm, attenuation within a polystyrene system is 1250 dB-mm/m, for example, whereas for epoxy is 1550 dB-mm/m. MDPE on the other hand shows modelled rates of 1240 dB-mm/m. Although these differences are large, such high attenuation rates would result in the signals not being measurable within a very short propagation distance. Consequently, the effect would not influence measurements in the field.

Attenuation of the A0 mode within polymeric systems is different to that observed in the liquid systems. Sharp local peaks may be observed at 1 and 1.5 MHz-mm, dependent on the material. The sharpness of the maxima has not been seen in any other models, within this investigation or published work, suggesting that the results may be erroneous. This could be a result of different mode paths converging which can occur when the solutions for similar wave modes reside relatively closely as a function of frequency and phase velocity. The results shown in Figure 4.27 are therefore unreliable, however the magnitudes of attenuation may still be approximated. Given this, it can be concluded that polymeric systems are more attenuating than liquid systems.

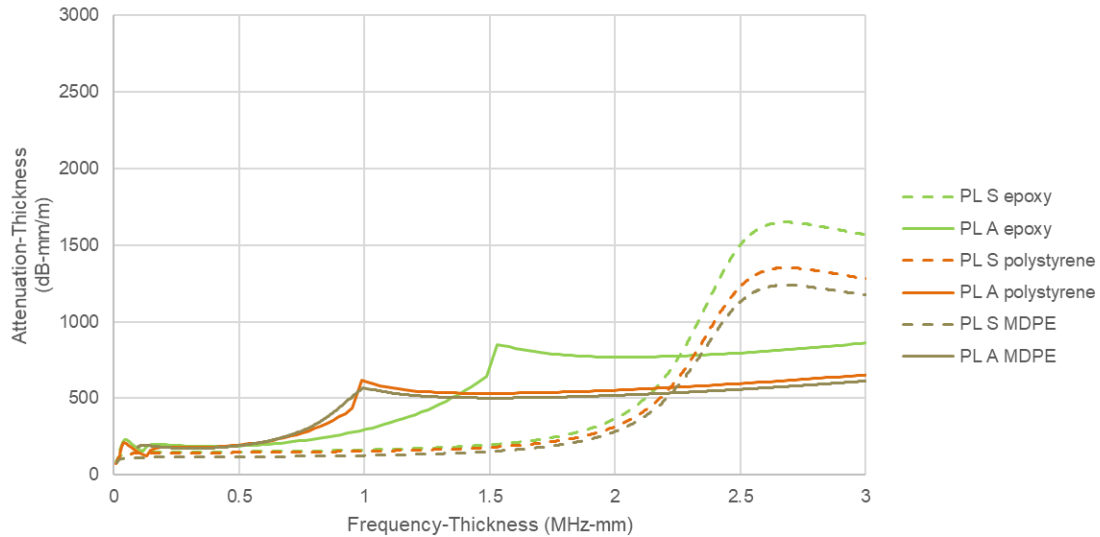


Figure 4.27 Disperse modelling results for attenuation-thickness as a function of frequency-thickness with internal polymeric materials and an external soil environment.

4.1.5.3 Solids: Stiff materials

Figure 4.28 shows attenuation behaviours for stiff materials. It is immediately apparent that the stiff materials behave very differently to one another, but also to other materials.

Comparing Figure 4.28 with Figures 4.26 and 4.27, attenuation within concrete systems is over double that seen for polymeric or liquid systems in Figures 4.27 and 4.26 respectively. By 1 MHz-mm attenuation is modelled at around 500 dB-mm/m for the S0 mode and 200 dB-mm/m for the A0 mode. These rates are much higher (+400 dB-mm/m) than the polymeric materials in Figure 4.27, though are of a comparable magnitude (1×10^2).

By 2.25 MHz-mm however, attenuation of the S0 mode has drastically increases to 2000 dB-mm/m whilst, after this point, then fluctuates sharply and in an unrealistic way. This behaviour implies that the model is erroneous, at least for frequency-thicknesses between 2.25 and 2.7 MHz-mm. From literature, however, attenuation within concrete is known to be high (Beard and Lowe, 2003) and vary dependent on the properties of the concrete (Li et al., 2017). Therefore, like with the polymeric models, although the wave behaviours are unrealistic, the magnitude of attenuation is likely reliable.

Attenuation within steel systems on the other hand is comparable to air (at 20c) and considerably lower than the polymeric systems. At 1 MHz-mm attenuation is modelled at 35 dB-mm/m, this is equivalent to air in Figure 4.26, whilst the observed propagation behaviours are also the same. The similarities between the models suggests that most of the wave energy is travelling within the steel and is not affected by a solid steel, rather than hollow, system. Such a conclusion agrees with the finding of Section 4.1.3.

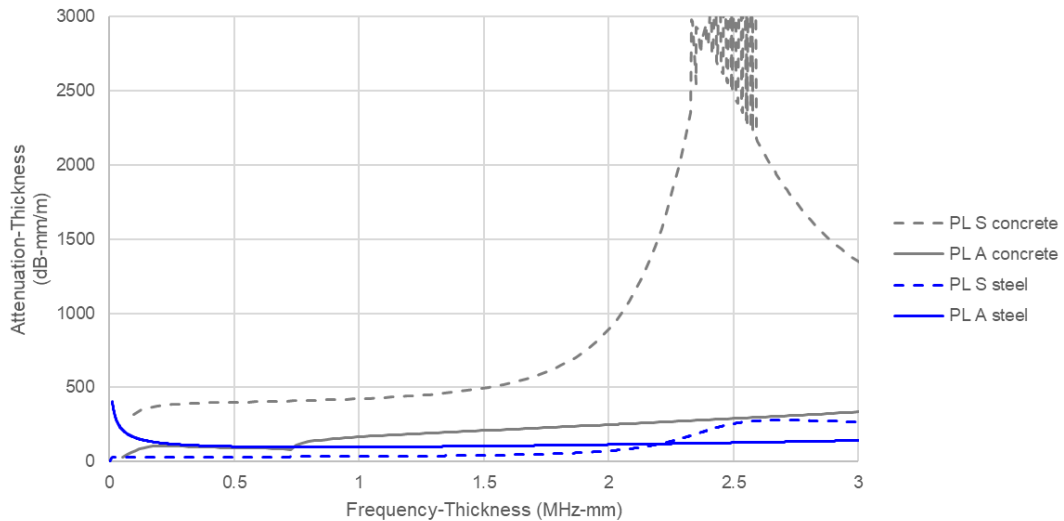


Figure 4.28 Disperse modelling results for attenuation-thickness as a function of frequency-thickness with internal solid materials and an external soil environment.

4.1.6 Case studies

4.1.6.1 Buried utility pipes

Four, generalised buried pipeline systems were modelled using Disperse. These included: a water filled pipe buried to depths of 0.6 and 1.2 m, and a gas filled pipe buried to cover depths of 0.6 and 1.2 m (Figure 4.29). These systems were designed using information from literature (Thames Water, 2015, Severn Trent, 2016, Water UK, 2017) with the material properties (Table 4.10) modelled to a resolution of 1 m with respect to variations resulting from depth (Figure 4.30).

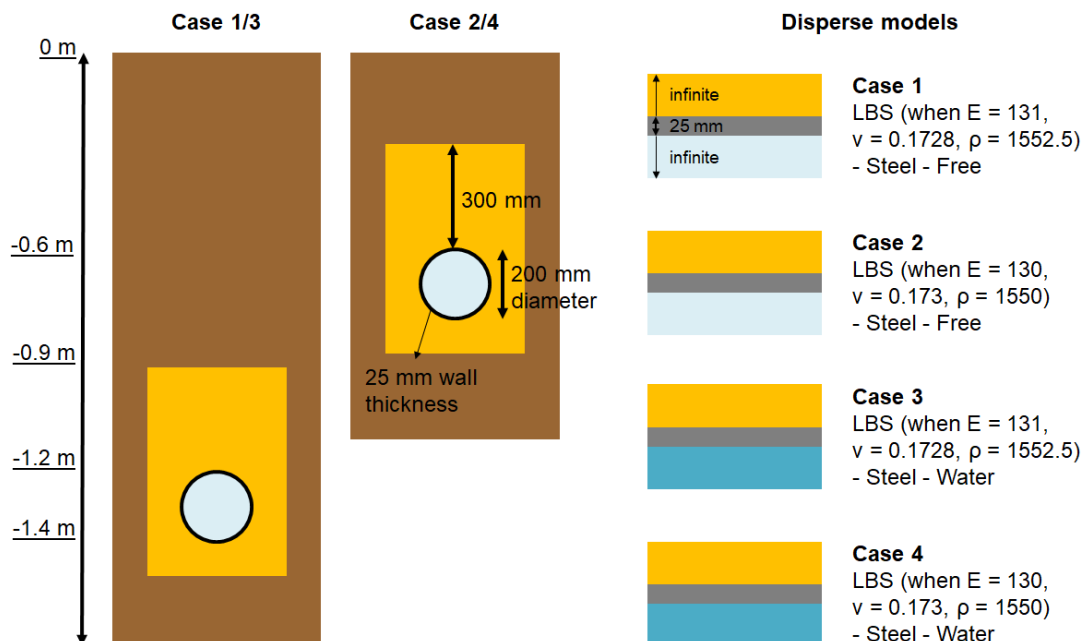


Figure 4.29 The four pipe model systems investigated (Cases 1 to 4).

Table 4.10 Typical parametric value ranges for describing London Clay and Leighton Buzzard Sand to a depth of 40 m.

Material	ρ (kg/m ³)	ν	E (MPa)	References
London Clay (LC) (undrained)	2000 at 0 m 2200 at 40 m	0.1 at 0 m 0.25 at 40 m	100 at 0 m 130 at 40 m	Gasparre et al., 2007 Hight et al., 2003 Nishimura et al., 2007
London Clay (LC) (drained)	2000 at 0 m 2200 at 40 m	0.1 at 0 m 0.25 at 40 m	100 at 0 m 250 at 40 m	Gasparre et al., 2007 Nishimura et al., 2007
Leighton Buzzard Sand (LBS)	1550 at 0 m 1650 at 40 m	0.173 at 0 m 0.165 at 40 m	130 at 0 m 170 at 40 m	Cabalar et al., 2010 Kumar and Madhusudhan, 2012 Cavallaro et al., 2001
Steel	7932	0.2865	216900	Disperse Program

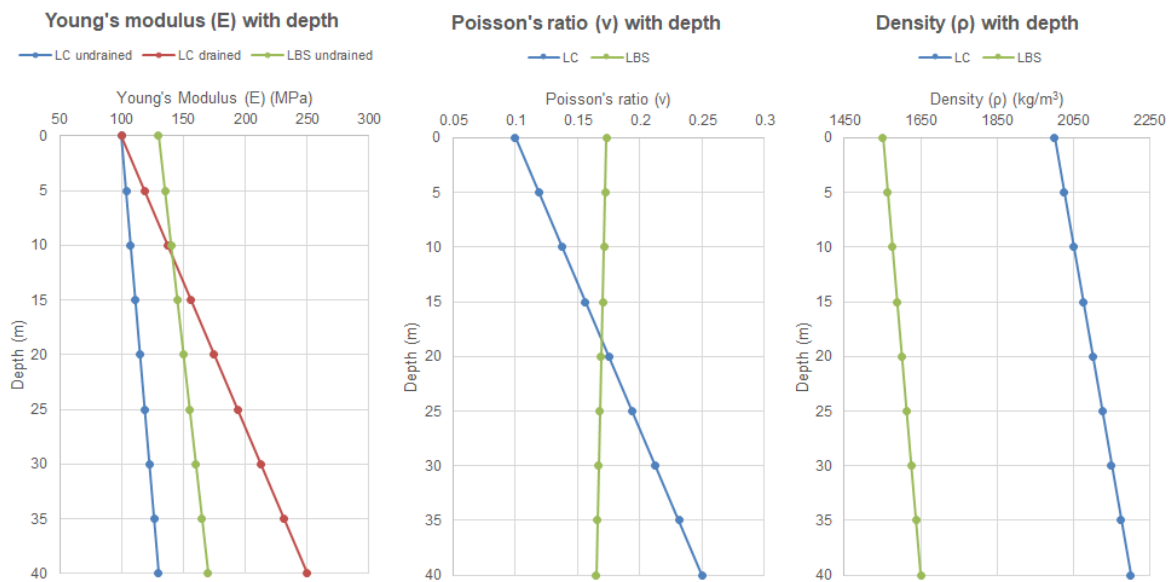


Figure 4.30 Variations in typical soil properties for London Clay and Leighton Buzzard Sand as a function of depth.

Figure 4.29 shows the models as both cross-sections of the whole system, and the tri-layer plate models tested within Disperse. The tri-layer models consisted of an external, infinite layer of LBS with depth appropriate properties (to represent a varying width between 100 and 300 mm), a 25 mm thickness steel layer to represent a plate or pipe, and an internal layer of either a free boundary (to represent most gaseous media) or an infinite layer of liquid water at 20° C dependent on the model.

The results of the models in Figure 4.29 are shown in Figure 4.31, with Figure 4.31b showing the same results but focusing on frequencies between 78 and 82 kHz. Frequencies of 80 kHz are known to be generated by the types of soil-steel interactions in which we are interested (Jiang et al., 2007, and Michlmayr et al., 2013, Smith and Dixon, 2019) and it was therefore important to understand soil behaviours at over this range.

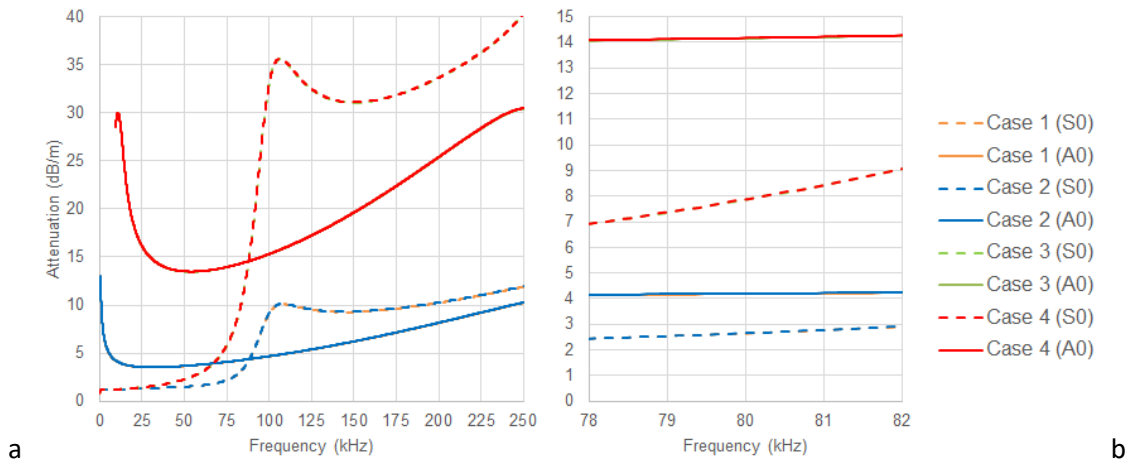


Figure 4.31 Disperse modelling results for the buried utility pipe case studies.

Generally, Figure 4.31 shows that attenuation rates within both pipe systems are relatively low, especially before 80 kHz. With respect to measurement of the signals, this means that signal could potentially propagate long distances and still be detectable. It can also be seen that a small change in burial depth has a minimal effect on attenuation with the modelled results being near identical. At 80 kHz for example, attenuation of the S0 mode at 0.6 m depth is 2.64 dB/m in the free environment and 7.89 dB/m in the water environment. By 1.2 m depth, these values become 2.67 and 7.90 dB/m, an increase of 0.03 and 0.01 dB/m respectively. These increases in attenuation are equivalent to <0.5% change.

Assuming that these models are for pristine condition systems i.e. undamaged steel and homogenous material properties, the differences in attenuation can be treated as negligible. Damages and inhomogeneities in the field would affect wave propagation and attenuation in the same way making depth-based differences indistinguishable. Carandente et al. (2010) for example show that Lamb waves may be used to detect defects in plates and are thus sensitive to discontinuities. Furthermore, Su et al. (2006) state that Lamb waves are highly sensitive to damages.

Figure 4.31 also shows that the internal medium has a strong influence on attenuation, as also shown previously in Section 4.1.4. By 80 kHz for example, attenuation of the S0 mode more than doubles between the environments to create a 5.25 dB/m difference between the air and water filled systems. For a small amplitude signal, this makes a large difference.

Three clear observations from Figure 4.31 may therefore be drawn:

- Small changes in burial depth have a minimal effect on wave attenuation.
- The internal medium of a pipe, i.e. the substance being transported, has a major effect on wave attenuation.
- Propagation below 80 kHz experiences relatively low attenuation with distance.

4.1.6.2 Pile foundations: Cylinder and H style

Along with buried utility pipes, propagation and attenuation through cylindrical and H-pile style piles were also investigated within Disperse. Figure 4.32 shows cross-sections of the models investigated as well as the tri-layer plate systems modelled within Disperse. The same soil properties as in the pipe models were used (Table 4.10 and Figure 4.30), whilst exact specifications of the models are shown in Table 4.11. It should be noted that for each pile type, both minimum and maximum thicknesses were modelled to account for different real-world geometries dependent on a pile's application.

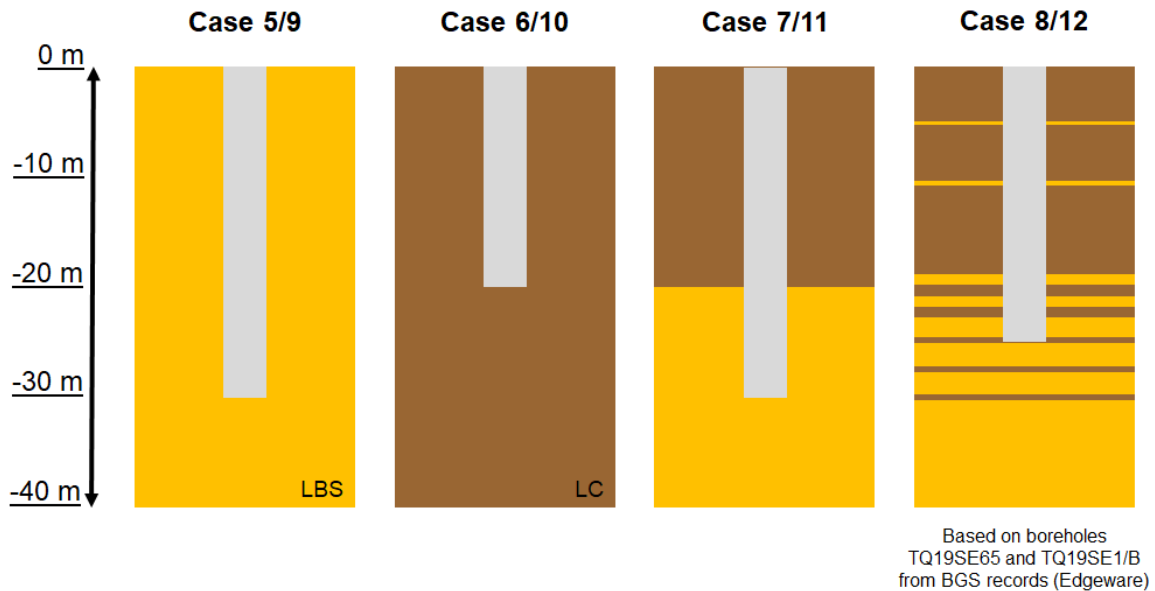


Figure 4.32 The eight pile model systems investigated (Cases 5 to 12).

Table 4.11 Specific plate geometries for the pile foundation models (Cases 5 to 12).

Case ID	Model	Tri-layer plate system	Plate thickness (mm)
5	Cylindrical pile	Free – Steel – LBS	10
6		Free – Steel – LC	
7		Free – Steel – LBS/LC	
8		Free – Steel – LBS/LC	
9	H pile	LBS – Steel – LBS	10 or 30
10		LC – Steel – LC	
11		LBS/LC – Steel – LBS/LC	
12		LBS/LC – Steel – LBS/LC	

The results of these models are shown in Figure 4.33 as percentage signal strengths with foundation depth. The top row shows models for a cylindrical pile within four different external environments, whilst the middle and bottom rows show models for a H pile within four different environments and at two different web thicknesses (10 and 30 mm, middle and bottom respectively). Models were

conducted for every 1 m of depth in order to take account of changes in the soil properties. The results therefore have a 1 m depth resolution.

Given that both pile types have been modelled at a wall/web thickness of 10 mm (top and middle rows), a direct comparison between these results can be made. It is seen that the cylindrical models, (soil-steel-free systems) are less attenuating than the H-pile web models (soil-steel-soil systems). In a pure LC environment for example, the cylindrical model for the S0 mode at 50 kHz loses around 99% of its energy after 12 m of propagation. The H-pile model on the other hand is only able to propagate 6 m before losing the same amount of energy. As the only difference between these models is their third environment, the difference in attenuation may be attributed to this change with Section 4.1.3 suggesting that as soil and steel, as in the H-pile environment, have a smaller impedance mismatch than air and steel, as in the cylindrical environment, energy transmission into the environment will be greater.

Comparing only the H piles models, different web thicknesses appear to have a significant effect on attenuation with models for the 30 mm web generally less attenuating than the 10 mm web. These findings are concurrent with those of Section 4.1.2; in which it was shown that plate thickness is inversely related to attenuation; as plate thickness increases, attenuation decreases.

As plate thickness increases however, attenuation only decreases until approximately 2.25 MHz-mm at which point the S0 mode become more attenuating. This is shown for the S0 mode at 80 kHz in the 30 mm web thickness model. At a frequency of 80 kHz, the frequency-thickness for a 30 mm web equates to 2.4 MHz-mm (0.08×30). This value is greater than the cross-over point making the mode more attenuating in this circumstance. At 50 kHz though, the frequency-thickness only equates to 0.5 MHz-mm (0.05×10) and is therefore less attenuating as with the other models.

A final observation from Figure 4.33 is the effect of frequency on attenuation. It is known that higher frequencies tend to attenuate at a faster rate than lower frequencies as more wave cycles occur within the same time period. This is shown for all S0 modes but only holds true for the A0 modes when propagating in the highest thickness web; in smaller thickness webs, the A0 modes at 80 kHz are less attenuating than the S0 modes at 50 kHz. As seen in Figure 4.33, and discussed in Section 4.1.2, this may be a result of the frequency-thicknesses being relatively low in value; there may be potential inaccuracies in the modelling process that could cause anomalous results. Alternatively, the results may be an accurate reflection of the environment and relate to unknown properties of the system. Further investigation is needed.

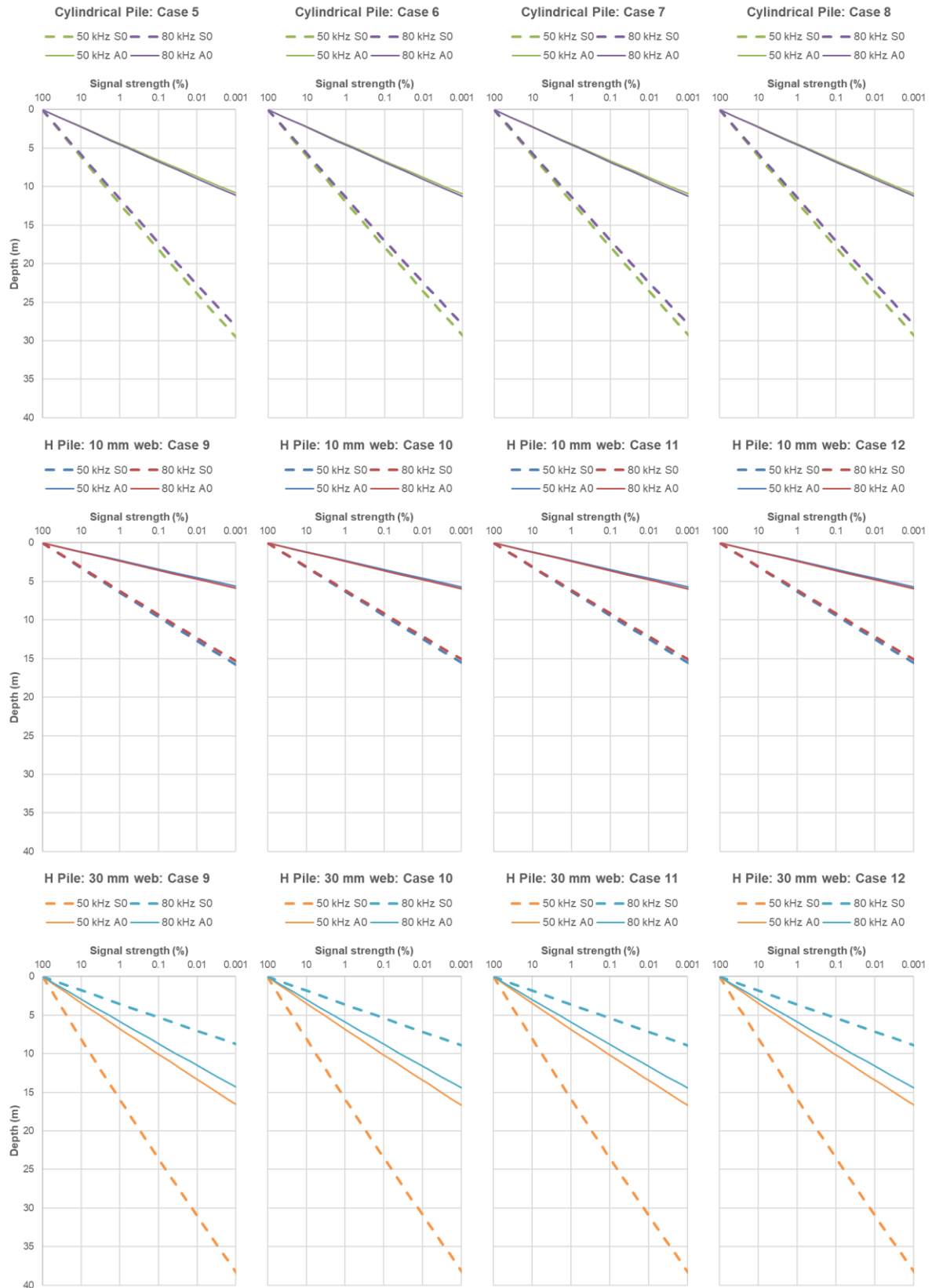


Figure 4.33 Results showing calculated signal strengths with depth for the two pile models investigated: cylindrical with a 10 mm wall thickness (top), and H-piles with 10 mm and 30 mm web thicknesses respectively (middle and bottom).

Three overall observations for propagation and attenuation within pile environments can therefore be made:

- Cylindrical style piles have a greater propagation potential than H-style piles.
- The S0 mode is less attenuating than the A0 mode at lower frequencies and thicknesses. At higher frequencies in larger thickness webs however this is not necessarily the case.
- Attenuation of the A0 mode appears to be lower for higher frequencies in certain soil-structure systems.

4.1.6.3 Pile foundations: Off-shore monopiles

Propagation and attenuation within an example off-shore monopile system were also investigated. For this, a study was designed around the reference model NREL 5MW OWT (Figure 4.34); a 60 mm thickness, 6 m diameter off-shore steel monopile. The reference model is buried to a depth of 36 m in soil before then continuing through 20 m of water and protruding into the air. Consequently, several tri-layer steel plate models were run to study the different system environments with results shown in Figures 4.35 and 4.36.

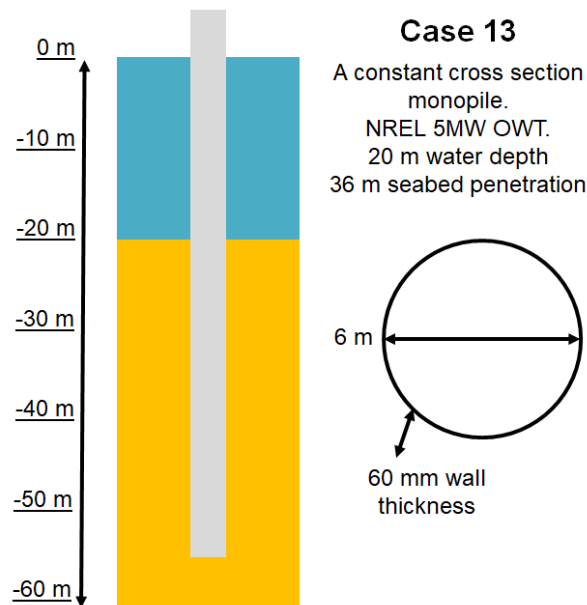


Figure 4.34 The monopile system model investigated (Case 13).

Figure 4.35 shows how attenuation varies within a monopile dependent on the internal and external environments, along with the modelled wave propagation for the S0 mode at 50 kHz. Figure 4.36 on the other hand shows how the attenuation relates to overall signal strengths with propagation from a source at depth to the surface.

Other than the free bound environment, it is clear that the other environments are relatively highly attenuating reducing the signal strength by over 90% within the first 3 m of propagation. An exception

to this is the asymmetric wave mode within the water environment. From literature though (Zhu et al., 2004, and Li et al., 2019), it is known that in this environment the A0 mode can travel as a Scholte wave, rather than Lamb wave, and therefore retains more of its energy.

Figure 4.35 also shows that within the soil-steel-soil environment, attenuation varies with the changing soil conditions associated with depth. Until approximately 10 m the modelled values of attenuation gradually increase with increasing depth, however after this point the values start to decrease. This suggests that one of the parameters used to describe the soil has become dominant, changing the mechanisms controlling attenuation. As may be seen in Figure 5.36 however, the percentage signal strength by 10 m of propagation within a soil-steel-soil environment is $<0.001\%$ so this effect is unlikely to be seen in the field.

For monitoring purposes, the signals of interest would realistically occur within the soil-steel-soil environment where soil-steel interactions happen. Signals within this environment would be indicative of structural movements opposed to environmental interactions (e.g. wind and wave transported bodies). Within this environment however, attenuation is relatively high with 99% of both the S0 and A0 wave modes attenuated by 4 m propagation whether measured at 50 or 80 kHz.

Contrasting with the pipe and pile models, attenuation of the S0 mode is also greater than that of the A0 mode throughout due to the high frequency-thickness products inherent to the structure. At 80 kHz for example, the S0 mode only has 0.08% of its signal strength left by 2 m propagation whereas the A0 mode still retains 0.49% of its energy. Although these percentage signal strengths are both relatively small, their difference is still significant when considering detection thresholds.

Although unlikely to be generate AE, wave attenuation behaviours within the air-steel-water environment should also be considered. When a signal is generated within the soil, it will need to propagate to a sensor for detection; this sensor will not necessarily reside within the same generation environment.

Most likely, the detecting sensor would be placed above the water level and consequently, generated signals will need to propagate through the air-steel-water environment. From Figure 4.36 it can be seen that none of the modelled waves would propagate the full 20 m of the modelled system without losing most of their signal strength. The symmetric modes for example would retain $<0.001\%$ signal strength after 10 m of propagation. Consequently, monitoring the stability of off-shore monopiles using this method would require adaptations. For measurable results, the AE sensors would need to be placed underwater, near to the water-soil boundary.

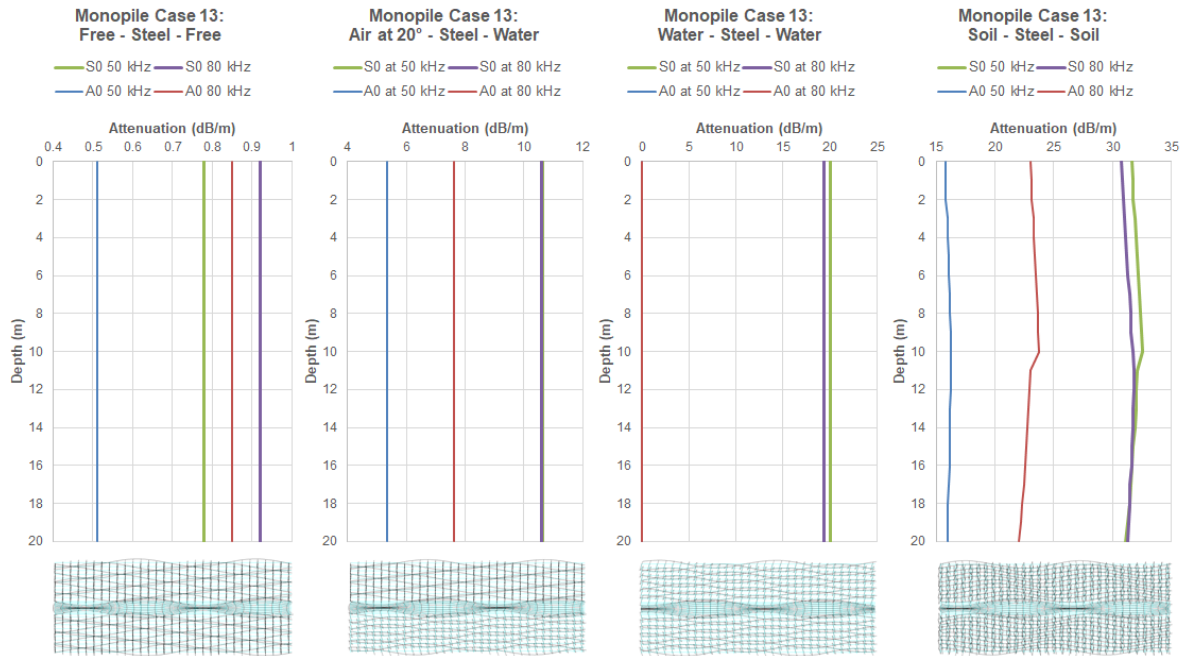


Figure 4.35 Environmental results for the offshore monopile model as dB measurements within each metre's depth.

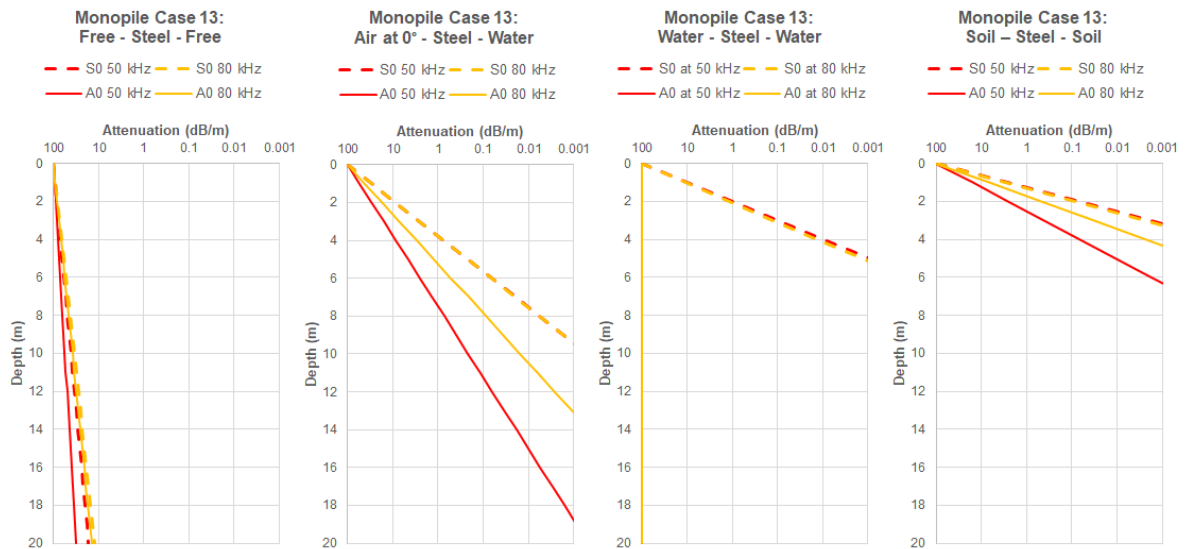


Figure 4.36 Environmental results for the offshore monopile model.

4.2 Small-scale laboratory experiments

Small-scale laboratory experiments using lengths of steel pipe (Section 3.2.5) were performed to investigate the effects of three structural factors on wave propagation and attenuation. These three factors were pipe length (propagation distance), pipe diameter (shell radius), and the presence of screw joints. This section presents the results as two studies: an investigation into pipe radius, within which propagation distance is also considered, and an investigation in the effect of screw joints.

4.2.1 Investigating pipe radius using propagation distances

The effects of pipe radii were investigated systematically by considering attenuation (dB-mm/m) with propagation distance (m) in two different diameter steel pipes (Section 3.2.5). Results of the study are shown in Figure 4.37.

Figure 4.37 shows measured signal amplitudes as a function of distance for tests conducted on two steel pipes, one with a 20 mm external diameter and one with a 48 mm external diameter. The measurements were collected at 0.25 m intervals where, for each distance, three pencil lead breaks were performed (Amplitudes 1, 2, and 3).

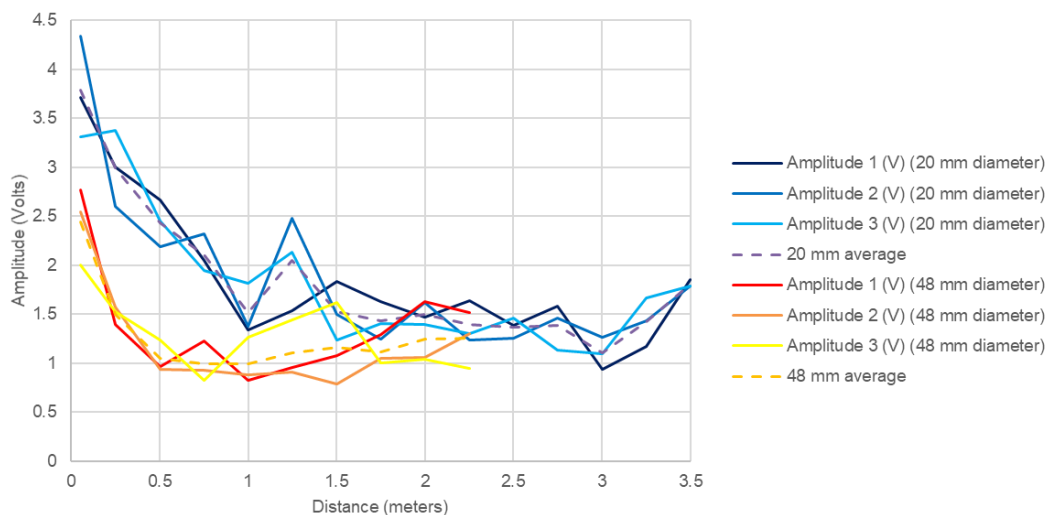


Figure 4.37 The measured effect of shell radius on wave propagation at various distances for steel pipes of different radii.

Two initial observations may be made from the figure: (1) the signal strength generally decreases with increasing propagation distance, and (2) the signals measured from the larger 48 mm diameter pipe are generally smaller.

Considering pipe diameter, Figure 4.37 suggests that the larger diameter pipe has a stronger influence on signal attenuation. At 0.5 m propagation for example, the average signal strength is around 2.5 V in the 20 mm pipe but only 1 V in the 48 mm pipe; This is 60% smaller.

However, simply comparing the measured signal amplitudes at corresponding distances does not take into account the variability in initial signal strength. Figure 4.37 shows that at 0.05 m (the smallest possible distance between source and sensor centre given attachment methods), the signal amplitudes vary by up to 2.4 V; Average signal strengths of approximately 3.8 and 2.5 V were measured for the 20 and 48 mm pipes respectively. Consequently, the signals should not be compared directly and should instead be made proportional to one another using respective signal strengths (Table 4.12).

Table 4.12 The measured average, calculated strength and change in strength of signals propagating through air-steel-air pipe systems of different diameters.

Distance (m)	Average signal strength (V)		% of initial signal		Difference in % distance	
	20 mm pipe	48 mm pipe	20 mm pipe	48 mm pipe	20 mm pipe	48 mm pipe
0.05	3.79	2.44	100.00	100.00	-	-
0.5	2.44	1.50	64.38	61.48	- 35.62	- 38.52
0.75	2.11	1.05	55.67	43.03	- 8.71	- 18.45
1	1.51	1.00	39.84	40.98	- 15.83	- 2.05
1.25	2.05	0.99	54.09	40.57	+ 14.28	- 0.41
1.5	1.53	1.10	40.38	45.08	- 13.71	+ 5.51
1.75	1.43	1.16	37.73	47.54	- 2.65	+ 2.46
2	1.5	1.11	39.58	45.49	+ 1.85	- 2.05
2.25	1.39	1.24	36.68	50.82	- 2.9	+ 5.33
2.5	1.37	-	36.15	-	- 0.53	-
2.75	1.39	-	36.68	-	+0.53	-
3.0	1.10	-	29.02	-	- 7.66	-
3.25	1.42	-	37.47	-	+ 8.45	-
3.5	1.81	-	47.76	-	+ 10.29	-

Table 4.12 gives the average signal strengths (V) with propagation distance (m) for both pipes, along with their relative signal strengths (%) with respect to the initial measurement (i.e. at 0.05 m). Additionally, the changes in strength across each distance interval have been calculated as a percentage loss or gain. The values in Table 4.12 demonstrate that signal strengths are a more appropriate way of comparing signal attenuation with propagation along different diameter pipes. Figure 4.38 therefore illustrates this visually, comparing the relative signal strengths with propagation (Figure 4.38a) and the how this signal strength changes for every 0.25 m propagated. (Figure 4.38b)

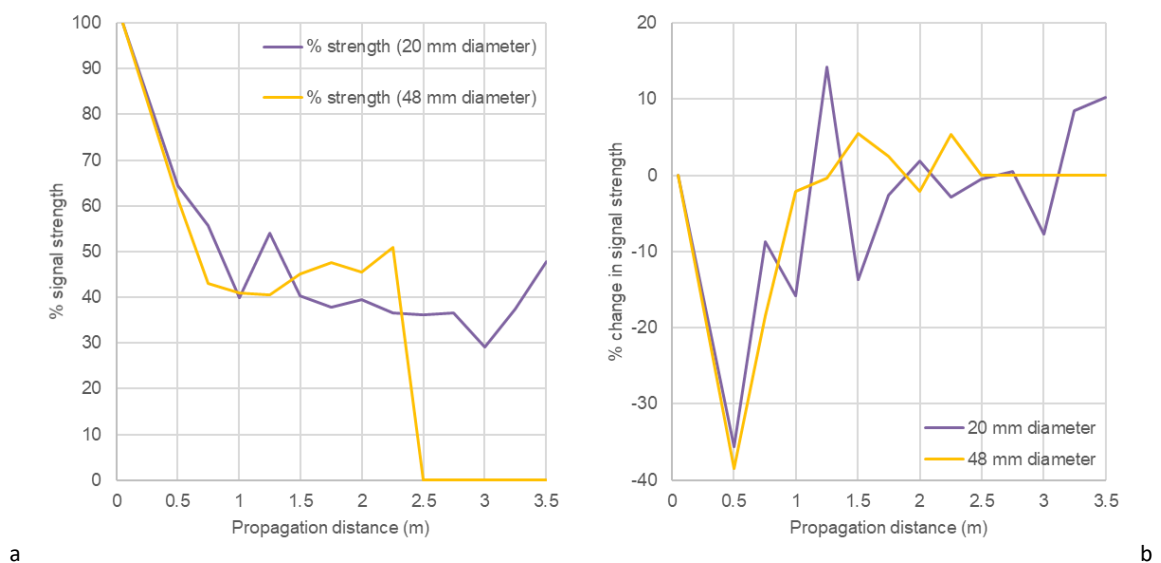


Figure 4.38 (a) The measured relative signal strengths (% initial) and (b) how this changes over 0.25 m intervals with propagation through 20 mm and 48 mm diameter steel pipes in air.

Figure 4.38 shows that for both the 20 and 48 mm diameter pipes the signal decreases substantially during the first metre of propagation (to just 40% initial strength in both cases) before then continuing to decrease at a much decreased rate, in the case of the longer 20 mm pipe, or remain relatively stable, in the case of the 48 mm pipe; This links back to initial observation (1).

In some cases, the signal strength can be seen to increase again. This is demonstrated clearly in Figure 4.38b with positive plotted changes, examples being at 1.5 and 2.25 m. This is likely as a result of signal reflections and multimodal signals superimposing, therefore making the measured signal appear higher. Moreover, dependent on the exact positioning of the input signal source the phase of the signal may affect the results. This effect is less however prevalent in the 20 mm diameter pipe for which propagation was measured over a greater distance and reflections had less effect.

Regardless, Figure 4.38 also shows that the calculated signal strengths remain relatively similar throughout propagation irrespective of the different pipe radii. This suggests that pipe radius has a negligible influence on attenuation and agrees with the computational models shown in Figure 4.17. Furthermore, any small differences in the observed attenuation may be assumed a result of flaws and defects within the pipe structure.

4.2.2 Investigating screw jointed pipes

The influence of connecting screw joints on wave propagation and attenuation within pipes was investigated using multiple sensor-joint set ups (Figure 4.39), as discussed in Section 3.2.5. Figure 4.40 shows the results of the tests in which signals were transmitted through a joint, whilst Figure 4.41 shows the results of tests in which the joint acted as a reflection point. The results are shown as signal voltages (V) against the relative propagation distances between the signal and sensor, opposed to sensor positioning.

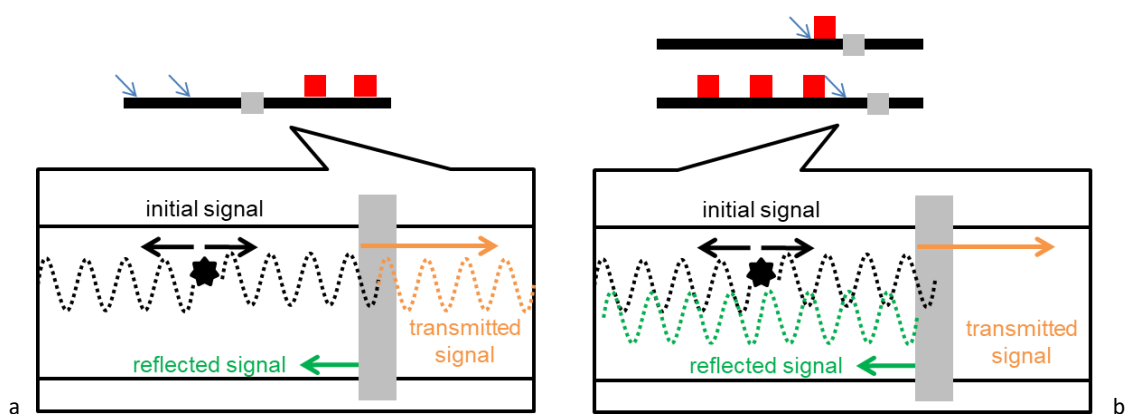


Figure 4.39 The sensor-joint set ups for investigating (a) signal transmission through a screw joint and (b) signal reflection at a screw joint.

Figure 4.40 shows signal strength with propagation as a result of wave transmission through a screw joint. Linear regression has been performed over the data to show the overall trend. It can be seen that the signal voltages vary over a 0.18 V range (0.15 to 0.33 V) for the individual tests conducted, even when over the same propagation distance. This may be a result of the initial signal strengths varying but could also be due to small differences in the sensor-structure coupling method, as discussed in Section 5.3.2.

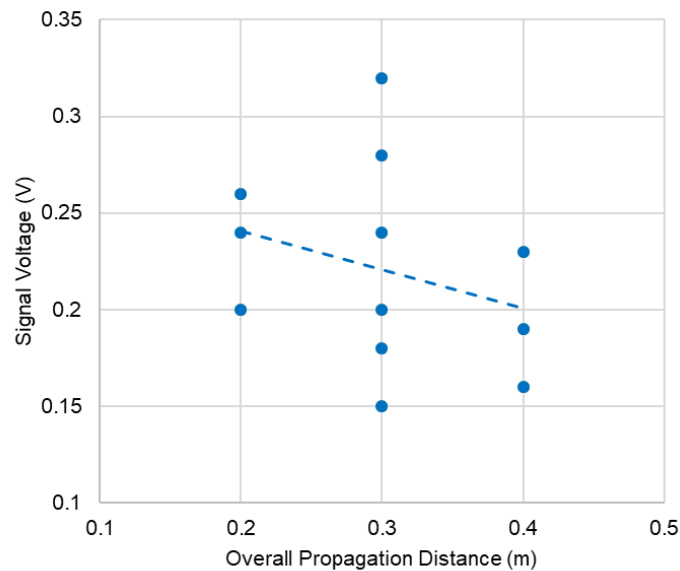


Figure 4.40 The measured effect of a screw joint on wave transmission for different propagation distances.

Despite these variations, a negative relationship between signal strength and propagation distance may still be concluded whereby signal strength decreases as propagation distance increases; this conclusion was also drawn in Figure 4.37. Furthermore, the plotted trend shows an attenuation value of around 0.2 V/m, equivalent in this case to around 83% of the signal strength being left after 1 m propagation, or 1.4 dB/m. Given that Section 4.1.1.4 suggested typical attenuation rates between 0.15 and 1.4 dB/m, this implies that the screw joint has a negligible effect on wave propagation.

Figure 4.41 on the other hand, shows signal strength with propagation as a result of reflection at a screw joint. Comparatively, the voltages plot over a much wider range (0.09 to 5.2 V) as a result of the direct signals also having been measured. Notably, the experimental set up also appears to have had a strong influence on the signal strength.

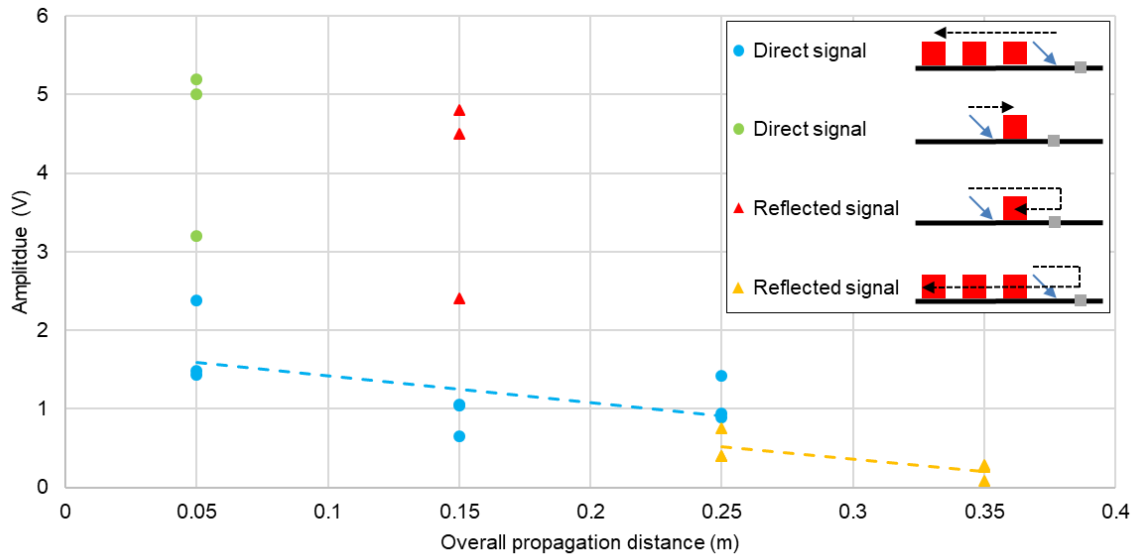


Figure 4.41 The measured effect of a screw joint on wave reflection for different propagation distances.

Comparing the direct (plotted as circles) and reflected (plotted as triangles) signals, a clear shift in the relative signal strengths can be seen; reflected signals are always weaker as a result of energy transmission at the joint.

Under the first set up (green circle to red triangle plots), the direct signals plot between 3.2 and 5.2 V whilst the reflections plot between 2.4 and 4.8 V. Mathematically, this is a maximum and average loss of around 54 to 15% signal strength, respectively, and suggests that anywhere between 46 and 85% of the signal energy is transmitted at the joint.

Under the second set up (blue circles to yellow triangles), similar observations can be made with the direct signals plotting between 0.65 and 1.05 V and the reflected signals plotting between 0.4 and 0.75 V for the same propagation distance (0.1 m). Mathematically, this is a maximum and average loss of around 62 to 33% signal strength and suggests that anywhere between 38 and 67% signal strength is transmitted at the joint.

These results are comparable to those of Alleyne and Cawley (1996) and Long et al. (2003) who find that, on average, between 80 and 95% of a signal is transmitted through various joint types (e.g. butt-welds, metal-metal ball and spigot). This is with exception to flange joints for which Alleyne and Cawley (1995) found to transmit very little acoustic energy. Consequently, given the shown variabilities in signal strength as a result of the collection method, the results in Figures 4.40 and 4.41 show that joints have a small but sometimes significant effect on the propagation and attenuation of AE.

Also using the second set up (blue circles to yellow triangles), Figure 4.41 additionally provides information on attenuation as a result of propagation. This is highlighted by linear trend lines showing that the signal strength decreases with increasing propagation. For the direct signal a rate of decrease of 3.4 V/m can be calculated, equivalent to a 56% signal loss or 5 dB/m. This is relatively high with much lower values (<1 dB/m) expected. This value is however likely to be erroneous due to the multiple initial signals from which it was calculated, each of differing strength.

4.3 Large-scale laboratory experiments

Large-scale laboratory tests investigating propagation and attenuation within different burial systems were performed as discussed in Section 3.6. Several set ups were used to investigate the influence of both pipe structures and burial systems. This allowed for the effects of each to be distinguished.

4.3.1 Propagation within a free bound pipe

Propagation behaviours as a result of pipe structures were primarily investigated using empty box tests representing a free-steel-free system. By using a free bound system, the effects of any external media were largely removed and ensured that observed wave behaviours were a result of the system structure. Two forms of data were collected, frequency data and raw waveforms, from which wave shapes, amplitude and attenuation, and velocity data could be extracted.

Figure 4.42 shows example frequency spectra, as averaged amplitudes (dB) against frequency (kHz), for two variants of a pencil lead break in the free bound system. The variants were for 0.5 (Figure 4.42a) and 0.9 mm (Figure 4.42b) diameter leads. Three spectra are shown on each graph, representing the three propagation distances tested (0.05, 5.5 and 6.5 m as labelled). These tests were repeated numerous times with the frequency spectra shown being representative. Additional tests demonstrating the repeatability of the test are given in Appendix 3.0.

Two observations may be made from Figure 4.42: (1) the different lead diameters produce similar frequency spectra; and (2) these spectra remain the same with propagation.

Comparing Figure 4.42a and Figure 4.42b it can be seen that the different lead diameters produce very similar frequency spectra. The spectra are relatively broadband, although tend towards lower frequencies (< 60 kHz). Local peaks are seen around 24, 43, and 50 kHz. Given that pencil lead breaks as a source are known to produce relatively broadband signals (Section 2.5.1), the peaks seen may therefore represent measured phenomena, such as background noise, but could also indicate resonance within the pipe.

Interestingly, the spectral shape does not change as a result of propagation. Comparing the three spectra in Figure 4.42a, although the strength of each frequency varies, the general spectrum remains the same. This suggests that wave propagation within the pipe is not becoming distorted with distance.

Figure 4.43 shows corresponding raw waveforms for the pencil lead break in Figure 4.42. It shows measured signal amplitudes (V) as a function of time (s) for three sensors located on top of the pipe at 0.05, 5.5 and 6.5 m from the initial source signal. Several observations may be made with respect to the wave shapes, signal amplitude, and wave velocities as a result of both the changing source lead diameter and the signal propagation distance.

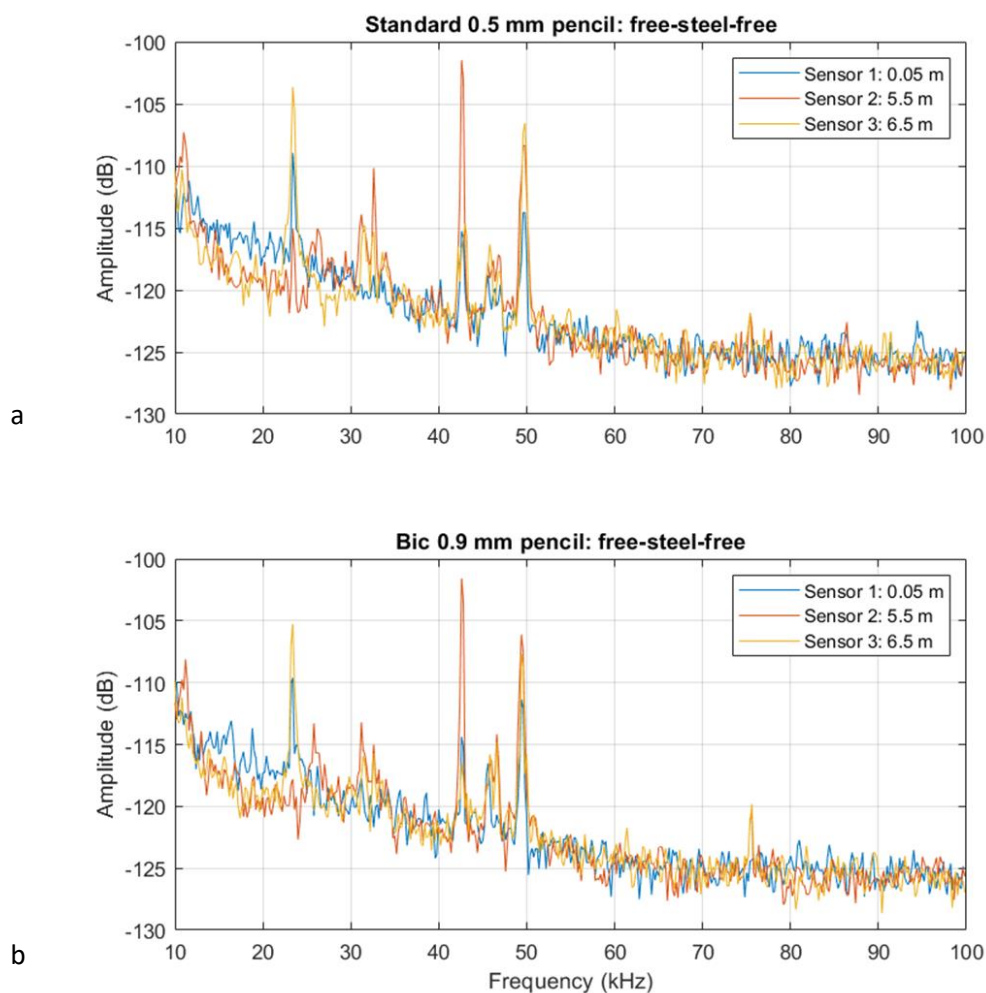


Figure 4.42 Averaged measured frequency spectra for the propagation of (a) a 0.5 mm pencil lead break signal and (b) a 0.9 mm pencil lead break signal through a 9 m, jointed steel pipe forming a free-steel-free system.

Figure 4.43 shows that the shape of the signals remains similar irrespective of the source pencil; Figure 4.43a and Figure 4.43b appear the same. The signals are relatively short in duration, between 0.11 and 0.13 s long, and start as an initial peak which then decays exponentially. Notably though, the

shape of the signal changes with propagation distance, spreading out over time. This is a known phenomenon occurring as the various modes within the multi-modal signal travel at slightly differing wave speeds and therefore having increasingly different arrival times.

Figure 4.43 also shows small peaks within the signals, most notably towards the start of each signal. These are likely a result of reflections as, given typical wave speeds of around 4000 to 6000 m/s (Fuller and Fahy, 1982, Shehadeh et al. 2008, Baik et al., 2010) within steel, reflected signals caused by the open ends of the pipe will occur within < 0.005 s of the initial break time.

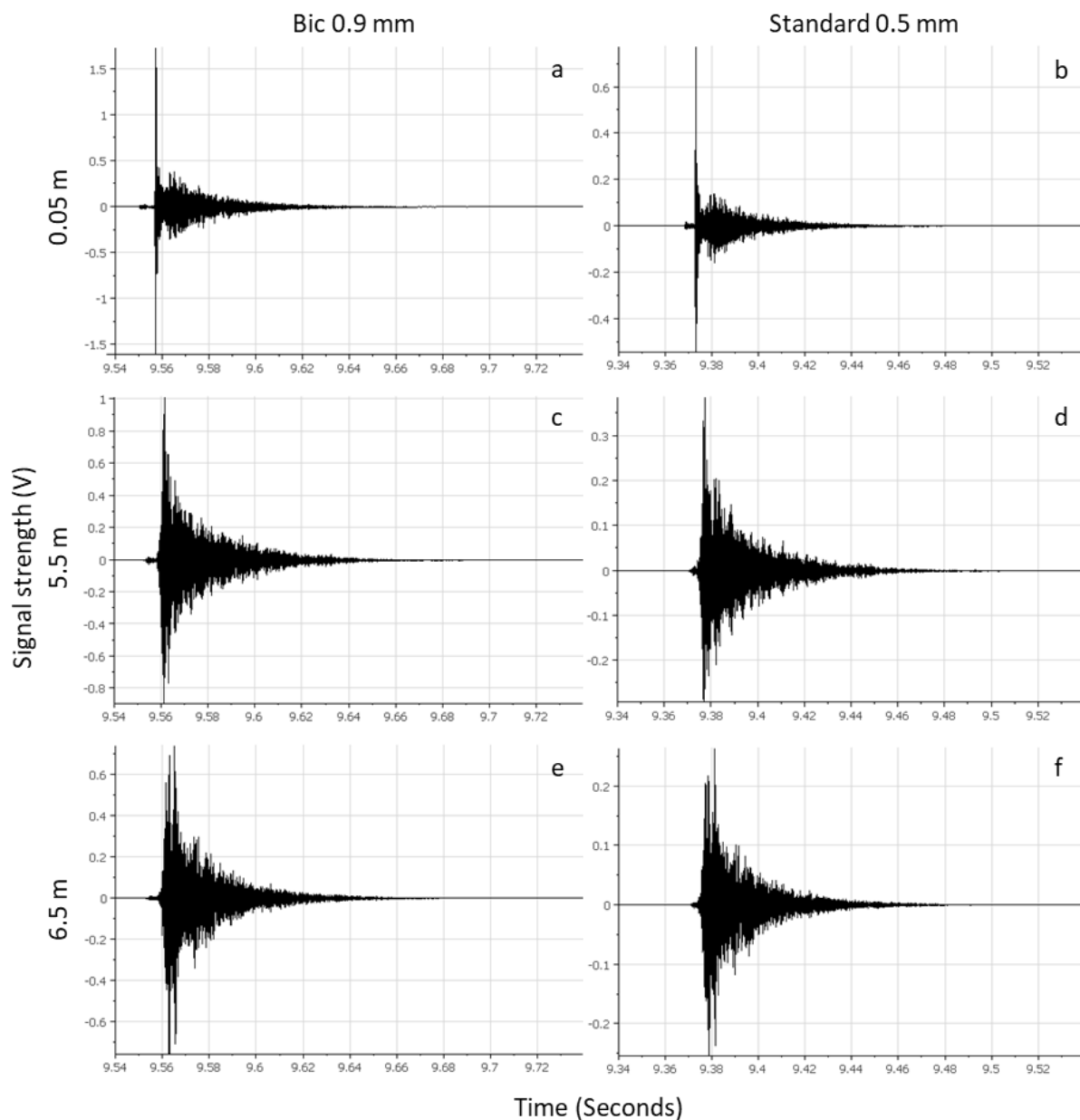


Figure 4.43 Example measured signal amplitudes with propagation along a 9 m, 42.4 mm OD diameter, 3.2 mm wall thickness steel pipe in a free-steel-free environment. Signals were measured at (a and c) 0.05, (b and d) 5.5, and (e and f) 6.5 metres and input using a Bic 0.9 mm pencil lead and standard 0.5 mm pencil lead.

The approximate wave speeds within experiments can be calculated from the peak amplitudes within the raw data. These are shown in Figure 4.44 for the all test conducted, split dependent on the propagation system (i.e. before or after a joint and with or without a surrounding backfill).

Figure 4.44 shows the calculated wave speeds vary between 3494 and 5188 m/s dependent on the test set up. Focusing on an air-steel-air system, an average wave speed of 4714 m/s may be calculated before transmission through a screw joint. This compares to an average speed of 4191 m/s after transmission, a decrease of 12%, and implies that propagation is slowed by the presence of the joint.

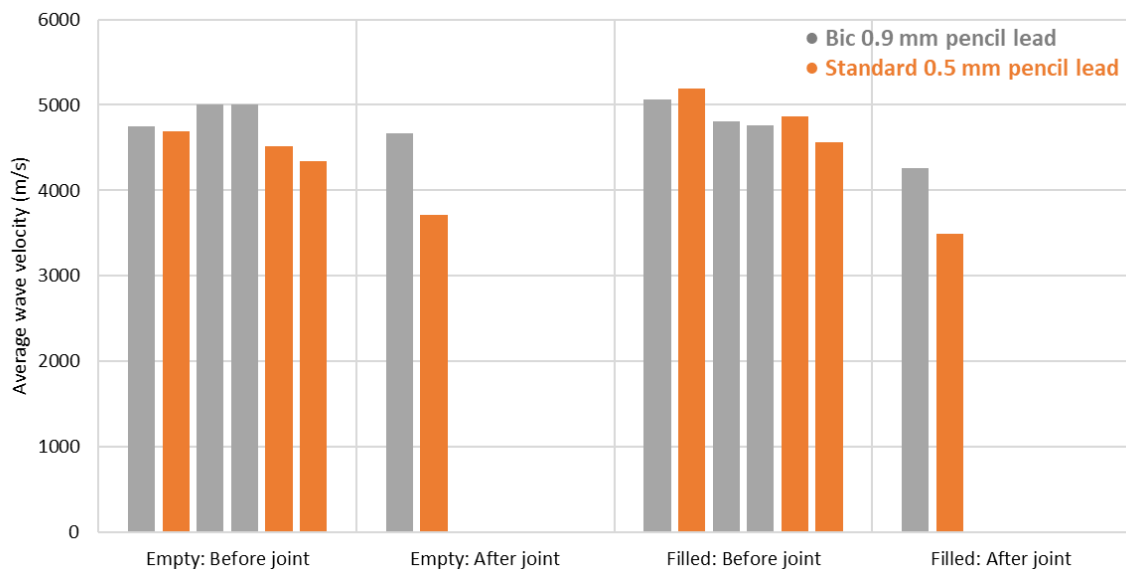


Figure 4.44 Average measured wave velocities (m/s) for propagation in an air-steel-air or air-steel-LBS pipe system before and after transmission through a screw joint.

Figure 4.45 similarly plots averaged peak amplitudes for all tests conducted. Like Figure 4.44, these have been split to represent measurement before (< 5.5 m) and after transmission (6.5 m) through a screw joint in filled and free bound burial systems. Additionally, the initial signal amplitudes (0.05 m) were also recorded.

The figure shows that a range of amplitudes were measured dependent on propagation distance, transmission through the screw joint, the presence of a backfill, and the initial source. Additionally, it should be noted that Figure 4.45 shows measurements from the two pencil lead variants.

Focusing on the initial source signals, these can be seen to range in magnitude from 0.59 to 2.16 V. This is a result of the different diameter pencil leads used to induce the signals. Comparing these with Figure 4.43, it is shown that the 0.5 mm lead generally produces smaller strength signals. Sause (2011) states that 'slight deviations' in the pencil lead can 'cause differences in the test signals'. Nevertheless,

changes in the measured amplitudes as a result of propagation within the system are still distinguishable.

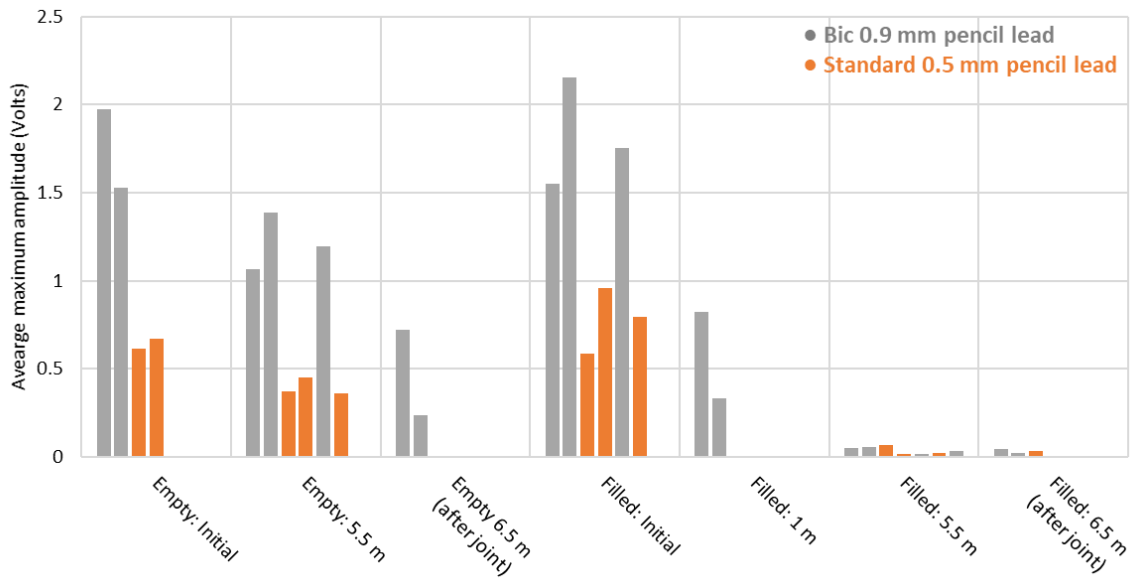


Figure 4.45 Average measured peak amplitudes (V) for propagation in air-steel-air and air-steel-LBS pipe systems before and after transmission through a screw joint.

After 5.5 m propagation, significant attenuation of the signals can be seen with the average signal strength reducing to around 0.80 V. This is in comparison to an initial strength of 1.20 V and demonstrates a 33% loss, which is a 10% difference to that of Disperse models (Figure 4.46) for high frequencies.

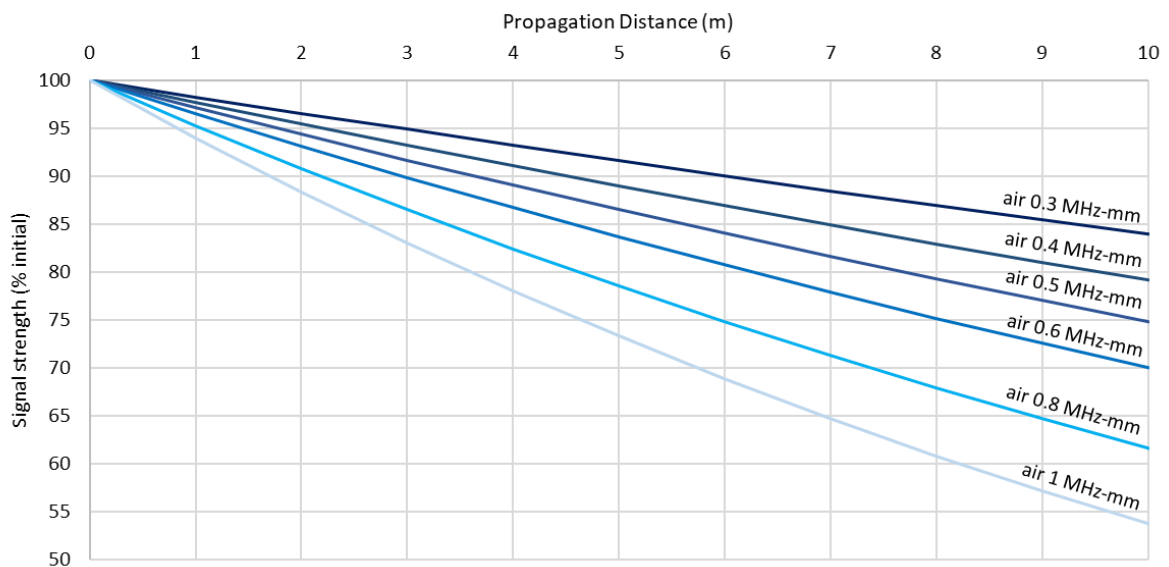


Figure 4.46 Signal strength with propagation distance in a modelled air-steel-air (free bound) system at frequency-thicknesses between 0.3 and 1 MHz-mm.

After propagation through a screw joint (6.5 m), the signals become further attenuated averaging a signal strength of 0.48 V (60% of that at 5.5 m). This is much smaller than the initial signal and suggests that significant attenuation has occurred both as a result of propagation distance and transmission through a screw joint. Section 4.2.2 suggested that losses at a joint should be <20% (i.e. >80% of the signal should be transmitted), although propagation distance was not taken account of in these measurements. Taking account of propagation by assuming between 3 and 7% of the signal may be lost over 1 m, 73% of the signal strength should still be measurable. Consequently, the attenuation levels seen as a result of jointing in the free bound large-scale experiments do not appear comparable to models or literature (Alleyne and Cawley, 1996, Long et al., 2003). There could be many reasons for this relating to both the physical properties of the waves measured (i.e. frequency and phase at the point of measurement) and the measurement system (i.e. inadequate sensor-structure coupling or sensor sensitivity). Modelling limitations were discussed in Section 4.1.1.6.

4.3.2 Propagation in a buried pipe system

Propagation and attenuation behaviours within a buried pipe system were investigated alongside a free bound system to compare effects. Like Figure 4.42, Figure 4.47 shows exemplar frequency spectra for two pencil lead break variants but in a buried system. Both similarities and differences may be seen.

Figure 4.47 shows that for both pencils, very similar frequency spectra are formed. The signals are relatively broadband, although tend towards frequencies below 60 kHz, with small peaks detectable around 23 and 40 to 50 kHz. Comparing Figure 4.47 with Figure 4.42, for the free bound and buried systems respectively, the general shape and positioning of the spectral peaks remain unchanged however the amplitude of the overall signal decreases with maxima of -115 dB compared with the previous -110 dB. Moreover, the change in the amplitudes of the peaks are also significantly smaller although distinguishable. Notably, the effects of propagation still remain negligible despite potential interactions with the burial material.

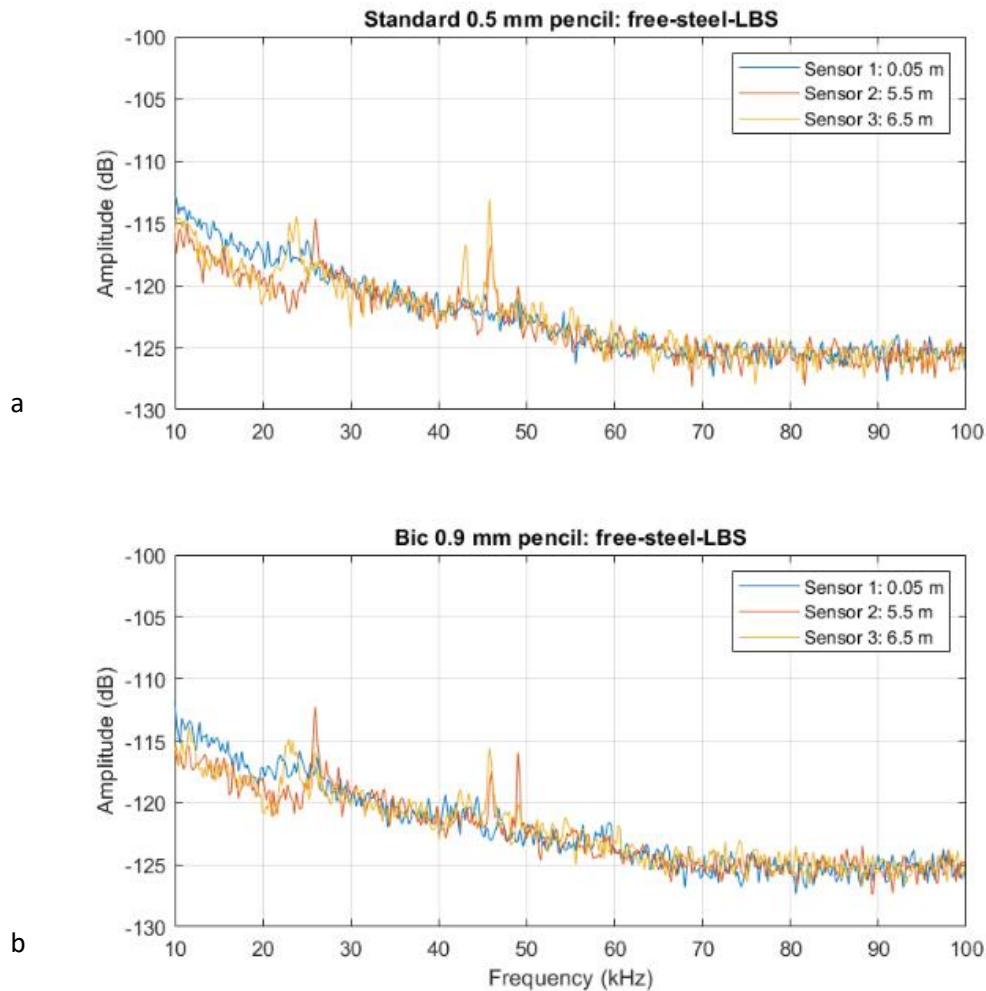


Figure 4.47 Averaged measured frequency spectra for the propagation of (a) a 0.5 mm pencil lead break signal and (b) a 0.9 mm pencil lead break signal through a 9 m, jointed steel pipe forming a free-steel-LBS (buried) system.

In Section 4.3.1, Figure 4.44 plotted the approximated wave speeds for each test. For the free bound system, it was found that an average wave of 4714 m/s could be calculated before transmission and 4191 m/s after transmission through the joint. For the backfilled system, a similar speed of 4784 m/s was calculated before transmission. This is slightly faster than the free bound system (+2%, before transmission), and therefore suggests that the burial environment has very little effect on the speed of propagation. Given that generated AE should travel through the steel, this was expected.

After transmission however, this speed decreases to 3877 m/s within the soil bound system. This is a drop of 19% and suggests that the presence of a screw joint had a significant effect. For the free bound system though, a drop of only 12% was seen. This difference may be a result of inherent measurement errors, i.e. source or coupling quality, but could also be a result of complex geometries interacting with the burial system. Regardless, it may be concluded that, although propagation speeds appear unaffected by the burial system, the structure of the waveguide can have a significant effect.

In terms of attenuation, Figure 4.45 showed measured amplitudes at various propagation distances. As discussed in Section 4.3.1, a range of initial amplitudes were recorded as a result of the different pencil lead sources used. An average value of 1.30 V may be calculated for the buried pipe tests.

After 5.5 m propagation, the average amplitude decreases to 0.04 V, or 3%, demonstrating a significant loss in signal strength as a result of the backfill. Comparing this with the free bound system, this is a 63% difference. Disperse models suggest that around 14% of the signal should be left (of the S mode) and, given that the measured signal will have been multimodal, a stronger signal was expected. However, as discussed in Section 4.1.1.6, the Disperse model cannot take account of numerous factors, such as the superposition and cancellation of wave modes and phase, which effect attenuation. Consequently, a signal strength of 3% after 5.5 m propagation is still plausible and further testing would likely increase the value with the effects of non-modellable factors averaged out.

After propagation through the screw joint (6.5 m), the signal then becomes further attenuated to 0.03 V. This is a further 25% loss, although the precision of the measurements is not considered in this statistic. As discussed, an approximate loss of up to 20% is expected at joints. A loss of 25% is therefore reasonable, agreeing with the findings of previously conducted small-scale experiments and published literature (Alleyne and Cawley, 1996, ^bLong et al., 2003).

4.4 Chapter summary

Wave propagation and attenuation within buried structure systems has been investigated using a combination of computational modelling and small- and large-scale experiments. The investigation was parametric, largely studying the influence of individual variables, whilst case studies investigating and comparing propagation and attenuation within typical buried structure systems were also performed. Additionally, the validity of the computational modelling methods used for investigations was tested.

Computational models showed that wave propagation is controlled by several factors including the physical geometry of a structure, the burial system and burial depth (which influences density and stiffness), and a signal's wave properties. Structurally, plate and cylinder models showed little difference in terms of propagation though the thickness of the plate/wall was inversely related to attenuation. Moreover, the radius of a pipe structure was shown to have a negligible influence. Therefore, tri-layer plate models could be used to accurately model most buried shell structures.

Both the internal and external materials within a burial system heavily influenced the observed wave attenuation. By parametrically studying three material properties, ρ , E , and ν , their individual effects could be established and the influence of materials with different mechanical properties therefore

obtained. Furthermore, case studies for typical steel structures were also performed in Disperse. These included utility pipes, pile foundations, and an off-shore monopile (i.e. wind turbine).

Although Disperse models were found to be accurate, the limitations of computational models were also considered. It was concluded that to further improve the accuracy of model outputs, numerous alternative factors, such as damages and wave distortion, would need to be considered. Using Disperse, this was not possible.

Experiments using both small- and large-scale configurations for air-steel-air pipe systems were also conducted. These provided validation to Disperse models, as the results could be compared, but also allowed for different phenomena to be studied. It was shown that joints within pipes, for example, could strongly affect wave propagation and attenuation, whilst the source signal, despite being induced using consistent methods, varied and therefore effected the measured signals.

Chapter 5: Results: Characterising AE signals

5.0 Results: Characterising AE signals

Evolving soil behaviours (i.e. strength and deformation) can be understood by characterising AE behaviours and developing relationships between these and other soil properties (OB2). Characterisation in this context means to understand and interpret stages of shearing and/or volume change under a range of stress levels and rates of shearing based on signal properties including frequency, amplitude, and the number of RDCs within a unit period. Additionally, alternative parameters including b-values, which provide an estimate of the relative abundance of differing strength AE events, have also been used as a behavioural indicator.

This chapter therefore presents a series of results characterising AE signals using various experiments including large direct shear box tests investigating shear interactions at a soil-steel plate interface (Section 5.1), large-scale laboratory tests investigating AE within buried pipe systems (Section 5.2) and flow noise (Section 5.4), and small-scale laboratory tests characterising the potential bias of the AE data acquisition method and equipment (Section 5.3).

5.1 Soil-steel interaction generated AE: Shear box testing

A programme of large direct shear box tests (Table 3.15) was performed to investigate the effects of several processes and properties on AE generation at a soil-steel interface. These included the processes of compression and shearing, and the properties of particle size (through soil type), normal stress, and shearing rate.

Following sample preparation, each test was conducted in two stages: a compression stage (during which normal stress application to a target value occurred), and the subsequent shearing of the sample (for which the target normal stress was maintained). These stages are illustrated in Figure 5.1 and considered separately in Sections 5.1.1 and 5.1.2 respectively.

5.1.1 Compression

Following sample preparation (Section 3.5.1), each sample underwent a period of compression during which a normal stress was applied to reach a target value and then maintained. Soil-steel interaction generated AE as a result of compressional mechanisms during this period could then be investigated, the result of which are shown in Figure 5.2 to 5.7.

Figures 5.2 to 5.7 show relationships between various parameters with time during the period in which each sample was being compressed. Furthermore, Figures 5.17 to 5.25 show additional relationships as functions of different parameters. From these, the effects of particle size and normal stress have been studied.

5.1.1.1 Particle size

The effects of particle size during compression were considered throughout the program of shear tests by repeating numerous experiments with two materials, LBS and PG. Figures 5.2 and 5.3 show cumulative RDCs and RDC rates/second, respectively, as functions of time during the period.

Figure 5.2 shows that the cumulative RDCs increase throughout compression. This was expected as a result of the graphs being cumulative. Notably however, the accumulation rates only vary over a small range and are different for each material.

Figures 5.2b and 5.2d, for example, show that the RDCs for PG tests accumulate with an approximate rate of around 3×10^4 RDCs per 100 seconds. For LBS tests, the rate is respectively lower ranging between 0.5 and 1.5×10^4 RDCs per 100 seconds (Figures 5.2a and 5.2c). Note that the rate of normal stress application was equal for all tests.

Given that the accumulation rates remain similar for each material, likely as a result of the compression, i.e. normal force, being applied with the same method throughout, this suggests that the particle sizes are affecting RDC production. Although, inherent differences in the particle morphologies (i.e. roundness) and packing structures may have also had an influence. Figure 5.3 therefore studies the RDC rates as a function of time.

Figure 5.3 shows that the RDC rates vary drastically in time fluctuating between 0 and 850 RDCs/second dependent on the test. Considering particle size, the PG tests, which have greater particle sizes, appear to have a higher emission rate than the LBS tests. This suggests that particle size affects AE generation during compression and different generation mechanisms may be involved. The relative vertical displacements during compression should however also be considered.

Figure 5.4 shows the vertical displacements (i.e. volume change as a result of settlement) experienced in each test as a function of time during compression. The figure shows that each sample decreases in height throughout compression, initially at a very rapid rate which then decreases over time. Final vertical displacements range between approximately 3.6 and 5.6 mm.

Comparing the effects of particle size, there is a distinct difference between the measured displacements with PG tests experiencing higher overall displacements (4.2 to 5.6 mm) compared to LBS tests (3.6 to 4.1 mm). This implies that PG as a granular material may be more compressible/difficult to achieve dense packing, which could relate to the particle size distribution and grain morphologies. It may therefore be inferred that more structural changes occur within the PG samples during compression, consequently generating higher levels of AE as seen in Figure 5.3.

The initial densities to which the samples were placed should however be considered, despite the same compaction method being used for each (Section 3.5.1).

Table 5.1 shows the initial densities, along with further related data, for the twelve tests shown. It can be seen that the initial densities of the PG tests are generally higher with an average relative density of around 69% whilst the LBS tests have a similar, but slightly lower, relative density of 67%. Given that these are so similar however, it may be concluded that the greater AE generation seen during compression of the PG tests is not a result of the initial density.

Table 5.1 Initial densities and related density data for shear box tests using LBS and PG materials.

		Initial density (kg/m ³)	Initial void ratio	Relative density (%)	Density interpretation
Constant rate	LBS 75 kPa	1623.26	0.62	37.44	Medium
	LBS 150 kPa	1669.19	0.58	67.81	Dense
	LBS 225 kPa	1689.63	0.56	80.80	Dense
	PG 75 kPa	1712.44	0.59	55.70	Medium
	PG 150 kPa	1717.33	0.59	58.79	Medium
	PG 225 kPa	1757.63	0.55	83.61	Dense
Stepped rate	LBS 75 kPa	1668.30	0.58	67.24	Dense
	LBS 150 kPa	1670.96	0.57	68.95	Dense
	LBS 225 kPa	1690.96	0.56	81.64	Dense
	PG 75 kPa	1714.82	0.59	57.21	Medium
	PG 150 kPa	1729.93	0.58	66.68	Dense
	PG 225 kPa	1777.33	0.54	95.33	Very dense
	Average LBS	1635.38	0.58	67.31	Dense
	Average PG	1751.58	0.57	69.53	Dense

Moving towards signal properties, Figure 5.5 shows dominant frequencies as a function of time for the same tests. The frequencies can be seen to vary between certain values (23, 32, 40 and 60 kHz) with no apparent pattern, although do vary over a much wider range for the LBS tests compared to the PG tests.

Figures 5.5a and 5.5c, for example, plot results for the LBS tests. The figures show that the dominant frequencies range between approximately 23 and 75 kHz. Figures 5.5b and 5.5d on the other hand, show much smaller variations between approximately 23 and 40 kHz for the PG tests. This suggests that different AE generating mechanisms may be dominating within the different materials during compression.

Relatedly, Figure 5.6 shows corresponding amplitudes for the dominant frequencies during compression. The amplitudes similarly appear to vary randomly with no apparent trend, fluctuating between extremes of -90 and -30 dBv. Notably however, the ranges of amplitude change dependent on the material with PG material varying between extremes of -90 and -50 dB and LBS between -90

and -30 dB. This implies that LBS materials are either louder, producing stronger signals, or more frequent, with signals superimposing. Given the results shown in Figure 5.3 though, the former is more likely to be the case during compression.

Calculated from the amplitude data, Figure 5.7 shows b-values for each test during compression. It can be seen that the b-values remain relatively stable, varying over a range of around 0.02 throughout the duration of compression. Additionally, although the b-values fluctuate throughout, there is an overall negative trend with the b-values decreasing over time indicating an increasing proportion of higher magnitude AE events.

Comparing the two materials, b-values tend to remain higher in the LBS samples than the PG samples with approximate values ranging between 0.12 and 0.14 and 0.10 and 0.12 respectively. This is likely a result of grain size and potential morphology.

5.1.1.2 Normal stress

During compression, normal stress appears to have little influence over some parameters and a clear effect on others. This is likely a result of compression being conducted using the same process for each and any distinguishable differences therefore not occurring until previously tested normal stresses have been surpassed. The effects of normal stress were considered by repeating each experiment using three different normal stresses, 75, 150, and 225 kPa, and with new specimens each time.

Figures 5.2 and 5.3 show cumulative RDC and RDC rate/minute, respectively, in which normal stress can be seen to have an effect. Figure 5.2 for example shows that the rate at which the RDCs accumulate in time remains approximately constant irrespective of the final normal stress magnitude. The final cumulative RDCs, however, vary as a result of a longer compression period for higher normal stresses.

Figure 5.3 similarly shows that the RDC rates/minute remain approximately comparable whilst overlapping. This is with exception to Figure 5.3a, for which the data collected under 225 kPa appear anomalous, and 5.3d, for which the data collected under 225 kPa are clearly anomalous. When not overlapping, i.e. after 75 or 150 kPa, the RDC rates arguably increase.

Contrastingly, Figure 5.4 shows that the rate of vertical displacement varies during a period of overlap however the final vertical displacements, after the target normal stress has been reached, are higher for higher normal stresses. This is with exception to the stepped LBS test under 225 kPa (Figure 5.4a), for which the result appears anomalous. Removing this anomaly, the figure indicates that normal stress affects vertical displacement during compression.

Figures 5.5 to 5.7 on the other hand (AE parameters frequency, amplitude and b-values), all appear to be negligibly affected by normal stress with the results varying across similar parametric ranges or exhibiting comparable behaviours regardless of normal stress magnitude. Figure 5.5 for example shows that the dominant frequencies fluctuate in time between 23 and 75 kHz, these fluctuations remaining unaffected by the normal stress. Similarly, Figure 5.6 shows that the corresponding amplitudes are also largely unaffected. Figure 5.7, though, shows that during compression the b-values remain approximately constant despite the different normal stresses, before then decreasing as a shear stress is introduced. B-values are therefore influenced significantly by shearing, but compression has a negligible effect. This is discussed in Section 5.1.2.

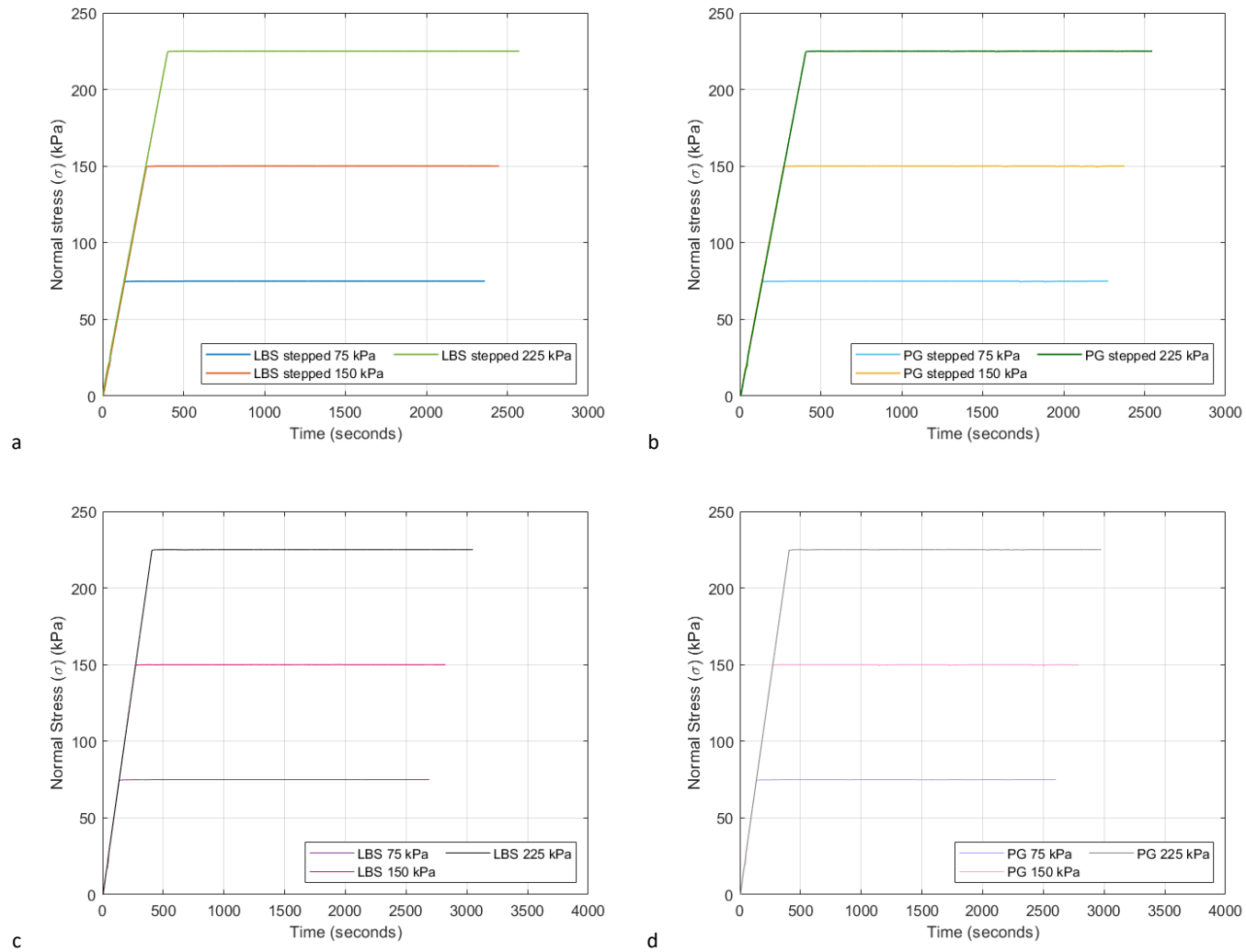


Figure 5.1 Normal stress with time for (a) stepped rate LBS tests, (b) stepped rate PG tests, (c) constant rate LBS tests and (d) constant rate PG tests for their duration.

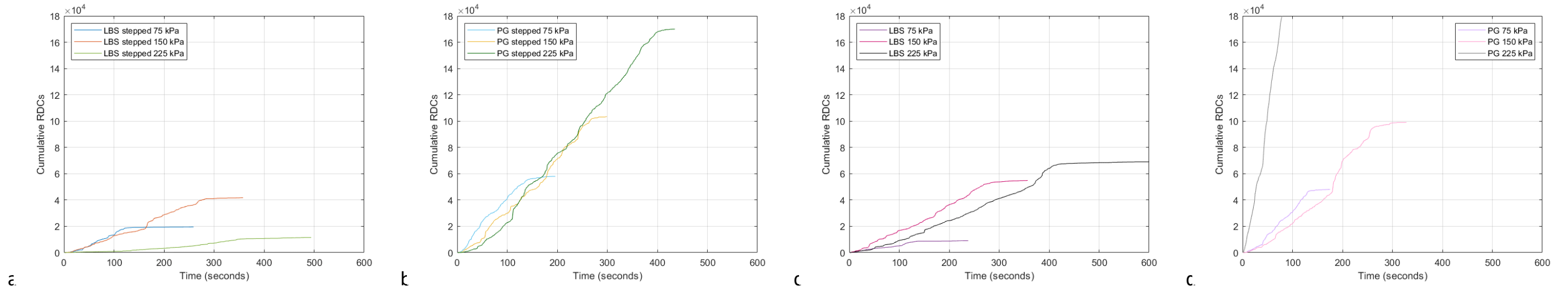


Figure 52 Cumulative RDCs with time for (a) stepped rate LBS tests, (b) stepped rate PG tests, (c) constant rate LBS tests and (d) constant rate PG tests during compression only.

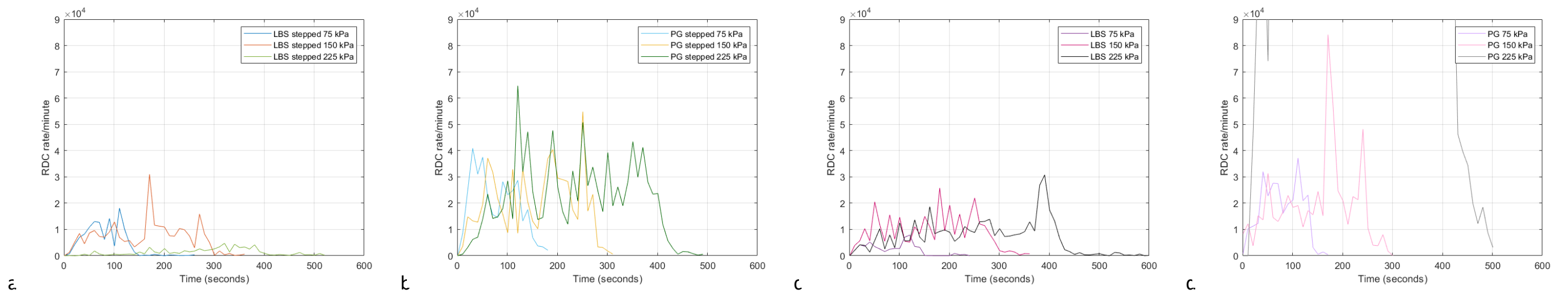


Figure 53 RDC rate/minute with time for (a) stepped rate LBS tests, (b) stepped rate PG tests, (c) constant rate LBS tests and (d) constant rate PG tests during compression only.

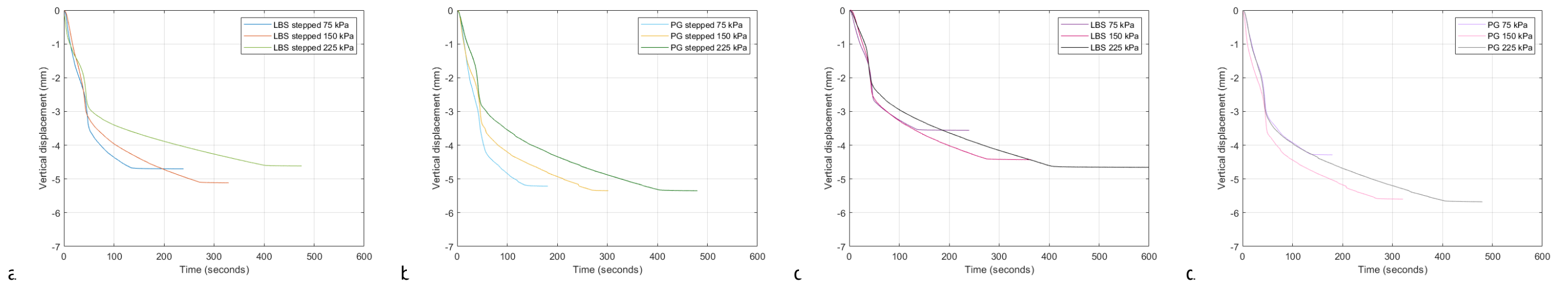


Figure 54 Vertical displacement with time for (a) stepped rate LBS tests, (b) stepped rate PG tests, (c) constant rate LBS tests and (d) constant rate PG tests during compression only.

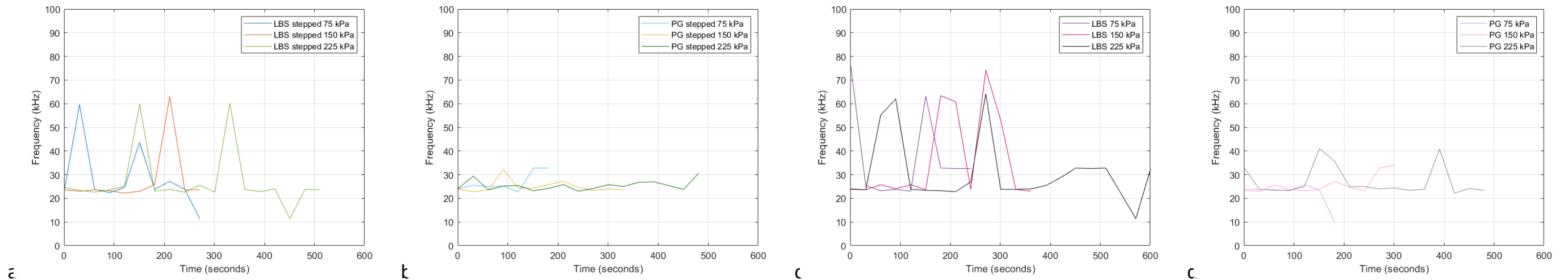


Figure 55 Frequency dominance with time for (a) stepped rate LBS tests, (b) stepped rate PG tests, (c) constant rate LBS tests and (d) constant rate PG tests during compression only.

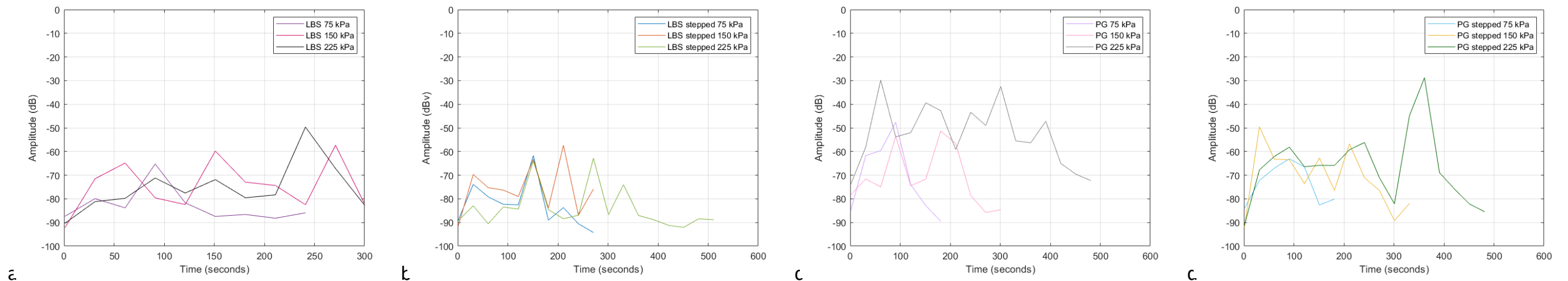


Figure 56 Amplitude with time for (a) stepped rate LBS tests, (b) stepped rate PG tests, (c) constant rate LBS tests and (d) constant rate PG tests during compression only.

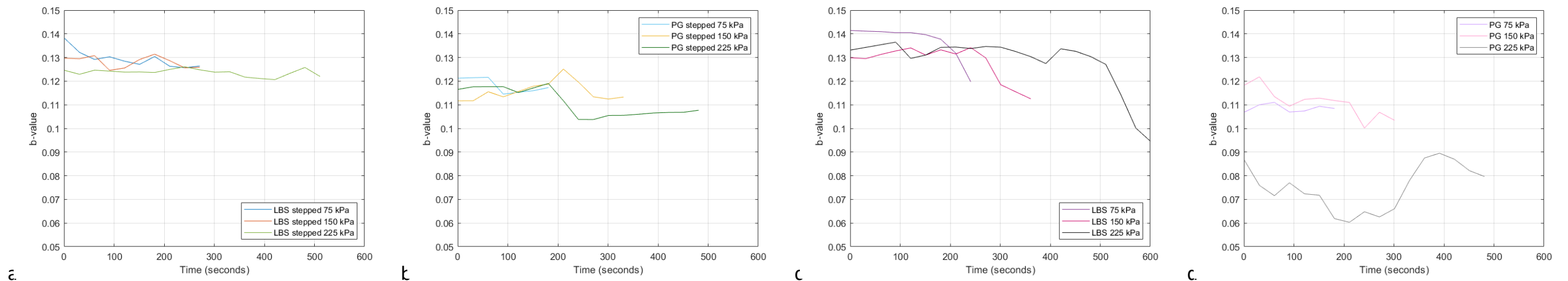


Figure 57 b-values with time for (a) stepped rate LBS tests, (b) stepped rate PG tests, (c) constant rate LBS tests and (d) constant rate PG tests during compression only.

5.1.2 Shearing

Following compression, each sample was subject to a period of shearing during which internal shear stresses affected behaviours (Figure 5.12). Dependent on the test, shearing was performed over a minimum shear displacement of 25 mm. Figures 5.10 to 5.16 show the relationships for the same parameters as discussed in Section 5.1.1, but as a function of shear displacement, to study parametric behaviours during the shearing period. Moreover, Figures 5.20 to 5.25 shows further parametric relationships for the full duration of each test (compression and shearing stages are both presented) for comparison, alongside additional tests not previously plotted. Four influential factors were considered: particle size, normal stress, mobilised shear stress, and shear rate.

5.1.2.1 Particle size

Figure 5.10 shows RDC rates/second as function of shear displacement. As displacement increases the RDC rate behaviours differ dependent on the shearing regime, although always increase initially during shear strength mobilisation. This is discussed in Section 5.1.2.3.

With respect to particle size, with exception to PG under 225 kPa (Figure 5.10d), the RDC rates are generally much lower in the PG tests compared to the LBS tests. At a shear rate of 1 mm/minute, for example (10 to 15 mm displacement in Figures 5.10a and 5.10b, and 0 to 40 mm displacement Figures 5.10c and 5.10d), RDC rates peak around 6000 RDCs/second in LBS and 4000 RDCs/second in PG (excluding PG under 225 kPa in Figure 5.10d). Similar results are shown in Figures 5.23b and 5.23d where the different materials show different AE production, whilst Zhang et al. (1990) state that 'AE activity decreases with increasing grain size'.

This observation contradicts that of the compressional stage of the experiment for which the PG tests were more emissive (Figure 5.3). During shearing though, more soil-steel interactions will occur with smaller grain sizes due to a larger number of grain contacts at the soil-steel interface.

Figure 5.11 then shows vertical displacements as a function of shear displacement. The figure shows that the displacement behaviours vary dependent on the soil type, although in nearly all cases LBS experiences higher vertical displacement (i.e. more settlement) than PG. Final vertical displacement for the LBS tests (Figures 5.11a and 5.11c), for example, range between 0.4 and 1.4 mm whereas, for the PG tests (Figures 5.11b and 5.11d), these are much smaller at 0.1 to 0.7 mm.

Like with RDC rates (Figure 5.10), this behaviour is contradictory to that seen during the compressional stage (Figure 5.4) where higher displacements were recorded in the PG samples. The behaviour, however, still relates to grain size, with dilation seen to occur for several of the PG tests (Figure 5.11b). Given that it is known that volumetric changes are governed by the state parameter, where the state

parameter may be defined as the difference between the initial void ratio and the void ratio on the critical state line for the same imposed stress, this implies that the material in these cases was denser than the critical state density and consequently dilated it shear. When dense, granular particles can become interlocked which, when sheared, become free and cause dilation as seen.

Figure 5.13 plots shear stress as a function of shear displacement throughout shearing. The figure shows that shear stresses begin to build within the soils, initially increasing rapidly, but at a decreasing rate, before then continuing to increase at a much slower and decreasing rate. The change from a rapid to slow increase always occurs between 2 and 4 mm displacement, however varies in terms of the shear stress reached by this point. For all tests though, the mobilised shear stress at this point is always slightly higher for PG samples under comparable conditions.

This observed difference is likely a result of the larger grains within PG providing a greater resistance to shearing. Relatedly, it can also be seen that more fluctuations in shear stress can be seen in PG tests when compared to LBS tests. This is likely also a result of more significant stick-slip behaviour. Similar results were observed by Han et al. (2018).

Investigating acoustic behaviours, Figure 5.14 shows that the range of frequencies dominating the LBS (Figures 5.14a and 5.14c) tests is slightly greater than PG (Figure 5.14b and 5.14d); extremes of 10 to 100 kHz and 10 to 95 kHz measured respectively. This is also emphasised in Figure 5.18 for which data points are plotted as a function of normal stress. Additionally, Figure 5.14 suggests that lower frequencies generally dominate PG compared to LBS soils with Figure 5.8 showing a basic statistical analysis (binning) of the dominant frequencies.

Figure 5.8 plots the number of times measured dominant frequencies fall into frequency categories of 10 kHz increments. The figure shows that a different range of mechanisms may be dominating in the two materials with fewer higher frequencies seen for the PG. This most likely relates to grain size; larger grains are expected to have lower resonant frequencies. Comparing Figures 5.14 and 5.15 however, frequency and amplitude (i.e. energy) are not related despite the observed link between grain size and amplitude and therefore insinuated link between frequency and amplitude.

Figure 5.15 shows that a range of signal amplitudes and behaviours were observed, varying dependent on both the shearing regime and soil type. Notably, like with the compressional stage, the range in amplitudes measured for PG is much greater compared to LBS, although a maximum of -15 dB is reached for both. This should be expected as the larger particles within the PG have a greater potential energy during slip-stick behaviours whilst there are fewer particles within the sample to release stored energy.

Figure 5.15 also shows that the variations in amplitude are greater for the PG tests. Table 5.2 summarises this statistically, showing goodness of fits, as coefficients of determination (R^2) values, for second order polynomials superimposed over the amplitude-shear displacement data. By measuring the goodness of fit, variations (i.e. fluctuations) over the overall trend can be established with smaller R^2 values indicating a worse fit and therefore more variation.

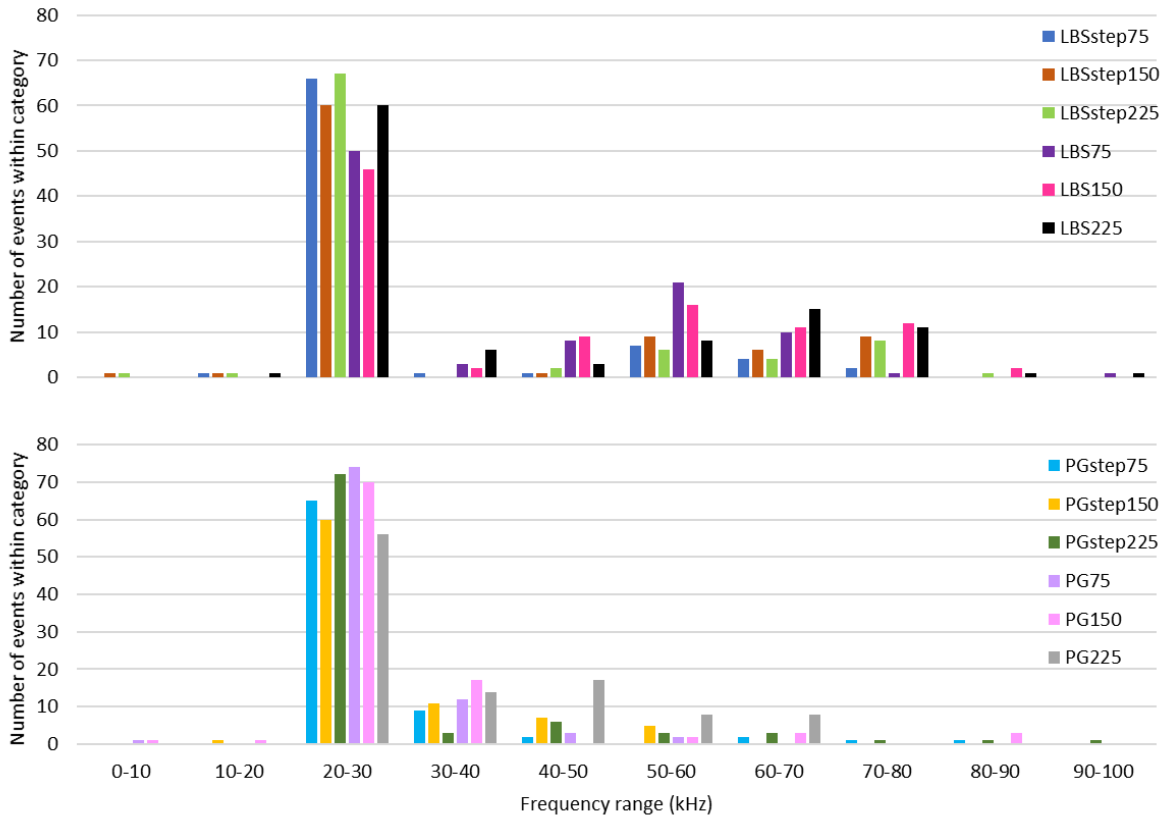


Figure 5.8 Statistical analysis on the occurrence of dominant frequencies (within 10 kHz bins) during shearing for stepped and constant rate tests with LBS (top) and PG (bottom).

Table 5.2 Goodness of fit as R^2 values for second order polynomials superimposed onto the amplitude data.

Test ID	R^2 value	Test ID	R^2 value
LBS step 75 kPa	0.3882	PG step 75 kPa	0.347
LBS step 150 kPa	0.443	PG step 150 kPa	0.2523
LBS step 225 kPa	0.5762	PG step 225 kPa	0.0745
LBS 75 kPa	0.2055	PG 75 kPa	0.168
LBS 150 kPa	0.4014	PG 150 kPa	0.2099
LBS 225 kPa	0.5224	PG 225 kPa	0.0266

Finally, Figure 5.16 shows corresponding b-values as a function of shear displacement. Like during compression, a difference in the magnitude of values can be seen between the PG and LBS tests. The difference is however small with the b-values generally greater in PG samples, averaging 0.0844, compared to 0.0780 in the LBS.

Higher b-values generally imply a higher number of low energy events were occurring. This is contradictory to the findings of Figure 5.15 in which it was suggested that PG produced more higher energy events. However, this statement does not consider the overall number of events whilst the signal amplitudes may have been formed from multiple, superimposing events.

Furthermore, several of the figures, including b-values, only show representative data (i.e. every 10 or 30 data points) due to the size of the datasets. Plotting the data in this way was a trade-off between readability and representation; general trends are visible however some data is lost from view. The datasets remained complete for other analysis such as the calculation of means, modes, and data ranges, however, so additional observations could still be made.

5.1.2.2 Normal stress

As with the compressional period, the influence of normal stress during shearing was investigated for three normal stresses. These were kept constant at 75, 150, or 225 kPa. Their influence on mechanical behaviours is shown in Figures 5.10 to 5.13 and on acoustic behaviours in Figure 5.14 to 5.16.

Figure 5.10 shows how different normal stresses affect RDC rates during shearing. It can be seen that higher normal stresses yield higher AE rates, a behaviour also observed by Smith and Dixon (2019). Higher RDC rates as a result of higher normal stresses were expected due to the higher work being done, and therefore potential energy, at the sample boundaries. This is with exception to the results in Figure 5.10b which shows a lot of overlap and suggest that under 225 kPa the test is less emissive. Given the results match those of other published works, the test under 150 kPa in Figure 5.10d may however be assumed anomalous.

RDC rates are also plotted in Figure 5.17 as a function of normal stress and Figure 5.23 as a function of shear stress for different shearing rates and shearing regimes. It is clear from Figure 5.17a that as the normal stress is increased, both the averaged minimum and maximum RDC rates also increase. Under 75 kPa, for example, minimum and maximum RDC rates of around 0.6×10^5 and 2.2×10^5 RDCs/minute were calculated, whilst under 225 kPa these increase to 1.2×10^5 and 5×10^5 RDCs/minute. The RDC rates have therefore doubled as normal stress has tripled.

Figure 5.17c however shows that there can be a large variation in the RDC rates under the same normal stress. Under 150 kPa, a range spanning 1.3×10^5 RDCs/minute was recorded for various tests under the same shearing conditions. This range is considerable but, given the number of influential and sometimes uncontrollable variables that can affect AE production, not unreasonable. Differences in the grain sizes, grain distributions, grain morphologies, and resulting fabric structures as the samples would all affect AE generation.

Figure 5.23 also shows RDC rates but as a function of shear stress (where shear stress is a function of normal stress and friction). Of importance, the figure is split to show results before and after the mobilisation of peak shear strength. This is opposed to being split by soil type, as in all other figures. The mobilisation of peak shear strength is important, marking the point at which surface friction is overcome and a shear zone develops; it is known that the thickness of the shear zone is dependent on the roughness of the surface.

Prior to mobilisation, the RDC rate increases at an increasing rate regardless of soil type, normal stress, or shear rate. This is also illustrated in Figures 5.10 and 5.13 where the RDC rates can be seen to initially rise steeply, coinciding with an initial rise in shear stress.

After mobilisation however, the RDC rates appear to plateau and form clusters around certain values. For the constant shear tests, single, clear clusters form. For the stepped (i.e. increasing increments of shearing velocity) shear tests though, several clusters form around increasing RDC rates demonstrating how the RDC rates increase with increasing shear rate (Section 5.1.2.3).

Figure 5.11 shows measured vertical displacements. The influence of normal stress on volumetric behaviour appears to be mixed with some tests clearly effected, such as in Figure 5.11c, and others not. Figure 5.11c clearly shows that higher normal stresses result in higher vertical displacements during shearing; for each normal stress tested there is a distinctive increase in the amount of displacement measured. Under 75 kPa, for example, a final vertical displacement of just under 0.4 mm was measured during shearing whilst under 225 kPa this increases to around 1.4 mm.

Figure 5.11a contrastingly suggests that the opposite is true with the test under 225 kPa recording the least vertical displacement (around 0.5 mm) and the test under 75 kPa recording the most (around 0.8 mm). Given the differing results, this would imply that factors other than normal stress may also be influencing the vertical displacement such as the differences in initial relative densities between samples; these can significantly influence volumetric behaviour during compression and shearing.

Figure 5.12 plots the shear rates for which each series of tests were conducted (a controlled variable) whilst Figure 5.13 plots the resultant shear stresses (a dependent variable).

The effects of normal stress on shear stress are very clear with three distinct bands of stress visible, dependent on both the sample material (Section 5.1.2.1) and normal stress. These are:

- 30 to 50 kPa shear stress under 75 kPa normal stress;
- 70 to 90 kPa shear stress under 150 kPa normal stress;
- And 110 to 130 kPa under 225 kPa normal stress.

The calculated interface friction angles for LBS-steel and PG steel were approximately 27.5 and 30.1 degrees, respectively.

Comparatively, the effects of normal stress on acoustic behaviours during shearing are unclear. Figure 5.14 for example shows that frequency dominance fluctuates seemingly randomly for all normal stresses tested.

Figure 5.14 shows that the dominance of different frequencies as a function of shear displacement vary similarly for each of the tested normal stresses, whilst the frequencies to which the dominance fluctuates within each test also remain approximately the same. This is weakly illustrated in Figure 5.18 too, where the occurrence of difference frequencies shows no clear dependent on normal stress. Furthermore, Figures 5.21 and 5.24 demonstrate that although clustering around different frequencies occurs, the range and spread of the frequency clusters do not appear to be affected by the normal stress. Similarly, Figure 5.15 suggests that signal amplitudes are also not significantly affected by normal stress with similar behavioural trends observable for each test.

Figure 5.16 shows that b-values measured from LBS reduce proportionally as normal stress increases; however, the inverse relationship between b-values is less clear for PG. Figure 5.19 additionally shows the b-values as a function of normal stress are spread over a large and approximately equal range for the different normal stresses tested. Furthermore, only weak clustering can be seen around some values which remain the same for each test.

5.1.2.3 Shear rate

The effects of shear rate on mechanical and acoustic behaviours were investigated using two shearing regimes, stepped shear and constant shear, over shearing rates ranging between 0.002 and 2 mm/minute. For the stepped rate tests, the shear rate was incrementally increased by 0.25 mm/minute (Figure 5.12) starting from 0.5 and ending at 2 mm/minute throughout shearing. For the constant rate tests, constant shear rate of 1 mm/minute was applied throughout.

Figure 5.10 shows RDC rates measured during both regimes. For the stepped rate tests (Figure 5.10a and 5.10b), it can be seen that increasing the shear rate incrementally causes AE activity (RDC rates) to increase in stepped but changing increments. Smith and Dixon (2019) show similar findings (Figures 2.11 and 2.17) and Dixon and Spriggs (2007) show that shear rates can be interpreted using measured AE rates (Figure 2.7). Additionally, Figure 5.26 suggests that RDCs per unit time are proportional to imposed shear rates. Interestingly however, although the shear rate remains constant for the duration of each test step (i.e. each constant shear velocity increment) in Figure 5.10a and 5.10b, the RDC rates

do not, appearing to peak at the start of each new shear increment and then gradually reduce to remain around a mean value.

One explanation for this relates to amount of work done. Every time the shear rate is increased, the amount of work being done on the sample per unit time (i.e. the energy put into) also increases. This increases the potential energy of the sample and therefore the energy available to be dissipated in the form of RDCs (heat and sound), hence increasing the RDC rate. As the shear rate then remains constant, the acceleration of the sample returns to 0 and the energy input is therefore less. Consequently, the RDC rates decrease.

In the constant rate tests (Figures 5.10c, 5.10d, 5.20c and 5.20d) where, apart from the PG tests under 75 and 150 kPa, the RDC rates can be seen to initially rise steeply before peaking and gradually decreasing – mirroring the mechanical mobilised shear strength vs shear displacement response. Notably though, this behaviour is not consistent for each shear rate and instead varies. This variation is emphasised in Figure 5.26a which shows average RDC rates as a function of shear rate. A clear increase in the RDC rates can be seen as the shear rate increases, illustrated with second order lines of best fit over the range of shear rates investigated, however the rate of increase decreases at a decreasing rate despite the shear rate increasing at a constant rate.

This decrease indicates that AE production may be limited with relation to energy availability, which in turn, may be influenced by numerous phenomena including a possible change in the dominant AE generation mechanism(s) which, relatedly, may produce lower energy and therefore less measurable AE. Furthermore, changes in the levels of friction between particles may influence AE production with Figure 5.13 showing that shear stress, which as discussed in Section 5.1.2.1 is related to friction, also exhibits a decreasing rate of change with increasing shear rate and/or displacement. Moreover, the initial grain fabric may influence friction and shear stress with Figure 5.26c showing that, although a positive trend between shear rate and RDC rate production can be deduced, for the numerous tests conducted at 1 mm/minute shearing rate, there is a wide variation in AE production (around 1×10^5 to 2.5×10^5 RDCs/minute) which is likely due to variations in soil behaviour (e.g. the initial fabric).

The effects of shear rate on vertical displacement are shown and compared in Figure 5.11 for the stepped and constant shearing regimes. With exception to the results in which dilation is seen (Section 5.1.2.1), the vertical displacements are seen to continue to increase at a decreasing rate irrespective of the shear rate or shear regime. Furthermore, the relationships mostly plot as smooth, opposed to segmented, lines suggesting that changes in the shearing rate do not visibly affect the way in which vertical displacement occurs.

Notably however, the vertical displacements for constant shear tests are on average greater than those of the stepped shear tests with respect to both the overall settlement (at 35 mm displacement for comparison purposes) and the change in displacement as a result of shearing. The constant shear tests (Figures 5.11c and 5.11d) for example show maximum vertical displacements of approximately 1.3 mm during shearing, whilst the stepped shear tests (Figures 5.11a and 5.11b) show maximum vertical displacement of around 0.6 mm. This could indicate that shearing at a maintained rate allows for different longer-term changes within the internal fabric of the materials to evolve, however could also relate to the differing densities and inherently varying internal structures of the initial samples. Table 5.1 for example shows that of the twelve tests, all six constant rate tests had lower initial densities than the equivalent stepped rate tests.

Figure 5.13 shows that during shearing, shear stresses remain relatively unaffected by the shear rate and any sudden changes to it (as with the stepped regime). Figure 5.14 on the other hand shows that shear rate effects the frequency of generated AE with Figure 5.14a and 5.14b showing that the dominance of different frequencies fluctuates more at lower shear rates than higher shear rates. This is emphasised in Figures 5.18a, 5.18b, 5.21a, and 5.21b for which the slow tests, that predominantly consist of slower shearing rates, plot across a relatively wide and distributed spread of frequencies during shearing and indicate that a wider variety of AE generating mechanisms may be occurring. Alternatively, this observation could also indicate the dominance of a singular, or just a few, mechanisms at higher shear rates.

This trend is further illustrated in Figure 5.8 which plots the number of high frequency (>35 kHz) events that occur within every 5 mm of displacement, and therefore correspond to changes in shear rate, throughout shearing. Generally, the number of higher frequency events decreases with progressive displacement; the highest number of events (9) is recorded at 0.75 mm/minute and the lowest (0) during the latter, faster stages of shearing. Figures 5.14c and 5.14d additionally support these findings. Fluctuations in the dominance of frequencies are seen consistently throughout, implying that the changes in frequency are not a function of displacement but shear rate.

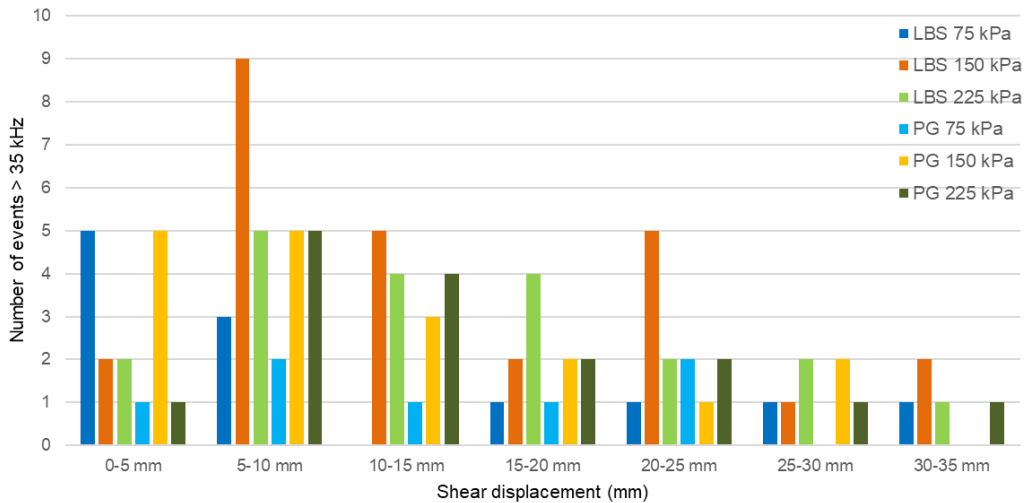


Figure 5.9 Number of higher (>35 kHz) AE events for every 5 mm displacement during stepped shear rate tests.

Relating to frequency, Figure 5.15 shows that as shear rates increase the corresponding amplitudes of generated AE also increase but at a decreasing rate. Figure 5.15a, for example, shows that under a shear rate of 0.75 mm/minute (5 to 10 mm displacement) the average amplitude fluctuates around -56.76 dB whereas by 1.75 mm/minute (25-30 mm displacement) this has increased to -49.53 dB. Contrastingly, at a constant shear rate (Figures 5.15c and 5.15d), the amplitudes appear to remain stable, fluctuating around an average value of -60 dB. This relationship is similar to that of the RDC rates, and hence both altitude and RDC rate behaviours show the same trends.

Calculated from the amplitudes, Figure 5.16 then shows that b-values may be seen to generally decrease during the stepped shearing regime but remain relatively constant, fluctuating slowly around a mean, during constant shearing. These behaviours are comparable to those observed in Figure 5.15 where for the stepped shearing regime the measured amplitudes can be seen to generally increase in average value, and for the constant shearing regime remain relatively stable. This shows that b-values are sensitive to changes in shear rate, whereas they were shown not to be significantly influenced by stress level earlier.

As discussed in Section 5.1.2.1, higher b-values suggest that a higher number of lower energy events were occurring. Given that the b-values decrease during the stepped shearing regime, the proportion of higher magnitude events increases (i.e. b-value reduces) as shearing velocities increase. Figures 5.15a and 5.15b showed that although the amplitude of events increased, this was at a decreasing rate; a higher proportion of low to high amplitude events may therefore be assumed. Moreover, the relative stability of b-values during constant shearing suggests a relatively consistent ratio of high to low amplitude events. Figure 5.15 reflects this.

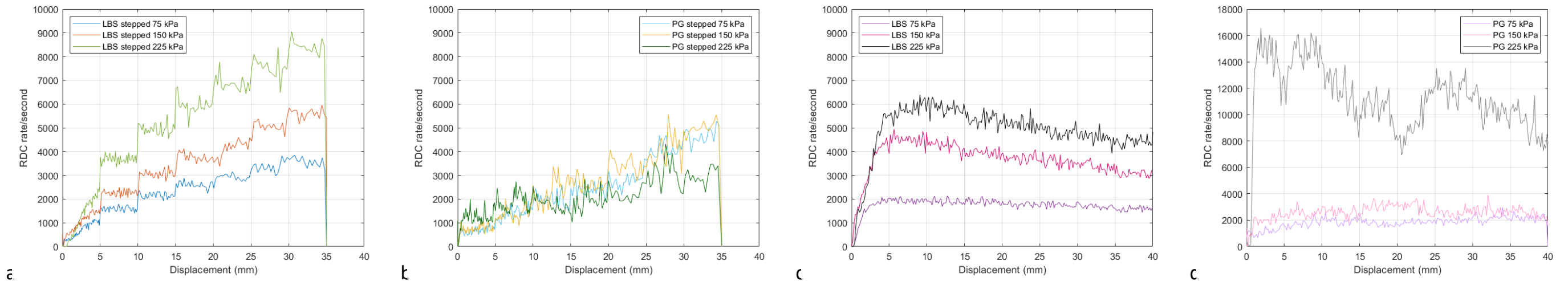


Figure 5.10 RDC rate/second with shear displacement for (a) stepped rate LBS tests, (b) stepped rate PG tests, (c) constant rate LBS tests and (d) constant PG tests.

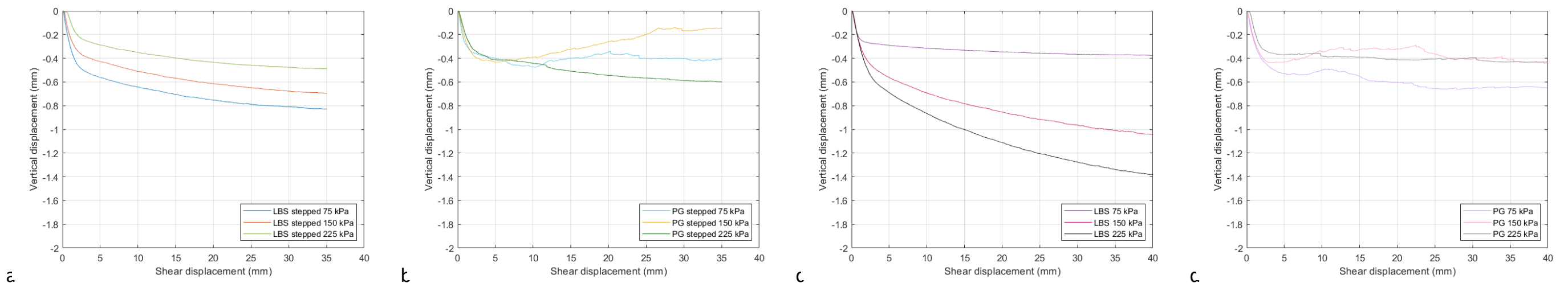


Figure 5.11 Vertical displacement with shear displacement for (a) stepped rate LBS tests, (b) stepped rate PG tests, (c) constant LBS tests and (d) constant rate PG tests during shearing only.

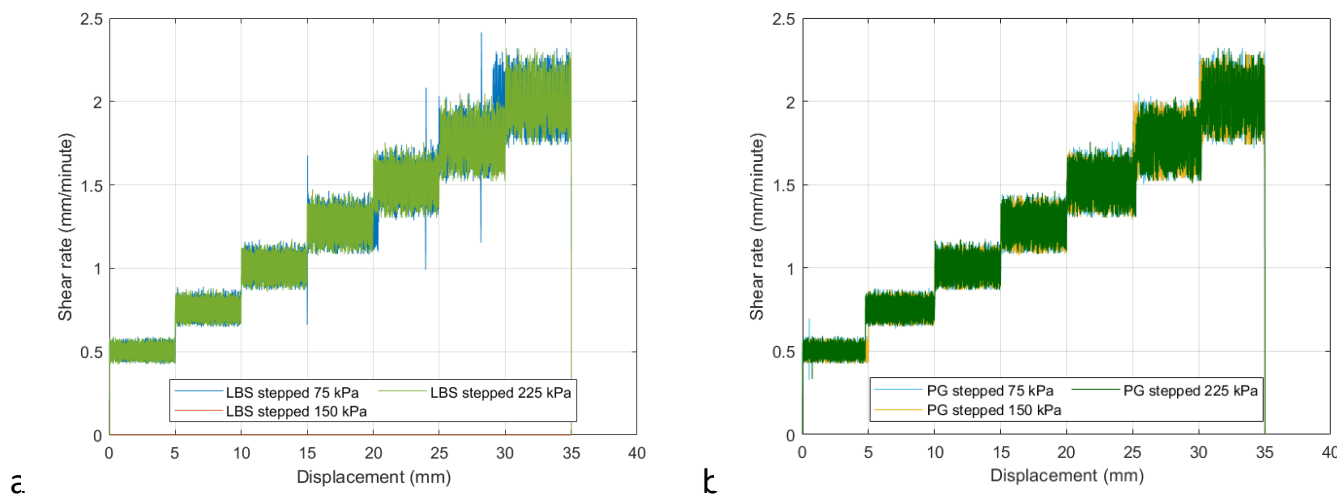


Figure 5.12 Shear rate with shear displacement for (a) stepped rate LBS tests and (b) stepped rate PG tests.

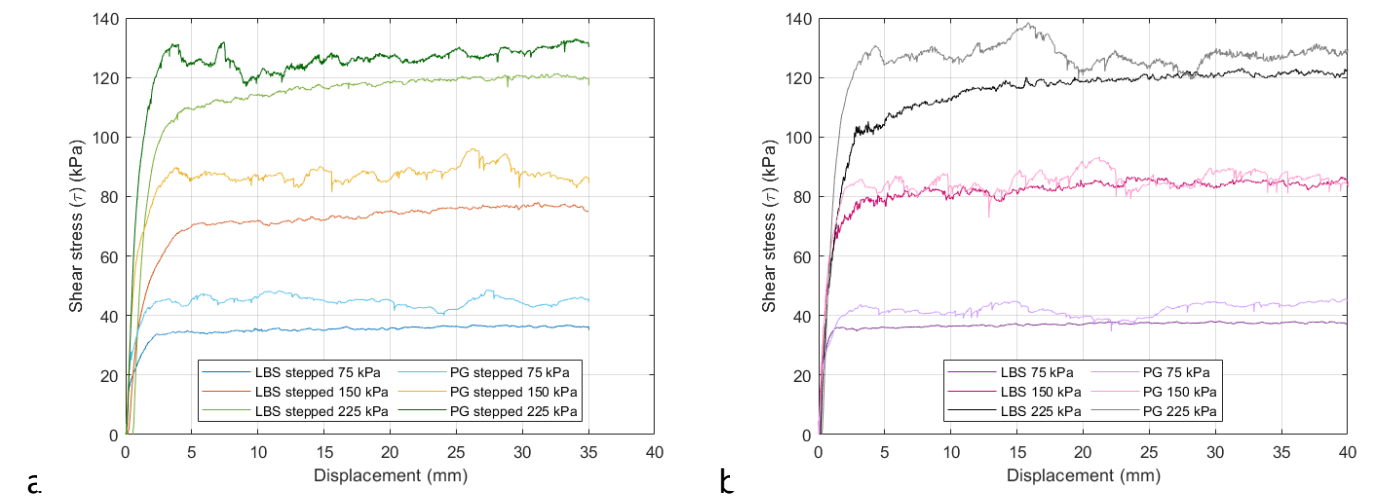


Figure 5.13 Shear stress with shear displacement for (a) stepped and constant rate LBS tests and (b) stepped and constant rate PG tests.

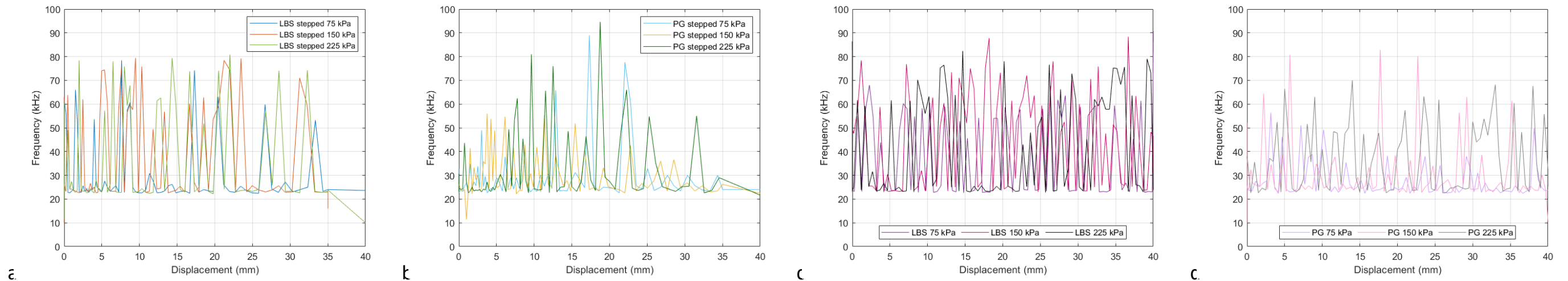


Figure 5.14 Dominant frequencies with shear displacement for (a) stepped rate LBS tests, (b) stepped rate PG tests, (c) constant rate LBS tests and (d) constant rate PG tests.

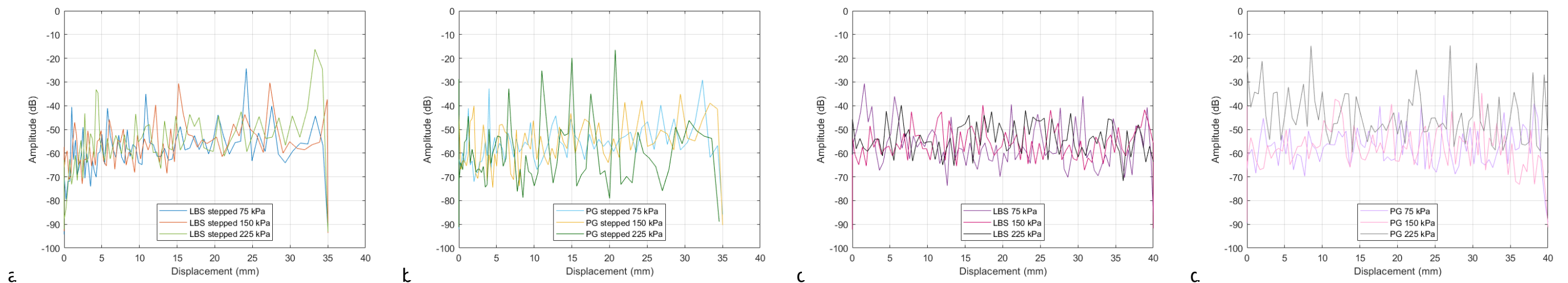


Figure 5.15 Amplitude with shear displacement for (a) stepped rate LBS tests, (b) stepped rate PG tests, (c) constant rate LBS tests and (d) constant rate PG tests.

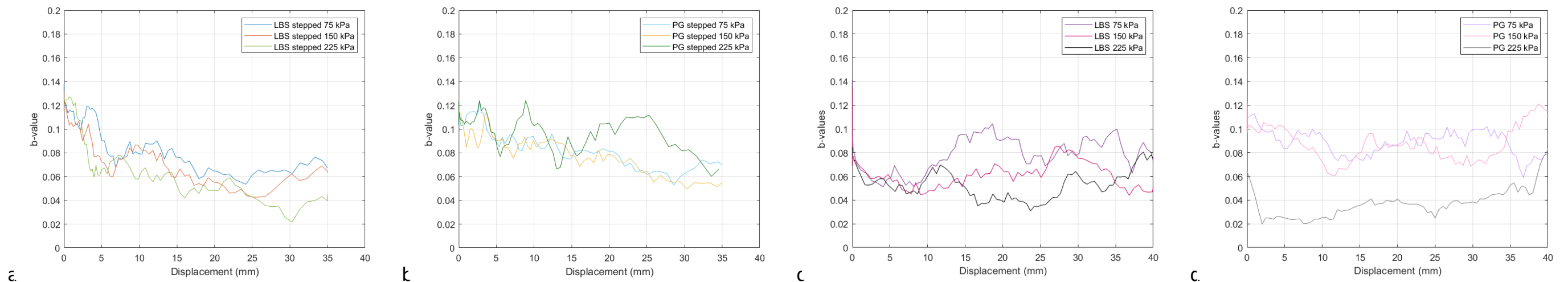


Figure 5.16 b-values with shear displacement for (a) stepped rate LBS tests, (b) stepped rate PG tests, (c) constant rate LBS tests and (d) constant rate PG tests.

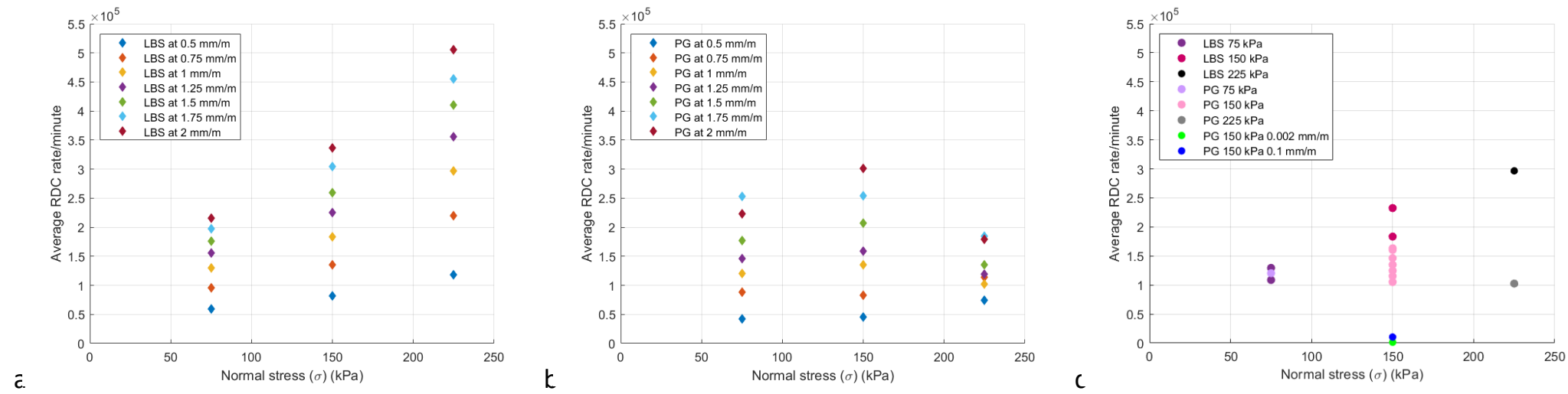


Figure 5.17 Separated and averaged RDC rates/minute with normal stress for (a) stepped rate LBS tests, (b) stepped rate PG tests and (c) constant rate LBS tests and PG tests (at target normal stress).

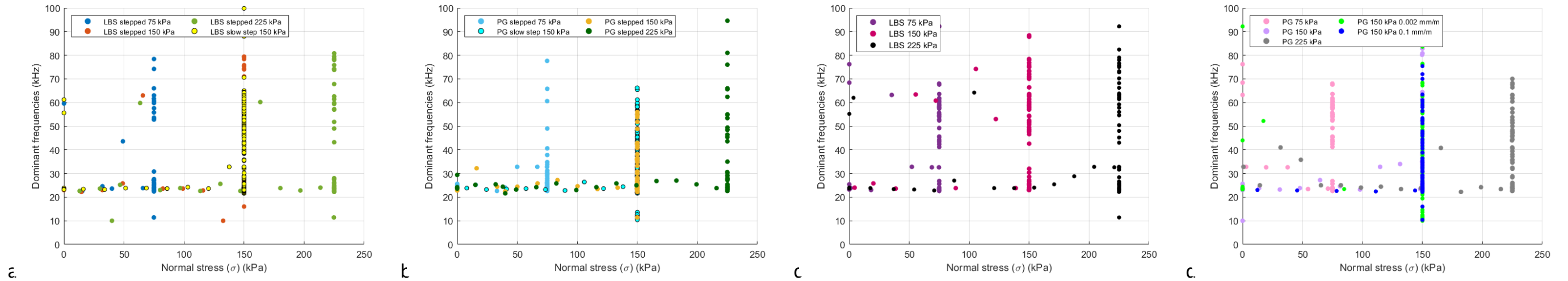


Figure 5.18 Cluster behaviours for dominant frequencies with normal stress for (a) stepped rate LBS tests, (b) stepped rate PG tests, (c) constant rate LBS tests and (d) constant rate PG tests during compression (before target normal stress) and shearing (at normal stress).

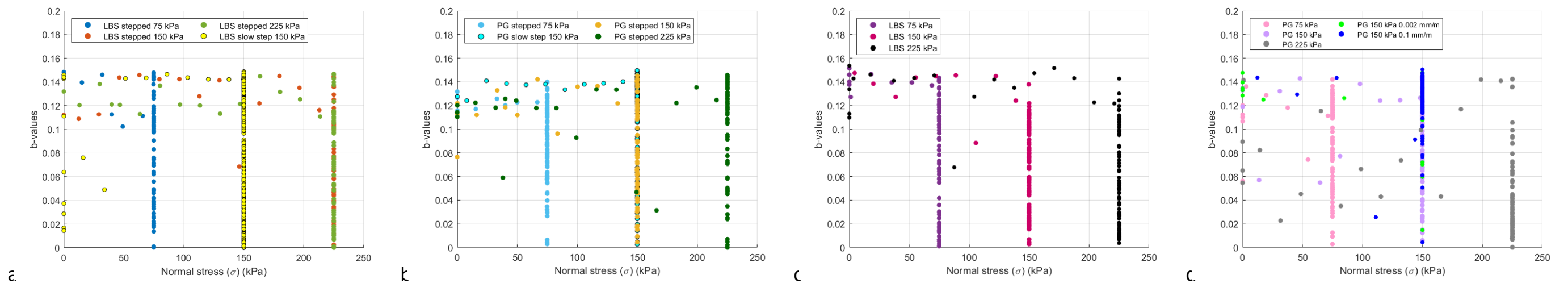


Figure 5.19 Cluster behaviours for b-values with normal stress for (a) stepped LBS tests, (b) stepped PG tests, (c) constant LBS tests and (d) constant PG tests during compression (before target normal stress) and shearing (at normal stress).

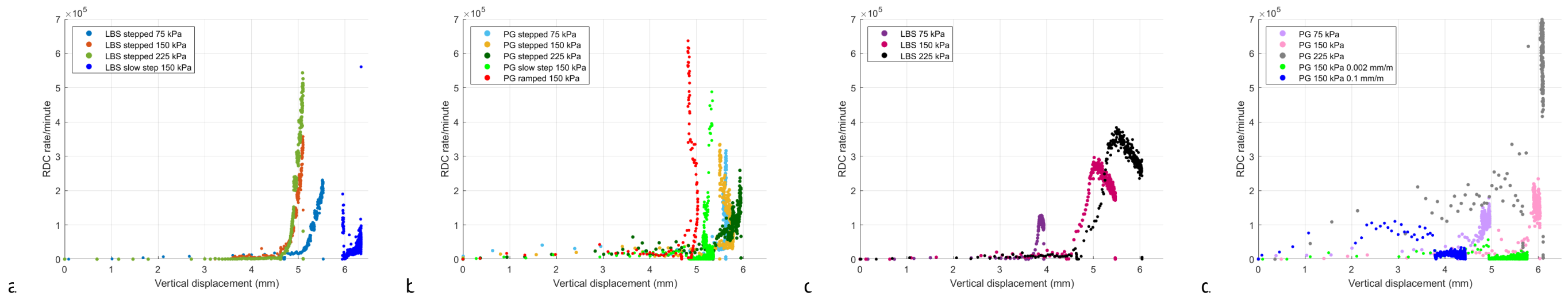


Figure 5.20 Cluster behaviours for RDC rate/minute with vertical displacement for (a) stepped rate LBS tests, (b) stepped rate PG tests, (c) constant rate LBS tests and (d) constant rate PG tests.

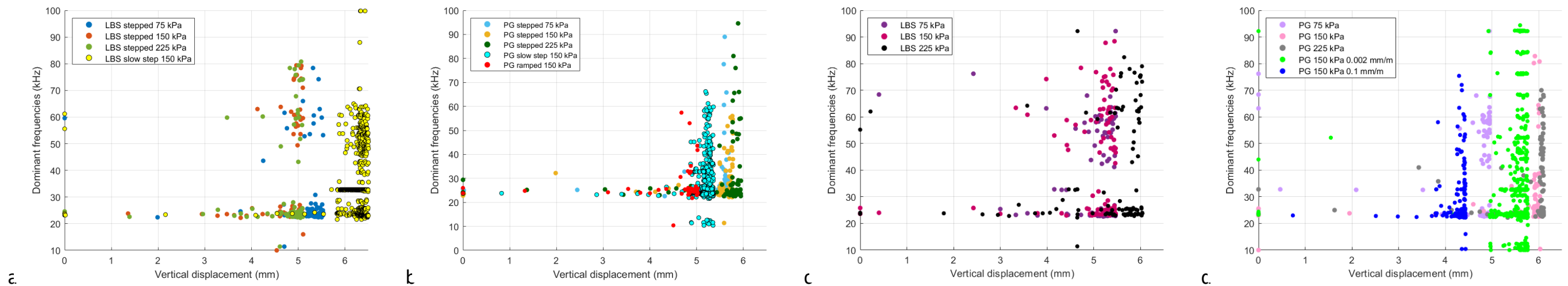


Figure 5.21 Cluster behaviours for dominant frequencies with vertical displacement for (a) stepped rate LBS tests, (b) stepped rate PG tests, (c) constant rate LBS tests and (d) constant rate PG tests.

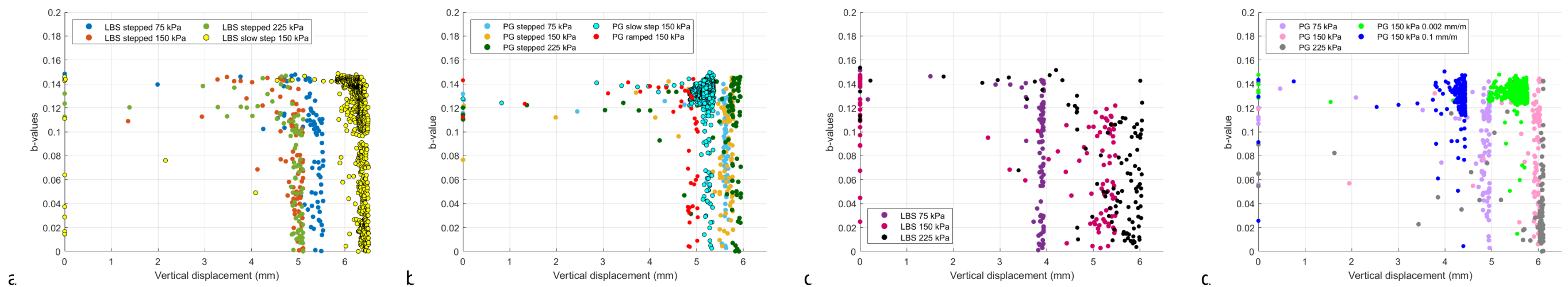


Figure 5.22 Cluster behaviours for b-values with vertical displacement for (a) stepped rate LBS tests, (b) stepped rate PG tests, (c) constant rate LBS tests and (d) constant rate PG tests.

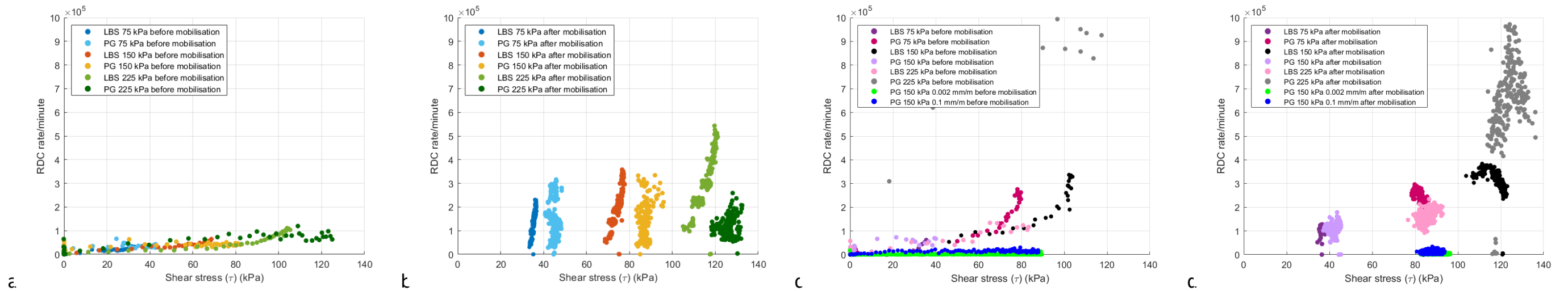


Figure 5.23 Cluster behaviours for RDC rate/minute with shear stress for (a) stepped rate LBS and PG before and (b) stepped rate LBS and PG tests after mobilisation, and (c) constant rate LBS tests and PG tests before and (d) constant rate LBS tests and PG tests after mobilisation.

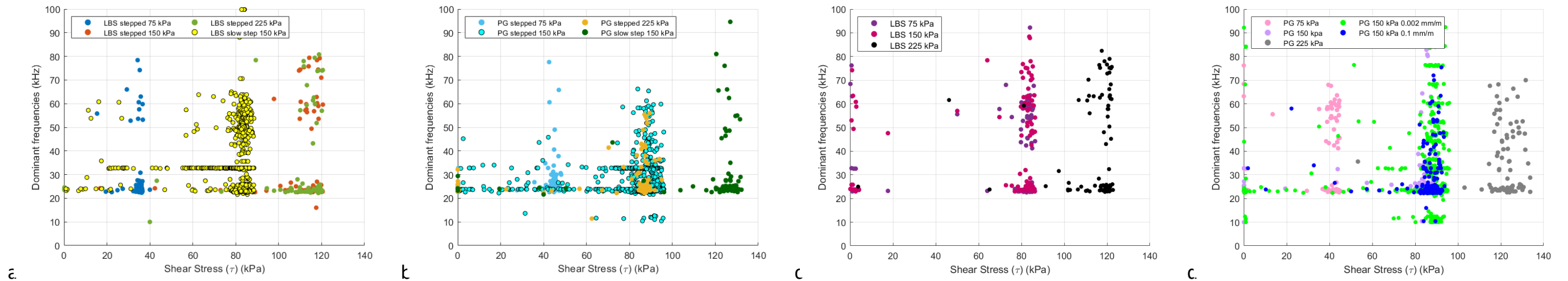


Figure 5.24 Cluster behaviours for dominant frequencies with shear stress for (a) stepped rate LBS and PG and (b) stepped rate LBS and PG tests, and (c) constant rate LBS tests and PG tests and (d) constant rate LBS tests and PG tests.

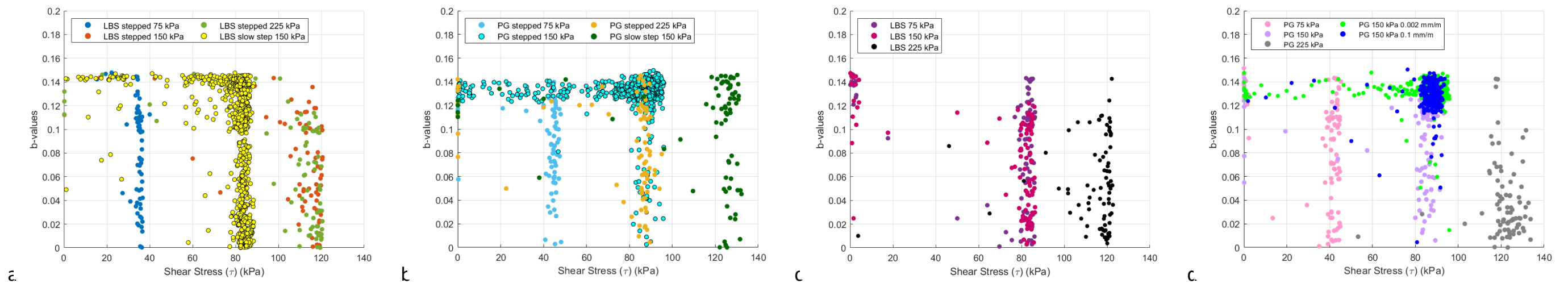


Figure 5.25 Cluster behaviours for b-values with shear stress for (a) stepped rate LBS and PG and (b) stepped rate LBS and PG tests, and (c) constant rate LBS tests and PG tests and (d) constant rate LBS tests and PG tests.

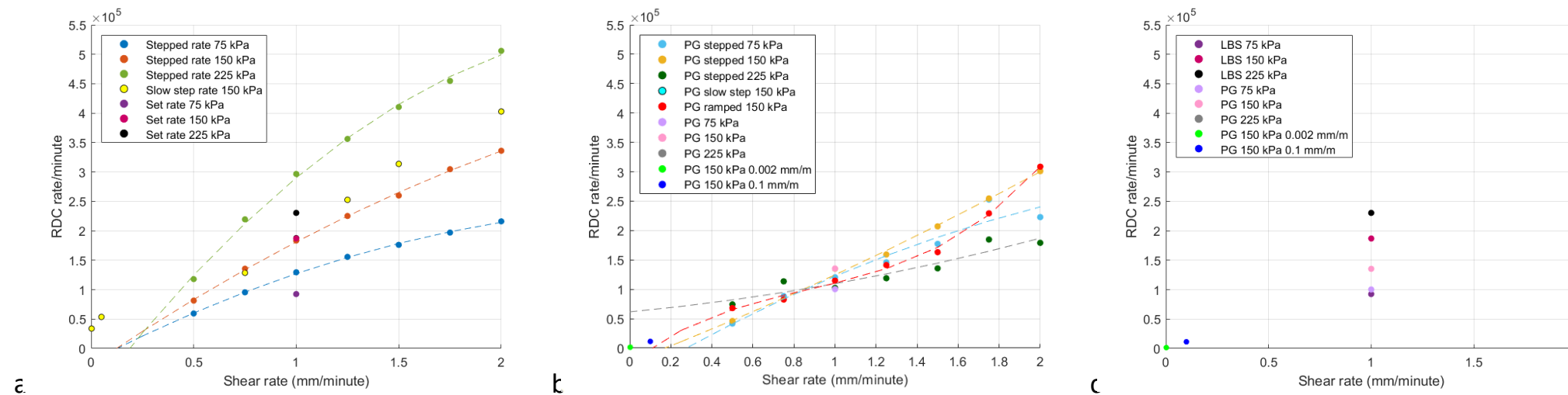


Figure 5.26 Cluster behaviours for RDC rate/minute with shearing rate for (a) a variety of LBS tests and (b) a variety of PG tests after mobilisation, and (c) constant rate LBS tests and PG tests during shearing.

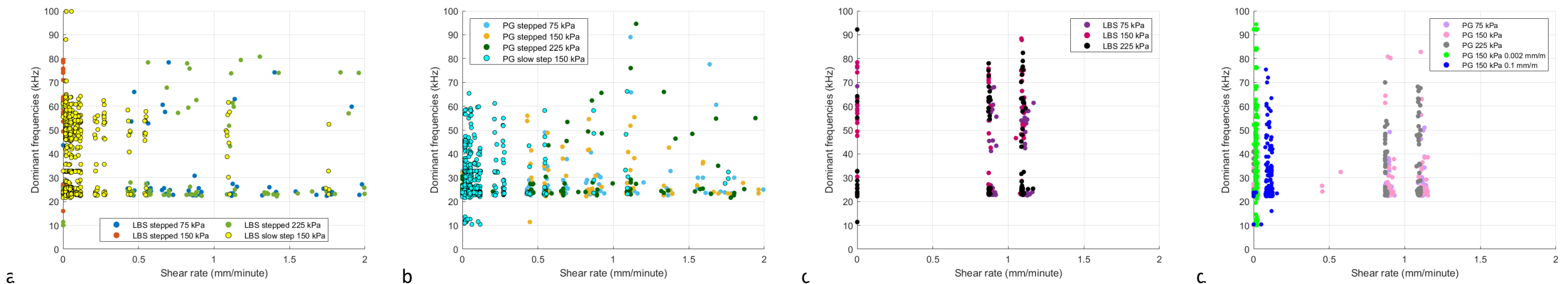


Figure 5.27 Cluster behaviours for dominant frequencies with shearing rate for (a) stepped rate LBS and PG and (b) stepped rate LBS and PG tests, and (c) constant rate LBS tests and PG tests and (d) constant rate LBS tests and PG tests during shearing.

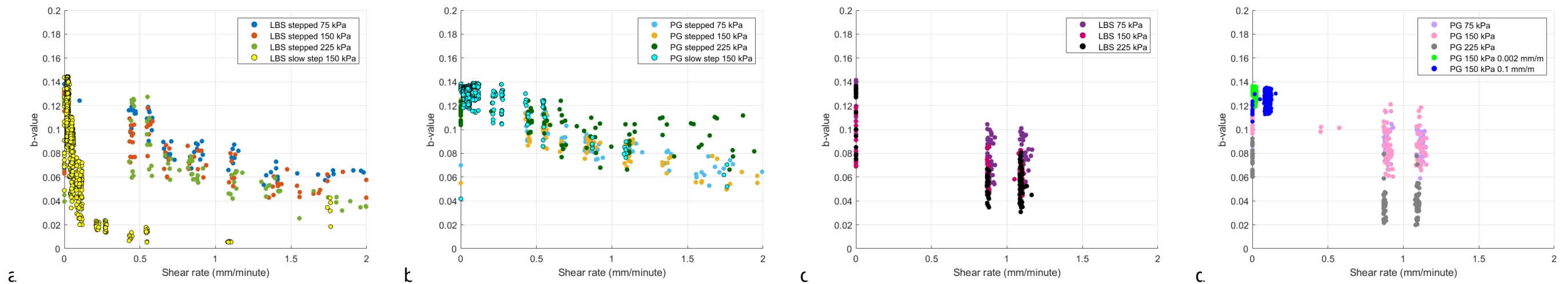


Figure 5.28 Cluster behaviours for b-values with shearing rate for (a) stepped rate LBS and PG and (b) stepped rate LBS and PG tests, and (c) constant rate LBS tests and PG tests and (d) constant rate LBS tests and PG tests during shearing.

5.1.3 Influence of plate roughness

The influence of plate roughness on AE generation was considered throughout the programme of shear box tests by taking roughness measurements at the start and end of each experiment. Additionally, high resolution scans using an Alicona Infinite Focus system (which captured high resolution optical images that have a 3D micro-coordinate system to compute shape and roughness measurements) were taken along a cross-section perpendicular to the grain (i.e. steel rolling direction) of the plate before any shearing experiments were conducted.

The results of the initial scan are shown in Figure 5.29 as a distribution plot, depth profile, and 3D model. It is shown that the plate was initially relatively smooth with most defects being between -0.5 and $+0.5$ μm in depth whilst a depth profile suggests that measurements larger than this were a result of occasional macro-defects (e.g. at 3.8 mm along the path); these are also shown in the 3D model.

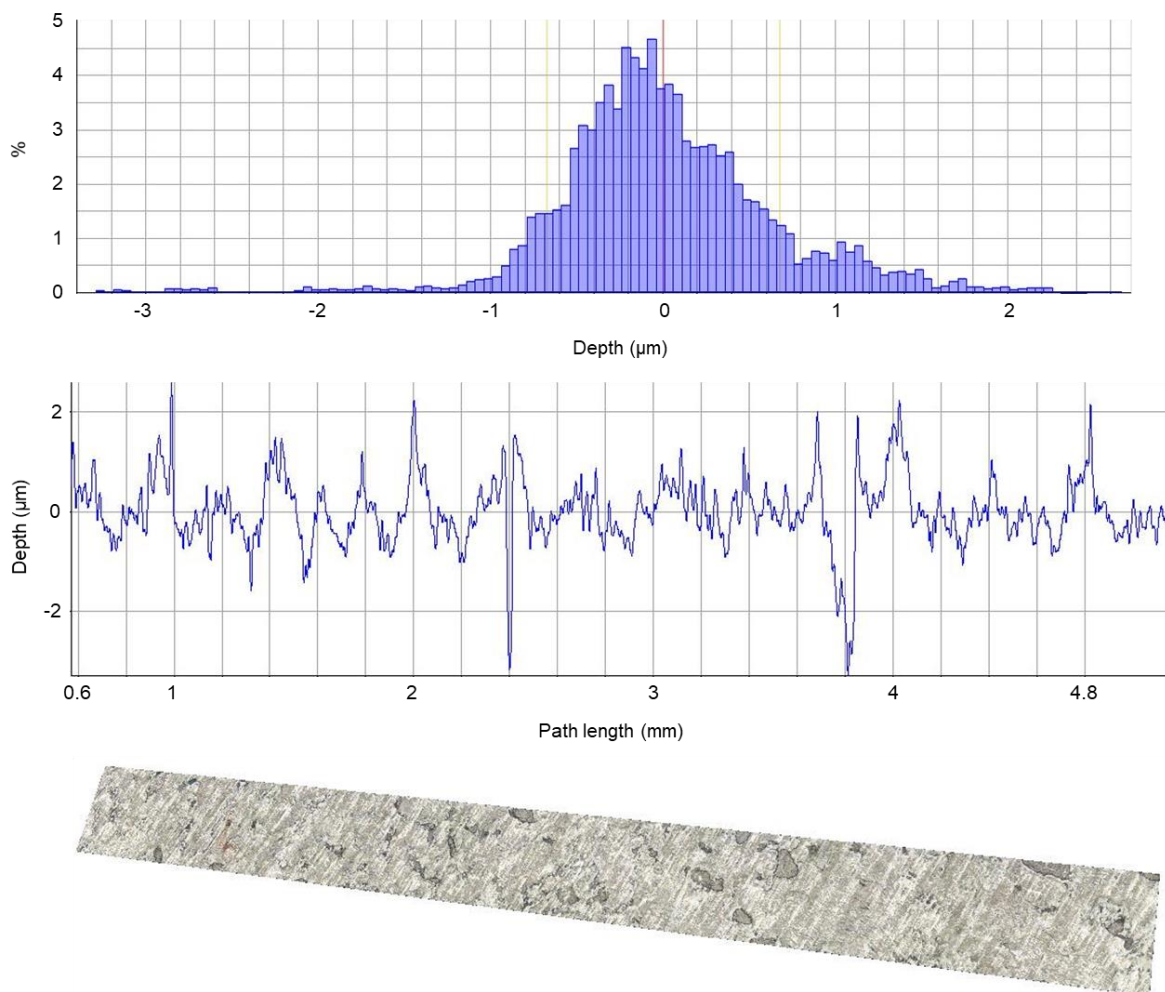


Figure 5.29 Plate roughness measurements taken before the programme of shear tests commenced as (a) a distribution plot of defect depths, (b) profile of depth along a cross-section against the grain of the plate, and (c) a 3D model of the profile.

During shearing, the surface of the plate changed as a result of soil-steel interactions. Measurements recorded during the programme of shearing are summarised in Figure 5.30 which shows all recorded roughness measurements (μm) as a function of position, orientation, and time (where position and orientation link to Figure 3.27 and time relates to chronological shearing episodes). Of note, the roughness measurements are presented as roughness averages (Ra) where each Ra were calculated as arithmetic averages of the absolute values of profile heights over each evaluation length (μm).

Figure 5.30 has been split to show measurements parallel and perpendicular to the shearing direction. It can be seen that as more shearing experiments are conducted, the roughness of the plate generally increases. This occurs regardless of whether the measurements are taken with or against the grain and is indicated by the superimposed black arrows for each grid position-orientation combination. The measurements taken against the grain, however, show roughness values of up to twice those of the measurements taken with the grain; this should be expected as grooves, analogous to striations, will be created in the direction of shearing by particle-plate interactions.

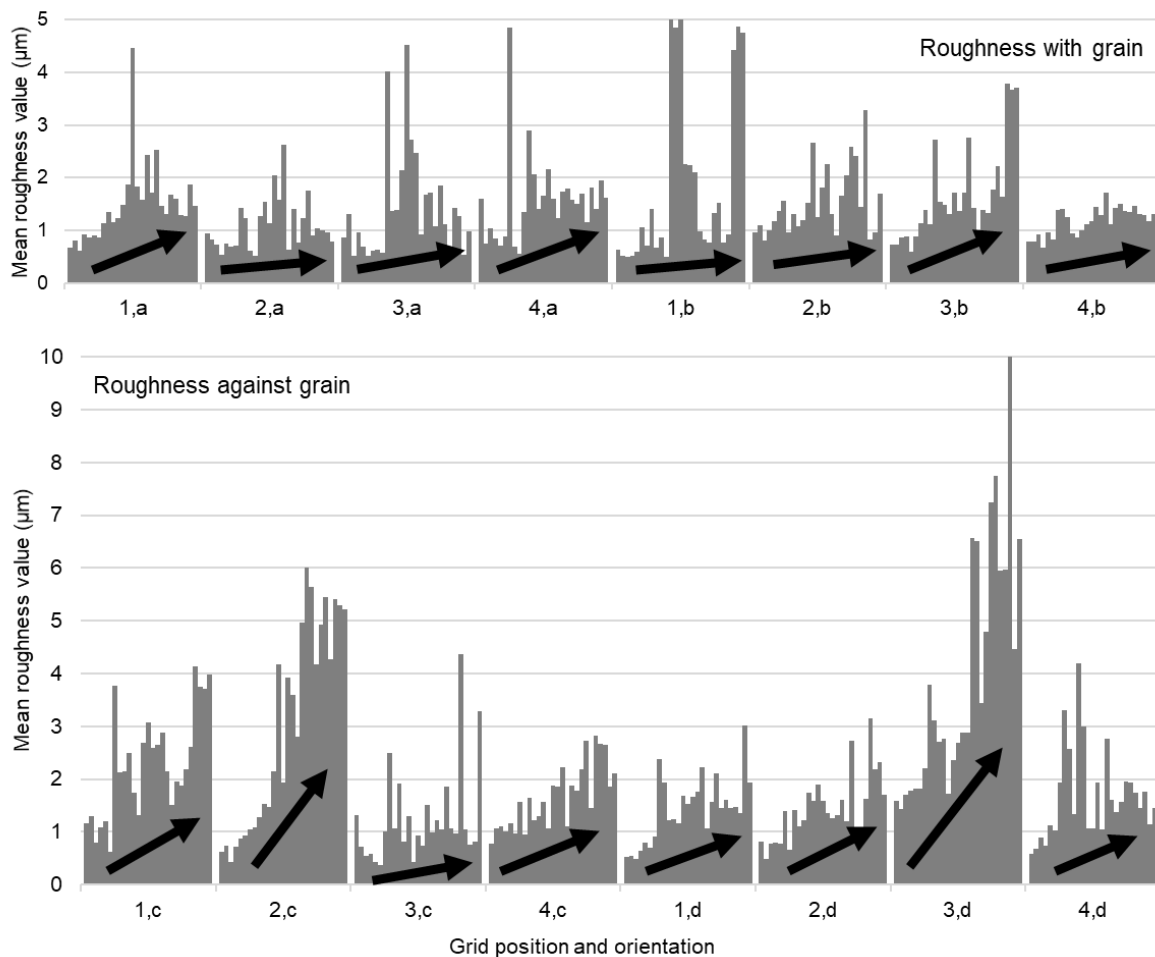


Figure 5.30 Plate roughness measurements with respect to position, orientation and time during shear box experiments. Superimposed arrows depict the general trend of each dataset.

5.2 Soil-steel interaction generated AE: Laboratory experiments

AE generated by soil-steel interactions was investigated using a large-scale laboratory set up in which a steel pipe was buried within an LBS annulus. The LBS was then stressed using multiples of 20 lb weights to cause soil-steel interactions measured using piezoelectric transducers (Section 3.6). Example results are shown in Figures 5.31 and 5.33.

Figure 5.31 shows an example signal measured during the large-scale experiments, by one sensor, plotted as an amplitude with time. The time is relative and taken over a period in which weights were being added to the soil. Several defined peaks can be seen in the signal, partly as a result of the weights being added in 20 lb increments (in this example 5) and partly as a result of the numerous particle reactions occurring with each addition. Signal reflections from pipe ends and joints should additionally be considered. The voltages measured are very small with a maximum of 0.005 V in this example, and a maximum signal of 0.04 V within the test series (Weighted 1 in Table 3.8). Notably a continuous background noise of < 0.0015 V was measurable throughout, although appropriate filtering could be applied to remove it; the noise remains during periods of no activity.

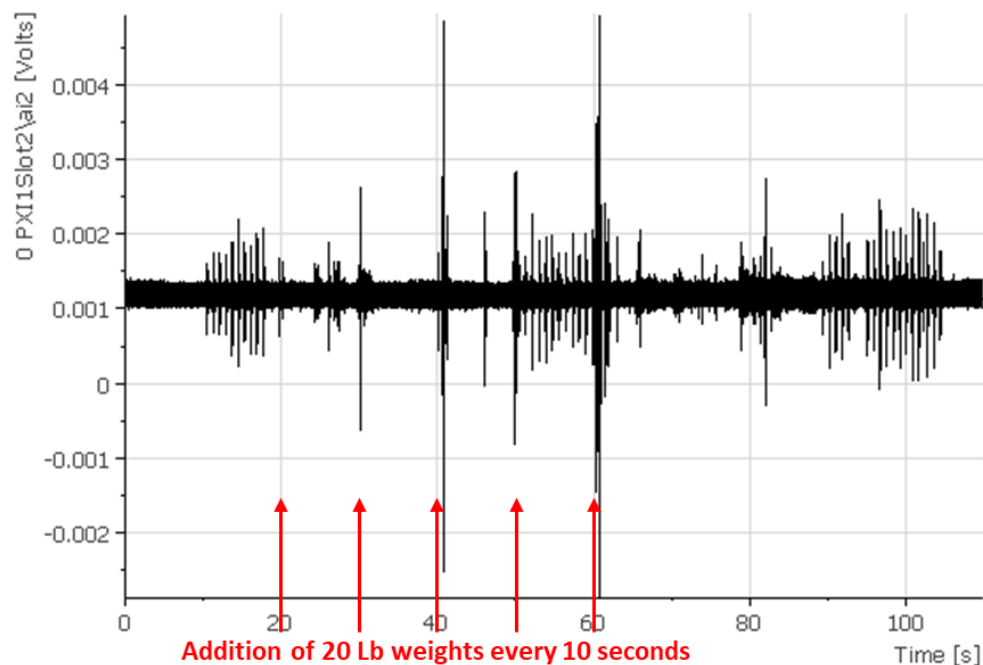


Figure 5.31 Signal amplitude (Volts) with relative time (seconds) during the addition of 100 lbs of weights to the top of a free-steel-soil pipe system.

Figure 5.32 relatedly plots the corresponding frequency spectrum for the example signal in Figure 5.31, but for three sensors at different distances. The figure shows that the resulting signal was relatively broadband, although tending towards higher frequencies, with small but distinguishable peaks visible around 25 and 45 kHz. The peaks at 25 and 45 kHz suggest that AE of these frequencies

were being generated within the system as a result of soil-steel interactions. Table 2.5 showed that grain friction has been observed to produce frequencies including 25 and 45 kHz, whilst Section 5.1.2 demonstrated that a range of frequencies generally between 20 and 80 kHz were plotted. Consequently, the large-scale buried pipe experiment, shear box experiments, and published works are all in agreement and it is likely that grain friction generated AE has occurred.

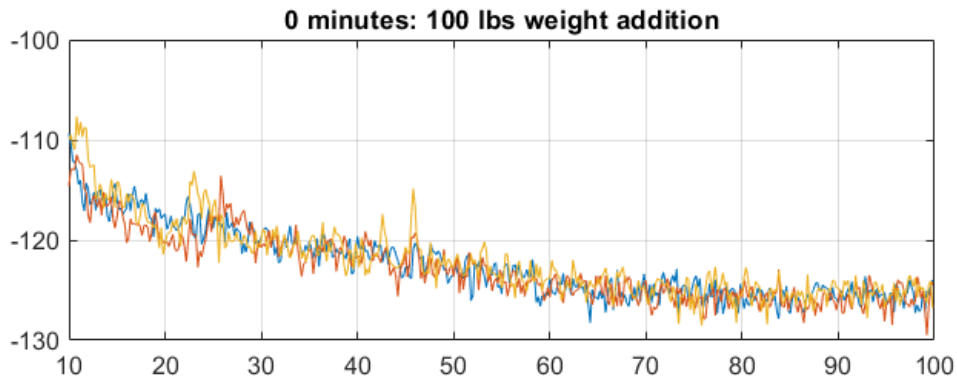


Figure 5.32 Frequency spectra measured during the addition of 100 lbs of weights to the top of a free-steel-soil pipe system.

Figure 5.33 shows more signal amplitudes with time for a similar weighted test. The figure however shows results for all three sensors and includes the addition, removal and increased addition of weights.

Comparing Figures 5.32 and 5.33 many similarities are observable. Peak voltages range between 0.003 and 0.03 V, whilst numerous signal peaks can be seen with the addition of individual weights and multiple soil-steel interactions. Notably though, a difference in the signals measured can also be seen for the different weights, and therefore applied normal stresses. For sensor 3 the initial addition of weights creates signals peaking at 0.027 V (after 100 Lbs has been added), whereas the re-addition of weights causes smaller signals peaking at 0.016 V. This implies that the soil undergoes less restructuring as less soil-steel interactions have occurred with Smith (2015) suggesting that soil behaviour is dependent on stress history.

Furthermore, signal peaks, albeit much smaller in voltage, may also be seen during the removal of weights and suggest that the soil continues to restructure as the normal stresses change. This effect was monitored by also measuring RDCs. However, given the very small signals detected, did not provide sufficient data.

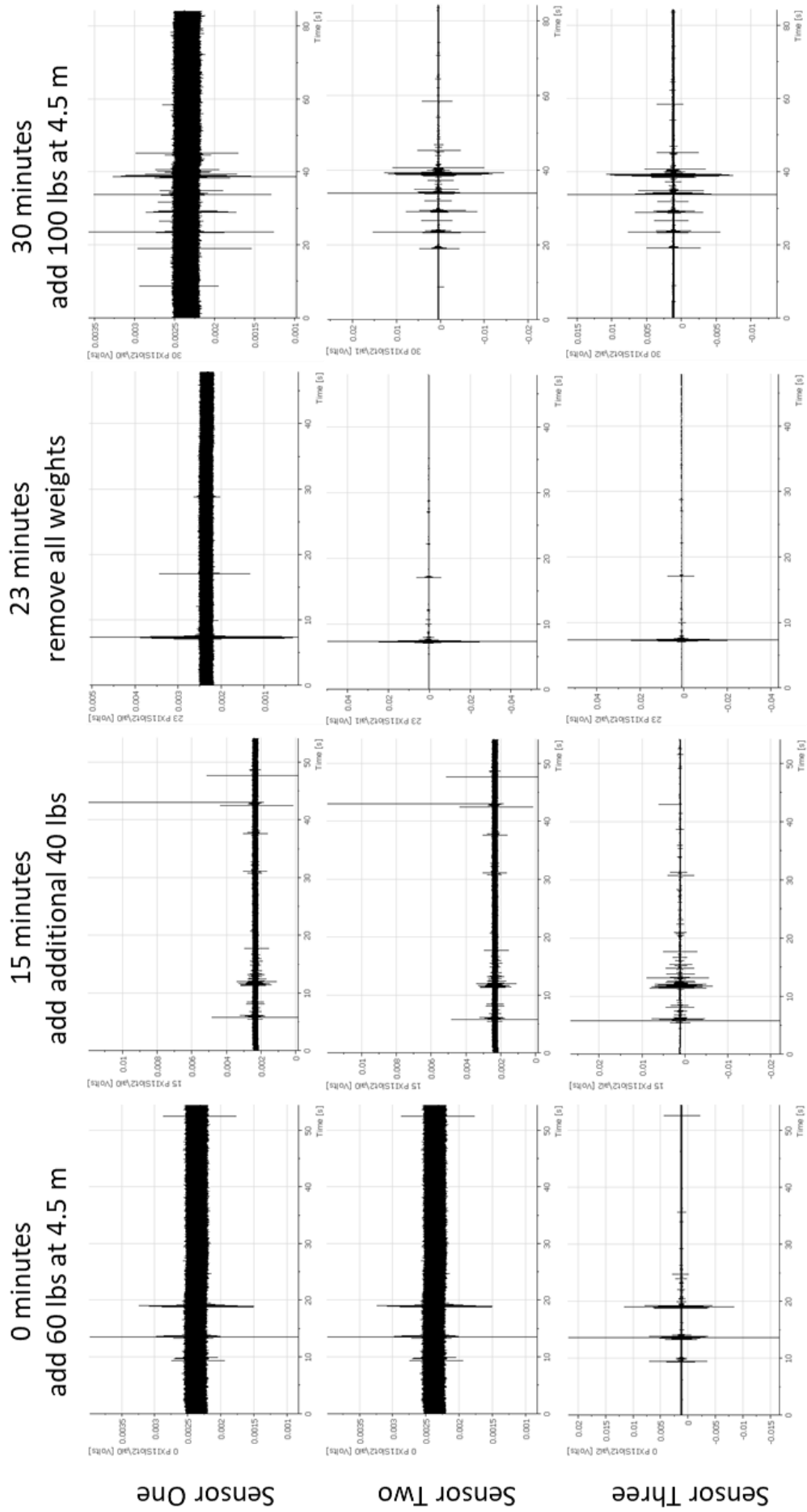


Figure 5.33 Signal amplitude (Volts) measured with relative time (seconds) during the addition, removal and re-addition of weights to the top

of a free-steel-soil pipe system in 20 lb increments.

5.3 AE equipment

The measurement and collection of AE data was orchestrated using equipment as described in Section 3.1. Although the AE measured can be considered representative, bias and errors within the result, as a result of the methodology and inherently differing sensitivity of individual components, should always be considered during their analysis.

5.3.1 Signal input sources

The signals from two input sources were compared against several criteria in order to ascertain the best source for experimentation whilst also characterising the signals generated. The sources used were pencil lead breaks, with a 0.9 mm Bic mechanical pencil, and the dropping of a 10 g ball bearing from a height of 10 cm, aided by a guide tube. Other sources were considered but found to be inappropriate (Section 3.2.1).

Figure 5.34 shows example results for the raw waveforms of a pencil lead break (left) and a dropped ball bearing (right). These are shown as time-amplitude graphs (seconds-Volts). Comparatively, Figure 5.35 shows the calculated frequency-amplitude spectra (kHz-Volts) for the same tests. It should be noted that several repeat tests were conducted at multiple propagation distances as described in Section 3.2.1; the results shown in Figures 5.34 and 5.35 are only representative.

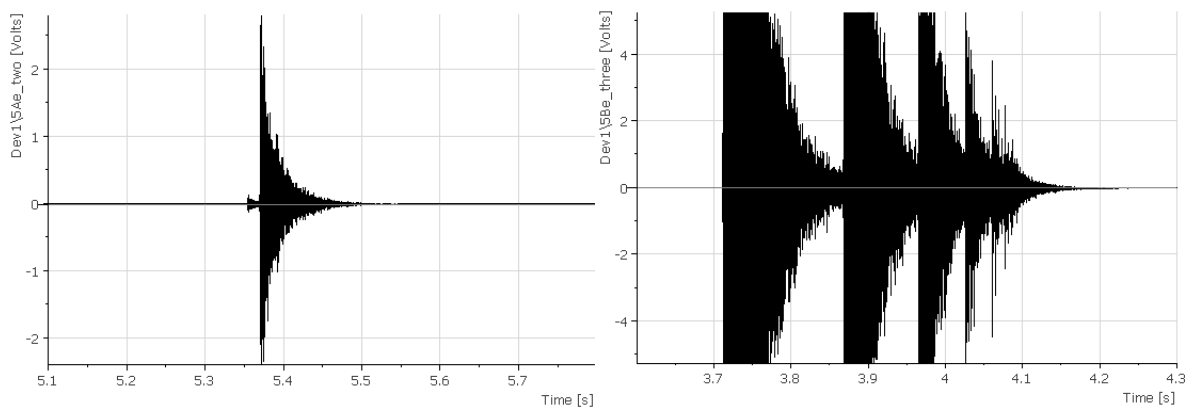


Figure 5.34 Raw waveforms for the measured amplitudes (Volts) of a pencil lead break test (left) and a dropped ball bearing test (right) after 4 m propagation in a steel pipe.

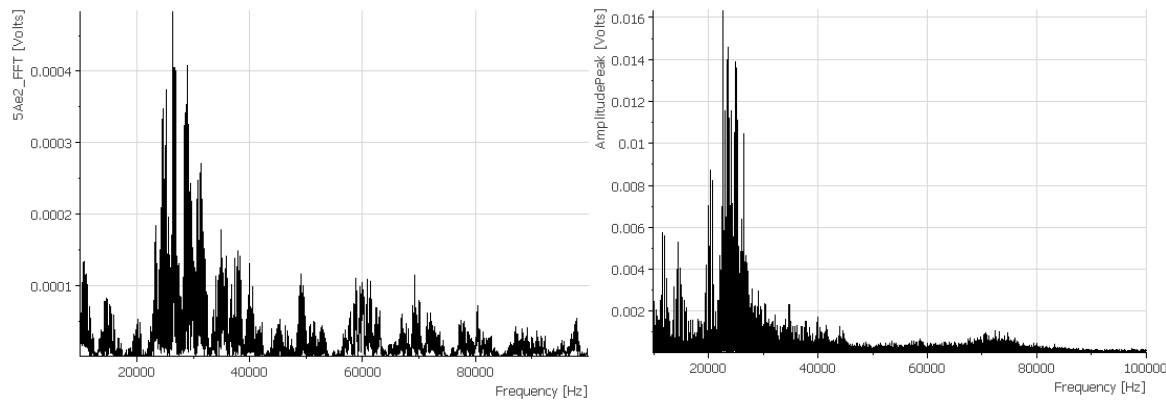


Figure 5.35 Calculated frequency spectra for a pencil lead break test (left) and a dropped ball bearing test (right) after 4 m propagation in a steel pipe.

Figures 5.34 and 5.35 show that the two sources produced very different waveforms from which several distinguishing features can be determined. These features are summarised in Table 5.3.

Table 5.3 A comparison of the signal characteristics for a pencil lead break and a dropped ball bearing.

Property	Pencil lead break	Dropped ball bearing
Relative amplitude (at 4 m propagation)	> 4 Volts	< 3 Volts
Average signal duration	0.20 seconds	0.50 to 0.59 seconds
Frequency range (at 4 m propagation)	23 to 50 kHz	20 to 30 kHz
Peak frequencies (at 4 m propagation)	23 to 30, 33, 38 kHz	21, 23 to 25 kHz

An ideal signal for acoustic testing should represent a Dirac delta function. A Dirac delta function may generally be defined as very short in duration, infinite in amplitude, and broadband in frequency (Figure 3.9).

Considering signal durations, Figure 5.34 suggests that pencil lead breaks are more appropriate sources as their signal duration is much shorter than that of a dropped ball bearing. Considering signal amplitudes however, the dropping of a ball bearing produces a much higher amplitude and therefore has a greater propagation potential than a pencil lead break. The signal created by the ball bearing, though, is formed from several transient signals within a small burst. This type of signal is more representative of soil-steel interactions, which would occur in small bursts from multiple locations within the field, however, for understanding simple wave propagation the input of multiple, uncontrolled signals within a short time period forms complex signals which make modal analysis complicated.

The multiple transient signals produced by the ball bearing can be seen to be very similar in shape though. This implies that the dropping of a ball bearing provides a very reproducible signal. Other ball bearing drop tests confirm this, generating the same signal. This is unlike the pencil lead breaks which,

although producing similar signal shapes, range in amplitude and sometimes contain secondary signals, such as seen in Figure 5.34. These secondary signals are likely caused by the initial pencil contact and/or uneven breakage, although given that they are so small can be easily filtered out or left to attenuate.

In terms of frequency content, the calculated frequency spectrum for a pencil lead break suggests frequency dominance across a range of 23 to 50 kHz. Peaks within this range may be seen at 23, 30, 33 and 28 kHz. Comparatively, a frequency range of 20 to 30 kHz may be seen for the dropped ball bearing with peaks at 21, 23 and 25 kHz. The signals produced by pencil lead breaks are therefore more broadband than dropped ball bearings, which, considering the range of frequencies known to be generated by soil-steel interactions (Section 2.3.2) again makes pencil lead breaks more appropriate signal sources.

5.3.2 Sensor-structure coupling

The sensitivity of an R3 α piezoelectric transducer to variations in coupling method was investigated by focusing on two main variants: the use of a couplant and the strength of contact. This was done in order to characterise signal variation as a result of instrumentation.

Six variations as discussed in 3.2.2 were used, the results of which are summarised in Figure 5.36. Figure 5.36 shows the measured (left) and average (right) signal voltages for the different tests.

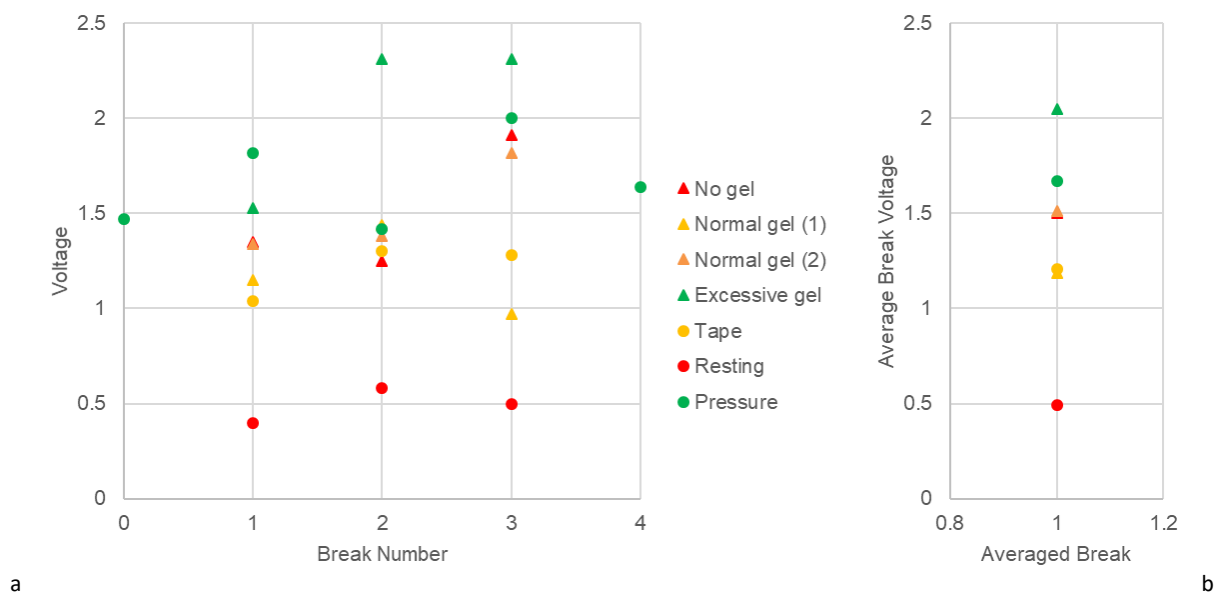


Figure 5.36 (a) Measured and (b) averaged voltages of pencil lead break signals with different sensor-structure couplings.

Figure 5.36 shows that the smallest measured amplitude was recorded when the sensor was resting on, rather than attached with pressure to, the structure. Contrastingly, the largest measured signal was recorded when an excessive amount of silicone gel couplant was used. The extreme

measurements were the result of different variation types, although relationships within variations types are still identifiable.

In terms of contact pressures, for example, it can be seen that increasing the contact pressure increased the strength of the measured signal. For a small contact pressure, represented by resting the sensor on the structure, a relatively small average amplitude was measured at 0.5 V; this was the smallest of all the variants. Applying a medium contact pressure, however, drastically increased the signal strength to over double those of the resting tests, averaging 1.2 V, whilst applying even more pressure further increased the signal strength again, although not as much. Furthermore, the additional use of cable ties, increasing the contact pressure again, raised the average signal strength to 1.7 V. The sensor-structure contact pressure was therefore heavily influential.

In contrast, the use of a couplant showed no clear relationship to signal strength. For the tests conducted with no couplant (no silicone gel), signals strengths can be seen to be on par with those in which a normal, pea-sized amount of gel was used. When an excessive amount of couplant was used though, a clear difference could be seen.

For the tests in which an excessive amount of silicone gel was used, the average strength of the measured signal rose by 50% in comparison to the normal tests. Overall, this set up yield the greatest signal strength for all the variants tested suggesting that the use of a couplant affected sensor sensitivity. However, given that no differences in signal strength were seen between the use of no and a pea sized amount of couplant, it is possible that there is a threshold to the amount of couplant required to affect signal strength.

Variations in the amplitude of the initial signal should also be considered as, although the signals were input with the same method, Suase (2011) shows that the angle of break and length and free lead can affect the signal; these parameters were not well controlled during testing. Consequently, the reliability of the results is reduced. To fully investigate the effects, at least two sensors would be required; one sensor to establish the quality of the input signal and one to test the sensitivity of different methods of attachment.

5.3.3 Sensor bias

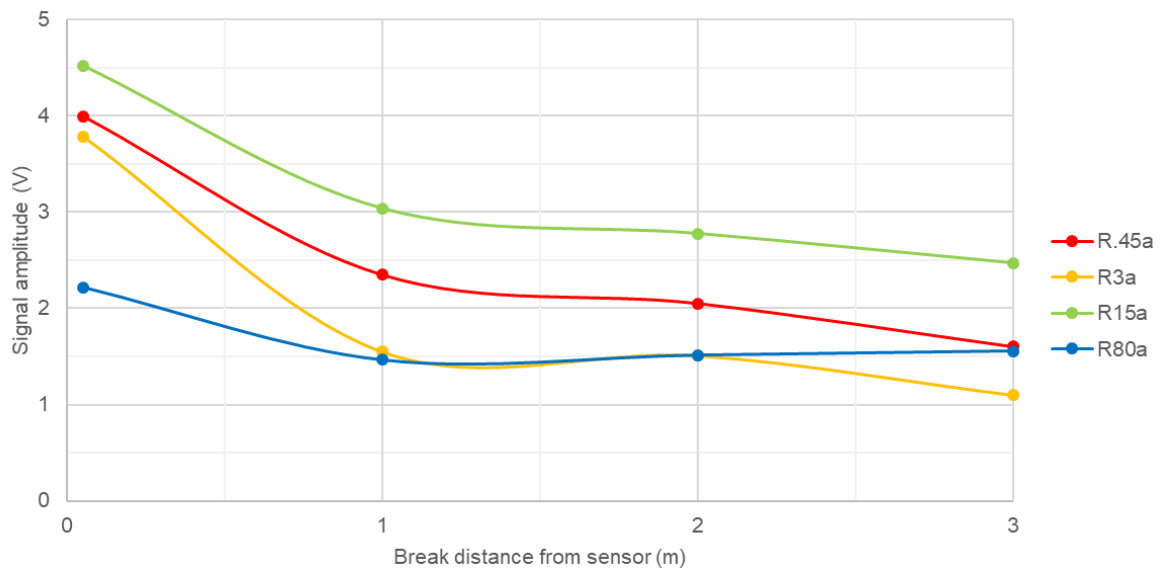
Bias as a result of the resonant frequencies inherent to different piezoelectric transducers was investigated using four sensors from MISTRAS alpha series. Specifications for each sensor are summarised in Table 5.4 whilst further information may be found in Appendix 4.0.

Table 5.4 Specifications summary for alpha series piezoelectric transducers (MISTRAS).

Name	R.45 α	R3 α	R15 α	R80 α
Resonant frequency (kHz)	20	29	75	200
Operating range (kHz)	5-30	25-70	50-400	200-1000
Peak sensitivity (dB)	85	80	80	58

Figures 5.37 and 5.38 show the results of the investigation. Figure 5.37 shows the averaged signal amplitudes (Volts) over four propagation distances (m), whilst Figure 5.38 shows the corresponding average frequency spectra (kHz) for the four sensors at 2 m propagation. Several observations may be made from each.

It can be seen from Figure 5.37 that the responses from the four sensors change dependent on propagation distance. The highest measured amplitudes, for example, were recorded by the R15 α sensor for each distance whilst the R.45 α sensor consistently recorded amplitudes around 0.5 V smaller. The lowest amplitudes on the other hand were recorded by a mixture of the R80 α and R3 α sensors with the responses from the R80 α and R3 α sensors practically the same at propagation distances of 1 and 2 m. These variations in response suggest that other factors, such as those described in Sections, may be influencing the measurements alongside the frequency response of each sensor. Figure 5.38 however, investigates the frequency responses at 2 m propagation.

**Figure 5.37** Average measured signal amplitudes with propagations distance for four different piezoelectric transducers.

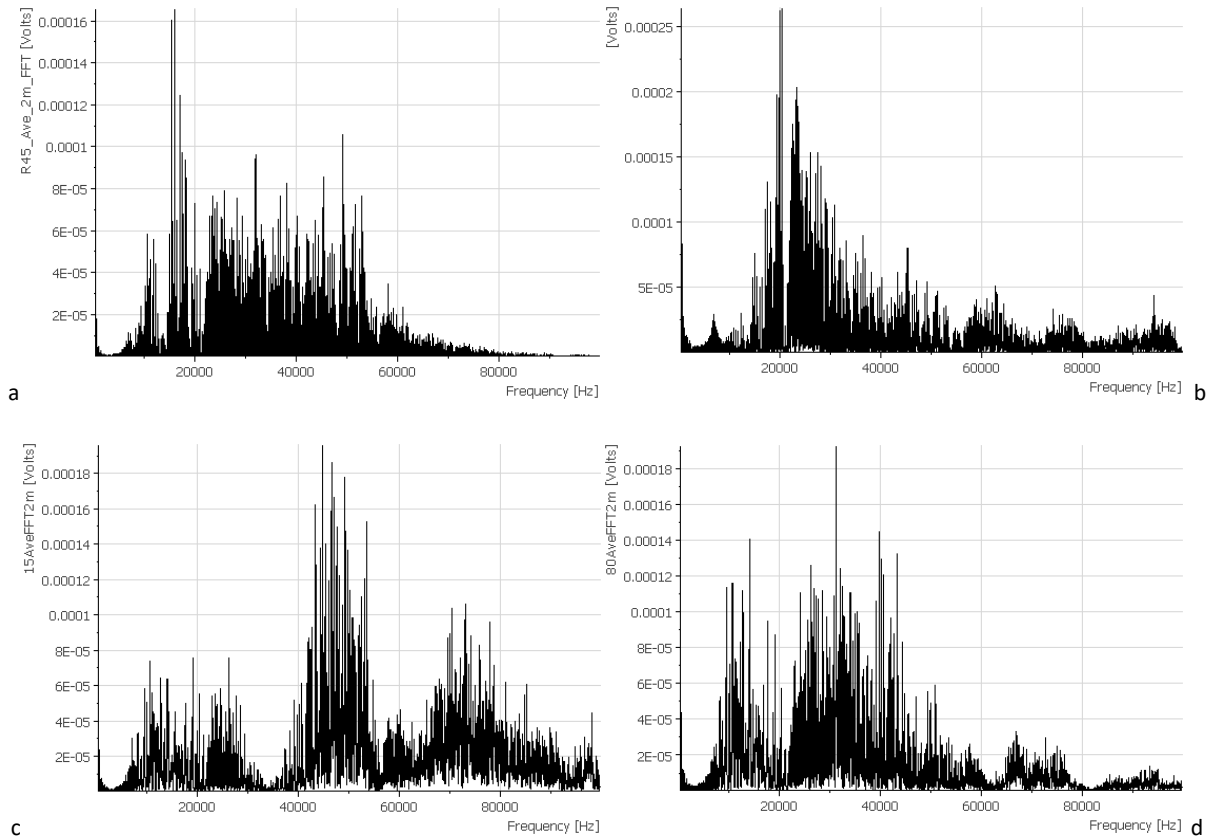


Figure 5.38 Average measured frequency spectra for four piezoelectric transducers: (a) R45, (b) R3, (c) R15, and (d) R80.

Figure 5.38 shows the average recorded frequency spectra (kHz) for the four sensors at 2 m propagation. The responses have been cut at 100 kHz as this was the filter limit and frequencies above this are therefore a result of aliasing. It can be seen that each spectrum is different, peaking at a variety of frequencies. This may be a result of inhomogeneities in the sources used but is more likely a result of the different sensor responses. Figure 5.38a for example, shows a strong peak between 15 and 20 kHz; specifications suggest it should peak at 20 kHz. Similarly, Figure 5.38b shows peaks between around 18 and 20 kHz; specification suggest peaks at 29 kHz. The frequency spectra seen are therefore in accordance with the manufacturing specifications, affecting the results recorded.

The responses are not necessarily centred around the suggested resonant frequencies however with Figure 5.38c, for example, showing three ranges over which the sensor response was greater. This is most likely a combined result of inherent differences in the actual response of each sensor (i.e. the specifications listed are what the manufacturers aim for, the actual response, although fitting the criteria, may vary a little), variations in the source signal, and characteristic of the band-pass filters in the amplifiers. Table 5.5 therefore summarises the key features for each frequency spectrum for different propagation distances and sensors. A lot of cross-over may be seen.

Table 5.5 The spectral features for different transducers at different propagation distances.

Propagation distance (m)		0.05	1	2	3
R.45 α	Dominant frequency range(s) (kHz)		22 to 56	10 to 17	10 to 16
			64 to 77	22 to 53	22 to 49
	Peak (kHz)		27	31	32
	Local peak(s) (kHz)		11, 46, 74	14, 40, 67	45, 67, 72
R3 α	Dominant frequency range(s) (kHz)	14 to 46	14 to 40	14 to 53	14 to 63
	Peak (kHz)	20	19	20	20
	Local peak(s) (kHz)	23, 35, 93	35, 59, 95	23, 28, 45	23, 28
R15 α	Dominant frequency range(s) (kHz)	10 to 30	22 to 30	10 to 29	10 to 29
		40 to 65	38 to 55	40 to 56	
		68 to 90	56 to 90	66 to 90	
	Peak (kHz)	48	46	45	48
	Local peak(s) (kHz)	11, 60, 73	25, 60, 71	26, 54, 73	

5.4 Extraneous AE: Water flow

The characterisation of water flow within pipes was studied experimentally using small-scale laboratory tests. Various results from this study are shown in Figure 5.39 which plot signal amplitudes as a function of time. Figure 5.41 relatedly shows the corresponding frequency spectra (kHz).

Figure 5.39 shows example results for raw waveform data (amplitudes) as a function of time (seconds). Four tests are shown to represent the range of flow speeds tested. These are: test 7 (Figure 5.39a), in which the flow speed was varied throughout; test 17 (Figure 5.39b), which had an average flow speed of 0.07 m/s; test 26 (Figure 5.39c), which had an average flow speed of 0.24 m/s; and test 19 (Figure 5.3d), which had an average flow speed of 0.56 m/s.

For test 7 (Figure 5.39a), during which the flow speed was varied, the figure shows that signal amplitudes varied between approximately 0.05 and 0.25 V and illustrates that flow speed effects AE generation. This effect is most likely as a result of temporarily increased turbulence as the water flow is disturbed (i.e. acceleration or deceleration) and interactions with the pipe wall increase. Moreover, considering that the strongest signals were measured at the start and end of the tests, it can be inferred that greater changes in the flow speed generate stronger signals (i.e. greater disturbances to flow generate greater turbulence). Contrastingly though, Figure 5.39a also shows that when there is no water flow (i.e. at the start, 0 to 4 seconds, and end, > 34 seconds, of the test) an average and relatively constant voltage of around 0.008 V can be seen. This may however be attributed to background or electronic noise.

For the constant rate flow tests, relatively constant signals can be seen during both periods of water flow as well as periods of no water flow although to different levels. At flow speeds of 0.07 m/s for example (Figure 5.39b), the signal remains relatively stable and fluctuates around a mean value of

0.1 V. At 0.24 m/s (Figure 5.39c), however, the signal is less stable and fluctuates within a 0.05 V range which averages a higher signal strength of 0.2 V. By 0.56 m/s (Figure 5.39d) though, the signal then fluctuates around a decreased average amplitude of 0.025 V.

During periods of changing water flow, i.e. acceleration and deceleration (when the tap is turned on and off), like with Figure 5.39a, Figure 5.39d shows that the signal increases in amplitude. This suggests that the water flow was more turbulent. Figures 5.39b and 5.39c do not show this however, instead remaining relatively constant throughout flow. This may be explained by comparing the starting and finishing amplitudes of Figures 5.39a and 5.39d (during known periods of accelerating or decelerating water flow) which can be seen to range between around 0.1 and 0.3 V. Given that the measured amplitudes within Figures 5.39b and 5.39c sit within this range, it is possible that the flow regime as a result of acceleration, constant flow, or deceleration in these tests does not change throughout; changes in flow speed are therefore not registered as changes in amplitude. This is emphasised in Figure 5.40 which shows that between signal amplitudes of around 0.13 and 0.18 V, the flow regime is turbulent within the pipe used for experimentation.

Figure 5.40 shows average signal amplitudes (Volts) as a function flow speed (m/s) and Reynold's number for all flow rate tests conducted. Boundaries for the three flow regimes, laminar, transitional, and turbulent, have additionally been superimposed (red dashed line). The figure is therefore a summary of results and enables a relationship between amplitude and flow speed to be established. This is shown as a third order polynomial (black dashed line) over the range tested.

Flow speeds ranging between 0.005 and 0.56 m/s were measured during testing. The highest signal amplitude occurred at an approximate flow speed of 0.2 m/s; this is also the point at which the flow regime changes from transitional to turbulent, implying that flow regime can have a significant affect on acoustic noise. During laminar and transitional flow regimes, the average signal strength can be seen to increase at an increasing rate. During turbulent flow (>0.2 m/s) it can then be seen to initially decrease at an increasing rate before appearing to continue to decrease linearly. The transition from laminar to turbulent flow at 0.2 m/s is therefore pivotal, but also demonstrates that AE noise may not be used to determine flow rates or regimes; the solutions are non-unique in terms of amplitude.

Overall, the measured signal strengths range between 0.01 and 0.2 V for the tested range of flow speeds. These are generally lower than the threshold value used in AE data collection and 1000 times greater than those measured by Husin et al. (2013), who suggest signals of 0.01 mV at flow velocities of 0.8 m/s. The values are however much smaller than those detected by Gao et al. (2015) who suggest amplitudes ranging between 0.5 and 1 V for flow velocities between 5 and 9.5 m/s, although these are much faster than those measured in this experiment. Additionally, the equipment and settings

used were different in each case and the sensitivities of sensors and amplification used during data collection are not considered in the comparisons. Considering this, and the non-unique nature of the solutions, amplitude may not be the best characterisation property. More in depth investigation would be required to confirm this though.

The frequency content of signals was consequently studied with Figure 3.41 showing example frequency spectra for the four selected flow tests. Most notably, it can be seen that flow noise is relatively low frequency with most energy concentrated below 40 kHz. For the variable speed test (Figure 3.41a), two peaks can be seen, one at 17 and one at 22 kHz. For the constant rate tests though (Figures 3.41b 3.41c 3.41d), only one peak can be seen at 17 kHz. This suggests changing flow speeds generate a wider range of frequencies and, linking to previous discussions, may be a result of a changing flow regime. Constant flow rates on the other hand appear to generate a constant signal, in this case 17 kHz.

These frequency results contradict those of published works (Table 5.6) with numerous authors suggesting that much higher frequency signals should be measured. As discussed though, it should be considered that the recorded frequencies will be heavily dependent on the sensors and filters applied during data acquisition. Consequently, for the instrumentation set up used during the investigation, a 17 kHz signal can be assumed correct.

Table 5.6 A comparison of frequency, flow speed, and sensor information for published works on fluid flow in pipes.

Media	Frequency range	Flow velocity	Sensor details	Reference
Water	10 to 40 kHz	0 to 0.5 m/s	R3 piezoelectric transducer coupled with silicone gel and cable ties	Laboratory experiments
Water	0 to 70 Hz and 170 to 180 Hz	35 to 90 m/s	Laser doppler vibrometer, Polytec PDV 100	Dinardo et al. (2018)
Pressurised water/gas	< 100, > 500 kHz	5 to 9.5 m/s	Piezoelectric ultrasonic sensors	Gao et al. (2015)
Pressurised water/gas	100 to 500 kHz	0.3 to 2 m/s	Piezoelectric AE sensor, PICO type 150-750 kHz	Husin et al. (2013)
Pressurised water/gas	50 to 150 kHz	0 to 0.07 m/s	Piezoelectric probe with AMSY-5 (Vallen-System)	Fang et al. (2013)
Pressurised water/gas with sand particles	100 to 500 kHz	5.5 to 8.5 m/s	Piezoelectric ultrasonic sensors	Gao et al. (2015)

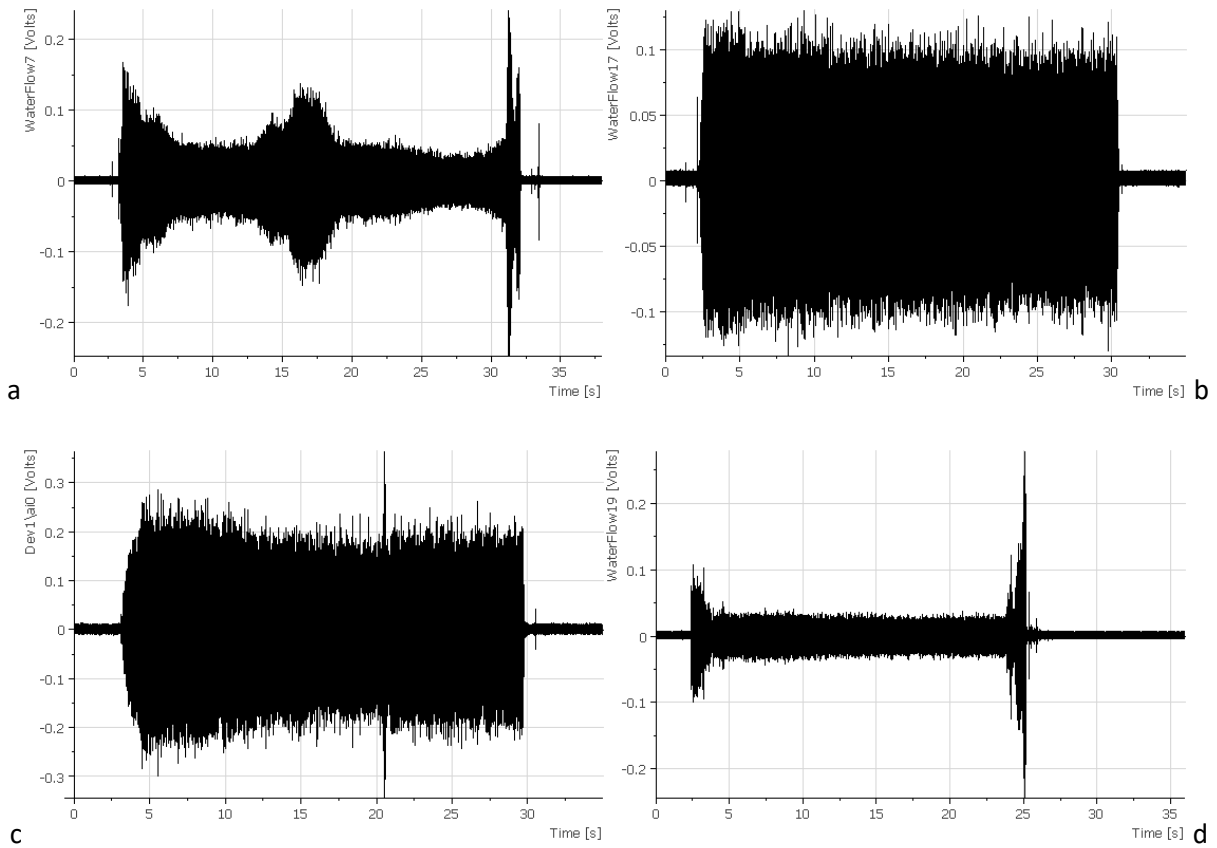


Figure 5.39 Raw waveforms (amplitude (v) verse time (seconds)) for water flow tests: (a) 7 (variable flow rate), (b) 17 (0.07 m/s), (c) 26 (0.24 m/s), and (d) 19 (0.56 m/s).

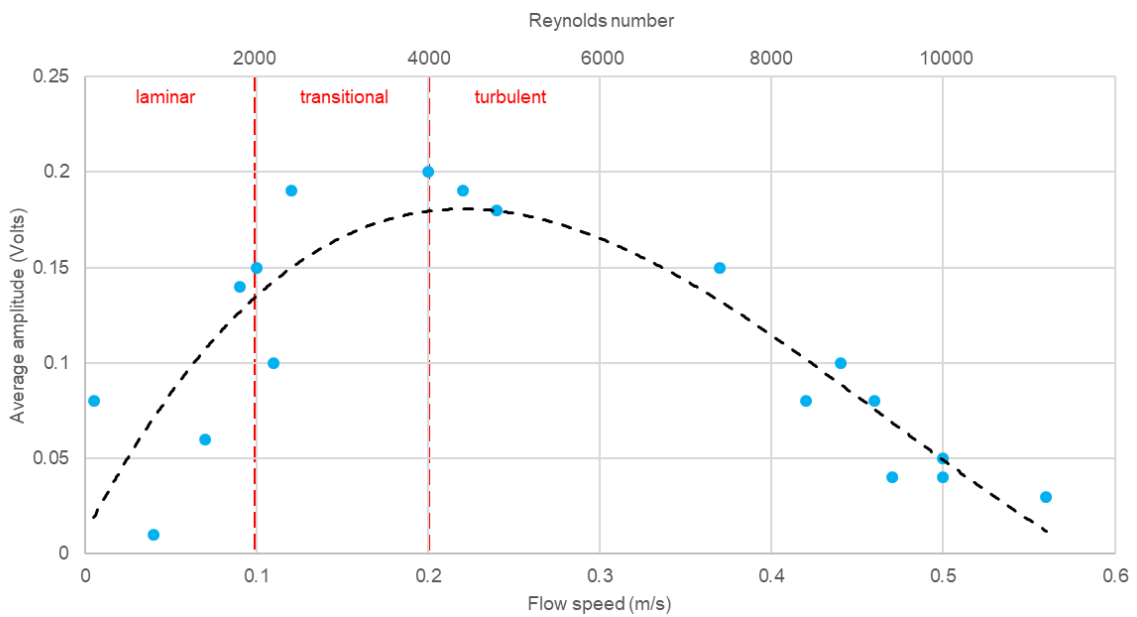


Figure 5.40 Average measured AE signal amplitude with water flow rate where the blue dots represent data point, the black dashed line is a third order polynomial best fit, and the red dashed lines represent typical boundaries defining the flow regime.

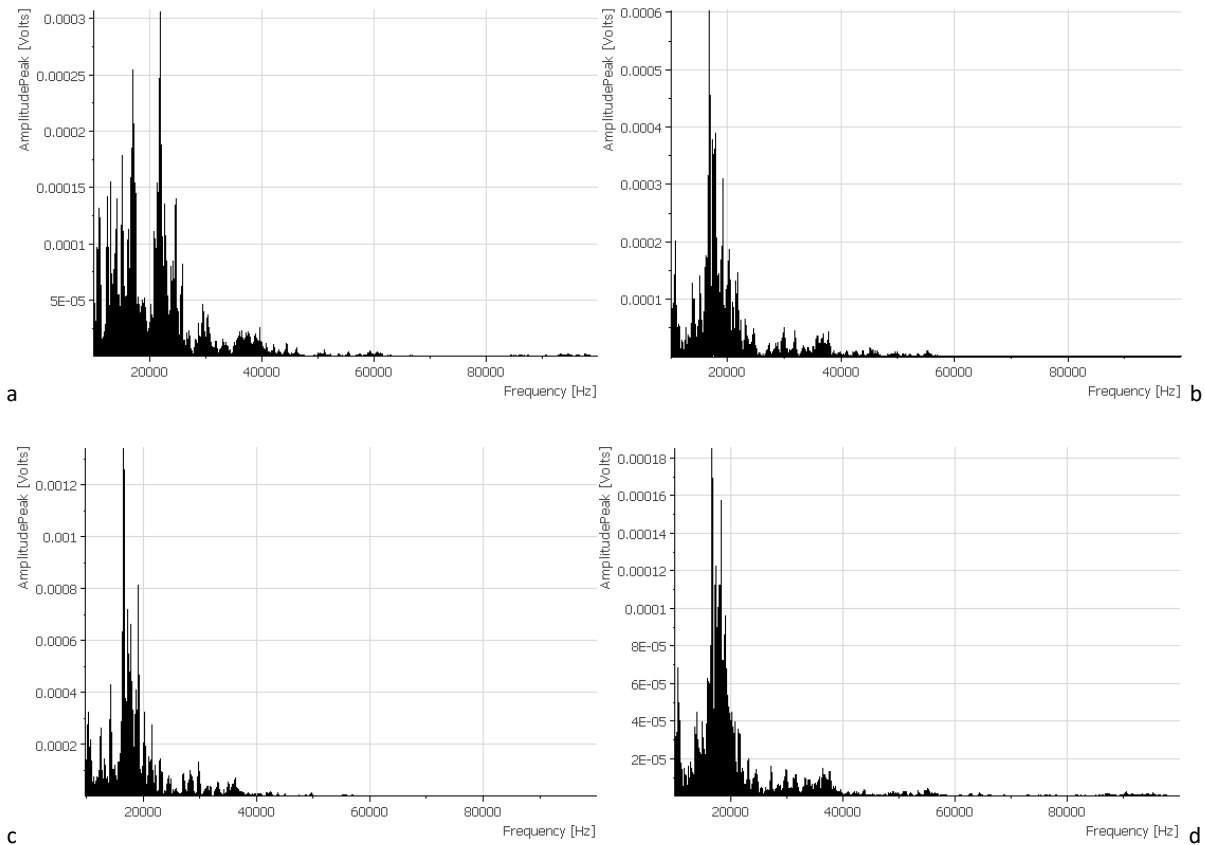


Figure 5.41 Whole test frequency spectra for water flow tests: (a) 7 (variable flow rate), (b) 17 (0.07 m/s), (c) 26 (0.24 m/s), and (d) 19 (0.56 m/s).

5.5 Chapter summary

The characterisation of AE generated from sources including water flow noise and soil-steel interactions has been investigated using a variety of experimental methods. The methods by which results were attained (e.g. input sources and sensor-structure coupling) were also studied.

Large direct shear box tests allowed for the influence of physical parameters on the mechanical and acoustic properties of soil-steel interactions to be studied. Most notably it was found that soil type, and the normal stresses subject to it, heavily influenced both mechanical and acoustic behaviours during compression and shearing. During shearing, the rate and way in which (i.e. constant or stepped increasing) a sample was sheared also influenced the observed behaviours. Clear empirical relationships were observed between measured AE parameters and imposed mechanical behaviours.

Following from this, large-scale experiments conducted on a buried steel pipe showed that changes in the external stresses to a system generated AE as a result of soil-steel interactions which, although small, were still measurable. The observed behaviours could be linked.

Small-scale tests investigating the AE data collection equipment revealed that pencil lead breaks provided ideal signals for determining wave propagation behaviours (linking to Chapter 4) whilst the

connection methods and choice of sensor effected the results obtained. Small-scale tests investigating water flow noise however showed that this was minimal and could be removed using simple filtering techniques both during and after the collection of data.

Chapter 6: Discussion: The development of a framework

6.0 Discussion: The development of a framework

The development of a framework for understanding soil-steel generated acoustic emissions in buried steel structures has two stages: (1) employing steel infrastructure as waveguides to create an effective AE sensor network (OB4) through understanding propagation within buried structures (OB3), and (2) interpreting subsequently measured AE behaviours within buried infrastructure environments (OB5) through the characterisation of AE sources and behaviours under different conditions (OB2).

These stages were summarised in Figure 1.3 which showed the steps involved in the development a framework and their place within the thesis structure. The figure also showed that there are numerous factors influencing the generation and propagation behaviours of AE which must be considered during development.

6.1 Stage 1: Employing steel infrastructure as waveguides

The first stage of the framework is to inform the development of an AE sensor network for monitoring buried infrastructure systems (OB4). This stage aims to create an efficient sensor network whereby the sensor spacing is cost effective (i.e. minimal sensor usage) whilst ensuring measured signals are still able to provide adequate information on ground/structure conditions.

Chapter 4 presented the results of investigations studying propagation and attenuation behaviours and how they are influenced by various factors including the structural geometry and burial conditions of a steel element. Moreover, the sensitivity of different sensors, sensor attachment methods, and analysis methods used to collect data were also investigated. Several conclusions were drawn regarding these influencing factors:

- Geometry
Attenuation is proportional to plate/wall thickness but relatively unaffected by shell radius. Geometry therefore affects wave propagation and consequently sensor spacings within a monitoring network.
- Burial system
Both the external and internal environments affect attenuation. The properties and condition of a burial soil therefore also affect sensor spacings.
- Connection methods
The sensitivity and mounting method of a piezoelectric sensor affects the signal measured. The choice of sensors and connection methods within a network thus affects the quality of results.

Figure 6.1 illustrates these findings showing an example of a buried pipe system where different influential factors have been labelled and colour coded; black factors relate to the structural geometry, blue factors relate to the generated AE, and red factors relate to the burial system. Additionally, the results presented in Section 4.1.6 demonstrated the affects for example case studies.

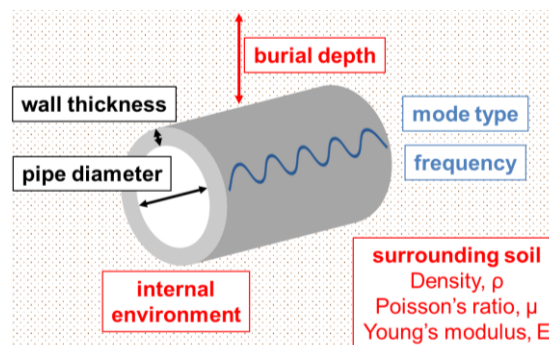


Figure 6.1 The factors influencing wave propagation and attenuation within an example pipe burial system where the pipe is considered a waveguide.

It should be noted that the factors in Figure 6.1 can change at a local scale, and thus, several questions much be considered whilst developing a sensor network.

1. What is the network measuring?
 - a. What are the AE sources and what frequencies/modes are likely to be generated?
 - i. What is the most appropriate sensor and coupling method to use?
 - ii. Are there extraneous AE sources?
 - iii. What limitations need to be imposed to ensure data is captured effectively?
 - b. How accurate does the system need to be?
 - i. What limitations can to be imposed to ensure data is captured effectively?
2. What is the structure-system like and how will this effect propagation and attenuation?
 - a. What are the internal/wall/external materials, and can they be quantified?
 - b. What is the structural geometry?
 - c. What is access like? (e.g. by foot only, regular maintenance hatches, etc.)
 - d. Do these factors (materials, geometry, and access) remain constant?

With these considerations, three overall steps for the design of a physical network are determinable: choosing appropriate hardware (physical equipment such as a sensor), choosing appropriate software (data capture considering limitations), and deploying the system with appropriate sensor spacings and attachment. These steps are illustrated in Figure 6.2 which emphasises their relation to the networks physical design. Furthermore, Figure 6.2 shows that after the deployment of a network system, data

capture, processing, and interpretation can then occur; these processes form stage 2 of the framework.

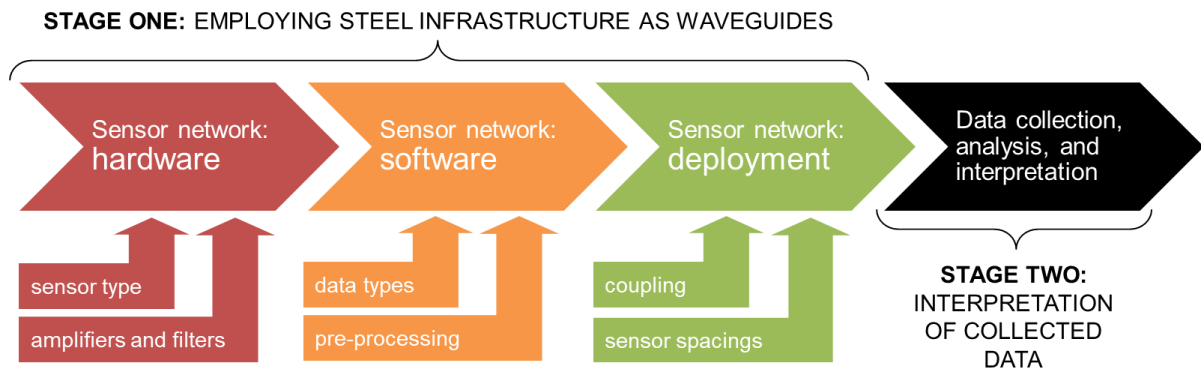


Figure 6.2 The three steps to developing a physical sensor network (stage 1), choosing appropriate hardware, choosing appropriate software, and deploying the physical network, for the collection, analysis and interpretation of AE data (stage 2).

6.1.1 Step 1: Hardware

As shown in Chapter 2, the fundamental design for an AE monitoring system (Figure 2.4) has been around since the 1980's. As technology has advanced, adaptations have been made to this design resulting in the most recent Slope ALARMS system (Figure 2.5). The purpose of the present thesis however is to use a passive waveguide, rather than the active waveguide as in a Slope ALARMS system, and thus the design must be altered to accommodate this. Such a design is summarised in Figure 6.3 whilst further explanation follows.

Waveguide: The aim of this work is to employ existing steel infrastructure as waveguides, therefore, other than assessing the appropriateness of the structure as a waveguide, this part of the system does not need to be considered.

Transducer: For soil-steel deformations, a sensor capable of measuring frequencies between 20 and 100 kHz is most appropriate (as shown by the results presented in Sections 2.3.3 and 5.1). A MISTRAS R3 α piezoelectric transducer by Physical Acoustics is ideal with an operating frequency range of 25 to 70 kHz and a resonant frequency of 29 kHz. Alternative sensors of similar specifications would also be suitable, although their attachment (in step 3) should be considered.

Amplifiers: Amplification of the measured signals is beneficial for later interpretation as it improves the signal-to-noise ratio through minimising electronic noise. Soil-steel interactions have been shown to produce measurable signals between -60 and -50 dB when recorded with a gain of 20 dB. A gain of 20 dB, where gain is a ratio of the output to input signals, has a magnification effect of ten times with

respect to the output voltage. Different gains may result in too much or too little amplification and consequent data loss, however this is dependent on the system set up.

Filters: Linking with the pre-processing suggested for step 2, filtering AE data as it is collected reduces the processing and storage of irrelevant data such as noise. To do this, bandpass filters between 10 kHz and 100 kHz are recommended. These can be inbuilt into amplifying equipment but may also be added as additional instrumental. Both have benefits.

Analogue-to-digital convertor or DAQ systems: For later computational processing, continuous analogue signals collected by a sensor should be discretely digitalised as a function of time and/or frequency using instrumentation. In an AE sensor network of multiple sensors, this component must be capable of taking several individual and simultaneous inputs for conversion such as with a DAQ system.

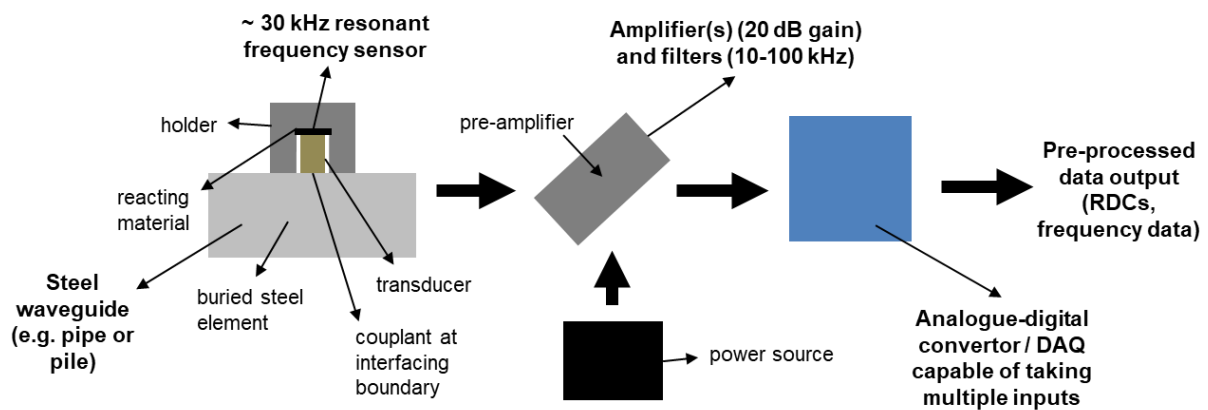


Figure 6.3 The proposed hardware required for employing steel infrastructure as waveguides in the field.

6.1.2 Step 2: Software

For the experiments conducted in Chapters 4 and 5, relatively simple LabVIEW programs were used to manage the recording of select data sets to appropriate capture (sampling) rates. The types of data collected, and its subsequent handling, are important to later analysis.

Data types: In terms of acoustic behaviours, RDCs and FFTs must be measured. From these parameters, absolute values and behavioural trends can be quantified whilst additional parameters, such as b-values, can be calculated. Chapter 5 showed that additional data collection, such as relative deformation and stress levels, was invaluable to fully understand AE behaviours in relation to deformation. However, the measurement of these parameters requires additional sensors/instrumentation to be set up during step 1 which are not necessary to an AE sensor network.

Processing: Linking with step 1, and to ensure that data is captured efficiently, frequency and amplitude filters should be applied to remove extraneous data such as electronic and environmental

noise. The removal of noise is aided by amplification, however further processing is still beneficial. A bandpass frequency filter between 10 kHz and 100 kHz should therefore be used to eliminate environmental and electronic noise as well as reduce the effects of potential aliasing during data collection. Additionally, for the measurement of RDCs a cut-off filter between 0.01 and 0.1 mV is suggested to remove unwanted environmental noise if necessary.

Capture rate: The capture (sampling) rate of different parametric values is a trade-off between the processing and power capabilities of the hardware, and the detail of real-time measurements desired. For frequency data, the Nyquist frequency must also be considered. The value (i.e. worth) of different data sets additionally varies, therefore, having different capture rates dependent on the parameter but also varying these rates independently in time, situation dependent, may be most appropriate; capture rates therefore link with stage 2 of the framework, data analysis and interpretation. This is illustrated in Figure 6.4 which shows a cycle of questions to consider when setting the rates.

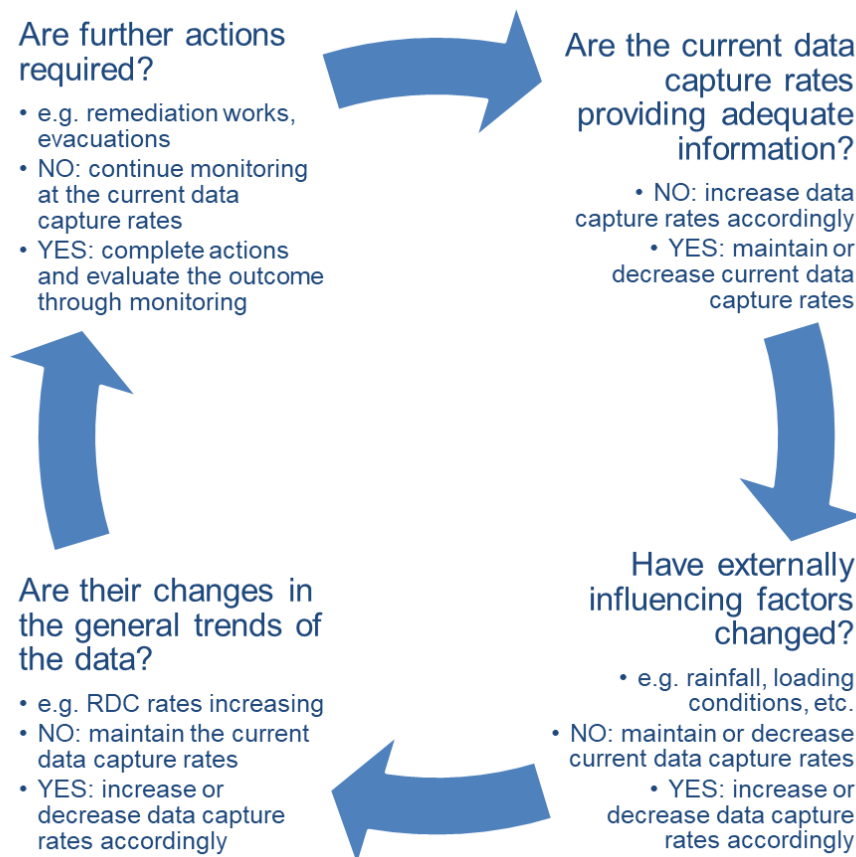


Figure 6.4 The cyclical nature of questions to consider when setting data capture (i.e. sampling) rates.

5.1.3 Step 3: Deployment

The physical deployment of an AE sensor network needs to consider factors such as sensor attachment and sensor spacings.

Attachment: For accurate results, the sensor should be attached using a consistent method. For steel structures, a specifically designed magnetic holder for R3 α piezoelectric transducers (Physical Acoustics) provides this by maintaining the sensor position and providing a constant contact pressure. This is achieved through magnetism and a soft pad onto which the sensor attaches within the holder. Additionally, a couplant such as silicone grease should be used between the ceramic of the transducer and the steel structure. The couplant should be used in great enough quantity to exclude air from the gap and thus reduce the acoustic impedance, increasing the sensitivity of the sensor.

Spacings: Sensor spacings are determined by the attenuation of the soil-structure system but may also be influenced by physical access to a structure. For measuring soil-steel deformations, theoretical (i.e. exact modelled values whereby 0.1% of the initial S0 wave mode's signal strength should remain) and suggested sensor spacings are given in Figures 6.5 and 6.6. These are for a point source travelling to one sensor (Figure 6.4a); the spacings could therefore be doubled in the field due to the omni-directional nature of AE sources (Figure 6.4b).

Both theoretical and suggested spacings are given to take account of differences between data collected by computational or laboratory models, in which the environment can be controlled, and in the field. The potential influence of factors not considered or modellable within computational and/or laboratory environments will affect attenuation, though this effect is likely to be small. Therefore, by providing suggested spacings smaller than the theoretical spacings, a margin of error is available within which the effects of any factors not considered can be absorbed.

Additionally, for measuring alternative phenomena, and linking with the choice of sensor during stage 1 (hardware), different sensor spacings may also be more appropriate dependent on the purpose of the system (e.g. for NDT a much higher sensitivity at frequencies different to those generated by soil-steel interactions would be required).

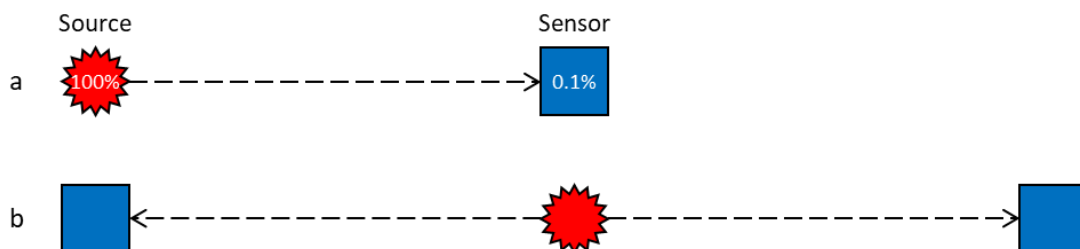


Figure 6.4 Suggested and realistic source-sensor spacings as a result of omni-directional AE sources in the field.

Figure 6.5 shows example signal strengths as a function of propagation distance for five burial systems: air-steel-air, air-steel-LBS, air-steel-clay, water-steel-air, and water-steel-LBS. These have been calculated for a burial depth of 5 m using the attenuation equation (Equation 6.1):

$$k = 20 \log \frac{Voltage_{in}}{Voltage_{out}} \quad [6.1]$$

Which when rearrange yields (Equation 6.2):

$$Voltage_{out} = \frac{Voltage_{in}}{10^{\frac{k}{20}}} \quad [6.2]$$

Where $Voltage_{in}$ and $Voltage_{out}$ refer to the input and output voltages (V), and k refers to the attenuation coefficient in dB/m.

For an air-steel-air system Figure 6.5 gives both theoretical and suggested sensor spacings at a variety of frequency-thickness products, as depicted by labelled arrows. The theoretical spacings have been picked at the point where 0.1% of the signal strength remains, whilst the suggested spacings have been calculated at 90% (rounded down to the nearest metre or decimetre dependent on magnitude) of this value. Suggested spacings at 90% were chosen to account for energy losses as a result of non-modellable phenomena such as defects and inhomogeneities in the materials. In the field measured signals will however be a superposition of multi-modal waves and sources, potentially counteracting this effect. Additionally, the signals would be omnidirectional, rather than unidirectional as assumed in the figure. The suggested spacings are therefore on the conservative side.

Figure 6.5 also illustrates the dependence of, and consequently large variation in, attenuation at different signal frequencies and steel element thicknesses (represented by signal strength). At 30 kHz, for example, sensor spacings of 355 m are suggested, by 80 kHz however this has decreased to 175 m; 175 m is less than half of 355 m. Thus, for an air-steel-air system it is important to have a prior understanding of the nature of the signals being measured i.e. a need to measure soil-steel interactions at 50 kHz, for example.

Alongside frequency-thickness, the burial system also significantly influences signal strengths; a clear difference in the magnitude of signal strength can be seen between air and soil bound systems. As a result, Figure 6.6 shows the same data at different scales in order to focus on material-bound systems.

Figure 6.6 plots signal strength with propagation distance for the four material-bound systems. The figure is split to emphasise the effects of internal media on soil bound systems (water and air). Like in Figure 6.4, Figure 6.6a shows that frequency-thickness affects signal strength for air-buried systems;

for a water-steel-air system, a difference in spacings of 6 m is seen for a 0.3 MHz-mm change in frequency thickness.

For the soil buried systems however, the differences seen significantly decrease to ≤ 1 m. Thus, suggested spacings irrespective of frequency-thickness can be made using conservative values. These are 15 m for gaseous internal materials (i.e. air or natural gas) and 3 m for internal water.

6.1.4 Stage 1: Summary

The instrumentation (i.e. hardware) and software used to form a sensor network are dependent on the application of the network. Additionally, data storage and power capacities need to be considered during design. For monitoring soil-steel deformation, the use of amplifiers, filters, and a sensor with a resonant frequency of around 30 kHz are recommended.

The physical deployment of an AE system is governed by both the attenuation within a system and the sensitivity of the AE system. Sensor spacings for five environments are suggested and may be summarised into four statements with respect to steel-air and steel-soil systems. These statements focus on propagation of the S0 mode, however, the superposition of different waves and additional attenuation, expected as a result of non-modellable phenomena, were also considered as follows:

- For air-steel-air systems, the sensor spacings are strongly dependent on the frequency-thickness product of interest. To ensure adequate data at a variety of frequencies is captured, spacings of ≤ 100 m are suggested. For efficiency however, larger spacings could be used dependent on the plate/wall thickness of the steel structure.
- For air-steel-soil systems (with typical clay or sand properties), sensor spacings of ≤ 15 m are suggested; differences as a result of the soil types considered were minimal. Propagation distances of this value have been successfully used in the field by Smith et al. (2017).
- For water-steel-air systems, the presence of water significantly increases attenuation and so spacings between 6 and 11 m are suggested dependent on the frequency-thickness of interest.
- For water-steel-sand systems, sensor spacings of only 3 m are suggested due to the expected high attenuation of the system; spacings of ≤ 3 m are likely to be appropriate to most soils. Shehadeh et al. (2008), however, found that approximately 0.06% of a signal was still measurable after 5 m propagation. Although, in their experiments the signal would have been a superposition of waves modes rather than the singular S0 mode used to generate Figure 6.6. This implies that propagation distances have the potential to be greater in the field.

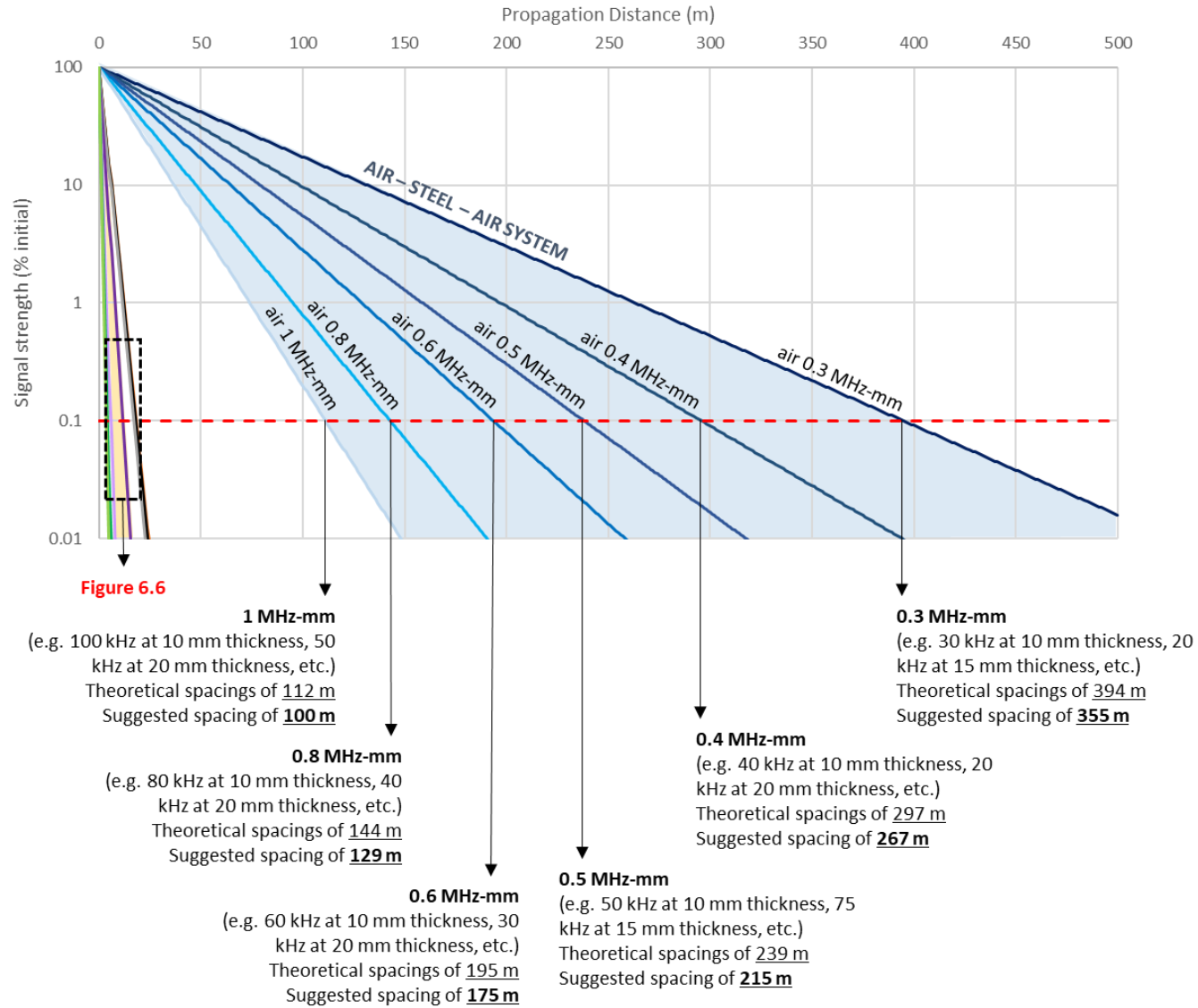


Figure 6.5 Signal strength with propagation for five burial systems and the consequent suggested sensor spacings for an air-steel-air system at different frequency-thickness products.

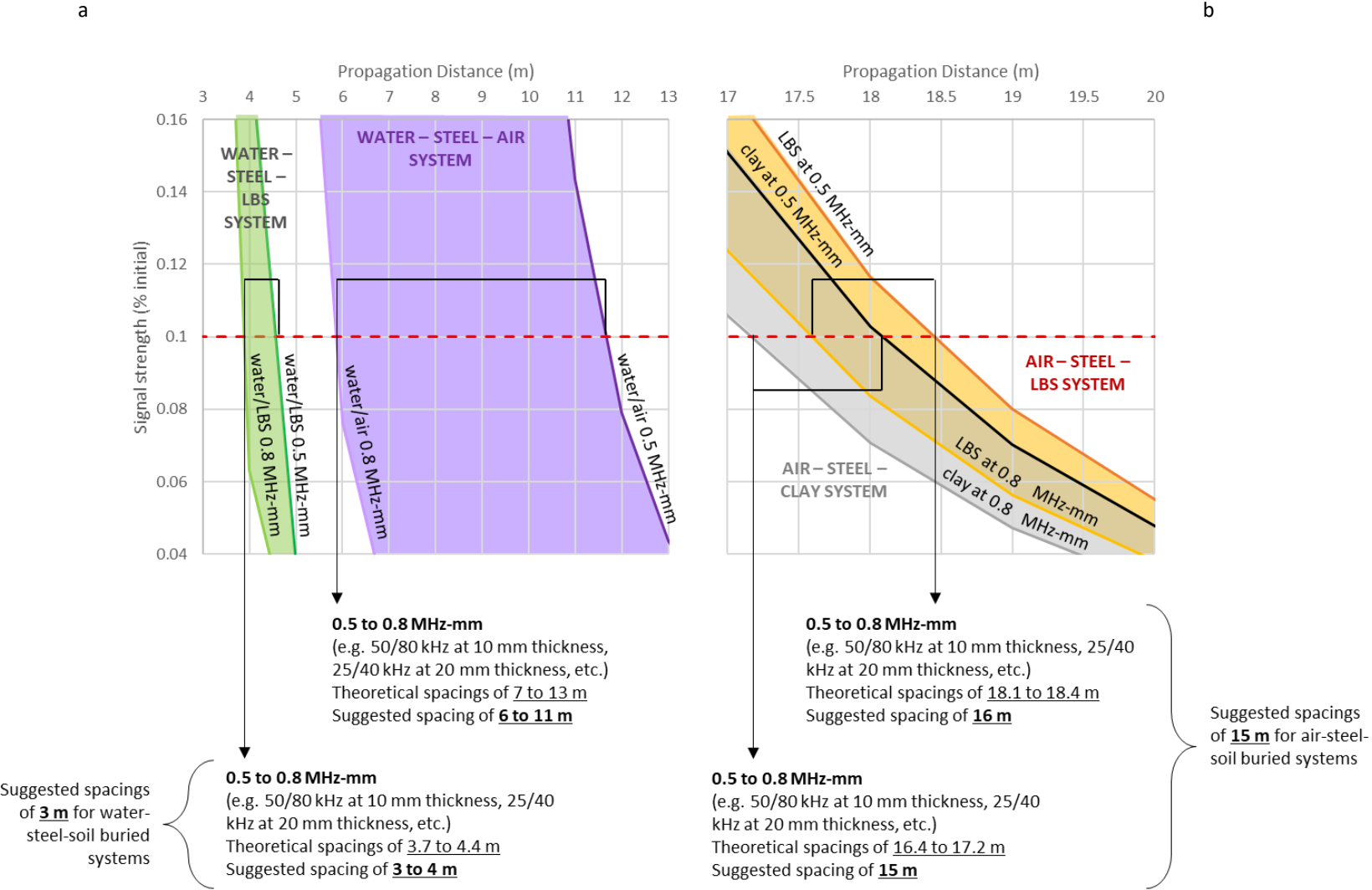


Figure 6.6 Signal strength with propagation and consequent suggested sensor spacings for (a) water filled burial systems in air and LBS and (b) air filled burial systems in LBS and clay for frequency-thickness products of 0.5 and 0.8 MHz-mm.

6.2 Stage 2: Interpreting AE behaviours in buried infrastructure systems

The second stage of the framework is to inform the interpretation of AE data collected by the sensor network developed in stage 1 (OB5). Stage 2 aims to provide a quantitative understanding of absolute and observed behaviours of AE through direct analysis of RDC and amplitude data, as well as the relating analysis of frequency and b-value data. Furthermore, additionally measured stress and displacement behaviours can also be used to strengthen and evaluate interpretations.

Chapter 5 presented the results of an investigation regarding AE generation and the evolution of AE generation within different system conditions (soils, stresses, and shearing rates). Moreover, the relationships between additional parametric data, such as stress and displacement, and collected AE data (RDCs, frequency, b-values) were analysed. The investigation allowed for several outcomes, dependent on the interpretation of AE behaviours, to be established. To do this, like with stage 1, the process can be broken down into three overall steps. These are summarised in Figure 6.7.

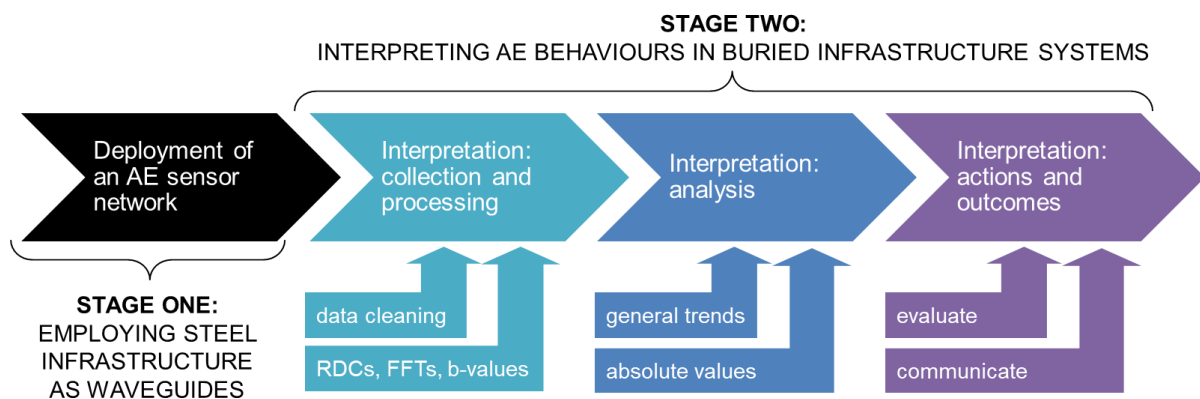


Figure 6.7 The three steps for interpreting AE behaviours in buried infrastructure systems (stage 2), collecting and processing AE data via a physical sensor network (stage 1), analysing the collected data, and using the analysis to interpret the conditions of the buried infrastructure system and provide relating actions and outcomes.

6.2.1 Step 1: Collection and processing

Linking to the software step (step 2) in stage one of the framework, the types of data and sampling rates to which these data are captured need to be determined and continually evaluated in order to provide the best interpretation possible. Furthermore, the captured data needs to either be stored or digitally transferred for future analysis (Stage 2: Step 2). This can be aided by cleaning (post-processing) and processing the captured data.

Data cleaning: To minimise the amount of data stored and transferred, whilst also improving its quality, data cleaning should occur; this may also be termed post processing. Data cleaning may involve processes such as: further filtering to remove aliasing effects, such as additional broadband frequency filters over 10 to 100 kHz; trimming in the time domain to remove excess data and focus on

periods of interest; and statistical analysis to summarise the data and data trends. Several of these cleaning techniques were employed in Chapter 5 to produce the results shown, whilst further data processing techniques follow.

Parametric data: With respect to the data types collected, the suggested system in Stage 1 is designed to measure cumulative RDCs (amplitude data) as a function of time and calculate FFTs (frequency spectra as a function of amplitude) at user defined time intervals. Further data such as raw waveforms may also be collected, however these create huge digital files which can slow the system and fill up available storage. From just RDC and FFT data, five data types are available to calculate:

- Cumulative RDCs with time
 - RDC rates with time
- Frequency spectra as a function of amplitude
 - Signal amplitudes (relating to frequencies)
 - b-values (relating to frequencies)

Moreover, statistical analysis of the available data allows for absolute values and general trends to be identified. By using several analytical methods, a more in-depth interpretation can be made.

Averaging: Averaging is known to reduce the effects of anomalous results and provide a single representative value. Averaging therefore allows for a large dataset to be represented as data points such as in Figure 5.14. Dependent on the data though, averages are not always representative. Other statistical parameters such as the mode (the value that occurs the most) and median (the value in the middle of a range) may be more appropriate.

Maximums: By focusing on data maxima, extremes and/or dominance can be identified. These may be absolute values or data envelopes with time or displacement. Maxima are beneficial as they allow for peaks and worse case scenarios (e.g. shear rates) to be distinguished. Moreover, dominant frequencies can be identified, the information allowing for other properties or phenomena to then be approximated (e.g. normal stress or AE generation mechanisms).

Point trends: Point based averages allow for the general trend of data to be determined when there is a high variation in measured values. For RDC and frequency data, this can be particularly useful as both can vary significantly in value over very short periods of time. Point averages therefore remove data extremes, which as discussed can be very useful, instead allowing for longer term spatial and temporal relationships to be determined without removing short term variations such as with other regression techniques.

Parametric functions: The sensitivity of different parameters to different phenomena may vary. By comparing the relationships between different parametric functions, differing parametric behaviours may therefore be seen and better interpretations made. RDC data for example is primarily dependent on the external material (e.g. grain size) and condition (e.g. normal and shear stresses) and can thus provide information on how they may be changing or influencing soil-steel interactions whilst frequency data is similarly dependent on the external material (e.g. grain size). Furthermore, extraneous signals such as internal water flow may also be indicated within frequency data.

Data storage and transferral: The storage and transfer of measured data is important to the analysis, evaluation, and communication of findings in future steps of the framework. Collected data, however, can have a very large digital file size. There are several solutions to storing and/or transferring data:

- Develop a system with large storage capacities from which data may be infrequently collected and analysed. This is an expensive method with the potential to lose large amounts of data if anything goes wrong with the storage. Furthermore, real-time monitoring would not be possible.
- Develop a system with small storage capacities where data is collected to capacity and overwritten unless certain criteria are met. If these criteria are met, the data should be kept or transferred via an automated system. This is a cheaper but more complex way of storing and transferring data. Like with a system of large storage capacities, there is still a chance of data being lost but the amount of data transferred.
- Develop a system that regularly transfers data. This is the chosen method as it allows for near real-time analysis and interpretation of measured AE behaviours and therefore reduced reaction times in the event of actions being required. Moreover, data is not lost as a result of storage capacity. Transfers should be through an automatic wired or wireless (i.e. cabled, satellite or wifi) system in order to ensure regularity. There is a small potential for data to be lost during transfer, whilst collection and transfer will be limited by the computational power and energy available. The benefits of regular data transferal far outweigh these risks though.

6.2.2 Step 2: Analysis

Relating to step 3, there are two desired outcomes of the analysis stage: (1) to assess the condition of the soil-steel-system and determine if deformation has or is occurring, and (2) to subsequently assess the condition of the buried steel structure by inference. Additionally, quantitative information on parameters such as shear rate and normal stress is desirable in order to provide context to the assessments and allow for risks to be appropriately analysed. The outcomes of this risk assessment

then determine whether actions (e.g remediation or evacuation) are required. Quantitative information is consequently invaluable.

To address these two outcomes, both the temporal trends within, and the absolute values of measured and calculated AE data have been used to develop an interpretive framework. Figure 6.8 focuses on the first outcome, assessing the condition of a soil-steel system and determining if deformation has or is occurring. The figure shows several scalar frameworks whereby the sign and magnitude of linear gradients over specific time periods have been related to soil behaviours. The scalar frameworks are for the parameters RDC rates, amplitude, and b-values.

Figures 6.9, 6.10 and 6.11 on the other hand show further frameworks for determining the likely normal stress (kPa) and shear rate (mm/minute) of an sand-steel system using quantitative data. Figure 6.9 is more general, using observed parametric frequency and b-value ranges to determine the likely normal stress being subject to a system, as well as the likely state of the soil (i.e. under compression or shearing). Figure 6.10 however, more specifically relates absolute calculated RDC rates with shear rates whilst Figure 6.11 similarly relates absolute measured amplitudes to RDC rates.

Several observations may be drawn from the figures:

- Zero gradients (i.e. horizontal trends) do not necessarily mean there is no change in condition.
 - Zero gradients over a prolonged period suggest no change however zero gradients over a short period, especially at a change of sign, suggest an important change in conditions.
- Higher RDC rates are indicative of faster shear rates whilst a sudden increase in the RDC rate suggests that the shear rate is increasing and/or the shear plane has been mobilised.
 - Staron et al. (2006) suggest that a sudden increase in RDC rate could signify imminent failure.
- A negative gradient for the parameter of amplitude indicates decreasing shearing rates and/or shearing activity whilst a positive gradient indicates increased shearing rates or compression.
 - The greater the gradient, the higher the rate of increase or decrease within specified ranges.
- Higher normal stresses generate a wider range of higher frequencies but a smaller range of b-values. Additionally, higher normal stresses generate more RDCs, particularly at faster shear rates, whilst higher amplitudes further indicate faster shear rates.

Notably though, the figures also show that there is a lot of cross-over in the solutions presented; by using one parameter only, e.g. the RDC rate, several of the figures suggest multiple interpretations

and are therefore non-unique. By using the figures (i.e. components) collectively (i.e. to form a framework), a greater understanding of the problem may consequently be gained. Section 6.2.2.1 therefore shows how the frameworks may be used with an exemplar data set of known conditions.

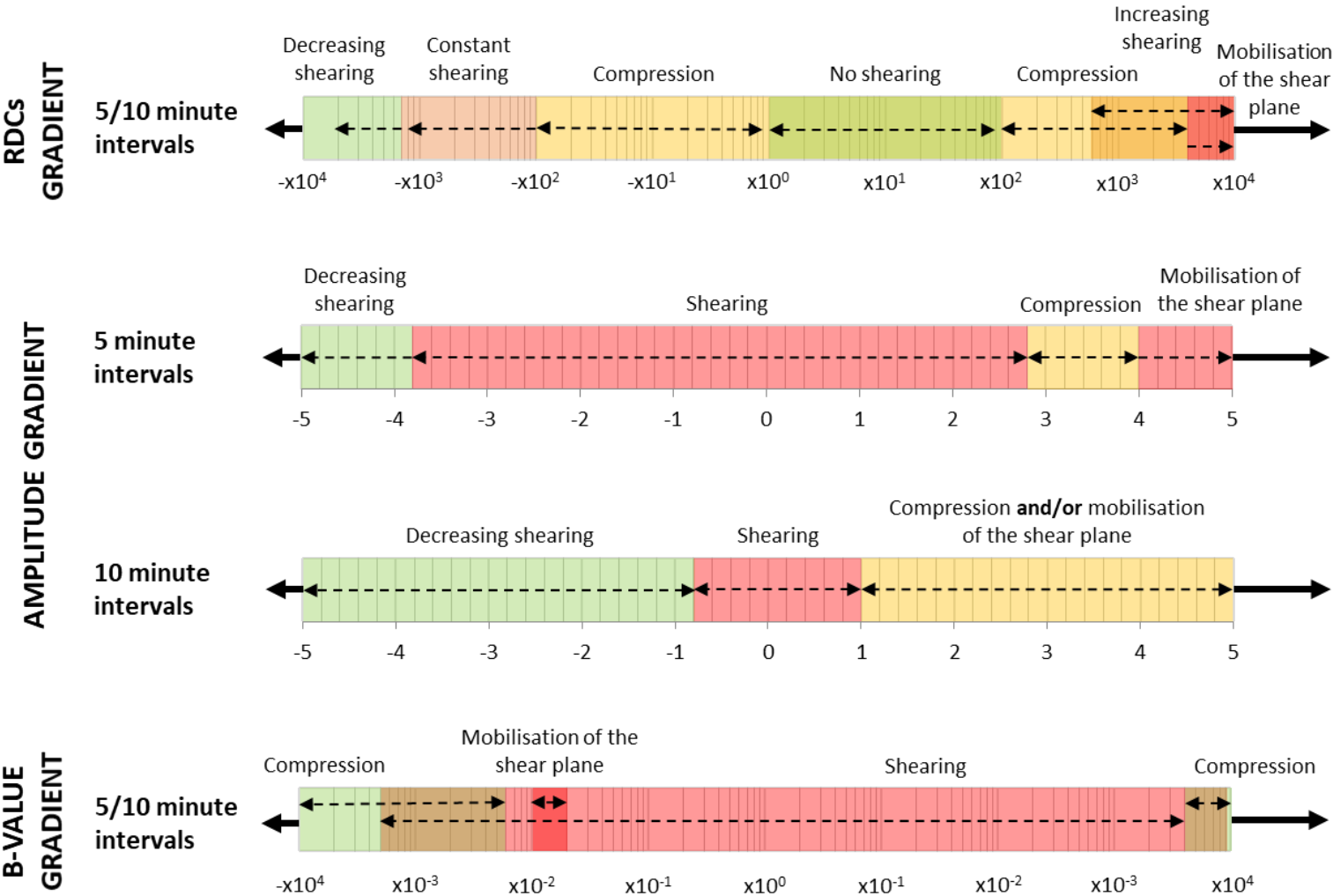


Figure 6.8 Scalar frameworks for determining the state of an LBS type soil-steel system using parameter-time linear gradients over 5- and 10-minute periods. The parameters include RDC rates (per minute), amplitude (dBV) and b-values. The suggested soil states have been colour coded to represent the risk posed by a system where green indicates least risk and red indicated most risk.

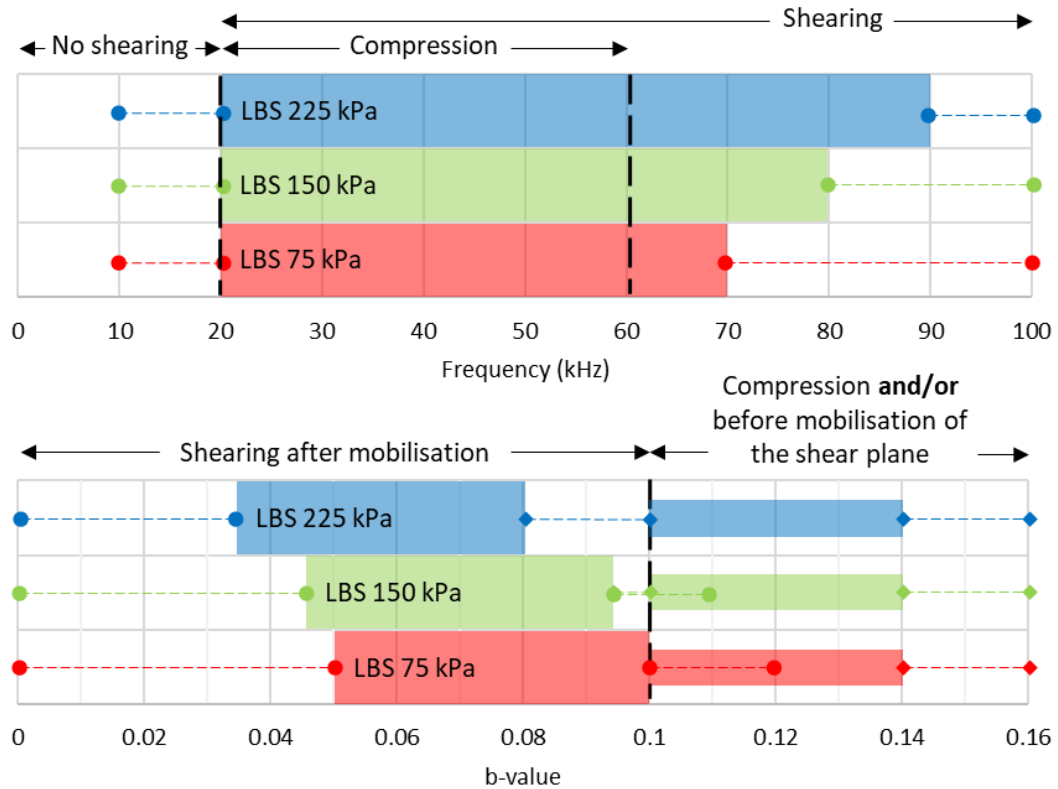


Figure 6.9 Frameworks for determining the likely normal stress and shear state of an LBS-steel system using observed parametric ranges of frequencies (kHz) and b-values for the conditions tested.

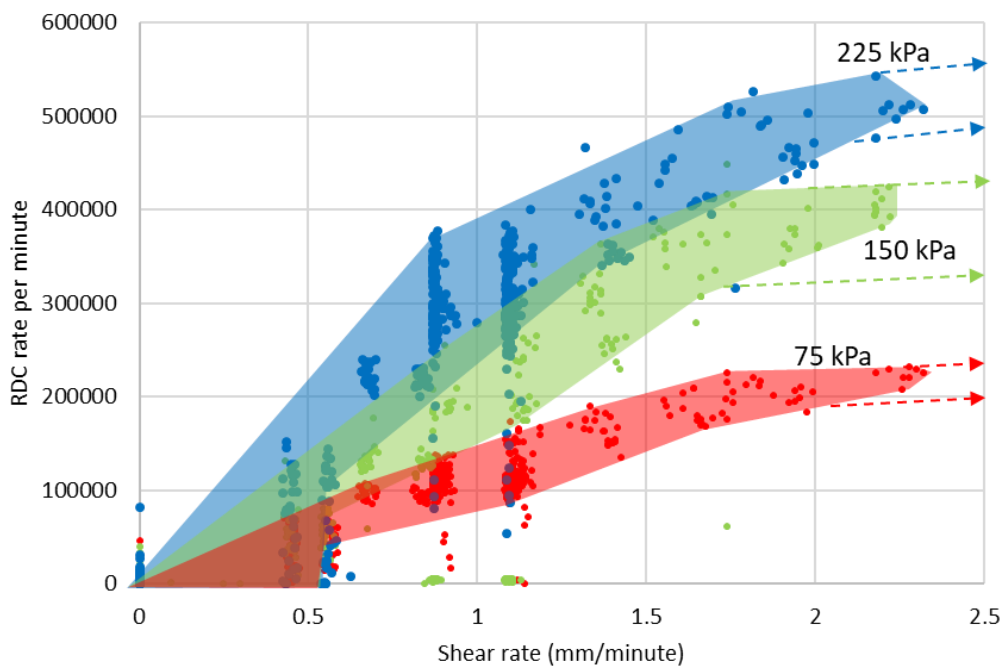


Figure 6.10 Shear rates (mm/minute) as a function of RDC rate (per minute) for three normal stresses, 75, 150, and 225 kPa. The points represent a mixture of constant and stepped rate shear tests.

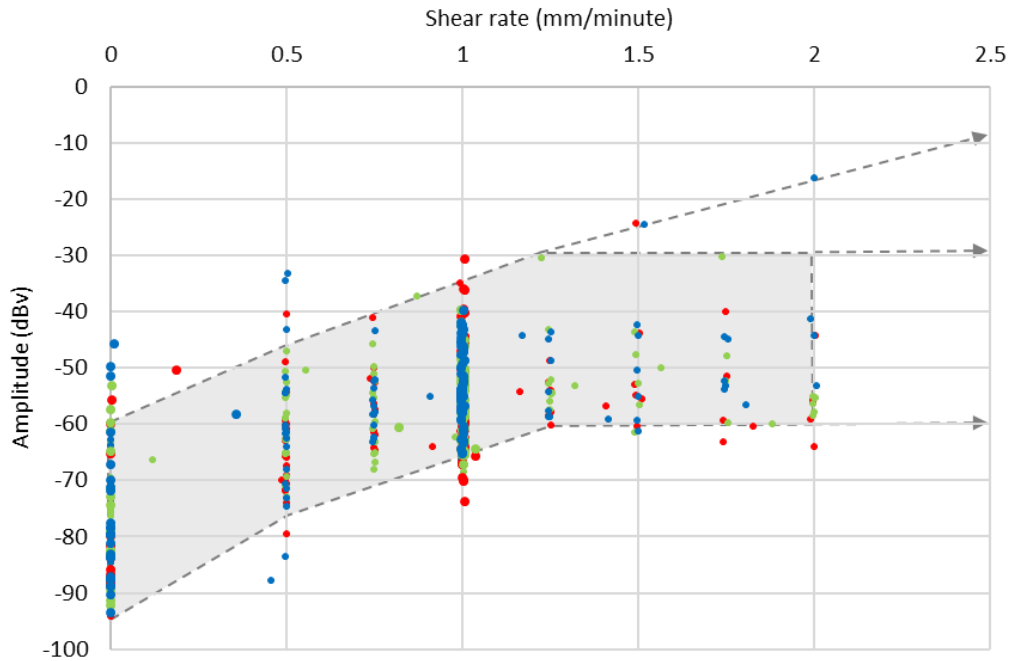


Figure 6.11 Shear rate (mm/minute) as a function of measured amplitude (dBv) at different normal stresses where red points were recorded under 75 kPa, green points under 150 kPa and blue points under 225 kPa. The points represent a mixture of constant and stepped rate shear tests.

6.2.2.1 Example one: LBS under 150 kPa normal stress and sheared at 1 mm/minute

To evaluate the series of graphs forming the interpretative AE framework in Figures 6.8 to 6.11, an analytical interpretation over 5 minute time intervals has been performed on an LBS sample tests which was under 150 kPa and sheared at 1 mm/minute over 40 mm. Table 6.1 and Figure 6.12 show the results.

Figure 6.12 consists of three graphs showing (a) RDC rate, (b) amplitude and (c) b-value data for the test. Superimposed grey rectangles indicate the period over which the sample was compressed to reach a target value of 150 kPa, whilst a black dashed arrow indicates the point at which the shear plane mobilised. The data has been plotted in 5 minute intervals over which average parametric values and linear gradients for each time interval have been taken. These are summarised in Table 6.1 along with interpretations formed from these values, in correspondence with the developed frameworks in Figures 6.8 to 6.11, and the known processes/changes in conditions with respective timings.

Table 6.1 shows that the interpretations made from Figures 6.8 to 6.11 generally match the real processes that occurred during the experiment although some uncertainty may be seen. For example, the mobilisation of the shear plane occurs either between 5 and 10, or 10 and 15 minutes dependent on which parameter is used for interpretation. Similarly, the parametric frameworks for amplitude and b-values distinguish between compression and shearing whereas the RDCs framework

distinguishes between constant and/or changing shearing regimes. There are consequently disparities in the individual interpretations, although a generalised interpretation may still be made using combined interpretations.

Table 6.1 Comparing the framework interpretations for various parameters at different time intervals with known processes.

Time (minutes)	Parameter	Gradient	Average value	Interpretation from gradients	Interpretation from averages	Known processes
0 to 5	RDCs	2803	8729	Compression / Before mobilisation	<0.5 mm/minute	Compression: 0 to 7 minutes
	amplitude	3.7	-75		Compression	
	b-value	0.0006	0.128			
5 to 10	RDCs	51727	85305	Mobilisation of the shear plane / Compression before mobilisation	<0.6 mm/minute	Shearing commences: 7 minutes Mobilisation of the shear plane: 9 minutes
	amplitude	4.3	-65		<1 mm/min	
	b-value	-0.01	0.118		Compression	
10 to 15	RDCs	5891	264389	Compression / Shearing / After mobilisation	0.9 to	
	amplitude	-1.0	-57		1.4 mm/minute	
	b-value	-0.002	0.073		Shearing	
15 to 20	RDCs	-3420	262108	Constant shearing / Shearing	0.9 to	
	amplitude	0.30	-54		1.4 mm/minute	
	b-value	-0.004	0.064		Shearing	
20 to 25	RDCs	-3715	243140	Constant shearing / Compression	0.8 to	
	amplitude	1.69	-54		1.3 mm/minute	
	b-value	-0.001	0.050		Shearing	
25 to 30	RDCs	-2733	227310	Constant shearing / Shearing	0.8 to	
	amplitude	-1.72	-55		1.3 mm/minute	
	b-value	0.003	0.057		Shearing	
30 to 35	RDCs	-2491	219327	Constant shearing / Shearing / Compression	0.7 to	
	amplitude	2.47	-55		1.2 mm/minute	
	b-value	-0.0008	0.063		Shearing	
35 to 40	RDCs	-2729	208464	Constant shearing / Shearing	0.7 to	
	amplitude	-1.02	-59		1.2 mm/minute	
	b-value	0.004	0.074		Shearing	
40 to 45	RDCs	-3740	189911	Constant shearing / Shearing	0.6 to	
	amplitude	0.17	-56		1.2 mm/minute	
	b-value	-0.005	0.065		Shearing	
45 to 50	RDCs	-7902	137554	Decreasing shearing / Compression	0.4 to	Shearing stops abruptly: 47 minutes
	amplitude	-7.77	-55		07 mm/minute	
	b-value	0.0002	0.049		Shearing	

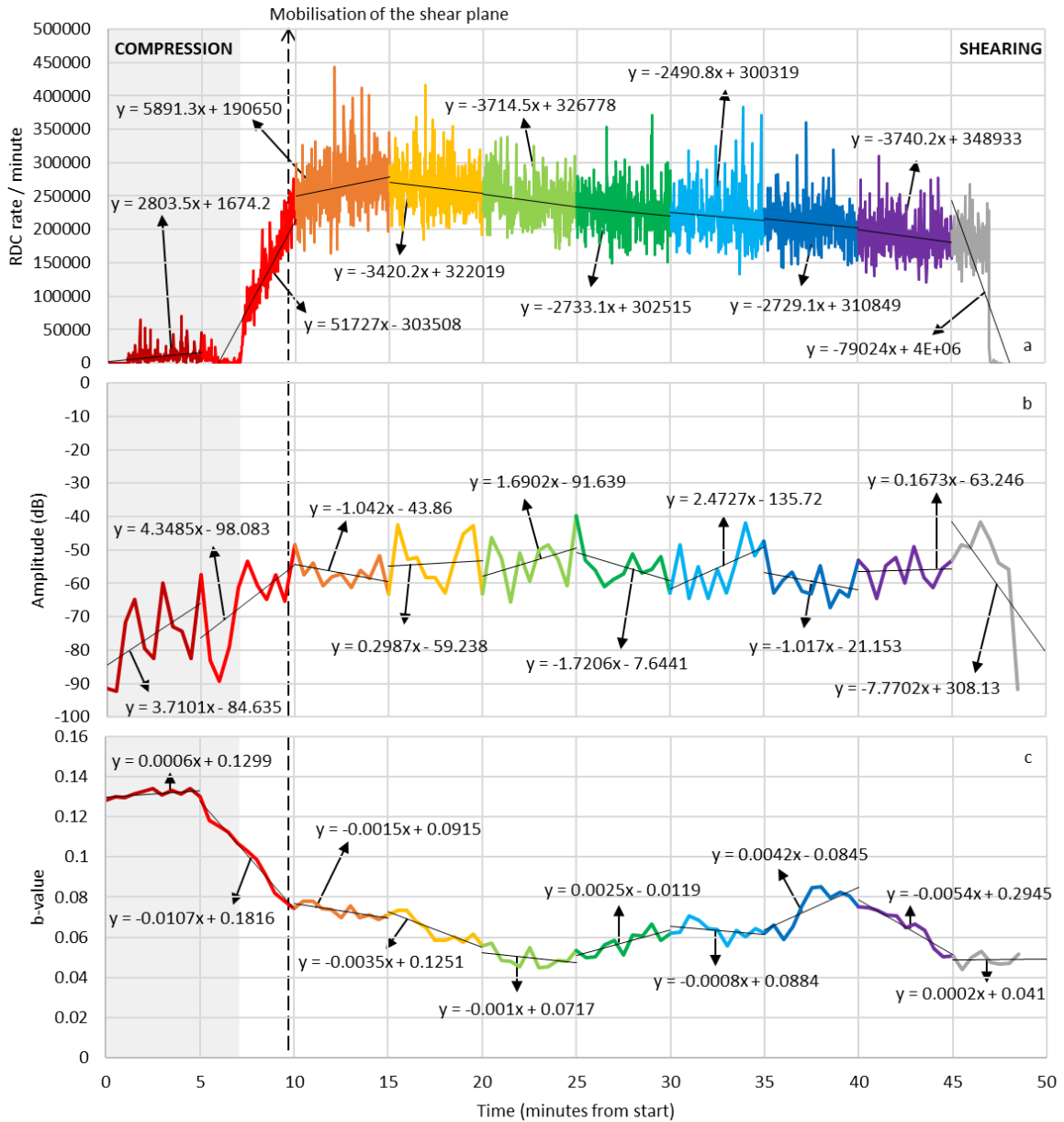


Figure 6.12 (a) RDC rate, (b) amplitude, and (c) b-value data with time for an LBS sample test under 150 kPa and sheared at 1 mm/minute over 40 mm. The data is plotted in 5 minute time intervals, as denoted by changing colours, for which linear gradients have been superimposed. The grey rectangle represents the period during which the sample was being compressed, as labelled, whilst the black dashed arrow indicates the point at which mobilisation of the shear plane occurred.

6.2.3 Step 3: Actions and outcomes

Although not within the scope of the thesis, the interpretations made from collected AE and relating data aim to provide an insight into the actions and outcomes needed to avoid potential problems relating to soil deformation.

To do this, two questions should be asked:

- What is the failure level of a system? Is deformation indicated and to what extent (magnitude and/or rate)?

- And what is the consequent state of the buried asset; What are the design limitations of the buried structure-system?

One or more of several actions can then be take. These may include:

- Continued monitoring at a decreased level
- Continued monitoring at a maintained level
- Continued monitoring at an increased level
 - Additional instrumentation beneficial to understanding
 - Increased data capture and analysis rates needed
- Remediation works
- Evasive actions such as public safety alerts (e.g. text messages and warnings within media) and voluntary or mandatory evacuations

Koerner et al. (1981), for example, provide suggested actions dependent on the rate of AE. These are summarised in Table 6.2 which splits the suggested actions into interpretations and their respective action.

Table 6.2 Suggested actions as a result of interpretations using qualitative AE levels. From Koerner et al. (1981).

AE level	Suggested interpretations	Suggested actions
None	The system is stable	Monitoring is only required at long-time intervals or when there is a change in conditions
Moderate	Deforming slightly, the system should be considered marginally stable	Continued monitoring until there is a change in conditions and a revaluation should occur
High	Substantial deformation, the system is unstable	Immediate remediation works should be conducted whilst continued monitoring allows for their effects to also be monitored
Very high	Large deformation, the system should be considered in a state of failure	Emergency precautions necessary for safety (i.e. the evacuation of nearby public)

The actions suggested by Koerner et al. (1981) are however qualitative. Figures 6.8 to 6.11 on the other hand are quantitative. Combining Table 6.2 and Figures 6.8 to 6.11, a quantitative framework of outcomes can therefore be established as an extension to Koerner et al.'s work (1981).

The potential impact of this quantitative framework, and the research behind it, is of great significance to practitioners; there is scope to reduce the effects of numerous short- and long-term impacts of deformation, whether economic, environmental, or social. The continued monitoring or increased monitoring of soil-structure and alternative systems, for example, allows for timely interventions to be made when required. This reduces the financial, environmental, and social costs of later intervention, at which point the damage caused by deformations could be irreversible and/or be costly to repair in terms of time, money, and resources. Moreover, timely interventions reduce the possibility of indirect impacts, such as the long-term mental health problems known to be caused by fatalities or imbalanced ecosystems as a result of contamination.

Additionally, the research behind the development of the framework is of great academic value, furthering our understanding of AE and clarifying its potential use as a monitoring tool. AE has been shown to be quantitatively interpreted using different methods, whilst the propagation and attenuation potential of S0 wave modes through various buried structure systems has been demonstrated. This is useful not just for monitoring AE caused by soil-steel interaction during deformation but also the structural health of various structures; it is known that propagation changes as a result of defects. The system may also be extended to be used on other structures, not just those investigated.

Following this statement, the current framework likely falls under a Technology Readiness Level (TRL) of 4 (Section AP5.0); the system, as a set of two components (i.e. stages) has been tested in a laboratory environment.

6.3 Chapter summary

A framework for understanding soil-steel generated AE in buried steel structures has been developed in two stages: (1) the creation and deployment of an AE monitoring system with spacings dependent on the burial system (Figures 6.5 and 6.6), and (2) the development of analytical frameworks for interpreting collected, and subsequently calculated, AE data sets (Figures 6.8 to 6.11).

Each of these stages were split into three steps to ensure that a large range of different influential factors known to effect collection and/or interpretation were considered. The overall framework may therefore be summarised as a series of six steps over two stages, forming the flow diagram in Figure 6.13, the outcome of which is a framework as shown in Figure 6.14.

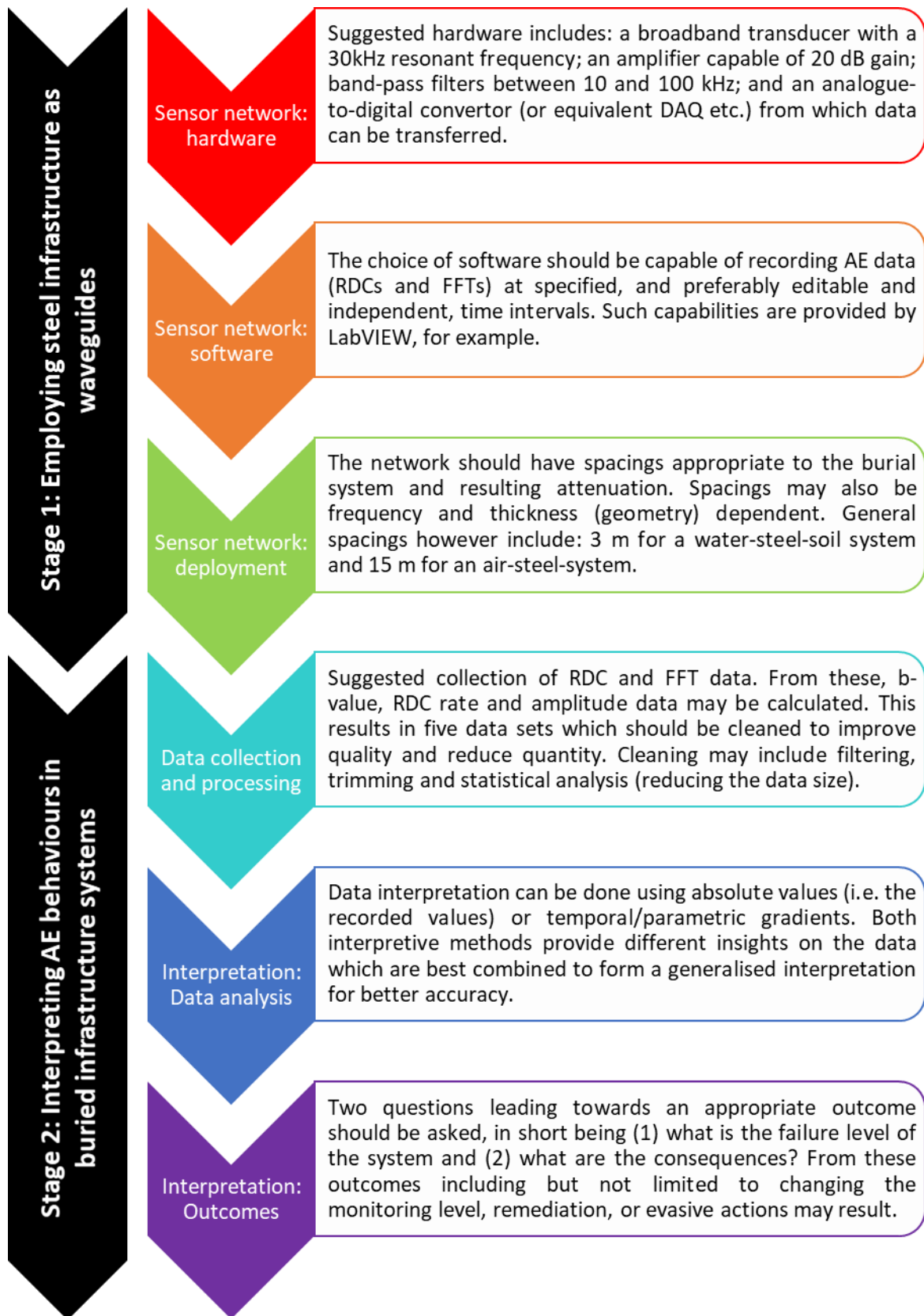


Figure 6.13 The summarised development of a two-stage framework for understanding soil-steel generated AE in buried steel structures, split into six steps.

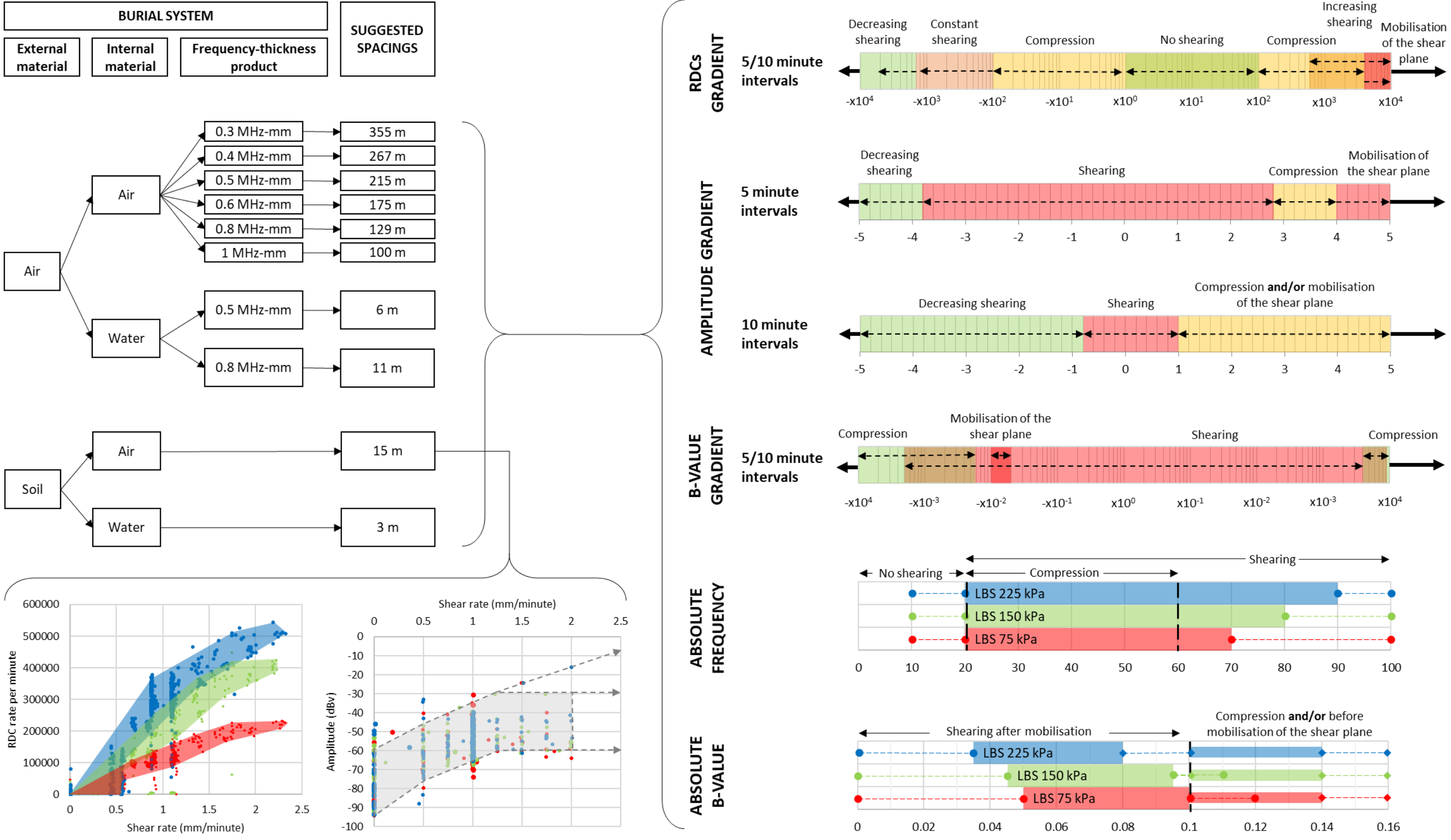


Figure 6.14 A two stage framework for deployment of a sensor network and subsequent interpretation and understanding of soil-steel generated AE in buried steel structures.

Chapter 7: Conclusions, limitations, and future work

7.0 Conclusions, limitations, and future work

The aim of this research was to develop a framework for understanding soil-steel generated acoustic emissions and their propagation in buried steel structures. To achieve this, five key objectives were set out as follows:

- OB1 To review knowledge of soil and AE behaviours, as well as the current monitoring systems for soil environments.
- OB2 To identify and characterise AE sources and behaviours in soil-steel systems.
- OB3 To investigate the propagation of AE through buried steel structures.
- OB4 To develop a framework to inform the creation of an AE sensor network.
- OB5 To develop a framework to inform the interpretation of detected AE.

These objectives were met using a series of investigative methods, including numerical simulations and small- and large-scale physical model experiments, the results of which are presented in several chapters. As stated in the introduction (Section 1.3), extensions to existing knowledge as well as new and original knowledge within the field of study have been contributed; these are summarised as a series of objective-by-objective conclusions in Section 7.1.

7.1 Conclusions

7.1.1 Objective 1

Chapter 2 formed a state-of-the-art review of current knowledge on topics including soil and structure stability, AE behaviours in soil-steel systems, and current monitoring systems within soil and soil-steel environments (OB1). From this a range of conclusions were drawn including:

- The increasing need for novel, accurate, and cost-effective monitoring systems to provide early warning of deterioration in buried infrastructure, especially within unstable environments. Currently available monitoring systems are prohibitively expensive or have technical limitation, preventing widescale use. The systems also typically provide only localised information at discrete time intervals; continuous and real-time monitoring systems are needed for early warning.
- Interpretation of AE generated by soils is still generally done on a qualitative basis using the qualitative framework published by Koerner and co-workers in the early 1980s. Quantification of slope displacement and stress levels using AE magnitudes has been done by Smith and Dixon (2018), however there is a gap in knowledge regarding a quantitative framework for

interpretation of soil-structure interaction-generated AE. This will enable decision makers to use AE to take actions, such as the evacuation of people or the undertaking of preventative measures.

- Numerous studies have investigated the propagation of ultrasonic waves in structural elements; however, no holistic framework exists that can be used to quantify AE attenuation in buried structure systems. An understanding of AE attenuation within buried structure systems would serve as guidance in the deployment of efficient sensor networks (e.g. sensor spacings) for AE monitoring.

7.1.2 Objective 2

An extensive programme of large direct shear box tests was conducted whereby mechanical behaviours and conditions (e.g. stress level, shearing velocity) were systematically varied to develop an understanding and quantify their influence on soil-structure interaction-generated AE. Chapter 5 presented the results of the study which investigated AE generated by compression and shearing mechanisms separately. The chapter showed that:

- The stress conditions subject to a soil sample strongly influence acoustic behaviours. Generally, AE activity increased proportionally with imposed normal stress during both compression and shearing mechanisms. However, the results indicate that the dominant AE frequency was not significantly influenced.
- Grain size was also shown to influence AE generation, though the effects differed dependent on whether the sample was being subject to compression or shearing. During compression, for example, PG produced more AE (RDCs) than LBS, whereas during shearing LBS was more emissive. A larger grain size did not necessarily increase the value of other AE parameters, with some either decreasing or showing no change.
- Shearing rate and shearing regime similarly affected acoustic behaviours. For the range of shear rates investigated (0.002 to 2 mm/minute, equivalent to slow to moderately-rapid soil movements) AE generation as a result of soil-steel interactions could be empirically related to shearing rate by a second order relationship. In addition, the measured and fully-mobilised shear stress were identifiable from AE data. All AE parameters investigated (e.g. RDCs, amplitude, b-values), except dominant frequency, were found to be related to shearing rate and mobilised shear stress.

7.1.3 Objective 3

Laboratory tests and computational models were performed to investigate wave behaviours within typical buried steel structure systems (OB3). The results of these were shown in Chapter 4. The chapter showed that:

- Wave behaviours are controlled by three categories of parameters: (1) the physical geometry of a structure or steel element, (2) the environment in which the element may be found, (3) and the properties of a wave propagating.
- Computationally, shell structures could be treated like plates in terms of their propagation and attenuation behaviours; little difference was seen in results for the same material system when modelled as a shell or plate. Joints within a pipe structure, on the other hand, increased attenuation to varying degrees, dependent on the joint type. Literature suggested that screw and welded joints transmitted most of a wave's energy, but both small- and large-scale testing conducted as part of this study showed significant reflection to occur at these joint types.
- Pipe radius was however proven to have minimal influence on the magnitude of attenuation in both computational and experimental investigations whilst wall thickness could be taken account of with frequency-thickness products. Changes in the material system (i.e. internal and external environments) were also found to influence attenuation. It was shown that increases in a soil's/ externals environment's ρ and E increased attenuation, decreasing at an exponential rate, though a clear relationship between v and attenuation was not quantifiable. In terms of internal materials, water caused significant attenuation, which when coupled with a soil burial, significantly decreased the propagation distance over which a signal could be detected. Computational models for four typical structural systems were subsequently conducted, for which propagation and attenuation behaviours were then analysed in detail.

7.1.3.1 Limitations

Limitations in the capabilities of computational models need to be taken into consideration when interpreting the results presented. Factors such as human error, simplified, and idealised conditions (e.g. isotropy and homogeneity) will influence results. In the field, measured signals are likely to be multi-modal, originating from a variety of sources, and become distorted during propagation due to inhomogeneous and anisotropic structural and environmental conditions.

A study was therefore performed to compare outputs of the Disperse program with measurements obtained using small- and large-scale laboratory experiments as well as published findings within literature. Generally, it was concluded that Disperse was able to provide accurate solutions with a relatively small error considering that variability in laboratory and field measurements should be

expected (e.g. precision/accuracy of sensors, sensor coupling variations, inhomogeneity, isotropy, etc.). Improved consistency between modelling, field, and/or laboratory results would only be achieved through the addition of realistic, representative variations during the construction of models, or through arduous and unrealistic control over variables in physical experiments.

7.1.4 Objective 4

Synthesis of the results produced by computational models, shear box, and small- and large-scale experiments enabled for a framework informing the creation of a sensor network, adaptable to varying forms of buried infrastructure within different environments, to be developed (OB4). This included information regarding the suitability of different steel infrastructure and provided recommendations on sensor spacings to take account of attenuation resulting from structural and environmental factors.

Sensor spacings were found to be largely dependent on the frequency-thickness product for simple burial systems, however the introduction of heavily attenuating internal or external materials drastically reduced this effect and lead to a smaller range of potential sensor spacings. The spacings suggested were conservative and focused only on the propagation of the fundamental S0 wave mode; literature implied that this mode was most likely to propagate within the systems of interest. However, in real, field conditions, a range of modes will propagate and be detected by the monitoring sensors, potentially increasing the possible propagation distances between sensors.

7.1.5 Objective 5

A framework to inform the interpretation of collected AE (OB5) was created using the results from a programme of large direct shear tests (Chapter 5). The development of this framework was shown in Chapter 6, which attempted to use both absolute AE values and rate of change of various AE parameters with time to establish relationships with mechanical behaviours.

The framework demonstrated that quantifiable relationships between various AE parameters in time can be used to determine the shearing and stress conditions of LBS type soils. Periods of increasing, maintained, or decreasing shear could be identified, alongside periods of compression. Furthermore, the point at which mobilisation of the shear plane occurs is shown to be identifiable using RDC rate time derivatives.

This framework demonstrated that monitoring individual AE parameters is not necessarily sufficient to interpret and quantify mechanical behaviour; monitoring combinations of AE parameters allowed for a greater level of interpretation, though a level of uncertainty should be kept in mind. For example,

combining RDC rates and RDC rate time derivatives allowed quantification of shearing rates (and their rate of change).

7.2 Recommendations for future work

Further research topics using a variety of investigative techniques are recommended to refine the current understanding of AE generation, propagation and attenuation within buried structure systems. These investigations will improve the frameworks developed, enable their application to a wider range of buried infrastructure systems (e.g. concrete) and progress the research through Technology Readiness Levels (TRLs) to develop proof of concept. These could include:

- Physical modelling-based investigations on:
 - wave behaviours within a wider variety of buried structures (i.e. concrete tunnels, retaining structures)
 - further analysis and characterisation of soil-structure generated signals (e.g. soil-concrete interaction, fine grains soil-steel interaction)
 - the influence of internal materials like water and gas (the physical models in this study had air as an internal environment)
 - layered flow, flow noise, contaminant noise, and other potential AE noise sources
 - the effects of different forms of pipe joints
 - large- and full-scale experiments on AE monitoring of buried pipe deformation
 - field trials of AE monitoring of buried infrastructure
- Physical shear box tests regarding:
 - the effects of different soil types (size, shape, grading) under different physical (wet, dry) and stress conditions (kPa)
 - the effects of different structure types and materials (e.g. concrete)
 - the effects of interface roughness and other properties like hardness
 - the rate of loading (increasing and decreasing)
 - stress history
 - pore-water pressures
 - increasing and decreasing shear rates and the rate of increase and decrease.
- Automated interpretations using machine learning.
 - Due to the quantitative nature of the measured AE, machine learning and automation of the interpretive processes should be relatively simple to introduce; specified interpretations are related to specific numerical measurements and measurement ranges. Numerous interpretations will still need to be formed, i.e. for different AE

parameters, from which an overall interpretation would then need to be chosen; this would add a level of complexity to the process.

The scope of the work discussed is therefore wide. Although many phenomena have been investigated - from which a basic framework informing the development of AE sensor networks and their subsequent interpretation has been established - there is significant potential for future work to improve the accuracy of the frameworks, investigate a range of new buried infrastructure applications, and progress the research through TRLs to develop a field-scale proof of concept (from TRL 4 to 5/6).

By providing proof of concept at a field-scale, stakeholders and decision makers could then be reassured that the benefits of such a system outweigh current pitfalls. Practically, however, further work on the placement of large-scale systems would need to be performed, potentially including the self-containment of the measurement system/elements of, as the current system requires mains power whilst large amounts of wiring would also be needed to connect system elements.

References

- Achenbach, J.D., 1973. Elastic wave propagation in solids. Amsterdam, London: North Holland Publishing Co.
- Afandi, M.I., Adinanta, H., Setiono, A. and Widiyatmoko, B., 2018, March. High resolution extensometer based on optical encoder for measurement of small landslide displacements. In *Journal of Physics: Conference Series*. IOP Publishing, 985(1).
- Aggelis, D.G., Soulioti, D.V., Sapouridis, N., Barkoula, N.M., Paipetis, A.S. and Matikas, T.E., 2011. Acoustic emission characterization of the fracture process in fibre reinforced concrete. *Construction and Building Materials*, 25(11), pp.4126-4131.
- Alleyne, D. and Cawley, P., 1995. The long range detection of corrosion in pipes using Lamb waves. In *Review of progress in quantitative nondestructive evaluation*. Springer, Boston, MA, pp. 2073-2080.
- Alleyne, D.N. and Cawley, P., 1996. The excitation of Lamb waves in pipes using dry-coupled piezoelectric transducers. *Journal of Nondestructive Evaluation*, 15(1), pp.11-20.
- Aristegui, C., Lowe, M.J.S. and Cawley, P., 2001. Guided waves in fluid-filled pipes surrounded by different fluids. *Ultrasonics*, 39(5), pp.367-375.
- ASTM, 2000. Standard test method for low strain integrity testing of piles. ASTM International, West Conshohocken, PA.
- ASTM E1316-20, 2000. Standard Terminology for Nondestructive Examinations. ASTM International, West Conshohocken, PA.
- Baik, K., Jiang, J. and Leighton, T.G., 2010. Acoustic attenuation, phase and group velocities in liquid-filled pipes: Theory, experiment, and examples of water and mercury. *The Journal of the Acoustical Society of America*, 128(5), pp.2610-2624.
- Barmopoulos, I. H., Ho, T. Y. K., Jardine, R. J. & Minh, A. N. (2009). The large displacement shear characteristics of granular media against concrete and steel interfaces. *Proceedings of the Research Symposium on Characterization and Behaviour of Interfaces*, Atlanta, GA, pp. 16–23.
- Bartoli, I., di Scalea, F.L., Fateh, M. and Viola, E., 2005. Modelling guided wave propagation with application to the long-range defect detection in railroad tracks. *NDT & E International*, 38(5), pp.325-334.
- Beard, F.D. 1961. Predicting slides in cut slopes. *Western Construction*, 36(72).

- Beard, F.D., 1962. Microseismic forecasting of excavation failures. *Civil Engineering*, 32(5), pp.50.
- Beard, M.D. and Lowe, M.J.S., 2003. Non-destructive testing of rock bolts using guided ultrasonic waves. *International journal of rock mechanics and mining sciences*, 40(4), pp.527-536.
- Beard, M.D., Lowe, M.J.S. and Cawley, P., 2003. Ultrasonic guided waves for inspection of grouted tendons and bolts. *Journal of Materials in Civil Engineering*, 15(3), pp.212-218.
- Berliner, M.J. and Solecki, R., 1996. Wave propagation in fluid-loaded, transversely isotropic cylinders. Part I. Analytical formulation. *The Journal of the Acoustical Society of America*, 99(4), pp.1841-1847.
- Bhattacharya, S. and Adhikari, S., 2011. Experimental validation of soil–structure interaction of offshore wind turbines. *Soil Dynamics and Earthquake Engineering*, 31(5-6), pp.805-816.
- Bhattacharya, S., 2014. Challenges in design of foundations for offshore wind turbines. *Engineering & Technology Reference*, 1(1), p.922.
- Bisoi, S. and Haldar, S., 2014. Dynamic analysis of offshore wind turbine in clay considering soil–monopile–tower interaction. *Soil Dynamics and Earthquake Engineering*, 63, pp.19-35.
- Bossy, E., Padilla, F., Peyrin, F. and Laugier, P., 2005. Three-dimensional simulation of ultrasound propagation through trabecular bone structures measured by synchrotron microtomography. *Physics in Medicine & Biology*, 50(23), p.5545.
- Boyle, A., Wilkinson, P.B., Chambers, J.E., Meldrum, P.I., Uhlemann, S. and Adler, A., 2017. Jointly reconstructing ground motion and resistivity for ERT-based slope stability monitoring. *Geophysical Journal International*, 212(2), pp.1167-1182.
- Bray, D.E. and Stanley, R.K. 1989. *Nondestructive evaluation*. New York: McGraw-Hill Book Co.
- Brunsdon, D. and Prior, D.B., 1984. *Slope instability*. Chichester: Wiley.
- Byrne, B.W., McAdam, R., Burd, H.J., Houlby, G.T., Martin, C.M., Zdravkovic, L., Taborda, D.M.G., Potts, D.M., Jardine, R.J., Sideri, M. and Schroeder, F.C., 2015, June. New design methods for large diameter piles under lateral loading for offshore wind applications. In *3rd International Symposium on Frontiers in Offshore Geotechnics (ISFOG 2015)*, Oslo, Norway, June, pp. 10-12.
- C4 offshore, 2019. Offshore turbine database. [online] Available at: <https://www.4coffshore.com/windfarms/turbines.aspx> [Accessed: 25/07/2019].

- Cabalar, A.F., Cevik, A. and Guzelbey, I.H., 2010. Constitutive modelling of Leighton Buzzard Sands using genetic programming. *Neural Computing and Applications*, 19(5), pp.657-665.
- Cadman, J.D. and Goodman, R.E., 1967. Landslide noise. *Science*, 158(3805), pp.1182-1184.
- Carandente, R., Ma, J. and Cawley, P., 2010. The scattering of the fundamental torsional mode from axi-symmetric defects with varying depth profile in pipes. *The Journal of the Acoustical Society of America*, 127(6), pp.3440-3448.
- Carswell, W., Johansson, J., Løvholt, F., Arwade, S.R. and DeGroot, D.J., 2014, June. Dynamic mudline damping for offshore wind turbine monopiles. In *ASME 2014 33rd International Conference on Ocean, Offshore and Arctic Engineering* (pp. V09AT09A025-V09AT09A025). American Society of Mechanical Engineers.
- ^aCarswell, W., Johansson, J., Løvholt, F., Arwade, S.R., Madshus, C., DeGroot, D.J. and Myers, A.T., 2015. Foundation damping and the dynamics of offshore wind turbine monopiles. *Renewable energy*, 80, pp.724-736.
- ^bCarswell, W., Arwade, S.R., DeGroot, D.J. and Lackner, M.A., 2015. Soil–structure reliability of offshore wind turbine monopile foundations. *Wind energy*, 18(3), pp.483-498.
- Cavallaro, A., Maugeri, M. and Mazzarella, R., 2001. Static and dynamic properties of Leighton Buzzard sand from laboratory tests.
- Cawley, P., Lowe, M.J.S., Alleyne, D.N., Pavlakovic, B. and Wilcox, P., 2003. Practical long range guided wave inspection-applications to pipes and rail. *Materials evaluation*, 61(1), pp.66-74.
- Chai, L., Wu, X. and Liu, C.S., 2014. A universal scaling law of grain chain elasticity under pressure revealed by a simple force vibration method. *Soft matter*, 10(35), pp.6614-6618.
- Chen, S., Yang, C., Wang, G. and Liu, W., 2017. Similarity assessment of acoustic emission signals and its application in source localization. *Ultrasonics*, 75, pp.36-45.
- CLH-PS, n.d. CLH-PS. [online] Available at: <https://www.clh.es/section.cfm?id=2&side=224&lang=en> [Accessed:25/07/2019]
- Cody, G.D., Goldfarb, D.J., Storch, G.V. and Norris, A.N., 1996. Particle granular temperature in gas fluidized beds. *Powder Technology*, 87(3), pp.211-232.
- Coste, C. and Gilles, B., 1999. On the validity of Hertz contact law for granular material acoustics. *The European Physical Journal B-Condensed Matter and Complex Systems*, 7(1), pp.155-168.

- Cruden, D.M. and Varnes, D.J., 1996. Landslides: investigation and mitigation. Chapter 3-Landslide types and processes. Transportation research board special report, (247), pp.36-75.
- Cunfu, H., Hongye, L., Zenghua, L. and Bin, W., 2013. The propagation of coupled Lamb waves in multilayered arbitrary anisotropic composite laminates. *Journal of Sound and Vibration*, 332(26), pp.7243-7256.
- De Pue, J., Van Meirvenne, M. and Cornelis, W.M., 2015. Accounting for surface refraction in velocity semblance analysis with air-coupled GPR. *IEEE Journal of Selected Topics in Applied Earth Observations and Remote Sensing*, 9(1), pp.60-73.
- Design manual for roads and bridges, 1999. Rock bolts. [online] Available at: <http://bailey.persona-pi.com/Public-Inquiries/M4-Newport/C%20-%20Core%20Documents/6.%20Transport%20and%20Engineering/DMRB/vol2/section1/ba8099.pdf> [Accessed: 26/07/2019]
- di Scalea, F.L. and McNamara, J., 2004. Measuring high-frequency wave propagation in railroad tracks by joint time–frequency analysis. *Journal of Sound and Vibration*, 273(3), pp.637-651.
- Dijkstra, T.A. and Dixon, N., 2010. Climate change and slope stability in the UK: challenges and approaches. *Quarterly Journal of Engineering Geology and Hydrogeology*, 43(4), pp.371-385.
- Dinardo, G., Fabbiano, L., Vacca, G. and Lay-Ekuakille, A., 2018. Vibrational signal processing for characterization of fluid flows in pipes. *Measurement*, 113, pp.196-204.
- Discover Water, 2018. Leaking Pipes [online] Discover Water. Available at: <https://discoverwater.co.uk/leaking-pipes> [Accessed: 10/07/2019]
- Dixon, N., Hill, R. and Kavanagh, J., 2003. Acoustic emission monitoring of slope instability: development of an active waveguide system. *Proceedings of the institution of civil engineers-geotechnical engineering*, 156(2), pp.83-95.
- Dixon, N. and Spriggs, M., 2007. Quantification of slope displacement rates using acoustic emission monitoring. *Canadian Geotechnical Journal*, 44(8), pp.966-976.
- Dixon, N., Moore, R., Spriggs, M., Smith, A., Meldrum, P. and Siddle, R., 2015. Performance of an acoustic emission monitoring system to detect subsurface ground movement at Flat Cliffs, North Yorkshire, UK. *Engineering Geology for Society and Territory*. Springer International Publishing, 2, pp. 117-120.

- Doanh, T., Abdelmoula, N., Gribaa, L., Nguyễn, T.T.T., Hans, S., Boutin, C. and Le Bot, A., 2017. Dynamic instabilities under isotropic drained compression of idealized granular materials. *Acta Geotechnica*, 12(3), pp.657-676.
- Engineering Toolbox, n.d. Absolute, Dynamic and Kinematic Viscosity [online] Available at: https://www.engineeringtoolbox.com/dynamic-absolute-kinematic-viscosity-d_412.html [Accessed: 20/02/2020]
- Fang, L., Lu, Q., Li, X., Liu, R. and Wang, X., 2013. Flow noise characterization of gas–liquid two-phase flow based on acoustic emission. *Measurement*, 46(10), pp.3887-3897.
- Fellows, R.F. and Liu, A.M., 2009. *Research methods for construction*. John Wiley & Sons,
- Ferdowsi, B., Griffa, M., Guyer, R.A., Johnson, P.A., Marone, C. and Carmeliet, J., 2013. Microslips as precursors of large slip events in the stick-slip dynamics of sheared granular layers: A discrete element model analysis. *Geophysical Research Letters*, 40(16), pp.4194-4198.
- FT pipelines. Pipe joints. [online] Available at: <https://ftpipelinesystems.co.uk/pipe-joints/> [Accessed: 25/07/2019]
- Fuller, C.R. and Fahy, F.J., 1982. Characteristics of wave propagation and energy distributions in cylindrical elastic shells filled with fluid. *Journal of sound and vibration*, 81(4), pp.501-518.
- Gao, G., Dang, R., Nouri, A., Jia, H., Li, L., Feng, X. and Dang, B., 2015. Sand rate model and data processing method for non-intrusive ultrasonic sand monitoring in flow pipeline. *Journal of Petroleum Science and Engineering*, 134, pp.30-39.
- Gardel, E., Seitaridou, E., Facto, K., Keene, E., Hattam, K., Easwar, N., Menon, N., 2009. Dynamical fluctuations in dense granular flows. *Philosophical Transactions of the Royal Society A* 367, pp.5109–5121.
- Gasparre, A., Nishimura, S., Minh, N.A., Coop, M.R. and Jardine, R.J., 2007. The stiffness of natural London Clay. *Géotechnique*, 57(1), pp.33-47.
- Gazis, D.C., 1959. Three-dimensional investigation of the propagation of waves in hollow circular cylinders. I. Analytical foundation. *The journal of the Acoustical Society of America*, 31(5), pp.568-573.
- Geotech, n.d. Foundation [online] Available at: <https://www.geotech.hr/en/differential-settlements/> [Accessed: 20/02/2020]

- Ghandourah, E.I.I., 2015. Large plate monitoring using guided ultrasonic waves (Doctoral dissertation, UCL (University College London)).
- Gilles, J., 2013. Empirical wavelet transform. *IEEE transactions on signal processing*, 61(16), pp.3999-4010.
- Gorman, M.R. and Prosser, W.H., 1991. AE source orientation by plate wave analysis.
- Greve, D.W., Neumann, J.J., Nieuwenhuis, J.H., Oppenheim, I.J. and Tyson, N.L., 2005, May. Use of Lamb waves to monitor plates: experiments and simulations. In *Smart Structures and Materials*, International Society for Optics and Photonics, pp.281-292.
- Grinsted, A., Moore, J.C. and Jevrejeva, S., 2004. Application of the cross wavelet transform and wavelet coherence to geophysical time series. *Nonlinear processes in geophysics*, 11(5/6), pp.561-566.
- Gutkin, R., Green, C.J., Vangrattanachai, S., Pinho, S.T., Robinson, P. and Curtis, P.T., 2011. On acoustic emission for failure investigation in CFRP: Pattern recognition and peak frequency analyses. *Mechanical systems and signal processing*, 25(4), pp.1393-1407.
- Haberland, C. and Rietbrock, A., 2001. Attenuation tomography in the western central Andes: A detailed insight into the structure of a magmatic arc, *Journal Of Geophysical Research-Solid Earth*, 106(B6), pp.11151-11167
- Han, F., Ganju, E., Salgado, R. and Prezzi, M., 2018. Effects of interface roughness, particle geometry, and gradation on the sand–steel interface friction angle. *Journal of Geotechnical and Geoenvironmental Engineering*, 144(12), p.04018096.
- Hardy Jr., H. R. 1992. Laboratory studies relative to the development of mechanical waveguides for acoustic emission monitoring of geologic structures, *Italian Journal of Nondestructive Testing and Diagnostics*, 13, (2), 32–38.
- Hayashi, T., Song, W.J. and Rose, J.L., 2003. Guided wave dispersion curves for a bar with an arbitrary cross-section, a rod and rail example. *Ultrasonics*, 41(3), pp.175-183.
- He, M.C., Miao, J.L. and Feng, J.L., 2010. Rock burst process of limestone and its acoustic emission characteristics under true-triaxial unloading conditions. *International Journal of Rock Mechanics and Mining Sciences*, 47(2), pp.286-298.

- Henkel, M., Noppe, N., Weijtjens, W. and Devriendt, C., 2018. Sub-soil strain measurements on an operational wind turbine for design validation and fatigue assessment. In *Journal of Physics: Conference Series*. IOP Publishing, 1037(5), pp. 052032.
- Hernández-García, A., Basaldúa-Sánchez, J.E., Martínez-Calzada, V., Samayoa-Ochoa, D. and Rodríguez-Castellanos, A., 2014. Reconstruction of the interface waves in elastic modles, analysed by indirect boundary element method (IBEM). *Pensee*, 76(10).
- Hesse, D. and Cawley, P., 2006. Surface wave modes in rails. *The Journal of the Acoustical Society of America*, 120(2), pp.733-740.
- Hight, D.W., McMillan, F., Powell, J.J.M., Jardine, R.J. and Allenou, C.P., 2003. Some characteristics of London clay. *Characterisation and engineering properties of natural soils*, 2, pp.851-946.
- Ho, T.Y.K., Jardine, R.J. and Anh-Minh, N., 2011. Large-displacement interface shear between steel and granular media. *Géotechnique*, 61(3), pp.221-234.
- Holford, K.M. and Carter, D.C., 1999. Acoustic emission source location. In *Key Engineering Materials*. Trans Tech Publications Ltd., 167, pp. 162-171.
- Holford, K.M. and Pullin, R., 2007. Current practice and applications of acoustic emission. In *Experimental Analysis of Nano and Engineering Materials and Structures*. Springer, Dordrecht, pp. 927-928.
- Hu, X., Zhang, M., Sun, M., Huang, K. and Song, Y., 2015. Deformation characteristics and failure mode of the Zhujiadian landslide in the Three Gorges Reservoir, China. *Bulletin of Engineering Geology and the Environment*, 74(1), pp.1-12.
- Huang, N.E., Shen, Z., Long, S.R., Wu, M.C., Shih, H.H., Zheng, Q., Yen, N.C., Tung, C.C. and Liu, H.H., 1998, March. The empirical mode decomposition and the Hilbert spectrum for nonlinear and non-stationary time series analysis. In *Proceedings of the Royal Society of London A: Mathematical, Physical and Engineering Sciences*. The Royal Society. 454(1971) pp. 903-995.
- Hung, M.H., Lauchle, G.C. and Wang, M.C., 2009. Seepage-induced acoustic emission in granular soils. *Journal of geotechnical and geoenvironmental engineering*, 135(4), pp.566-572.
- Hungr, O., Leroueil, S. and Picarelli, L., 2014. The Varnes classification of landslide types, an update. *Landslides*, 11(2), pp.167-194.

- Husin, S., Addali, A. and Mba, D., 2013. Feasibility study on the use of the Acoustic Emission technology for monitoring flow patterns in two phase flow. *Flow Measurement and Instrumentation*, 33, pp.251-256.
- Iliopoulos, A., Weijtjens, W., Van Hemelrijck, D. and Devriendt, C., 2017. Fatigue assessment of offshore wind turbines on monopile foundations using multi-band modal expansion. *Wind Energy*, 20(8), pp.1463-1479.
- Izakian, H., Pedrycz, W. and Jamal, I., 2015. Fuzzy clustering of time series data using dynamic time warping distance. *Engineering Applications of Artificial Intelligence*, 39, pp.235-244.
- Jiang, X.J., Wang, J.D., Jiang, B.B., Yang, Y. and Hou, L.X., 2007. Study of the power spectrum of acoustic emission (AE) by accelerometers in fluidized beds. *Industrial & Engineering Chemistry Research*, 46(21), pp.6904-6909.
- Jiang, Y., Wang, G. and Kamai, T., 2017. Acoustic emission signature of mechanical failure: Insights from ring-shear friction experiments on granular materials. *Geophysical Research Letters*, 44(6), pp.2782-2791.
- Johnson, P.A., Ferdowsi, B., Kaproth, B.M., Scuderi, M., Griffa, M., Carmeliet, J., Guyer, R.A., Le Bas, P.Y., Trugman, D.T. and Marone, C., 2013. Acoustic emission and microslip precursors to stick-slip failure in sheared granular material. *Geophysical Research Letters*, 40(21), pp.5627-5631.
- Knappett J.A., and Craig, R.F., 2012. *Craig's Soil Mechanics*. 8th ed. Abingdon: Spon Press, pp.171
- Koerner, R.M., McCabe, W.M. and Lord Jr, A.E., 1981. Overview of acoustic emission monitoring of rock structures. *Rock mechanics*, 14(1), pp.27-35.
- ^aKoerner, R.M., Lord Jr, A.E. and Deutsch, W.L., 1984. Determination of prestress in cohesive soils using AE. *Journal of Geotechnical Engineering*, 110(11), pp.1537-1548.
- ^bKoerner, R.M., Lord Jr, A.E. and Deutsch, W.L., 1984. Determination of prestress in granular soils using AE. *Journal of Geotechnical Engineering*, 110(3), pp.346-358.
- Korkolis, E. and Niemeijer, A.R., 2017. Insights into Earthquake Nucleation from Acoustic Emissions and Stick-slip Instabilities in Friction Experiments. In 79th EAGE Conference and Exhibition 2017.
- Kostis, H., 2018. Global Landslide Catalogue [online] Nasa. Available at: <https://svs.gsfc.nasa.gov/4632> [Accessed: 10/07/2019].
- Krathe, V.L. and Kaynia, A.M., 2017. Implementation of a non-linear foundation model for soil-structure interaction analysis of offshore wind turbines in FAST. *Wind Energy*, 20(4), pp.695-712.

- Kumar, J. and Madhusudhan, B.N., 2012. Dynamic properties of sand from dry to fully saturated states. *Geotechnique*, 62(1), pp.45-54.
- Lai, J., Yang, P.C., Yang, B.H. and Chang, D.W., 2017. Integrity Testing of Model Pile with Embedded Accelerometers. *DEStech Transactions on Materials Science and Engineering*, (ictim).
- Lee, M.W. and Waite, W.F., 2007. Amplitude loss of sonic waveform due to source coupling to the medium. *Geophysical Research Letters*, 34(5).
- Leinov, E., Lowe, M.J. and Cawley, P., 2015. Investigation of guided wave propagation and attenuation in pipe buried in sand. *Journal of Sound and Vibration*, 347, pp.96-114.
- Leinov, E., Lowe, M.J. and Cawley, P., 2016. Ultrasonic isolation of buried pipes. *Journal of Sound and Vibration*, 363, pp.225-239.
- Leroueil, S. 2001. Natural slopes and cuts: movement and failure mechanisms. *Géotechnique*, 51(3): 197–243.
- Lesny, K., Paikowsky, S.G. and Gurbuz, A., 2007. Scale effects in lateral load response of large diameter monopiles. In *Contemporary Issues In Deep Foundations*, pp.1-10.
- Li, F., Huang, L., Zhang, H. and Yang, T., 2017. Attenuation of acoustic emission propagation along a steel strand embedded in concrete. *KSCE Journal of Civil Engineering*, pp.1-9.
- Li, Z., Jing, L., Wang, W., Li, Y., Dubey, A., Lee, P. and Murch, R., 2018, May. Measurement and analysis of wave propagation in water-filled steel pipeline using iterative quadratic maximum likelihood algorithm. In *Proceedings of Meetings on Acoustics 175ASA*. Acoustical Society of America, 33(1) pp. 045001.
- Li, Z., Jing, L., Wang, W., Lee, P. and Murch, R., 2019. The influence of pipeline thickness and radius on guided wave attenuation in water-filled steel pipelines: Theoretical analysis and experimental measurement. *The Journal of the Acoustical Society of America*, 145(1), pp.361-371.
- Liu, C.H. and Nagel, S.R., 1992. Sound in sand. *Physical Review Letters*, 68(15), p.2301.
- Lo, K.F., Ni, S.H. and Huang, Y.H., 2010. Non-destructive test for pile beneath bridge in the time, frequency, and time-frequency domains using transient loading. *Nonlinear Dynamics*, 62(1), pp.349-360.
- Lockner, D., 1993, December. The role of acoustic emission in the study of rock fracture. In *International Journal of Rock Mechanics and Mining Sciences & Geomechanics Abstracts*. Pergamon, 30(7), pp. 883-899.

- London array, n.d. Offshore Construction. [online] Available at: <http://www.londonarray.com/the-project-3/offshore-construction/>. [Accessed: 18/12/2018].
- ^aLong, R., Cawley, P. and Lowe, M., 2003, November. Acoustic wave propagation in buried iron water pipes. In *Proceedings of the Royal Society of London A: Mathematical, Physical and Engineering Sciences*. The Royal Society, 459(2039), pp.2749-2770.
- ^bLong, R., Lowe, M. and Cawley, P., 2003. Attenuation characteristics of the fundamental modes that propagate in buried iron water pipes. *Ultrasonics*, 41(7), pp.509-519.
- Lord, A.E. and Koerner, R.M., 1974. Acoustic emission response of dry soils. *Journal of Testing and Evaluation*, 2(3), pp.159-162.
- Lowe, M.J., 1995. Matrix techniques for modelling ultrasonic waves in multilayered media. *IEEE transactions on ultrasonics, ferroelectrics, and frequency control*, 42(4), pp.525-542.
- Lowe, M. and Pavlakovic, B., 2013. DISPERSE user manual.
- Madarshahian, R., Soltangharai, V., Anay, R., Caicedo, J.M. and Ziehl, P., 2019. Hsu-Nielsen source acoustic emission data on a concrete block. *Data in brief*, 23, p.103813.
- Mair, K., Marone, C. and Young, R.P., 2007. Rate dependence of acoustic emissions generated during shear of simulated fault gouge. *Bulletin of the seismological Society of America*, 97(6), pp.1841-1849.
- Maji, A.K., Satpathi, D. and Kratochvil, T., 1997. Acoustic emission source location using lamb wave modes. *Journal of engineering mechanics*, 123(2), pp.154-161.
- Majmudar, T.S. and Behringer, R.P., 2005. Contact force measurements and stress-induced anisotropy in granular materials. *Nature*, 435(7045), pp.1079-1082.
- Mao, W. and Towhata, I., 2015. Monitoring of single-particle fragmentation process under static loading using acoustic emission. *Applied Acoustics*, 94, pp.39-45.
- Mao, W., Aoyama, S., Goto, S. and Towhata, I., 2015. Acoustic emission characteristics of subsoil subjected to vertical pile loading in sand. *Journal of Applied Geophysics*, 119, pp.119-127.
- Mao, W., Towhata, I., Aoyama, S. and Goto, S., 2016. Grain Crushing under Pile Tip Explored by Acoustic Emission. *Geotechnical Engineering*, 47(4), pp.164-175.
- Maze, G., Cheeke, J.D.N., Li, X. and Wang, Z., 2001. Coupled guided acoustic modes in water-filled thin-walled tubes. *The Journal of the Acoustical Society of America*, 110(5), pp.2295-2300.
- McLaskey, G.C. and Glaser, S.D., 2011. Micromechanics of asperity rupture during laboratory stick slip experiments. *Geophysical Research Letters*, 38(12).

- Menck, n.d. Walney extension. [online] Available at:
<https://www.menck.com/index.php/projects/walney> [Accessed: 25/07/2019]
- Menck, 2015. Amrumbank West. [online] Available at:
<https://www.menck.com/index.php/projects/amrumbank-west> [Accessed: 25/07/2019]
- ^aMichlmayr, G., Or, D. and Cohen, D., 2012. Fiber bundle models for stress release and energy bursts during granular shearing. *Physical Review E*, 86(6), p.061307.
- ^bMichlmayr, G., Cohen, D. and Or, D., 2012. Sources and characteristics of acoustic emissions from mechanically stressed geologic granular media—A review. *Earth-Science Reviews*, 112(3-4), pp.97-114.
- Michlmayr, G., 2013. Characteristics of force jumps and energy release during shearing of granular material-acoustic emissions measurements and fiber-bundle models (Doctoral dissertation, University of Natural Resources and Life Sciences, Vienna).
- Michlmayr, G., Cohen, D. and Or, D., 2013. Shear-induced force fluctuations and acoustic emissions in granular material. *Journal of Geophysical Research: Solid Earth*, 118(12), pp.6086-6098.
- Michlmayr, G., Chalari, A., Clarke, A. and Or, D., 2017. Fiber-optic high-resolution acoustic emission (AE) monitoring of slope failure. *Landslides*, pp.1-8.
- Mirsky, I., 1965. Wave propagation in transversely isotropic circular cylinders Part I: Theory. *The journal of the Acoustical Society of America*, 37(6), pp.1016-1021.
- Mishra, B.K. and Thornton, C., 2001. Impact breakage of particle agglomerates. *International Journal of Mineral Processing*, 61(4), pp.225-239.
- Montoto, M., Suarez del Rio, L.M., Khair, A.W. and Hardy Jr, H.R., 1984. AE in uniaxially loaded granitic rocks in relation to their petrographic character. *Ser. Rock Soil Mech.:(United States)*, 8(CONF-811036-).
- Mostafapour, A. and Davoudi, S., 2013. Analysis of leakage in high pressure pipe using acoustic emission method. *Applied Acoustics*, 74(3), pp.335-342.
- Naderi-Boldaji, M., Bahrami, M., Keller, T. and Or, D., 2017. Characteristics of acoustic emissions from soil subjected to confined uniaxial compression. *Vadose Zone Journal*, 16(7).
- National Instruments, 2020, Software filtering: Windowing - General Analog Concepts [online] Available at: <https://www.ni.com/en-gb/support/documentation/supplemental/06/software-filtering--windowing---general-analog-concepts.html> [Accessed: 20/02/2020]

- NDT Resources, n.d. Modes of sound wave propagation [online] Available at: <https://www.nde-ed.org/EducationResources/CommunityCollege/Ultrasonics/Physics/modepropagation.htm> [Accessed: 19/02/2020]
- NDT, 2007. Hsu-Nielson test [online] Available at: <https://www.ndt.net/ndtaz/content.php?id=474> [Accessed: 19/02/2020]
- Ni, S.H., Lo, K.F., Lehmann, L. and Huang, Y.H., 2008. Time–frequency analyses of pile-integrity testing using wavelet transform. *Computers and Geotechnics*, 35(4), pp.600-607.
- Ni, S.H., Isenhowe, W.M. and Huang, Y.H., 2012. Continuous wavelet transform technique for low-strain integrity testing of deep drilled shafts. *Journal of GeoEngineering*, 7(3), pp.097-105.
- Ni, S.H., Yang, Y.Z., Tsai, P.H. and Chou, W.H., 2017. Evaluation of pile defects using complex continuous wavelet transform analysis. *NDT & E International*, 87, pp.50-59.
- Nishimura, S., Minh, N.A. and Jardine, R.J., 2007. Shear strength anisotropy of natural London Clay. *Géotechnique*, 57(1), pp.49-62.
- NJUG, 2013. NJUG Guidelines on the Positioning and Colour Coding of Underground Utilities' Apparatus. [online] Available at: <http://streetworks.org.uk/wp-content/uploads/2016/09/V1-Positioning-Colour-Coding-Issue-8.pdf> [Accessed: 25/07/2019]
- Noda, S. and Hyodo, M., 2013. Effects of fines content on cyclic shear characteristics of sand–clay mixtures. In *Proceedings of the Eighteenth International Soil Mechanics and Geotechnical Engineering Conference* (pp. 1551-1554).
- Nordlund, E. and Li, C., 1990. Acoustic emission and the Kaiser effect in rock materials. In *The 31th US Symposium on Rock Mechanics (USRMS)*. American Rock Mechanics Association.
- Oelze, M.L., O'Brien, W.D. and Darmody, R.G., 2002. Measurement of attenuation and speed of sound in soils. *Soil Science Society of America Journal*, 66(3), pp.788-796.
- Okwori et al., 2016. Concrete repair, rehabilitation and retrofitting IV. An investigative study into the application of non-destructive testing techniques for integrity assessment of RC piles, pp.237-244.
- ^aOxford Dictionary, n.d. Wave. [online] Available at: <https://www.lexico.com/definition/wave> [Accessed: 19/02/2020]
- ^bOxford Dictionary, n.d. Infrastructure [online] Available at: <https://www.lexico.com/definition/infrastructure> [Accessed: 19/02/2020]

- Pannese, E. M., Take, W. A., Hoult, N. A., Yan, R., & Le, H., 2019. Bridge transition monitoring: Interpretation of track defects using digital image correlation and distributed fiber optic strain sensing. *Proceedings of the Institution of Mechanical Engineers, Part F: Journal of Rail and Rapid Transit*, 0954409719851626.
- Parisher, R.A. and Rhea, R.A., 2001. *Pipe drafting and design*. Gulf Professional Publishing.
- Pavlakovic, B., Lowe, M., Alleyne, D. and Cawley, P., 1997. Disperse: a general purpose program for creating dispersion curves. In *Review of progress in quantitative nondestructive evaluation* (pp. 185-192). Springer US.
- Pavlakovic, B.N., Lowe, M.J.S. and Cawley, P., 2001. High-frequency low-loss ultrasonic modes in imbedded bars. *Transactions-American Society of Mechanical Engineers Journal of Applied Mechanics*, 68(1), pp.67-75.
- Pelecanos, L., Soga, K., Chung, M. P., Ouyang, Y., Kwan, V., Kechavarzi, C., & Nicholson, D., 2017. Distributed fibre-optic monitoring of an Osterberg-cell pile test in London. *Geotechnique Letters*, 7(2), 152-160.
- Pollock, A.A., 1986. Classical wave theory in practical AE testing. *Progress in Acoustic Emission III-JAP Society of Non-Destructive Testing*, pp.708-721.
- Poncelet, O. and Deschamps, M., 1997. Lamb waves generated by complex harmonic inhomogeneous plane waves. *The Journal of the Acoustical Society of America*, 102(1), pp.292-300.
- Read, M.D., Ayling, M.R., Meredith, P.G. and Murrell, S.A., 1995. Microcracking during triaxial deformation of porous rocks monitored by changes in rock physical properties, II. Pore volumetry and acoustic emission measurements on water-saturated rocks. *Tectonophysics*, 245(3), pp.223-235.
- Rendon, E.A. and Manuel, L., 2014. Long-term loads for a monopile-supported offshore wind turbine. *Wind Energy*, 17(2), pp.209-223.
- Rose, J.L., Avioli, M.J., Mudge, P. and Sanderson, R., 2004. Guided wave inspection potential of defects in rail. *NDT & E International*, 37(2), pp.153-161.
- Rose, J.L., 2014. *Ultrasonic guided waves in solid media*. Cambridge University Press.
- Rouse, C., Styles, P. and Wilson, S.A., 1991. Microseismic emissions from flowslide-type movements in South Wales. *Engineering Geology*, 31(1), pp.91-110.
- Rumpf, H., 1962. The strength of granules and agglomerates. *Agglomeration (Conference)*, New York, Interscience, pp.379-414.

- Sakuma, T., Sakamoto, S. and Otsuru, T., 2014. Computational simulation in architectural and environmental acoustics. Springer Japan, pp. 296-297.
- Sause, M.G., 2011. Investigation of pencil-lead breaks as acoustic emission sources. *Journal of acoustic emission*, 29.
- Schneider, J.B., 2017. Understanding the finite-difference time-domain method. School of electrical engineering and computer science Washington State University, pp.181.
- Scholtès, L., Chareyre, B., Nicot, F. and Darve, F., 2009. Micromechanics of granular materials with capillary effects. *International journal of engineering science*, 47(1), pp.64-75.
- Severn Trent Water, 2016. Severn Trent design manual for self lay providers [online] Available at: https://www.stwater.co.uk/content/dam/stw/stw_buildinganddeveloping/STW-SLO-Design-Manual-Final-V1.1.pdf [Accessed:25/07/2019]
- Shehadeh, M. and Elghamry, M., 2005. Effect of internal and external environment on acoustic emission propagation in long steel pipes. In 9th International Conference on Mining, Petroleum, and Metallurgical Engineering.
- Shehadeh, M., Steel, J.A. and Reuben, R.L., 2006. Acoustic emission source location for steel pipe and pipeline applications: the role of arrival time estimation. *Proceedings of the Institution of Mechanical Engineers, Part E: Journal of Process Mechanical Engineering*, 220(2), pp.121-133.
- Shehadeh, M.F., Abdou, W., Steel, J.A. and Reuben, R.L., 2008. Aspects of acoustic emission attenuation in steel pipes subject to different internal and external environments. *Proceedings of the Institution of Mechanical Engineers, Part E: Journal of Process Mechanical Engineering*, 222(1), pp.41-54.
- Shehadeh, M.F., Elbatran, A.H., Mehanna, A., Steel, J.A. and Reuben, R.L., 2019. Evaluation of Acoustic Emission Source Location in Long Steel Pipes for Continuous and Semi-continuous Sources. *Journal of Nondestructive Evaluation*, 38(2), p.40.
- Smith, A. and Dixon, N., 2014. Acoustic emission monitoring of active waveguides to quantify slope stability.
- Smith, A., Dixon, N., Meldrum, P., Haslam, E. and Chambers, J., 2014. Acoustic emission monitoring of a soil slope: Comparisons with continuous deformation measurements. *Géotechnique Letters*, 4(4), pp.255-261.

Smith, A. and Dixon, N., 2015. Quantification of landslide velocity from active waveguide-generated acoustic emission. *Canadian Geotechnical Journal*, 52(4), pp.413-425.

^aSmith, A., Dixon, N., Meldrum, P., Haslam, E. and Chambers, J., 2014. Acoustic emission monitoring of a soil slope: Comparisons with continuous deformation measurements. *Géotechnique Letters*, 4(4), pp.255-261.

^bSmith, A., Dixon, N., Meldrum, P. and Haslam, E., 2014. Inclinator casings retrofitted with acoustic real-time monitoring systems. *Ground Engineering*, pp.1-6.

Smith, A., 2015. Quantification of slope deformation behaviour using acoustic emission monitoring (Doctoral dissertation, © Alister Smith).

Smith, A., Dixon, N. and Fowmes, G., 2017. Monitoring buried pipe deformation using acoustic emission: quantification of attenuation. *International Journal of Geotechnical Engineering*, 11(4), pp.418-430.

Smith, A. and Dixon, N., 2019. Acoustic emission behaviour of dense sands. [online] Available at: <https://dspace.lboro.ac.uk/dspace-jspui/handle/2134/36586> [Accessed: 25/07/2019]

Staron, L., Radjai, F. and Vilotte, J.P., 2006. Granular micro-structure and avalanche precursors. *Journal of Statistical Mechanics: Theory and Experiment*, 2006(07), pp.P07014.

Stein, D., 2004. *Rehabilitation and Maintenance of Drains and Sewers*. Brelin: Ernst & Sohn Verlag. ISBN 3-433-01316-0.

Su, Z., Ye, L. and Lu, Y., 2006. Guided Lamb waves for identification of damage in composite structures: A review. *Journal of sound and vibration*, 295(3-5), pp.753-780.

Suzuki, H., Kinjo, T., Hayashi, Y., Takemoto, M., Ono, K. and Hayashi, Y., 1996. Wavelet transform of acoustic emission signals. *Journal of acoustic emission*, 14, pp.69-84.

Terzaghi, K., 1950. *Geologic aspects of soft-ground tunnelling*. Wiley.

Thames Water, 2015. Mains design guidelines for self-lay organisations working in new developments. [online] Available at: <https://www.thameswater.co.uk/-/media/Site-Content/Developer-Services/Mains-design-guidelines.pdf> [Accessed: 25/07/2019]

Thames Water, 2019. [online] <https://www.thameswater.co.uk/help-and-advice/leaks/fixing-leaks> [Accessed: 13/06/2019]

- Tong, Z.W., Han, Q.B., Yin, C., Qi, L.H., Zhang, Y. and Zhu, C.P., 2016. Guided Waves in a Solid Rod Embedded in Infinite Medium with Weak Interface. In MATEC Web of Conferences, EDP Sciences, 44, pp.02012.
- Uhlemann, S., Smith, A., Chambers, J., Dixon, N., Dijkstra, T., Haslam, E., Meldrum, P., Merritt, A., Gunn, D. and Mackay, J., 2016. Assessment of ground-based monitoring techniques applied to landslide investigations. *Geomorphology*, 253, pp.438-451.
- UKPIA, 2019. Transportation, terminals and pipelines. [online] Available at: <https://www.ukpia.com/our-contribution/uk-downstream-oil-sector/transportation-terminals-and-pipelines/> [Accessed: 25/07/2019].
- USGS, n.d. Earthquake glossary [online]. Available at: <https://earthquake.usgs.gov/learn/glossary/?term=seismic%20wave> [Accessed: 19/02/2020]
- Varnes, D.J., 1978. Slope movement types and processes. Transportation Research Board Special Report, 176.
- Wang, Y.H. and Santamarina, J.C., 2007. Attenuation in sand: an exploratory study on the small-strain behaviour and the influence of moisture condensation. *Granular Matter*, 9(6), pp.365-376.
- Water UK, 2017. Self-lay code of practice. [online] Available at: <https://www.water.org.uk/self-lay-code-of-practice/> [Accessed:25/07/2019]
- Welker, P. and McNamara, S., 2011. Precursors of failure and weakening in a biaxial test. *Granular Matter*, 13(1), pp.93-105.
- Wilcox, P., Pavlakovic, B., Evans, M., Vine, K., Cawley, P., Lowe, M. and Alleyne, D., 2003, March. Long range inspection of rail using guided waves. In *Review of Progress in Quantitative Nondestructive evaluation: Volume 22*. AIP Publishing, 657(1), pp. 236-243).
- Wilkinson, P., Chambers, J., Uhlemann, S., Meldrum, P., Smith, A., Dixon, N. and Loke, M.H., 2016. Reconstruction of landslide movements by inversion of 4-D electrical resistivity tomography monitoring data. *Geophysical Research Letters*, 43(3), pp.1166-1174.
- Wille-Geotechnik, n.d. Large direct shear test systems. [online] Available at: https://www.wille-geotechnik.com/en/Large_Shear_Systems.html [Accessed: 26/07/2019]
- Wolfe, n.d. What is acoustic impedance and why is it important? [online] Available at: <https://newt.phys.unsw.edu.au/jw/z.html> [Accessed: 26/07/2019]

- Xie, Y., Rodriguez, S., Zhang, W., Liu, Z. and Yin, W., 2016. Simulation of an electromagnetic acoustic transducer array by using analytical method and FDTD. *Journal of Sensors*.
- Yamada, S. and Oshima, A., 2016. An attempting research on evaluating grain-size characteristics based on acoustic properties of soil for liquefaction assessment by Swedish Ram Sounding. *Japanese Geotechnical Society Special Publication*, 2(7), pp.321-326.
- Yang, Z. X., Jardine, R. J., Zhu, B. T., Foray, P. & Tsuha, C. H. C. (2010). Sand grain crushing and interface shearing during displacement pile installation in sand. *Géotechnique* 60, No. 6, 469–482, doi: 10.1680/geot.2010.60.6.469.
- Zand, 2018. Geo-hazard Monitoring of Pipelines using Strain Gauges. [online] The Applus+ Blog. Available at: <https://blog.applus.com/geo-hazard-pipelines-strain-gauges/> [Accessed: 28/10/2019]
- Zhang, J., Wong, T.F., Yanagidani, T. and Davis, D.M., 1990. Pressure-induced microcracking and grain crushing in Berea and Boise sandstones: Acoustic emission and quantitative microscopy measurements. *Mechanics of Materials*, 9(1), pp.1-15.
- Zhang, J., Lin, H. and Doolittle, J., 2014. Soil layering and preferential flow impacts on seasonal changes of GPR signals in two contrasting soils. *Geoderma*, 213, pp.560-569.
- Zheng, J. and Hryciw, R.D., 2015. Traditional soil particle sphericity, roundness and surface roughness by computational geometry. *Géotechnique*, 65(6), pp.494-506.
- Zheng, C., Ding, X., Kouretzis, G., Liu, H. and Sun, Y., 2018. Three-dimensional propagation of waves in piles during low-strain integrity tests. *Géotechnique*, 68(4), pp.358-363.
- Zhou, Y.C., Wright, B.D., Yang, R.Y., Xu, B.H. and Yu, A.B., 1999. Rolling friction in the dynamic simulation of sandpile formation. *Physica A: Statistical Mechanics and its Applications*, 269(2), pp.536-553.
- Zhu, J., Popovics, J.S. and Schubert, F., 2004. Leaky Rayleigh and Scholte waves at the fluid–solid interface subjected to transient point loading. *The Journal of the Acoustical Society of America*, 116(4), pp.2101-2110.
- Zigone, D., Voisin, C., Larose, E., Renard, F. and Campillo, M., 2011. Slip acceleration generates seismic tremor like signals in friction experiments. *Geophysical Research Letters*, 38(1).

Appendices

AP1.0 Landslides

Landslides may be initiated by a range of triggers and in a variety of materials and formats. Consequently, landslides can take on many forms. It is useful to be able to classify these, and more importantly their causative mechanism, as this can provide an understanding on the potential of future failures events. Hungr et al. (2014) offer such classification in the form of a 32-class landslide system based on the type of failure movement and material (Table AP 1.1).

The system consists of 32 major landslide classes based around 6 movement types for 2 materials: rock and soil. It is a modern adaptation of Varnes’s original 1978 classification system, allowing for more precise categorisation with simplistic descriptive terms (Section GL3.1) relating to modern terminology and understanding. Furthermore, sub-categories can be used in composite to describe more complex mass movements.

Table AP1.1 A modern adaptation of Varnes (1978) landslide classification system containing 32 sub-categories for six movement types. From Hungr et al. (2014).

Type of movement	Rock	Soil
Fall	1 Rock/ice fall	2 Boulder/debris/silt fall
Topple	3 Rock block topple 4 Rock flexural topple	5 Gravel/sand/silt topple
Slide	6 Rock rotational slide 7 Rock planar slide 8 Rock wedge slide 9 Rock compound slide 10 Rock irregular slide	11 Clay/silt rotational slide 12 Clay/silt planar slide 13 Gavel/sand/debris slide 14 Clay/silt compound slide
Spread	15 Rock slope spread	16 Sand/silt liquefaction spread 17 Sensitive clay spread
Flow	18 Rock/ice avalanche	19 Sand/silt/debris dry flow 20 Sand/silt/debris flow slide 21 Sensitive clay flow slide 22 Debris flow 23 Mud flow 24 Debris flood 25 Debris avalanche 26 Earth flow 27 Peat flow
Slope deformation	28 Mountain slope deformation 29 Rock slope deformation	30 Soil slope deformation 31 Soil creep 32 Solifluction

Understanding the type of material failure is important for understanding the mechanisms behind instability and consequent AE generation. Understanding material failure is however also important

for interpreting the effects of material failures on buried infrastructure. In engineering, it is therefore important to recognise the differing geotechnical characteristics of different materials within the classification system. Consequently, a supplementary classification table describing mechanical properties for different materials was developed by Hungr et al. (2014) to compliment the updated landslide classification system (Table AP 1.2).

Table AP1.2 The mechanical properties of different soils in the field (From Hungr et al., 2014).

Material name	Character descriptors	Simplified field description
Rock	Strong Weak	Strong-broken with a hammer Weak-peeled with a knife
Clay	Stiff Soft Sensitive	Plastic, can be moulded into standard thread when moist, has dry strength
Mud	Liquid	Plastic, unsorted remoulded, and close to liquid limit
Silt, Sand, Gravel, and boulders	Dry Saturated Partly saturated	Nonplastic (or very low plasticity), granular, sorted. Silt particles cannot be seen by eye.
Debris	Dry Saturated Partly saturated	Low plasticity, unsorted and mixed
Peat	-	Organic
Ice	-	Glacier

Further complimenting Table AP1.2, Cruden and Varnes (1996) suggest a system to quantitatively categorise landslide velocities based on magnitude (Table AP1.3). Classifying landslide velocities is useful for determining the potential severity of material failures and thus the response that should be taken (Hungr et al, 2014).

Table AP1.3 Landslide velocity scale (From Cruden and Varnes, 1996).

Velocity class	Description	Velocity (mm/s)	Typical velocity	Suggested response
7	Extremely rapid	5×10^3	5 m/s	Nil
6	Very rapid	5×10^1	3 m/min	Nil
5	Rapid	5×10^{-1}	1.8 m/h	Evacuation
4	Moderate	5×10^{-3}	13 m/month	Evacuation
3	Slow	5×10^{-5}	1.6 m/year	Maintenance
2	Very slow	5×10^{-7}	1.6 mm/year	Maintenance
1	Extremely slow	-	-	Nil

AP2.0 Windowing

The effects of window type when performing FFTs on collected waveform data were tested by collecting waveform data for a free-bound, small-scale pipe system. Figure AP2.1 shows an exemplar frequency spectrum from the study for three windows: rectangular (DIAdem’s default choice), Hanning and Cauchy.

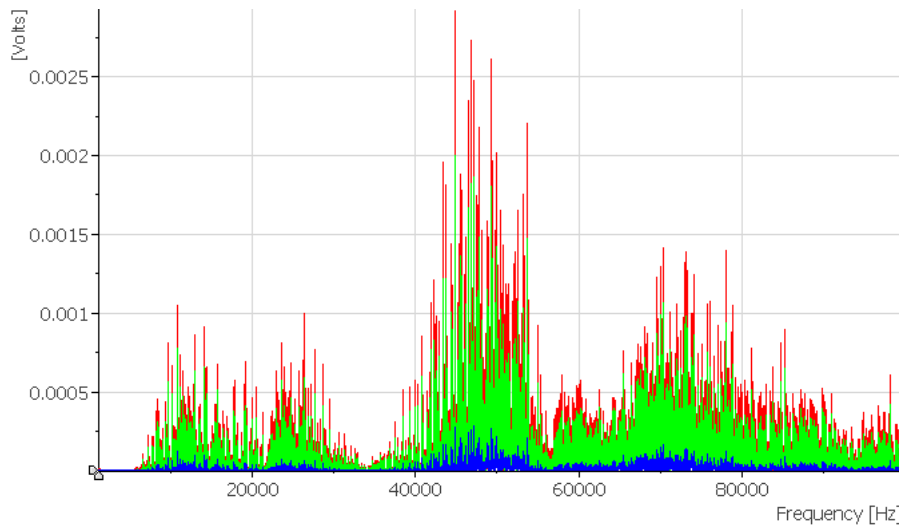


Figure AP2.1 Exemplar frequency spectra calculated in DIAdem from collected waveform data using three windows: rectangular (red), Hanning (green), and Cauchy (blue).

Figure AP2.1 shows that the different windows produce very similar frequency spectra for which the frequency peaks remain approximately constant, however, the magnitudes vary. This has been statistically analysed by comparing the differences between the spectra (i.e. subtracting one from the other), examples of which is shown in Figures AP2.2 and AP2.3 for the rectangular to Hanning and rectangular to Cauchy windows.

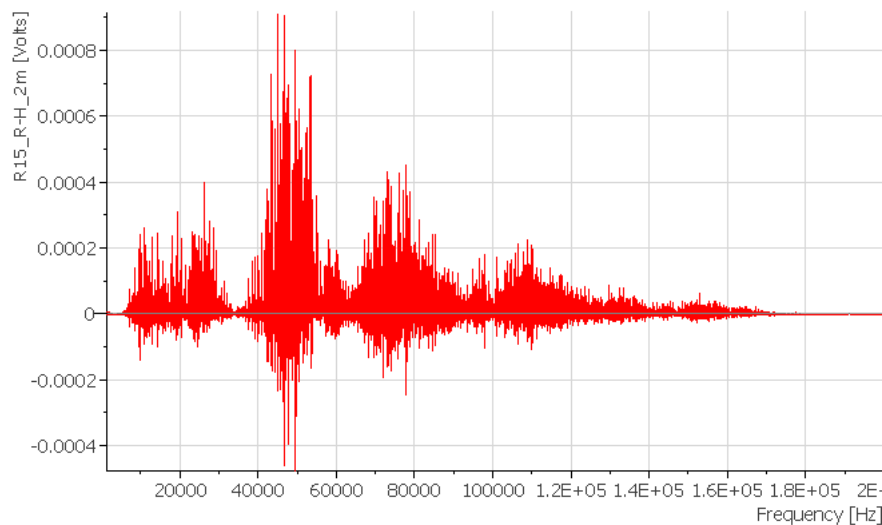


Figure AP2.2 An example of the difference between a rectangular and Hanning window for FFT calculations.

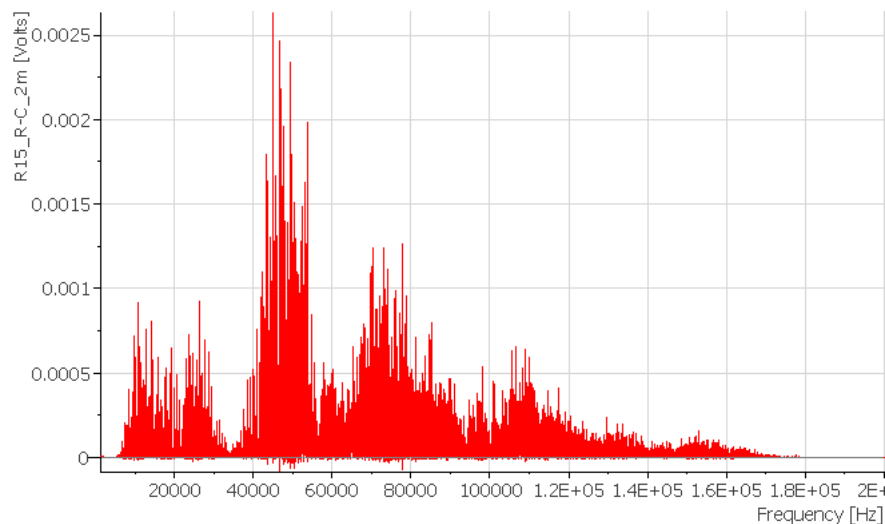


Figure AP2.3 An example of the difference between a rectangular and Cauchy window for FFT calculations.

Comparing Figures AP2.2 and AP2.3 several observations may be made:

- The difference between a rectangular and Cauchy window is much greater than a rectangular and Hanning window with maximum differences in amplitude of around 0.0026 V compared to 0.0009 V respectively. The peak signal strengths in Figure AP2.1 range between 0.001 and 0.003 V. This implies that the Cauchy window, for which differences of up to 0.0026 V were measured, produces a very weak spectrum.
- Differences between the rectangular and Hanning windows, however, vary between being positive and negative (i.e. some frequencies are stronger, and some are weaker dependent on the window), whereas for the rectangular and Cauchy window are generally positive (i.e. always weaker). This suggests that the windows may be more or less sensitive to different frequencies with the Cauchy and rectangular windows being the most similar of those tested.
- The general shape of each spectrum mirrors that of the rectangular spectrum shown in Figure AP2.1 confirming that the frequencies calculated are the same.

Given these observations, it may be concluded that, although there are differences in the spectra produced, important observations from each, such as frequency dominance, remain constant whilst the rectangular window, although the simplest window type, produces the strongest spectrum.

AP3.0 Large-scale testing: Repeatability tests

For each large-scale test, experiments were repeated by inputting and recording several pencil lead break signals conducted using the same method. These are shown in Figures AP3.1 to AP3.4 and compare the results of 0.5 and 0.9 mm diameter pencil leads in experiments studying both propagation through a joint (Figures AP3.1 and AP3.2), and the sensitivity of sensor placement (Figures AP3.3 and AP3.4). Furthermore, Tables AP3.1 to AP3.4 show the measured and calculated amplitudes, attenuation and wave velocities for each test. Good repeatability is apparent.

Table AP3.1 Amplitude, attenuation, and wave velocity results for empty (free-steel-free) large-scale laboratory tests investigating propagation and using a Bic 0.9 mm pencil.

	Sensor 1			Sensor 2				Sensor 3			
	Wave break (s)	Max. Amplitude (Volts)	Attenuation (% initial)	Wave break (s)	Max. Amplitude (Volts)	Attenuation (% initial)	Wave velocity (m/s)	Wave break (s)	Max. Amplitude (Volts)	Attenuation (% initial)	Wave velocity (m/s)
Break 1	8.42	2.15	100.00	8.43	0.95	44.14	5000.00	8.43	0.77	35.72	5000.00
Break 2	9.55	1.73	100.00	9.55	1.02	58.96	4583.33	9.55	0.74	42.83	3333.33
Break 3	9.56	1.72	100.00	9.56	1.04	60.47	4583.33	9.56	0.72	42.09	5000.00
Break 4	10.62	2.03	100.00	10.63	1.07	52.71	5000.00	10.63	0.67	32.76	5000.00
Break 5	9.47	2.23	100.00	9.47	1.25	56.05	4583.33	9.47	0.70	31.52	5000.00
Average	-	1.97	100.00	-	1.07	54.47	4750.00	-	0.72	36.99	4666.67
Variance	-	0.04	0.00	-	0.01	33.68	41666.67	-	0.00	21.91	444444.44

Table AP3.2 Amplitude, attenuation, and wave velocity results for empty (free-steel-free) large-scale laboratory tests investigating propagation and using a standard 0.5 mm pencil.

	Sensor 1			Sensor 2				Sensor 3			
	Wave break (s)	Max. Amplitude (Volts)	Attenuation (% initial)	Wave break (s)	Max. Amplitude (Volts)	Attenuation (% initial)	Wave velocity (m/s)	Wave break (s)	Max. Amplitude (Volts)	Attenuation (% initial)	Wave velocity (m/s)
Break 1	8.63	0.44	100.00	8.63	0.35	81.01	5500.00	8.63	0.21	48.28	1666.67
Break 2	8.45	0.70	100.00	8.45	0.37	52.92	4583.33	8.45	0.29	41.25	909.09
Break 3	8.15	0.75	100.00	8.15	0.47	63.14	4583.33	8.15	0.28	36.86	1000.00
Break 4	8.61	0.42	100.00	8.61	0.27	64.69	4230.77	8.61	0.16	36.97	10000.00
Break 5	9.37	0.78	100.00	9.37	0.39	49.87	4583.33	9.37	0.26	34.02	5000.00

	Sensor 1			Sensor 2				Sensor 3			
	Wave break (s)	Max. Amplitude (Volts)	Attenuation (% initial)	Wave break (s)	Max. Amplitude (Volts)	Attenuation (% initial)	Wave velocity (m/s)	Wave break (s)	Max. Amplitude (Volts)	Attenuation (% initial)	Wave velocity (m/s)
Average	-	0.62	100.00	-	0.37	62.32	4696.15	-	0.24	39.48	3715.15
Variance	-	0.02	0.00	-	0.00	119.78	180187.38	-	0.00	24.72	12118494.03

Table AP3.3 Amplitude, attenuation, and wave velocity results for empty (free-steel-free) large-scale laboratory tests investigating sensor placement and using a Bic 0.9 mm pencil.

	Sensor 1 (0.05)			Sensor 2 (5.5)				Sensor 3 (5.5)			
	Wave break (s)	Max. Amplitude (Volts)	Attenuation (% initial)	Wave break (s)	Max. Amplitude (Volts)	Attenuation (% initial)	Wave velocity (m/s)	Wave break (s)	Max. Amplitude (Volts)	Attenuation (% initial)	Wave velocity (m/s)
Break 1	11.17	1.51	100.00	11.17	1.32	87.42	5000.00	11.17	1.10	72.85	5000.00
Break 2	10.52	0.99	100.00	10.52	1.10	110.89	5000.00	10.52	1.15	115.93	5000.00
Break 3	10.97	1.36	100.00	10.97	1.31	96.32	5000.00	10.97	1.15	84.56	5000.00
Break 4	9.30	2.32	100.00	9.30	1.70	73.28	5000.00	9.30	1.32	56.90	5000.00
Break 5	9.63	1.45	100.00	9.63	1.51	104.14	5000.00	9.63	1.26	86.90	5000.00
Average	-	1.53	100.00	-	1.39	94.41	5000.00	-	1.20	83.43	5000.00
Variance	-	0.19	0.00	-	0.04	173.07	0.00	-	0.01	377.08	0.00

Table AP3.4 Amplitude, attenuation, and wave velocity results for empty (free-steel-free) large-scale laboratory tests investigating sensor placement and using a standard 0.5 mm pencil.

	Sensor 1			Sensor 2				Sensor 3			
	Wave break (s)	Max. Amplitude (Volts)	Attenuation (% initial)	Wave break (s)	Max. Amplitude (Volts)	Attenuation (% initial)	Wave velocity (m/s)	Wave break (s)	Max. Amplitude (Volts)	Attenuation (% initial)	Wave velocity (m/s)
Break 1	9.22	0.91	100.00	9.22	0.47	52.32	3928.57	9.22	0.46	51.21	3437.50
Break 2	9.96	0.72	100.00	9.96	0.46	63.49	5000.00	9.96	0.35	47.86	4583.33
Break 3	21.00	0.79	100.00	21.00	0.66	84.48	5000.00	21.00	0.52	66.67	5000.00
Break 4	9.73	0.41	100.00	9.73	0.31	74.76	3666.67	9.73	0.23	55.10	3666.67
Break 5	10.10	0.53	100.00	10.10	0.35	65.28	5000.00	10.10	0.23	43.02	5000.00
Average	-	0.67	100.00	-	0.45	68.06	4519.05	-	0.36	52.77	4337.50
Variance	-	0.03	0.00	-	0.02	118.17	353832.20	-	0.01	64.04	439652.78

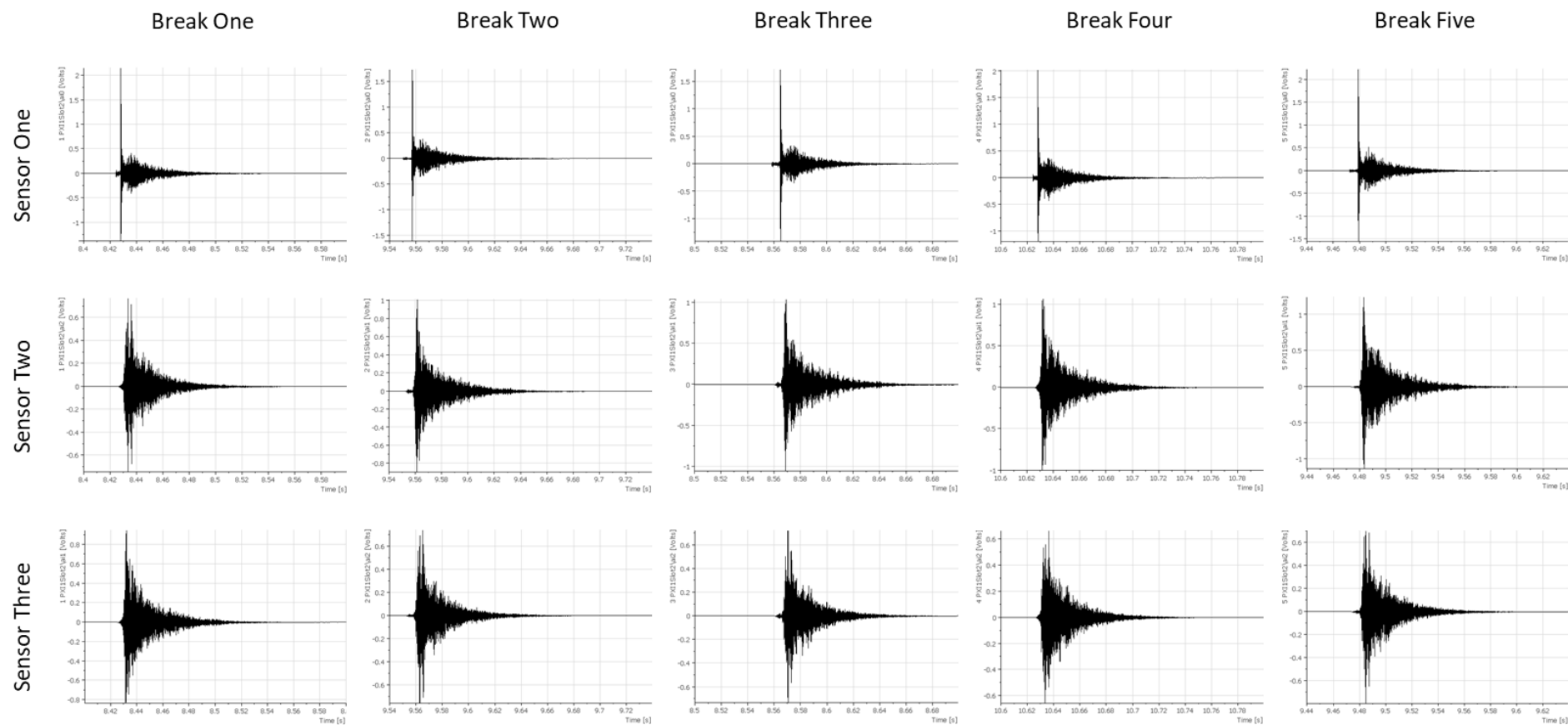


Figure AP3.1 Raw waveforms for empty (free-steel-free) large-scale laboratory tests investigating propagation and using a Bic 0.9 mm pencil.

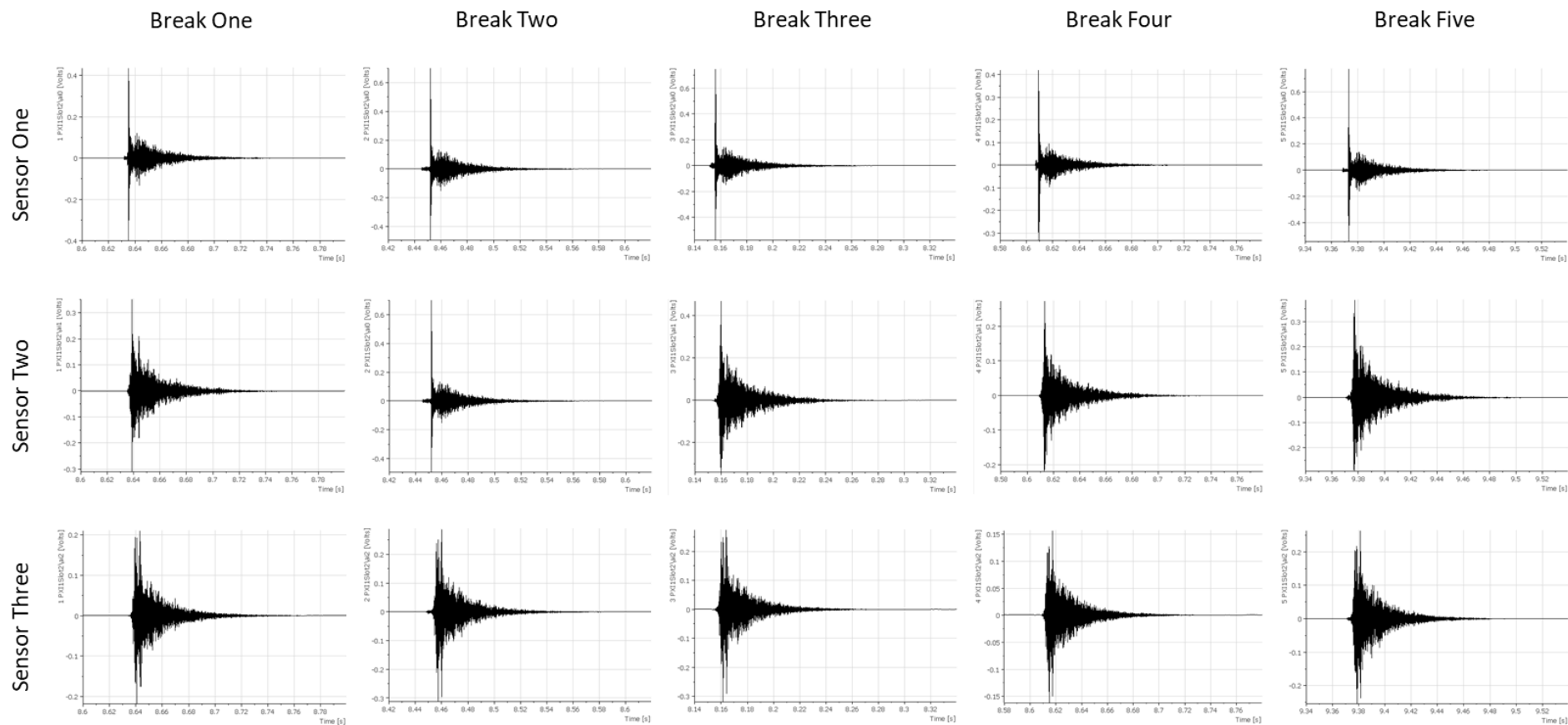


Figure AP3.2 Raw waveforms for empty (free-steel-free) large-scale laboratory tests investigating propagation and using a standard 0.5 mm pencil.

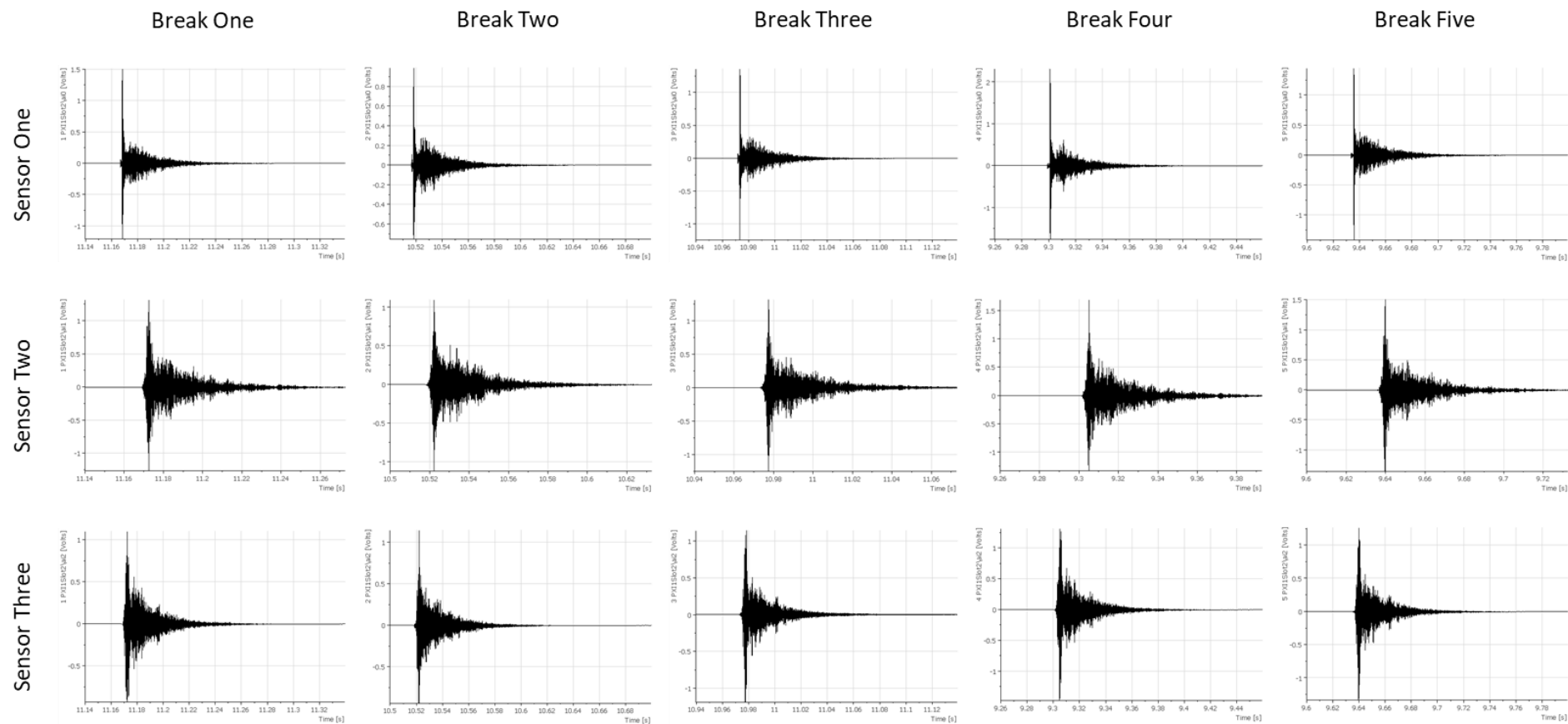


Figure AP3.3 Raw waveforms for empty (free-steel-free) large-scale laboratory tests investigating sensor placement and using a Bic 0.9 mm pencil.

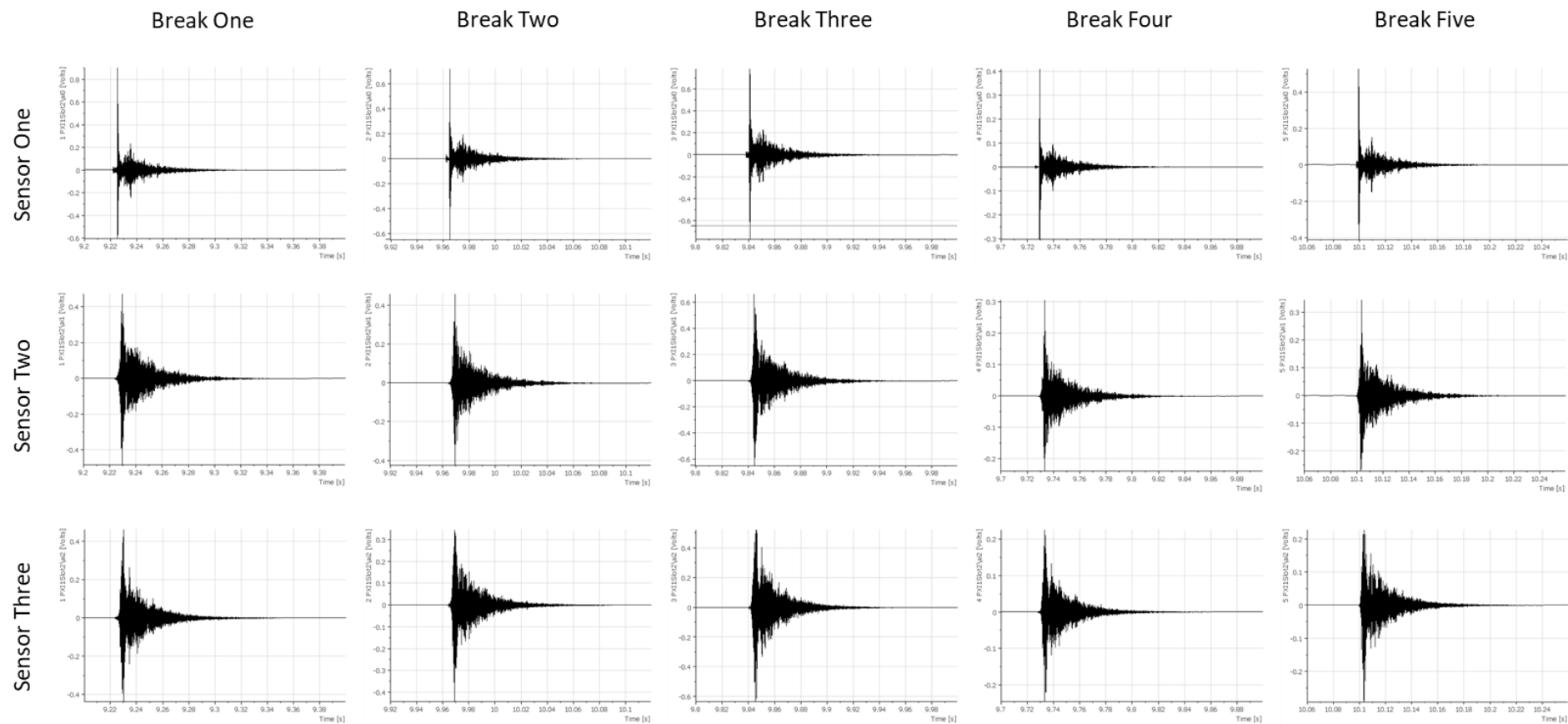


Figure AP3.4 Raw waveforms for empty (free-steel-free) large-scale laboratory tests investigating sensor placement and using a standard 0.5 mm pencil.

AP4.0 Piezoelectric transducers

Four piezoelectric transducers were tested and investigated during experimentation. The transducers were all produced by Physical Acoustic and included the R.45, R3 α , R15 α and R80 α , three of which were part of the alpha transducer series. Each was made from stainless steel and faced with a ceramic. The use of ceramics made sure that the sensor is isolated from the structure and ensured a low noise operation (Physical Acoustics).

Data sheets for each of the sensors can be found on the Physical Acoustics website, although a summary is provided below (Table AP4.1) along with suggested used for each sensor, whilst Figure AP4.1 shows the measured sensitivities (i.e. calibration) of each the sensors used during experiments, where available.

Table AP4.1 A comparison of the main features of four piezoelectric transducers (R.45, R3 α , R15 α , and R80 α) by Physical Acoustics.

	R.45	R3 α	R15 α	R80 α
Operating frequency range (kHz)	5 to 30	25 to 70	50 to 400	200 to 1000
Resonant frequency (kHz)	20	29	150	200
Temperature range (c)	-45 to 150	-65 to 175	-65 to 175	-65 to 175
Shock limit (g)	500	500	500	500
Size (mm)	28.6 mm diameter 40.6 mm height	19 mm diameter 22.4 mm height	19 mm diameter 22.4 mm height	19 mm diameter 21.4 mm height
Weight (g)	121	55	34	32
Suggested uses	Monitoring AE activity in very large structures.	Structural health monitoring of small to medium concrete and geological structures and leak detection in buried metal pipeline.	Monitoring common structures such as pipelines, vessels, bridges, storage tanks, etc., as well as factory and process monitoring.	Monitoring high noise environments such as brittle crack detection.

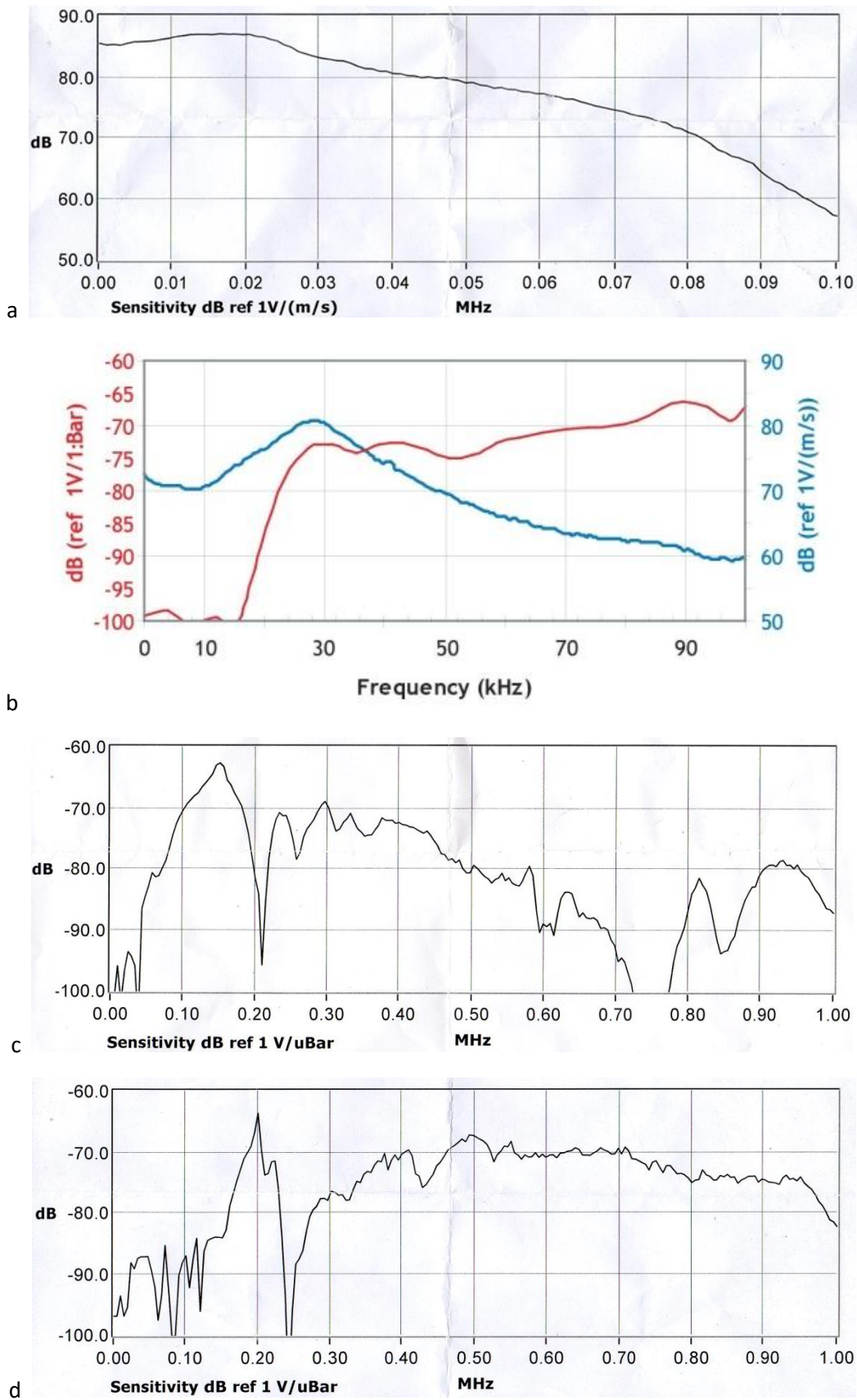


Figure AP4.1 The measured sensitivities of the (a) R.45, (c) R15, and (d) R80 sensors used during laboratory experiments and the (b) suggested sensitivity of the R3 sensor.

AP5.0 Technology Readiness Levels (TRLs)

Technology Readiness Levels (TRLs) form a staged system to estimate the maturity of a technology system with respect to its development. The method was first developed by NASA during the 1970s and is often displayed as a thermometer diagram, e.g. Figure.

The framework system described within this thesis sits within TRL4 with the various component of the system having been tested within laboratory experiments.

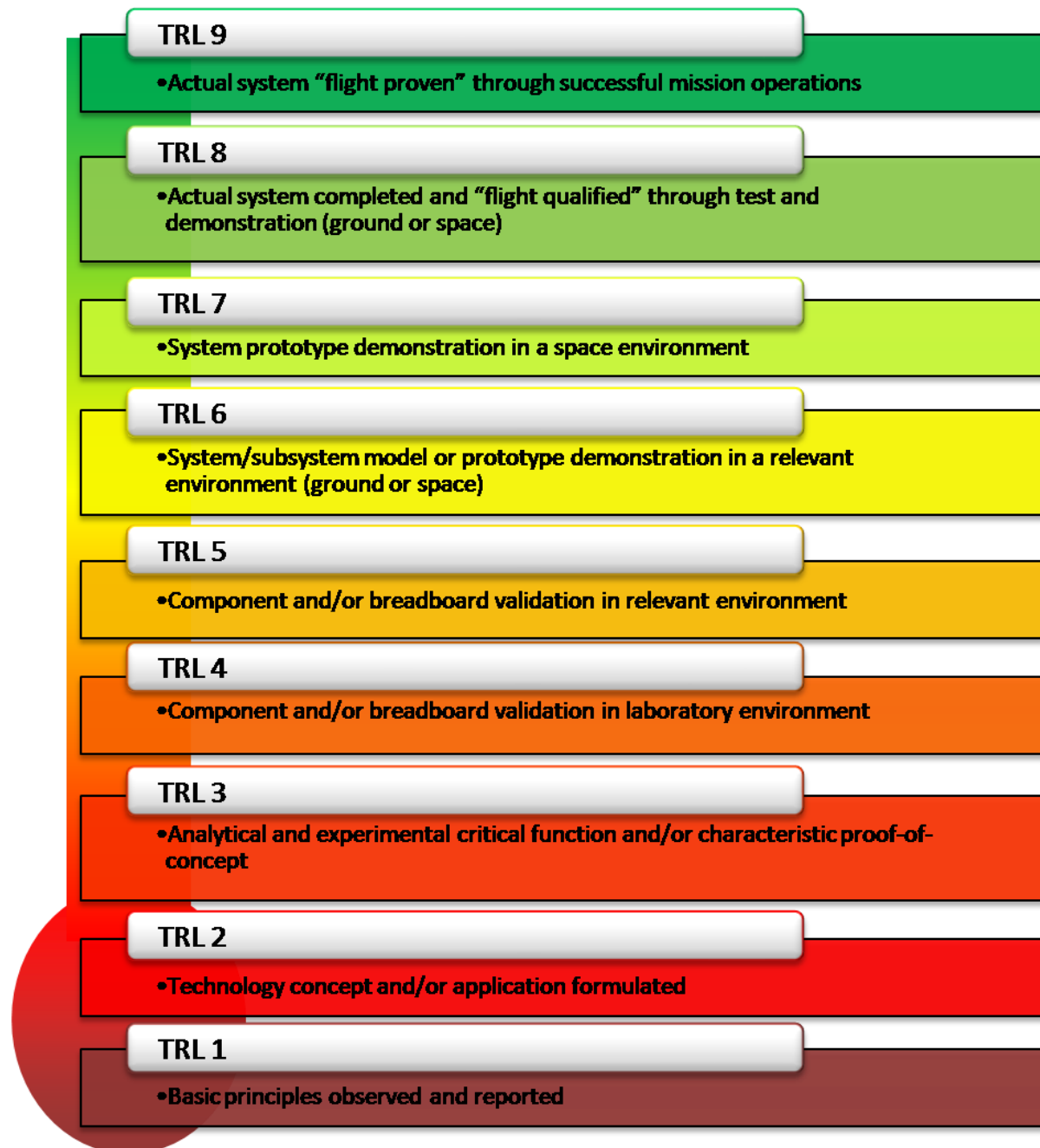


Figure AP5.1 Technology Readiness Levels (TRLs) as described by NASA, 2017.

Glossary

GL1.0 General terminology

Table GL1.0 A glossary of general terminology.

Abb.	Term	Definition
AE	Acoustic emission	An acoustic emission may be defined as elastic sound wave radiation away from a source. ASTM (American Society of Testing Material) (2016) define acoustic emission in E610-77 as "Acoustic Emission (AE)—the class of phenomena whereby transient elastic waves are generated by the rapid release of energy by a localized source or sources within a material, or the transient elastic wave(s) so generated. Acoustic emission is the recommended term for general use. Other terms that have been used in AE literature include (1) stress wave emission; (2) microseismic activity and (3) emission or acoustic emission with other qualifying modifiers."
-	AE count rate	An AE count is defined as 'the number of times the acoustic emission signal amplitude exceeds a present threshold during any selected portion of a test' (ASTM E1316-20, 2000)
Z	Acoustic impedance $z = \rho c$ (per unit area) $z = \rho c S$ (cross sectional)	The acoustic impedance is a measure of the opposition for acoustic flow between two mediums. It is therefore a value describing the efficiency of acoustic transmission using acoustic pressure and flow.
-	Acoustic intensity $I = \frac{1}{2}(\rho c)(A\omega)^2$	Acoustic intensity is the rate at which pressure fluctuations work on a unit area of fluid and is measured with the units Wm^{-2} . It is essentially loudness as is the amount of energy found from the product of particle velocity and sound pressure. Loudness however is measured in decibels.
-	Active waveguide	The active waveguide system was developed by Dixon et al. (2003) (Figure 2.5) for ground deformation using AE. Contrary to its name, the system is a passive monitoring tool that guides acoustic emissions (i.e. sound) passively created by soil particles interacting with a buried steel waveguide during deformation of the soil body.
-	Aliasing $f_{alias} = f_{sample} - (f_{record} - f_{sample}) $	Aliasing is an effect seen in signal analysis where the recording frequency was not high enough to properly record a waveform. Frequencies above the Nyquist (or used sampling rate) fold back and forth from the point of highest recorded frequency and zero, like a string within a box, to cause 'fake' spikes in a signal.
-	Anisotropy	See isotropy
-	Attenuation	Attenuation may be defined as the loss of energy per wave cycle and can be due to many different factors including energy transfer over distance, scattering and adsorption. It can however be specified in several ways including hysteretic damping, per wavelength or unit distance travelled, and Kelvin-Voigt damping where damping is proportional to particle velocity and therefore heavily frequency dependent (Lowe and Pavlakovic, 2013).
-	Bessel functions	Bessel functions are a special function forming a more complex solution to the differential wave equation. There are two common classes of the solution, the first and second. The third is known as a Hankel function.

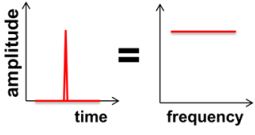
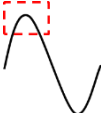
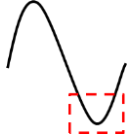
Abb.	Term	Definition
F _{cf}	Coulomb friction	Coulomb friction is the threshold value of frictional force required for a sliding or rotational movement to occur between two or more bodies. In the context of granular AE these are soil particles.
-	Dispersion	A waveform composed of varying harmonic waves of different wavelengths will eventually undergo separation of the different contributing waves due to their different wave speeds (this is assuming angular velocity and wave number are not proportional); this is known as dispersion.
-	Dirac Delta function	The Dirac Delta function is an infinitesimally short duration signal pulse of infinite amplitude in the time domain and representing all frequencies equally, to a value of 1, in the frequency domain. These are important features for signal processing as they allow for all and any changes that occur during signal propagation, whether time or frequency based, to be seen during analysis.
		
-	Extraneous	Of an external origin.
-	Frequency domain	Data within the frequency domain will always have an assigned frequency for each individual datum. Data may therefore be expressed with dependency on frequency.
-	Half-space	Either of the two spaces developed when a Euclidian space is divided by a plane or boundary. Usually there is only a single boundary within a space, thereby creating two half-spaces, with any other boundaries considered to be far away so have no influence.
-	Hertzian Contact Law	The Hertzian contact law describes localised stresses between two curved surfaces that are in contact.
-	Isotropy	Isotropy for an object refers to a property having the same properties or magnitude in different directions. Anisotropy therefore refers to a property being directionally dependent.
-	Kaiser effect	The Kaiser effect may be defined as 'The absence of detectable acoustic emission until previously applied stress levels are exceeded'. (Nordlund and Li, 1990)
LBS	Leighton Buzzard Sand	Leighton Buzzard Sand is the name given to a type of sand material (where sand is defined as having a grain size between 0.06 and 2 mm) found in Leighton Buzzard, UK. It is an industry standard sand.
-	Normal mode	A normal mode is the characteristic pattern of motion for a system when all sinusoidal components are moving with the same frequency and with a fixed phase relation. Lamb waves may often be referred to as normal modes.
PG	Pea Gravel	Pea Gravel is the name given to a rounded form of gravel material (where gravel is defined as having a grain size between 2-4 mm) technically formed from pebbles (>4<20 mm in diameter).
-	Picking	In seismology, picking is the generally accepted method for manually, automatically, or as a combination of both, selecting and reading information for a point of interest. Often, this is the point in time at which the first break of a wave occurs.
μ	Poisson's ratio	Poisson's ratio describes the proportional squashing and lengthening of a material in different directions so as to keep the same volume under compression.

Abb.	Term	Definition
Re	Reynolds number $Re = \frac{\rho VL}{\eta}$	Reynolds number is a dimensionless number based on diameter used to assess the state of flow. Flow may be laminar, transient or, turbulent with values below ~2300 considered laminar, values above ~4000 considered turbulent and, anything in between considered transient.
G	Shear modulus	Shear modulus is also known as the modulus of rigidity and refers to the ability of a material to resist transverse deformations, known as shearing.
s	Slowness $\frac{1}{v}$	Slowness is the inverse of velocity. It is often used in mathematical manipulations in order to keep linearity and make simplify the extraction of solutions.
-	Spectral leakage	Spectral leakage usually occurs as a result of windowing during processing. The leakage appears as aliased frequencies (non-realistic) within the signal as a result of harsh boundaries at window edges. Accuracy is therefore decreased as 'fake' frequencies are shown to exist.
-	Time domain	Data within the time domain will always have an assigned time stamp for each individual datum. Data may therefore be expressed with a dependency on time.
TRL	Technology Readiness Level	Technology Readiness Levels (TRLs) are a concept originally developed by NASA to estimate the maturity of a technology system with respect to its development, from the first ideas to fully working and integrated systems within the world. See Section AP5.0.
η	Viscosity	Viscosity (η) is a measure of a fluids resistance to flow or deformation by shear or tensile stresses and can be denoted in two ways, dynamic (absolute) or kinematic. Dynamic viscosity is a measure of the internal resistance between assumed non-turbulent flow layers within a material; it is written as a force per unit area. Kinematic viscosity however is the ratio of dynamic viscosity to the materials density, therefore removing units of force (Engineering Toolbox).
-	Wave equation	The wave equation is a mathematical expression describing the basic motion of a wave. More complex wave motion can be achieved with the addition of more functions to the base equation. It can be expressed in multiple formats.
-	Wave mode	The wave mode is most easy to understand on a standing wave where the number of nodes, points that are always zero in amplitude, and the sinusoidal movement between them define the mode of the wave. The wave mode is therefore directly related to frequency.
-	Wave packet	A wave packet is a short burst or envelope of localised wave movement/action which can be dispersive. It is essentially a pulse of energy containing multiple frequencies and therefore a travelling localised disturbance.
-	Waveguide	A waveguide is usually a pipe or tube that allows for easy propagation, and consequent confinement, of a wave along its length.
E	Young's modulus	In a solid, Young's modulus is a property of a material describing its elasticity in one dimension only, such as a metal rod being stretched. It describes the ability to withstand such a force. Young's modulus is similar to Bulk modulus; however bulk modulus is three dimensional.

GL2.0 Wave terminology

GL2.1 Wave parameters and properties

Abb.	Term	Definition
ω	Angular frequency $\omega = \frac{2\pi}{T} = 2\pi f$	Angular frequency is the amount of 'angle' a waveform will complete in one second and is measured in radians per second. Angle here refers to the proportion of a sine wave, in full equalling 2π . Frequency and angular frequency are linked by the equation angular frequency (ω) = $2\pi f$, therefore angular frequency is always going to be greater than frequency in arbitrary value. It is useful due to angle, in terms of radians, being a constant everywhere whilst degrees are something we have 'decided' as a unit.
K	Bulk modulus	The bulk modulus is a property of a material describing its elasticity or compressibility; it is therefore how the material responds in shape with a load pressure. Material properties are important to wave propagation.
f_c	Corner frequency Cut-off frequency	See cut-off frequency A cut-off frequency, sometimes known as a corner frequency, is a critical frequency after which wave propagation will no longer occur and/or starts to 'roll off' and dramatically reduce in amplitude. It is the point between the stop band and pass band of a filter.
f	Frequency $f = \frac{1}{T} = \frac{c}{\lambda}$	The number of full wave cycles, usually measured by the number or amplitude peaks or troughs, to travel past a point in a defined in one second is known as frequency and measured in Hertz (Hz); this is the SI unit.
V _{gr}	Group velocity	The speed at which the overall shape of a wave travels is known as the group velocity and is generally made from a combination of different harmonics of varying amplitude, wavelength etc. The group velocity may also be explained as the velocity at which energy is transported and is therefore very important.
$f_{Nyquist}$	Nyquist frequency $f_{Nyquist} \geq 2f$	The Nyquist frequency is the minimal sampling frequency, or rate, that must be used to fully record a waveform. It is equal to twice the highest expected frequency within a signal. In reality frequencies higher than the Nyquist are generally used anyway for insurance.
ϕ	Phase angle $\phi = kx = \frac{2\pi \cdot x}{\lambda}$	The phase angle relates a distance in space to a fraction of a wavelength. It describes the fractional distance of a wave cycle that has elapsed or may be different from another cycle.
V _{ph}	Phase velocity	The phase velocity of a wave is the velocity at which one point of a phase is displaced, or the speed of the wave shape moving.
-	Wave crest	A wave crest, or peak, is the maximum local positive amplitude a singular wave cycle reaches.
-	Wave mode	The wave mode is most easy to understand on a standing wave where the number of nodes, points that are always zero in amplitude, and the sinusoidal movement between them define the mode of the wave. The wave mode is therefore directly related to frequency.
k	Wave number $\kappa = \frac{2\pi}{\lambda}$	The wavenumber is the number of complete wave cycles in a specified distance, often one metre, and usually denoted as 'k'. This is different to angular frequency (see above), which is for a singular point. It is measured in radians per metre.
-	Wave peak	See wave crest (or wave trough)

Abb.	Term	Definition
-	 Wave trough	A wave trough is the maximum local negative amplitude a singular wave cycle has.
-	 Wave cycle	Wave cycle is the term used for one full wave shape, usually measured from peak to peak or trough to trough (a classic cosine wave) or sometimes 0 amplitude returning to 0 amplitude (a classic sine wave consisting of one crest and one trough).

GL2.2 Wave types

Table GL2.2 A glossary of wave types.



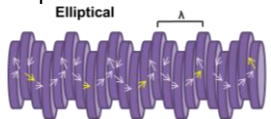
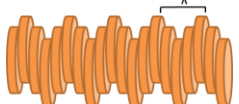
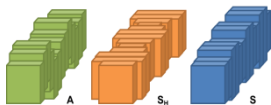
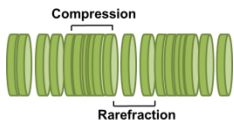

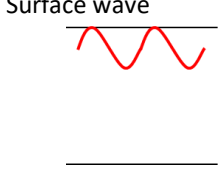
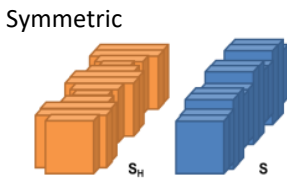
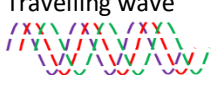
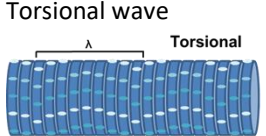

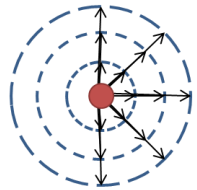
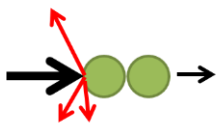
Abb.	Term	Definition
A	Asymmetric 	Asymmetric waves are termed due to their particle motions. See shear waves.
-	Bulk (body) wave 	Bulk, or body, waves travel through the bulk and therefore within a material body rather than at the surface or in plates. Shear and longitudinal waves can be body waves.
-	Elliptical wave 	Elliptical waves have a rotational particle motion with respect to axes perpendicular to the direction of propagation. They are consequently a cross between longitudinal and flexural waves.
-	Flexural wave 	Also sometimes known as secondary or shear waves, flexural waves have particle motions which are left and right (or up and down) with respect to the propagation direction. Shear waves can only travel through solids or materials that have a high enough shear strength.
-	Harmonic wave	A harmonic wave has a steady state and therefore defined wavelength. It is a scaled version of an original, first harmonic wave, for which the scale is an integer multiple.
S, S _H or, A	Lamb wave 	Lamb waves are also known as plate waves and propagate in layers up to only a few wavelengths thickness. This is opposed to surface waves. They may also sometimes be referred to as normal modes. There are three forms of Lamb wave: S, S _H and, A; where S waves have symmetric movements and A waves are asymmetric.
L	Longitudinal wave	Also sometimes known as primary or compressional waves, longitudinal wave have particle motions which are forward and backward with respect to the propagation direction. This creates compressions and

Abb.	Term	Definition
		rarefactions as areas of more and less dense particles are created with propagation.
-	Plane wave	A wave of constant frequency and amplitude with infinitely long wave fronts, a surface of constant phase, which are perpendicular to the direction of travel, is known as a plane wave. Plane waves are a mathematical abstract but may be approximated.
-	Plate wave	See Lamb wave.
-	Rayleigh wave	Rayleigh waves are surface waves that propagate at solid-free boundaries. They have an elliptical, retrograde particle motion.
-	Scholte wave	Scholte waves are surface waves that can form at the boundary of solid-liquid half-spaces. They have retrograde, elliptical particle motions.
-	Standing wave 	Standing waves are non-propagating waves. The wave fluctuates between stationary nodal points of constant amplitude zero.
-	Stationary wave	See standing wave.
-	Stoneley wave	Stoneley waves are surface waves that can form at the boundary of solid-solid half-spaces. They have clockwise, elliptical particle motions.
-	Surface wave 	Surface waves form in materials greater than a few wavelengths thick. They are displacements that decay exponentially with distance from a surface (Achenbach, 1973) and will therefore only ever appear to propagate within a few wavelengths of a surface or boundary. There are three types of surface wave, Rayleigh, Scholte and, Stoneley, their formation dependent on the boundary at which they form.
S	Symmetric 	Symmetric waves are termed due to their particle motions. Similarly to asymmetric waves, their particles move up and down or side to side at a perpendicular to the direction of wave travel. The particle motions are however symmetrical with respect to the direction of travel, somewhat like a compressional wave.
-	Transient wave	A transient wave is a signal pulse that travels in time. This is opposed to a travelling wave which is harmonic and therefore has a steady state.
-	Travelling wave 	A travelling wave is harmonic and therefore has a steady state. Unlike a stationary wave, the peaks and troughs of a travelling wave move in the direction of wave propagation so that there are no nodal points.
-	Torsional wave 	Torsional waves are body waves that propagate with particle motions which rotate back and forth around an axis in the direction of propagation. They produce an effective twisting motion where in cross-section a particle will first rotate clockwise then anti-clockwise.

GL2.3 Wave attenuation

Table GL2.3 A glossary of wave attenuation terms.

Abb.	Term	Definition
-	Absorption 	Absorption is a process of energy transformation where one energy form changes into another. In the case of propagating waves this is usually from the form of kinetic, vibrational energy to that of heat energy. The propagating wave energy is therefore reduced as a result of some of it transforming to heat during particle interactions.
-	Coupling	Coupling occurs between adjacent bodies or layers of media. It is the effective sharing of energy between two or more adjacent bodies and will often present as two or more separate waves.
-	Extrinsic attenuation	Extrinsic refers to an external influence. Extrinsic attenuation therefore refers to attenuation as a result of external influences such as a surrounding medium.
-	Geometric spreading 	Geometric spreading can occur in two or three dimensions; it is not applicable to one dimensional propagation as plate waves may be assumed. Geometric spreading can be described as the spreading out of a wave's energy homogeneously around the edges or across the surface of a circle or sphere respectively. As a circle or sphere grows the energy packages remain the same in total number but become less densely positioned, thus making it appear that in any one direction the energy is reducing with distance.
-	Intrinsic attenuation	Intrinsic is defined as natural or belonging to. Intrinsic attenuation therefore refers to attenuation as a result of the wave propagating material's properties.
-	Scattering 	Scattering occurs when energy is reflected and propagated in a different direction to that of the main propagation. The overall energy in the wave field is therefore maintained however the energy in the direction of propagation is reduced. Energy is not lost or transformed during this process.

GL3.0 Material instability terminology

GL3.1 Landslide movement classifications

Table GL3.1 A Glossary of landslide movement classifications.

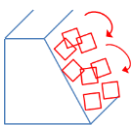
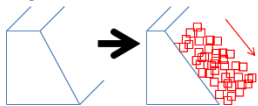
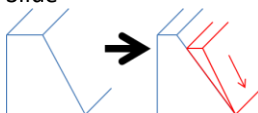
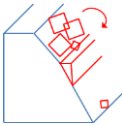

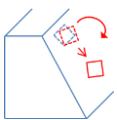
Abb.	Term	Definition
-	Fall 	A fall type motion describes the collective movement of multiple fragments. The term 'fragments' refers to the relatively smaller parts of a larger mass which may individually detach, fall, roll and bounce to collectively create a fall type failure.
-	Flow 	A flow is the collective flow-like motion of multiple fragments to form a mass slide of fragments. A slide however refers to a whole mass movement rather than individual fragment behaviour.
-	Slide 	The sliding or slumping of a whole mass along a plain is known as a slide. A slide type movement describes a mass movement rather than the collective movement of individual fragments. This is a flow.

Abb.	Term	Definition
-	Slope deformation 	Slope deformation encompasses all slope failure mechanisms such as slides and topples but is extremely slow or unmeasurable and although a type of failure can be described better as a partial failure or deformation.
-	Spread 	A spread failure defines the stretching (elongation) or spreading of a mass over a larger than original area is known as a spread failure. For solids this is limited in size and may occur as the sequential toppling of blocks to a different level, as depicted.
-	Topple 	A topple motion consists of the forward rotation of singular or multiple individual fragments.

GL3.2 Soil mechanisms and interactions

GL3.2 A glossary of soil mechanisms and interactions.

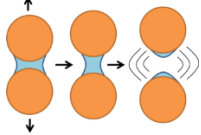
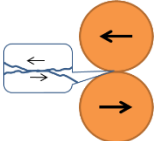
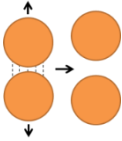
Abb.	Term	Definition
-	Adhesive bonds (solid bridges)	Solid bridges are physical connections between particles. They can be created in a number of different ways including: <ul style="list-style-type: none"> • Sintering (heat and pressure causing solidification without melting) • Chemical reactions • The melting of extremities and outer surfaces of particles can create molten bridges connecting particles which then solidify. • The addition of bonding agents, of an inorganic nature, can create liquid bridges with then solidify forming solid connections between particles. • The crystallisation of dissolved materials can create solid bridge bonds between particles. An example is the crystallisation of salts and minerals forming veins within rock cracks.
-	Apparent cohesion	Apparent cohesion is the extrapolated value of cohesion at zero normal effective stress when a linear failure envelope model is assumed when connecting points of peak stress. It is not a real value but an artefact of the model and hence apparent (Knappett and Craig, 2012).
-	Capillary bridges 	Capillary bridges are liquid connections between particles. There are two forms: free bridges, formed when pore spaces are semi-filled with liquid and, viscous binders formed by non-freely moving liquids and therefore non-constant liquid pressures. Viscous binders are stronger than free liquid bridges as a result of stronger surface tension forces. When void spaces are completely filled with liquid and grains are encapsulated, bridges will not form but there is a certain tensile strength.
-	Closed bonds 	Closed bonds are the interlocking of particles as a result of shape and are therefore associated more with fibrous, flat shaped, and bulky particles.
-	Cohesion	In soils the contribution to shear strength that is independent of particle friction is known as cohesion. It is a resistance force to shear.

Abb.	Term	Definition
-	Electrostatic forces	Oppositely charged particles with have encounter small attractive forces. The amount of charge absorbed by a particle depends on the material from which it is formed and its motion.
-	Intermolecular forces 	Intermolecular forces are dominant at very short-range distances between particles, therefore closely packed particles with have stronger intermolecular forces. The dominant force is known as the Van der Waals force. It is a weak attractive force. Rumpf (1962) estimated Van der Waals forces to be in the order of 1×10^{-20} kg/cm ² and therefore have negligible effect.
-	True cohesion	True cohesion, opposed to apparent cohesion, is the real value of cohesion within a soil at zero normal effective stress (Knappett and Craig, 2012).

GL4.0 Signal processing terminology

GL4.1 Processing and characterisation methods

Table GL4.1 A glossary of signal processing and characterisation methods.

Abb.	Term	Definition
-	Average	An average, also known as the arithmetic mean, is the central value within a discrete set of values. The average is calculated by summing every value within the data set and dividing it by the number of values within the data set and is meant to be representative of the data set.
XSD	Cross spectral density (power spectral density)	The XSD, similarly to the XWT, quantifies the similarity, or coordination of two signals subject to a FT and therefore exposes areas of high common power. It uses cross-correlations to do this.
XWT	Cross wavelet transform	The XWT, similarly to the XSD, quantifies the similarity, or coordination, of two signals subject to a WT and therefore exposes areas of high common power giving phase information (Grinsted et al., 2004).
DTWD	Dynamic time warping distance	The DTW tests works by finding an optimal match between different signals by stretching and compressing their shape through time. Signal segments may then be assigned to fuzzy shape-based clusters with an individual degree of membership dependent on the closeness of matching; segments within the same cluster are therefore comparable. Signals over different time periods and of different lengths are consequently comparable with this method. (Izakian et al., 2015, and Chen et al., 2017)
EDR	Edit distance real-number	The EDR test works out the number of edits (insert, delete, replace) required to transform one signal into another. The less edits, the closer matched the signals are. (Izakian et al., 2015)
EMD	Empirical Mode Decomposition	EMD is a modelling technique based on empirical observations rather than mathematical principles. The method identifies and separates the representative modes in a signal within the Fourier domain. EMD is an adaptable method meaning it must be changed for individual problems. There are therefore many slight method variants. (Huang et al., 1998, and Gilles, 2013)
FFT	Fast Fourier Transform	The FFT decomposes a signal into its constituent sine waves, each of which is representative of a particular frequency. A frequency spectrum relating to the significance of each sine wave within the waveform signal

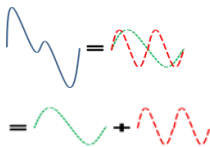
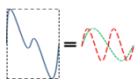
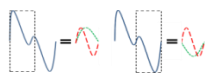
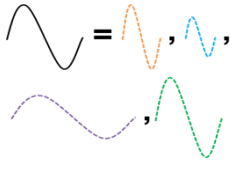
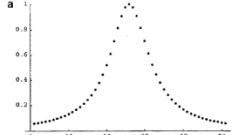
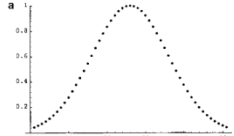
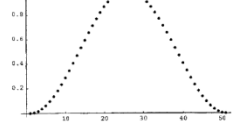
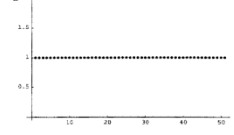
Abb.	Term	Definition
		can then be formed from the results. The FFT method and variations of it (including WFT and GT, see separate sections) are rigid techniques that do not require individual tailoring to a problem.
GT	Gabor Transform	The Gabor transform is a WFT (see WFT) where the window width is defined as a Gaussian function. The window width is therefore constant and of the order of the lowest frequency of the signal, consequently high frequencies are not located well in time (Suzuki et al., 1996).
LCSS	Longest common subsequence	The LCSS test is a measure of the longest signal sequence that can be found within two or more signals. The longer the sequence found, the more closely matched the signals are. (Izakian et al., 2015)
MSC	Magnitude square coherence	The MSC test can be performed in either the Fourier domain or the frequency domain and is a comparison in the similarity of spectra by amplitude. Spectral shapes are compared by creating an auto spectral density and a cross spectral density of the signals, from which a coherence spectrum may be defined to form a quantitative relationship.
-	Maxima	Maxima denote the highest values within a data set. This may be local, i.e. the highest point within a defined section of the data, or represent the highest value within the whole data set.
-	Minima	Minima denote the lowest values within a data set. This may be local, i.e. the lowest point within a defined section of the data, or represent the lowest value within the whole data set.
-	Point trend	Point trends can be used to show the general trend of a dataset by connecting data points at specified intervals. A 10-point trend would, for example, connect every 10 th data point within a data set.
-	Regression analysis	Regression analysis is a tool formed from statistical processes to determine a relationship(s) between multiple parameters, where one parameter is dependent on the other(s). regression analysis may include linear or non-linear regression. These can be achieved through various mathematical processes, an example being the least squares method.
-	Scalogram	A scalogram is similar to a spectrogram but instead defined for wavelet decomposition. It is the squared modulus of a continuous wavelet transform. Resolution is dependent on frequency.
-	Spectrogram	A spectrogram represents the spectral energy density of a defined local window in sine wave decomposition like from the squared modulus of a WFT. Time and frequency shifts are preserved by a spectrogram thus meaning there is a time frequency covariance.
WFT	Windowed Fourier Transform  	The WFT works in the same way as a FFT (see FFT) but only decomposes a selected time period, or window, of a signal into its constituent sine waves. To analyse the whole waveform several WFT's can be conducted by moving the window along. This gives time-frequency information, the resolution of which is dependent on the size of the window.
WTC	Wavelet coherence	The WTC test is used on data for which the WT has been applied. Similarly to the MSC, it compares spectral shapes to reveal phase information. It may therefore be thought of as a local coherence test

Abb.	Term	Definition
WT	Wavelet Transform 	<p>between two or more wavelet transforms in time-frequency space, although is less localised (temporally and spatially) than other methods. The WTC should not be confused with the cross wavelet transform (XWT) which shows areas of high common power. (Grinsted et al., 2004, and Chen et al., 2017)</p> <p>The WT decomposes a signal into its constituent wavelets (rather than sine waves as in the FFT). The wavelets are defined with a shape which may be scaled and transformed to fit different parts of an overall waveform. A spectrogram of scale and time can be formed to show where fits are achieved relating. The spectrogram does not provide a direct time-frequency relationship as is scaled; the relationship can be related afterwards via the scale. The WT is a rigid method that does not require individual tailoring to a problem.</p>

GL4.2 WFT window classifications

Table GL4.2 A glossary of WFT window classifications.

Abb.	Term	Definition
-	Cauchy window 	The Cauchy window used in WFTs has a narrow shape and does not touch zero at the extremities. It is consequently restricting but good at removing any spectral leakage.
-	Gabor / Gaussian window 	The Gabor window uses a Gaussian function to define the window width for WFTs. The function used is usually in the order of the lowest frequency found within a signal and therefore provides poor resolution at higher frequencies. It does not quite touch zero at the edges.
-	Hann (Hanning) window 	The Hann or Hanning window has been described as perfectly adequate for 95% of signal processing (National Instruments, 2020). It is a special case of cosine where $a=2$ and touches zero at the edges. This is opposed to, and must not be confused with, the Hamming window which has a very similar shape but does not touch zero at the extremities.
-	Rectangular window 	This is the simplest of window shapes used for WFTs. Everything within the shape is given a magnitude of 1 whilst everything outside has a magnitude 0. Spectral seepage can therefore be a problem and create aliasing, especially at <50% the Nyquist frequency.

GL5.0 AE measurement systems

Table GL5.0 A glossary of AE measurement systems.

Abb.	Term	Definition
-	Accelerometer	Accelerometers measure acceleration forces, or changes in velocity. They are an electromechanical device which can measure changes in

Abb.	Term	Definition
		other variables such as capacitance or stress which is then expressed as a proportional electronic signal.
ERT	Electrical Resistivity Tomography	ERT is a geophysical technique in which the resistivity of the sub-surface is measured and plotted as a scalar image to distinguish sub-surface features. Sub-surface resistivity is measured using an array of spaced probes through which a current is then passed and measured.
-	Extensometer	Extensometers measure changes in the length of an object, or specimen elongation. There are many different forms of the instrument which can be contact or non-contact. Contact instrumentation will physically measure lengths whilst non-contact instrumentation works by tracking the distances between chosen markers.
-	Fibre optics	Fibre optics can be used to accurately measure small deformations and strains with high resolution. The system is formed from fibre optic cables through which light of different wavelength are passed and are attached to an interrogator. Changes in the light path effect the measured travel times, reflections and therefore phase of the light within. From this, deformation and strain may therefore be interpreted.
GPR	Ground penetrating radar	GPR is a geophysical method that uses radar to distinguish subsurface features. Dependent on the feature of interest, different frequency pulses are sent into the ground, reflected back, and measured by the instrument at the surface. Post-processing then allows for sub-surface features to be identified.
-	Inclinometer	An inclinometer is an instrument that measures angles of slopes. It consists of two components, the casing and measurement system. Inclinometers casings are often used in boreholes and provide a uniform and guided path with which the measurement system can be lowered to measure. As a slope deforms the borehole and casing will also deform therefore measured angles will change.
InSAR	Interferometric synthetic-aperture radar	InSAR is a form of remote sensing technique that uses and compares radar images of the Earth's surface to measure surface deformations. This is done by comparing the phase of waves returning to a satellite or aircraft, from which a map of changes may be created and interpreted with very high resolution.
LIDAR	Light imaging detecting and ranging	LIDAR is a form of remote sensing technique that uses laser lights to measure changes in distance as a function of return time and wavelengths. From these differences, a high-resolution map of a surface can be formed and compared with past and future surveys.
NDT	Non-Destructive Testing	Non-Destructive Testing a non-intrusive method, comprising of several methods, to investigate and evaluate the structural health and/or the material properties of a system of system component without causing damages.
-	Piezometer	A piezometer is an instrument that measures the presence of a liquid or gas. They are often installed in boreholes to measure changing ground water conditions.
-	Remote sensing	Remote sensing is a measurement technique where the acquisition of data is performed without physical contact and often from distance. Generally, remote sensing refers to the monitoring techniques of LIDAR and InSAR which use satellite or air-borne monitoring methods.
-	Seismometer	A seismometer measures seismic movements and ground motions using moments. They are usually combined with some form of timing and

Abb.	Term	Definition
-	Slope ALARMS	<p>recording device and will produces a seismograph depicting ground motions. Seismographs may be physical or electronic.</p> <p>Slope ALARM systems measure AE caused by interactions with a buried steel waveguide. The systems comprise of a piezoelectric transducer affixed to a steel waveguide, from which signals are measured, amplified, filtered, digitalised and stored or sent wirelessly to further storage for processing and analysis. The measured AE can be used to determine the health and stress conditions of the structural system.</p>
-	Strain gauge	<p>Strain gauges measure the strain type forces (pressure, tension, weight, etc.) on an object. They work by converting the forces into a proportional electrical resistance which can be measured and analysed.</p>
-	Tiltmeter	<p>A tiltmeter is a form of inclinometer with which small changes in the vertical level are measured. Tiltmeters can measure dynamically (continuously) whereas inclinometers tend to be static. The instruments may be mechanical or electrical.</p>